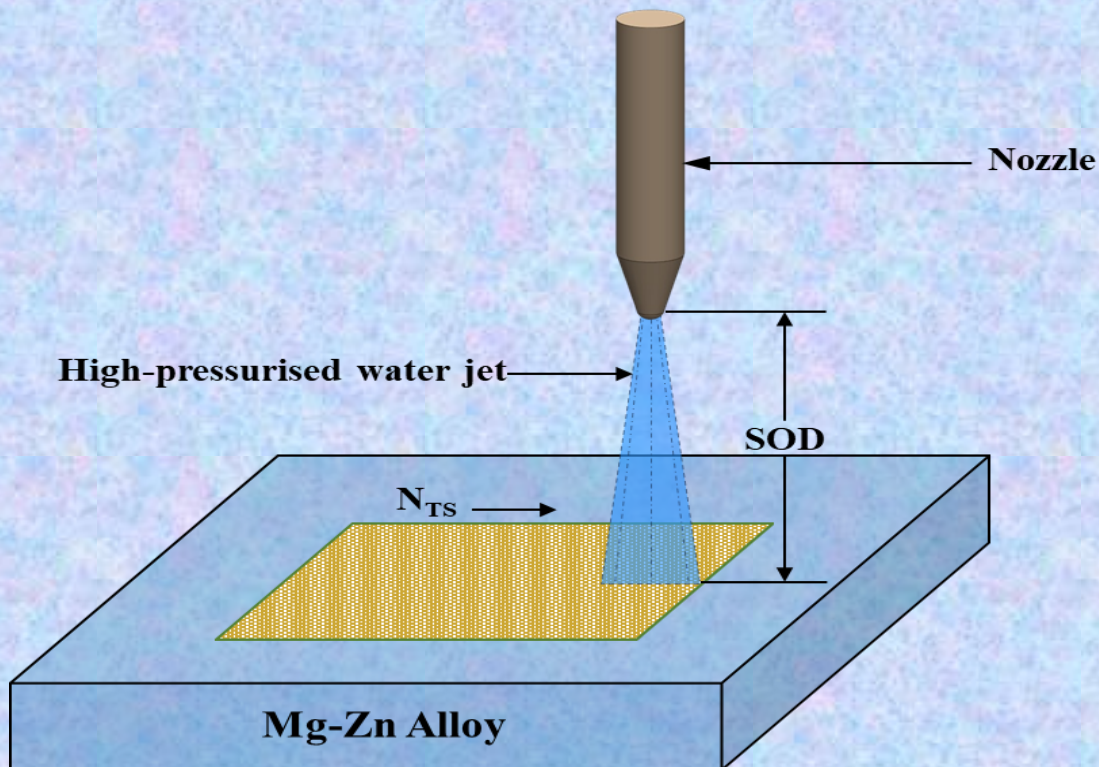


ISBN : 978-81-957455-5-5

**PROCESSING OF ADVANCED MATERIALS
and
FABRICATION OF PRODUCTS - XXX**



Editors

Ajay Kumar • T. S. Srivatsan



PROCESSING OF ADVANCED MATERIALS
And
FABRICATION OF PRODUCTS - XXX
Ajay Kumar
T.S. Srivatsan

Published & Printed by:
TANEJA SALES CORPORATION
Registered Office:
20, Satnam Park, Krishna Nagar, Delhi - 110051
Ph. : 9312231302
Email : tanejasalescorp@gmail.com
www.tanejasalescorp.in

First Published 2024

ISBN : 978-81-957455-5-5

All rights reserved. No part of this publication may be reproduced, stored in a retrieval system or transmitted, in any form or by any means, mechanical, photocopying, recording or otherwise, without prior written permission of the author or publisher.

PREFACE

This bound volume contains the papers presented at the **Thirtieth International Conference on Processing of Advanced Materials and Fabrication of Products [PAMFP – XXX]** held at the **Indian Institute of Technology Hyderabad [IIT Hyderabad Campus]**, Hyderabad, Andhra Pradesh, **INDIA, 11 - 13 December 2024**. The International Association for Processing of Materials and Fabrication of Products [IA PMFP] and IIT Hyderabad [Hyderabad, Andhra Pradesh, INDIA] were prime sponsors of this scholarly technical event, i.e., conference, spread over three days. It is the thirtieth in a series of conferences on Processing of Advanced Materials, bringing together engineers, technologists, and researchers from industry, universities and national/government laboratories, working on aspects and intricacies related, relevant and applicable to the processing, fabrication, characterization and evaluation of

- (a) Materials spanning biomaterials, composites [to include metal-matrix composites, ceramic-matrix composites, and polymer-matrix composites], fuel cell materials, functionally-graded materials, high-energy materials, intermetallic(s), magnetic materials, foam materials, nanomaterials and nanocomposites, phase-change materials, porous materials and super-conducting materials, and
- (b) Many marvels of manufacturing to include Additive manufacturing, Green manufacturing, Sustainable manufacturing, Artificial Intelligence (AI) and Machine Learning (ML), and MEMS/NEMS, for potential use on a spectrum of products spanning the domains of both performance-critical and non-performance critical.

Researchers were encouraged to present and discuss their findings, observations, inferences and potentially viable applications or outcomes resulting from their study.

The earlier conferences on Processing and Fabrication of Advanced Materials were held as follows:

- (1) The ***first*** conference was held in Cincinnati (USA) in **1991**
- (2) The ***second*** was held in Chicago (USA) in **1992**
- (3) The ***third*** was in Pittsburgh (USA) in **1993**
- (4) The ***fourth*** in Cleveland (USA) in **1995**
- (5) The ***fifth*** in Cincinnati (USA) in **1996**

- (6) The *sixth* in Singapore (Singapore) in **1997**
- (7) The *seventh* in Rosemont, Illinois (USA) in **1998**
- (8) The *eighth* in Singapore (Singapore) in **1999**
- (9) The *ninth* in St. Louis (USA) in **2000**
- (10) The *tenth* in Indianapolis (USA) in **2001**
- (11) The *eleventh* in Columbus (USA) in **2002**
- (12) The *twelfth* in Pittsburgh (USA) in **2003**
- (13) The *thirteenth* in Singapore (Singapore) in **2004**
- (14) The *fourteenth* in Pittsburgh (USA) in **2005**
- (15) The *fifteenth* in Cincinnati (USA) in **2006**
- (16) The *sixteenth* in Singapore (Singapore) in **2007**
- (17) The *seventeenth* in New Delhi (India) in **2008**
- (18) The *eighteenth* in Sendai (Japan) in **2009**
- (19) The *nineteenth* in Auckland (New Zealand) in **2010**
- (20) The *twentieth* in Hong Kong City (Hong Kong) in **2011**
- (21) The *twenty first* in Guwahati (India) in **2012**
- (22) The *twenty second* was in Singapore (Singapore) in **2013**
- (23) The *twenty third* was held in Roorkee (India) in **2014**
- (24) The *twenty fourth* was held in Kansai (Japan) in **2015**
- (25) The *twenty fifth* was held in Auckland (New Zealand) in **2017**
- (26) The *twenty sixth* was held in Jeonju (S. Korea) in **2017**
- (27) The *twenty seventh* was held in Jonkoping (Sweden) in **2019**.
- (28) The *twenty eighth* was held in Chennai (India) in **2020**
- (29) The *twenty ninth* was held in Tirupati (India) in **2024**.

This conference is a collection of papers provided by students, practicing engineers, technologists, researcher scientists and academicians from a few countries. The abstracts, to include plenary, invited and contributed papers that were accepted for oral presentation at the **three-day scholarly technical event** were divided into sessions. A total of PQ papers accepted and received in time have been chosen for inclusion in the bound volume. The technical papers neatly compiled and assembled in the bound volume cover a broad spectrum of topics that assuredly represent the very diverse nature of the field of materials, products and applications.

We, the conference organizers from both the International Association for Processing of Materials and Fabrication of Products [IA PMFP] and the Indian Institute of Technology, Hyderabad [IIT H], extend our warmest thanks and appreciation to all of the ‘concerned’ individuals for their inspired interest, energetic enthusiasm and sustained willingness to both participate and contribute.

As conference co-organizers, we also extend our heartfelt thanks and gratitude to the following:

- (a) Professor **Dr. B. S. Murthy** [Director IIT Hyderabad] for his “valued” understanding and enthusiastic willingness in allowing IIT H to be the “dedicated” co-sponsor and “dependable” host of this scholarly technical event being held within the intellectual confines of the “glowing” pastures of IIT Hyderabad.
- (b) Professor **Mohan Sangeneni** for his energetic and enthusiastic willingness to step-in and provide the needful guidance, suggestions, recommendations and even observations with specific reference to extending an invitation to “key” individuals at appropriate locations for the purpose of their contribution both by way of participation and physical presence at the technical event (conference). He was also generous in providing the needful motivation, encouragement and words of wisdom, based on personal experience(s), in putting forth the appropriate workshops that were held immediately prior to this scholarly technical event or conference.
- (c) A strong dose of gratitude, appreciation, admiration and applause is generously extended to the Conveners: (i) Professor **Saswata Bhattacharya** (IIT Hyderabad), (ii) Professor **Pinaki P. Bhattacharjee** (IIT Hyderabad), (iii) Professor **Kishalay Mitra** (IIT Hyderabad), (iv) Professor **Rajesh Korla** (IIT Hyderabad), (v) Professor **Gopinath Muvvala** (IIT Hyderabad), and (vi) **Dr. Nagendra Pratap Singh** (MSRUAS, Bangalore) for their energetic and enthusiastic willingness to step in and extend “valued” help and support on a few key intricacies specific to conduct of this international scholarly technical event or conference.
- (d) The two organizing secretaries, (i) Professor **Ashok Kamaraj** (IIT Hyderabad), and (ii) Dr. **Govind Narayan Sahu** (IIT Tirupati and IA-PMFP), for diligently executing the tasks periodically assigned to them for the purpose of ensuring smooth conduct of all intricacies specific to this conference.
- (e) The **Students, Research Scholars** and **Technical Staff** in the Department of Materials Science and Metallurgical Engineering (MSME) at IIT Hyderabad.
- (f) The Professional Conference Managing unit **Connexions Orbis Pvt Ltd.** [New Delhi, India], has been a source of immense strength and inspiration by being very understanding,

supportive and patient through the entire process initiating from the moment of conception of this scholarly technical event to be held within the confines of an academic institution devoted to nurturing, fostering and promoting excellence in higher education to enable in both enlightenment and enrichment to completion culminating in compilation and presentation of impressive bound volume(s) as a “valued” outcome of this intellectual scholarly endeavor. We, the conference organizers, extend abundance of thanks, “valued” appreciation and boundless gratitude to Mr. Niranjana Kumar (*Managing Member*) and Mr. Hemant Tripathi (*Managing Member*) of **Connexions Orbis Pvt. Ltd.**, for their sustained interest, involvement, meticulous attention to the specifics essential for orderly execution of all intricacies specific to systematic and methodical execution of all the desired essentials pertaining to this scholarly technical event while concurrently ensuring timely completion and presentation of the bound volume. Their diligent, dedicated and dynamic execution of all required intricacies did certainly help in ensuring successful completion of the specifics pertaining to the bound volume(s).

- (g) Extra special thanks of recurring order is also extended to the publishers **Taneja Sales Corporation** (Delhi 110006, India) (Managing Director: Mr. Amit Taneja) and all involved and contributing staff for their diligent and dedicated efforts in ensuring timely publication and release of this impressive bound volume having archival value.

As editors of this bound volume we anticipate that it would be of immense value and use to the following:

- (a) *Graduate students* in Materials Engineering, Metallurgical Engineering, Manufacturing, Mechanical Engineering and Industrial Engineering.
- (b) *Practicing engineers and Researchers*, and
- (c) *Scientists and Scholars*.

This bound volume also offers potentially viable avenues for new perspectives and directions in the domain enveloping science and engineering of (i) Existing materials, (ii) Advanced materials, (iii) Emerging materials, and (iv) Sustainable materials and all related, relevant and applicable manufacturing processes to include (i) Additive manufacturing, (ii) “Green manufacturing”, (iii) Smart manufacturing, and (iv) Manufacturing techniques for advanced materials specific to information technology applications.

CHAIR

Dr. T. S. Srivatsan, PhD., F AAAS, FASM, FASME, F IAAM

Professor (Emeritus)

Department of Mechanical Engineering

The University of AKRON

Akron, OHIO 44325-3903, **USA**

E-Mail: tsrivatsan@uakron.edu

Phone: +1-330-608-8355



CONVENORS

Professor **Saswata Bhattacharya**, PhD
Department of Materials Science & Metallurgical Engineering
Indian Institute of Technology (IIT) Hyderabad
Kandi 502284, Sangareddy
Telangana, **INDIA**
E-Mail: saswata@msme.iith.ac.in

Professor **Pinaki Prasad Bhattacharjee**, PhD
Department of Materials Science & Metallurgical Engineering
Indian Institute of Technology (IIT) Hyderabad
Kandi 502284, Sangareddy
Telangana, **INDIA**
E-Mail: pinakib@iith.ac.in

Professor **Kishalay Mitra**, PhD
Department of Chemical Engineering
Indian Institute of Technology (IIT) Hyderabad
Kandi 502284, Sangareddy
Telangana, **INDIA**
E-Mail: kishalay@che.iith.ac.in



Dr. Ajay Kumar, PhD
Assistant Professor
Department of Mechanical Engineering
Indian Institute of Technology (IIT) Tirupati
Tirupati - 517619, Dist. – Tirupati
Andhra Pradesh, **INDIA**.
E-Mail: drajaykumarp@iittp.ac.in



CO-CONVENORS

Professor Rajesh Korla, PhD

Department of Materials Science & Metallurgical Engineering

Indian Institute of Technology (IIT) Hyderabad

Kandi 502284, Sangareddy

Telangana, INDIA

E-Mail: rajeshk@msme.iith.ac.in

Professor Gopinath Muvvala, PhD

Department of Mechanical & Aerospace Engineering

Indian Institute of Technology (IIT) Hyderabad

Kandi 502284, Sangareddy

Telangana, INDIA

E-Mail: mgopinath@mae.iith.ac.in



Dr. Nagendra Pratap Singh, PhD

Associate-Dean Research

M. S. Ramaiah University of Applied Science

[MSRUAS]

Bangalore, Karnataka, INDIA

&

IA-PMFP

E-Mail: nagendra.singh4565@gmail.com;
director.tce@msruas.ac.in



ORGANIZING SECRETARY

Professor Ashok Kamaraj
Department of Materials Science & Metallurgical Engineering
Indian Institute of Technology (IIT) Hyderabad
Kandi 502284, Sangareddy
Telangana, INDIA
E-Mail: ashokk@msme.iith.ac.in

:



Dr. Govind Narayan Sahu
Department of Mechanical Engineering
Indian Institute of Technology (IIT) Tirupati
Tirupati - 517619, Dist. – Tirupati
Andhra Pradesh, INDIA.

&

IA PMFP
E-Mail: govinds@iittp.ac.in



ORGANIZING COMMITTEE

No.	Member	Affiliation	Country
1.	Prof. Saswata Bhattacharya	IIT Hyderabad	India
2.	Prof. Pinaki Prasad Bhattacharjee	IIT Hyderabad	India
3.	Prof. Kishalay Mitra	IIT Hyderabad	India
4.	Dr. Ajay Kumar	IIT Tirupati & IA-PMFP	India
5.	Prof. Rajesh Korla	IIT Hyderabad	India
6.	Prof. Gopinath Muvvala	IIT Hyderabad	India
7.	Dr. Nagendra Pratap Singh	MSRUAS & IA-PMFP	India
8.	Prof. Ashok Kamaraj	IIT Hyderabad	India
9.	Dr. Govind Narayan Sahu	IIT Tirupati & IA-PMFP	India
10.	Prof. S. Mohan	IIT Hyderabad	India
11.	Prof. B. Vaidhyanathan	Loughborough University & IA-PMFP	UK
12.	Dr. Shankar Venugopal	Mahindra & Mahindra & IA-PMFP	India
13.	Dr. Arcot A Somashekar	University of Auckland New Zealand & IA-PMFP	
14.	Prof. V.V. Rao	IIT Tirupati & IA-PMFP	India

INTERNATIONAL ADVISORY COMMITTEE

No.	Member	Affiliation Country
1.	Prof. Ramamoorthy Ramesh	Rice University USA
2.	Dr. Anil K. Sachdev	General Motors Company USA
3.	Prof. Andre Katterfeld	Otto-von-Guericke Univ. Germany
4.	Prof. Dr.-Ing. habil. Thorsten Halle	Otto-von-Guericke Univ. Germany
5.	Prof. Eric MacDonald	University of Texas USA
6.	Prof. Raman Singh	Monash University Australia
7.	Prof. Surya Kalidindi	Georgia Institute of Technology, USA
8.	Prof. S. Mohan	IIT Hyderabad India/USA
9.	Prof. Nikhil Gupta	NYU USA

NATIONAL ADVISORY COMMITTEE

No.	Name	Affiliation Location
1.	Prof. B. S. Murty	IIT Hyderabad Hyderabad
2.	Prof. Gandham Phanikumar	IIT Madras Chennai
3.	Prof. Satish V. Kailas	IISc Bangalore Bangalore
4.	Prof. Satyam Suwas	IISc Bangalore Bangalore
5.	Dr. Vikas Kumar	DRDO Hyderabad

ABOUT EDITORS of the BOUND VOLUME



Dr. Ajay Kumar is the *Assistant Professor* in the Department of Mechanical Engineering, **Indian Institute of Technology (IIT) Tirupati** India. Prior to joining IIT Tirupati, he was (i) a postdoctoral fellow at Washington State University (WSU) Pullman, USA, and (ii) University of Wisconsin Milwaukee (UWM) USA.

He obtained his

- (a) B.E. (Mechanical) from Madhav Institute of Technology and Science (MITS) [Gwalior (Madhya Pradesh) India],
- (b) M.Tech. (Materials Engineering) from Maulana Azad National Institute of Technology (MANIT) [Bhopal (Madhya Pradesh) India], and
- (c) Ph.D. from the Indian Institute of Science (IISc) [Bengaluru India].

His major areas of research interests include Advanced Metal Casting, Metal Forming, Tribology and Surface Engineering and Advanced Materials Characterization.

- He is focusing at constructing a quantitative and predictive understanding of the phenomena underlying the materials development for industrial applications by employing a variety of experimental and computational tools to establish process-structure-property relationships in materials.
- He has published 4 patents, more than 30 papers in respected international journals, and 9 book chapters.

- Dr. Ajay Kumar received the Tribology Society of India Best Paper Award (Academic Research) in National Tribology Conference 2014.
- He is fellow member of Centre for Education Growth and Research (CEGR).
- He has received 'CHANDRAN MENON MEMORIAL AWARD'—for Applied Research and Innovative Technology for 2022–23.



Dr. T.S. Srivatsan, is **Professor (Emeritus)** in the Department of Mechanical Engineering at **The University of Akron** (Akron, Ohio, USA). He received his **Bachelor of Engineering** degree in Mechanical Engineering (**B.E.**, 1980) from **Bangalore University** (Bangalore, India) and graduate degrees [**Master of Science** in Aerospace Engineering (**M.S.** 1981) and **Doctor of Philosophy** in Mechanical Engineering (**Ph.D.** 1984) from **Georgia Institute of Technology** (Atlanta, Georgia, USA). **Dr. Srivatsan** joined as the faculty in The Department of Mechanical Engineering at The University of Akron in August 1987. Since joining, he has instructed undergraduate and graduate courses in the areas of: (i) Advanced Materials and Manufacturing Processes, (ii) Mechanical Behavior of Materials, (iii) Fatigue of Engineering Materials and Structures, (iv) Fracture Mechanics, (v) Introduction to Materials Science and Engineering, (vi) Mechanical Measurements, (vii) Design of Mechanical Systems, and (viii) Mechanical Engineering Laboratory. His research areas currently span the following areas: (a) Fatigue and Fracture behavior of advanced materials to include monolithic(s), intermetallic, Nano-materials and metal-matrix composites; (b) Processing techniques for advanced materials and nanostructure materials; (c) Inter-relationship between processing and mechanical behavior; (d) Electron Microscopy; (e) Failure Analysis; and (f) Mechanical Design. A synergism of his efforts has helped in measurable ways to advance the science, engineering and technological applications of materials in a wide variety of products spanning both performance-critical and non-performance-critical.

Dr. T. S. Srivatsan has authored/edited/co-edited **SEVENTY [70] books** and **SIX [5] monographs** in areas cross-pollinating mechanical design; processing and fabrication of advanced materials; deformation, fatigue and fracture of ordered intermetallic materials; machining of composites; failure analysis; technology of rapid solidification processing of materials; manufacturing techniques for engineering and engineered materials; and High Entropy Alloys: Innovations, Advances and Applications. He serves as **co-editor** of *International Journal on Materials and Manufacturing Processes* and on the **editorial advisory board** of five other journals in the domain of *Materials Science and Engineering*. His research has enabled him to deliver over two-hundred and forty-plus (**275+**) technical presentations in national and

international meetings and symposia; technical/professional societies; and research and educational institutions. He has also authored and/or co-authored over eight-hundred plus (**800+**) archival publications in international journals (**415**), chapters in books (**15**), proceedings of national and international conferences (**280**), reviews of books (**79**), and technical reports (**76**). As on October 2024 his citation index” H” is **58**, “i10 index” is **211** and well over **12200 google scholar citations AND a Research Interest Score of 4564 [to be ranked within the top 2 percent of researchers spread throughout the world]**. Besides, he has personally mentored, supervised and successfully graduated over **75** students at the graduate degree level {Master of Science (MS) + Doctor of Philosophy (PhD) + Post-Doctoral Research Scholars}, and advised, inspired. mentored and supervised over **900+** students at the undergraduate level.

In recognition of his efforts, contributions and its impact on furthering science, technology and education **Dr. T. S. Srivatsan** has been elected as: (a) **FELLOW of ASM International**, (b) **FELLOW of American Society of Mechanical Engineers (ASME International)**; (c) **FELLOW of American Association for the Advancement of Science (AAAS)**, (d) **IAAM Scientist Award** (2023), *International Association of Advanced Materials* [IAAM (Ulrika, Sweden)], (e) **IAAM Scientist Award** (2024), *International Association of Advanced Materials* [IAAM (Ulrika, Sweden)], and (f) **FELLOW of International Association for Advanced Materials** [IAAM (Ulrika, Sweden)].

Dr T. S. Srivatsan has also been recognized as:

- (a) ***Outstanding Young Alumnus*** of Georgia Institute of Technology (Atlanta, Georgia, USA),
- (b) ***Outstanding Research Faculty***, The University of Akron (Akron, Ohio, USA).
- (c) ***Outstanding Research Faculty***, the College of Engineering at The University of Akron (Akron, Ohio, USA), and
- (d) **Alexander M. Scott *Distinguished Service Award*** of The Minerals, Metals and Materials Society [TMS] (Pittsburgh, PA, USA).

Also, **Dr. T. S. Srivatsan** has the distinct honor of being chosen, in recent years, for inclusion in the following:

- ♠ Elected to *WHO's WHO in AMERICAN EDUCATION: 7th edition* 2005-2006
- ♠ Elected to *WHO's WHO in the MIDWEST* 1992-2004
- ♠ Elected to *WHO's WHO in TECHNOLOGY* 1994-2004
- ♠ Elected to *WHO's WHO in the WORLD: 23rd edition* 2005-2006
- ♠ Elected to *WHO's WHO in AMERICA: 59th edition* 2005

- ♠ Elected to *WHO's WHO in SCIENCE and ENGINEERING: 8th edition*
2005
- ♠ *WHO's WHO among AMERICA's TEACHERS: 7th edition*
2005 - 2006
- ♠ *WHO's WHO among Executives and Professionals: Cambridge*
2007
- ♠ Leader and Professional "Honors Edition"
Princeton Premier Registry
2007 - 2008
- ♠ *WHO's WHO among Executives and Professionals: Cambridge*
2009 - 2010
- ♠ Elected to *WHO's WHO in AMERICA: 63rd edition (Marquis)*
2010 - 2011
- ♠ *WHO's WHO among Executives and Professionals: Cambridge*
2011 - 2012
- ♠ *WHO's WHO among Executives and Professionals: Cambridge*
2015 - 2016
- ♠ Leader and Professional "Honors Edition"
Princeton Premier Registry
2007 - 2008
- ♠ Elected to *WHO's WHO in AMERICA: 66th edition (Marquis)*
2016 - 2018
- ♠ Albert Nelson MARQUIS LIFETIME ACHIEVEMENT AWARD
2018
- ♠ Elected to *WHO's WHO in WORLD (Marquis)*
2018 - 2019
- ♠ Elected to *WHO's WHO in WORLD (Marquis)*
2020 - 2021
- ♠ Elected to *WHO's WHO in Education (Marquis)*
2020
- ♠ Elected to *WHO's WHO in AMERICA: 70th edition (Marquis)*
2021 - 2022
- ♠ Elected to *WHO's WHO in Marquis Industry Leaders (Marquis Publications)*
2021
- ♠ Elected to *WHO's WHO in Top Professionals [Top Educator] (Marquis Publications)*
2022

Over the years, **Dr. T. S. Srivatsan** has offered and/or extended his knowledge and expertise in research services to the following: (i) U.S. Government [U.S. Air Force and U.S. Navy], (ii) National Research Laboratories, and (iii) Industries related to aerospace, automotive, power-generation, leisure-related products, and applied medical sciences.

**Messages
for the
30th PAMFP 2024
Conference**



Dr. Sanjay Kumar Jha
CMD, Mishra Dhatu Nigam (MIDHANI)
Hyderabad India

It is heartening to know that the 30th International Conference on Processing of Advanced Materials and Fabrication of Products, 2024 is being organized at IIT Hyderabad from 11th to 13th December, 2024. The conference is organized to bring together scientists, technologists, researchers, engineers, industry leaders for exploring the new vistas with respect to recent advances, emerging trends in spectrum of products spanning both performance-critical and non-performance critical.

The underlying theme of this conference i.e., ‘Design and Manufacturing of Sustainable Materials, Process and Products’ and ‘Sustainable Metallurgy and Energy-Efficient Materials for Transition & Decarbonization in Metal Manufacturing Sectors’ is the need of the hour and occupies a significant role in achieving the Hon’ble Prime Minister’s vision of “Viksit Bharat-2047”.

To achieve the “Viksit Bharat” vision, it is absolutely important to integrate ‘innovation’ and ‘sustainability’ in the field of design and manufacturing of advanced materials to minimize the environmental impact. The significance of sustainability and environmental stewardship is expected to grow in the realms of manufacturing and design in future and are likely to influence the main priorities for advancing manufacturing operations and technologies.

Recognizing this importance, I am glad to know that IIT-Hyderabad has been playing a very significant role in this direction and taken up the initiative. May this conference foster

new collaborations and improve understanding of sustainability in manufacturing and design, and to enhance applications of AI/ML for process optimization.

Warm Regards,

Dr. Sanjay Kumar Jha
CMD,
Mishra Dhatu Nigam (MIDHANI)
Hyderabad India



Prof. B.S. Murty
Director, IIT Hyderabad

Dear Participants,

We live in an era marked by rapid technological advancements. The technology is evolving so unprecedented pace that redefines our lives and brings innumerable possibilities. “Viksit Bharat”, a developed India, requires a multifaceted approach that embraces the contributions of various fields.

We should create solutions that address pressing societal challenges, improving quality of life for all. Our focus should extend beyond mere technological advancement and empower communities and promote sustainability. We should envision a future where technology enriches lives and fosters a more equitable world.

Metallurgists and Material Scientists play a significant role in Viksit Bharat, by designing materials and technologies that keep India ahead of others, making our Bharat not only a global player but a global leader.

Thank you.

Jai Hind.

Prof. B.S. Murty

Director, IIT Hyderabad



Prof. T. Srivatsan
President of International Association for
Processing of Materials and Fabrication of Products
[IA PMFP]

Greetings, cheers and abundance of thanks I extend to each one of you either opting to be physically present in person and make your presence felt or tuning in on-line to make your “valued” presence felt and participating by way of delivering your presentation. In the last few days and weeks, I have been fortunate to receive messages from individuals, both involved and committed to investigating, contributing and furthering the prevailing knowledge base in the domains specific to Materials (to include both Science and Engineering) and Manufacturing Processes (to include Manufacturing Technologies), congratulating me for 33 years [1991-2024] of dedicated, diligent and devoted commitment to the execution and delivery on aspects specific to both promoting and furthering the prevailing knowledge base specific to the Processing of Materials as a viable outcome for the fabrication of products for use in a spectrum of applications.

This technical event being held at Indian Institute of Technology (IIT) (Hyderabad), India., is the 30th in a series of conferences on the specific topic of “**Processing of Advanced Materials**”, with the prime objective of bringing together engineers, technologists, and researchers from nations scattered through the globe and intimately associated with industries, universities and national/government laboratories, and committed to working on aspects and intricacies related, relevant and applicable to the processing, fabrication, characterization and evaluation of

- (a) Materials spanning biomaterials, composites [to include metal-matrix composites, ceramic-matrix composites, and polymer-matrix composites], fuel cell materials, functionally-graded materials, high-energy materials, intermetallic(s), magnetic

materials, foam materials, nanomaterials and nanocomposites, phase-change materials, porous materials and super-conducting materials, and

- (b) Many marvels of manufacturing to include Additive manufacturing, Green manufacturing, Sustainable manufacturing, Artificial Intelligence (AI), Machine Learning (ML), and MEMS/NEMS, for potential use on a spectrum of products spanning the domains of both performance-critical and non-performance critical.

In net essence the “Theme” of this Scholarly Technical Event is on the following two key aspects:

1. The Design and Manufacturing of Sustainable Materials, Process and Products
2. Sustainable Metallurgy and Energy-Efficient Materials for Transition & Decarbonization in Metal Manufacturing Sectors

The key participants are encouraged to present and discuss their findings, observations, inferences and even the potentially viable outcomes culminating from their study

The earlier conferences on “**Processing and Fabrication of Advanced Materials**” have been held in seven nations to include the following: (i) Hong Kong (# 1), (ii) India (# 6), (iii) Japan (# 2), (iv) New Zealand (# 2), (v) Singapore (# 4), (vi) S. Korea (# 1), (vii) Sweden (# 1) and (viii) USA (# 12).

As organizers we have made every effort to ensure that each one of you in attendance, has an excellent experience that spans the domain of education with the prime objective of (i) enabling and ensuring enlightenment for all of the participants and interested attendees, and (ii) importantly encouraging and promoting entrepreneurship, growth and prosperity. Giving due consideration to the scale and caliber of the qualified and intellectually inclined individuals that we have been able to attract, encourage and even reward, this scholarly technical event the “**Thirtieth International Conference on the topic of Processing of Advanced Materials and Fabrication of Products**” does look forward to meeting the desired objectives specific to enabling excellence in the execution of research and possibly entrepreneurship by way of development of products for selection and use in a large number of applications. In essence, this conference seeks to bring out excellence, while concurrently striving to enable and promote (i) diversity and (ii) celebrate accomplishments and achievements made possible either independently or through

collaboration. Our key objective is to both nurture and promote the overall wellbeing of research done by each one of you while concurrently ensuring a platform for the presentation of your research with an emphasis on innovations and findings and the possibility of entrepreneurship that does necessitate the need for both stewardship and direction (focus).

Srivatsan T S

President (IA PMFP)

TABLE OF CONTENT

Advance Materials and Manufacturing Technology

1.	Synthesis and characterization of metallic nanoparticles via Laser ablation synthesis in solution	1-15
2.	Optimization of Water Jet Pressure, Feed Rate and Abrasive Flow Rate in Abrasive Waterjet Machine to enhance Kerf Taper, Surface Roughness and Materias Removal Rate of Aluminium 6061 using Response Surface Methodology and Grey Relational Analysis	16-31
3.	Optimization of Kerf Taper, Material Removal Rate and Surface Roughness of POLYOXYMETHYLENE in Abrasive Waterjet Machining	32-47
4.	Influence Of Water-Jet Peening On Environment-Induced Degradation And Surface Characteristics Of A Magnesium-Zinc Alloy	48-51
5.	Optimizing Laser Machining Parameters For Enhanced Surface Quality And Structural Integrity Of Magnesium Alloy Composites	56-71
6.	Analysis Of Abrasive Aqua Jet Machining Characteristics Of A Hybrid Composite Using Waste Wire-Reinforced Carbon Fiber	72-86
7	Mechanical Response Of Hybrid Glass/Kevlar Epoxy Polymer Composite Reinforced With Multi- Wall Carbon Nanotubes	87-97

8.	Mechanical Response Of 3d Printed Reinforced Nylon For Use In Performance-Specific Applications	98-111
9.	Role Of Isothermal Surface Oxidation In Influencing Microstructure And Mechanical Response Of A Novel Shape Memory Alloy.	112-122
10.	Advanced Processing and Optimization of NiOx as a Hole Transport Layer in Perovskite Solar Cells	123-137
11.	Squeeze Cast Dispersion Strengthened Quaternary Aluminum Alloy Metal Matrix Composite: Damping Behavior	138-153
12.	Comparative Study of Heat Source Models to Analyse Thermal Effect on Precise Modelling of Arc Welding Process	154-170
13.	Mechanical and Microstructure Analysis of AlSi10Mg Alloy Fabricated by Selective Laser Melting Process	171-192
14.	Improved Bandgap Prediction of 2D Materials using Ensemble of Hyperparameter Optimized Boosting Algorithms	193-207
15.	Fusion 360 Based Composite Leaf Spring Design	208-222
16.	Manufacturing of hollow parts with light weight for automotive industry: A case Study	223-232
17.	Modelling and Analysis of Essential Parameters in Green Sand Process to Minimize Shrinkage Porosity in Grey Iron Components	233-241
18.	Duplex treatment of Nitriding and PVD coating – An Insight	242-252

19.	Diamond-Like Carbon Coating – Tribological applications	253-268
20.	Case Study On Repair Welding Of Nickel Aluminium Bronze Alloy Casting (Bs1400 Ab2-CuAl10Fe5Ni5) Using Tungsten Inert Gas Welding Process	269-283
21.	Development of IoT based Real Time Weld Defect Monitoring System For GMAW	284-297
22.	Drilling Analysis of Coir Fiber/Pine Needle Powder Reinforced Hybrid Epoxy Composite	298-309
23.	Establishing a process map of microstructural and phase changes through molten pool thermal history for ex-situ and in-situ laser cladding of TiN/Inconel 625 MMC	310-323
24.	Fabrication and Analysis of Dual Hardness Steel Through Laser DED	324-334
25.	Graphite oxide embedded polyaniline hybrids for high frequency electromagnetic wave attenuation and EMI shielding	335-347
26.	Identifying the advancements of friction stir welding: Innovations in Numerical modeling and simulation	348-362
27.	Sustainable Machining Of Nitinol Shape Memory Alloy Using Near-Dry Electrical Discharge Machining Process	363-381
	Addictive Manufacturing	
28.	Study on deposition characteristics of Ti6Al4V alloy fabricated through Wire Arc Additive Manufacturing using TIG and MIG-CMT Mode	383-395

29.	Optimizing WAAM Process Parameters to Enhance Microstructure and Mechanical Properties of Aluminum 1050: An Experimental Approach	396-417
30.	Steady-State Thermal analysis of Inconel Material lab manufactured 3D Metal Printed Exhaust valve for IC Engines: An innovative approach	418-431
	Polymers and Biomaterials	
31.	“Bio-inspired Synthesis of Metal oxide Nanoparticles from Neltuma juliflora (Sw.) Raf. Leaf Extract for Antimicrobial and Antioxidant activities.”	433-446
32.	Enhancing Polyoxymethylene (POM) Strength for Gearing Applications through Alumina Reinforcement and Comprehensive Testing	447-458
33.	Biodegradable microneedle patches for enhanced and efficient transdermal drug delivery	459-475
34.	Transport, EMISE and Humidity Sensing studies of Polyaniline-Cobalt Ferrite Nanocomposites	476-492
35.	Transport properties and EMI SE studies of Silver decorated Polyaniline-Banana carbon ternary nanocomposites	493-509
36.	Adjustable Prosthetic Feet for the Age Group of 5-10 Years	510-522
37.	Fabrication And Characterization Of Biodegradable Composite Materials Using Bamboo Fibers As Reinforcement And Natural Binder As Matrix	523-533

38.	The Mechanical Properties Of Epoxy Based Bamboo Fibre Reinforced Composite: An Experimental Study	534-543
39.	Dynamic Mechanical and Tribological Properties of Multimaterial Hydrogel Film Under Physiological Solutions for Biomedical Applications	545-560
40.	Fabrication And Characterization Of Biodegradable Composite Disposable Plates Using Natural Fibers And Starch	561-567
41.	Fault Tree Analysis of FDM 3D Printer for Improved Maintainability	568-573

**ADVANCE MATERIALS
AND
MANUFACTURING
TECHNOLOGY**

Synthesis and Characterization of Metallic Nanoparticles via Laser ablation Synthesis in Solution

**Mayur A. Makhesana^{1*}, Kaushik M. Patel²,
Nilesh D. Ghetiya³, Shruti C. Bhatt⁴**

*^{1,2,3,4}Mechanical Engineering Department,
Institute of Technology, Nirma University,
Ahmedabad 382481, India*

**Corresponding Author E-mail:
mayur.makhesana@nirmauni.ac.in*

Abstract

Conductive inks made of metallic nanoparticles have drawn a lot of interest because of their effectiveness and affordability. Because of the numerous conceivable material combinations and qualities, NP-based inks facilitate the creation of novel applications. Due to its high thermal conductivity and printability, silver and copper NP based ink is one of the conductive inks that is frequently utilized in a variety of applications. The process for producing nanoparticles from solid material by irradiating it while it is immersed in a liquid medium is called pulsed laser ablation in liquid (PLAL), often referred to as laser ablation synthesis in solution (LASiS). Using LASiS, copper NPs were produced, and the impact of the process parameters was studied using DI water as liquid medium by analysing ultraviolet-visible (UV-Vis) spectra, mean size, distribution, and viscosity. The findings revealed that the pulse repetition frequency of 50 kHz, scanning speed 1.5 m/s, and ablation time of 30 minutes has resulted in desired characteristics of Cu NPs. The feasibility of produced Cu NPs for inkjet printing is established through viscosity measurements of produced colloids by adding IPA and glycerol at different volume fraction.

Keywords: Copper nanoparticles, LASiS, synthesis, particle size, viscosity

Introduction

The process for producing nanoparticles from a solid substance by irradiating it while it is immersed in a liquid medium—typically DI water—is called pulsed laser ablation in liquid (PLAL), often referred to as laser ablation synthesis in solution (LASiS) [1]. A variety of NPs

have been produced using LASiS, including silicon, carbon [2,3], silver [4,5], gold [6], titanium [7], and magnesium [8,9]. Conductive inks have been the focus of a lot of research lately because of their importance in flexible electronic devices and printing technologies [10]. The need for highly conductive printable tracks has increased across a wide range of industries, including solar cells, thin-film transistors, smart textiles, flexible displays, wearable technologies, and smart packaging. Medication delivery, printed electronics, and implantable medical devices are just a few of the numerous uses for these NPs. Since metal NPs like copper (Cu) [11], gold (Au) [12] and silver (Ag) [13] have a resistivity that is similar to that of the bulk material, they are most frequently utilized in conductive inks. These liquid-suspended conductive particles can function as ink because they are a liquid at room temperature. When applied and dried, the inks can create conductive patterns, making it easier to handle and print than molten metal.

NPs are commonly produced by physical and chemical processes. The two main physical processes that are employed are evaporation condensation and laser ablation. LASiS as a physical technology has garnered a lot of attention in the literature because of its environmentally benign nature and capacity to control the mean size and distribution of nanoparticles. The main advantage is that NP development at specific sizes can be stopped without the use of hazardous ligands. The process is therefore environmentally benign and chemically safe, waste is reduced, and no by-products are created, which makes it appealing for the large-scale production of functional nanomaterials. When compared to the chemical technique, LASiS drastically lowers the amount of post-processing required for the production of nano colloids. Nanoparticle size, yield, ablation efficiency, morphology, and chemical composition are all influenced by the liquid medium. These variables all have an impact on the nanoparticles' mechanical and electrical characteristics, which show how useful they are in the various technology sector. Due to its ease of usage, DI water is a commonly utilized liquid medium. Without the use of further chemicals, the as-fabricated colloid can be used as conductive ink to create flexible sensors [14].

Because of the numerous conceivable material combinations and qualities, NP-based inks facilitate the creation of novel applications. Due to its high thermal conductivity and printability, Ag NP based ink is one of the conductive inks that is frequently utilized in a variety of applications. This material conducts well in both its metallic and oxide phases, therefore there is no technological risk in using it. For the production of high-quality printed electronic devices, less ink will be

required due to the ink's high conductivity. Silver nanoparticles (AgNps) are among the most researched and utilised nanomaterials globally because of their utility in applications in the various fields [15,16]. However, the waste by products of the well-known chemical synthesis method has a negative impact on the environment. Furthermore, post-production washing procedures to eliminate ligands can be required based on the application's surface purity requirements [17]. Post-production polymers that are bonded to the nanoparticle surface are also possible, and it has been observed that they negatively impact the conductivity of nanocolloid printed circuits [18]. Ligand-free Np production and the potential for single-step functionalization are made possible by LASiS to get over these problems. The development of LASiS can greatly reduce the amount of post-processing required in comparison to chemical synthesis. Moura et al. [19] created Ag nanoparticles using nanosecond laser ablation in liquid, and they experimentally examined the impact of the liquid medium and laser fluence on the size, shape, and structure of the resulting nanoparticles. The characteristics of Ag nanoparticles and their rate of formation were shown to be significantly influenced by the liquid media and changing laser fluence. By laser ablation of silver target in distilled water, Dorrnanian et al. [20] created 6–12 nm silver nanoparticles. The average size of NPs has been found to decrease with increasing laser fluence. Nikolov et al. [21] produced metallic nanoparticles (NPs) by pulsed laser ablation of Ag and Au objects immersed in double-distilled water. For twenty minutes, the targets are subjected to different wavelengths of laser pulses. Valverde-Alva et al. [22] used the pulsed photoacoustic (PA) method to laser-ablate Ag-NPs in ethanol. A peak for plasmon absorption at around 400 nm was visible in the colloids' absorption spectra. The PA analysis revealed a considerable reduction in the creation rate of Ag-NPs in the first several hundred laser pulses. Zamiri et al. [23] investigated the impact of laser repetition rate on laser ablation production of silver nanoparticles in the presence of starch as a stabilizer. Stability measurements showed no discernible changes in flocculation, agglomeration, or mean particle size. Zeta potential analyses, however, revealed that the ideal double layer charge is attained at 30 Hz. As a result, small size and improved stability appears to be present in the synthesis of Ag-NP using the laser ablation synthesis in solution (LASiS) method. Silver nanoparticles were generated by Freeland et al. [24] using a novel laminar flow "semi-batch" production technique. The colloids may be used to thin-film print anti-microbial surfaces and were manufactured in less than 15 minutes. It was discovered that using a mild ionic liquid for Np manufacturing provided size

quenching and a route to better size control throughout the production process. Recently, Sreenilayam et al. [25] used a flow-based LASiS system to create additive-free silver (Ag) NP inks with average particle size of 32 nm with 30 min ablation time and 20 kHz, frequency. The XPS study showed that the as-produced LASiS Ag NP colloids were stable over a 12-month period ($\xi = -47$ mV).

Conductive inks made of metallic nanoparticles have drawn a lot of interest because of their effectiveness and affordability. Copper nanoparticles were created by Satriyani and Khumaeni [26] using a pulse laser ablation technique with a pulse Nd:YAG laser. A pure copper metal was exposed to a pulse Nd: YAG laser (1064 nm, 50 mJ) with different frequencies. The result shows that Cu NPs with a sphere-like shape and an average diameter of 12 nm were effectively produced. NPs were effectively produced by using a copper plate [27]. Comparative tests were conducted to examine the effects of different solvents such as DI water, butanol, ethylene glycol, hexane, and acetonitrile on the properties of Cu NPs. The efficiency of the generated copper nanoparticles in reducing aromatic nitro compounds, such as 4-nitrophenol and nitrobenzene, was also assessed. Gondal et al. [28] employed PLAL to produce copper oxide nanostructures. Additionally, they investigated the effects of oxidizing media (hydrogen peroxide and deionized water) on the final materials' optical characteristics, shape, and composition. Optical examinations revealed a notable red shift (3.34–2.5 eV) in the band gap energy when compared to PLAL synthesis without hydrogen peroxide in the liquid media. The characteristics of particle production and modification in ethyl alcohol, as well as the influence of trace amounts of oxidizing and acid-base species on the properties of the NPs in water colloids, were investigated during NP formation using PLAL. It has been determined that a competitive adsorption mechanism, not the carbon shell formation, is responsible for the resistance to deep oxidation of Cu NPs seen in an ethyl alcohol dispersion [29]. PLAL was used to produce carbon nanoparticles (CNPs) in three different liquid media. The as-fabricated NPs were applied to paper substrates as conductive inks. While the nano colloids generated in ethanol had extra peaks and higher absorbance from 210 to 300 nm, DI water exhibited three unique UV-Vis absorbance peaks at 200, 216, and 225 nm. It was found that the characteristics of the NPs were greatly affected by the liquid medium employed for PLAL [30].

The review of literature revealed the research conducted on producing copper nanoparticles for a variety of uses using (PLAL). However, very limited research is reported that look at the relationship between the NP characteristics and viscosity achieved with different solvents

for inkjet printing applications. In addition, it aims to combine the characteristics of copper nanoparticles generated through PLAL with the influence of laser processing variables on the properties. Using LASiS, copper NPs were produced, and the impact of the laser frequency, scanning speed, and ablation time was studied using DI water as liquid medium. Ultraviolet-visible (UV-Vis) spectra, average size, concentration, and viscosity were evaluated. To our knowledge, this is the novel study that, analyzed the size distributions and morphologies of Cu NPs produced through LASiS in de-ionized (DI) water to achieve desired viscosity for it's possible application for inkjet printing.

Experimental Details

Materials and Experimental Set-up

Copper targets with a purity of 99.99% was the material employed for the experiments. The DI water was used in the colloid production of NPs. Disc with a diameter of 8 mm and 4 mm thickness was produced by mechanically polishing and machining the copper plate with silicon carbide up to 1200 grit. The prepared samples were then rinsed with DI water after being cleaned for 30 minutes in an ultrasonic bath.

Copper NPs were produced using the Laser Ablation Synthesis in Solution technique, illustrated in Figure 1. Consistent laminar flow is maintained at the ablation region. A picosecond-pulsed Nd:YAG laser (1064 nm), a maximum output power of 1.2 W, and a pulse width of 700 ps was utilized. The target was placed inside a 3D-printed and customized flow cell. The removal of any masking effects was made possible by the flow of solvent, which allowed effective NP production. The operating fluence was kept at 1.83 J/cm^2 , and the spot size of the laser beam was regulated at $120 \text{ }\mu\text{m}$. At a speed of 2.5 mm/s , the beam scanned across the target surface in an Archimedean spiral path. The effect of pulse repetition frequency of the laser set at 10, 50, and 100 kHz, laser scan speed (1 m/s, 1.5 m/s, and 2 m/s), and ablation time 10, 20, and 30 min.

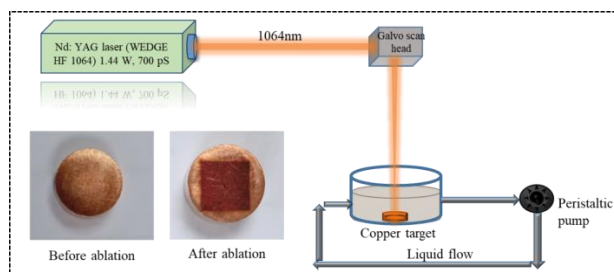


Figure 1 Schematic of experimental setup used to produce Cu NPs

Material Characterization

Multiple analytical techniques were used to determine the morphology and size of the colloid. The NP mean diameter, concentration, and size distribution was measured by means of dynamic light scattering (DLS). Each sample was subjected to twenty runs/measurements on the DLS apparatus, which were then averaged to get raw data on the mean diameter of the nanoparticles and their size distribution. A TEM equipped with a field emission gun and an objective lens was utilised. A copper mesh TEM grid was used for the analysis, and 40 μL of the sample was applied. It was then left to evaporate at room temperature. The optical properties were assessed using a UV-Vis spectrometer. A viscometer (Brookfield Cone/Plate Rheometer) was utilised to measure colloidal viscosity for five minutes at 25 °C and 60 RPM.

Results and Discussion

Visual inspection and Ultraviolet–Visible Spectroscopy

A beaker filled with deionized (DI) water and the Cu NPs are shown in Figure 1 following ten minutes of laser ablation. After ten minutes of laser ablation, the liquid medium's colour changed from colourless to brown in Figure 2. The colour shift that has been observed has been previously reported in the literature, and it is ascribed to the presence of Cu NPs in the liquid media. The presence of Cu NPs contributes for the colour shift before and after PLAL; a minor increase in the brown color's intensity is correlated with higher NP yield in all liquids. Visual inspection thus showed that the NP yield increased as the pulse repetition frequency, scanning speed, and ablation time were increased.

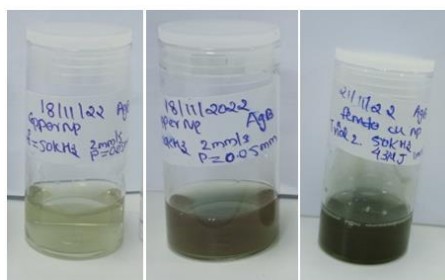


Figure 2 Images of the copper NP sample produced at different processing parameters

Following experiments, each sample were subjected to UV-Vis analysis to confirm the existence of Cu NPs; the related extinction spectra are shown in Figure 3. The pattern of deionized (DI) water was deducted from the whole spectrum in order to separate the contribution of Cu NPs. To do this, a reference sample of DI water was added to the

device while the colloid spectrum was being recorded. In overall, every spectrum that was collected showed a steady trend with peak around 295 nm. As previously mentioned, the rise in pulse repetition frequency, laser scan speed, and ablation duration attributed to the higher concentration of NPs in the liquid. This is explained by the higher energy that the increased frequency and scan speed provides, which allows for more target material to be vaporized or ablation and, as a result, more NPs to be produced [31]. It's interesting to note that, in comparison to other levels, the absorbance of the resultant NPs generated at a 50 KHz frequency, 1.5 m/s scanning speed, and 30 min ablation time was noticeably greater. Furthermore, the absorbance of the resultant Cu NPs showed a linear drop across all parameters at increasing wavelengths after 300 nm, eventually reaching a saturation point.

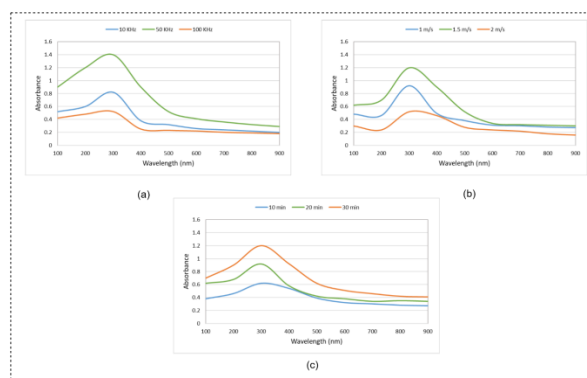


Figure 3 UV-Vis absorption spectrum with varying (a) pulse repetition frequency (b) scanning speed (c) ablation time

Average size and concentration of NPs

The average size and number of NPs generated by PLAL were evaluated using Dynamic Light Scattering (DLS) analysis at different pulse frequency, scanning speeds, and ablation time. NPs generally had typical diameters between 120 and 240 nm, as seen in Figure 4. Additionally, Figure 4 demonstrated that samples produced at 50 kHz, 1.5 m/s, and 30 minutes ablation time had a smaller size range than other samples produced at different levels. Figure 5 shows how the mean sizes of NPs are affected by changes in laser parameters. Notably, the mean size consistently decreased as the frequency and scanning speed increased from 10 to 50 kHz and 1 to 1.5 m/s. Figure 4 shows how the mean sizes of NPs vary in response to variations in the pulse repetition frequency while keeping the laser scan speed and the ablation time at different settings. The general pattern indicates a decrease in nanoparticle size as frequency increases

from 10 to 50 kHz. The increased heating of the target material brought on by the combined effect of several laser pulses at greater repetition rates is the cause of this pattern. The size and shape of the produced NPs are probably going to be influenced by these enhanced thermal effects, which could result in the creation of smaller particles [32]. The transition from intermittent to regular ablation is responsible for this occurrence. Which is characterized by the plume shielding effect's recurrent modulation that affects particle ejection and morphological features [33]. However, at greater scanning speed (2 m/s), the plume shielding effect is eliminated and the ablation process reaches a steady state. Shorter ablation times led to the production of larger NPs. The influence of ablation time is explained by the direct effect of laser power on the thermodynamic properties of cavitation bubbles and the resulting plasma. Moreover, the local concentration of ablated particles rises with time due to liquid confinement. This increases the length of the cavitation bubbles by facilitating the plasma plume's rise to higher temperatures and pressures.

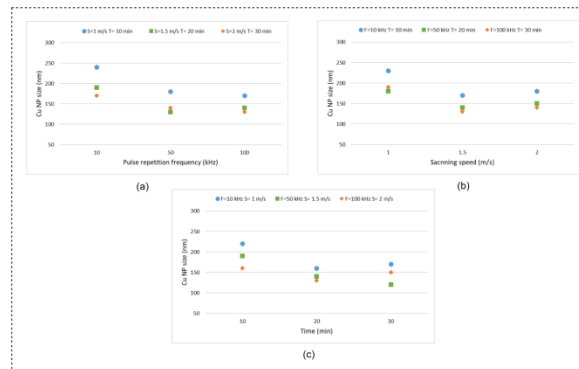


Figure 4 Variation in NPs' mean diameter with varying (a) pulse repetition frequency (b) scanning speed (c) ablation time

Analyses of nanoparticle concentration were performed and Figure 5 (a–c) shows the results. To assess the effect of changing one parameter on particle concentration, two variables were kept constant in each graph. These results showed that when frequency increased from 10 to 100 kHz, the concentration of NPs rose from 2.2×10^8 to 2.82×10^8 particles/mL. Similarly, the concentration of nanoparticles increased from 2.1×10^8 to 2.84×10^8 particles/mL when the ablation time was increased from 10 to 30 minutes. This finding is consistent with the visual examination results, which showed that higher frequency and ablation time increased the production of nanoparticles. On the other hand, the concentration of nanoparticles decreased as the

scanning speed increased from 1 to 2 m/s. Furthermore, at lower scanning speeds, a wider size distribution was noted, which might be the result of particle fragmentation [34]. It's also important to note that the NPs may agglomerate or undergo further oxidation and delay growth after being released into the liquid medium [35]. In this instance, agglomeration is anticipated since the stability of the NPs is low due to the lack of a stabiliser. Under pulsed laser ablation, the concentration of NPs in a liquid is affected by the scanning speed. Higher scanning speeds usually result in lower nanoparticle concentrations, whereas lower scanning speeds often result in higher concentrations.

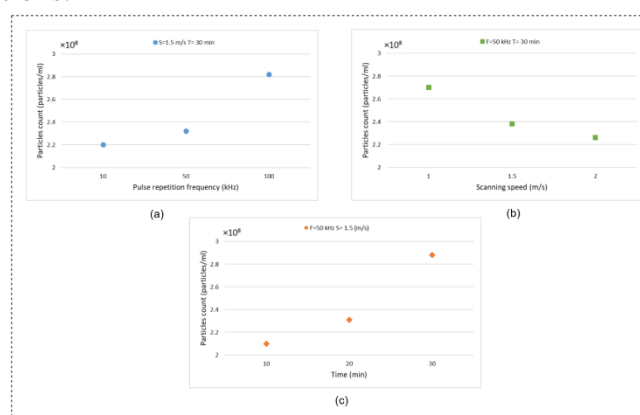


Figure 5 Variation in NPs' concentration with varying (a) pulse repetition frequency (b) scanning speed (c) ablation time

Scanning Transmission Electron Microscopy

With varying acceleration voltages and magnifications. A TEM image of dried Cu NPs obtained at a frequency of 50 kHz, a scanning speed of 1.5 m/s, and under 30 minutes ablation is shown in Figure 6. As DI water serves as the surrounding medium, all of the NPs have a similar shape, a combination of spherical and non-spherical forms with some aggregation that leads to cluster formation. Spherical particles are likely to form when growth is driven by atoms nucleating in the condensed phase in a liquid medium with a constant dipole moment. As seen in the image, these images verify the existence of spherical and nanoscale NPs with a few clusters and agglomerations. Thermal evaporation is the main process that underlies pulsed laser ablation. Larger particles undergo melting and vaporization into atoms or molecules as a result of the laser's high temperature generation on their surfaces. These atoms subsequently reorganize into smaller nanoparticles with the same or different shapes depending on the laser settings and surrounding material.

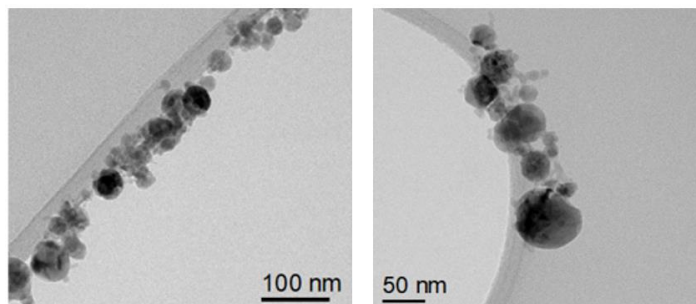


Figure 6 TEM images of copper nano colloids at acceleration voltage 10 kV and 20 kV

Viscosity Measurements

Since PLAL can accurately control nanocolloid properties, such as nanoparticle size, concentration, stability, and colloid viscosity, its applicability in inkjet printing is quite promising. The produced additive-free Cu NPs have potential uses in the fabrication of ink for inkjet printing. The particle size, density, concentration, and viscosity of the ink are crucial to the printing process. To prevent issues like excessive flow or printer head obstruction, it is crucial to maintain the proper ink viscosity, which normally ranges from 1 to 20 mPa.s. The viscosity of the Cu NPs was modified by adding various solvents in order to meet the viscosity specifications suitable for inkjet printers. As illustrated in Figure 7 illustrates the change in viscosity of NP colloids with the addition in isopropyl alcohol (IPA) and glycerol with different volumetric ratios. The viscosity within the range of 1.05 to 2.2 mPa.s was achieved with varying IPA volume fraction. Whereas 0.8 volume fraction of glycerol resulted in highest viscosity value of 9.88 mPa.s making it suitable for inkjet printing application. The chemical reaction between NPs and the solvent is one of the variables that might alter the liquid's viscosity. Different viscosity measurements were obtained by changing the quantities of glycerol, a highly viscous and non-toxic solvent, with water.

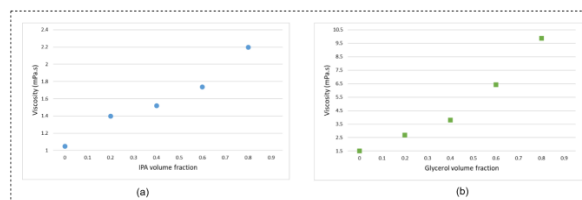


Figure 7 Variation in dynamic viscosity at different volume fraction of (a) IPA (b) glycerol

Conclusions

This study explored the use of liquid pulsed laser ablation to generate copper nanoparticles for potential inkjet printing application. The effects of variables like scanning speed, ablation time, and pulse repetition frequency on the optical properties, size, concentration, and viscosity of the generated NPs were investigated.

1. The results showed that for all tested samples, higher NP yield was associated with increased frequency, scanning speed, and ablation time. Additionally, as frequency increased from 10 to 50 kHz, the optical absorbance raised, which was explained by the liquid's greater NP concentration. A distinct peak was obtained around 295 nm.
2. The DLS measurements revealed that the mean size of NPs decreased as the frequency and scanning speed increased from 10 to 50 kHz and 1 to 1.5 m/s. Larger NPs were produced as a result of shorter ablation time. The direct impact of laser power on the thermodynamic characteristics of cavitation bubbles and the ensuing plasma explains the effect of ablation time. The production of spherical Cu NPs with consistent size was evidenced from TEM analysis.
3. Viscosity measurement of produced samples was carried out to establish the use of produced colloids for inkjet printing application. The viscosity within the range of 1.05 to 2.2 mPa.s was achieved with varying IPA volume fraction. Whereas 0.8 volume fraction of glycerol resulted in highest viscosity value of 9.88 mPa.s making it suitable for inkjet printing application.

References

- [1] Fazio, E.; Gökce, B.; De Giacomo, A.; Meneghetti, M.; Compagnini, G.; Tommasini, M.; Waag, F.; Lucotti, A.; Zanchi, C.G.; Ossi, P.M.; et al. Nanoparticles engineering by pulsed laser ablation in liquids: Concepts and applications. *Nanomaterials* 2020, 10, 2317.
- [2] B. Freeland, R. McCann, P. O'Neill, S. Sreenilayam, M. Tiefenthaler, M. Dabros, M. Juillerat, G. Foley, D. Brabazon, Real-time monitoring and control for high efficiency autonomous laser fabrication of silicon nanoparticle colloids, *Int. J. Adv. Manuf. Technol.* 114 (2021) 291–304, <https://doi.org/10.1007/S00170-021-06772-6>.
- [3] A.V. Shabalina, T.I. Izaak, T.S. Kharlamova, D.O. Martynova, I.N. Lapin, V. A. Svetlichnyi, Ag/SiO_x nanocomposite

- powders synthesized from colloids obtained by pulsed laser ablation, *Colloids Surf. A Physicochem. Eng. Asp.* 553 (2018) 80–88, <https://doi.org/10.1016/j.colsurfa.2018.05.047>.
- [4] E. McCarthy, S.P. Sreenilayam, O. Ronan, H. Ayub, R. McCann, L. McKeon, K. Fleischer, V. Nicolosi, D. Brabazon, Silver nanocolloid generation using dynamic laser ablation synthesis in solution system and drop-casting, *Nano-Struct. Nano-Objects* 29 (2022), 100841, <https://doi.org/10.1016/j.nanoso.2022.100841>.
- [5] P. Wagener, S. Ibrahimkuty, A. Menzel, A. Plech, S. Barcikowski, Dynamics of silver nanoparticle formation and agglomeration inside the cavitation bubble after pulsed laser ablation in liquid, *Phys. Chem. Chem. Phys.* 15 (2013) 3068, <https://doi.org/10.1039/c2cp42592k>.
- [6] A.E. Urusov, A.V. Petrakova, P.G. Kuzmin, A.V. Zherdev, P.G. Sveshnikov, G. A. Shafeev, B.B. Dzantiev, Application of gold nanoparticles produced by laser ablation for immunochromatographic assay labeling, *Anal. Biochem.* 491 (2015) 65–71, <https://doi.org/10.1016/J.AB.2015.08.031>.
- [7] D. Blažeka, J. Car, N. Krstulovi, Concentration Quantification of TiO₂ Nanoparticles Synthesized by Laser Ablation of a Ti Target in Water, 2022.
- [8] A. Nyabadza, M. Vázquez, S. Coyle, B. Fitzpatrick, D. Brabazon, Magnesium nanoparticle synthesis from powders via pulsed laser ablation in liquid for nanocolloid production, *Appl. Sci.* 11 (2021) 10974, <https://doi.org/10.3390/APP112210974>.
- [9] F. Abrinaei, M.J. Torkamany, M.R. Hantezadeh, J. Sabbaghzadeh, Formation of Mg and MgO nanocrystals by laser ablation in liquid: effects of laser sources, *Sci. Adv. Mater.* 4 (2012) 501–506, <https://doi.org/10.1166/sam.2012.1309>.
- [10] S.P. Sreenilayam, I.U. Ahad, V. Nicolosi, V.A. Garzon, D. Brabazon, Advanced materials of printed wearables for physiological parameter monitoring, *Mater. Today* 32 (2020) 147–177, <https://doi.org/10.1016/j.mattod.2019.08.005>.
- [11] M. Grouchko, A. Kamyshny, S. Magdassi, Formation of air-stable coppersilver core-shell nanoparticles for inkjet printing, *J. Mater. Chem.* 19 (2009) 3057–3062, <https://doi.org/10.1039/B821327E>.

- [12] N. Zhao, M. Chiesa, H. Sirringhaus, Y. Li, Y. Wu, B. Ong, Self-aligned inkjet printing of highly conducting gold electrodes with submicron resolution, *J. Appl. Phys.* 101 (2007) 064513, <https://doi.org/10.1063/1.2496249>.
- [13] J. Neddersen, G. Chumanov, T.M. Cotton, Laser ablation of metals: A new method for preparing SERS active colloids, *Appl. Spectrosc.* 47 (1993) 1959, <https://doi.org/10.1366/0003702934066460>.
- [14] Letzel, A.; Santoro, M.; Frohleiks, J.; Ziefuß, A.R.; Reich, S.; Plech, A.; Fazio, E.; Neri, F.; Barcikowski, S.; Gökce, B. How the re-irradiation of a single ablation spot affects cavitation bubble dynamics and nanoparticles properties in laser ablation in liquids. *Appl. Surf. Sci.* 2019, 473, 828–837.
- [15] Nyabadza, A.; Vázquez, M.; Coyle, S.; Fitzpatrick, B.; Brabazon, D. Review of Materials and Fabrication Methods for Flexible Nano and Micro-Scale Physical Property Sensors. *Appl. Sci.* 2021, 11, 8563.
- [16] Cao L, Bai X, Lin Z, et al. The preparation of Ag nanoparticle and ink used for inkjet printing of paper based conductive patterns. *Materials (Basel)*. 2017;10 (9):1004.
- [17] Lee SH, Jun BH. Silver nanoparticles: synthesis and application for nanomedicine. *Int J Mol Sci.* 2019;20(4):865–888.
- [18] Rehbock C, Jakobi J, Gamrad L, et al. Current state of laser synthesis of metal and alloy nanoparticles as ligand-free reference materials for nano-toxicological assays. *Beilstein J Nanotechnol.* 2014;5(1):1523–1541.
- [19] C.G. Moura, et al., Effects of laser fluence and liquid media on preparation of small Ag nanoparticles by laser ablation in liquid, *Opt. Laser Technol.* 97 (2017) 20–28.
- [20] D. Dorrnian, S. Tajmir, F. Khazanehfar, Effect of laser fluence on the characteristics of Ag nanoparticles produced by laser ablation, *Soft Nanosci. Lett.* 3 (2013) 93–100.
- [21] A.S. Nikolov, et al., Characterization of Ag and Au nanoparticles created by nanosecond pulsed laser ablation in double distilled water, *Appl. Surf. Sci.* 257 (2011) 5278–5282.
- [22] M.A. Valverde-Alva, et al., Synthesis of silver nanoparticles by laser ablation in ethanol: A pulsed photoacoustic study, *Appl. Surf. Sci.* 355 (2015) 341–349.

- [23] R. Zamiri, et al., The effect of laser repetition rate on the LASiS synthesis of biocompatible silver nanoparticles in aqueous starch solution, *Int. J. Nanomed.* 8 (2013) 233–244.
- [24] Freeland, B., McCann, R., Alkan, G., Friedrich, B., Foley, G., & Brabazon, D. (2020). Stable nano-silver colloid production via Laser Ablation Synthesis in Solution (LASiS) under laminar recirculatory flow. *Advances in Materials and Processing Technologies*, 6(4), 677-685.
- [25] Sreenilayam, S.P., McCarthy, É., McKeon, L., Ronan, O., McCann, R., Fleischer, K., Freeland, B., Nicolosi, V. and Brabazon, D. (2022). Additive-free silver nanoparticle ink development using flow-based Laser Ablation Synthesis in Solution and Aerosol Jet printing. *Chemical Engineering Journal*, 449, 137817.
- [26] Satriyani, C. M., & Khumaeni, A. (2019, May). Synthesis of colloidal copper nanoparticles using pulse laser ablation method. In *Journal of Physics: Conference Series* (Vol. 1217, No. 1, p. 012019). IOP Publishing.
- [27] Begildayeva, T., Lee, S. J., Yu, Y., Park, J., Kim, T. H., Theerthagiri, J., ... & Choi, M. Y. (2021). Production of copper nanoparticles exhibiting various morphologies via pulsed laser ablation in different solvents and their catalytic activity for reduction of toxic nitroaromatic compounds. *Journal of Hazardous Materials*, 409, 124412.
- [28] Gondal, M. A., Qahtan, T. F., Dastageer, M. A., Saleh, T. A., Maganda, Y. W., & Anjum, D. H. (2013). Effects of oxidizing medium on the composition, morphology and optical properties of copper oxide nanoparticles produced by pulsed laser ablation. *Applied surface science*, 286, 149-155.
- [29] Goncharova, D. A., Kharlamova, T. S., Lapin, I. N., & Svetlichnyi, V. A. (2019). Chemical and morphological evolution of copper nanoparticles obtained by pulsed laser ablation in liquid. *The Journal of Physical Chemistry C*, 123(35), 21731-21742.
- [30] Nyabadza, A., Vázquez, M., Fitzpatrick, B., & Brabazon, D. (2022). Effect of liquid medium and laser processing parameters on the fabrication of carbon nanoparticles via pulsed laser ablation in liquid towards paper electronics. *Colloids and Surfaces A: Physicochemical and Engineering Aspects*, 636, 128151.

- [31] Hamad, A.H. Effects of Different Laser Pulse Regimes (Nanosecond, Picosecond and Femtosecond) on the Ablation of Materials for Production of Nanoparticles in Liquid Solution. In High Energy and Short Pulse Lasers; Viskup, R., Ed.; IntechOpen: Rijeka, Croatia, 2016.
- [32] Claverie, F.; Fernández, B.; Pécheyran, C.; Alexis, J.; Donard, O.F. Elemental fractionation effects in high repetition rate IR femtosecond laser ablation ICP-MS analysis of glasses. *J. Anal. At. Spectrom.* 2009, 24, 891–902.
- [33] Liang, L.; Yuan, J.; Lin, G. Effect of the scanning speed on the microgroove formation regime in nanosecond-pulsed laser scanning ablation of cermet. *Int. J. Adv. Manuf. Technol.* 2020, 107, 97–107.
- [34] Bajaj, G.; Soni, R.K. Effect of liquid medium on size and shape of nanoparticles prepared by pulsed laser ablation of tin. *Appl. Phys. A* 2009, 97, 481–487.
- [35] Lee, C.; Kim, N.R.; Koo, J.; Lee, Y.J.; Lee, H.M. Cu-Ag core-shell nanoparticles with enhanced oxidation stability for printed electronics. *Nanotechnology* 2015, 26, 455601.

Optimization of Water Jet Pressure, Feed Rate and Abrasive Flow Rate in Abrasive Waterjet Machine to enhance Kerf Taper, Surface Roughness and Material Removal Rate of Aluminium 6061 using Response Surface Methodology and Grey Relational Analysis

**K. Karthik¹, S. Tamil Selvan² S. Vishnudharsan³,
B. Vignesh⁴, K. Karthick⁵, S. Mahesh Kumar⁶**

¹²³⁴⁵⁶ *Department of Mechanical Engineering,
Coimbatore Institute of Technology,
Tamil Nadu, 641014, India*

Abstract

The purpose of this study is to optimize different input process variables in abrasive waterjet (AWJ) cut surfaces in order to maximize material removal rate, minimize surface roughness and reduce Kerf Taper. This method is good for cutting materials that are sensitive to temperature changes. Three input process parameters were varied in three levels. Kerf taper, Material removal rate, and surface roughness are all assessed as outcome variables. Aluminium grade 6061 is employed because of the material's extensive technical and structural applications. Response Surface Methodology and Grey Relational Analysis are the effective optimization strategies used in this study. Pressure (K) (110 Bar), Feed Rate (M) (100 mm/min), and Abrasive Flow Rate (V) (350 g/min) are the optimized input parameters obtained from the optimization processes. The material removal rate rises during the rise of abrasive particles flow rate and nozzle speed. The material removal rate is directly influenced by the rate of flow of abrasive particles and the traverse speed. Increased pressure and decreased feed rate have an inverse effect on surface roughness. Both optimization strategies may be used to compute the results.

Keywords: Abrasive Waterjet Machining, Kerf Taper, Grey Relational Analysis, Surface Roughness, MRR, Response surface Methodology.

Introduction

Abrasive waterjet (AWJ) cutting is a versatile machining process widely used for its ability to cut various materials without generating excessive heat. This study aims to optimize the input process variables in AWJ cutting surfaces to maximize material removal rate (MRR), minimize surface finish, and reduce Kerf Taper. The method holds great potential for cutting materials sensitive to temperature changes. Three key input process parameters, namely water jet pressure, feed rate, and abrasive flow rate, were varied at three levels to investigate their impact on the output factors.

Abrasive Waterjet (AWJ) is now a widely used, non-traditional method. In this procedure, water and abrasive are combined under intense pressure. A very small nozzle with high pressure discharges water. The two main categories of waterjets are water jets with abrasive (AWJM) and without abrasive (WJM). For industrial applications, the first offers special abilities [8]. The machining process makes use of the high-pressure water coming from the nozzle. The removal of material in waterjet cutting can be compared to a supersonic process [11].

Mechanical characteristics were determined by S. Athul [1]. By using a pin-on-reciprocating tribometer, a numerical wear model is created to validate and analyze the wear characteristics of Al 6061 alloy as it slides against the hard-counter face of En31 steel at a high temperature. Regarding the machining of magnesium-silicon-based aluminium alloys using an abrasive water jet.

Sreenivasulu Reddy [2] focused on process parameter optimization for multicriteria decision-making. The DEAR technique and Taguchi-based design of trials are used to identify the best input parameters [11] with desired response in AWJM. The taguchi technique was unable to concurrently optimize both replies in the maximum-minimum scenario.

Shu Wang [3] investigated the cutting profile in aluminium alloy using an AWJ. By examining the cut contour, process parameter performance is assessed. It was discovered that the material size and movement of the nozzle had a significant impact on the cutting front's contour. The jet lag increases as the nozzle moves more quickly.

Adnan Akkurt [4] used a variety of materials, including pure Al-6061, to study the impact of traverse speed on surface quality in AWJM. Cutting specimens of each material at various feed rates results in specimens of 5 mm and 20 mm thickness for the experiment. It is determined by measuring the surface roughness of each experiment

that pure aluminium does not have the same surface quality as the Al-6061 aluminium alloy in AWJ cutting applications.

The impact of parameters in the water jet machining process was investigated by Jennifer Milaor Llanto [5]. In researching ways to improve AWJM application, the author's thorough review found that aluminium work parts received 53% of the attention. A total of 27% of recent investigations have demonstrated that feed rate significantly affects AWJ cutting performance, with statistics of 22% abrasive flow and 20% water pressure. Due to its superior performance and affordable pricing, garnet with a mesh size of #80 got 90% utilization in the AWJM application.

Using an experimental study, Karthik K [6] developed a regression equation that includes jet pressure, nozzle speed, and abrasive particle flow rate for the rate of material removal and kerf top width. The research material is 304 stainless steel that is 15 mm thick. The experimental parameter was subjected to three degrees of change, and to maximize the outcomes, response surface techniques and grey relational analysis were utilized.

Material Selection

Aluminium alloy 6061 plates of 15 mm thickness are chosen as the target material in this experiment. The following is a list of the material's qualities and its chemical makeup (Tables 1 and 2). Numerous applications call for the use of aluminium alloy 6061 in various sectors like automobiles (truck sections and body panels), structural (bridge structures), marine (ship constructions), aeroengine applications (rotors), and boiler making are just a few of the heavy-duty applications.

Table 1. Al 6061 - Chemical Composition

Element	% By Weight
Manganese	0.0 to 0.15
Iron	0.0 to 0.70
Magnesium	0.80 to 1.20
Silicon	0.40 to 0.80
Copper	0.15 to 0.40
Zinc	0.0 to 0.25
Titanium	0.0 to 0.15
Chromium	0.04 to 0.35
Others	0.0 to 0.15
Aluminium	Balance

Table 2. Al 6061 - Mechanical properties

Mechanical Properties	Metric
Ultimate Tensile Strength	312 MPa
Tensile Yield Strength	275 MPa
Shear Strength	206 MPa
Fatigue Strength	97 MPa
Modulus of Elasticity	69 GPa
Shear Modulus	26.5 GPa

The nozzle and orifice of the device are 1.03 mm and 0.3 mm in size, respectively [5]. Garnet of 80 mesh size is used in all cutting trials. Greater stand-off lengths are less prone to cause abrasive obstructions, which will slow down cutting, than smaller stand-off distances. 2 mm is the stand-off distance.

Strength-to-Weight Ratio: AL 6061 delivers good strength and stiffness while being relatively lightweight thanks to its high strength-to-weight ratio. This makes it useful in areas like aircraft, automotive, and sporting goods where weight reduction is important. Despite being lightweight, AL 6061 has impressive strength qualities, as seen by its tensile yield strength of 275 MPa and ultimate tensile strength of 312 MPa.

Experimental Design

The water pressure was chosen based on the equipment limits (the highest level that the pump could produce was 380 bar) [8]. The nozzle traverse speed was chosen based on a predefined minimum water pressure [12]. Lower traverse speeds were then chosen with enough spacing. This method ensures that all of the parameter combinations in Table 3 achieve at least 90% through cuts.

Table 3. AWJM Input parameters with levels.

AWJM Input Parameters	1 st Level	2 nd Level	3 rd Level
Jet Pressure (Bar) - K	90	100	110
Feed Rate (mm/min) - M	80	90	100
Abrasive Flow Rate (g/min) - V	250	300	350

The flow rates of abrasives were chosen based on common uses and equipment layout. Because it is difficult to adjust the pressure for each trial, the initial set of tests were carried out while framing the run order, with the pressure (Level 1) remaining constant. Changing the abrasive particle flow rate and nozzle feed rate. In the next series of tests, pressure (Level 2) was chosen, and the other factors were adjusted while the pressure remained constant [12].

The L27 OA configuration offers the advantage of adaptability, allowing you to tailor the orifice size to meet the specific needs of the cutting application. This versatility enhances material compatibility, cutting efficiency, and speed while providing a cost-effective solution for abrasive water jet cutting machining.

Measurement of Material Removal Rate (MRR)

Material Removal Rate (MRR) is determined as the product of kerf area and nozzle speed (traverse speed). The MRR was calculated using the following equation, Eq. 1. Fig. 1. depicts the kerf area.

$$\text{MRR} = \text{Kerf Area} \times \text{Traverse Speed} \quad (1)$$

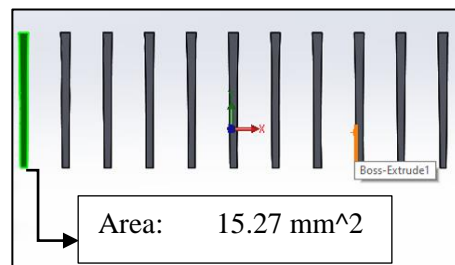


Figure. 1. Measurement of Kerf Area.

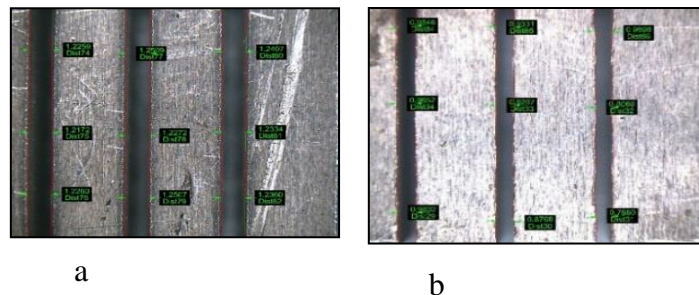


Figure. 2. (a) Kerf Top Width, (b) Kerf Bottom width

Measurement of kerf parameters

The kerf parameters are measured using the video measuring machine; the output 2D drawing file from the video measuring machine is imported into CAD software (Fig. 1) for measuring the kerf top and bottom of the cut surface (Fig. 2). The measured values are tabulated in Table 4.

Measurement of Roughness of Cut Surface

Using the surface roughness tester in Fig. 3, each cut's surface roughness is determined by placing the probe on the surface to be measured and given free movement. On both sides of the cut, the roughness is computed and the average is used. Each cut's averages are determined, and the numbers are reported in Table 4 [7].

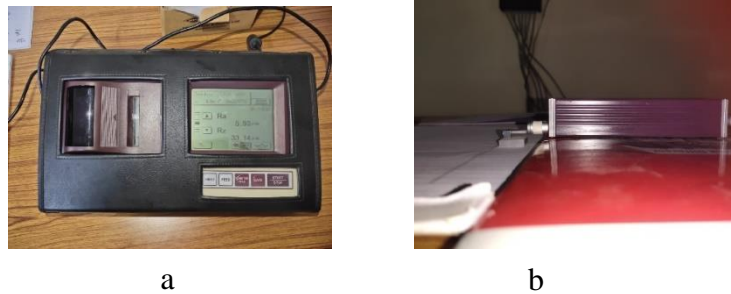


Figure 3. (a) Roughness Tester, (b) Probe on workpiece surface

Table 4. Response Table

Run Order	Water Pressure (K) (Bar)	Feed Rate (M) (mm/min)	Abrasive Flow Rate (V) (g/min)	MRR (mm ³ /min)	KTW (mm)	KBW (mm)	Surface Roughness (μm)
1	90	80	250	1300.80	1.2429	0.8198	16.5717
2	90	90	250	1422.00	1.2401	0.7939	18.5483
3	90	100	250	1541.00	1.2314	0.6583	18.6467
4	90	80	300	1284.80	1.2333	0.8471	17.3800
5	90	90	300	1366.20	1.2149	0.7900	14.9417
6	90	100	300	1465.00	1.2207	0.7367	14.5483
7	90	80	350	1212.00	1.2255	0.8014	13.7067
8	90	90	350	1325.70	1.2209	0.7642	13.1883
9	90	100	350	1397.00	1.2198	0.7578	12.9733
10	100	80	250	1252.00	1.2293	0.9114	14.1483
11	100	90	250	1397.70	1.2292	0.8155	13.2733

12	100	100	250	1489.00	1.2145	0.8262	13.2317
13	100	80	300	1265.60	1.2295	0.8737	13.0900
14	100	90	300	1355.40	1.2325	0.8323	12.9033
15	100	100	300	1481.00	1.2252	0.7879	11.6417
16	100	80	350	1249.60	1.2352	0.9032	10.7200
17	100	90	350	1352.70	1.2300	0.8395	11.0100
18	100	100	350	1475.00	1.2174	0.7915	10.8900
19	110	80	250	1218.40	1.2088	0.9056	11.4700
20	110	90	250	1351.80	1.2043	0.8309	12.6467
21	110	100	250	1448.00	1.2012	0.8489	12.5050
22	110	80	300	1238.40	1.2130	0.9242	9.5300
23	110	90	300	1321.20	1.2084	0.8894	9.4150
24	110	100	300	1496.00	1.2056	0.8616	8.7967
25	110	80	350	1203.20	1.2139	0.9677	10.4033
26	110	90	350	1345.50	1.2102	0.9102	11.3517
27	110	100	350	1527.00	1.2075	0.8615	9.8433

Grey Relational Analysis

Grey Relational Analysis (GRA) is an optimization technique to find the optimum solution by using the normalized data. It is generally applied to multi-parameter optimization problems by providing importance to individual responses. The goal is to raise the MRR and KBW while lowering the KTW and surface roughness [9].

Normalization of Data

Hence the original data are converted into a comparable array of values ranging from 0 to 1. MRR and KBW are to be maximized, i.e., a "larger, the better" sequence of normalization is adopted to scale the MRR and KBW responses between 0 and 1 with the following formula, Eq. 2.

$$x_i^*(p) = \frac{x_i(p) - \min(x_i(p))}{\max(x_i(p)) - \min(x_i(p))} \quad (2)$$

KTW and surface roughness are to be minimized; hence, the "smaller the better" sequence of normalization is adopted to scale the KTW between 0 and 1 with the following formula, Eq. 3.

$$x_i^*(p) = \frac{\max(x_i(p)) - x_i(p)}{\max(x_i(p)) - \min(x_i(p))} \quad (3)$$

Grey Relational Coefficient Calculation

The following formula can be used to compute the Grey relational coefficient, Eq. 4.

$$GRC_i(p) = \frac{\Delta_{\min} + \varepsilon \Delta_{\max}}{\Delta_{oi}(k) + \varepsilon \Delta_{\max}} \quad (4)$$

Grey Relational Grade Calculation

The below formula can be used for Grey Relational Grade (GRG) calculation, Eq. 5.

$$GRG_i = \frac{1}{n} \sum_{k=1}^n GRC_i(p) \quad (5)$$

Grey Relational Analysis Result

The findings of the Grey Relational Grade (GRG) calculation are presented in Table 5. The greatest GRG in experimental cut 27 is connected to the ideal process parameters, and this is the last stage in the procedure.

Table 4. Result of GRA

Input Parameters	Values
Water pressure (K)	110 Bar
Feed rate(M)	100 mm/min
Abrasive flow rate(V)	350 g/min
Response	
Material Removal Rate (MRR)	1527.00 mm ³ /min
Kerf Top Width (KBW)	1.2075 mm
Kerf Bottom Width (KBW)	0.8615 mm
Surface Roughness	9.8433 μm

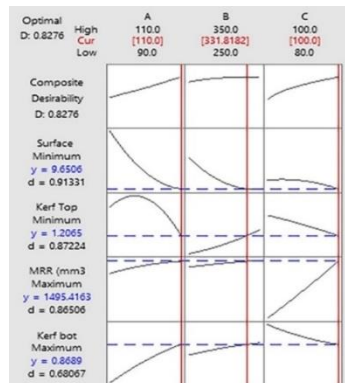


Figure. 4. Response Graph of Input and Output Process Parameters

Response Surface Methodology

In this method, the objective is to find the optimum response and the variables corresponding to this response. The Response Surface Methodology (RSM) aids in determining the response surface's chorography, including local minimum, maximum, and ridge lines, as well as the area where the optimal value was discovered [13]. The experimental data are to be evaluated in a statistical model [9]. Graphs that indicate as pressure increases, the MRR will rise and the KTW value will assume a parabolic form; as a result, the program locates a "sweet spot" that shows the perfect figure to fulfill both goals. According to the graph that depicts the relationship between traverse speed and the responses, the material removal rate increases as traverse speed increases but the kerf top width decreases, therefore the highest permissible value of traverse feed is recommended [10]. According to the previous graph, abrasive flow rate has a minimal impact on MRR but a significant impact on KTW. As a result, the software chooses a number where KTW is the least.

Contour Plot for the Responses

Responses and the factors K and M are related

The connection between the components K and M (waterjet pressure and abrasive flow rate) and outputs is depicted in the following Fig. 5 [13]. Maximum MRR is seen to occur at higher values of K. When the pressure is between 100 and 110 bars and the flow rate is between 250 and 350 g/min, the sand flow rate has less of an impact on the larger material than the water pressure. A satisfactory surface roughness necessitates water pressure between 100 and 110 bars [10].

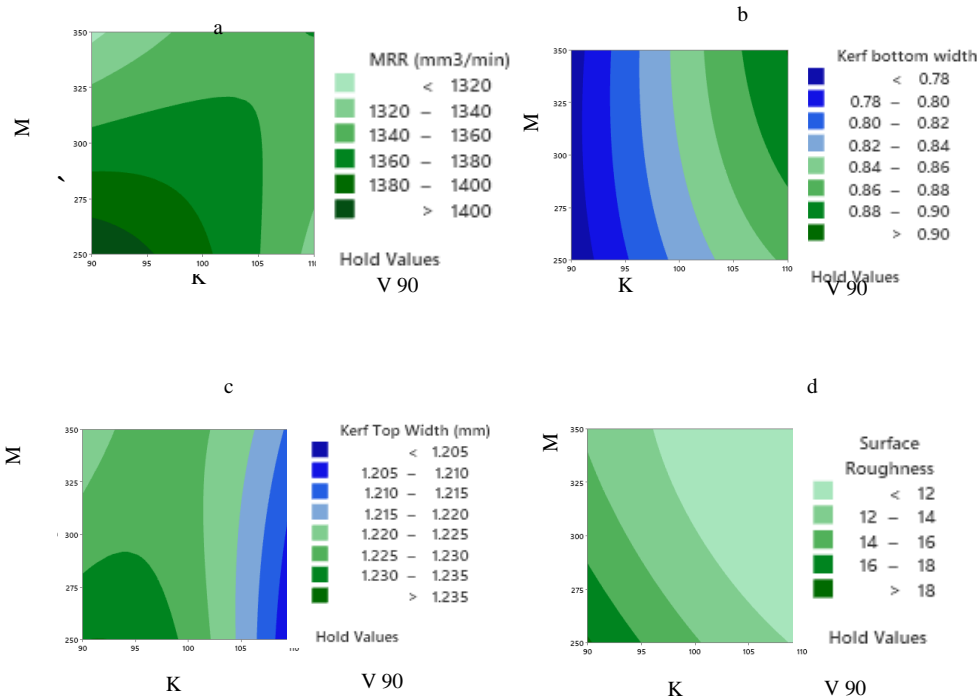
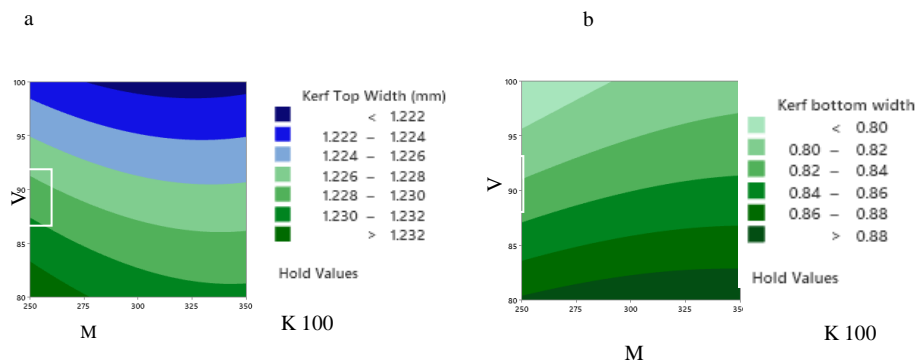


Figure 5. (a),(b),(c),(d) Correlation between the outputs and the Factors K and M.

Responses and the factors M and V are related

The association between the results and factors V and M (feed rate and Abrasive flow rate respectively) is displayed in Fig. 6. Below [10]. Greater values of M and V have been shown to provide higher values of MRR and satisfactory surface roughness when abrasive flow rate ranges between 250 - 350 g/min and feed ranges between 96 -100 mm/min.



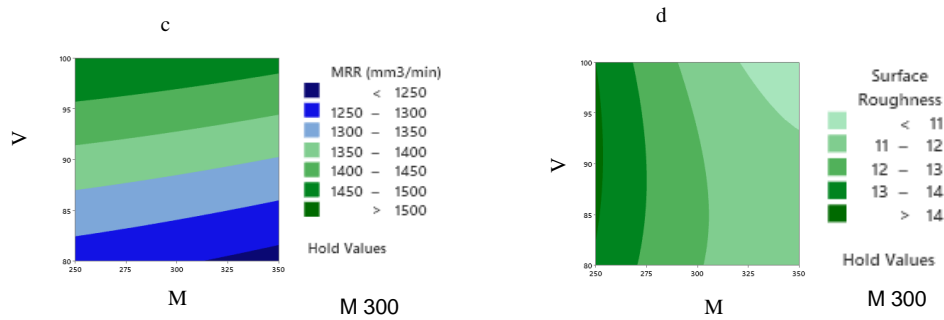


Figure 6. (a),(b),(c),(d) Correlation between the Outputs and the Factors

Responses and the factors V and K are related

The link between the results and parameters K and V (water pressure and feed rate, respectively) is shown in Fig. 7 below. Excellent surface quality and a greater MRR have been seen when both K and M expand. When the pressure fluctuates between 100 and 110 bars and the feed rate fluctuates between 95 and 100 mm/min [10].

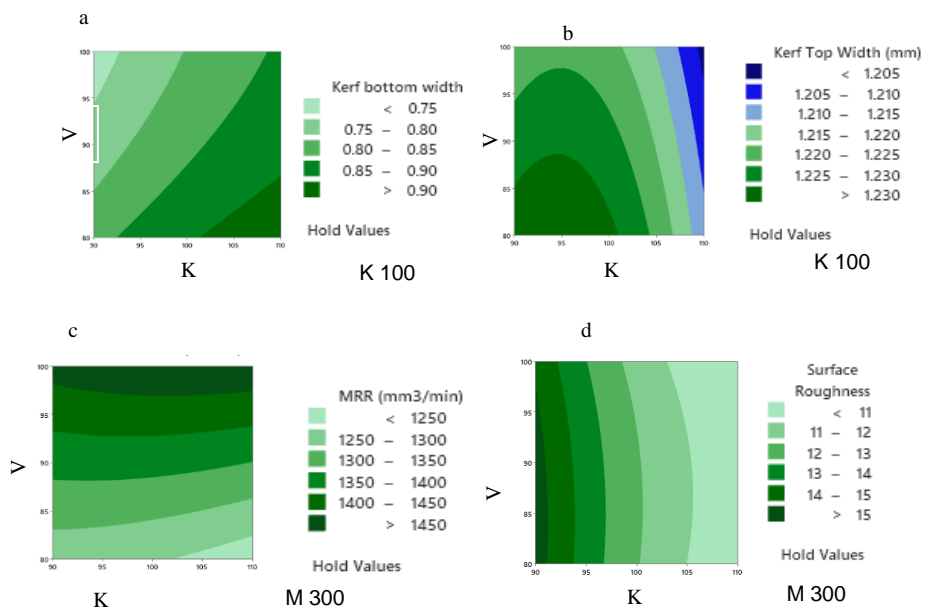


Figure 7. (a),(b),(c),(d) Correlation between the Outputs and the Factors V and K.

Results

The best values for the input parameters discovered using the two optimization techniques are tabulated in Table 6, and the response graphs for each output are shown in Fig. 4.

Table 6. Result from optimization technique

Parameters	Grey Relational values	Response Surface Values
Input		
Pressure (K)	110 Bar	110 Bar
Feed Rate (M)	100 mm/min	100 mm/min
Abrasive Flow Rate (V)	350 g/min	331.8281 g/min
Output		
Optimum MRR	1527 mm ³ /min	1492.07 mm ³ /min
Optimum KTW	1.2075 mm	1.2052 mm
Optimum KBW	0.8615 mm	0.8645 mm
Optimum Ra	9.8433 μm	9.9826 μm

The findings from the two approaches are comparable, and the error is less than 10%. Therefore, it is possible to find the optimal process parameters for machining utilizing AWJM employing both GRA and RSM.

The Regression Equation for various responses are given below,

$$\begin{aligned} \text{MRR (mm}^3/\text{min)} &= 3392 - 16.6 K - 6.71 M - 13.6 V - 0.0956 K^*K - 0.00086 M^*M \\ &\quad + 0.0374 V^*V + 0.0644 K^*M + 0.1713 K^*V + 0.0046 M^*V \end{aligned} \quad (5)$$

$$\begin{aligned} \text{Kerf Top Width (mm)} &= 0.883 + 0.01321 K - 0.001387 M - 0.00075 V - 0.000090 K^*K \\ &\quad + 0.000000 M^*M - 0.000004 V^*V + 0.000011 K^*M + 0.000007 K^*V + 0.000001 M^*V \end{aligned} \quad (6)$$

$$\text{Surface} = 169.1 - 2.411 K -$$

$$\begin{aligned}
 \text{Roughness } (\mu\text{m}) &= 0.270 M + 0.487 V + 0.00814 K^*K + 0.000236 M^*M - \\
 &\quad 0.00248 V^*V + 0.001479 K^*M + 0.00103 K^*V - \\
 &\quad 0.000553 M^*V \\
 \text{Kerf bottom width (mm)} &= 1.45 + 0.0153 K - 0.00109 M - 0.0295 V - \\
 &\quad 0.000108 K^*K \quad (8) \\
 &\quad - 0.000002 M^*M + 0.000085 V^*V + 0.000017 K^*M \\
 &\quad + 0.000075 K^*V + 0.000007 M^*V
 \end{aligned}$$

Where,

MRR – Material Removal Rate, K – Pressure, M – Abrasive flow rate,
V – Traverse speed

Validation of the Results

Table 7. Validation of Result

Input Parameters		Values
Water pressure (K)		110 Bar
Feed rate(M)		100 mm/min
Abrasive flow rate(V)		350 g/min
Response		
Material Removal Rate (MRR)	Trial 1	1548 mm ³ /min
	Trial 2	1475 mm ³ /min
	Trial 3	1541 mm ³ /min
Kerf Top Width (KBW)	Trial 1	1.2050 mm
	Trial 2	1.2125 mm
	Trial 3	1.2154 mm
Kerf Bottom Width (KBW)	Trial 1	0.8512 mm
	Trial 2	0.8418 mm
	Trial 3	0.8617 mm
Surface Roughness	Trial 1	9.7327 μm
	Trial 2	9.6452 μm
	Trial 3	9.5892 μm

Conclusions

This study looked at how output responses like material removal rate (MRR), kerf profile, and surface roughness were affected by water pressure, abrasive particle flow rate, and nozzle feed rate.

The main conclusions to be drawn are the following:

- As the water pressure rises, the rate of material removal rises, while surface roughness and kerf taper both fall.
- Surface roughness and kerf taper fall while MRR rises when abrasive particle flow rate and nozzle movement speed increase.
- Finding the ideal input process parameter value can be accomplished using either the Grey relational analysis or the Response Surface methodology.
- The impacts of three input process variables—water jet pressure, feed rate, and abrasive flow rate—on the outcomes of material removal rate (MRR), kerf profile, and surface polish were examined in this study. Based on the required output responses, the optimization methods helped identify the optimal input parameter values for water pressure (110 Bar), feed rate (100 mm/s), and abrasive flow rate (350 g/min).
- The study found that the water pressure significantly affects the rate of material removal. The rate of material removal increased along with the water pressure. This is explained by the water jet's larger kinetic energy at higher pressures, which leads to more effective cutting and faster material removal rates. Additionally, the enhanced surface smoothness and decreased kerf taper were made possible by the higher water pressure. Cleaner cuts with less surface roughness and better dimensional accuracy were produced as a result of the enhanced cutting power and energy.
- It is significant to note that the Response Surface Methodology (RSM) or the Grey Relational Analysis may both be used to determine the best input process parameter values. Both approaches offer useful tools for enhancing the process variables and obtaining the desired end results. A multi-criteria decision-making method that may take into account the relationship between several input and output characteristics is the Grey relational analysis. It enables the determination of the ideal parameter values depending on how closely the actual

performance matches the ideal. RSM, on the other hand, uses mathematical models to forecast how input parameters and output responses will interact. The ideal parameter values can be found by doing experiments at various parameter levels and fitting response surfaces.

References

- [1] Athu, S., Premnath, G., Sunil, B., Rajeev, V.R., Elevated Temperature Wear Behavior of Aluminium Alloy (Al 6061), *National Conference on Latest Trends in Mechanical Engineering*, 2018 <https://www.researchgate.net/publication/328580734>
- [2] Sreenivasulu Reddy., Chaitanya Goteti., Optimization of Process Parameters for Multi Criterion Decision Making in Abrasive Water Jet Machining of Magnesium - Silicon Based Aluminium Alloys, *International Journal of Modern Manufacturing Technologies*, ISSN 2067-3604, Vol. XIII, P.1, 2021.
- [3] Shu Wang., Dong Hu., Fengling Yang., Chuanlin Tang., Peng Lin., Exploring cutting front profile in abrasive water jet machining of aluminum alloys, *The International Journal of Advanced Manufacturing Technology*, V.112, P.845–851, 2020. <https://doi.org/10.1007/s00170-020-06379-3>
- [4] Adnan Akkurt., Mustafa Kemal Kulekci., Ulvi Seker., Fevzi Ercan., (2004), Effect of feed rate on surface roughness in abrasive waterjet cutting applications, *Journal of Materials Processing Technology*, V.147, P. 389–396 2004. <https://doi.org/10.1016/j.jmatprotec.2004.01.013>
- [5] Jennifer Milaor Llanto., Majid Tolouei-Rad., Ana Vafada., Muhammad Aamir., Recent Progress Trend on Abrasive Waterjet Cutting of Metallic Materials, *Journal of applied Sciences MDPI*, V.11(8), P.3344, 2021. <https://doi.org/10.3390/app11083344>
- [6] Karthik, K., David Smith Sundar Singha., Harivignesh, M., Gopi Karthick, R., Praveena, M., Optimization of Machining Parameters in Abrasive Water Jet Cutting of Stainless Steel 304, *Materials Today Proceedings*, V.46, P. 1384-1389, 2021. <https://doi.org/10.1016/j.matpr.2021.02.489>
- [7] Shu Wang., Dong Hu., Fengling Yang., Peng Lin., (2021), Investigation on kerf taper in abrasive waterjet machining of

aluminium alloy 6061-T6, *Journal of Material Research and technology*, V.15, P.427-433, 2021.
<https://doi.org/10.1016/j.jmrt.2021.08.012>

- [8] Zhong., Yu., A study of the cutting Performance in multi pass AWJM of alumina ceramics with controlled nozzle oscillation, *The International Journal of Advanced Manufacturing Technology*, V.27(7), P.693-702, 2004. <http://dx.doi.org/10.1007/s00170-004-2256-7>
- [9] Senthilkumar, N., Optimization of Process Parameters in Abrasive Water Jet Machining, *International Journal of Innovative Research in Science*, V.5, P.2347-6710, 2016. <http://www.ijirset.com-2319-8753>
- [10] Joel, C., Jeyapoovan,T., Pinninti Praneeth Kumar., (2020), Experimentation and optimization of cutting parameters of abrasive jet cutting on AA6082 through response surface methodology, V.44, P.3564-3570, 2020.
<https://doi.org/10.1016/j.matpr.2020.09.452>
- [11] Gnanavelbabua, A., Saravanan, P., Rajkumar, K., Karthikeyand, S., Baskarane, R., Effect of Abrasive Waterjet Machining Parameters on Hybrid AA6061-B4C- CNT Composites, *International Conference on Materials, Manufacturing and Modelling (ICMMM)*, V.5, P. 13438-13450 2018.
<https://doi.org/10.1016/j.matpr.2018.02.338>
- [12] Yasuyuki Nakamura., Kazuya Sano., Yoshitugu Morishita., The Study on Abrasive Water Jet for Predicting the Cutting Performance and Monitoring the Cutting Situation in the Water, *J. Eng. Gas Turbines Power*, V. 133(6), P. 064501(3), 2011.
<https://doi.org/10.1115/1.4002252>
- [13] Shiva Dayal Rao, B., Abhijeet Sethi., Alok Kumar das., Fiber laser processing of GFRP composites and multi-objective optimization of the process using response surface methodology, *Journal of Composite materials*, V.53, P.11, 2018.
<https://doi.org/10.1177/0021998318805139>

Optimization of Kerf Taper, Material Removal Rate and Surface Roughness of POLYOXYMETHYLENE in Abrasive Waterjet Machining

**K.Karthik¹, A.Mani sankar², B.Atchaya³,
P.Mahalakshmi⁴, U.Manoj⁵, and N.Sathish kumar⁶**

¹²³⁴⁵⁶ *Department of Mechanical Engineering,
Coimbatore Institute of Technology,
Tamil Nadu, India*

Abstract

Abrasive water jet machining (AWJM) is an advanced machining technique. It swiftly removes material from extremely hard and brittle substances without inducing distortion or altering the microstructure, using a blend of high-pressure water and abrasive particles. As a result, it has quickly established itself as one of the most prominent manufacturing technologies. The effects of various AWJM input parameters on POM removal rate (MRR), kerf angle, and surface roughness (SR) have been investigated in this study. On POM material, design of experiments (DOE)-approved experiments are carried out by adjusting input parameters like traverse speed (TS), abrasive flow rate (AFR), and water pressure (WP). The data collected is optimized by Grey Relational Analysis, Response Surface Methodology, and aggression optimization. All these are carried out using MINITAB software.

Introduction

Polyoxymethylene (POM), a high-performance engineering thermoplastic, exhibits exceptional mechanical properties, chemical resistance, and dimensional stability. Its robust mechanical characteristics [1], including high strength, stiffness, and fatigue resistance, combined with its low coefficient of friction [2], make it ideal for applications demanding durability and precision. POM's resistance to a wide range of solvents, acids, and alkalis, along with its hydrophobic nature, ensures its suitability in diverse chemical environments. Moreover, its high melting point, good thermal conductivity, and low thermal expansion [3] contribute to its versatility in various industries. The polymer's dimensional stability, electrical

insulating properties, and excellent machinability further enhance its appeal for applications ranging from automotive components to medical devices. Mainly in the automotive industry Its chemical resistance, particularly resistance to petrol and diesel fuel, protects the endurance and integrity of these parts [4].

Abrasive water jet machining (AWJM), a versatile and precise cutting technology, employs a high-pressure water jet combined with abrasive particles to effectively process a wide range of materials, including metals, non-metals, and composites. The process's key advantages include exceptional precision, minimal heat-affected zones, and the ability to cut complex shapes without the need for specialized tooling. Critical parameters influencing AWJM performance encompass pressure, abrasive flow rate, abrasive type, stand-off distance, and cutting angle. AWJM's versatility and efficiency have established it as a valuable tool for industries such as metalworking, aerospace, and automotive, where demanding cutting applications require precise and complex results. [5]

Abrasive water jet machining (AWJM), precise cutting technology, offers numerous advantages for processing polyoxymethylene (POM), a high-performance engineering thermoplastic renowned for its exceptional mechanical properties and chemical resistance. AWJM's ability to produce precise cuts with minimal heat-affected zones is particularly beneficial for preserving POM's material integrity, ensuring optimal performance in demanding applications. The technology's versatility allows for the efficient cutting of complex shapes and geometries in POM, enabling manufacturers to create intricate components with precision and efficiency. [6]

Abrasive Water Jet Machining (AWJM) requires careful consideration of various input parameters to achieve optimal results. These parameters include hydraulic factors like water pressure, flow rate, and orifice diameter; abrasive characteristics such as type, particle size, and flow rate; cutting conditions like stand-off distance, traverse speed, angle, and passes; as well as mixing and acceleration parameters related to the chamber and tube design [7]. Our investigation focused on the influence of pressure, transverse speed, and abrasive flow rate.

To optimize parameters like pressure, transverse speed, and abrasive flow rate in Abrasive Water Jet Machining (AWJM), a comprehensive approach combining ANOVA, Grey Relational Analysis (GRA), and Response Surface Methodology (RSM) is effective. ANOVA identifies significant factors, GRA quantifies relationships under uncertainty [8], and RSM models and predicts optimal settings [9].

Materials

Table 1 Chemical Properties of POM

Property	units
Melting Range	165-175°C
Specific Heat	1.8 to 2.2 J/g·°C
Density	1.41 to 1.43 g/cm ³ ,
Young's Modulus	2,500 to 3,500 Mpa
Electrical Resistivity	10 ¹⁴ to 10 ¹⁶ Ω·cm
Poisson's Ratio	0.2 to 0.4

Polyoxymethylene with a thickness of 35 mm was designated as the target material for this investigation. The following is a breakdown of its chemical properties (Table 1). Its Rockwell hardness is 122, which is 6% higher than nylon, and its moisture absorption is 0.9%, which is 14% lower than nylon. Popular choice for numerous applications in different sectors like automobiles (engine mounts and structural elements), industrial machinery (heavy-duty gears), construction and manufacturing (machinery bases), and consumer products (electronic device cases).

The nozzle and orifice of the device are 1.03mm and 0.3mm in size, respectively. Garnet of 80 mesh size is used in all cutting trials. Greater stand-off lengths are less prone to cause abrasive obstructions, which will slow down cutting, than smaller stand-off distances. 3 mm is the stand-off distance. The polymer's dimensional stability, electrical insulating properties, and excellent machinability further enhance its appeal for applications ranging from automotive components to medical devices. Mainly in the automotive industry Its chemical resistance, particularly resistance to petrol and diesel fuel, protects the endurance and integrity of these parts.

Experimental Design

The water pressure was chosen based on the equipment limits (the highest level that the pump could produce was 380 Bar) [10]. The nozzle traverse speed was chosen based on a predefined minimum

water pressure [11]. Lower traverse speeds were then chosen with enough spacing. This method ensures that all of the parameter combinations Table 2. chosen to achieve at least 90% through cuts.

The flow rates of abrasives were chosen based on common uses and equipment layout. Because it is difficult to adjust the pressure for each trial, the initial set of tests were carried out while framing the run order, with the pressure (Level 1) remaining constant. Changing the abrasive particles flow rate and nozzle feed rate. In the next series tests, pressure (Level 2) was chosen, and the other factors were adjusted while the pressure remained constant [11].

Table 2. AWJM Input parameters with levels.

AWJM Input Parameters	1st Level	2nd Level	3rd Level
Jet Pressure (Bar) - K	80	100	120
Feed Rate (mm/min) - M	40	55	70
Abrasive Flow Rate (g/min) - V	200	250	300

The L27 OA configuration offers the advantage of adaptability, allowing you to tailor the orifice size to meet the specific needs of the cutting application. This versatility enhances material compatibility, cutting efficiency, and speed while providing a cost-effective solution for abrasive water jet cutting machining.

Measurement Of MRR:

MRR (material removal rate) is calculated based on the kerf profile area and the feed rate and traverse speed of the nozzle. The following equation was used to calculate the MRR. Kerf Area is illustrated in Figure 1.

$$\text{MRR} = \text{Kerf Area} \times \text{Traverse Speed}$$

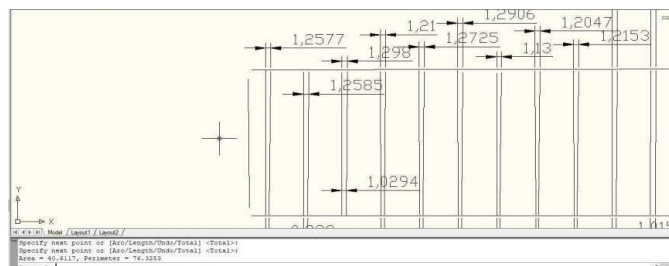


Figure 1. Measurement of Kerf Area.

Measurement of Kerf Parameters:

The Kerf parameters like Kerf Top Width (KTW), Kerf Bottom Width (KBW), and Kerf Area were measured using Video Measuring Machine (VMM). The output 2D drawing file from the video measuring machine is imported into CAD software Fig. 1 for measuring the kerf top and bottom of the cut surface Fig. 2. The measured values are tabulated in Table 3.

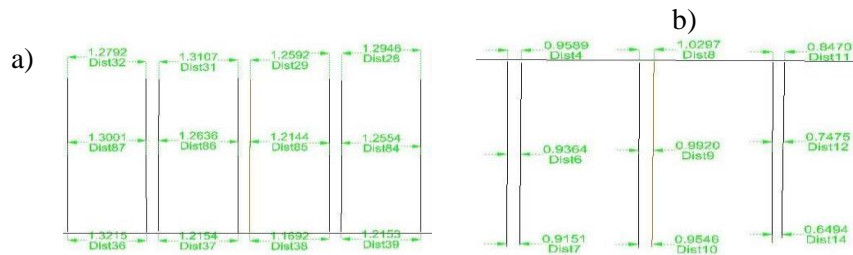


Figure 2. (a)Kerf Top width, (b)Kerf Bottom width

Measurement of Roughness of Cut Surface

Using the surface roughness tester in Fig. 3, each cut's surface roughness is determined by placing the probe on the surface to be measured and given free movement. On both sides of the cut, the roughness is computed and the average is used. Each cut's averages are determined and the numbers are reported in Table 3 [12].

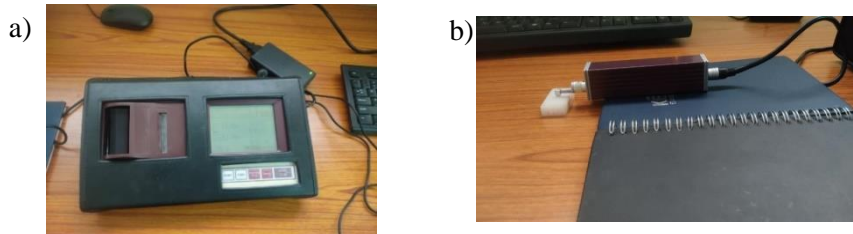


Figure 3. (a)Surface roughness tester, (b) Measurement of surface roughness on POM

Table 3. Response Table

RUN ORDER	WATER PRESSURE (BAR)	FEED RATE (mm/min)	ABRASIVE FLOW RATE (g/min)
1	80	40	200
2	80	40	250
3	80	40	300
4	80	55	200
5	80	55	250
6	80	55	300
7	80	70	200
8	80	70	250
9	80	70	300
10	100	40	200
11	100	40	250
12	100	40	300
13	100	55	200
14	100	55	250
15	100	55	300
16	100	70	200
17	100	70	250
18	100	70	300
19	120	40	200
20	120	40	250
21	120	40	300
22	120	55	200
23	120	55	250
24	120	55	300
25	120	70	200
26	120	70	250
27	120	70	300

GREY RELATIONAL ANALYSIS

Grey Relational Analysis (GRA) is a method used to find the best solution among multiple options by analysing normalized data. It's particularly useful for problems with many factors to consider, assigning different levels of importance to each factor. The aim is to increase MRR and KBW while decreasing KTW and surface roughness.

Normalization of Data

Hence the original data are converted into a comparable array of values ranging from 0 to 1. MRR and KBW are to be maximized, i.e., a "larger the better" sequence of normalization is adopted to scale the MRR and KBW responses between 0 and 1 with the following formula Eq.1:

$$x_i^*(p) = \frac{x_i(p) - \min(x_i(p))}{\max(x_i(p)) - \min(x_i(p))} \quad (1)$$

KTW and surface roughness are to be minimized; hence, the "smaller the better" sequence of normalization is adopted to scale the KTW between 0 and 1 with the following formula Eq.2:

$$x_i^*(p) = \frac{\max(x_i(p)) - x_i(p)}{\max(x_i(p)) - \min(x_i(p))} \quad (2)$$

Grey Relational Coefficient Calculation

The following formula can be used to compute the Grey relational Coefficient Eq.3:

$$GRC_i(p) = \frac{\Delta_{min} + \varepsilon \Delta_{max}}{\Delta_{0i}(k) + \varepsilon \Delta_{max}} \quad (3)$$

Grey Relational Grade Calculation

The below formula can be used for Grey Relational Grade (GRG) calculation Eq.4:

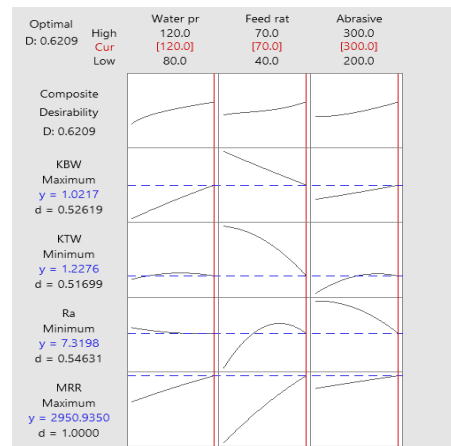
$$GRG_i = \frac{1}{n} \sum_{k=1}^n GRC_i(p) \quad (4)$$

Grey Relational Analysis Result

The findings of the Grey Relational Grade (GRG) calculation are presented in Table 4. The greatest GRG in experimental cut 27 is connected to the ideal process parameters, and this is the last stage in the procedure.

Table 4. Result of GRA.

INPUT PARAMETERS	
Pressure	120 (bar)
Feed rate	70 (mm/min)
Abrasive flow rate	300(g/min)
RESPONSES	
Optimum KBW	1.0307(mm)
Optimum KTW	1.2186(mm)
Optimum MRR	2945.87(mm ³ /min)
Optimum surface roughness	6.876(μ m)

**Figure 4.** Response Graph of Input and Output Process Parameters

Response Surface Methodology

The primary objective of this study is to identify the optimal response and the corresponding variables influencing it. Response Surface Methodology (RSM) is employed to elucidate the response surface topography, including local minima, maxima, and ridge lines, as well as the region of optimal value. Experimental data are subjected to statistical modeling to establish relationships between variables and responses.

Graphical analyses reveal that as pressure increases, material removal rate (MRR) rises while kerf top width (KTW) exhibits a parabolic trend. This suggests an optimal operating point where both MRR and KTW are optimized. Similarly, increasing traverse speed enhances

MRR but diminishes KTW, necessitating a careful balance to achieve the desired outcome. The influence of abrasive flow rate on MRR is minimal, whereas KTW is significantly impacted. Consequently, the software selects an abrasive flow rate that minimizes KTW while maintaining acceptable MRR levels.

Contour plot for the responses

Responses and the factors M and V are related

The association between the results and factors V and M (feed rate and abrasive flow rate, respectively) is displayed in Fig. 5 below [13]. Greater values of M and V have been shown to provide higher values of MRR and satisfactory surface roughness when abrasive flow rate ranges between 200 g/min and 300 g/min and feed rate ranges between 63 mm/min and 70 mm/min.

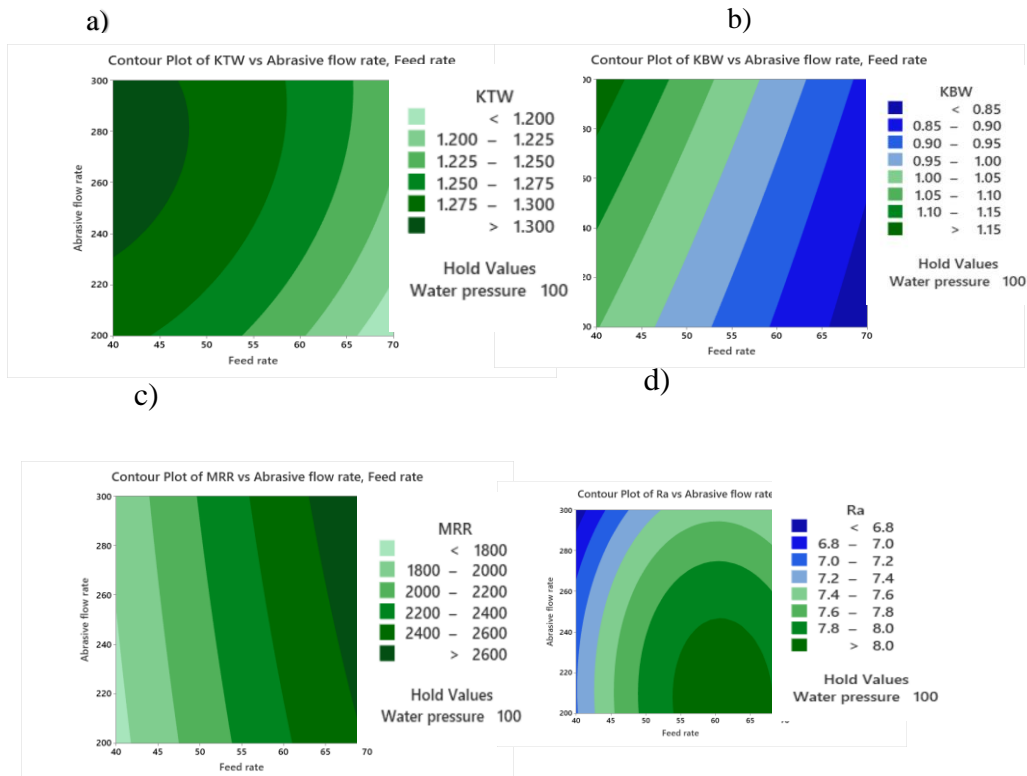
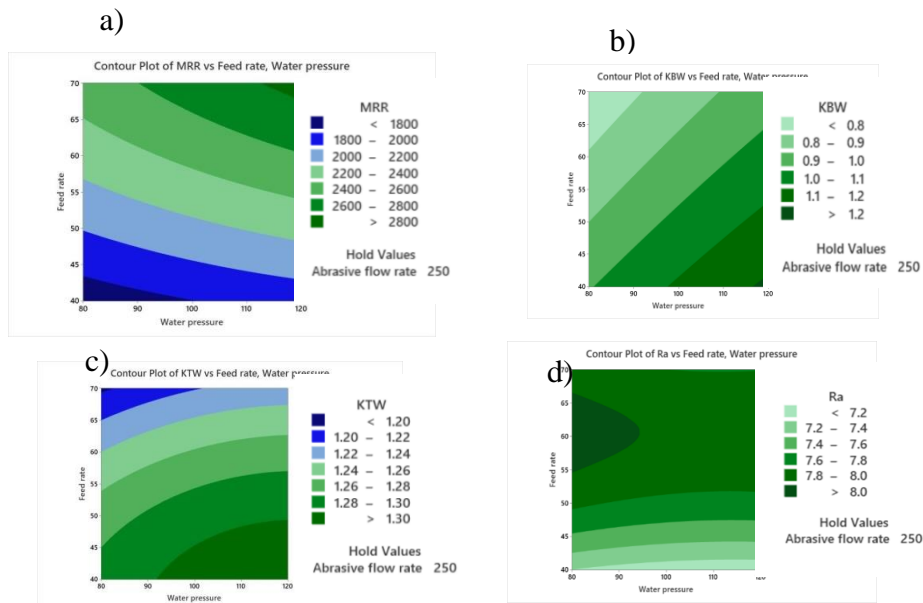


Figure 5 (a), (b), (c), (d) Correlation between the Outputs and the Factors M and V.

Responses and the factors V and K are related

The link between the results and parameters K and V (water pressure and feed rate, respectively), is shown in Fig. 6 below. Excellent surface



quality and a greater MRR have been seen when both K and M expand. When the pressure fluctuates between 97 bar and 110.5 bar and the feed rate fluctuates between 55 mm/min - 70 mm/min.

Figure 6. (a),(b),(c),(d) Correlation between the Outputs and the Factors V and K

ANALYSIS OF VARIANCE (ANOVA)

In this comprehensive study, ANOVA (Analysis of Variance) was employed as a robust statistical tool to meticulously quantify the contributions of water pressure, feed rate, and abrasive flow rate to the performance of Abrasive Water Jet Machining (AWJM). By conducting a series of controlled experiments with varying levels of these parameters and meticulously measuring key indicators such as kerf bottom width, kerf top width, material removal rate, and surface roughness, ANOVA provided valuable insights into the intricate relationships between these parameters and the overall process efficiency [8]. The study demonstrated that all three parameters significantly influenced the AWJM process, with water pressure and abrasive flow rate having the most pronounced effects on kerf width

and material removal rate, while feed rate had a more significant impact on surface roughness.

Percentage of contribution

Percentage contribution of MRR

The percentage contribution of input parameters such as water pressure, feed rate, and abrasive flow rate to the output parameter MRR (material removal rate). Feed rate is the highest percentage contributing factor (88.19%) on material removal rate, whereas abrasive flow rate is the lowest contributing factor Fig 7.

Percentage contribution of KTW

The percentage contribution of input parameters for kerf top width. Here, the feed rate contributes the most, whereas the least influencing factor is water pressure (7.09%). The error that occurs in this distribution is 16.93% Fig 8.

Percentage contribution of KBW

The feed rate contributes about 50%, and the second highest percentage contributing factor is the water pressure (37.5%). The kerf bottom width is almost negligibly affected by the abrasive flow rate Figure 9.

Percentage contribution of Surface roughness

For surface roughness, the feed rate is the highest percentage contributing factor, and also the abrasive flow rate has a significant effect on the surface roughness, about 28.979% Fig 10.

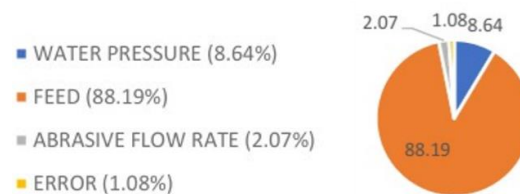


Figure 7. Percentage contribution of MRR

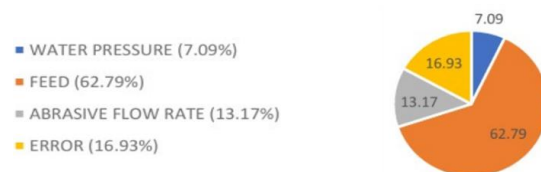


Figure 8. Percentage contribution of KTW

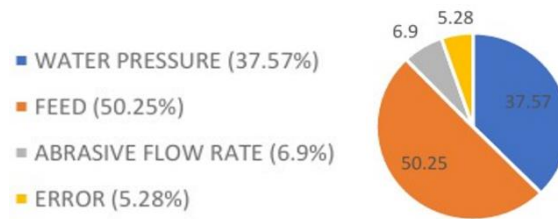


Figure 9. Percentage contribution of KBW



Figure 10. Percentage contribution of surface roughness

Optimization of Parameters using Regression Method

This study employs regression techniques to model and analyze the relationship between output variables such as kerf width, surface roughness, and material removal rate (MRR) and input factors like water pressure, traverse speed, and feed rate in abrasive water jet machining (AWJM). We collect experimental data to develop regression models that represent these relationships. For instance, we use a linear regression model to predict the impact of pressure and speed variations on surface roughness. The developed regression model also facilitates multi-response prediction, allowing for the simultaneous optimization of multiple outputs. We plot a response graph on this basis to visually represent the effects of input parameters on the multiple responses and identify optimal operating conditions.

In the context of multiple response prediction, the standard error of fit (SE) represents the standard deviation or uncertainty associated with the predicted values. Smaller values indicate more precise predictions, and here 0.0146 is the more precise prediction. Typically, we construct confidence intervals for the estimated response variable values or model predictions using the 95% confidence level. We expect individual future observations of the response variable to fall within a range of values provided by the 95% prediction interval. It accounted for both the uncertainty in the estimated values and the variability of future observations. [9]

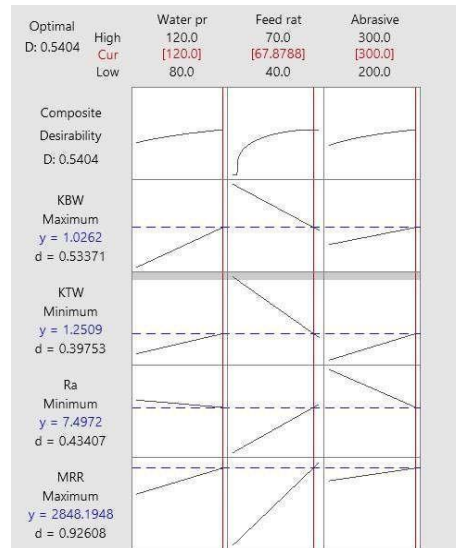


Figure 11. Response graph from regression method

This graph, Fig. 11, depicts the optimized values of kerf bottom width, kerf top width, surface roughness, and material removal rate obtained from the regression method.

RESULT AND DISCUSSION

Table 4. Result from optimization technique

PARAMETERS	GREY RELATIONAL ANALYSIS	RESPONSE SURFACE METHODOLOGY	REGRESSION OPTIMIZATION
INPUT PARAMETERS			
Pressure	120 Bar	120 Bar	120 Bar
Feed Rate	70 mm/min	70 mm/min	67.87 mm/min
Abrasive Flow rate	300 g/min	300 g/min	300 g/min
OUTPUT PARAMETERS			
Optimum MRR	2945.87 mm ³ /min	2950.93 mm ³ /min	2848.19 mm ³ /min
Optimum KTW	1.2186 mm	1.2276 mm	1.2508 mm
Optimum KBW	1.0307 mm	1.0217 mm	1.0262 mm
Optimum Ra	6.8760 μm	7.3198 μm	7.4971 μm

The values obtained by the three methods are in the same range, and the percentage change in value is less than 10%. Hence all three methods are recommended for obtaining the optimized process parameters for machining using AWJM.

Conclusion

Optimization of process parameters of AWJM on polyoxymethylene is carried out successfully. And the following conclusions are made:

- The optimized parameters for cutting polyoxymethylene of approximately 37mm thickness (± 5 mm) are a water pressure of 120 bar and an abrasive flow rate of 300 g/min.
- The feed rate ranges between 67.87 mm and 70 mm, while the material removal rate (MRR) is optimized to 2848.19 mm³/min to 2950.93 mm³/min.
- Kerf dimensions are optimized with a Kerf Top Width (KTW) of 1.2186 mm to 1.2508 mm and a Kerf Bottom Width (KBW) of 1.0217 mm to 1.0307 mm, along with a surface roughness (Ra) of 6.8760 μ m to 7.4971 μ m.

References

- [1] Rong xin Guo, "Experimental investigations on tensile strength and fracture toughness of a polyoxymethylene fiber reinforced concrete," *Theoretical and Applied Fracture Mechanics*, vol. 130, 2024. <https://doi.org/10.1016/j.tafmec.2023.104250>.
- [2] Rustamov, Ibrohim, "Filler processing and mixing effects of polyoxymethylene/graphene nanocomposite on tribo-mechanical performances," *Tribology International*, vol. 201, p. 110267, 2025. <https://doi.org/10.1016/j.triboint.2024.110267>.
- [3] J. Zhang, "Poly(lactic acid)/polyoxymethylene blends: Morphology, crystallization, rheology, and thermal mechanical properties," *Polymer*, vol. 69, pp. 103-109, 2015. <https://doi.org/10.1016/j.polymer.2015.05.050>.
- [4] Kneissl, Lucas M., "Mechanical properties and tribological performance of polyoxymethylene/short cellulose fiber composites," *Polymer Testing*, vol. 128, no. 108234, 2023. <https://doi.org/10.1016/j.polymertesting.2023.108234>.
- [5] Chen, Ming, "Method of ensemble modeling for abrasive water

- jet machinability of metal materials," *Journal of Manufacturing Processes*, vol. 110, pp. 291-302, 2024. <https://doi.org/10.1016/j.jmapro.2024.01.004>.
- [6] Kumar, U. Ashok, "Influence of abrasive water jet cutting on glass fibre reinforced polymer (GFRP) composites," *Materials Today: Proceedings*, vol. 27, pp. 1651-1654, 2020. <https://doi.org/10.1016/j.matpr.2020.03.554>.
- [7] N. Sathishkumar, "Process parameters optimization in machining of duplex 2205 stainless steel alloy using AWJM technique," *Materials Today: Proceedings*, vol. 46, pp. 1390-1395, 2021. <https://doi.org/10.1016/j.matpr.2021.02.491>.
- [8] Raja, M. Ayyanar, "Parametric investigation and optimization of AWJM process on stir cast al7075/basalt composite materials using Taguchi based grey relational analysis," *Materials Today: Proceedings*, vol. 60, pp. 815-821, 2022. <https://doi.org/10.1016/j.matpr.2021.09.398>.
- [9] K. Karthik, "Optimization of machining parameters in abrasive water jet cutting of stainless steel 304," *Materials Today: Proceedings*, vol. 46, pp. 1384-1389, 2021. <https://doi.org/10.1016/j.matpr.2021.02.489>.
- [10] Y. Zhong., " A study of the cutting Performance in multi pass AWJM of alumina ceramics with controlled nozzle oscillation," *The International Journal of Advanced Manufacturing Technology*, vol. 27(7), pp. 693-702, 2004. <https://doi.org/10.26190/unsworks/17795>.
- [11] Yasuyuki Nakamur., Kazuya Sano., Yoshitugu Morishita., "The Study on Abrasive Water Jet for Predicting the Cutting Performance and Monitoring the Cutting Situation in the Water," *J. Eng. Gas Turbines Power*, vol. 133(6), p. 064501(3), 2011. <https://doi.org/10.1115/1.4002252>.
- [12] Shu Wang., Dong Hu., Fengling Yang., Peng Lin., "Investigation on kerf taper in abrasive waterjet machining of aluminium alloy 6061-T6," *Journal of Material Research and technology*, vol. 15, pp. 427-433, 2021. <https://doi.org/10.1016/j.jmrt.2021.08.012>.
- [13] Joel, C., Jeyapoovan,T., Pinninti Praneeth Kumar., "Experimentation and optimization of cutting parameters of

abrasive jet cutting on AA6082 through response surface methodology,," *Materials Today: Proceedings*, vol. 44, pp. 3564-3570, 2020. <https://doi.org/10.1016/j.matpr.2020.09.452>.

INFLUENCE OF WATER-JET PEENING ON ENVIRONMENT-INDUCED DEGRADATION AND SURFACE CHARACTERISTICS OF A MAGNESIUM-ZINC ALLOY

A. Arun ¹, S. Santosh ^{1} and T.S. Srivatsan ²**

¹Department of Mechanical Engineering

Sri Sivasubramaniya Nadar (SSN) College of Engineering
Old Mahabalipuram Road, Kalavakkam 603110, Tamil Nadu,
India

²Department of Mechanical Engineering

The University of Akron
Akron, Ohio 44325, USA

***Presenter and Corresponding Author: santoshs@ssn.edu.in*

Abstract

In this work, the results of a recent research study aimed at examining the impact of water jet peening on resistance to environment-induced degradation or corrosion resistance and surface characteristics of a Magnesium-Zinc [Mg-Zn] alloy will be highlighted. The research study essentially examined the influence of water-jet peening input variables, namely, traverse speed (N_{TS}), number of passes, and standoff distance (SOD) on the chosen Mg-Zn alloy. To understand the effects and impact of the variables specific to water-jet peening, the surface topography, and X-ray diffraction analysis were systematically conducted and the results analyzed. An investigation was conducted to analyse the magnitude of improvement in both the hardening effect and roughening effect that occurs as a outcome of the water-jet peening process. The peened surfaces exhibited a **35.38%** increase in microhardness and a **22.56 %** decrease in surface roughness. The test results did demonstrate promising improvements in the resistance of the chosen Mg-Zn alloy to environment-induced degradation or corrosion. Specific details will be highlighted and discussed.

Keywords : Mg-Zn alloy, Water-jet peening, environment-induced degradation, characteristics of surface.

Introduction

Magnesium (Mg) and its alloys are now the preferred material for orthopedic fracture fixing implants due to their various advantages. These properties include osseointegration, osteoconductivity,

antimicrobial, biocompatibility, resorbability, osteoinductivity, angiogenesis, antioxidants, and the ability to prevent drug-induced osteonecrosis. One of the lightest structural metals available is magnesium, with a specific gravity of 1.74. Consequently, steel-based components are giving way to composites and alloys based on magnesium^[1]. However monolithic magnesium is easily worn down and corroded, which could lead to the implant failing before its time. Surface changes, coatings, heat treatments, peening, and alloying can improve magnesium's corrosion and wear qualities. Due to the fact that osteoblastic cells cling to and multiply on the surface of an implant, the topography of that surface is extremely important. Zn is regarded as a viable choice for alloying with magnesium since it is biodegradable, non-toxic, naturally occurring as a trace element in humans, and required to regulate human metabolism. In order to enhance the resistance of a variety of materials against corrosion, surface modification techniques have been developed^[2]. However, each has its own restrictions. Processing Mg alloy offers significant challenges such as flame ignition, fracture propagation, and high heat generation, which can affect properties and lead to material failure in the bio-environment.^[3] Additionally, several researches have demonstrated the relevance of scratched surface roughness for bio-implants during the course of their development. Peening is a mechanical working process that enhances the mechanical properties of a material by causing residual compressive stress caused by plastic deformation near its surface^[4]. Surface morphology can be improved by using water jet peening, a cutting-edge technique for superficial treatments. Deformation is caused by the surface treatment, which ultimately results in altered grain boundaries and increased strength^[5]. By efficiently modifying the surface and adding compressive residual stress to the subsurface, the waterjet peening (WJP) method can improve fatigue life without affecting the chemical characteristics of the alloys. The high-pressure water from the nozzle is separated into three zones: continuous (ideal for machining), droplet (good for peening), and dispersed (suitable for cleaning). Water jet peening process parameters are SOD- standoff distance, N_{TS} - nozzle traverse speed, W_{JP} -Water jet pressure, and several passes that are suitable candidates for the water jet peening operations. Muruganandam et al^[6] have conducted the effect of water jet process variables of peening on AZ31B Mg alloy. W_P , SOD, N_{TS} , and number of passes are chosen for the study. It was found that the microhardness of the AZ31B Mg alloy peened surface has significantly improved and decreased the surface roughness of the water jet peened AZ31B Mg alloy. M. Lieblich et al^[7] have analysed the high W_{JP} -peened biomedical

Ti6Al4V ELI alloy. The flat plate is peened with response factor roughness using abrasiveless high-pressure water jets. Water jet peened surface improved three microhardness and reduced the Ra. Azhari et al. [8] discovered showed increasing the number of water jet passes by more than twice reduced the surface roughness of peened surface.

In this present work, Mg-Zn alloy was peened by a water jet with process parameters of standoff distance (SOD), traverse speed (N_{TS}), water jet pressure (W_{JP}), and no of passes chosen for this study. The water jet peened surfaces were examined by microhardness, the roughness of peened surface with the interaction of SOD, and N_{TS} , with fixed parameters of W_{JP} . The surface characteristics are examined by SEM, and phase identification is checked by X-ray diffraction analysis, the water jet peened mg-Zn alloy is used by the biomedical industry to strengthen the material behavior.

Materials and Methods

Water jet Peening studies were conducted using a high-pressure WJ machine configuration (Aquajet G010, made by Aqua Jet Machine Tool, India). The basis material was a magnesium-zinc alloy. The peening operation takes place on a plate measuring 10×7×3 mm. Figure 1 represents the schematic view of water jet peening with Mg-Zn alloy. During water jet peening, input parameters are the number of passes, traverse speed (N_{TS}), standoff distance (SOD), and fixed water jet pressure (W_{JP}) selected based on the previous study as indicated in Table 1. The jet nozzle follows a straight-pass track, and the nozzle impingement angle is 90°. The average roughness (Ra) of the water jet-peened Mg-Zn alloy surface was assessed using an SJ-210 Mitutoyo surface tester, and the microhardness of the surface was examined using an Innovates 400TM series Vicker hardness tester. The five indentations were made on the cutting surface with the use of a diamond indenter, and the average indentation value was recorded. XRD analysis of unpeened and peened Mg-Zn alloy was taken by using a Malvern Panalytical diffractometer with a (2 θ , and 90°) 0.026 scan step size, $\lambda=1.5405\text{\AA}$. SEM morphology of peened surfaces is taken by the Thermo Scientific ApreoS high-resolution FESEM.

Effect of input variables on the roughness of water jet peened surfaces

Figure 2 represents the effect of water jet input variables on the (Ra-surface roughness) of the peened Mg-Zn alloy. In this analysis, SOD varies from 60 mm to 120 mm, and nozzle traverse speed is 1200 to 2100 mm/min. Increasing the SOD creates more divergence in the

water jet, with a high traverse rate and small steps over distance. From the figure, the SOD is 60 mm, the nozzle jet traverse speed is 1200 mm/min, with a W_{JP} of 140 MPa, and the number of passes is 2. The peened surface roughness was achieved at 6.918 μm . On the other hand, SOD is increased by 60 to 90 mm and N_{TS} is 1700 mm/min. With the same level of constant parameters, the roughness of peened surfaces is reduced by 28.12%, SOD is 120 mm, N_{TS} is 2100 mm/min, W_{JP} is 140 MPa, and the number of passes is 2. The R_a is reduced by 36.34%. From those observations, increasing the SOD with high traverse speed reduced the surface roughness of water jet-peened surfaces. As SOD grows, the water jet's impact energy is dispersed across a broader region, allowing for a more uniform peening effect ^[9]. A bigger SOD lets the water jet cover a greater area with more constant energy, resulting in lower surface roughness (R_a), and also the high traverse rates of the nozzle moving the designed peened surface move rapidly due to this interaction time between the material and waterjet being very short ^[10]. This phenomenon reduces the energy, and smooth surfaces are formed in the peened region.

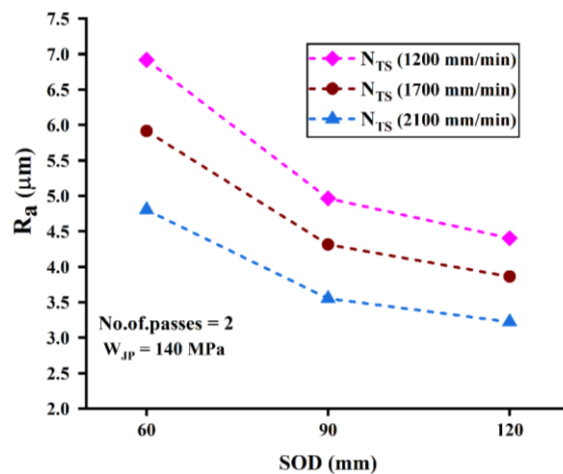


Figure 2. Effect of Surface roughness (R_a) of SOD Vs nozzle traverse speed (N_{TS})

Effect of input variables on the microhardness of water jet peened surfaces

Figure 3 illustrates how the microhardness of the peened magnesium zinc composition is affected by the water jet input factors. In this analysis, the N_{TS} was 1200 to 2100 mm/min, the SOD varied from 60 mm to 120 mm, the W_{JP} was fixed at 140 MPa, and the number of passes was 2. Fig. 3, it was represented that SOD is 60 mm to 120 mm, N_{TS} varies from 1200 to 2100 mm/min, and the microhardness of the water jet-peened Mg-Zn alloy increased by about 15.7% compared to

the unpeened surface. As the SOD increases from 60 to 120 mm, Increased jet pulse amplitude causes recurrent impact. Both surface and underlying layers undergo elastic-plastic deformations^[11]. As peened surfaces advance across the treated zone, they plastically deform and change its characteristics. Near-surface layers have the biggest work-hardening gradient. The water jet's intensity rises with standoff distance because water droplets disintegrate more between the nozzle and the target^[12]. It is possible to explain the consequence of the rise in hardness on the peened surface in accordance with the intensity of the water globules that are responsible for the phenomenon.

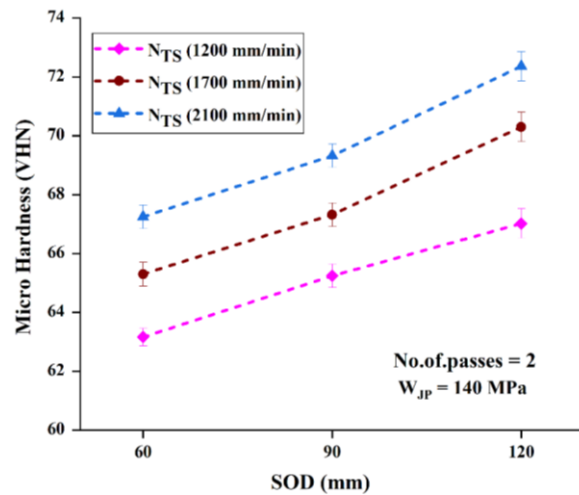


Figure 3. Effect of Microhardness of SOD Vs nozzle traverse speed (N_{TS})

SEM analysis of waterjet peened surface of Mg-Zn alloy

Fig. 4 shows the SEM analysis of the water jet-peened Mg-Zn alloy on the input parameters (SOD = 120 mm, N_{TS} = 2100 mm/min, W_{JP} = 140 MPa, and number of passes = 2). It is observed that waterjet-peened surfaces form scratches, pits, cavities, and rough surface regions due to the erosive action of the water jet over the material surface. The reason behind this is A water bubble made a quick impact on the surface of the substance, which resulted in the production of erosion. The section of the surface that is smooth is the one in which the rate of erosion is low and the likelihood of peening action is higher in this particular location. Multiple flaws around the groove indicated that it had been damaged repeatedly by the extended peening activity, resulting in deep grooves in the most peened location. Due to material surface stretching during peening, pits, and craters may indicate intergranular fracture, resulting in an increase in surface roughness.

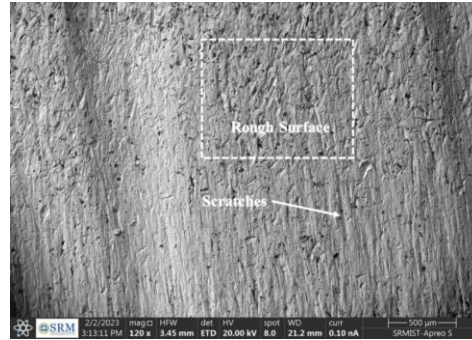


Figure 4. SEM image of Water jet Peened Mg-Zn Alloy (SOD = 120 mm, NTs = 2100 mm/min, W_{JP} = 1400 MPa)

XRay Diffraction analysis of unpeened and peened Mg-Zn Alloy

The XRD graph of base Mg-Zn and water jet-peened Mg-Zn alloy with different water jet variables are illustrated in Fig. 5. The Mg-Zn alloys are composed mainly of magnesium (α -Mg). The XRD pattern shows that water jet peening does not create new peaks or crystals on the specified sample surfaces. In comparison between the unpeened and peened surfaces, the XRD pattern confirmed that all the major peaks (Mg and Zn) are present in both the Mg-Zn and water jet-peened surfaces. In the water jet peened sample (SOD = 120 mm, N_{TS} = 2100 mm/min, W_{JP} = 140 MPa), this manifested itself as a significance of differences in the roughness of the Mg-Zn alloy. In conclusion, the selection of peened variables, such as the no.of.passes, SOD, WJP, and N_{TS} has significant importance in increasing the surface superiority of peened regions.

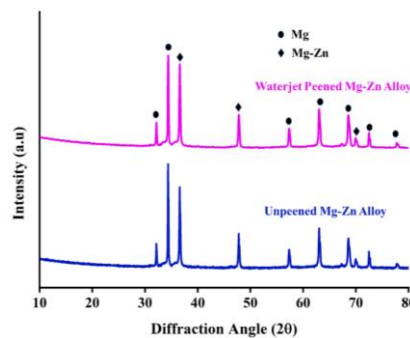


Figure 5. XRD pattern of unpeened and peened Mg-Zn alloy

Conclusions

In this experimentation analysis, the Mg-Zn alloy was water jet peened by varying the water jet input parameters, which are SOD, nozzle jet traverse speed, and fixed parameters of water jet pressure.

The experimentation techniques are followed by the double-pass jet. The following conclusions were reported:

- The surface roughness was reduced by 36.34%. From those observations, increasing the SOD with high traverse speed reduced the surface roughness of water jet-peened surfaces. As SOD grows, the water jet's impact energy is dispersed across a broader region, allowing for a more uniform peening effect.
- The microhardness (VHN) improved by 15.12% as the SOD increases to 60 mm to 120 mm.
- SEM analysis confirmed the waterjet peening erosion effects and smooth surface.
- XRD patterns confirm that an increase in the Ra of the double-peened process makes it more difficult for peaks to develop on the surface, which in turn makes it possible to reduce the peaks.
- Water jet peening of Mg-Zn suitable method for increasing the surface integrity.

References

- [1] Predko, P.; Rajnovic, D.; Grilli, M. L.; Postolnyi, B. O.; Zemcenkovs, V.; Rijkuris, G.; Pole, E.; Lisnanskis, M. Promising Methods for Corrosion Protection of Magnesium Alloys in the Case of Mg-Al, Mg-Mn-Ce and Mg-Zn-Zr: A Recent Progress Review. *Metals (Basel)*, 2021, 11 (7), 1133. <https://doi.org/10.3390/met11071133>.
- [2] Liu, X.; Sun, J.; Zhou, F.; Yang, Y.; Chang, R.; Qiu, K.; Pu, Z.; Li, L.; Zheng, Y. Micro-Alloying with Mn in Zn–Mg Alloy for Future Biodegradable Metals Application. *Mater Des*, 2016, 94, 95–104. <https://doi.org/10.1016/j.matdes.2015.12.128>.
- [3] Jaiswal, S.; Dubey, A.; Lahiri, D. In Vitro Biodegradation and Biocompatibility of Mg–HA-Based Composites for Orthopaedic Applications: A Review. *J Indian Inst Sci*, 2019, 99 (3), 303–327. <https://doi.org/10.1007/s41745-019-00124-w>.
- [4] Xie, L.; Wen, Y.; Zhan, K.; Wang, L.; Jiang, C.; Ji, V. Characterization on Surface Mechanical Properties of Ti–6Al–4V after Shot Peening. *J Alloys Compd*, 2016, 666, 65–70. <https://doi.org/10.1016/j.jallcom.2016.01.119>.
- [5] Lesyk, D. A.; Soyama, H.; Mordiyuk, B. N.; Dzhemelinskyi, V. V.; Martinez, S.; Khripta, N. I.; Lamikiz, A. Mechanical Surface Treatments of AISI 304 Stainless Steel: Effects on Surface

- Microrelief, Residual Stress, and Microstructure. *J Mater Eng Perform*, 2019, 28 (9), 5307–5322. <https://doi.org/10.1007/s11665-019-04273-y>.
- [6] Muruganandhan, R.; Mugilvalavan, M.; Thirumavalavan, K.; Yuvaraj, N. Investigation of Water Jet Peening Process Parameters on AL6061-T6. *Surface Engineering*, 2018, 34 (4), 330–340. <https://doi.org/10.1080/02670844.2017.1394564>.
- [7] Lieblich, M.; Barriuso, S.; Ibáñez, J.; Ruiz-de-Lara, L.; Díaz, M.; Ocaña, J. L.; Alberdi, A.; González-Carrasco, J. L. On the Fatigue Behavior of Medical Ti6Al4V Roughened by Grit Blasting and Abrasiveless Waterjet Peening. *J Mech Behav Biomed Mater*, 2016, 63, 390–398. <https://doi.org/10.1016/j.jmbbm.2016.07.011>.
- [8] Azhari, A.; Schindler, C.; Godard, C.; Gibmeier, J.; Kerscher, E. Effect of Multiple Passes Treatment in Waterjet Peening on Fatigue Performance. *Appl Surf Sci*, 2016, 388, 468–474. <https://doi.org/10.1016/j.apsusc.2015.11.195>.
- [9] Sourd, X.; Zitoune, R.; Hejjaji, A.; Salem, M.; Hor, A.; Lamouche, D. Plain Water Jet Cleaning of Titanium Alloy after Abrasive Water Jet Milling: Surface Contamination and Quality Analysis in the Context of Maintenance. *Wear*, 2021, 477, 203833. <https://doi.org/10.1016/j.wear.2021.203833>.
- [10] Xie, J.; Rittel, D. The Effects of Waterjet Peening on a Random-Topography Metallic Implant Surface. *European Journal of Mechanics - A/Solids*, 2018, 71, 235–244. <https://doi.org/10.1016/j.euromechsol.2018.03.022>.
- [11] Srivastava, M.; Hloch, S.; Gubeljak, N.; Milkovic, M.; Chattopadhyaya, S.; Klich, J. Surface Integrity and Residual Stress Analysis of Pulsed Water Jet Peened Stainless Steel Surfaces. *Measurement*, 2019, 143, 81–92. <https://doi.org/10.1016/j.measurement.2019.04.082>.
- [12] Mardi, K. B.; Dixit, A. R.; Pramanik, A.; Hvizdos, P.; Mallick, A.; Nag, A.; Hloch, S. Surface Topography Analysis of Mg-Based Composites with Different Nanoparticle Contents Disintegrated Using Abrasive Water Jet. *Materials*, 2021, 14 (19), 5471. <https://doi.org/10.3390/ma14195471>.

OPTIMIZING LASER MACHINING PARAMETERS FOR ENHANCED SURFACE QUALITY AND STRUCTURAL INTEGRITY OF MAGNESIUM ALLOY COMPOSITES

A. Arun¹, P. Vignesh², S. Santosh^{1*} and T.S. Srivatsan³

¹ *Department of Mechanical Engineering*
Sri Sivasubramaniya Nadar (SSN) College of Engineering
Old Mahabalipuram Road
Kalavakkam 603110, Tamil Nadu, INDIA

² *Centre for Sustainable Materials And Surface Metamorphosis*
Chennai Institute of Technology
Chennai-600069, Tamil Nadu, INDIA

³ *Department of Mechanical Engineering*
The University of Akron
Akron, Ohio 44325, USA

* Corresponding Author: santoshs@ssn.edu.in

Abstract

The machining of magnesium alloy-based composites, i.e., AZ31/YSZ, using the technique of laser technology does offer a noticeable advancement in the development of lightweight, high-strength materials for the purpose of selection and use in a spectrum of industrial applications. In this paper, the results of a recent research study aimed at investigating the laser machining process parameters for the magnesium alloy (AZ31) that is reinforced with yttria-stabilized zirconia (YSZ) particles with the primary focus on optimizing surface quality while concurrently minimizing thermal damage is presented and adequately discussed. The specifics of this novel research exercise did focus on a systematic evaluation of the effects of laser power (P) nozzle distance (N_D), and Nozzle cutting speed (N_S) on (i) surface roughness (SR), (ii) material removal rate (MRR), and (iii) microstructural integrity of the engineered magnesium alloy composite. The test results revealed that a precise control of these parameters can significantly enhance both the machining efficiency and surface finish while concurrently reducing the formation and presence of defects, such as fine microscopic cracks and the heat-affected zone. This novel research study does provide a valuable

insight into the laser machining characteristics of the engineered AZ31/YSZ composites, contributing to the progressive development of novel manufacturing techniques for performance-specific composite materials.

Keywords: Laser Machining; Magnesium Alloy (AZ31); Reinforcement; Yttria-Stabilized Zirconia (YSZ); Surface Quality; Thermal Damage; Material Removal Rate.

Introduction

Magnesium alloys have in recent years gradually evolved to become a major class of lightweight structural materials due on account of their outstanding features, which essentially includes (i) high specific strength, (ii) light weight, and (iii) ease of machining. Magnesium is the third most widely used structural metal, behind aluminum and steel [1]. The magnesium-based alloys and composites have unique properties such as (i) high strength, (ii) positive damping capacity, and (iii) low density. It is non-magnetic in nature and has effective elastic shielding [2]. Among the several magnesium alloys used in technical contexts, AZ31 (Mg-Al-Zn) is among the most prevalent. The term "AZ31" refers to the alloy's key alloying elements, namely aluminum (Al) at about 3% and zinc (Zn) at about 1%, with magnesium (Mg) making up the remainder [3].

To improve the performance of the AZ31 alloy, researchers have over the years made every effort to systematically investigate the potentially viable reinforcing techniques. The mechanical characteristics, wear resistance and thermal stability of magnesium alloys can be improved by adding ceramic reinforcements. Yttria stabilized zirconia (YSZ) is a promising ceramic material due on account of its high hardness, wear resistance, and high-temperature stability. Stabilized with YO_2 , the YSZ ceramic material maintains the cubic phase of zirconia at room temperature, while concurrently offering improved mechanical characteristics and thermal stability [4]. The YSZ can improve the AZ31 magnesium alloy by boosting hardness, wear resistance, and even corrosion resistance. The AZ31/YSZ composites often improve both the mechanical characteristics and tribological characteristics for the purpose of selection and use in a spectrum of advanced engineering applications. These composites are more easily manufactured using the technique of stir casting due essentially to their low cost and high production rate. Refinement in grain size, reduction in porosity and overall reinforcing uniformity are all enhanced by this method. The AZ31/YSZ

composites were applicable for usage in (i) the automotive sector to make lightweight components and brake components (ii) the Aerospace industry, (iii) biomedical applications, (iv) electronic and consumer goods, and (v) the defence and military applications [5]. The AZ31/YSZ composite has superior machinability, and is often a popular choice for components that need to be precision machined primarily because it can be machined quickly and with minimum wear on the tools.

Laser-based machining uses laser technology's precision, speed, and adaptability to machine metals, ceramics, and composites. The lasers can often generate complicated shapes, remove material faster, while concurrently providing more precision when cutting the AZ31 magnesium alloys. Laser-based machining often involves the use of an intensive laser beam to thermally eject the material from the surface of a workpiece [6]. Additive Manufacturing (AM), heat treatment, and water jet techniques, all make use of aluminum, which possesses a combination of unusual qualities or characteristics. In addition, a mixture of magnesium and aluminum can provide exceptional toughness, in addition to providing high flexibility and good resistance to corrosion. The machining surface quality of the AZ31 magnesium alloy was also assessed by Lopez et al. [7]. In their experiment, they found that decreasing the nozzle cutting speed (N_s) did reduce the cutting surface quality. Demir et al. [8] examined how to cut AZ31 Mg alloy stents using a continuous wave laser. The primary aim of this investigation was to study how the laser interacted with the AZ31/Mg alloy. This independent study confirmed pulse duration to be the most significant element, which did improve the machined quality of the surface. Wang et al. [9] studied laser machining of the magnesium alloys utilizing both air and water medium, as well as an interplay of the laser factors. Their independent findings clearly revealed that immersion of the chosen magnesium alloys did improve overall machine quality to the same extent as the air medium. Guo et al. [10] examined the influence of fiber laser machining on the AZ31B Mg alloy using both the empirical and the computational method. Based to these findings, the highest possible temperature of the AZ31B Mg can be enhanced by increasing the time of machining to reducing the nozzle cutting speed. In their independent study on laser cutting of the AZ3Mg alloy, Demir et al. [11] found that high temperatures during melting did contribute to reducing the cutting quality while concurrently increasing the surface roughness.

From a careful study of the published literature on machined AZ31 Mg-based alloys, in this present study the AZ31 Mg alloy and yttria-stabilized zirconia (YSZ) composite developed using the

technique of ultrasonic-assisted stir casting process, and the manufactured AZ31 Mg/YSZ composite were precision machined using fiber laser machining with the key input variables being the following: (i) laser power (P), (ii) nozzle cutting speed (N_s), and (iii) nozzle distance (N_D), with the responses being (i) surface roughness (SR), and (ii) material removal rate (MRR). This investigation is based on use of the RSM-BBD technique. The fiber laser parameter interaction for the developed AZ31Mg/YSZ composite cutting quality study was based on an experimental study aimed at minimizing the surface roughness, heat-affected zone, and the presence of fine microscopic cracks in the machined region.

Materials and Methods

The study utilized AZ31 magnesium alloy, produced by Exclusive Magnesium Pvt. Ltd. [Hyderabad, Andhra Pradesh, INDIA] as the matrix material. The yttria-stabilized zirconia (YSZ) reinforcing material was acquired from Oerlikon Metco. [USA]. The selection of yttria-stabilized zirconia (YSZ) as the reinforcement was based on its exceptional hardness and thermal stability.

Fabrication of AZ31/Yttria-stabilized Zirconia Composite by Ultrasonic-Assisted Squeeze Casting (UASC):

The UASC process essentially involved heating the AZ31 alloy to a temperature of 700 °C in an atmosphere of inert argon until it becomes molten. Afterwards, the liquid alloy was agitated for a period of 15 minutes using a tungsten stirrer. The pre-heated yttria-stabilized zirconia (YSZ) particles, at a temperature of 250 °C, were then introduced to the molten alloy and constantly agitated for another 10 minutes to ensure that they were evenly dispersed [12]. Subsequently, the temperature was reduced to 500 °C to attain the semi-solid state. This was followed by stirring. This procedure does ensure a complete breakdown of any particle agglomeration. Afterwards, the temperature of the molten material was raised to 720 °C, and an ultrasonic treatment was conducted using acoustic waves with a power of 2.5 kW. The procedure involved the use of a titanium probe to prevent an aggregation of the reinforcing particles and to concurrently aid in dispersing the gas bubbles that were trapped. Finally, the mixture of components was put into a warm steel mold that measured diameter of 50 mm and 150 mm in length. The mold was heated beforehand for the purpose of ensuring rapid solidification and 50 MPa pressure was supplied. Ultimately, the as-cast ingots were extracted from the mold. Following solidification of the composite melt, samples for microstructural analysis were obtained by cutting the as-cast composite

ingot using a wire-cut EDM machine. The microstructural samples were then manually polished using SiC impregnated sandpaper [600 grit, 800 grit, and 1200 grit] and then polished using diamond paste to obtain a near mirror-like surface finish. The microstructure and worn surfaces of the AZ31/5% YSZ composite samples were analysed in scanning electron microscope [Model: Carl-Zeiss].

Fiber Laser Machining setup for the AZ31Mg/YSZ composites

The AZ31Mg/YSZ composite was cut using a high-power fiber laser (Trumpf 3060) and a copper-based conical nozzle was used. Nitrogen-assisted gas was used in the experiment. It also serves as a cooling agent, helping to dissipate the heat that is generated during the laser machining process. Thermal distortion is minimized as a result of this cooling process, and the material is kept from either distorting or melting to an excessive degree. Because nitrogen gas is inert, it contributes to the establishment of a protective environment on the machined region, thereby contributing to reducing or preventing the formation and presence of oxides. A graphical illustration of the fiber laser setup and the AZ31Mg/YSZ composite is as shown in **Figure 1**. The fiber laser input settings and levels are highlighted in **Table 1**.

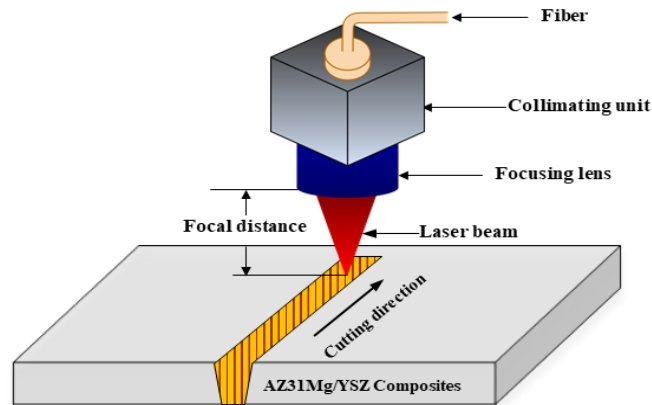


Figure 1. Schematic illustration of fiber laser cutting of the AZ31Mg/YSZ composite

Table 1. Fiber laser input variables levels and their range

Input process variables	Symbol	Unit	Levels		
			-1	0	1
Laser Power	P	W	500	750	1000
Nozzle cutting speed	N _S	m/min	1.5	2.25	3
Nozzle distance	N _D	Mm	0.5	1	1.5

The primary objective of the study was to improve the MRR and to concurrently minimize the SR without appreciably affecting the characteristics of the chosen material. The set of 15 experiments, using a combination of three input factors specific to laser-based machining, using the RSM-BBD technique is provided in **Table 2**. The material removal rate (MRR) was compute by the weight reduction both before machining and after machining using Equation 1 [13]. The surface roughness (SR) value was measured using a 2-D roughness tester [Model: Mitutuyo SJ-210]. The arithmetic average value for surface roughness (SR) was then recorded.

$$MRR = \frac{W_b - W_a}{\rho \times t} \text{ (mm}^3\text{/min)}$$

In this equation:

cut,

sample (mm),

(g/mm³).

W_b is Weight of sample before cutting,

W_a is weight loss of the sample after the laser

t is thickness of the AZ31Mg/YSZ composite

ρ is the Density of AZ31Mg/YSZ composite

Table 2. Experimental run for the fiber laser machining

Run	Input variables			Output	
	Power (P)	Cutting speed (N _s)	Nozzle distance	MRR	SR
	W	m/min	mm	mm ³ /min	μm
1	750	3	0.5	4.713	3.881
2	1000	1.5	1	5.292	4.673
3	500	1.5	1	3.805	3.745
4	1000	2.25	0.5	5.432	4.415
5	750	1.5	1.5	4.48	3.993
6	750	2.25	1	4.515	3.985
7	750	2.25	1	4.51	4.033
8	1000	3	1	5.215	4.548
9	750	3	1.5	4.278	3.785
10	1000	2.25	1.5	5.213	4.562
11	750	1.5	0.5	4.514	3.815
12	500	3	1	3.964	3.713
13	500	2.25	0.5	4.003	3.654
14	750	2.25	1	4.502	3.989
15	500	2.25	1.5	3.801	3.575

Result and Discussions

Characterization of the AZ31/YSZ As-cast Composite

The SEM image showing the microstructure of the AZ31 magnesium alloy composite reinforced with 5 % Yttria-stabilized zirconia (YSZ) particles is shown in **Figure 2**. The microstructure is characterized by an even distribution of the YSZ particles throughout the matrix of the AZ31 alloy. The Yttria-stabilized zirconia (YSZ) particles, denoted by yellow arrows, exhibit a near-uniform dispersion, thereby revealing efficient processing of the composite material that

guarantees optimal reinforcement through the matrix. The AZ31 matrix did display a near uniform grain structure, suggesting that it underwent controlled solidification following the use of secondary processes, such as either rolling or extrusion. These processes result in the presence of smaller grains with a concomitant improvement of noticeable order in the mechanical properties. The interface between the yttria-stabilized zirconia (YSZ) particles and the magnesium alloy metal matrix appears to be tightly bonded, with no visible gaps or separation. This suggests a strong interfacial bonding, which is essential for the transfer of the load during mechanical testing. Furthermore, the noticeable absence of secondary phases, or porosity, does indicate a composite material of superior quality with minimal number of imperfections.

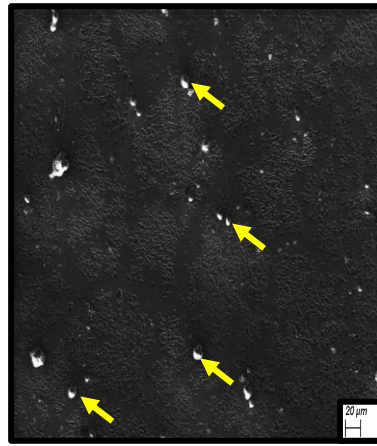


Figure 2. Scanning electron micrograph of the AZ31/5% YSZ composite

Statistical analysis (ANOVA) of MRR and SR

The ANOVA outputs for the MRR and SR are summarized in **Table 1**. The p values for both MRR and SR are < 0.01 , which does make the measurements noteworthy. It suggests that a minimum of one of the factors that are independent has a considerable impact on the response factors. The F values for both the MRR and the SR are 870.32 and 608.19 [with 95% confidence level]. The developed model was significant in level, the R^2 , adj R^2 , Predicted R^2 , and Adequate Precision for the response of material removal rate was 99.94%, 99.82 %, 99.01 %, and 87.081 %. Similarly for the surface roughness (SR) it was 99.1%, 99.76 %, 99.72 %, and 74.56%. From the ANOVA results the adequate precision in value is more than the (S/N) ratio of 4, which means the selected model was both desirable and suitable for

use in optimization techniques. The regression equation for MRR and SR developed model is given by Equation 2 and Equation 3.

Table 2. ANOVA responses for MRR and SR

Source	Sum ²		F-value		p-value		
	MRR	SR	MRR	SR	MRR	SR	
Model	4.08	1.7705	870.32	608.19	< 0.0001	< 0.0001	Significant
P (W)	3.89	1.5400	7472.69	4761.27	< 0.0001	< 0.0001	
N _S (mm/min)	0.0008	0.0119	1.5	36.78	0.2755	0.0018	
N _D (mm)	0.099	0.0028	190.17	8.52	< 0.0001	0.0338	
P × N _S	0.0139	0.0023	26.74	6.98	0.0036	0.0459	
P × N _D	0.0001	0.0127	0.1388	39.13	0.7248	0.0015	
N _S × N _D	0.0402	0.0187	77.21	57.82	0.0003	0.006	
P ²	0.0286	0.1120	54.92	346.20	0.0007	< 0.0001	
N _S ²	0.0029	0.0001	5.56	0.44	0.0649	0.5352	
N _D ²	0.0009	0.0565	1.65	174.76	0.2553	< 0.0001	
Residual	0.0026	0.0016					
Lack of Fit	0.0025	0.0001	19.51	0.0442	0.0491	0.9845	In significant
Pure Error	0.0001	0.0015					
Cor Total	4.08	1.7721					
				R ²	0.9994	0.9991	
				Adj (R ²)	0.9982	0.9976	
				Pre (R ²)	0.9901	0.9972	

$$\begin{aligned} \text{MRR (mm}^3/\text{min)} = & 2.052 + 0.0014 \times P + 0.7405 \times N_s + 0.2825 \times \\ & N_D - 0.000314 \times (P \times N_s) - 3.4e^{-05} \times (P \times N_D) - 0.2673 \times (N_s \times \\ & N_D) + 1.408e^{-06} \times P^2 + -0.0497 \times N_s^2 + 0.061 \times \\ & N_D^2 \end{aligned} \quad (2)$$

$$\begin{aligned} \text{SR (}\mu\text{m)} = & 3.4904 - 0.00258 \times P + 0.2757 \times N_s + 1.099 \times N_D - \\ & 0.00012 \times (P \times N_s) + 0.00045 \times (P \times N_D) - 0.18233 \times (N_s \times N_D) + \\ & 2.786e^{-06} \times P^2 - 0.0110 \times N_s^2 - 0.494917 \times N_D^2 \end{aligned} \quad (3)$$

Analysis of Material Removal Rate on Fiber Laser Input Parameters

The 3-D surface plot of material removal rate (MRR) on a machined AZ31Mg/YSZ composite with laser input parameters is shown in **Figure 3 (a–b)**. The effect of laser power (P) and nozzle traverse speed (Ns) on MRR of the fiber laser-machined AZ31Mg/YSZ is shown in **Figure 3 (a)**. It indicates that the maximum MRR is 5.448 mm³/min, which is achieved for a high-level laser power (P = 1000 W), a nozzle travel speed of 3 m/min, and a nozzle distance of 0.5 mm. The reason behind this is that rapid vaporization or melting can be easily achieved by increasing the laser power, which does help in the transfer of more energy to the substance. A greater MRR is the end result of faster material ablation, or cutting, that is made possible by an increased energy density. The AZ31 magnesium alloy is a reflective material, and during laser machining, the intensity of laser interaction on the alloy does prevent the occurrence of oxidation and other hazardous effects. The inert gas, i.e., nitrogen (N₂), does aid in preventing oxidation, which does happen quickly. This can and does essentially aid in the following: (i) speed up the removal of material, (ii) provide cleaner cuts, and (iii) lessen the possibility of oxides accumulating on the surface. On the other hand, material removal can be reduced by 29.80% by decreasing the laser power to 500 W, cutting speed (Ns) to 1.5 m/min, and nozzle distance (N_D) to 0.5 mm. With lower laser power and minimum cutting speed delivered to the AZ31Mg/YSZ composite, the energy delivered may not be adequate to efficiently melt, or evaporate, the material at a fast enough rate, resulting thereby in a slower cutting process and noticeable reduction in material removal rate (MRR) [15]. The amount of time that the laser beam spends interacting with the material is increased when the nozzle cutting speed (N_s) was decreased. While this might appear to enhance material removal, in reality, it often leads to inefficient usage of the energy. The longer exposure can cause excessive heating, resulting in

melting of the material instead of efficient ablation, thereby reducing the material removal rate (MRR).

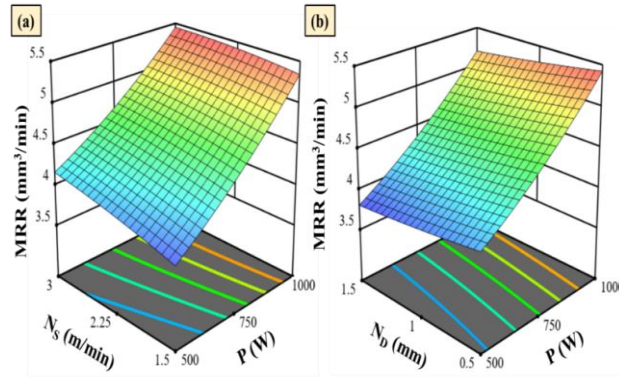


Figure 3 (a-b). 3D interaction plot for the MRR (mm³/min)

Analysis of Surface Roughness on Fiber Laser Input Parameters

The 3-D surface map of surface roughness (SR) on a machined AZ31Mg/YSZ composite is shown in **Figure 4 (a-b)**. The combination effects of fiber input variables on surface roughness of the machined regions of the AZ31Mg/YSZ composite is shown in **Figure 4(a)**. It was identified that maximum value of the surface roughness was 4.667 μm , with input variables of laser power ($P=1000$ W), nozzle speed (N_s) of 1.5 m/min, and a nozzle distance of (N_d) of 1 mm. The surface roughness (SR) of the cutting edge was gradually minimised when the laser power was reduced by various levels. The cutting speed (3 m/minute to 1.5 m/minute) had a greater effect on roughness than laser power (P). The surface roughness (SR) was found to be 3.712 μm for a nozzle speed of 3 m/minute and at a laser power (P) of 500 W. Increasing the nozzle speed (N_s) from 1.5 m/minute to 3 m/minute did decrease the value of surface roughness (SR) by 20.4 percent. In **Figure 4 (b)** is shown an interplay between the laser power (P) and the nozzle distance (N_d). When the gap between the nozzle and the surface was increased from 0.5 mm to 1.5 mm, there was a noticeable improvement in the SR. This raise was further influenced by laser power (P), which ranged from 500 W to 1000 W. By adjusting the nozzle distance, the laser beam was able to stimulate the surface of the AZ31Mg/YSZ composite. This led to a larger cut size, and the high laser power (P) did result in an observable increase in the ablation rate. Additionally, a material with high deposition spatters around the cutting region was removed, thereby contributing to increasing the surface roughness (SR) [16].

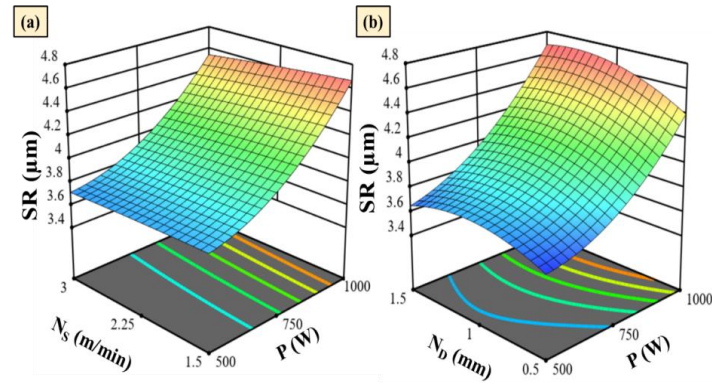


Figure 4 (a-b). 3D surface plot for SR (μm)

Perturbation analysis for MRR and SR

The perturbation curve for fiber laser input variables affecting the MRR and SR of the machined AZ31Mg/YSZ composite sample is shown in Figure 5 (a,b). Based on the perturbation curves, it is clear that a variation in the variables does result in noticeable patterns for the output values. The perturbation curve for the material removal rate (MRR) with various input variables, such as: (i) laser power (P), (ii) nozzle speed (N_s), and nozzle distance (N_D) is shown in Figure 5(a). It was found that both laser power (P) and nozzle speed (N_s) when raised from the reference points did increase the material removal rate (MRR) indicating a positive trend. Similarly, the curve for N_D does reveal an observable decrease in the material removal rate (MRR).

Figure 5 (b) represents the surface roughness (SR) in the perturbation curve for the variation in laser parameters. Laser power, nozzle distance (N_D) increases the surface SR increases. The high SR does affect the surface quality due to high energy interaction between the work materials. More spatters are formed around the cutting region, thereby affecting quality of the cut. With an increase in the laser power, surface roughness can decrease, resulting in a smoother surface, but upon reaching an appropriate power level, it can climb, indicating excessive power. The surface roughness decreases with decreasing cutting speed up to a certain point, after which a further decrease in the cutting speed does result in an increase in roughness due to thermal-induced damage. The curve for nozzle distance (N_D) does have the tendency to show a decreasing trend in surface roughness with a decrease in the nozzle distance (N_D), indicative of a smoother surface up to a certain point.

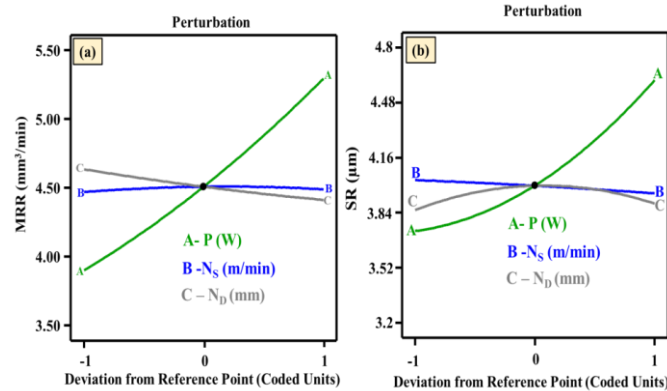


Figure 5. Perturbation analysis curves for:
(a) Material Removal Rate, and
(b) Surface Roughness

Optimization of Fiber Laser Input Parameters for the AZ31Mg/YSZ alloy.

The ramp function as a set of optimal process parameters for fiber laser input variables is shown in **Figure 6(a)**. The goal of the optimization technique was to achieve a high MRR and minimum SR on the machined AZ31mg/YSZ composite. The optimum values were found based on multi-objective desirability techniques for the fiber laser parameters, i.e., (i) laser power (P) is 810 W, (ii) nozzle speed (N_s) of 3 m/minute, and (iii) nozzle distance (N_D) of 0.5 mm. The response values for the optimized condition were found to be a MRR (material removal rate) of 4.877 mm³/min and a SR (surface roughness) of 3.975 μm. The combined desirability value was achieved at 0.776.

Based on the optimization results, a confirmation test was conducted, and the values and responses are summarized in **Table 4**. It was confirmed that the predicted value and the experimental value differed in percentage by less than 5. This then confirms that the optimized parameters are suitable for fiber laser machining of the chosen and studied AZ31Mg/YSZ composites.

Table 4. Confirmation analysis of Predicted value and Experimental value for fiber laser machining of the AZ31Mg/YSZ composites

Fiber laser-optimized level variables			Predicted value		Experimental value		Error %	
P (W)	N _s (m/min)	N _D (mm)	MRR (mm ³ /min)	SR (μm)	MRR (mm ³ /min)	SR (μm)	MRR (mm ³ /min)	SR (μm)
810	3	3.3	4.877	3.974	5.013	3.853	2.712	3.044

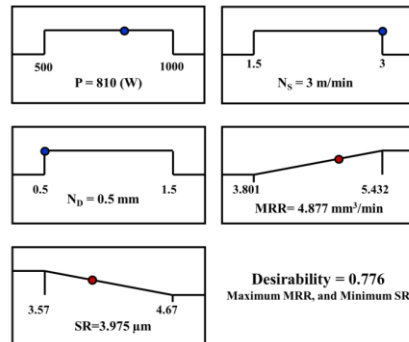


Figure 6. Ramp plot for fiber laser input variables

Conclusions

1. The AZ31Mg/5%YSZ composites were fabricated using the ultrasonic-assisted strip casting techniques, and the Yttria-stabilized zirconia (YSZ) particles were used as a stabilizer to improve strength of the composites.
2. Scanning electron microscopy observation of the microstructure was used to confirm the presence of AZ31Mg and YSZ particles in the composite microstructure..
3. Fiber laser machining of the AZ31 Mg/ YSZ composites, based on the RSM-BBD technique was conducted using fiber laser input parameters, such as (i) laser power (P), (ii) nozzle traverse speed (Ns), and (iii) Nozzle distance (N_D). The responses, i.e., MRR and SR were analysed.
4. ANOVA results confirm laser power to be the most significant variable for enhancing MRR and obtaining better surface quality. 3D surface plots revealed that the MRR was improved by increasing the laser power (P), and nozzle cutting speed

- (N_S). The SR was reduced by the lower nozzle distance (N_D) and minimum laser power (P).
5. Fiber laser optimized results were obtained by maximum MRR and SR the input variables are P = 810 W, N_D = 0.5 mm, and N_S = 3 m/minute. The responses of predicted values are a MRR = 4.877 mm³/min, and SR = 3.974 μm.
 6. The tests confirmed that both the predicted value and actual value are acceptable in their range.

References

1. Prasad, SV Satya, S. B. Prasad, Kartikeya Verma, Raghavendra Kumar Mishra, Vikas Kumar, and Subhash Singh. "The role and significance of Magnesium in modern day research-A review." Journal of Magnesium and alloys 10, no. 1 (2022): 1-61.
2. Asar, A. and Zaki, W., 2024. A comprehensive review of the mechanisms and structure of interpenetrating phase composites with emphasis on metal-metal and polymer-metal variants. Composites Part B: Engineering, p.111314.
3. Predko, P., Rajnovic, D., Grilli, M.L., Postolnyi, B.O., Zemcenkovs, V., Rijkuris, G., Pole, E. and Lisnanskis, M., 2021. Promising methods for corrosion protection of magnesium alloys in the case of Mg-Al, Mg-Mn-Ce and Mg-Zn-Zr: A recent progress review. Metals, 11(7), p.1133.
4. Bakhsheshi-Rad, H.R., Hamzah, E., Ismail, A.F., Daroonparvar, M.M.A.M., Yajid, M.A.M. and Medraj, M., 2016. Preparation and characterization of NiCrAlY/nano-YSZ/PCL composite coatings obtained by combination of atmospheric plasma spraying and dip coating on Mg–Ca alloy. Journal of Alloys and Compounds, 658, pp.440-452.
5. Rakshith, M. and Seenuvasaperumal, P., 2021. Review on the effect of different processing techniques on the microstructure and mechanical behaviour of AZ31 Magnesium alloy. Journal of Magnesium and Alloys, 9(5), pp.1692-1714.
6. Arun, A., Rajkumar, K. and Santosh, S., 2023. Fiber laser cutting study on ternary NiTiV shape memory alloy. Materials and Manufacturing Processes, 38(14), pp.1745-1754.
7. García-López, E., Ibarra-Medina, J.R., Siller, H.R., Lammel-Lindemann, J.A. and Rodriguez, C.A., 2018. Surface finish and

back-wall dross behavior during the fiber laser cutting of AZ31 magnesium alloy. **Micromachines**, 9(10), p.485.

8. Demir, A.G.; Previtali, B.; Ge, Q.; Vedani, M.; Wu, W.; Migliavacca, F.; Bestetti, M. *Biodegradable magnesium coronary stents: Material, design and fabrication.* **Int. J. Comput. Integrated Manuf.** 2014, 27, 936–945.
9. Wang, H., Xu, Y., Liu, J., Hu, Q., Wang, X., Ren, N., Zhou, W. and Ren, X., 2021. *Magnet-assisted laser hole-cutting in magnesium alloys with and without water immersion.* **Journal of Manufacturing Processes**, 61, pp.539-560.
10. H. Guo, J. Li, M. He, X. Wu, T. Sun, *Fiber laser cutting of AZ31 magnesium alloy: numerical and experimental investigation* (Applied Optics and Photonics China (AOPC2015)), SPIE, 2015.
11. A.G. Demir, B. Previtali, C.A. Biffi, *Fibre Laser Cutting and Chemical Etching of AZ31 for Manufacturing Biodegradable Stents*, **Adv. Mater. Sci. Eng.** 2013 (2013), 692635.
12. Vignesh, P., Ramanathan, S. & Ashok kumar, M. *Evaluation of the Wear Performance of Novel Titanium/Hydroxyapatite-Reinforced Mg–3Zn Hybrid Composites Fabricated by Squeeze Casting.* **J Bio Tribo Corros** 9, 38 (2023). <https://doi.org/10.1007/s40735-023-00756-7>
13. Balasubramaniyan, C., Rajkumar, K. & Santosh, S. *Fiber Laser Cutting of Cu–Zr Added Quaternary NiTi Shape Memory Alloy: Experimental Investigation and Optimization.* **Arab J Sci Eng** 48, 3665–3679 (2023). <https://doi.org/10.1007/s13369-022-07256-9>.
14. Khdair, A.I. and Melaibari, A.A., 2023. *Experimental evaluation of cut quality and temperature field in fiber laser cutting of AZ31B magnesium alloy using response surface methodology.* **Optical Fiber Technology**, 77, p.103290.
15. Jana, S., Olszta, M., Edwards, D., Engelhard, M., Samanta, A., Ding, H., Murkute, P., Isgor, O.B. and Rohatgi, A., 2021. *Microstructural basis for improved corrosion resistance of laser surface processed AZ31 Mg alloy.* **Corrosion Science**, 191, p.109707.
16. Fajardo, S., Miguélez, L., Arenas, M.A., de Damborenea, J., Llorente, I. and Feliu, S., 2022. *Corrosion resistance of pulsed laser modified AZ31 Mg alloy surfaces.* **Journal of Magnesium and Alloys**, 10(3), pp.756-768.

ANALYSIS OF ABRASIVE AQUA JET MACHINING CHARACTERISTICS OF A HYBRID COMPOSITE USING WASTE WIRE- REINFORCED CARBON FIBER

**C. Balasubramaniyan¹, S. Santosh² * A. Arun² and
T.S. Srivatsan³**

¹ *Department of Mechanical Engineering*
Sri Venkateswara College of Technology
Sriperumbudur 602105, Tamil Nadu, INDIA

² *Department of Mechanical Engineering*
Sri Sivasubramaniya Nadar (SSN) College of Engineering
Old Mahabalipuram Road
Kalavakkam 603110, Tamil Nadu, INDIA

³ *Department of Mechanical Engineering*
The University of Akron
Akron, Ohio 44325, USA

* Corresponding Author: santoshs@ssn.edu.in

Abstract

In today's engineering landscape, lightweight composite materials are increasingly sought after, yet their production often remains to be a challenge. This study explores a hybrid composite material, where carbon fiber is reinforced with waste wire taken from the Electrical Discharge Machining (EDM) process, specifically brass wire. The composite materials were created with varying weight fractions of used wire from the electric discharge machining process (5%, 10%, and 15%) along with a carbon fiber reinforced polymer matrix. The machinability of these hybrid composites was examined using abrasive aqua jet machining, with the key variables, namely (i) aqua jet pressure (A_{JP}), (ii) abrasive flow rate (A_{FR}) and (iii) nozzle traverse speed (N_{TS}), being adjusted. The machining outcomes were evaluated in terms of (i) kerf taper (K_T), and (ii) surface roughness (R_a). The purpose of this investigation was to identify the optimal process variables for effective abrasive aqua jet cutting of waste wire-reinforced carbon fiber polymer (CFRP) composites. Both the numerical technique and graphical optimization technique were used to

determine the best machining conditions. The results revealed that a higher aqua jet pressure and moderate traverse speed did minimize both surface roughness (R_a) and kerf taper (K_T). Mechanical properties, to include tensile strength and Shore D hardness, were also enhanced, particularly for the 10.0 weight percent incorporation of the used wire. The tensile properties were determined using a digital universal testing machine (UTM). The hybrid composite does show much promise for applications in protective casings for electronic devices and for certain aerospace structures.

Keywords: Carbon Fiber, Abrasive Aqua Jet, waste EDM wire, tensile test, Hardness. Sustainability.

Introduction

Rapid advancements in the domain specific to composite materials have significantly impacted various industrial applications, especially in those sectors that necessitate the need for lightweight and high-strength components. Hybrid composites, which combine various types of fibers, have engendered considerable attention due on account of their enhanced mechanical properties and versatility [1]. Hybrid composites, which combine two or more different types of fibers, have emerged as a prominent category due to their enhanced mechanical properties and tailored performance characteristics. Among these, carbon fiber reinforced composites (CFRCs) are particularly noteworthy for their excellent specific strength [σ/ρ] and stiffness, making these materials both necessary and essential for aerospace, automotive, and other high-performance-critical applications [2]. Among these, waste electric discharge machining (EDM) wire-reinforced carbon fiber composites have emerged as a promising candidate due to their sustainability and cost-effectiveness. Carbon fibers combined with wire reinforcements, do offer a potential solution to the numerous challenges associated with carbon fiber coupled with the critical need for environmentally friendly manufacturing processes. However, both manufacturing and machining of these advanced composites does present considerable challenges. Traditional machining methods, such as drilling and milling, often result in the following: (i) poor surface finish, (ii) rapid tool wear, and (iii) high operational costs due on account of the hardness and abrasiveness of the carbon fibers [3]. As a result, there is an increasing interest in alternative machining techniques that can effectively address these challenges

One such technique is abrasive aqua jet machining (AWJM). This is basically an innovative technology that uses a high-velocity jet

of water mixed with abrasive particles to cut through the hybrid composite. Abrasive aqua jet machining (AWJM) is predominantly advantageous for machining composite materials primarily because it minimizes thermal effects and mechanical stresses while concurrently reducing the likelihood of delamination and matrix cracking [4]. This technique also provides the flexibility to cut complex shapes with high precision and minimal tool wear, which are critical attributes for working with advanced composites. Despite its advantages, the machining characteristics of hybrid composites, especially those incorporating waste wire-reinforced carbon fibers, remain underexplored. The interplay between the abrasive grains, the water jet, and the composite component creates unique challenges and opportunities for optimising the machining settings to produce desirable outputs. [5].

Recent research has explored the application of abrasive aqua jet machining (AWJM) to a variety of composite materials. However, there is limited information available on its efficacy when applied to the hybrid composites, especially those incorporating recycled materials. The use of waste wire-reinforced carbon fibers (WRCF) represents a promising direction for sustainability in composite manufacturing. The wire reinforced carbon fibers (WRCF) not only offer a potential solution for the easy disposal of carbon fiber waste but also has the potential for reducing material cost and concurrently enhance the mechanical characteristics of the resultant composites [6]. Despite these advantages, the machining characteristics of hybrid composites that incorporate wire reinforced carbon fibers (WRCF) remain underexplored. This research aims to fill this gap by investigating the properties of abrasive aqua jet cutting of the hybrid composites made from waste wire-reinforced carbon fibers. By examining the key factors, such as (i) kerf taper, (ii) surface finish, and (iii) influence of different machining parameters, this study seeks to enhance the efficiency of AWJM while concurrently optimizing the machining process of the hybrid composite. The results of this investigation hold significant implications for the future of both composite manufacturing and recycling, while also offering potential pathways for more sustainable and efficient production techniques in various high-performance applications.

Experimental Procedure

Materials

The waste electric discharge EDM wire, with a diameter of 0.5 mm, is sourced from a Wire EDM machine [Model: YCM W350].

The carbon fiber and epoxy resin were provided by Suntech Polymers and Fibers [India]. The preparation of the waste wire-reinforced carbon fiber laminate is shown in **Figure 1**.

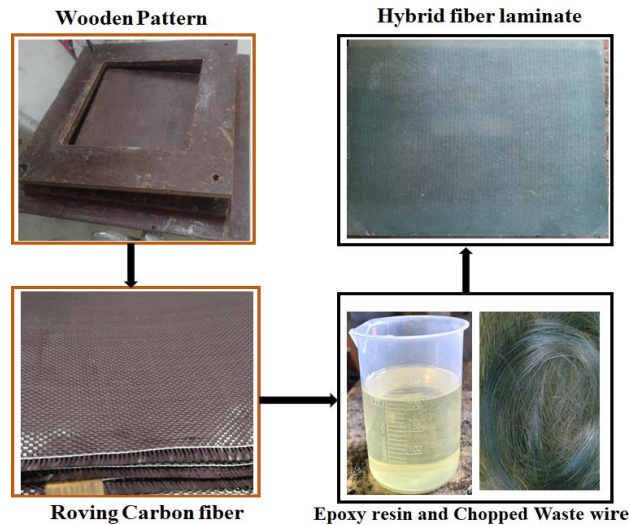


Figure 1. Fabrication of the hybrid laminate

Fabrication of Composite

The hybrid composites were fabricated using the hand layup method, incorporating varying amounts of waste wire reinforcement [ranging from 5 to 15 % of weight]. The specific weight ratios of the waste electrical discharge machining (EDM) wire reinforcements are listed in **Table 1**. Wooden molds were used for the fabrication process. The mold surfaces were pre-coated with wax so as to ensure easy removal of the finished laminate.

Table 1. Percentage of Waste EDM wire (W_S -Wire) reinforcement.

Samples	W_S -Wire -5	W_S -Wire -10	W_S -Wire -15
Percentage (%)	5	10	15

To cure the epoxy resin, approximately 1% catalyst and an accelerator were added. The longitudinal alignment of the fibers in the composite was maintained, thereby giving the material unidirectional properties. Epoxy resin mixed with the waste wire was applied to the carbon fiber layers, creating samples with waste wire contents of 5 weight percent, 10 weight percent, and 15 weight percent, designated as (i) W-Wire-5, (ii) W-Wire-10, and (iii) W-Wire-15. The composite laminates were

then cured at room temperature for 24 hours using a 15 kg load. This resulted in sizes of 250 mm × 250 mm × 5 mm.

Tensile test and Hardness Test

The specimens used to determine the ultimate tensile strength were cut in conformance with specifications provided in the ASTM D3039 standard, with the chosen composite containing 5 weight %, 10 weight %, and 15 weight % of waste wire reinforcement. The observed values were recorded. Additionally, the Shore Hardness of the hybrid composite, which measures the resistance of the material to indentation, was evaluated. A Shore Hardness gauge, equipped with a spring-loaded needle, was used for this measurement. The needle is pressed against the composite, and the corresponding hardness indicated by the needle of the gauge was recorded.

AWJM of Hybrid composite

The fabricated waste wire-reinforced laminates were machined utilizing an AWJ Machine [Type: Aqua Jet CNC]. The setup includes an abrasive hopper, a regulator valve, and a workspace with a size of 1250 mm x 3000 mm. Throughout both the trials and the machining operations, the nozzle was regularly inspected to maintain consistent performance. The abrasive aqua jet machining (AWJM) setup is shown in **Figure 2**. Table 2 shows the three categories of cutting factors that will be examined. The size of the reinforcing particles was standardized using an 80 mesh (garnet), and the diameter of the nozzle [1.2 mm] was kept constant.

Table 2. Input Variables for Abrasive aqua jet machining (AWJM)

Machining variables	Units	Levels		
Aqua jet pressure (A_{JP})	MPa	200	300	400
Nozzle traverse speed (N_{TS})	mm/min	150	200	250
Abrasive flow rate (A_{FR})	g/sec	3	4	5

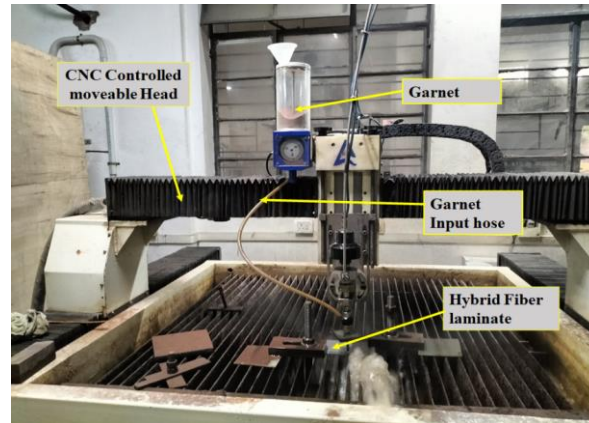


Figure 2. Aqua Jet machining setup loaded with hybrid composite

The adopted input variables were consistent with standard literature and industrial references. The design of expert software was utilized and it did generate a combination of 17 variable input parameters, which are shown in **Table 3**.

In this research study, machining of the hybrid composite using abrasive aqua jet machining (AWJM) was followed by the precise measurement of both R_a and K_T . The surface roughness (R_a) was evaluated by the SJ-210 tester [7]. For the purpose of accuracy, the surface roughness (R_a) was calculated three times on each specimen, and the average value was recorded. The kerf of the surface was assessed using a Video Measuring System. The Kerf taper was determined by measuring both the top Kerf width and the bottom Kerf width three times for each sample and then determining the average results. The Kerf taper was calculated using the following relationship or equation [8]

$$Kerf\ taper(K_T) \text{ (mm/mm)} = \frac{W_t - W_b}{2t} \quad (1)$$

where K_T = Kerf Taper, t = composite thickness, W_t , W_b are top width and bottom width.

Optimization of the Fabricated Hybrid Composite

The RSM-Response Surface Methodology was applied in this research study using the Box-Behnken Design (BBD) for the purpose of optimizing the experimental conditions. The BBD is advantageous due to its requirement for fewer experimental runs when compared to the Central Composite Design, making it a cost-effective approach while still delivering results that are both accurate and reliable [9]. By systematically assessing the combination of the chosen process

parameters and their effects on the responses, the BBD allows us to efficiently identify the optimal condition.

Table 3. Machining input parameters.

Run	A _{JP} (MPa)	N _{TS} (mm/min)	A _{FR} (g/sec)	K _T (mm)	Ra (μm)
1	300	200	4	2.176	2.933
2	300	150	5	1.987	2.805
3	300	200	4	2.289	3.061
4	200	200	5	3.212	4.085
5	300	250	5	2.879	3.701
6	300	250	3	2.759	3.573
7	200	200	3	3.113	3.957
8	300	200	4	2.397	3.189
9	300	150	3	1.871	2.677
10	200	250	4	3.334	4.213
11	400	200	5	1.612	2.421
12	400	250	4	1.764	2.549
13	400	150	4	1.325	2.165
14	300	200	4	2.511	3.317
15	300	200	4	2.634	3.445
16	400	200	3	1.447	2.293
17	200	150	4	2.998	3.829

Results and Discussion

Tensile and Hardness test

The tensile characteristics of the hybrid composite reinforced with waste EDM wire were evaluated, and the results are presented in **Figure 3 (a)**. The test results reveal that incorporating waste EDM wire into the composite matrix significantly enhances the tensile strength up to a certain threshold. Specifically, as the percentage of waste EDM wire reinforcement increases from 5 weight % to 10

weight %, the tensile strength of the composite shows an observable improvement. This is shown in **Figure 3 (a)**. This observed enhancement or improvement can be attributed to reinforcing effect of the wire, which does contribute to strengthening of the composite microstructure [10]. However, the study also indicates that a further increase in the waste wire content beyond 10 weight % did result in an observable reduction in the tensile strength. The observed fall or loss in tensile strength can be related to the creation and presence of a distinct interface with the waste wire and the epoxy resin, which does contribute to the presence of high "local" stress concentration and consequent weakening of the composite microstructure [11].

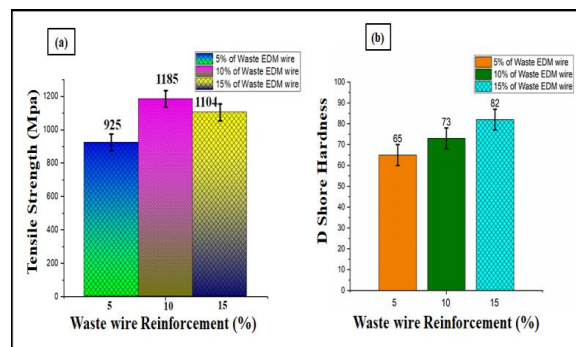


Figure 3: (a) Tensile strength, and (b) D Shore Hardness

The hardness properties of the hybrid composite, as influenced by an incorporation of varying percentages of the waste EDM wire, are shown in **Figure 3(b)**. The test results clearly demonstrate a substantial enhancement or improvement in hardness of the composite material with the addition of waste EDM wire. The observed increase in hardness is due to the formation and presence of a more rigid interphase between the carbon fiber and the waste wire, which is inherently harder than the epoxy matrix. The reinforcement provided by the waste wire not only enhances hardness of the chosen composite material but concurrently improves its resistance to deformation when under the influence of a load, thereby making it a more durable and resilient material [12].

Interaction of inputs on Kerf taper

An interaction between the various process parameters and their effect on kerf taper (K_T) of the hybrid composite is represented in **Figure 4 (a, b)**. In **Figure 4 (a)**, the impact of abrasive jet pressure (A_{JP}) and nozzle traverse speed (N_{TS}) on Kerf taper (K_T) are shown. The results clearly reveal the K_T to improves with an increase in the

nozzle traverse speed (N_{TS}). This is primarily due to an uneven erosion of the polymer material, leading to greater deviation of the Kerf taper [13]. Conversely, an increase in the abrasive jet pressure (A_{JP}) does tend to reduce the variation in Kerf width, as the high-pressure water jet effectively erodes the composite material, particularly for the composite with a lower amount of the reinforcement (5 weight %). It also indicates that a minimum Kerf taper width (K_T) was achieved for lower amounts of the waste EDM wire reinforcement (i.e., 5 weight %). This is primarily because a lower reinforcement content does lead to less interference with the cutting process, resulting in more uniform removal of the material [14].

In **Figure 4 (b)**, the interplay of abrasive flow rate (A_{FR}) and nozzle traverse speed (N_{TS}) is explored. The results clearly demonstrate that increasing the nozzle traverse speed (N_{TS}) while maintaining a constant abrasive flow rate (A_{FR}) does lead to higher Kerf taper (K_T) values, particularly at a high traverse speed. This is evident from the significant increase in Kerf taper (K_T) observed for the composite materials with a high waste wire reinforcement (15 weight %). A higher kerf taper (K_T) at increased nozzle traverse speed (N_{TS}) is basically due to the reduced time the garnet particles to interact with the composite. This does lead to less precision in the cuts and a greater material deviation. The optimal machining parameters for minimizing Kerf taper (K_T) involves maintaining a lower nozzle traverse speed and a lower percentage of waste EDM wire reinforcement to allow for a more controlled and precise removal of the material. This often results in reduced Kerf taper and improved machining quality.

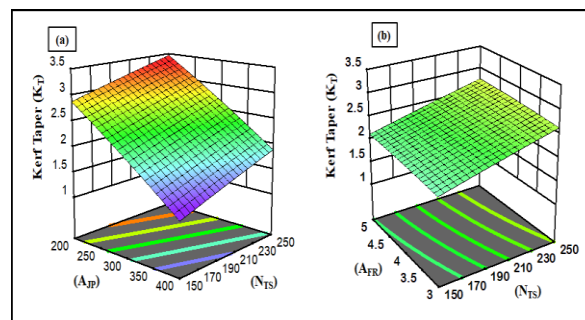


Figure 4 (a, b) Kerf taper interaction with process variables

Interaction of inputs on surface quality (Ra)

An interaction between the various process variables and their influence on the Ra in abrasive aqua jet machining (AWJM) of the

hybrid composite is shown in **Figure 5**. The impact of abrasive jet pressure (A_{JP}) and nozzle traverse speed (N_{TS}) on the surface roughness (R_a) is indicated in **Figure 5(a)**. The surface roughness (R_a) increases with a decrease in abrasive jet pressure (A_{JP}) and an increase in the nozzle traverse speed (N_{TS}). At lower abrasive jet pressure (A_{JP}), the cutting force exerted by the water jet is reduced, resulting in less effective removal of the material and thus a rougher surface. Conversely, a greater nozzle traverse speed (N_{TS}) does result in less time for the abrasive particles to interplay with the composite material, which often leads to increased surface roughness. The combined effect of these two parameters reveals that achieving a smoother surface does necessitate the need for a balance between sufficient jet pressure and optimal traverse speed to ensure a near even removal of the chosen material [15].

An interaction between abrasive flow pressure (A_{FR}) and nozzle traverse speed (N_{TS}) on surface roughness is represented in **Figure 5 (b)**. The R_a increases as the nozzle traverse speed (N_{TS}) increases, even when the abrasive flow rate (A_{FR}) is kept constant. A higher nozzle traverse speed (N_{TS}) implies a faster traverse of the nozzle over the material surface, often leading to incomplete cutting action and a rougher surface. On the other hand, a boost in the abrasive flow rate (A_{FR}) does result in a noticeable reduction in the R_a due to a higher volume of the abrasive particles both impacting and interacting with the material, which often helps in smooth removal of material. However, if the N_{TS} is too high, even a higher abrasive flow rate (A_{FR}) cannot compensate for the rapid traverse, resulting in an overall rougher surface [16].

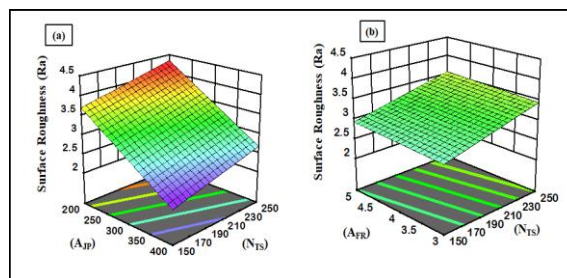


Figure 5 (a, b). Surface roughness interaction with the process variables

Perturbation Curve

The perturbation curves shown in **Figure 6** provide a useful insight into the impact of various input parameters on Kerf taper (K_T) and surface roughness (R_a). In **Figure 6 (a)**, is shown that A_{JP} has a

significant negative influence on Kerf taper (K_T). As the abrasive jet pressure (A_{JP}) increases, the Kerf taper (K_T) decreases sharply, suggesting that higher jet pressures often results in a more precise and narrower cut. This is primarily because a higher pressure enhances the cutting capability of the water jet, while concurrently reducing the tapering effect. Alternatively, the N_{TS} does show a positive influence on Kerf taper (K_T), meaning that as the traverse speed increases, the Kerf taper (K_T) also increases. This is essentially because of the shorter interplay time between the jet and the material, leading to less controlled cuts and greater tapering. The abrasive flow rate (A_{FR}) has a relatively minimal impact on Kerf taper (K_T), as indicated by the near-flat slope of the curve. This suggests that within the range of abrasive flow rate (A_{FR}) values studied, changes in the abrasive flow rate does not significantly affect the Kerf taper [17].

The perturbation curve for Ra is shown in **Figure 6 (a)**. Similar to K_T , the abrasive jet pressure (A_{JP}) has a noticeable effect on the Ra, with higher pressures leading to reduced surface roughness. This clearly indicates that a higher abrasive jet pressure (A_{JP}) facilitates a smoother cut by allowing the abrasive particles to more effectively remove material, thus producing a finer surface finish. The nozzle traverse speed (N_{TS}) again shows a positive correlation with the surface roughness (Ra), where increased traverse speed results in a rougher surface. This can safely be attributed to a faster movement of the nozzle over the material, which leaves less time for the abrasive particles to smoothen the surface. The abrasive flow rate (A_{FR}) exhibits a minimal but slightly negative influence on the surface roughness (Ra), indicating that an increased flow rate can marginally improve the surface finish by providing more abrasive particles to interact with surface of the material [18].

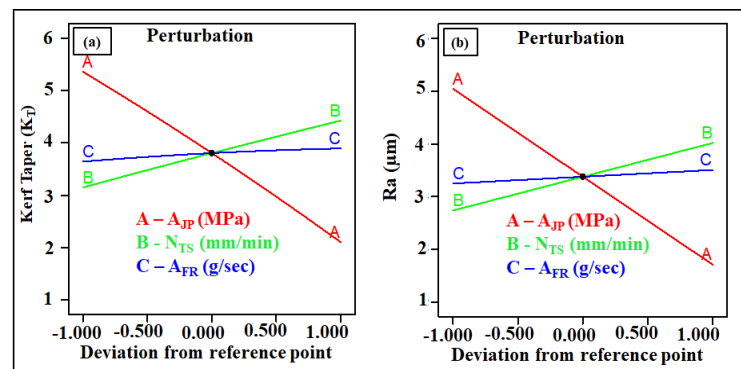


Figure 6. Perturbation of input parameters on (a) Kerf Taper (b) Surface Roughness

Optimization of the Inputs

An optimization of the input parameters for abrasive aqua jet machining was conducted to achieve minimal Kerf taper (K_T) and Ra in the hybrid composite. The optimized variables were determined to be an abrasive jet pressure (A_{JP}) of 393 MPa, a N_{TS} of 158 mm/min, and an abrasive flow rate (A_{FR}) of 3.3 g/sec. This is provided in **Table 4**. The predicted values for Kerf taper (K_T) Ra under these conditions was 1.263 mm and 2.104 μm , respectively.

Table 4. Optimization of the Process Parameters.

Input variables at Optimized level			Predicted value		Experimental values		Error %	
A_{JP} (MPa)	N_{TS} (mm/min)	A_{FR} (g/sec)	Kerf Taper K_T (mm)	Surface Roughness (Ra) (μm)	Kerf Taper K_T (mm)	Surface Roughness Ra (μm)	Kerf Taper K_T (mm)	Surface Roughness Ra (μm)
393	158	3.3	1.263	2.104	1.314	2.201	3.88	4.407

Experimental validation of these optimized parameters yielded actual kerf taper (K_T) and surface roughness (Ra) values of 1.314 mm and 2.201 μm , with an error percentage of 3.88 percent for K_T and 4.407 percent for the Ra. The slight discrepancies between the predicted value and the experimental value does provide a good correlation, suggesting the chosen parameters to effectively optimize the machining process [19]. The minor errors observed are within an acceptable range, confirming an overall robustness of the optimization method. These results demonstrate that precise control of abrasive jet pressure (A_{JP}), nozzle traverse speed (N_{TS}), and abrasive flow rate (A_{FR}) can significantly enhance machining quality by minimizing Kerf taper (K_T) and the surface roughness (Ra), which is represented in the ramp diagram in **Figure 7**.

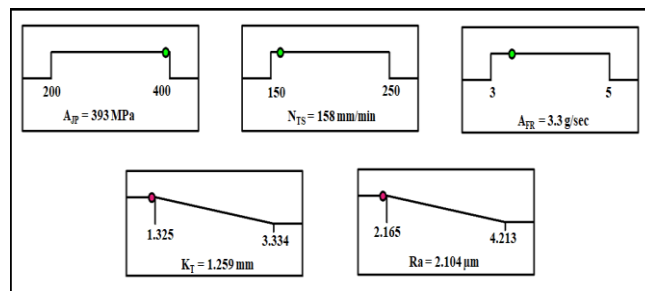


Figure 7. Ramp diagram for Optimization of the inputs

Conclusions

1. The hybrid composite was successfully fabricated using waste EDM wire-reinforced carbon fiber, demonstrating effective reinforcement integration. The inclusion of waste wire enhanced the mechanical properties while promoting sustainability by utilizing industrial waste. The composite's fabrication process was optimized to ensure both a uniform distribution and strong bonding between the matrix and the reinforcement.
2. Abrasive Aqua jet machining (AWJM) was used to effectively machine the hybrid composite. The process parameters were crucial in achieving optimal machining outcomes, with high precision cuts and minimal surface damage, making abrasive aqua jet machining (AWJM) a viable method for processing advanced composites.
3. The addition of waste EDM wire significantly influenced both the tensile strength and hardness of the composite. Tensile strength increased with wire reinforcement up to 10 weight percent beyond which it decreased due to issues specific to the interface. The hardness improved consistently, thereby indicating enhanced stiffness and durability, which is beneficial for structural applications.
4. 3-D analysis revealed that kerf taper was most affected by nozzle traverse speed (N_{TS}) and abrasive jet pressure (A_{JP}). A higher abrasive jet pressure (A_{JP}) reduced the Kerf taper, while a higher nozzle traverse speed (N_{TS}) increased it.
5. The surface roughness was predominantly influenced by abrasive jet pressure (A_{JP}) and nozzle traverse speed (N_{TS}), where a higher abrasive jet pressure (A_{JP}) and a lower nozzle traverse speed (N_{TS}) did result in a smoother surface. The study highlighted the need to optimize these variables carefully to achieve the desired surface finish, which is crucial for many applications.
6. The perturbation analysis revealed abrasive jet pressure (A_{JP}) to be the most critical parameter affecting both kerf taper and surface roughness. Raising the abrasive jet pressure (A_{JP}) generally led to reduced taper and roughness, while nozzle traverse speed (N_{TS}) and abrasive flow rate (A_{FR}) had a positive correlation, thereby indicating the necessity for a precise control of these parameters for obtaining optimal machining results.

7. Optimization of machining parameters yielded near optimal kerf taper and surface roughness values, with minimal deviations from the predicted outcomes. This study confirmed that a combination of abrasive jet pressure (A_{JP}) of 393 MPa, nozzle traverse speed (N_{TS}) of 158 mm/min, and abrasive flow rate (A_{FR}) of 3.3 g/sec is ideal for minimizing machining defects, thereby ensuring high-quality processing of the hybrid composite.

References

- [1] Sayam, A., Rahman, A.M., Rahman, M.S., Smriti, S.A., Ahmed, F., Rabbi, M.F., Hossain, M. and Faruque, M.O., 2022. *A review on carbon fiber-reinforced hierarchical composites: mechanical performance, manufacturing process, structural applications and allied challenges*. **Carbon Letters**, 32(5), pp.1173-1205.
- [2] Zhang, J., Lin, G., Vaidya, U. and Wang, H., 2023. *Past, present and future prospective of global carbon fibre composite developments and applications*. **Composites Part B: Engineering**, 250, p.110463.
- [3] Gao, T., Li, C., Wang, Y., Liu, X., An, Q., Li, H.N., Zhang, Y., Cao, H., Liu, B., Wang, D. and Said, Z., 2022. *Carbon fiber reinforced polymer in drilling: From damage mechanisms to suppression*. **Composite Structures**, 286, p.115232.
- [4] Thakur, R.K. and Singh, K.K., 2020. *Abrasive waterjet machining of fiber-reinforced composites: A state-of-the-art review*. **Journal of the Brazilian Society of Mechanical Sciences and Engineering**, 42(7), p.381.
- [5] Balasubramanian, C., Manohar, N.J. and Ezra, V., 2024. *Abrasive water jet machining (AWJM) on glass fiber composite reinforced with aluminium waste grain: An experimental investigation*. **Materials Today: Proceedings**, 98, pp.1-6.
- [6] Rani, M., Choudhary, P., Krishnan, V. and Zafar, S., 2021. *A review on recycling and reuse methods for carbon fiber/glass fiber composites waste from wind turbine blades*. **Composites part B: engineering**, 215, p.108768.
- [7] Balasubramanian, C., Rajkumar, K., Krishnan, B.S. and Arun, A., 2024. *Performance evaluation of abrasive water jet machining on spent garnet reinforced hybrid composite*. **Materials Today: Proceedings**, 98, pp.16-20.

- [8] Li, M., Lin, X., Yang, X., Wu, H. and Meng, X., 2021. *Study on kerf characteristics and surface integrity based on physical energy model during abrasive waterjet cutting of thick CFRP laminates*. **The International Journal of Advanced Manufacturing Technology**, 113, pp.73-85.
- [9] Balasubramaniyan, C., Rajkumar, K. *Identification of parametric conditions and the influence of laser interaction on the material removal and surface characteristics of 904 L steel super austenitic stainless steel*. **Int J Interact Des Manuf** (2024). <https://doi.org/10.1007/s12008-024-01987-9>
- [10] Sobuz, M.H.R., Saha, A., Anamika, J.F., Houda, M., Azab, M., Akid, A.S.M. and Rana, M.J., 2022. *Development of self-compacting concrete incorporating rice husk ash with waste galvanized copper wire fiber*. *Buildings*, 12(7), p.1024.
- [11] Reis, J.P., de Moura, M. and Samborski, S., 2020. *Thermoplastic composites and their promising applications in joining and repair composites structures: A review*. **Materials**, 13(24), p.5832.
- [12] Almushaikeh, A.M., Alaswad, S.O., Alsuhybani, M.S., Alotaibi, B.M., Alarifi, I.M., Alqahtani, N.B., Aldosari, S.M., Alsaleh, S.S., Haidyrah, A.S., Alolyan, A.A. and Alshammari, B.A., 2023. *Manufacturing of carbon fiber reinforced thermoplastics and its recovery of carbon fiber: A review*. **Polymer Testing**, 122, p.108029.
- [13] Arun, A., Rajkumar, K. and Vishal, K., 2023. *Process Parameters for Optimization in Abrasive Water Jet Machining (AWJM) of Silicon-Filled Epoxy Glass Fibre Polymer Composites*. **Journal of Inorganic and Organometallic Polymers and Materials**, 33(5), pp.1339-1356.
- [14] Pradhan, S. and Dhupal, D., 2023. *Machining of aluminium nitride ceramic with a AJM process using SiC abrasives: Experiments and simulation*. *Journal of Manufacturing Processes*, 95, pp.68-90.
- [15] Ozcan, Y., Tunc, L.T., Kopacka, J., Cetin, B. and Sulitka, M., 2021. *Modelling and simulation of controlled depth abrasive water jet machining (AWJM) for roughing passes of free-form surfaces*. **The International Journal of Advanced Manufacturing Technology**, 114(11), pp.3581-3596.
- [16] Jani, S.P., Senthil Kumar, A., Adam Khan, M. and Uthayakumar, M., 2020. *Surface roughness and morphology*

studies on machining hybrid composite material using abrasive water jet cutting process. **Surface Engineering of Modern Materials**, pp.125-148.

- [17] Speidel, A., Bisterov, I., Saxena, K.K., Zubair, M., Reynaerts, D., Natsu, W. and Clare, A.T., 2022. *Electrochemical jet manufacturing technology: From fundamentals to application*. **International Journal of Machine Tools and Manufacture**, 180, p.103931.
- [18] Bañon, F., Sambruno, A., González-Rovira, L., Vazquez-Martinez, J.M. and Salguero, J., 2021. *A review on the abrasive water-jet machining of metal–carbon fiber hybrid materials*. **Metals**, 11(1), p.164.
- [19] Balasubramaniyan, C. and Rajkumar, K., 2024. *Enhancing low-speed WEDM machining capabilities on Nitronic-50 with a constant frequency ultrasonic hybrid method*. Proceedings of the Institution of Mechanical Engineers, Part C: **Journal of Mechanical Engineering Science**, 238(8), pp.3468-3479.

MECHANICAL RESPONSE OF HYBRID GLASS/KEVLAR EPOXY POLYMER COMPOSITE REINFORCED WITH MULTI- WALL CARBON NANOTUBES

A. Arun¹, S. Santosh^{1*}, P. Kamaraj² and T.S. Srivatsan³

¹ *Department of Mechanical Engineering*
Sri Sivasubramaniya Nadar (SSN) College of Engineering
Old Mahabalipuram Road
Kalavakkam 603110, Tamil Nadu, INDIA

² *Department of Mechanical Engineering*
Sri Venkateswaraa College of Technology
Sriperumbudur 602105, Tamil Nadu, INDIA

³ *Department of Mechanical Engineering,*
The University of Akron
Akron, Ohio 44325, USA

Corresponding Author: santoshs@ssn.edu.in

Abstract

The prevailing situation necessitates the need for lightweight materials that can offer a combination of unaltered qualities. With resources quickly running out in terms of shorter service lives coupled with an inability to reduce, reuse, and recycle, the concept of sustainability is both gaining and becoming increasingly important. In this paper, the results of a recent study aimed at understanding and improving the properties of composite materials through hybrid fiber stacking and the use of nanofillers is well presented and adequately discussed. The desired composite materials were prepared using a simple hand layup process and subsequently cut using the technique of abrasive water jet machining (AWJM). Mechanical tests, to include tensile, flexural, impact, and hardness, were conducted using the standard machines. The test results revealed both the toughness and strength of the engineered hybrid composites reveal a noticeable increase with the inclusion of nanofillers. The observed increase in interlaminar bonding coupled with adhesion between the laminae was caused by the presence of nanofillers. Both load sharing and the resistance to failure of the engineered composite material were significantly influenced by

the presence of distinctive features. All of the experiments did reveal that a 0.3 weight percent (GKC0.3) lower nanofiller concentration had the most significant improvement. Upon comparison with the unfilled ones (GKC0), the flexural strength improved by 11.30 percent, impact toughness improved by 10 percent, and the hardness improved by well over 60 percent with an 18.19 percent improvement in tensile strength. The test findings clearly reveal that, for a given percentage of the composite material, adding hybrid layers of glass and Kevlar with multi-walled carbon nanotube (MWCNT) as the reinforcement did improve the existing characteristics of the engineered composite. As a result, numerous lightweight applications, to include automobiles and unmanned aerial vehicles [UAVs], can benefit from the use of this type of hybrid layered composite material.

Keywords : Glass Fiber, Kevlar fiber, Multi-walled carbon nanotube (MWCNT), Mechanical characteristics.

Introduction

Industry demands for lightweight materials with significant stiffness-to-weight ratio [E / ρ], extended fatigue life, remarkable strength-to-weight ratio [σ / ρ], and superior corrosion resistance in comparison to metallic materials are met by fiber-reinforced polymer composites. These industries include aerospace, automotive, railway, wind energy, and space. Polymer composites frequently utilise glass fibres as the reinforcing component. They consist of fine glass fibres, providing a blend of high tensile strength, rigidity, and impact resistance [1]. The incorporation of glass fibres into epoxy resin enhances the mechanical properties of the resulting composite, rendering it suitable for structural applications that necessitate a high strength-to-weight ratio [σ / ρ]. The Izod test specimen must be notched in compliance with ASTM D-256. The dimensions of the impact test specimen are as follows: The dimensions of the specimen are 64 mm \times 12.7 mm \times 3.2 mm. It includes a 2 mm deep 'V' notch centrally positioned with a 45° included angle. Glass fibers are also thermally stable and resistant to environmental deterioration, making them excellent for use in hostile environments and locations [2]. Kevlar, a para-aramid synthetic fiber, is well-known for its superior tensile strength and toughness, which often exceeds those of glass fibers. Kevlar fibers offer a distinct set of qualities, to include the following: (i) great strength, (ii) low weight, and (iii) good resistance to impact and abrasion. Kevlar strands add great toughness and impact resistance to an epoxy matrix [3]. This makes Kevlar-reinforced composites ideal for applications that demand exceptional durability, such as (i) bulletproof vests, (ii) helmets, and (iii) protective gear.

Multi walled Carbon nanotubes [MWCNTs] are cylindrical nanostructures made of several graphene sheets folded into tubes. Due on account of their mechanical, electrical, and thermal characteristics, the multi-walled carbon nanotubes [MWCNTs] are popular in composite material research. The presence of MWCNTs in an epoxy can improve tensile strength, modulus, and thermal conductivity. MWCNTs also increase electrical conductivity of the composite material, making it appropriate for EMI shielding and other electronic applications [4]. Among these options, fiber hybridization has received positive feedback because it accounts for changes in reinforcing behavior, which is a main load-bearing source in composite laminates. Developing hybrid polymer composites often entails a continuing need for novel materials that, in addition to being lightweight, have better functional features, such as (i) impact strength and (ii) durability [5]. Research on hybrid polymer matrix composites requires both a thorough study and organization, as evidenced by previous research studies [6-8]. A research performed by Randjbaran et al. [9] revealed that glass fiber is preferable to Kevlar fiber and should be used for the initial layer. Glass fiber should represent the initial layer. The amount of energy that is absorbed by glass fiber immediately following an impact is higher than that of Kevlar fiber. Vinay et al. [10] developed hybrid composites of synthetic fibers such as E-glass/carbon/Kevlar laminates. The composite revealed superior flexural and high hardness characteristics due to their strong adhesive bonding with the matrix of thermosets. A similar study for the hybridization polymer composites containing nanofillers was reported by Mohan et al. [11] and found that with multi-walled carbon nanotubes (MWCNT) concentration of 1 weight percent inclusion of the glass/flax fibers, prepared hybrid composites did reveal improved flexural strength by up to 28.26%, with the unfilled nanofiller having a lower compressive strength. Inclusion of 1 weight percent of MWCNT did enhance the compressive strength. Similar findings of incorporating MWCNTs at 2 percent, 3 percent, and 4 percent volume fraction in glass/carbon fiber composites did increase both the Young's Modulus and Flexural Strength when compared to the glass-Kevlar fiber reinforced plastic {G-KFRP}, resulting in a strong interlaminar bonding [12].

According to the published literature, utilizing an appropriate weight percent of multi-walled carbon nanotubes (MWCNT) in hybrid composites does improve the mechanical characteristics. It should be emphasized that very little research has been conducted on the effects of MWCNTs on Glass/Kevlar polymer composites with epoxy as the matrix. This study looks into how MWCNT with glass fibers and Kevlar fibers alters the mechanical characteristics. In this independent

research study, hybrid composites MWCNT were reinforced with 0 % MWCNT, 3 % MWCNT, and 5 % MWCNT using prepreg hand-layup compression molding procedure. The nano filler-induced hybrid polymer composites were then carefully evaluated using ASTM standards for tensile strength, flexural strength, impact strength, and hardness. Properties of the developed composite materials did reveal a noticeable improvement after the addition of hybrid layers of glass and Kevlar along with multi-walled carbon nanotube (MWCNT) reinforcement.

Materials and Methods

Bidirectional twill is woven using roving glass and Kevlar fibers, specifically Kevlar-29 and E-glass, which has a surface density of 200 gsm and 360 gsm. These fibers were sourced from Sakthi Fibers [Chennai, India]. To enhance properties of the composite material, functionalized multi-walled carbon nanotubes (MWCNTs) with a diameter of 10–30 nm and a surface area of 110–350 m²/g and provided by Adnano Technologies [India] were incorporated. The matrix material used for fabricating the hybrid polymer composites did include the epoxy resin (LY556) and a curing agent (HY951). These materials were selected to optimize the mechanical and functional characteristics of the resultant composite material by taking advantage of the following: (i) high tensile strength of Kevlar, (ii) durability of glass fibers, and (iii) unique properties of the multi-walled carbon nanotubes (MWCNTs). A combination of these materials coupled with a bidirectional twill weave does result in the engineering of a robust and versatile composite suitable for use in a spectrum of applications where strength and durability are critical.

Fabrication of composites

The hand lay-up approach was utilized to create the hybrid polymer composite with filler inclusion. The composites were fabricated using a wooden mold that measured 30 cm × 300 mm with MWCNT as the filler. The fabrication procedures for the hybrid polymer composites are shown in **Figure 1**. Initially, both the glass fibers and Kevlar fibers were cut to the desired size and subsequently cleaned with acetone two to three times. The multi-walled carbon nanotubes (MWCNT) fillers (3% and 5%) were combined with epoxy in a separate beaker. For about an hour, the nanofiller solution was agitated using a probe ultrasonication. The MWCNTs are evenly dispersed in the epoxy matrix that was maintained at a temperature 45°C and continuously stirred using a magnetic stirrer. In addition to ensuring evaporation of the volatile contaminants evaporate, this also

contributed to a reduction in viscosity of the epoxy. After the fillers have been evenly dispersed through the epoxy matrix, allow the mixture to come to ambient temperature before adding the hardener. The curing ingredient was combined with nanofillers and epoxy at a 10:1 ratio. The mold was then cleaned using wax. The fibers were injected into the mold using a roller so as to achieve equal thickness and dispersion. The top plate was put on top of the mold and left to cure for 24 hours. The designation of prepared hybrid composites is provided in **Table 1**.

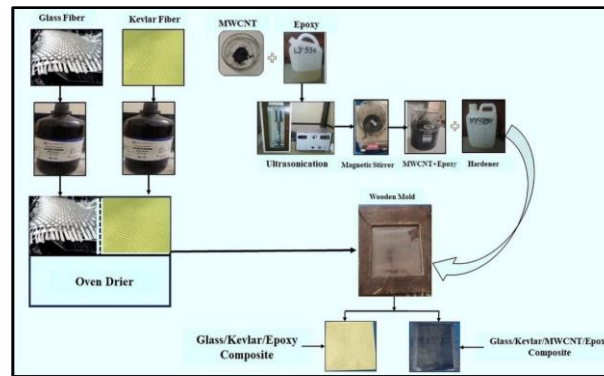


Figure 1. Preparation of Glass/Kevlar/MWCNT Epoxy Composite

Table 1. Designations of the Hybrid Composites

Symbol	Designation
GKC0	Glass/Kevlar/Epoxy 0% MWCNT hybrid polymer composite
GKC0.3	Glass/Kevlar/Epoxy 3% MWCNT hybrid polymer composite
GKC0.5	Glass/Kevlar/Epoxy 5% MWCNT hybrid polymer composite

Mechanical Testing and Characterization Standards

Abrasive water machine cut test samples to comply with the specifications outlined in the ASTM standards. The hybrid MWCNT composite specimens were subsequently subjected to tensile testing in accordance with ASTM D6380. The assessment was conducted via a computerised universal testing machine (UTM) [Model: Instron 4206]. The ASTM standard was adhered to in the fabrication of dog bone-shaped tensile specimens of 165 mm in length, 19 mm in width, and 3

mm in thickness, with a gauge length of 50 mm. The flexural test was performed in accordance with ASTM standard D790 (127 mm × 13 mm × 3 mm) with the three-point testing method. A Barcol hardness tester [PCE-1000 N] measuring 30 mm × 30 mm was employed to determine the hardness of the produced samples. This was executed in compliance with ASTM standard D 2583. A spring-loaded plunger was employed to assess the material's resistance to indentation, ranging from 300 kgf/mm² to 500 kgf/cm². Before testing commenced, the Barcol impresser was calibrated, and the dial indication of the scale was adjusted to zero. The Izod test specimen must be notched in line with ASTM D-256. The dimensions of the impact test specimen are as follows: The specimen is 64 mm × 12.7 mm × 3.2 mm. It includes a 2 mm deep 'V' notch at the centre with a 45° included angle.

Results and Discussions

Tensile results of Glass/ Kevlar/ MWCNT/ Epoxy hybrid composite

The tensile properties of GKC0, GKC0.3, and GKC0.5 hybrid composites are shown in **Figure 2**. The tensile strength without MWCNT, the glass/ Kevlar hybrid composite without MWCNTs (GKC0) was 221.09 MPa, and the tensile modulus was 17.17 GPa, which is shown in **Figure 2 (a-c)**. The addition of MWCNT did increase the load-sharing size of the hybrid polymer matrix, which is reflected by an observable increase in the strength values irrespective of the amount of multi-walled carbon nanotubes (MWCNT) inclusion. The composite with 0.3 weight percent MWCNT addition had the highest strength of 261.3 MPa. This is 18.19% higher than the composite with no MWCNT reinforcement. An incorporation of MWCNT into the matrix served as a link that improved the interfacial adhesion between the matrix and the reinforcing hybrid fibers. This was accomplished by enhancing the connection between the two materials [13]. Similarly, adding 5% MWCNT resulted in a lower strength value of 240.61 MPa. This is because of incorrect filler dispersion coupled with agglomeration during preparation.

The tensile modulus values for the samples under consideration is shown in **Figure 2 (c)**. The lower addition of 3% MWCNT fillers did reveal a maximum tensile modulus of 20.13 GPa, whereas the tensile modulus GKC0 sample was 17.17 GPa and the 5% MWCNT added sample had a tensile modulus of 19.05 GPa. The GKC0.3 sample did reveal the greatest percentage improvement, with a 17.0 % increase over the sample with no fiber reinforcement, i.e., GKCO.

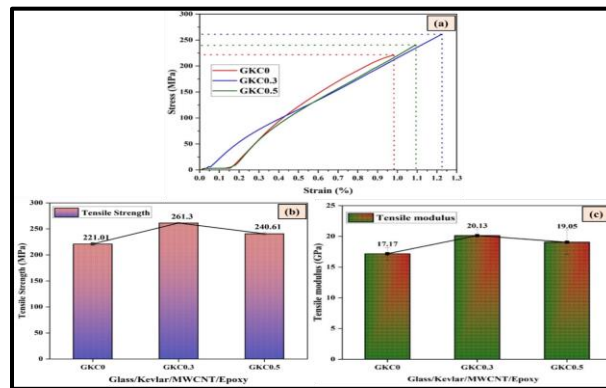


Figure 2. Tensile results of the Glass/ Kevlar/ MWCNT/ hybrid composites

- (a) Stress versus Strain
- (b) Tensile Strength, and
- (c) Tensile modulus

Flexural / Impact Characteristics of Glass/ Kevlar/ MWCNT/ Epoxy Composites

The flexural properties and impact of GKC0, GKC0.3, and GKC0.5 hybrid composites are represented in **Figure 3 (a, b)**. The flexural test was performed using the 3-point bending analysis on a Universal Test Machine (UTM). From **Figure 3(a)**, the flexural strength value of GKC0 is 450.12 MPa, for GKC0.3 it is 50.12 MPa, and for GKC0.5 it is 473.36 MPa. The GKC0.3 had high flexural strength, which was 11.30 % higher than that of the GKC0 hybrid composite. The 3% multi-walled carbon nanotube (MWCNT) addition exhibited noticeable improvement in strength of the composite due to delamination. The flexural modulus improved by the addition of multi-walled carbon nanotubes (MWCNTs), which creates a more uniform stress distribution within the composite by filling the gaps and voids at the interfaces between the reinforcing hybrid fibers and the matrix. The improved bonding reduces and/or minimizes the likelihood of pull-out of the reinforcing fibers or debonding under the influence of flexural loads, and thereby contributing to enhancing the resistance of the composite material to bending forces [14].

The impact strength of the GKC0, GKC0.3, and GKC0.5 hybrid polymer composites is shown in Figure 3(b). The reinforcing glass fiber and Kevlar fiber combination in the composite material is adequate enough to withstand an impact load. This in conjunction with the presence of fillers (i.e., multi-walled carbon nanotubes) does

contribute to enhancing the loading resistance. For the GKC0.3 composite, the lowest filler-added sample, did exhibit the maximum impact strength (243 kJ/m^2) when compared to the unfilled and the GKC0.5 composite (221 kJ/m^2). The maximum increase was approximately 10 percent more than that of an un-reinforced hybrid composite. Increased filler concentration did cause the formation and presence of fine microcracks, which tended to propagate quicker in the composite matrix due to agglomeration [15].

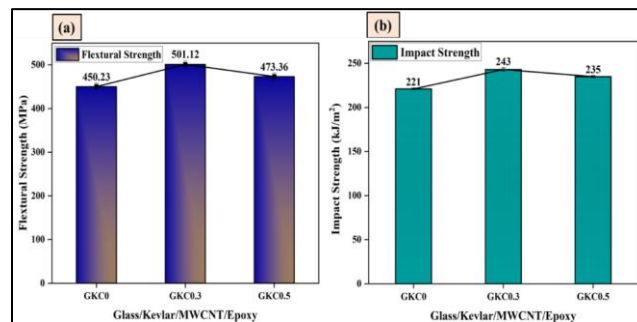


Figure 3. (a) Flexural strength
(b) Impact strength of Glass/ Kevlar/ MWCNT hybrid composite

Barcol Hardness of Glass/ Kevlar/ MWCNT/ Epoxy Composites

A Barcol Hardness testing device was used to assess the hardness of the produced samples. The hardness values based on the Barcol hardness testing is shown in **Figure 4**. When the well-dispersed GKC0.3 hybrid composite was subjected to indentation loading, the highest Barcol hardness number that was obtained was 40. This composite material did exhibit a high level of resistance to deformation of the matrix [16]. The reinforced multi-walled carbon nanotube (MWCNT) fillers do provide a solid link with the polymer chains, preventing free stretching while concurrently limiting plastic deformation. The hardest samples were the GKC0.3 and GKC0.5. This was 60 percent higher and 40 percent higher than the sample without GKC0 hybrid composites.

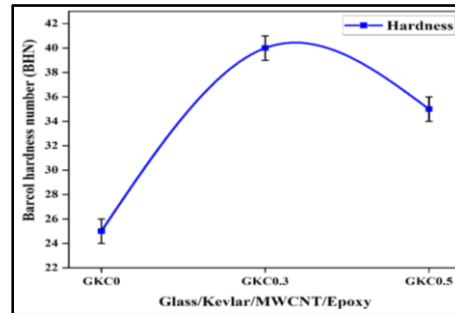


Figure 4. Barcol hardness graph for the Glass/ Kevlar/ MWCNT/ Epoxy composite.

Conclusions

1. Glass/Kevlar hybrid composites with multi-walled carbon nanotube (MWCNT) (3%) and 5%) epoxy-based polymer composites were made using hand layup techniques.
2. Almost all mechanical properties, including hardness, modulus, flexural strength, impact strength, and tensile strength, were achieved in compliance with ASTM guidelines.
3. When comparing the GKC0.3 composite to the unfilled hybrid multi-walled carbon nanotube (MWCNT) composite (GKC0), the GKC0.3 composite showed increases in tensile strength and tensile modulus of 18.19% and 17.23%, respectively.
4. In comparison to the GKC0 composite, without the MWCNT, the GKC0.3 composite did exhibit enhanced flexural strength by 11.30% and impact strength by 10%. The Barcol harness number also increased with a reduction of the multi-walled carbon nanotube (MWCNT) added to the hybrid composite.
5. According to mechanical characterization of the developed Glass/Kevlar 3% MWCNT hybrid polymer composite, it does possess a higher level of strength when compared to the other compositions, namely the GKC0 and GKC0.5 composites. Development of hybrid polymer composites does necessitate the need for a continuous search for innovative materials that, in addition to being lightweight, offer greater functional properties, such as (i) impact strength, and (ii) durability.

References:

1. Jayan, J.S., Appukuttan, S., Wilson, R., Joseph, K., George, G. and Oksman, K., 2021. *An introduction to fiber reinforced composite materials*. In **Fiber reinforced composites** (pp. 1-24). Woodhead Publishing.
2. Shafei, B., Kazemian, M., Dopko, M. and Najimi, M., 2021. *State-of-the-art review of capabilities and limitations of polymer and glass fibers used for fiber-reinforced concrete*. **Materials**, 14(2), p.409.
3. Al-Furjan, M.S.H., Shan, L., Shen, X., Zarei, M.S., Haj Mohammad, M.H. and Kolahchi, R., 2022. *A review on fabrication techniques and tensile properties of glass, carbon, and Kevlar fiber reinforced Polymer composites*. **Journal of Materials Research and Technology**, 19, pp.2930-2959.
4. Taraghi, I., Fereidoon, A. and Mohyeddin, A., 2014. *The effect of MWCNTs on the mechanical properties of woven Kevlar/epoxy composites*. **Steel Compos. Struct**, 17(6), pp.825-834.
5. Wolfs, Y., Verpoest, I. and Gorbatiikh, L., 2019. *Recent advances in fibre-hybrid composites: materials selection, opportunities and applications*. **International Materials Reviews**, 64(4), pp.181-215.
6. Arun, A., Rajkumar, K. and Vishal, K., 2023. *Process Parameters for Optimization in Abrasive Water Jet Machining (AWJM) of Silicon-Filled Epoxy Glass Fibre Polymer Composites*. **Journal of Inorganic and Organometallic Polymers and Materials**, 33(5), pp.1339-1356.
7. Alsaadi, M., Bulut, M., Erklığ, A. and Jabbar, A., 2018. *Nano-silica inclusion effects on mechanical and dynamic behavior of fiber reinforced carbon/Kevlar with epoxy resin hybrid composites*. **Composites Part B: Engineering**, 152, pp.169-179.
8. Joseph, L., Chakravarthi, E.K., Kumar, S., Jaya Narayanan, K. and Mini, K.M., 2023, May. *Nano filler incorporated epoxy based natural hybrid fiber confinement of concrete systems: Effect of fiber layers and nano filler addition*. In **Structures** (Vol. 51, pp. 320-331). Elsevier.

9. Randjbaran, E., Zahari, R., Abdul Jalil, N.A. and Abang Abdul Majid, D.L., 2014. *Hybrid composite laminates reinforced with Kevlar/carbon/glass woven fabrics for ballistic impact testing*. **The Scientific World Journal**, 2014(1), p.413753.
10. Vinay, H.B., Govindaraju, H.K. and Banakar, P., 2017. *Experimental study on mechanical properties of polymer-based hybrid composite*. **Materials Today: Proceedings**, 4(10), pp.10904-10912.
11. Mohan, K. and Rajmohan, T., 2018. *Effects of MWCNT on mechanical properties of glass-flax fiber reinforced nano composites*. **Materials Today: Proceedings**, 5(5), pp.11628-11635.
12. Swinker, K.R.J., Kanagasabapathy, H. and Neethi Manickam, I., 2022. *Effect of MWCNT on mechanical characterization of glass/carbon hybrid composites*. Proceedings of the Institution of Mechanical Engineers, Part E: Journal of Process Mechanical Engineering, 236(5), pp.2155-2163.
13. Cheon, J. and Kim, M., 2021. *Impact resistance and interlaminar shear strength enhancement of carbon fiber reinforced thermoplastic composites by introducing MWCNT-anchored carbon fiber*. **Composites Part B: Engineering**, 217, p.108872.
14. Xiao, C., Tan, Y., Wang, X., Gao, L., Wang, L. and Qi, Z., 2018. *Study on interfacial and mechanical improvement of carbon fiber/epoxy composites by depositing multi-walled carbon nanotubes on fibers*. **Chemical Physics Letters**, 703, pp.8-16.
15. Ahmed, A.K., Alwan, M.A. and Farhan, A.J., 2023. *Effect of Using Nano-Silica with Carbon/Kevlar Fiber Reinforced Epoxy on Energy Observation of Toughness*. **International Journal on" Technical and Physical Problems of Engineering**, 15(1), pp.241-247.
16. Shahabaz, S.M., Mehrotra, P., Kalita, H., Sharma, S., Naik, N., Noronha, D.J. and Shetty, N., 2023. *Effect of Al₂O₃ and SiC nano-fillers on the mechanical properties of carbon fiber-reinforced epoxy hybrid composites*. **Journal of Composites Science**, 7(4), p.133.

MECHANICAL RESPONSE OF 3D PRINTED REINFORCED NYLON FOR USE IN PERFORMANCE-SPECIFIC APPLICATIONS

**A. R. Anil Chandra ^{1*}, Jayaram R. Pothnis ²,
Sathyapal Hegde ³, T. S. Srivatsan ⁴**

¹ *Department of Mechanical Engineering*
B.M.S. College of Engineering
Bangalore 560 019, **INDIA**

² *Department of Aerospace Engineering*
Ramaiah Institute of Technology
Bangalore 560 054, **INDIA**

³ **Prasanna Technologies,**
Bangalore - 560 010, **INDIA**

⁴ *Department of Mechanical Engineering*
The University of Akron
Akron, OHIO 44325-3903, **USA**

* Corresponding author E-Mail: anilchandraar.mech@bmsce.ac.in

Abstract

Additive manufacturing (AM) or 3-dimensional (3-D) printing is currently the talk of the day as it has penetrated all walks of life spanning various industries including those related to aerospace engineering. This method is being employed even for the realization of critical components across industry sectors and this trend is expected to register an upward swing. Properties of a 3-D printed component does depend on various factors, such as (i) properties of the raw material, (ii) printing parameters, and (iii) post-processing of the 3-D printed material. Onyx® is a nylon material that is reinforced with micro carbon fiber and developed by Markforged®. This material is popular among a few others, such as (i) Polylactic acid (PLA), and (ii) Acrylonitrile butadiene styrene (ABS). In this paper, the results of a recent research study aimed at investigating and understanding the fatigue behaviour of Onyx® using uniaxial fatigue tests are presented. During the fatigue tests, the infra-red (IR) thermography technique was used to carefully analyze heat signature in the material prior to failure

followed by fracture. In addition to discussions on the fatigue response of the tested material, this work highlights the usefulness of infra-red (IR) thermography as a non-contact measuring system for applications in the area of structural health monitoring. Further, the utility of the technique can be extended even for the life prediction of Onyx® that is being chosen for use in structural applications.

KeyWords: 3-D printed Onyx, Additive Manufacturing, Fatigue behavior, Infra-Red Thermography

Introduction

Additive manufacturing (AM) techniques, such as (i) fused deposition modelling (FDM), and (ii) fused filament fabrication (FFF), commonly known as 3D printing, are being widely used for the printing of popular polymeric materials, such as (i) poly lactic acid (PLA), and (ii) acrylonitrile butadiene styrene (ABS). During the last decade, several publications in open literature have shown the printing direction to wield considerable influence on mechanical properties of such materials [1-3]. However, the directionality in properties is often not welcome in all engineering applications and hence researchers were in the pursuit (and still in pursuit) of “isotropic” materials that could be 3D printed.

Onyx® is a nylon material that is reinforced with micro carbon fiber and developed by Markforged® [4]. The results from a recent study by Nikiema et al. [5] revealed that Onyx®, to a large extent, could be a potential isotropic material since its mechanical properties do not vary significantly with the orientation angle on the printing platform. In the work, the authors reported a maximum deviation of 10 percent between the different orientations. Further, this material can be used as 3-D printing material or as a base material which can be combined with continuous fibers to form a composite 3-D printing material. This aspect provided the necessary impetus for successful adaptation of 3D printing technologies to composite materials so as to reduce the overall complexity of composite manufacturing, lower production cost while concurrently enabling a high degree of automation. However, this apparent “isotropic” behaviour of printed Onyx is also related to infill patterns and density [6,7]. A detailed review on the influence of 3-D printing parameters on the mechanical properties of polymeric materials can be found elsewhere [8].

Onyx® is an important material for the following reasons: Onyx's strength and stiffness are highly dependent on both the strength and stiffness of the reinforcing fibers as per the research conducted and findings obtained by David et al. [9]. They emphasized, in their

independent study, that the orientation of the carbon fibers is crucial since it can significantly affect and/or influence the mechanical properties of the composite material, far more than the printing direction. Additionally, the distinct mechanical properties of the fibers and the matrix did create a complex stress state in the composite structure. This complexity arises as a direct consequence of the bonding between the reinforcing fibers and the matrix, as well as spatial arrangement of the reinforcing fibers within the volume during printing [10]. The mechanical properties of the 3-D printed composite can be attributed to the following: (a) bond quality between the reinforcing fiber and the matrix, and (b) relationship between thickness of the material (number of layers) and ultimate tensile strength [11].

As in the case of metallic materials, polymeric materials develop accumulated damage due to repeated loads, which gradually propagates until they reach a critical value culminating in instant failure by fracture [12]. Loss or degradation in the property of interest specific to the chosen and studied material is an accumulated process during cyclic loading and is referred to as fatigue damage. In the case of composite materials, the fatigue process can be divided into three main stages, which are the following:

- (a) Early matrix cracking leading to crack nucleation,
- (b) Crack growth through the microstructure of the composite material culminating in
- (c) Failure by fracture.

The duration of each stage does depend on the conjoint and mutually interactive influences of (i) composition of the material, (ii) geometry, and (iii) loading conditions.

The nucleation stage is argued to be a material property in bulk materials but is not the case for a 3D printed material [13]. Hence, developing an understanding of the fatigue behaviour of 3D printed material does become a complex process [14-16]. Especially when materials are printed with features such as a hole, that may be required from the application point of view. Therefore, this study makes an attempt to understand the fatigue behaviour of 3-D printed Onyx material, an aspect requiring attention and at present very few studies on the topic have been reported in literature.

Maier et al. [17] discussed the potential aerospace applications of carbon-fiber-reinforced Onyx® due to their high glass transition temperature ($T_g=114^\circ\text{C}$) and tensile strength exhibited by the material apart from having better insulation (thermal and electrical), weather

resistant and wear resistant properties. Research by Martinez et al. [14] on the fatigue life of such 3D printed thermoplastics did indicate an initial linear response to the applied load that gradually transits to a non-linear response over time due to their inherent viscoelastic properties. Generally, in composites and polymeric materials, fatigue failure is preceded by the generation of heat due to the applied load resulting in an observable reduction in stiffness culminating in the occurrence of the following: (i) matrix cracking, (ii) matrix-fibre interface de-bonding, and (iii) delamination (inter-layer failure) [18,19]. The heat that is generated during the fatigue process becomes an important structural health monitoring parameter as was shown in a recent study [20]. One of the key advantages of using an infra-red thermal (IRT) approach for the purpose of fatigue characterization is that fewer number of test specimens are sufficient to accurately characterize the fatigue strength of the composite materials during cyclic stress-controlled high cycle fatigue [21, 22]. Infrared based thermal cameras have been used to study damage accumulation in fiber reinforced plastic materials [23-25]. Use of thermal camera for the early prediction of fatigue failure of 3-D printed Onyx material is yet to be reported in published literature and forms the primary aim of this research study.

Materials and Methods

The sequence of experiments conducted to characterize fatigue properties of the 3-D printed material Onyx® is shown in **Figure 1**.

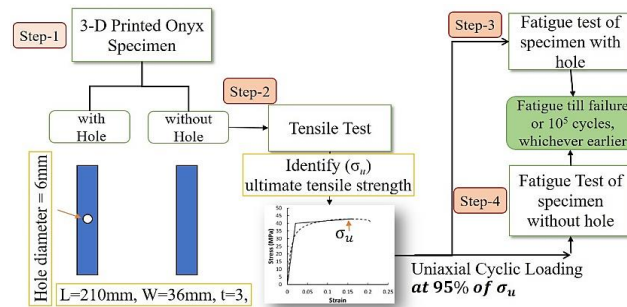


Figure 1. Flow chart of the experimentation procedure adopted in the present work

Specimen 3-D Printing

All the tensile and fatigue specimens used in the present research study were fabricated using the desktop 3D printer [Model: Markforged® Mark Two™]. Onyx®, which contains micro-carbon

fibers in a nylon matrix [26], was fed as the raw material to the 3D printer. Each 3D printed layer was pre-set to a thickness of 0.125 mm. Reducing the thickness does give finer detailing and a smoother surface finish but concurrently increases the printing time. A larger layer thickness will tend to reduce the printing time and can concurrently compromise on (i) surface finish, (ii) interlayer adhesion, and (iii) mechanical performance. Hence selection of layer thickness must be made based on “performance-specific applications”. Furthermore, it is worth noting that the 3D printer [Model: Markforged Mark Two™] provides options on selecting the material and printing parameters. The parameters selected in the present research study are provided in **Table 1** and shown in **Figure 2**. The printing parameters were similar for the specimen ‘with hole’ and the specimen ‘without hole’.

Table 1. Printing parameters selected from the Markforged Mark Two™ 3D printer software

Nozzle temperature	Layer thickness	No. of layers	Infill density
275°C	0.125 mm	24	100%

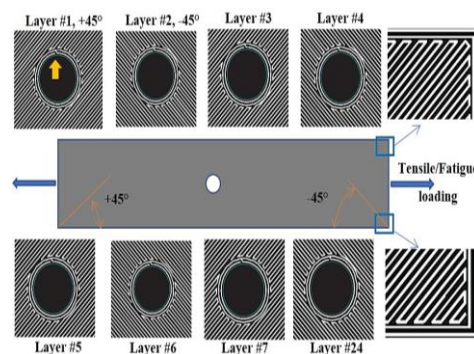


Figure 2. Schematic representation of 3D printing of Onyx® tensile and fatigue testing specimen and the printing direction with respect the loading direction (**Step-1**). The printing pattern at the edges of the specimen and near the hole is highlighted.

Tensile Test and Fatigue test

Ambient temperature tensile and fatigue tests were conducted using a 25kN MTS Landmark 370.25® servo-hydraulic universal testing machine:

- (a) The tensile tests were conducted under a displacement-controlled rate of 0.5 mm/minute. The specimens were similar in dimensions to those of the open hole fatigue (OHF)

specimens tested earlier [23]. The specimens were loaded until they fractured.

- (b) The fatigue tests were performed under tension–tension mode at a frequency of 6 Hz and a load ratio R (minimum load/maximum load) = 0.1. These parameters were chosen based on prior studies [23, 24].

An IR camera [Model E95, supplied by Teledyne FLIR, USA] with a thermal resolution of 464×348 pixels and sensitivity of 50 mK was used to monitor the surface temperature of the test specimens during testing. Calibration for emissivity was carried out prior to the tests very much in accordance with procedures described in our previous study and resultant publication [25]. An area of approximately 60 mm (length) \times 40 mm (width) with a specimen hole at the centre was chosen to monitor the temperature during fatigue testing.

Results and Discussions

Tensile Tests

The room temperature tensile test results of the two specimens: ‘with hole’ and ‘without hole’ are compared in **Figure 3a**. The specimen ‘with hole’ revealed a $\sim 9\%$ reduction in the tensile strength when compared to the test specimen ‘without hole’ and a $\sim 50\%$ reduction in % elongation to failure (% EL). Based on ultimate tensile strength (UTS, σ_u) of the specimen, the fatigue loading parameters were selected and shown in **Figure 3b**. The σ_{\max} for the test specimen ‘without hole’ was 22.33 MPa while the load ratio $[R]$ and test frequency were the same.

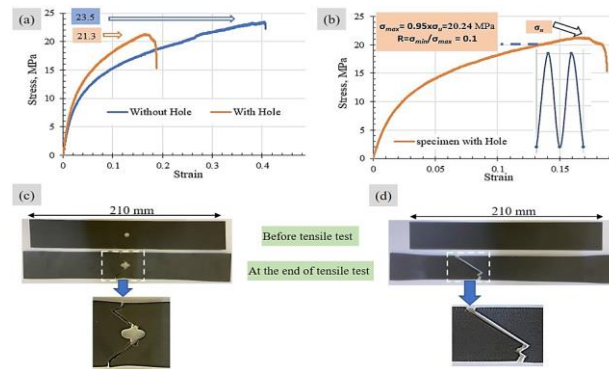


Figure 3. (a) A typical engineering tensile stress-strain plot of the two specimens (**Step-2**).

- (b) The rationale for selecting loading parameters for fatigue tests is depicted
 (c) Comparing the tensile specimen with hole, before and after failure, and
 (d) Comparing the tensile specimen without hole, before and after failure

The fracture surfaces of the two specimens, shown in **Figure 4**, does reveal two distinct features. The edges exhibit ‘fibrous texture’ due to extensive pulling between the surfaces while the ‘intermediate region’ did show delamination resulting in pull-out at 45° to the loading direction. The failure seems to have initiated from the hole, seen in **Figure 4a** and **Figure 4b**, that terminated with the edges showing unstable mode of fracture. This is possibly due to nature of the printing direction shown in **Figure 2**. The discontinuity during 3-D printing, highlighted by the yellow solid arrow in **Figure 2**, seems to be the cause of fracture initiating from the hole. ‘Front view’ indicates the first layer printed on the ‘bed’ while the ‘back view’ is the 24th layer on top of the specimen. The fracture surface at a higher magnification around the hole is shown in **Figure 5**. It is evident from the fractographic observations that failure initiated at the printing-induced defect resulting in a 9% reduction in tensile strength and essentially a 50% reduction in percent elongation to failure (%EL).

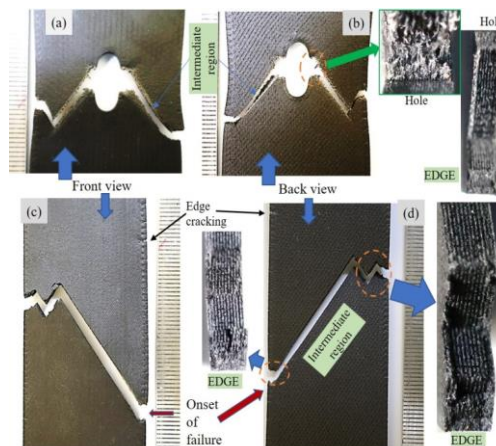


Figure 4. Failure mode of the (a,b) specimen with hole and the (c, d) specimen without a hole under quasi-static tensile test and the visible 24 layers. A millimetre scale is attached to the photograph.

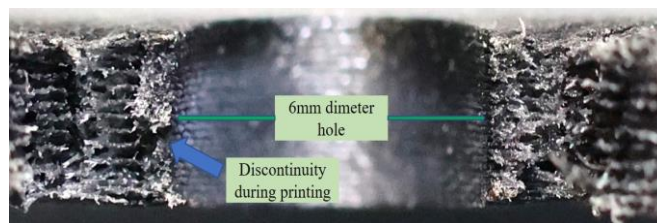


Figure 5. Tensile failure surface around the hole highlighting the ‘fibrous texture’ and defect leading to fracture. Loading direction is normal to the view.

Fatigue Characterization

During the fatigue tests, the test specimen was constantly monitored using a FLIR thermal IR camera [Model: E-95 model] from a distance of ~1m. Images were captured at regular intervals from the start of the test up until failure by fracture and this is shown in **Figure 6**. The rise in surface temperature (T) of the test specimen was plotted against the number of fatigue cycles (N) and is shown in **Figure 6a**. The temperature (T) versus cycles (N) plot shows three distinct regions: (i) an initial non-linear increase in temperature, this is followed by (ii) a long duration of constant temperature, and (iii) an abrupt increase in temperature resulting in failure by fracture. The maximum surface temperature recorded increased from 28 °C, at the start of the test, to 87.5 °C at the time of failure by fracture [$N_f = 94,343$ cycles]. The sequence of thermographs captured at various instances of time is shown in **Figures. 6b-f**. The temperature in the immediate vicinity of the hole instantly reduced to 51°C upon failure and is shown in **Figure 6g**.

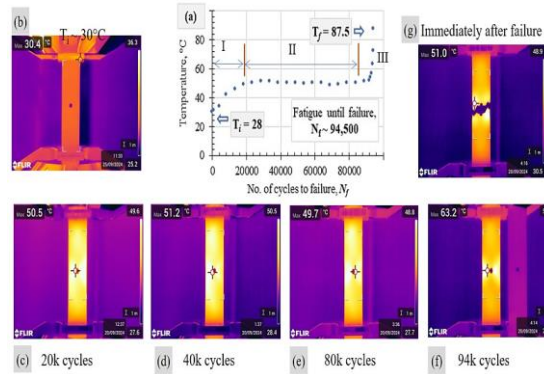


Figure 6. Constant amplitude fatigue testing at a frequency of 6 Hz (**Step-3**).

- (a) Test until 10^5 cycles or failure,
- (b-g) Thermal images of the specimen at various instances of fatigue testing

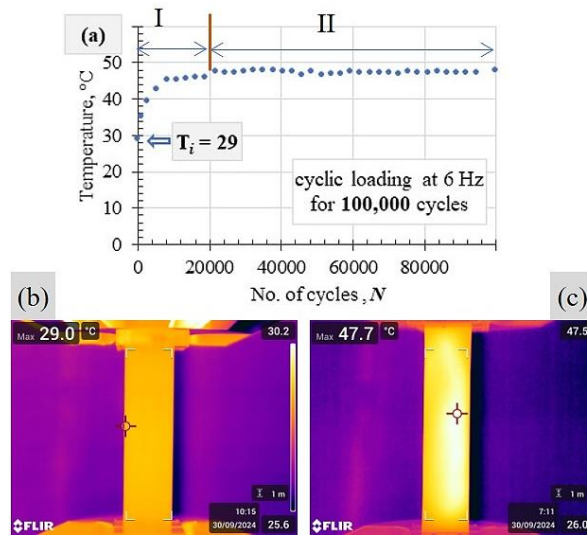


Figure 7. (a) Temperature of the specimen ‘without hole’ during fatigue testing (Step-4),
 (b) Thermogram of the specimen at the beginning of the test, and
 (c) Thermogram of the test specimen upon completing 10^5 cycles.

On the contrary, the test specimen ‘without hole’ lasted for complete 10^5 cycles. The temperature rise was similar, exhibiting a non-linear region for a short period of time followed by ‘iso-thermal’ region as shown in **Figure 7**. Although the test specimen could have exhibited region-III eventually, the test was terminated since it was beyond the scope of this research study. The present research study does clearly demonstrate that use of the thermal IR camera can give early warning of region III thereby preventing the occurrence of catastrophic failure.

High-temperature regions were observed on either side of the hole (**Figure 8**) and correspond to the regions of stress concentration in the test specimens. The damage initiated in the immediate vicinity of the hole and propagated towards the edges of the specimen. This does corroborate well with the observations made in previous section (**Figure 5**). Damage in the form of a crack appeared after 94,000 cycles and is shown in **Figure 8a**. An untested specimen ‘with hole’ is kept besides for the purpose of comparison of the surface temperature profile. The 6-mm diameter hole was stretched to 7.8 mm, equivalent to a strain of ~30%. The 36 mm wide specimen was reduced to 33.9 mm due to elongation at the centre and indicative of necking as shown in **Figure 8b**. The onset of region III in the temperature (T) versus number of fatigue cycles (N) plot corroborates well with the occurrence of plastic deformation resulting in ‘plastic zone’ ahead of

the notch [shown by dashed lines in **Figure 8c**]. The temperature distribution measured ahead of the ‘crack-tip’ showed a sudden drop near the periphery of the test specimen and is the inset shown in **Figure 8c**. A closer look at the fracture surface did indicate the damage to have propagated about 3 mm on both the sides of the hole prior to the onset of unstable propagation culminating in failure by fracture (see **Figure 9**). The unstable fracture seen in **Figure 9** is similar to the features shown in **Figure 4**.

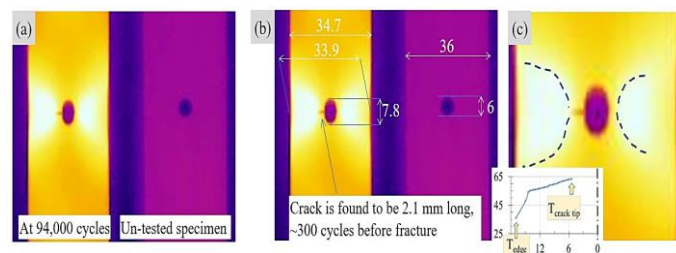


Figure 8. (a) Specimen with a hole showing fatigue crack just before failure.
 (b) Measurement of crack length and specimen deformation around the hole compared with untested specimen
 (c) Enlarged view of the specimen with hole highlighting the temperature distribution away from the crack tip.
 The area within the dashed line indicates higher temperature compared to far field.

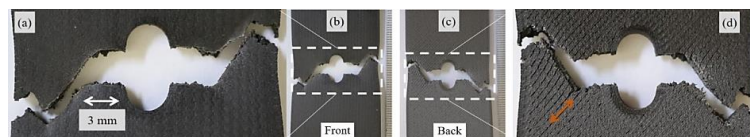


Figure 9. (a) Close-up micrograph of the (b) front portion of the specimen with hole,
 (c) Back side of the specimen and its
 (d) Enlarged view indicating printing direction in coloured arrow.

Conclusions

A 3-D printed Onyx® specimen ‘with hole’ was tested for both tensile properties and fatigue properties. For the purpose of comparison, test specimen ‘without hole’ was printed and tested under similar conditions. A thermal infra-red (IR) camera was used to monitor the heat signature during the fatigue tests. The following are the key findings of this research study:

1. The 3-D printed Onyx® specimen exhibits very good elongation to failure (~40%)
2. The test specimen ‘with hole’ lasted for ~94,500 fatigue cycles before failure at a stress ratio of $R = 0.1$. However, the test specimen ‘without hole’ did not fail even after 10^5 cycles. The maximum stress during cyclic loading was 95% of the ultimate tensile strength of the material.
3. A clear heat signature was evident prior to failure.
4. For the test specimen containing a “hole”, the pattern of failure was distinctly different under quasi-static tensile loading and constant amplitude fatigue loading.

Based on the observations, it is safely concluded that the 3-D printed Onyx® appears to be a good candidate for performance specific applications requiring a combination of good ductility and fatigue properties. Use of thermal IR camera in health monitoring of such materials in structural applications can prove to be beneficial for the purpose of detection of damage and failure. Further work is planned to understand the Visco-elastic behaviour of Onyx® vis-à-vis its fatigue performance and the usefulness of thermal IR camera in both damage prediction and monitoring.

Acknowledgements

The authors profusely thank (i) the Principal, B.M.S. College of Engineering, Bengaluru, (ii) the Head of the Department, Mechanical Engineering, for supporting the research activities. (iii) The technical support rendered by the staff, Mr. Praveen Bharadwaj in 3D printing of the specimens, and (iv) Mr. Mahesh S. (Research Scholar, VTU, Belagavi) for operating the UTM is acknowledged. (v) Also, thanks to the Head, R&D Department, for permitting the use of BSNCSIS facility in BMSCE. (vi) Thanks, are also due to M/s.Eagle Electricals, Bengaluru, for supplying with FLIR® thermal IR camera for the academic work.

References

- [1] M. Daly, M. Tarfaoui , M. Chihi, C. Bouraoui. Int. J. Adv. Manuf. Technol. 126, p.5307–5323 (2023). <https://doi.org/10.1007/s00170-023-11486-y>
- [2] D. Popescu, A. Zapciu, C. Amza, F. Baci, R. Marinescu, Polymer Testing, 69, pp. 157-166, (2018) <https://doi.org/10.1016/j.polymertesting.2018.05.020>.
- [3] M.N. Ahmad, A. Yahya . Designs. 7(6), p. 136. (2023) <https://doi.org/10.3390/Designs7060136>
- [4] <https://Markforged.Com/Materials/Plastics/Onyx> (accessed on 16 October 2024)
- [5] D. Nikiema, P. Balland, A. Sergent, Chinese Journal of Mechanical Engineering: Additive Manufacturing Frontiers, 2(2) , p.100075 (2023) <https://doi.org/10.1016/j.cjmeam.2023.100075>
- [6] L.G. Blok, M.L. Longana, H. Yu, B.K.S. Woods, Additive Manufacturing 22, pp. 176-186, (2018) <https://doi.org/10.1016/j.addma.2018.04.039>
- [7] M. T. Birosz, D. Ledenyák, M. Andó. Polym. Test., 113, p. 107654, (2022) <https://doi.org/10.1016/j.polymertesting.2022.107654>
- [8] D. Popescu, A. Zapciu, C. Amza, F. Baci, R. Marinescu, Polym. Test., 69, pp. 157-166, (2018) <https://doi.org/10.1016/j.polymertesting.2018.05.020>
- [9] C. Dávid, K. Peter, B. Jozef, B. František, Materials Research Proceedings, 34, pp 6-13, (2023) <https://doi.org/10.21741/9781644902691-2>
- [10] K. Ramachandran, M. N.Azadani, P. Ravichandran, N. B. Shivaprakash, M. Obi, C. L. Gnanasagaran, Prog. Addit. Manuf. 9, 2089–2097 (2024). <https://doi.org/10.1007/s40964-024-00565-5>
- [11] A.D. Pertuz-Comas, J.G. Díaz, O.J. Meneses-Duran, N.Y. Niño-Álvarez, J. León-Becerra. Polymers 14(17), p. 3586, (2022) <https://doi.org/10.3390/polym14173586>
- [12] S. Abbasi, R. Ladani, C. Wang, A. Mouritz, Compos. Part A-Appl. S., 147 (2021), p. 106440 <https://doi.org/10.1016/j.compositesa.2021.106440>
- [13] L. Safai, J. S. Cuellar, G. Smit, A. A. Zadpoor, A Review Of The Fatigue Behavior Of 3D Printed Polymers, Additive Manufacturing,

- Vol. 28, 2019, Pp. 87-97, ISSN 2214-8604,
<https://doi.org/10.1016/J.Addma.2019.03.023>
- [14] M. J. Martinez, J V. Soriano, J. S. Trinidad-Rendon, S. G. T. Cedillo, J C. Pérez, M C. Gonzalez. J. Compos. Sci., 8(1), 12 (2024),
<https://doi.org/10.3390/Jcs8010012>
- [15] A. Panerai, A. Canegrati, L.M. Martulli, M. Kostovic, G. Rollo, A. Sorrentino, M. Carboni, A. Bernasconi, I. J Fatigue, 174, , p. 107711, (2023) <https://doi.org/10.1016/J.Ijfatigue.2023.107711>
- [16] T. Jollivet, C. Peyrac, F. Lefebvre, Procedia Engineering 66 p. 746 – 758 (2013) <https://doi.org/10.1016/j.proeng.2013.12.128>
- [17] R. Maier, A. M. Istrate, A. Despa, A. C. Mandoc, S. Bucaciuc, R.Stoica, Materials, 15(14), (2022) p.5069;
<https://doi.org/10.3390/ma15145069>
- [18] L. Safai, J.S. Cuellar, G. Smit, A.A.Zadpoor, Additive Manufacturing, 28, (2019), p 87-97,
<https://doi.org/10.1016/j.addma.2019.03.023>
- [19] S. Shiri, M. Yazdani, M.A. Pourgol, Mater. Des., 88 (2015), p. 1290-1295, <https://doi.org/10.1016/j.matdes.2015.09.114>
- [20] F. W. Panella and A. Pirinu, I. J. Fatigue 152 1064032022
<https://doi.org/10.1016/j.ijfatigue.2021.106403>
- [21] J. Montesano , H. Bougherara, Z. Fawaz, Composites Part B: Engineering; 97: 137-143. (2014)
<https://doi.org/10.1016/j.compositesb.2013.12.053>
- [22] Z. Stankovičová, V. Dekýš, M. Uhříčik, P. Novák, B. Strnadel, Machine Modelling and Simulations 2017 EDP Sciences, 2018 MATEC Web Conf. 157, (2018)
<https://doi.org/10.1051/mateconf/201815705021>
- [23] J.R. Pothnis, A.K. Hajagolkar, A.R. Anilchandra, R. Das, S. Gururaja, Composite Structures 324 p.117557, (2023)
<https://doi.org/10.1016/J.Compstruct.2023.117557>
- [24] S. Gururaja, N. Manoharan, J.R. Pothnis, A.R.A Chandra, In: A. Beese, R.B.Berke, G.Pataky, S.Hutchens, (Eds) Fracture, Fatigue, Failure And Damage Evolution, Proceedings Of The Society For Experimental Mechanics Series. Springer, (2023)
https://doi.org/10.1007/978-3-031-17467-4_3
- [25] A.R.Anilchandra, J.R.Pothnis, A.K. Hajagolkar, , S. Hegde, , S. Gururaja, In: C.V. Chandrashekara, N.R. Mathivanan, K. Hariharan, (Eds) Recent Advances In Materials And Manufacturing. Lecture

Notes In Mechanical Engineering. Springer, Singapore. 2024
https://doi.org/10.1007/978-981-97-3654-6_27

[26] Onyx—Micro Carbon Fiber Filled Nylon that Forms the Foundation of Markforged Composite parts. Available online: <https://markforged.com/materials/plastics/onyx> (accessed on 16 October 2024).

Role Of Isothermal Surface Oxidation In Influencing Microstructure And Mechanical Response Of A Novel Shape Memory Alloy.

B. Maalolan¹, S. Santosh² and T.S. Srivatsan³

^{1,2} *Department of Mechanical Engineering*
Sri Sivasubramaniya Nadar College of Engineering
Old Mahabalipuram Road
Kalavakkam 603110, Tamil Nadu, India

³ *Department of Mechanical Engineering*
The University of Akron
Akron, Ohio 44325, USA

Abstract

Alloys that have the potential to retain the original form when susceptible to external stimuli such as thermomechanical changes are called Shape Memory Alloys (SMAs). The nickel-titanium (Ni-Ti) alloy “Nitinol” is favoured due on account of to its high recoverable strain, wear resistance, capability to withstand large deformation and acceptable mechanical performance. To reduce the martensite, start temperature (Ms) of the chosen Ni-Ti alloy, cobalt is added. Studies have shown that a non-reactive oxidation layer is formed on the top layer of the chosen NiTi alloy at room temperature. However, at the higher temperature the formation and presence of a passive oxidation layer does depend on both the composition and surface treatment given to the chosen material due to oxidation of the surface. At the higher temperatures, the NiTi tends to easily react with oxygen in the atmosphere resulting in the formation and presence of oxides. Isothermal oxidation tests were carried out on the chosen alloy by heating it in an incinerator at temperatures of 450, 550, 650 and 750°C for 60 minutes with the prime intent of examining the structure of the oxide. Differential Scanning Calorimetry (DSC) and X-ray diffraction (XRD) were performed on the oxidized sample. The microstructure of the NiTiCo alloy test specimens subsequent to oxidation was examined and analyzed using a scanning electron microscope (SEM). XRD results reveal the presence of the B2 austenite phase in the microstructure of the oxidized sample. The addition of cobalt did cause a notable drop in the transition temperature. As the temperature at which isothermal surface oxidation is performed is increased, the

transition temperatures are also increased. Scanning electron microscopy observations did reveal the temperature at which isothermal surface oxidation occurred. Also, it is noted that at a higher temperature oxidation occurs and greater is grain size of the surface oxides. In this paper, the results of the scanning electron microscopy observations is presented and adequately discussed.

Keywords: NiTiCo shape memory alloy; Isothermal oxidation; Scanning electron microscopy, Microstructure, Mechanical Properties

Introduction

SMA's are the sub-classification of shape memory materials (SMM), which can retain their original form when exposed to an external stimulus [1-6]. An alloy, which can exhibit a 1 way Shape Memory Effect (SME) when it is distorted at a temperature below the critical temperature (T_c) and reverts back to the initial shape upon heating above the T_c . The alloy needs to be further distorted to achieve the shape memory effect primarily because it retains its original, undeformed shape as it cools. If it is kept in mind that an alloy that has two separate geometries, one at the lower temperatures and one at the higher temperature, it will display a 2 way SME. A binary shape memory alloy displays a SME both when heated and when cooled. When this impact lacks any outside force, it is said to have an intrinsic bidirectional effect. A material is considered to exhibit super-elasticity when it is distorted by minor forces and instantly recovers to its original shape after the external forces have been removed. If the deforming force has been removed, an indestructible eyeglass frame made of super-elasticity can be bent or twisted without losing its original shape [7].

Nickel-titanium alloys are identified to be the most commercial shape memory alloy. Nitinol is often referred to as the parent of shape memory alloys (SMA's) due on account of the following: (i) its corrosion resistance, (ii) excellent fatigue strength, (iii) high recoverable strain, (iv) mechanical performance, (v) large deformation and good wear resistance, (vi) excellent damping qualities, and (vii) anti-ferromagnetic nature [8]. Nitinol exhibits a density of 6.5 g/cm^3 and melts over a temperature range of 1240°C - 1310°C . The transformation temperature can alter dramatically because of the addition of a ternary element [10-11].

Non-reactive oxides are manifested on the outer layer of Ni-Ti alloys at room temperature. However, their behaviour upon exposure to higher temperatures, depends on both the composition and surface

treatment of the materials as a direct consequence of surface oxidation [12]. Chu et al., deduced that the activation energy of Ni50-Ti50 for the purpose of oxidation was 226 kJ mol^{-1} [13]. Chan et al studied and found that the temperature at which oxidation occurs does influence the formation of oxides on the surface [14]. Another independent study [13] did thoroughly examine the oxidation of a Ti50Ni50 alloy in laboratory air at temperatures ranging from 700 °C to 1000°C. However, there was no evidence of scale spalling. The oxidation kinetics of the titanium metal does follow an exponential law at temperatures below 400 °C, a cubic law at temperatures between 400 °C - 600 °C, and a parabolic law at temperatures above 600 °C. Fristov and co-workers examined the isothermal oxidation of Ni-Ti shape memory alloys (SMAs) at temperatures ranging from 300 °C to 800°C [15]. Their independent research found that the Ni-Ti alloys did reveal various oxidation behaviour at temperatures both above 500 °C and below 500°C [16].

Fasching et al concluded from their exhaustive study that the transition temperature of the Ni-Ti alloy can be lowered by the addition of Cobalt [17]. They further noted and recorded and noted that an introduction of cobalt did enhance both the yield stress and work hardening coefficient of the Ni-Ti alloy. The addition of cobalt to Ni-Ti alloy did lower the martensite start [M_s] temperature as determined by Santosh et al. [18]. Gu and co-workers [19] did investigate the bio-reactive oxide layer surface on NiTi alloys. Heating the NiTi alloy to temperatures above 600°C can and does generate a protective layer of titanium dioxide (TiO_2) on the surface. Treatment temperatures spanning from 300 °C to 400 °C did result in a thin coating of nickel oxide.

The current research investigates the effect of mechanical properties and microstructure during surface oxidation of a NiTiCo alloy. In the present study, the NiTiCo alloy was subjected to exposure to oxygen across a temperature range of 450, 550, 650 and 750 °C. The characteristics of oxidised alloys were determined using a DSC and a SEM.

Materials and Methods

The NiTiCo alloy was used to investigate its oxidation behaviour. Raw nickel, titanium and cobalt of high purity were procured, and the surface impurities were removed by cleaning with acetone. The raw materials were then melted using a high-density graphite crucible. A covering of glass wool stopped the vacuum induction furnace's water-cooled copper coil from coming in direct

contact with the crucible. A zirconia coated steel mold was warmed to 525°C for one-full hour to prevent thermal incompatibility during casting of the molten alloy. The vacuum chamber was then shut, and the vacuum steadily increased as the crucible pot containing the charge and the heated mold was then placed inside. The induction current was used to heat both the charge and the crucible. The chamber was fed with argon gas under pressure and heated to 300°C. The alloy melted at 1400°C and was then put into a heated mold. The 3-mm thick cast alloy was then subject to the following procedure:

- (a) Taken out from the mold,
- (b) Plated with delta glaze (in order to avoid oxidation)
- (c) Homogenised at 900°C for three hours.

Hot rolling at 900°C was subsequently then used to decrease the thickness to 1-mm. The plate prepared is cut into 4 samples that measured 350 mm *150 mm in dimension. The samples were then kept in a furnace at temperatures of 450, 550, 650 and 750°C. The samples were heated for full 60 minutes in a crucible pot.

The test samples were then smoothened and etched using an etchant consisting of a mixture of (i) nitric acid (HNO₃), (ii) CH₃COOH, and (iii) hydrofluoric acid (HF) in equal parts. A scanning electron microscope [Model: QUANTA 400] with energy dispersive spectrum (EDS) facility was used for the purpose of analysis of the following: (i) layout of platelets, (ii) matrix, (iii) grain boundaries, and (iv) precipitate particles. DSC was then done to appreciate the reaction of isothermal surface oxidation on the transitional temperature. At a heat transfer rate of 20°C, the transformation/transition temperature was evaluated using the DSC [Model: NETZSCH-204]. A transition from the austenite (A) to martensite (M) did happen during the cooling cycle and the transition from M to A did happen during the heating cycle. The heating cycle involves an endothermic reaction (gradual absorption of heat) and the cooling cycle did involve an exothermic reaction (release of heat).

XRD studies were carried out on the oxidized sample at room temperature to identify the different phases present in the microstructure using an XRD equipment [**Model:** X'Pert Pro PANalytical] with CuK α radiation and a step angle range of 20-90 degrees. The CuK α has a wavelength of 1.54 λ and a voltage of 45kV. The rate of scanning was set to 0.01° for every second. The experiment did use CuK α radiation with an aperture, receiving slit and anti-scatter widths of 2-mm, 0.2-mm, and 2-mm respectively.

Results and Discussions

The Ni-Ti-Co alloy was successfully made using the technique of vacuum induction melting. The 4 test samples cut from 1-mm thick sheet were heated in a furnace that was maintained at temperatures of 450, 550, 650 and 750°C. Both DSC and XRD were carried out on the oxidised sample. The microstructure of the NiTiCo alloy test specimens subsequent to oxidation was carefully examined and analyzed using a SEM.

The XRD diffractogram of the oxidized samples at 450, 550, 650, and 750 °C. Each diffraction pattern accords with a different temperature at which the isothermal surface oxidation was performed. The XRD test results reveal the presence of the B2 austenite phase thus enabling in concluding that the martensite transition temperature is well below room temperature. The X-ray diffraction study also reveals the maximum diffraction intensity to correspond with the plane (011). As noted in **Figure 1**, due to a lower transformation temperature only the B2 phase exists, unlike the NiTi alloy where both martensite and B2 phase coexist as noted by other researchers in their independent studies [20-21].

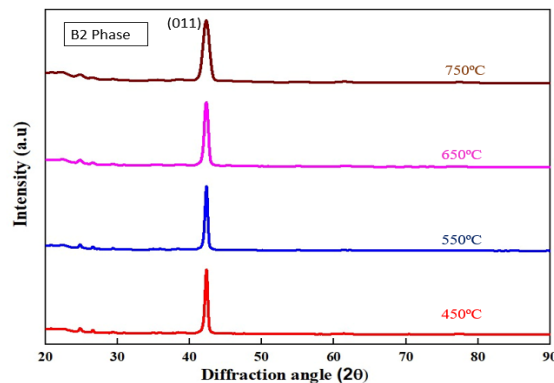


Figure 1. X-ray diffraction (XRD) patterns for the NiTiCo alloy

The room temperature XRD clearly reveals that all the alloys display the appearance of the B2 austenite phase. The diffraction intensity of the planes (012), (001) and (111) was found to be minimal in the diffractogram and when indexed together the peaks are not easily visible.

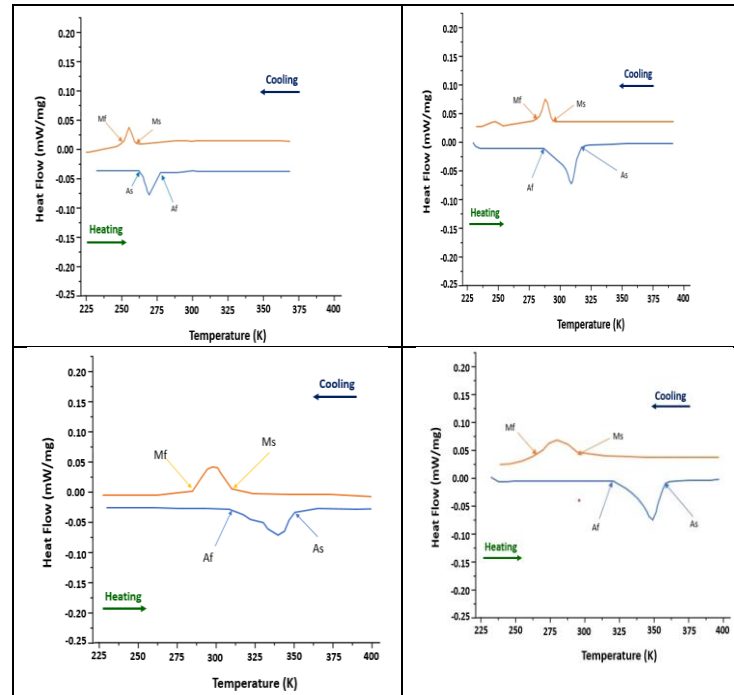


Figure 2. (a) DSC thermogram of oxidized sample at 450°C;
 (b) DSC thermogram of oxidized, sample at 550°C;
 (c) DSC thermogram of oxidized sample at 650°C;
 (d) DSC thermogram of oxidized sample at 750°C

As previously discovered by the authors, the addition of cobalt does lower the transition temperature [13, 17-18]. The transition of B2 to M does occur during a single cooling stage, as is shown in **Figure 2**. The transformation of martensite (M) to the B2 phase does occur during the heating period. The martensite finish temperature (M_f), martensite start temperature (M_s), austenite start temperature (A_s), and austenite finish temperature (A_f) and the transition temperatures of martensite (M) and the B2 phase, are shown in **Figure 2a**, **Figure 2b**, **Figure 2c**, and **Figure 2d**. These temperatures do reveal a noticeable increase as the rate of oxidation increases.

The SEM image of the oxidized sample at 450°C is shown in **Figure 3**. We did observe that the formed oxide layer is thin and we could see scratch marks in the micrograph taken using a SEM. The scratch marks were created during fine polishing of the test sample prior to oxidation. The size of the oxide grain was very small.

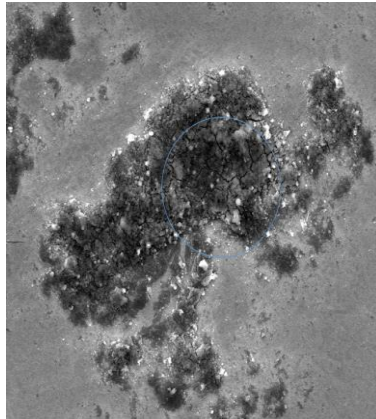


Figure 3. Scanning electron micrograph of the oxidised sample at 450°C.

The SEM micrograph of the oxidised sample at 550°C is shown in **Figure 4**. The oxide layer grain size is bigger than its counterpart of 450°C. We also note the formation and presence of a fine layer of titanium dioxide (TiO_2). We do observe the diffusion of titanium in the oxide layer.

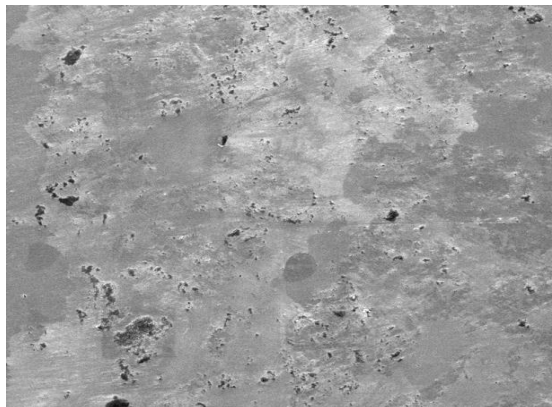


Figure 4. Scanning electron micrograph of the oxidized sample at 550°C.

At the higher temperature range of 650-750°C, size of the grain in the oxide layer was noticeably bigger than at the low temperature. Thus, we conclude that greater the temperature of the isothermal surface oxidation, then greater is the grain size of the oxide layer. From the scanning electron micrographs, we do observe the titanium dioxide (TiO_2) layer to be exposed to a higher temperature. Also, based entirely on observations we infer that no visible martensite phase to exist in the oxidized sample thus reaffirming results of the X-ray diffraction (XRD). A much complex microstructure was observed in

the micrographs that were taken using a scanning electron microscope (SEM). Oxidation of nickel (Ni) is difficult than that of titanium (Ti) [18]. Thus, the formation and presence of titanium dioxide (TiO_2) is easily visible on the outer scale. This is shown in the micrographs of **Figure 5a** and **Figure 5b**.

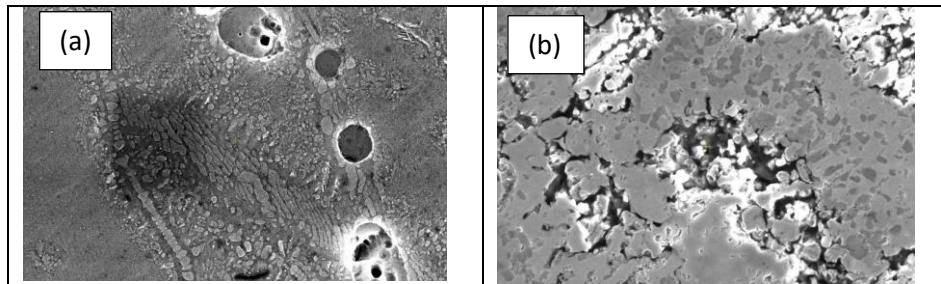


Figure 5. Scanning electron micrographs of the oxidized sample at (a) 650°C, and (b) 750°C

Conclusions

The role of isothermal surface oxidation on microstructure and mechanical properties of a NiTiCo was extensively studied using the techniques of XRD, SEM and DSC. Following are the key findings

1. The XRD results and SEM observations do reveal the microstructure of the oxidised samples to contain the B2 phase with NO martensite phase being present. The X-ray diffraction (XRD) studies also reveal the maximum diffraction intensity to correspond well with the plane (011).
2. The addition of cobalt does cause a significant decrease in the transition temperature. As the temperature at which the isothermal surface oxidation is performed is increased, the transition temperatures are also noticeably increased.
3. At 450°C, formation and presence of the oxide layer is thin and from scanning electron micrographs we do see scratch marks. The scratch marks are formed during polishing prior to oxidation. The grain size of the oxide layer was noticeably small.
4. At the higher temperatures, we did observe from the scanning electron micrographs the synthesis of titanium dioxide (TiO_2) on the surface.
5. Higher the temperature of isothermal surface oxidation, greater is the grain size of the oxide layer

References

- [1] K. Otsuka, C.M. Wayman, in *Shape Memory Materials*, Cambridge University Press, Cambridge, 1998, pp. 1–90.
- [2] Maalolan, B., & Santosh, S. (2024). *A review on CuAlNi shape memory alloys: Production methods, applications and current trends*. **Materials Today: Proceedings**. <https://doi.org/10.1016/j.matpr.2024.03.026>
- [3] S. Santosh, G. Nithyanandh, J. Ashwath, K.L. Kishore, *Comparison of Internal friction measurements on Ni-Ti reinforced smart composites prepared by Additive Manufacturing*, **J. Alloys Compd.** 924 (2022) 166027, <https://doi.org/10.1016/j.matpr.2022.09.538>
- [4] V. Sampath, R. Srinithi, S. Santosh, P.P. Sarangi, J.S. Fathima, *The Effect of Quenching Methods on Transformation Characteristics and Microstructure of a NiTiCu Shape Memory Alloy*, **Trans. Indian Inst. Met.** 73 (6) (2020) 1481– 1488, <https://doi.org/10.1007/s12666-020-01909-9>
- [5] S. Santosh, A.N. Tuan, 7 - *NiTi-based ternary shape-memory alloys. Micro and Nano Technologies, Nickel-Titanium Smart Hybrid Mater.* (2022) 123–137, <https://doi.org/10.1016/B978-0-323-91173-3.00006-7>
- [6] E. Hornbogen, in *Advanced Structural and Functional Materials*, Springer, Heidelberg, 1991, p. 133, <https://doi.org/10.1007/s11661-003-0186-x>
- [7] W.B. Jefrin Harris, Achudha Vagheesan Dehaleesan, Santosh Sampath, Anirudh Venkataraman Krishnan. "A state-of-the-art review on electric discharge machining of shape memory alloys", **Materials Today: Proceedings**. 72, <https://doi.org/10.1016/j.matpr.2022.09.538>
- [8] L. Selvaraj an, C. Sathiya Narayanan, R. Jeyapaul *Optimization of Process Parameters to Improve Form and Orientation Tolerances in EDM of MoSi -SiC Composites*. **Materials and Manufacturing Processes**. (2014) P956. <https://doi.org/10.1080/10426914.2014.962041>
- [9] Manjeri, R. M., D. Norwich, F. Sczerzenie, X. Huang, M. Long, and M. Ehrlinspiel. "A study of thermo-mechanically processed high stiffness NiTiCo shape memory alloy." **Journal of Materials Engineering and Performance** 25 (2016): 894–900. <https://doi.org/10.1007/s11665-016-1932-8>

- [10] Zarinejad, Mehrdad, and Yong Liu. "Dependence of transformation temperatures of NiTi-based shape-memory alloys on the number and concentration of valence electrons." **Advanced Functional Materials** 18, no. 18 (2008): 2789-2794. <https://doi.org/10.1002/adfm.200701423>
- [11] Bozzolo, Guillermo, Ronald D. Noebe, and Hugo O. Mosca. "Site preference of ternary alloying additions to NiTi: Fe, Pt, Pd, Au, Al, Cu, Zr and Hf." **Journal of alloys and compounds** 389, no. 1-2 (2005): 80-94. <https://doi.org/10.1016/j.jallcom.2004.07.051>
- [12] Duerig, T., A. Pelton, and D. J. M. S. Stöckel. "An overview of nitinol medical applications." **Materials Science and Engineering: A** 273 (1999): 149-160. [https://doi.org/10.1016/S0921-5093\(99\)00294-4](https://doi.org/10.1016/S0921-5093(99)00294-4)
- [13] Chu, C. L., S. K. Wu, and Y. C. Yen. "Oxidation behavior of equiatomic TiNi alloy in high temperature air environment." **Materials Science and Engineering: A** 216, no. 1-2 (1996): 193-200. [https://doi.org/10.1016/0921-5093\(96\)10409-3](https://doi.org/10.1016/0921-5093(96)10409-3)
- [14] Chan, C. M., Trigwell, S., & Duerig, T. (1990). *Oxidation of an NiTi alloy. Surface and interface analysis*, 15(6), 349-354. <https://doi.org/10.1002/sia.740150602>
- [15] Khanna, A. S. (2002). *Introduction to high temperature oxidation and corrosion*. ASM international.
- [16] Firstov, G. S., R. G. Vitchev, H. Kumar, Bart Blanpain, and Jan Van Humbeeck. "Surface oxidation of NiTi shape memory alloy." **Biomaterials** 23, no. 24 (2002): 4863-4871. [https://doi.org/10.1016/S0142-9612\(02\)00244-2](https://doi.org/10.1016/S0142-9612(02)00244-2)
- [17] Fasching, Audrey, D. Norwich, T. Geiser, and Graeme W. Paul. "An evaluation of a NiTiCo alloy and its suitability for medical device applications." **Journal of materials engineering and performance** 20, no. 4-5 (2011): 641-645. <https://doi.org/10.1007/s11665-011-9845-z>
- [18] Santosh, S., and V. Sampath. "Effect of ternary addition of cobalt on shape memory characteristics of Ni-Ti alloys." **Transactions of the Indian Institute of Metals** 72 (2019): 1481-1484. <https://doi.org/10.1007/s12666-019-01591-6>
- [19] Gu, Y. W., Tay, B. Y., Lim, C. S., & Yong, M. S. (2005). *Characterization of bioactive surface oxidation layer on NiTi*

- alloy. **Applied Surface Science**, 252(5), 2038-2049.
<https://doi.org/10.1016/j.apsusc.2005.03.207>
- [20] Jing, R. R., and Liu, F. S. (2007). *The influence of Co addition on phase transformation behavior and mechanical properties of TiNi alloys*. **Chinese Journal of Aeronautics**, 20(2), 153-156. [https://doi.org/10.1016/S1000-9361\(07\)60024-7](https://doi.org/10.1016/S1000-9361(07)60024-7)
- [21] Lekston, Z., & Łągiewka, E. (2007). X-ray diffraction studies of NiTi shape memory alloys.

Advanced Processing and Optimization of NiOx as a Hole Transport Layer in Perovskite Solar Cells

¹K Shashank Kumar, ²Pradyumna J

^{1,2}*Department of Centre for Sensors & Vision Technology,
Central Manufacturing Technology Institute,
Bengaluru*

Abstract

Recent advancements in perovskite solar cells (PSCs) highlight the critical role of hole transport layers (HTLs) in enhancing charge carrier extraction and transport. Nickel oxide (NiO) has emerged as a promising inorganic HTL material for PSCs, valued for its high hole mobility, chemical stability, optical transparency, and compatibility with various perovskite materials. This study focuses on the fabrication and optimization of NiO thin films as HTLs, utilizing electron beam evaporation deposition (EBED) on Glass/ITO substrates with thicknesses ranging from 30 nm to 50 nm. Post-deposition samples were thermally oxidized for the conversion of Nickel to Nickel oxide. The structural, morphological, optical properties of Nickel oxide films were analyzed using advanced characterization techniques. Findings indicate that optimized NiO layers enhance charge extraction, transport, and reduce recombination, thereby improving PSC performance. This work highlights the importance of NiO layer thickness and composition in developing efficient and high-performance PSCs.

Introduction

Perovskite solar cells (PSCs) have emerged as a transformative technology in the field of photovoltaics due to their high power conversion efficiencies, low material costs, and potential for scalable production. Unlike traditional silicon-based solar cells, PSCs utilize perovskite-structured compounds that exhibit exceptional light absorption, favorable bandgaps, and high defect tolerance, making them highly efficient in capturing and converting sunlight into electricity. However, while PSCs have shown remarkable laboratory efficiencies—approaching those of commercial silicon cells—their long-term stability, scalability, and environmental sensitivity present significant challenges that must be overcome for commercial viability (Djurišić et al., 2015). Research in recent years has focused on optimizing the architecture of PSCs, with particular attention to the

design and development of hole transport layers (HTLs), which are crucial for efficient charge extraction and overall device performance (Kim et al., 2014). In PSCs, the role of the HTL is to selectively extract and transport positive charge carriers (holes) generated in the active perovskite layer while blocking electrons, thus ensuring efficient charge separation and transport to the electrodes. An effective HTL enhances the power conversion efficiency (PCE) of PSCs by reducing recombination losses and providing stable interfaces within the cell structure. Among various materials explored as HTLs, nickel oxide (NiO) has gained significant interest due to its exceptional stability, compatibility with the perovskite layer, and tunable electrical and optical properties (Aydın et al., 2018). NiO, a p-type semiconductor with a wide bandgap, offers a suitable energy level alignment with perovskite materials, which facilitates efficient hole extraction and transport. Additionally, NiO is relatively low-cost, abundant, and environmentally benign compared to conventional HTL materials, making it an attractive choice for sustainable PSC applications (Liu et al., 2018; Di Girolamo et al., 2020). Nickel oxide (NiO) has garnered attention as an efficient hole transport material for PSCs due to its unique physical and chemical properties. NiO offers a favourable valence band alignment with perovskite active layers, enabling efficient hole extraction and transport to the electrode. Its wide bandgap and excellent chemical stability contribute to an effective hole transport process, minimizing recombination losses and enhancing the operational lifespan of PSCs. Additionally, NiO is optically transparent, facilitating maximum light absorption in the active layer, and exhibits favourable doping properties that enable modulation of its conductivity. NiO's wide bandgap (3.7–4.0 eV) and high transparency enable it to act as an effective HTL that minimizes parasitic absorption and allows for high optical transmission, which is critical for capturing more incident light in the perovskite layer (Yin et al., 2019). Its favorable energy level alignment with the perovskite layer reduces potential energy barriers, thus enhancing hole extraction and improving overall device efficiency. Unlike organic HTLs, NiO's inorganic nature imparts greater thermal and chemical stability to PSCs, which is essential for prolonged operational lifetimes (Nkele et al., 2020). Additionally, the chemical robustness of NiO makes it less susceptible to environmental degradation factors such as moisture and UV exposure, addressing one of the main limitations of PSCs. Recent studies have reported impressive improvements in PSC performance using NiO-based HTLs, with devices achieving efficiencies exceeding 20% (Liu et al., 2018). The enhancement in performance has been accomplished through various fabrication methods such as solution

processing, sputtering, atomic layer deposition (ALD), and chemical vapor deposition (CVD), with each technique influencing the structural, electronic, and optical properties of NiO in unique ways.

Different fabrication methods for NiO-based HTLs have been explored to optimize their properties for PSCs, each presenting distinct advantages and limitations. Solution-based methods, such as spin-coating and combustion synthesis, offer low-cost, low-temperature processing compatible with flexible substrates, making them attractive for scalable manufacturing. These methods have produced PSCs with high PCEs, but they can sometimes lead to inconsistencies in film quality, requiring careful control of processing conditions to ensure uniformity (Liu et al., 2018). Sputtering and e-beam evaporation, on the other hand, allow for better control over film thickness and composition, yielding high-quality films with excellent reproducibility and scalability (Abzieher et al., 2019). Plasma-assisted ALD is another promising technique for NiO deposition, as it enables precise control over film properties, such as thickness and stoichiometry, at low temperatures. This method is particularly suitable for PSCs requiring ultrathin HTLs to enhance charge extraction without increasing series resistance. However, ALD equipment is relatively expensive, which may limit its accessibility for large-scale production (Koushik et al., 2019).

This study aims to provide an in-depth examination of NiO as an HTL in PSCs, focusing on its structural, electrical, and optical properties and how these contribute to device performance. It also reviews current deposition techniques and evaluates their effectiveness in enhancing stability and efficiency. Through this investigation, we aim to highlight the transformative potential of NiO in the development of next-generation PSCs and underscore the ongoing research required to harness this potential fully.

Materials and Methods

Materials

Indium tin oxide (ITO)-coated glass substrates size of 20mm X 20 mm were sourced from SHILPENT Enterprises, featuring a surface resistivity of less than 10 ohms per square. Nickel pellets, with 99.995% purity, along with acetone, isopropanol, and deionized water, were employed in the substrate cleaning process to ensure optimal surface quality for deposition.

Preparation for Deposition of Nickel

The ITO substrates were prepared by a systematic cleaning process to ensure optimal surface conditions for deposition, targeting dust and impurities on the surface. Each substrate was sequentially immersed and agitated in separate petri dishes: first in acetone for 5 minutes, then in isopropyl alcohol for another 5 minutes, and finally rinsed with distilled water to eliminate any residual solvents. After this, the substrates were dried with nitrogen gas and then heated on a hot plate at 120°C for 10 minutes to remove any remaining moisture and improve surface adhesion for the subsequent deposition process.

Deposition of Nickel

Electron-beam evaporation, a physical vapor deposition (PVD) technique, employs a high-voltage electron gun to focus an electron beam on the source material, heating it to its vaporization point. This process occurs within a vacuum chamber to prevent contamination and reduce interactions with gas molecules. As the electron beam strikes the source (evaporant), kinetic energy transforms into thermal energy, causing rapid evaporation. The resulting vapor plume travels in a direct path due to the low-pressure environment, condensing onto a substrate above to form a thin film.

For this study, nickel pellets (99.995% pure) were deposited onto indium tin oxide (ITO) substrates at thicknesses of 30 nm, 40 nm, and 50 nm using the Kenosistec KE 500EI electron-beam evaporator. Following deposition, heat treatment was applied to oxidize the nickel into nickel oxide, optimizing its properties as a hole transport layer.

Thermal Annealing of Deposited Nickel films

In this study, thermal annealing was employed to convert nickel (Ni) thin films into nickel oxide (NiO) using a muffle furnace set to 450°C. The choice of this annealing temperature was based on prior studies indicating that temperatures in the range of 400–500°C effectively promote oxidation while preserving thin-film uniformity. In preparation for a controlled thermal gradient annealing of nickel-deposited samples, a muffle furnace was employed based on Mustafa et al. [1]. Initially, the furnace interior was cleaned to avoid contamination. Nickel-deposited samples were placed on a clean metal plate inside the furnace, beginning at room temperature. The heating process involved a series of ramps: an initial ramp of 2 minutes to 100°C with a 2-minute soak, followed by a 4-minute ramp to 200°C and a 10-minute soak (buffered by +25°C). A gradual 6-minute ramp raised the temperature to 325°C with a 30-minute soak, and a final ramp to 425°C for one hour. After reaching the target temperature of

450°C, the furnace was switched off to allow samples to cool overnight. This controlled ramping process was crucial for achieving uniform thermal treatment.

Characterization Techniques for NiO Thin Films

To enhance the performance of nickel oxide (NiO) as a hole transport layer (HTL) in perovskite solar cells, various characterization techniques are essential for analyzing and optimizing its properties. These techniques assess critical parameters such as morphology, crystallinity, optical properties, electrical conductivity, and interfacial compatibility with perovskite materials. Here's a detailed overview of key characterization techniques commonly used for NiO thin films.

Morphological and Structural Analysis

Scanning Electron Microscopy (SEM) - Energy dispersive spectroscopy (EDS)

SEM-EDS enables imaging the surface morphology and elemental composition of NiO films at high resolution. By providing high-resolution images, SEM helps assess the surface roughness, grain size, and uniformity. SEM images can reveal surface defects, cracks, or pinholes, which, if present, may lead to undesirable charge recombination in the device. Energy Dispersive Spectroscopy (EDS) is an analytical technique that detects and identifies the elemental composition within a sample. This provides both qualitative and quantitative insights into major, minor, and trace elements within the material. SEM-EDS was obtained on Zeiss, Ultra55.

X-Ray Diffraction (XRD)

XRD is used to determine the crystallinity, crystal structure, and phase composition of NiO films. Analyzes the crystal structure of a material by measuring the diffraction pattern of X-rays. This helps in identifying the specific crystalline phases. Crystallinity can have a major impact on charge transport. XRD is also useful for detecting impurities or secondary phases that may form during film fabrication.

XRD scans were obtained on Rigaku, Smartlab X-ray diffractometer and scan ranges from 10° to 90°.

Chemical Composition and Surface Analysis

X-Ray Photoelectron Spectroscopy (XPS)

XPS is a critical tool for analyzing the surface composition, elemental state, and chemical bonding in NiO films. XPS depth profiling can also reveal information about the NiO perovskite interface, which is

important for understanding interfacial recombination mechanisms. XRD scans was obtained on Kratos,AxisDLD.

Optical Properties Characterization

UV-Visible Spectroscopy

UV-Visible spectroscopy provides information on the optical absorption of NiO films, which is essential for understanding their transparency and bandgap. For optimal performance, NiO films are expected to have a broad bandgap, typically around 3.7 to 4.0 eV, which is essential to permit adequate light to pass through to the perovskite layer.

UV-Visible spectroscopy scans were obtained on Shimadzu UV 3600 scan ranges was between 300-800 nm.

Results and Discussion

Morphological Analysis

Surface morphology of NiO layers onto the glass/ITO substrate was investigated using scanning electron microscopy as presented the surface morphology of NiO film at 450 °C shows no cracks due to the suitable limit of temperature. However, by increasing the reaction temperature to 450°C, the Ni metals begin to grow into NiO, forming gradually separated grains (defective or non-uniformly structure) of NiO layers with some uncompleted Ni–O reaction on the sample. These unreacted Ni metal on NiO layers would increase the sample conductivity during the experiments with the formation of more electrons. The SEM image of the NiO layer annealed at 450°C with a 40 nm thickness that exhibits coarse grains provides valuable insight into the film morphology. From figure 1 its shows coarse grain formation can indicate a crystalline structure with larger grain boundaries, which could impact the materials electronic properties. Such a morphology may enhance the charge transport properties by reducing resistance pathways. However, coarse grains might also contribute to increased surface roughness, potentially affecting the interface contact with the perovskite layer. Controlling the annealing temperature and deposition parameters is crucial to balancing grain size for optimal device performance.

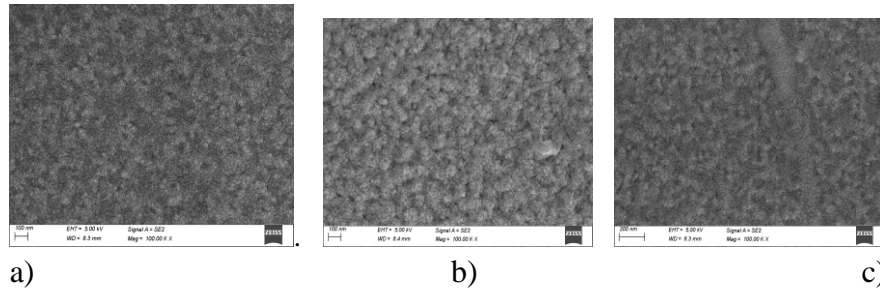


Figure.1 SEM images of the NiO films which were annealed at 450° C
a) 30nm NiO, b) 40nm NiO, c) 50nm NiO

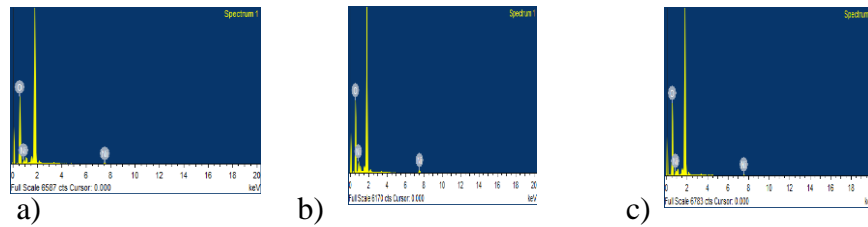


Figure.2 EDS Spectrum of the NiO films a) 30nm NiO, b) 40nm NiO, c) 50nm NiO

Table 1 EDS spectrum of annealed NiO films at different thickness

Element	Weight (%)			Atomic (%)		
Thickness of NiO film	30 nm	40 nm	50 nm	30 nm	40 nm	50 nm
O K	92.54	84.37	93.32	97.85	95.19	98.09
Ni K	7.46	15.63	6.68	2.15	4.81	1.91
Totals	100	100	100	100	100	100

The EDS analysis of the annealed NiO layers reveals variations in oxygen content and atomic weight percentage across NiO thicknesses of 30 nm, 40 nm, and 50 nm. These investigation shows annealed Nickel exhibits high content of oxygen and conversion to NiO and exhibit the most favorable stoichiometric balance, which is essential for efficient hole transport in its role as a hole transport layer (HTL) in photovoltaic applications. From the Table 1 the EDS analysis for the annealed NiO layers at thicknesses of 30 nm, 40 nm, and 50nm the 30 nm NiO layer exhibits an oxygen content of 92.54%, whereas the 40

nm layer shows a reduced oxygen content at 84.37%, and the 50 nm layer demonstrates an increased oxygen content of 93.32%. These results suggest that the 50 nm NiO layer achieves a more complete oxidation, which may enhance its structural integrity and electronic performance, while the lower oxygen content in the 40 nm layer could indicate partial oxidation or the presence of oxygen vacancies, potentially affecting charge transport and recombination properties. The atomic weight percentage analysis further corroborates these findings, with values of 97.85% for the 30 nm layer, a drop to 95.19% for the 40 nm layer, and an increase to 98.09% for the 50 nm layer. This trend in atomic weight aligns with the oxygen content data, as the higher atomic weight in the 50 nm layer reflects a composition closer to stoichiometric NiO. The deviation observed in the 40 nm layer suggests a non-stoichiometric composition, which may require optimized deposition or annealing conditions to achieve the desired purity and structural properties for high-performance applications. These compositional distinctions underscore the influence of film thickness on NiO quality and highlight the importance of precise thickness control in fabricating effective NiO-based HTLs for perovskite solar cell applications.

The X-ray Diffraction (XRD) analysis of Nickel Oxide (NiO) as a Hole Transport Layer (HTL) shows diffraction peaks at approximately 20°, 40°, 45°, and 65°, which offer valuable insights into the crystalline structure and phase integrity of the material. From figure.3 it shows the XRD patterns peaks at 40° and 45° are associated with the (111) and (200) planes of cubic NiO, affirming the presence of a polycrystalline cubic phase. These planes are crucial as they indicate well-aligned crystal domains, which facilitate efficient charge transport. The peak at 65° may be attributed to higher-index planes such as (220), confirming extended crystalline order.

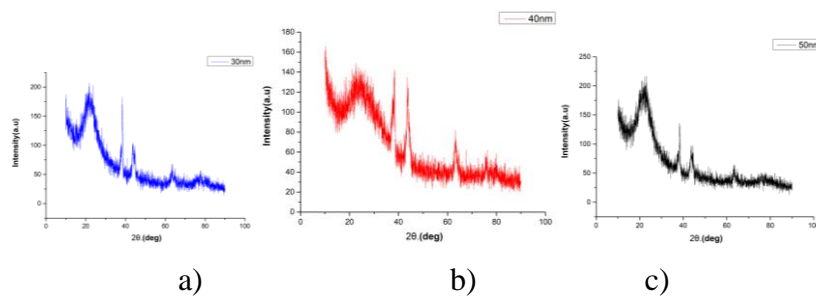


Figure.3 XRD patterns of the NiO films a) 30nm NiO, b) 40nm NiO, c) 50nm NiO

The broad nature and noise of the peaks indicate a degree of structural imperfection, suggesting either fine grain size or partial amorphous content due to suboptimal growth or incomplete crystallization. Such broadened peaks imply microstructural inconsistencies that may influence electronic properties by increasing charge carrier trapping sites and reducing mobility. The sharper, well-defined peaks represent higher crystallinity, which enhances charge transport by minimizing recombination and improving hole mobility in HTLs. Heat treatment plays a pivotal role in optimizing crystallinity. For NiO, annealing at approximately 450°C promotes phase stabilization and oxygen diffusion, leading to the formation of stoichiometric NiO and suppressing secondary phases like NiO₂ or Ni₂O₃. The presence of any secondary phases, which may appear as minor peaks, can detrimentally affect charge transport properties, thereby reducing the performance of the HTL in device applications. This analysis underscores the necessity of refined deposition and annealing processes to achieve a high-quality crystalline NiO layer, optimizing its use in perovskite solar cells for enhanced power conversion efficiency and device stability.

Chemical Composition and Surface Analysis

The X-ray photoelectron spectroscopy (XPS) analysis of NiO as a hole transport layer (HTL) typically reveals a prominent peak around 530 eV in the binding energy spectrum, corresponding to the O 1s core level. From the figure shows the peak is associated with the oxygen lattice in nickel oxide and indicates the presence of Ni–O bonds, which are characteristic of NiO.

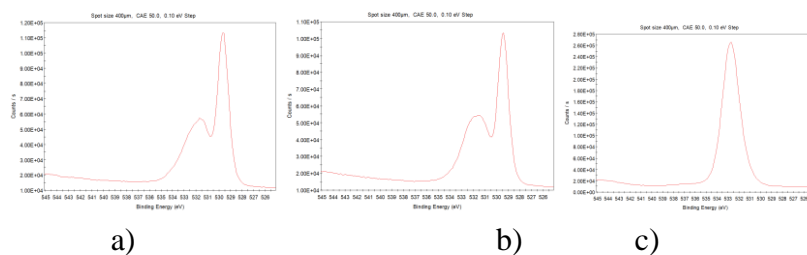


Figure.4 XPS spectrum of the NiO films a) 30nm NiO, b) 40nm NiO, c) 50nm NiO

The analysis of this peak, along with any shifts or additional shoulder features, can provide insights into the chemical state, stoichiometry, and potential defect levels within the NiO layer, which are crucial for assessing its electronic properties and overall

effectiveness as an HTL in perovskite solar cells. The X-ray photoelectron spectroscopy (XPS) analysis of the NiO layer, particularly the peak around 530 eV corresponding to the O 1s binding energy, is indicative of oxygen in the Ni–O lattice structure. This peak confirms the successful formation of NiO with a stoichiometric oxygen component. This peak frequently serves as a reference point to confirm the phase purity of the NiO layer and to assess potential non-stoichiometric oxygen defects or adsorbed surface species, which may influence the electronic structure and efficiency of hole transport. The shifts in the O 1s peak or additional features (e.g., shoulders around 531–532 eV) suggest the presence of hydroxyl groups, oxygen vacancies, or chemisorbed species on the NiO surface. For effective application as a hole transport layer (HTL), maintaining a balance between sufficient oxygen content and minimal defect density is essential. Optimizing Adjusting the annealing temperature and deposition techniques for NiO can affect these XPS peak features, subsequently influencing the stability and performance of the device.

Optical Properties Characterization

UV-Vis spectroscopy technique evaluated the optical properties of the nickel oxide (NiO) layer, a critical factor in determining its effectiveness in solar cell applications. This technique provides precise measurements of light absorption from the ultraviolet to visible spectrum, allowing for accurate estimation of the NiO film's bandgap energy. The absorption spectrum also serves to detect potential impurities or structural defects, contributing to quality control in the deposition process. Analysis revealed that a 40 nm NiO layer demonstrated superior absorption characteristics, particularly with peak absorbance between 350 nm and 370 nm. This finding highlights a significant correlation between film thickness and optical performance, indicating that a 40 nm layer optimizes light absorption, which is essential for efficient hole transport. Such optimization is crucial to enhancing solar cell efficiency by ensuring the hole transport layer supports effective charge movement with minimal energy dissipation.

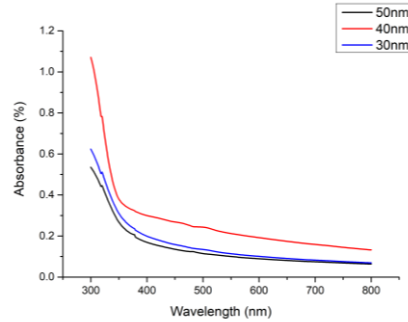


Figure. 5 Absorbance graph of NiO films

From the figure.5 shows the transmittance coefficient results indicate that the 40 nm nickel oxide (NiO) layer experiences significant photon transmission loss, suggesting that while it effectively absorbs photons, it transmits fewer to subsequent layers. This reduction in transmittance adversely affects the structural efficiency of the solar cell device, particularly impacting its Incident Photon-to-Electron Efficiency (IPCE) and overall power conversion efficiency (PCE). Although a lower transmittance might be acceptable in configurations where the hole transport layer (HTL) is the bottom-most layer on ITO glass, alternative stacking configurations could lead to considerable IPCE losses, ultimately diminishing device efficiency. These findings emphasize the critical need to balance absorption and transmission properties when optimizing the NiO layer for high-performance perovskite solar cell (PSC) configurations.

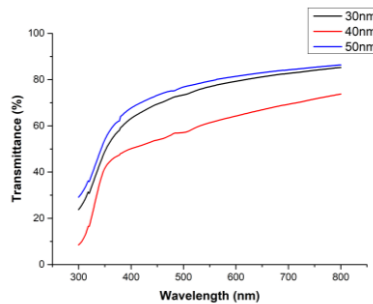


Figure.6 Transmittance graph of NiO films

Conclusion

In this study, the properties of nickel oxide (NiO) layers annealed at 450°C were comprehensively analyzed to evaluate their suitability as hole transport layers (HTLs) for perovskite solar cells. The findings from Scanning Electron Microscopy (SEM), Energy Dispersive Spectroscopy (EDS), X-ray Diffraction (XRD), X-ray Photoelectron

Spectroscopy (XPS), and UV-Vis spectroscopy provide a detailed understanding of the structural, compositional, and optical characteristics of NiO thin films at varying thicknesses (30 nm, 40 nm, and 50 nm). In conclusion, this study investigates the importance of precise control over NiO film thickness, annealing conditions, and compositional purity in optimizing NiO for use as a hole transport layer in perovskite solar cells. While thicker NiO layers (50 nm) exhibited improved oxidation and stoichiometric balance, thinner layers (30 nm) demonstrated partial oxidation, which could affect the electronic properties and charge transport efficiency. The 40 nm NiO layer, although exhibiting favorable absorption properties, presented challenges related to photon transmission. Therefore, careful optimization of deposition and annealing parameters is essential to enhance the performance and stability of NiO-based HTLs in perovskite solar cells.

Acknowledgments

We acknowledge and express our sincere gratitude to our institution Central Manufacturing Technology Institute and our director of the Institute, Dr. Nagahanumai, for providing the necessary facilities to conduct this research. We also acknowledge the CeNSE, MNCF, Indian Institute of Science, Bengaluru, for their support and for providing characterization facilities essential for this study.

References

1. Aboulsaad, M., Tahan, A. E., Soliman, M., El-Sheikh, S. M., & Ebrahim, S. (2019). Thermal oxidation of sputtered nickel nano-film as hole transport layer for high performance perovskite solar cells. *Journal of Materials Science: Materials in Electronics*, 30(22), 19792–19803.
2. Abzieher, T., Moghadamzadeh, S., Schackmar, F., Eggers, H., Sutterlüt, F., Farooq, A., Kojda, D., Habicht, K., Schmagel, R., Mertens, A., Azmi, R., Klohr, L., Schwenzer, J. A., Hetterich, M., Lemmer, U., Richards, B. S., Powalla, M., & Paetzold, U. W. (2019). Electron-Beam-Evaporated nickel oxide hole transport layers for Perovskite-Based photovoltaics. *Advanced Energy Materials*, 9(12).
3. Aydın, E., Troughton, J., De Bastiani, M., Ugur, E., Sajjad, M., Alzahrani, A., Neophytou, M., Schwingenschlögl, U., Laquai, F., Baran, D., & De Wolf, S. (2018). Room-Temperature-Sputtered Nanocrystalline Nickel Oxide as Hole Transport Layer for p-i-n

Perovskite Solar Cells. *ACS Applied Energy Materials*, 1(11), 6227–6233.

4. Djurišić, A. B., Wu, Y., Yue, Y., Liu, J., Zhang, W., Yang, X., Chen, H., Bi, E., Islam, A., Grätzel, M., & Li, H. (2015). Efficient and stable large-area perovskite solar cells with inorganic charge extraction layers. *Science*, 350(6263), 944–948.
5. Kim, J. H., Liang, P., Williams, S. B., Cho, N., Chueh, C., Glaz, M. S., Ginger, D. S., & Jen, A. K. (2014). High-Performance and environmentally stable Planar heterojunction perovskite solar cells based on a Solution-Processed Copper-Doped nickel oxide Hole-Transporting layer. *Advanced Materials*, 27(4), 695–701.
6. Koushik, D., Jost, M., Dučinskas, A., Burgess, C. H., Zardetto, V., Weijtens, C. H. L., Verheijen, M. A., Kessels, E., Albrecht, S., & Creatore, A. A. (2019). Plasmaassisted atomic layer deposition of nickel oxide as hole transport layer for hybrid perovskite solar cells. *Journal of Materials Chemistry C*, 7(40), 12532–12543.
7. Nkele, A. C., Nwanya, A. C., Shinde, N. M., Ezugwu, S., Mâaza, M., Shaikh, J. S., & Ezema, F. I. (2020). The use of nickel oxide as a hole transport material in perovskite solar cell configuration: Achieving a high performance and stable device. *International Journal of Energy Research*, 44(13), 9839–9863.
8. Pang, S., Chang, J., Dong, H., Chen, D., Xi, H., & Hao, Y. (2019). Efficient NIO hole transporting layer obtained by the oxidation of metal nickel film for perovskite solar cells. *ACS Applied Energy Materials*, 2(7), 4700–4707.
9. Wang, T., Ding, D., Wang, X., Zeng, R., Liu, H., & Shen, W. (2018). HighPerformance Inverted Perovskite Solar Cells with Mesoporous NiO Hole Transport Layer by Electrochemical Deposition. *ACS Omega*, 3(12), 18434–18443.
10. Yin, X., Guo, Y., Xie, H., Que, W., & Kong, L. B. (2019). Nickel oxide as efficient hole transport materials for perovskite solar cells. *Solar RRL*, 3(5).
11. Liu, Z., Chang, J., Lin, Z., Zhang, L., Yang, Z., Chen, D., Zhang, C., Liu, S., & Hao, Y. (2018). High-Performance Planar Perovskite Solar Cells Using Low Temperature, Solution–Combustion-Based

Nickel Oxide Hole Transporting Layer with Efficiency Exceeding 20%. *Advanced Energy Materials*, 8(19).

12. Di Girolamo, D., Di Giacomo, F., Matteocci, F., Marrani, A. G., Dini, D., & Abate, A. (2020). Progress, highlights and perspectives on NiO in perovskite photovoltaics. *Chemical Science*, 11(30), 7746–7759.
13. X. Yan, J. Zheng, L. Zheng, G. Lin, H. Lin, G. Chen, B. Du, F. Zhang, Optimization of sputtering NiO films for perovskite solar cell applications. *Mater. Res. Bull.* **103**, 150–157 (2018)
14. P. Yang, J. Wang, X. Zhao, J. Wang, Z. Hu, Q. Huang, L. Yang, Magnetron-sputtered nickel oxide films as hole transport layer for planar heterojunction perovskite solar cells. *Appl. Phys. A* **125**, 481 (2019)
15. H. Lee, Y.T. Huang, M.W. Horn, S.P. Feng, Engineered optical and electrical performance of rf-sputtered undoped nickel oxide thin films for inverted perovskite solar cells. *Sci. Rep.* **8**, 5590 (2018).
16. A. Venter, J.R. Botha, Optical and electrical properties of NiO for possible dielectric applications. *S. Afr. J. Sci.* 107, 1–2 (2011)
17. J. Tauc, Optical properties and electronic structure of amorphous Ge and Si. *Mater. Res. Bull.* 3, 37–46 (1968)
18. S. Hietzschold, S. Hillebrandt, F. Ullrich, J. Bombsch, V. Rohnacher, S. Ma, W. Liu, A. Köhn, W. Jaegermann, A. Pucci, W. Kowalsky, E. Mankel, S. Beck, R. Lovrincic, Functionalized nickel oxide hole contact layers: work function versus conductivity. *ACS Appl. Mater. Interfaces* 9, 39821–39829 (2017)
19. A. Jayendran, *Englisch für maschinenbauer*, 2nd edn. (Springer, Germany, 1997), pp. 43–49
20. S. Mrowec, Z. Grzesik, Oxidation of nickel and transport properties of nickel oxide. *J. Phys. Chem. Solids* 65, 1651–1657 (2004)
21. L.D.L.S. Valladares, A. Ionescu, S. Holmes, C.H.W. Barnes, A.B. Domínguez, O.A. Quispe, J.C. González, S. Milana, M. Barbone, A.C. Ferrari, H. Ramos, Y. Majima, Characterization of Ni thin films following thermal oxidation in air. *J. Vac. Sci. Technol.* 32, 051808 (2014)

22. U. Kwon, B.G. Kim, D.C. Nguyen, J.H. Park, N.Y. Ha, S.J. Kim, S.H. Ko, S. Lee, D. Lee, H.J. Park, Solution-processible crystalline NiO nanoparticles for high-performance planar perovskite photovoltaic cells. *Sci. Rep.* 6, 30759 (2016)
23. N. Srivastava, P.C. Srivastava, Realizing NiO nanocrystals from a simple chemical method. *Bull. Mater.* 33, 653–656 (2010)
24. Q. Dong, Y. Fang, Y. Shao, P. Mulligan, J. Qiu, L. Cao, J. Huang, Solar cells. Electron-hole diffusion lengths > 175 μm in solution-grown $\text{CH}_3\text{NH}_3\text{PbI}_3$ single crystals. *Science* 347, 967–970 (2015)
25. G. Magdy, M.E. Harb, A.M. Elshaer, L. Saad, S. Ebrahim, M. Soliman, Preparation of electrolytic quasi-solid-state nanofibers for dye-sensitized solar cells. *JOM* 71, 1944–1951 (2019)
26. M.M. Lee, J. Teuscher, T. Miyasaka, T.N. Murakami, H.J. Snaith, Efficient hybrid solar cells based on meso-superstructured organometal halide perovskites. *Science* 338, 643–647 (2012).

SQUEEZE CAST DISPERSION STRENGTHENED QUATERNARY ALUMINUM ALLOY METAL MATRIX COMPOSITE: DAMPING BEHAVIOR

**S. A. Srinivasan¹, S. Santosh¹, S.P. Kumaresh babu²,
T. S. Srivatsan³**

¹Department of Mechanical Engineering
Sri Sivasubramaniya Nadar College of Engineering
Kalavakkam, Tamil Nadu. INDIA

²Department of MME
National Institute of Technology
Tiruchirappalli. Tamil Nadu, INDIA

³Department of Mechanical Engineering
The University of Akron
Akron, Ohio, USA

Abstract

Aluminium – “The metal with the wings” was extensively used in aerospace applications and it was believed that aluminium and its alloys were meant for that particular engineering application. The quaternary Al-Zn-Mg-Cu alloy occupied a predominant position in aerospace-related applications for well over a decade. This research study focuses on hybrid composites preparation of the VAL12 matrix strengthened by the presence of nanocrystalline lanthanum zirconate dispersoids using the squeeze casting process and involving the use of compo-casting technique. The nanocomposites examined for their grain growth and mechanical properties were subjected to diffraction studies to confirm the presence of dispersoids in the aluminum alloy metal matrix composite [AMMC] and traces of the MgZn_2 “laves” phase was identified, which helps in strengthening of the hybrid composite. The electron beam surface diffraction (EBSD) results following metallographic preparation and examination did confirm that presence of second-phase particles in the microstructure, which effectively restrains growth of the recrystallized grains. This is due to particulate stimulated heterogeneous nucleation and the Zener pinning effect. Since solidus temperature of the rare earth oxides

is higher, which is favorable for the formation of randomly oriented grains. The composite material's ability to dissipate the elastic strain energy was carefully examined through damping studies. Distortion of the metal matrix was observed by witnessing the β transition zone to occur at 147 - 153 °C for the monolithic alloy and at 212 – 237 °C for the chosen composite material with 6 percent lanthanum zirconate (LaZ). The presence of rare earth compounds in the VAL12 matrix does increase the thermal stability, which can be seen as an increase in the damping coefficient [$\tan \delta = 0.225$] for the composite material.

Keywords: VAL12, lanthanum zirconate (LaZ) (rare earth, Squeeze casting, Damping behavior.

Introduction

With an observable increase in industrial regulations and market demands in the industries spanning automobile and aerospace, the development and emergence of lighter structural and high-performance engineering components has become an essential task to both address and deliver or act upon. An increase in the degree of the industrialisation is one of the driving factors in an era driven by an increased emphasis on consumption of non-ferrous metals for use in a spectrum of engineering applications that permeate the world around us. Decreasing the metallic utilisation and concurrently reducing the production stages and involvement of the labour force are the key segments every industry is looking forward. Hence, the combined properties from both cast components and deformed components are under demand, particularly for applications specific to both automobile and aerospace. This demand does create an extensive possibility for the utilization of cast components and the development of productive methods in casting. The drive towards invention of novel cast aluminium alloys has happened in recent years. This is essentially because the standard cast alloys do not cater to the needs specific to rigorous industrial requirements and technology advancements.

Among the numerous nonferrous alloys, the aluminium alloys are chosen for use in important applications in the industries spanning aircraft, aerospace, and automobile engineering. The structural assembly of an aircraft is generally made using both sheet stock and extruded parts, which are often held together by the rivets made from the quaternary aluminum alloy Al-Zn-Mg-Cu) [the 7xxx.x series alloys]. These alloys apart from

providing high strength also possess good damping properties [1]. The prevailing perspective on the cast aluminum alloys belonging to Al-Zn-Mg-Cu have in recent years changed from the earlier belief that they possess low castability with noticeable advancements in the emergence of new and novel manufacturing techniques. The primary need of any industry is to develop high strength aluminium alloy, which provide a combination of good mechanical properties at both room temperature and high temperatures when compared one-on-one with the conventional alloys. The properties should be in such a way that the new system of alloys shall be tailored as per the demand of the industry. Further, they should offer better cast ability, corrosion resistance and improved wear resistance for the purpose of industrial applications [2].

The alloys chosen for use in the industries spanning automobile and aerospace generally provide better corrosion resistance and are mechanically stronger. The structural materials are generally alloyed for the purpose of enhancing workability to obtain the desired structure with no compromise in mechanical strength. Squeeze casting, which is one of the novel processes used to obtain better densification needs must be addressed towards obtaining the optimum operating conditions specific pertaining to a particular alloy. VAL12 is a promising cast aluminum alloy with aluminum as the prime element followed by zinc, magnesium, and copper as its major constituents, providing the essential and desired properties. With the properties governed by the ratio of Zn:Mg, the cast aluminum alloy, VAL12, finds application in bonnets, boot lids, doors, load carrying arms and suspension joints. Recently several successful efforts have been made and reported on this alloy using new and improved casting process. The application of squeeze-cast components as a viable replacement for the conventional wrought components does considerably reduce the overall structural weight while concurrently minimizing the necessity for secondary processing operations, such as (i) stamping, (ii) forging, and others to obtain the desired properties [2,3].

The properties of alloys can be improved by an introduction of dispersed phases into the alloy matrix since there does exist a restriction in compositional constituency of an alloy due to solid solubility limit. [4]. In recent years, the rare earth particulate reinforcements are gaining increased popularity since they do not decrease the casting fluidity as in the case of the oxide reinforcements and increase viscosity of the melt resulting in non-Newtonian behaviour. The hydrodynamic interaction

between the liquid melt and reinforcing particulates and the non-hydrodynamic interaction between the particulates does affect fluidity of the liquid melt. This in turn does exert an influence on the solidification characteristics. The presence of engulfed nucleation sites by the particulate reinforcements does result in the formation of smaller dendrites and finer grains upon solidification.

The VAL12 cast alloys manufactured by conventional casting processes, have a tendency to undergo inter-granular fracture upon being subjected to loading. This one property does worsen the overall mechanical stability of the alloy. Introduction of particulates to the matrix does stimulate a transition from inter granular fracture to intra granular fracture providing a positive note on overall adaptability of the alloy. [5]. The influence of rare earth addition on microstructure and the effect of temperature during the casting process was investigated for the Al-Zn-Mg-Cu quaternary alloy that was fabricated using the squeeze casting process [6]. It was inferred that with an increase in the melt temperature the average grain size increased from 32 μm to 51 μm in the temperature range 720 °C to 780 °C. Beyond 740 °C, a steep rise in the grain size was observed. To identify the influence of rare earth addition, both lanthanum and cerium were added in (i) 0 percent, (ii) 1 percent, (iii) 2 percent, and (iv) 3 percent, to the melt that was held at 780 °C. The higher melt temperature, the presence of rare-earth (RE) element did considerably reduce the grain size to 30 μm due to the presence of more nucleation sites. [5-7]. On the other hand, the influence of squeeze casting on the cast aluminum alloy VAL12 was compared by **Lei Lu** et al. (2014) with an Al-Zn-Mg-Cu alloy that contained reduced zinc percentage when compared to VAL12. The effect of squeeze casting process was seen on an overall refinement of the microstructure. The mechanical properties of the squeeze cast samples did reveal considerable increase in tensile strength almost twice than that of gravity die casting. At a higher solutionizing treatment the strength increased to a maximum of 590 MPa, with a concomitant reduction in strain [7].

This alloy when strengthened by silicon and chrome, the fatigue life of base alloy was 3,075 cycles (maximum), whereas, it was 2,993 cycles and 1,413 cycles for the silicon-containing and chromium-containing alloys. An investigation of the fracture morphology revealed that the fatigue cracks initiated at the surface and tended to propagate along the grain boundaries. No inter- grain fracture was observed due to

the presence of reinforcements in the cast aluminum alloy metal matrix [8]. Another study specific to mechanical property of the VAL12 alloy strengthened by the addition of zirconium and scandium did reveal the zirconium addition to refine the microstructure, dendritic morphology was alleviated and mechanical properties were enhanced. Further addition of the element scandium (Sc) and an incorporation of the squeeze casting process to the liquid melt did result in attaining fine and uniaxial-shaped grains, which in turn contributed to increasing the mechanical properties. The zinc and copper phases present in the grain boundary did have an impact on elongation of the alloy [9,10].

Though this cast aluminum alloy has several practical applications in the industry specific to aerospace, very few notable studies have been reported on the VAL12 alloy and its mechanical performance. This investigation aims to provide report on dampening behavior of the squeeze cast hybrid composite with the lanthanum zirconate (LAZ) dispersed through the cast aluminum alloy VAL12 matrix with an insight into understanding of the fracture mechanism.

Methodology

Table 1. Elemental constituents of VAL12

Element	Zn	Mg	Cu	Al	Mn	Fe	Si	Other
Composition (wt%)	7.46	2.20	1.39	88.25	0.21	0.18	0.12	0.19

The material used in the present investigation is VAL12 with chemical composition given in Table 1, and strengthened with $\text{La}_2\text{Zr}_2\text{O}_7$ (LAZ) dispersoids. Synthesis of the LAZ [11] and details specific to preparation of the composite material have been reported by the authors [12]. The grounded samples made from the castings were used to conduct metallurgical characterization studies and mechanical property evaluation of the as-cast aluminum alloy metal matrix composites [AMMCs]. The Pan Analytical X-ray diffractometer [Model: DY 1656] was used for the purpose of phase analysis and the formation of intermetallic compounds at a scan rate of 1° /minute, and using $\text{CuK}\alpha$ radiation. The optical microscope [Model: Leica D2700M] and electron micrograph [Model: TESCAN – Vega3 L.M.U] was observed to detect the presence of second-

phase particles and their distribution within the aluminum alloy metal matrix, In accordance with ASTM standards, the mechanical properties of the aluminum alloy metal matrix composites (AMMCs) were determined using a hardness tester [Model: Matsuzawa], a densitometer [Model: Mettler Toledo], and a Tensiometer [Model: Instron]. The damping capacity of the composites was evaluated using a DMTA – DMS6100 analyzer at room temperature to 300 °C and a test frequency of 1 Hz.

Results and Discussion of the Results.

Metallurgical studies and Mechanical behavior

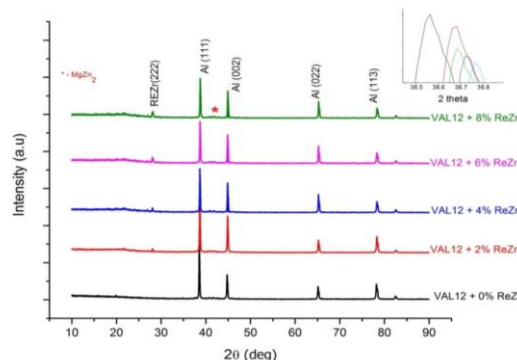


Figure 1. X-ray diffraction patterns

The X ray diffraction pattern for the aluminum alloy reinforced with LAZ dispersoids is shown in **Figure 1**. The presence of lanthanum zirconate dispersoids was confirmed and intensity of the reinforcement peak did increase with an increase in mass percentage of the reinforcements in the cast aluminum alloy metal matrix. Fine trace of the ‘Laves’ phase (MgZn_2) was seen in all of the composites containing 6 percent and 8 percent dispersoids, which initially forms as heterogeneous nucleus, with additional distribution contributing to the mechanical strength. N.A.Belov (1995) [5] did report on the characteristics of the MgZn_2 eutectic intermetallic and observed it to play a vital role in contributing to improving mechanical strength of the alloy. S. Wang et al (2018) [12] observed in their study of the MgZn_2 intermetallic that they

did play a key role in determining both the ductile and brittle characteristics. Presence of the 'laves' phase[MgZn_2] was easily seen at very fine levels in the aluminum alloy composites with the presence of lanthanum zirconate. The composite with 8% (by weight) dispersoids did reveal fine traces of the MgZn_2 phase. The formation and presence of the MgZn_2 is also associated with a high nucleation rate due to the presence of dispersoids in the aluminum alloy metal matrix and a thermodynamic difference between the matrix and the reinforcements [13]. No other intermetallic phases were observed in the XRD pattern of the cast test specimens. The aluminum peak shift and inconsistency are caused by a difference in thermodynamic stability of the dispersoids and the metal matrix. A decrease in the Al peak intensity can be witnessed with the aid of inset graphs. The presence of graphite was not seen in the X-ray diffraction study.

Table 2. Mechanical Properties of the Hybrid Composites

Sample	Theoretical density (g/cc)	Actual density (g/cc)	Porosity level (%)	Hardness (Hv)	Yield Strength (MPa)	UTS (MPa)	Strain (%)
VAL12 + 1%Gr	2.832	2.786	5.22	94.04	95	133	17.19
VAL12 + 1% Gr + x $\text{La}_2\text{Zr}_2\text{O}_7$							
x = 2%	2.858	2.743	4.55	137.58	105	180	12.04
x = 4%	2.888	2.764	4.02	152.00	140	216	10.20
x = 6%	2.918	2.801	4.29	160.05	195	235	9.41
x = 8%	2.948	2.809	4.00	169.20	190	210	8.36

The consolidated mechanical test results on the hybrid composites is provided in **Table 2**. It can be noticed that in the case of all castings, 95% of the theoretical density was attained for the casting due to the liquid forging operation caused by the squeeze pressure applied to the melt. The density results clearly reveal the presence of good interfacial bonding and cohesion between the aluminum alloy metal matrix and the reinforcing

dispersoids. The observed minor increase in density of the composite containing 8% dispersoids can be attributed to a reduction in both shrinkage and gas porosity, which are both mitigated by a higher volume fraction of the reinforcement in the aluminum alloy metal matrix. The most significant enhancement in tensile strength (UTS) relative to 6% LAZ in the microstructure did result in 76 % improvement in strength when compared to the unreinforced matrix alloy.

The presence of a large amount of the reinforcing dispersoids did contribute to reducing the overall strain carrying capability of the composites, which tends to behave in a material brittle. The volume fraction of dispersoids in to the aluminum alloy metal matrix differs based on density, which in turn decides the maximum amount of dispersoids that can be accommodated in the metal matrix [14]. Also, it was observed that though there is an appreciable increase in both harness and tensile strength due to the presence of the reinforcement, there does result in a noticeable reduction in the strain. The presence of more amounts of second-phase particles in the microstructure of the composite material does restrict the elongation causing as a result the presence of “localized” stress and localized strain around the reinforcing dispersoids. An enhancement in strength of the composites when compared one-on-one with the matrix alloy can be attributed to a work hardening effect that is essentially caused by the dispersoids in the matrix aided by the squeeze casting pressure applied on the molten metal. The thermal mismatch between the reinforcing dispersoids and aluminum alloy matrix causes stress concentration, which in turn contributes to increasing the dislocation density with a concomitant increase in strength of the composite microstructure. At few cases there was a decrease in strength with the addition of zirconia. This could be attributed to an agglomeration of the reinforcing particles in the microstructure of the composite, weakened bonding at the boundaries resulting in de-bonding of the reinforcing dispersoids from the aluminum alloy metal matrix [15]. To have a better understanding of the material behavior under stress conditions, the fracture surface morphology of the test specimens deformed in tension was studied. This is presented in the following section.

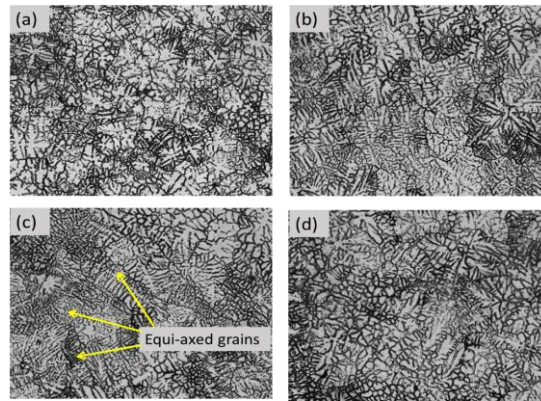


Figure 2. Optical micrographs of the VAL12 hybrid composite

The micrographs (**Figure 2**) reveal that the combined phases of zirconia and lanthanum oxide in lanthanum zirconate does aid in enabling a very fine microstructure. Equiaxed grains were seen in the hybrid composites containing lanthanum zirconate dispersoids of 4 weight percent and more. The fine grains are obtained due to increasing thermal mismatch between the rare earth oxide and the metal matrix. The presence of rare earth oxides in the matrix does act as localized nucleation sites, which favors the occurrence of solidification. Among the several reasons for the presence of near equiaxed shaped grains are a few important features that can be attributed to the following: (i) restriction in fluid flow, (ii) localized solidification, and (iii) thermodynamic interaction between the matrix and the rare earth dispersoid particles [16]. From the scanning electron micrographs, it can be inferred that the addition of rare earth zirconate (REZr) does refine the grains to a great extent, which is seen in **Figure 3**. The hybrid composites with 6 percent REZr does reveal a fine microstructure with the reinforcements occupying the inter-grain positions along the grain boundary. The inset shows the presence of REZr particulates. Scanning electron micrograph of the hybrid composite containing 8 weight percent REZr does reveal a sizeable number of striations, which essentially occurs due to straining of the composite. The presence of increased amount of dispersoids in the chosen aluminum alloy metal matrix does act as nucleation sites, which induces an increased level of triaxial state of stress around the reinforcing particulates during solidification.

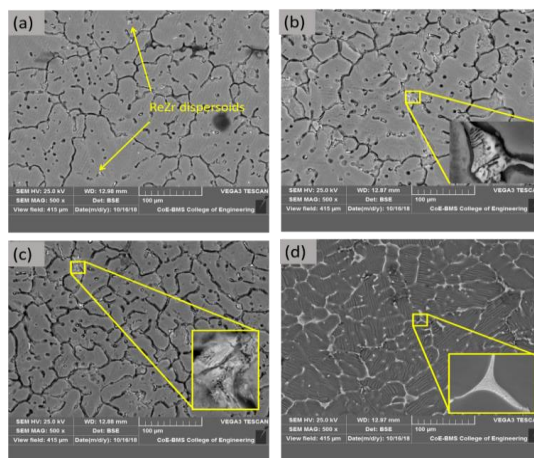


Figure 3. Scanning electron micrographs of the VAL12 hybrid composite

Damping behavior

DMTA is evolving to be one of the important study conducted on a material in the field of Rheology, which essentially involves the study of deformation of the chosen material. This rheological phenomenon unlike other techniques like creep, does record response of the chosen material against an oscillatory force that is applied to it, with the lag becoming a measure of the damping co-efficient [$\tan \delta$]. The present investigation on damping behavior does involve observing the ability of the chosen material to store energy [Storage modulus – elastic portion] and its ability to lose energy [the loss modulus – viscous portion] in a given environment. The ratio between these provides a measure of damping capacity ($\tan \delta$) of the material.

The dynamic response of the hybrid composites containing $\text{La}_2\text{Zr}_2\text{O}_7$ dispersoids is shown in **Figure 4**. The graphs reveal a loss in the storage modulus with an increase in temperature. This is essentially because the molecules gain free volume with an increase in temperature and molecular motion is facilitated to occur. Bending and stretching of the metallic bond is gradual for the case of the unreinforced VAL12 composite. The storage modulus of this curve can be observed to be essentially smooth without any appreciable distortion. When the DMTA curves for the hybrid composites are closely observed, an inconsistency in the β zone can be seen. For the hybrid composites containing the REZr

dispersoids, it can be clearly seen that the β transition temperature is in the range of 200 °C – 225 °C. The transition temperature does increase the working range of the composites by approximately 60 °C when compared to the other hybrid composites. The presence of rare earth compounds in the VAL12 alloy metal matrix does increase the thermal stability, which can be seen as a measure of an increase in damping co-efficient. The values obtained from the DMTA tests are tabulated in **Table 3**.

Table 3. Damping co-efficients of hybrid composites

Sample	Tan δ	β transition zone
Val 12 + 1 Gr	0.092	
VAL12 + 1% Gr + x La₂Zr₂O₇		
x = 2%	0.220	215 °C – 238 °C
x = 4%	0.215	212 °C – 240 °C
x = 6%	0.214	212 °C – 237 °C
x = 8%	0.225	205 °C – 238 °C

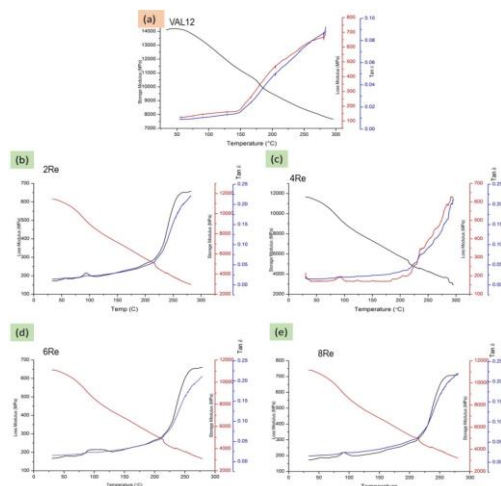


Figure 4. DMTA graphs for the VAL12 + 1% Gr + x La₂Zr₂O₇ hybrid composites (a) x = 0%, (b) x = 2%, (c) x = 4%, (d) x = 6%, and (e) x = 8%

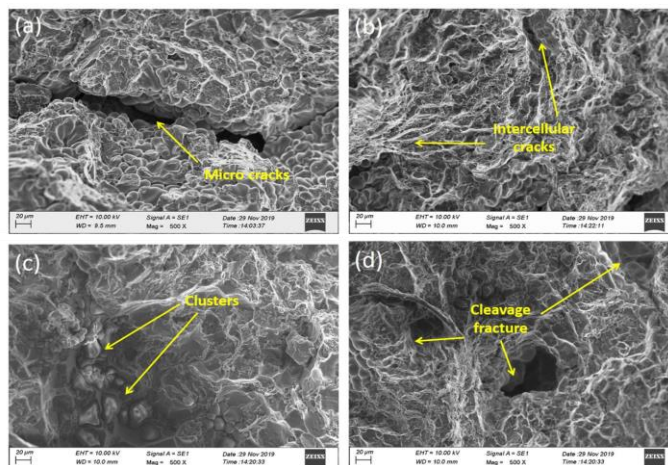


Figure 5. Fractographs of the DMTA test samples of the VAL12 + 1% Gr + x $\text{La}_2\text{Zr}_2\text{O}_7$ hybrid composites
(a) x = 2%, (b) x = 4%, (c) x = 6%, (d) x = 8%

At the temperatures is lesser than the β transition temperature range, the damping capacities become invariable and does increase with an increase in the temperature. The hybrid composites containing the LAZ dispersoids reveal almost twice the damping capacity as that of the monolithic VAL12 counterpart without a noticeable sacrifice in the mechanical properties. The damping capacities values clearly reveal that the hybrid composites are structurally sound primarily because of the inherent thermal stability of the rare earth elements [17]. The reason for good damping capacity of the LAZ hybrid composites can be attributed to the presence of second-phase particles in the microstructure, which arrests the dislocations while concurrently improving the intrinsic damping capacity of the chosen and studied composite material. The fabrication process does provide for better densification coupled with minimal porosity, which is an influencing factor from a fabrication point of view [18].

From the fractographic examination, as shown in Figure 5, the presence of clusters of dispersoids can be clearly seen through the microstructure of the composite. In this condition, damping of the composites is essentially due to the internal sliding friction that is caused

by the detached dispersoids due to poor bonding. The grain boundaries also play a key role in determining damping capacity of the composite material. The presence of second-phase LAZ dispersoids in the VAL12 metal matrix does refine the grain structure, which can be seen from the previous results. The refinement in grain size and structure is mainly due to the occurrence of localized nucleation around the reinforcing dispersoids. The thermal mismatch between the LAZ dispersoids and the aluminum alloy metal matrix does develop a stress field around them – comprising of both compressive stress and tensile stress. The dissipation of energy at and around these locations occurs as the grain boundary area increases when a refinement in grain size occurs, which in turn contributes to increasing the damping behaviour of the hybrid composites.

Scanning electron micrographs also reveal a transformation from ductile fracture to the brittle fracture mode due to presence of dispersoids in the metal matrix. The ductility of the hybrid composites is reduced when compared one-on-one with the VAL12 matrix alloy due to the presence of the dispersoids. The strain that was measured during the tensile test is in agreement with this. Further, fractographic observations did reveal presence of dimples along with few microscopic cracks, which are the “key” initiation points for failure of the chosen material (Figure 5 (a), and Figure 5 (b)). The crack is favored to grow along the grain boundary regions, gradually propagates into the intercellular region culminating in failure by rupture or fracture. Figure 5(c) and Figure 5(d) reveal mixed failure modes showing both cleavage and particulate pull out. The propagation of fine microscopic cracks does weaken the boundary between the reinforcing dispersoids and metal matrix causing as a result the dispersoids to be pulled out of the metal matrix due essentially because of weakening of the bond between the interfaces. The presence of clustered dispersoids, which are sensitive to premature damage does result in poor strain, which is shown in **Figure 7** [19]. The fractographic observations substantiate along with the tensile test results and in all cases, fracture was observed to occur both for the matrix and the reinforcement providing an indication of better bonding between them.

Conclusions

The hybrid composites were successfully fabricated using the technique of squeeze casting of the VAL12 cast aluminum alloy as the matrix and $\text{La}_2\text{Zr}_2\text{O}_7$ dispersoids as reinforcement, with varying weight percentages [0%, 2%, 4%, 6% and 8%] and 1% graphite. The following are the key findings specific to fabrication of the hybrid composites:

1. The combined effect of stirring and squeezing helps in attaining a better dispersion of the dispersoids through the composite microstructure and better densification of the hybrid composite. The graphite added to the composite acts as solid lubricant and improves the wetness of the molten melt, which in turn aids in metal pouring and facilitates in fine dispersion of the reinforcing dispersoids.
2. The diffraction studies confirm the presence of dispersoids in the aluminum alloy metal matrix composites (AMMCs) along with fine traces of the MgZn_2 'laves' phase, which helps in strengthening of the hybrid composite.
3. The grain size of the hybrid composites containing the $\text{La}_2\text{Zr}_2\text{O}_7$ dispersoids was fine. An increase in the number of nucleation sites coupled with thermal mismatch between the lanthanum zirconate and VAL12 matrix are the primary reasons that aid in attaining a finer and near equiaxed shaped grains.
4. EBSD results confirm the presence of second-phase particles to effectively restrain the growth of the recrystallized grains growth due to the conjoint and mutually interactive influences of particulate stimulated heterogeneous nucleation and the Zener pinning effect. The solvus temperature of lanthanum zirconate is higher, which results in the formation of the randomly oriented grains.
5. The mechanical properties reveal hardness of the material to be directly proportional and the strain is inversely proportional to the percentage of reinforcement in the composite microstructure. The hybrid composites containing lanthanum zirconate does exhibit almost twice the tensile strength of the unreinforced aluminum alloy.

6. The damping behavior of the composites reinforced with $\text{La}_2\text{Zr}_2\text{O}_7$ dispersoids does reveal a positive trend with respect to an increase in reinforcement percentage and attaining > 0.2 damping coefficient, which is preferred for small roller applications.

References

1. I.N.Fridlyander, A.V.Dobromyslov, E.A.Tkachenko and O.G.Senatorova. **Met. Sci. Heat Trea.**, 47(7-8), 269-75 (2015).
2. Zolotarevsky, Vadim & Belov, N. and Glazoff, Michael. (2007). Chapter 5. Industrial Casting Aluminum Alloys, pp.327-396 Casting Aluminum Alloys, Elsevier, Amsterdam (2007).
3. Ryazantsev, V.I., V.A. Fedoseev and V.N. Matsnev. **Weld. Int.**, 15, 56–59 (2001).
4. N. A. Belov. **Met. Sci. Heat Trea.**, 53 (9-10), 420-27 (2012).
5. Belov, N.A. **Met. Sci. Heat Trea.**, 37, 237–42 (1995).
6. Fan, C.H., Y.B. Zhu and N. Yang (2013) **Adv. Mater. Res.**, 779–780, 78–83 (2013).
7. Lu, L., D. Zhang and Y. Li. **Mater. Sci. Forum.**, 788, 187–192 (2014).
8. Kim, I., Y. Park, K. Kim and I. Kim. **Mater. Sci. Forum.**, 449–452, 617–20 (2004).
9. Wang, Z., J. Xu, Z. Zhang, B. Li and D. Li. **Adv. Mater. Res.**, 652–654, 2455–59. (2013).
10. Srinivasan S.A, Kumaresh Babu, John Berchmans L, Usmaniya Mehana, **Mat. Res. Exp.**, 6(10) 104001 (2019).
11. S.A. Srinivasan, S.P. Kumaresh Babu. **J. Inst. Eng. India Ser. D** (2020) Doi:10.1007/s40033-020-00224-3.
12. Wang, S., Y. Zhao, H. Guo, F. Lan and H. Hou. **Materials**, 11, 1–11 (2018).
13. Honda, K., W. Yamada and K. Ushioda. **Mater. Trans.**, 49, 1395–1400 (2008).
14. Srivatsan, T.S. **J. Mater. Sci.**, 27, 4772–4781 (1992).

15. Abdizadeh, H., H.R. Baharvandi, and K.S. Moghaddam. **Mater. Sci. Eng A.**, 498, 53–58 (2008).
16. Tahiri, H., S.S. Mohamed, H.W. Doty, S. Valtierra and F.H. Samuel Effects of Grain refining on columnar to equi-axed transition in aluminium alloys in Aluminium alloys - Recent trends in processing, characterisation, mechanical behaviour and application, Intech open science publishing (2017).
17. Deng, C. F., D. Z. Wang, X.X. Zhang and Y.X. Ma. **Mater. Lett.**, 61, 3229–31 (2007).
18. Siva prasad, D. and C. Shoba. **J. Mater. Res. Technology**, 5, 123–130 (2016).
19. Wu, H.Y. J. Mater. **Process. Technol.**, 101, 76–80 (2000)

Comparative Study of Heat Source Models to Analyse Thermal Effect on Precise Modelling of Arc Welding Process

¹Ganta Venkateswara Rao, ²Saurav Suman, ³Laldinenga,
⁴Milan Kr. Maity, ⁵Vijay Mandal

^{1,2,3,4,5}*Department of Mechanical Engineering,
NIT Mizoram,
Aizawl, India*

Abstract

In this study, thermo-mechanical elastic plastic 3D finite element analysis has been performed for single pass submerged arc welding of 10mm thick corrosion and oxidation resistant AISI 304 steel plate for square butt joint with no edge preparation. Five different heat source models were employed to model the heat deposition from a moving heat source during welding. Element birth and death techniques were also used to imitate the addition of a weld molten pool in the weld gap during welding. Temperature-dependent mechanical and physical properties were also considered for the base plate and weld material. The analysis was performed using an FE software package of ANSYS APDL. The thermal effect of all the heat sources was compared by altering their design parameters and comparing them with the experimental results. It was found that the volumetric heat sources show better thermal gradients than the surface heat source models. Moreover, the volumetric heat source model was found more suitable for emulating the addition of weld material in the weld gap during the welding process.

Keywords: FEM; Welding; Modelling; ANSYS; Thermo-mechanical; Elastic- Plastic; AISI 304 steel

Introduction

Welding is one of the most important joining techniques available and is widely used in different industries like aerospace, automobiles, maritime, nuclear power plants, construction, etc. Since high concentrations of heat are involved in welded joints and their vicinity, it causes deformation or residual stress, which leads to degradation in ultimate or fatigue strength or structural stability and manufacturing accuracy. Conducting trials to gather data on residual stress is highly

costly and time-consuming. Therefore, computational analysis is essential as it provides a fast and effective method of calculating different data. At present, many researchers sum up many combinations of heat source models for numerical simulation of the temperature field, residual stress, distortion, etc., and their computational predictions were compared with an actual experimental result and used the outcome for improving welding processes. Kiyoshima et al. compared a variable heat source model. A moving heat source model and an instantaneous line heat source model were utilized to evaluate their impact on welding residual stress and distortion in a multi-pass J-groove joint. They found out that the heat source model has a significant influence on welding distortion. Additionally, they discovered that while a variable-length heat source could not predict welding distortion well, it could predict welding residual stress well.[1]. Ghosh and Chattopadhyay attempted to get the analytical solution for the thermal field that a moving heat source with various forms induces in a semi-infinite body, i.e., oval, double ellipsoidal, and conical forms, and found out that oval shape heat source is the best suitable heat source for heat input of submerged arc welding process[2] [3]. Hongyuan *et al.* derived a general double ellipsoidal heat source model from an existing double ellipsoidal heat source model, which contains all the characteristics of its predecessor. In addition, it can deal with external disturbances like magnetic field interference, cases when welding wires are not perpendicular to the work, etc. [3].

Besides the above researchers, many others have proposed different heat source models from the late 1930s. In those days, the most widely used analytical technique for determining the thermal history of welds was Rosenthal's application of Fourier's fundamental theory of heat flow to moving heat sources. To analyze heat flow in weldment, several authors have used FEM to overcome the limitations of Rosenthal analysis. Various authors proposed a Gaussian flux distribution (W/m^2) applied to the workpiece's surface and heat distribution throughout the molten zone to reflect the arc's digging action [4]. The profound investigation made by the early researchers has been continuing till today. Three unlike heat source models, viz. variable heat source (VHS), instantaneous line heat source (ILHS), and a moving heat source model (MHS), have been compared to find their influenced-on welding residual stress and distortion[1], [5]. Among three distinct heat source models, a comparison of the temperature, distortion, stress, coarse, and dense mesh has been made: heat source models with circular discs, extended Gaussian heat sources, and

extended point heat source models from the simulations of a bead on plate welding process. The expanded point heat source model simplified the extended Gaussian heat source model[6]. A Ghosh considered the double elliptic paraboloid moving heat source volume to analyze the transient heat distribution on a welded plate analytically and numerically[7]. Wang et al. proposed a combined heat source model known as the polynomial heat source model to improve the accuracy of finite element (FE) models, which follows Gaussian heat density distribution.

A circular heat source was employed to measure the effect of surface heating, while a polynomial equation was used to represent the volumetric heat power source. The effects of the double ellipsoidal heat source model with the first, second, and third-order polynomials were investigated in the fusion zone. It was discovered that the disc's source effectively explained an "irregular curvature" and modified the fusion zone boundary's shape. To evaluate the polynomial heat source further, comparisons between the simulation and experimental data included the double ellipsoid and conical heat source model with the polynomial heat source, and it has been found that the polynomial heat source did the best [8]. Li et al. further suggested a uniform-Gaussian distributed heat source model, a combination heat source model, to replicate the residual stress field of T welding S355 steel. The heat distribution in the molten pool was described by combining a Gaussian surface with a uniform-volume heat source. The power supplied to the system was divided proportionately to the new combined heat source, and the heat in the molten pool with heat from the arc is the total heat flow. The simulation results of residual stress distributions show that the uniform Gaussian heat source model is adequate for forecasting residual and deformation stress during T welding [9]. An investigation has been made for a comprehensive methodology to analyse the thermal analysis of welding. The Gaussian conchoidal heat distribution model was used in the study to choose a surface heat source. A comparison of simulated and measured heat cycles at different distances from the weld line has been made. The heat source abruptly surged in temperature when it got to the weld line nodes, peaked, and then progressively dropped down as it progressed. This study also mentioned that increased welding current increased temperature at constant welding speed. Also, the temperature of the weldment is less when the welding speed is higher since the heat source is introduced for a short time.

Also, it has been mentioned that the temperature change depends significantly on heat input. A new volumetric heat source model named the parabolic Gaussian heat Source (PGHS) model has been proposed for predicting weld bead shape when welding thin titanium alloy sheets with a plasma arc[10]. A simulation was carried out using the proposed model, which included two types of heat sources: conical and modified conical. The PGHS model can predict PAW's weld bead geometry more accurately than the other models for full penetration welding. Also, the PGHS model predicts that the weld pool shape is larger than the other two. The predicted weld bead geometry comparisons with the experimental measurement show that the PGHS model offers a suitable temperature field and weld bead shape in PAW of thin alloy sheets with Ti-6Al-4V[11]. For a wider range of geometries and welding procedures, the double-ellipsoidal distribution was changed to a double-ellipsoidal-conical heat power density to describe transient temperature fields precisely, like electron-beam welding, keyhole-laser or an arc welding operation in a deep, narrow groove wherein applying a double-ellipsoidal heat power density model is not as suitable. Experimental results of GTAW and EBW and their respective simulation results were compared[12]. The double Bi-Ellipsoid model Excel characterized the geometry, displaying the lowest percentage deviations between the experimental and numerical maximum temperatures.[13]. The author has also implemented a the submerged arc welding process is simulated using a double ellipsoidal heat source model on P91 steel weld to replicate both the addition of heat and molten weld pool during the welding[14], [15], [16], [17], [18]. However, a circular disc shape heat source model was employed to model surface heating in various thermal mitigation techniques for in-situ control over welding distortion and residual stresses[19], [20], [21].

The literature review shows that very few studies have been found comparing the various heat source models to simulate the fusion welding process effectively. Moreover, some authors specifically compared the two or three heat source models only depending on their specific welding process or materials. Hence, the present work presents a consolidated comparative study of five heat source models, both 2D and 3D, to observe their thermal effect on the peak temperature, rate of heating and cooling, thermal gradient across the weld plate, etc. Finally, the simulated and experimental findings are compared for the time-temperature profile.

Heat Source Models

As mentioned, five types of heat source models were chosen for the current comparative studies. The same is explicated below and categorized based on their governing equations, shape & size, dimensions, etc.

Double ellipsoidal heat source model

It was developed by Goldak *et. al.* (1984) as an improvement of the semi-ellipsoidal heat source, which combines two semi-ellipsoidal heat sources as shown in Fig, and since then, it has been used in several works as it gives an accurate result in a low penetration welding process especially[4].

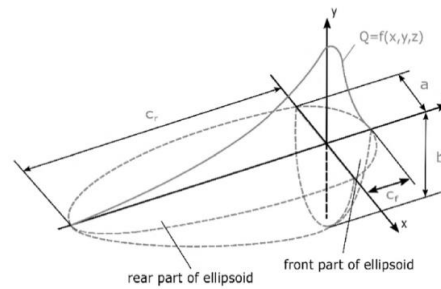


Figure 1 Double Ellipsoidal Heat Source Model [4]

The rear and front part of the heat source is given as the following equations

$$q(x,y,z) = \frac{6\sqrt{3}QF_r}{\pi abc_r\sqrt{\pi}} e^{\frac{-3x^2}{a^2}} e^{\frac{-3y^2}{b^2}} e^{\frac{-3z^2}{c_r^2}} \quad (1)$$

$$q(x,y,z) = \frac{6\sqrt{3}QF_f}{\pi abc_f\sqrt{\pi}} e^{\frac{-3x^2}{a^2}} e^{\frac{-3y^2}{b^2}} e^{\frac{-3z^2}{c_f^2}} \quad (2)$$

Q represents the total energy input, a and b are the semi-axes along the x and y directions, and c_r and c_f are the heat source's front and rear semi-axes, respectively. The heat deposited in fraction, F_r and F_f, represent the heat apportionments of the heat flux in the rear and front quadrants, respectively, where F_f + F_r = 2.

Considering a moving heat source, the above equations can be rewritten as

$$q_r(x,y,z,t) = \frac{6\sqrt{3}QF_r}{\pi abc_r\sqrt{\pi}} e^{\frac{-3x^2}{a^2}} e^{\frac{-3y^2}{b^2}} e^{\frac{-3(z+v(\tau-t))^2}{c_r^2}} \quad (3)$$

$$\text{And } q_f(x,y,z,t) = \frac{6\sqrt{3}QF_f}{\pi abc_f\sqrt{\pi}} e^{\frac{-3x^2}{a^2}} e^{\frac{-3y^2}{b^2}} e^{\frac{-3(z+v(\tau-t))^2}{c_f^2}} \quad (4)$$

where lagging parameter, welding time, and welding speed are represented by t , v , and τ , respectively. One more heat source model taken into account in this research is-

Conical heat source model

Although a Double Ellipsoidal heat source can analyse the deeper thermal field of weld penetration, it is still not applicable to electron beam welding, laser beam welding, or any other welding process which are high-density keyhole welding process[12].

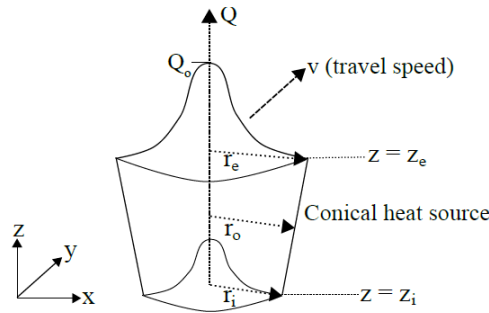


Figure 1 Conical Heat Source Model [9]

To consider a configuration produced by the said welding processes, which is a weld of high depth-to-width ratio, a conical heat source, as shown in Figure 1, is commonly used. The governing equations are given as

$$q(x, y, z) = Q_0 \exp\left(\frac{-3r^2}{r_0^2}\right) \quad (5)$$

where Q_0 is the maximum heat source intensity (Wm^{-3}), r is the radial distance of the heat source center and is represented as

$$r = \sqrt{x^2 + y^2} \quad (6)$$

where r_0 is the radius of the heat source and is decreasing linearly from top to bottom and is represented as

$$r_0(z) = r_e + \frac{r_i - r_e}{z_i - z_e} (z - z_e) \quad (7)$$

where z_e and z_i represent the top and bottom surface's z coordinates, and r_e and r_i represent the upper and lower radii. where $H = z_e - z_i$. Q_0 can be further represented as [9]

$$\eta P = \int_0^H \int_0^{2\pi} \int_0^{r_0} Q_0 \exp\left(\frac{-3r^2}{r_0^2}\right) dr d\theta dh \quad (8)$$

$$\text{or } Q_0 = \frac{9\eta P \exp(3)}{\pi(\exp(3)-1)} \cdot \frac{1}{(z_e - z_i)(r_e^2 + r_i^2 + r_e r_i)} \quad (9)$$

where η is the power efficiency, and P is the welding power source.

Cylindrical heat source model

This Heat source model is also used to simulate the temperature field, which involves a welding process with high-density energy that produces a high width-to-depth ratio profile. Figure 2 shows the cylindrical heat source model[22].

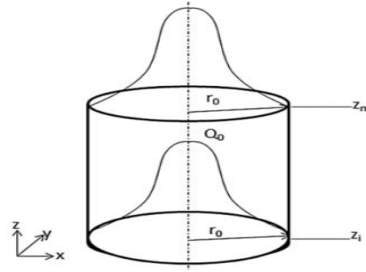


Figure 2 Cylindrical heat source model[22]

The Gaussian distribution of heat energy is also followed by this heat source model, which is provided as

$$q(x,y,z) = \frac{Q_0}{\pi r_0^2 H} \exp\left(\frac{-3r^2}{r_0^2}\right) \quad (10)$$

Where Q_0 maximum volumetric heat source intensity and H is the height of the model, r_0 is the radius of the heat source model, and r is the radial distance from the volumetric heat source center and is given as

$$r = \sqrt{x^2 + y^2} \quad (11)$$

Considering a moving heat source, Eq. (11) can be shown as

$$q(x,y,z,t) = \frac{Q_0}{\pi r_0^2 H} \exp\left(\frac{-3(x^2 + (y + v(\tau - t))^2)}{r_0^2}\right) \quad (12)$$

Here, t , the lagging parameter, and welding speed are represented by v , τ , and t , respectively.

Cubical heat source model

It is a volumetric heat source model following a Gaussian heat distribution in **Error! Reference source not found.** [23].

It is represented mathematically as

$$q(x,y,z) = \frac{Q_0}{D^3} \exp\left(\frac{-3r^2}{D^2}\right) \quad (13)$$

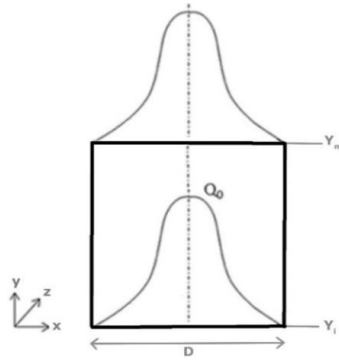


Figure 4 Cubical Heat Source Model [23]

where r is the radial distance from the center of the volumetric heat source, D is the length of the cubical heat source, and Q_0 is the maximum intensity of the heat source.

$$r = \sqrt{x^2 + y^2} \quad (14)$$

Considering a floating heat source in the z -direction, Eq. 14 represented as

$$q(x,y,z,t) = \frac{Q_0}{D^3} \exp\left(\frac{-3(x^2 + (z + v(\tau - t))^2)}{D^2}\right) \quad (15)$$

Where v , τ , and t are the welding speed, lagging parameter, and welding time.

Circular disk heat source model

A surface heat flux heat source model following a Gaussian energy distribution is represented by Eq. 16 and also shown in Figure 3 [24], [25].

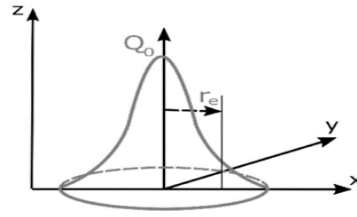


Figure 3 Circular disk heat source model[24], [25]

$$q(r) = \frac{3Q_0}{\pi r_e^2} \exp \left[-3 \left(\frac{r}{r_e} \right)^2 \right] \quad (16)$$

In this equation, r is the radial distance from the heat source center, Q_0 is the highest surface heat source intensity, and here is the radial dimension of the heat source where 95% of the heat flux is deposited.

When the heat source moves along y direction over the surface, Eq. 17 becomes

$$q(x, y, t) = \frac{3Q_0}{\pi r_e^2} \exp \left[-3 \left(\frac{x + (y + v(\tau - t))}{r_e} \right)^2 \right] \quad (17)$$

where lagging parameter, welding time, and welding speed are represented by t , v , and τ , respectively.

FE Model, Boundary Conditions, and Material Properties

Two rectangular blocks measuring 150×75×10 mm have been developed for the finite element analysis, as illustrated in Figure 4. The temperature-dependent material characteristics of AISI 304 steel are displayed in Figure 4 (b)[26]. The meshing was done so that a fine mesh was used near the weld line for better results, and a coarser mesh was used in an area far from the weld bead. An element of solid 70 with total nodes of 13288 and total aspects of 6450 has been used for the analysis. The element death and birth technique has been employed to incorporate a heat source. The welding parameters are set at 450 V with 26.5 A. The welding speed was 5.3 mm/sec.

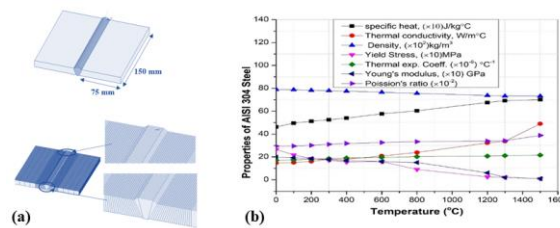


Figure 4 (a) 3D model and meshing of AISI 304 Steel plate butt joint (b) Material properties of AISI 304 steel [26]

Transient Heat Conduction Equation

A rectangular coordinate system (x, y, z), a transient heat governing equation for homogenous, isotropic material with heat generation is given by

$$\frac{\partial}{\partial x} \left[K \frac{\partial T}{\partial x} \right] + \frac{\partial}{\partial y} \left[K \frac{\partial T}{\partial y} \right] + \frac{\partial}{\partial z} \left[K \frac{\partial T}{\partial z} \right] + Q = \rho C_p \frac{\partial T}{\partial t} \quad (18)$$

Where x, y , and z are the cartesian coordinates and represent the transverse, thickness, and longitudinal direction, ρ Is the density of the plate material (kg/m^3), K is the thermal conductivity ($\text{W/m}^\circ\text{C}$), Q is the internal heat generation rate (W/m^3), and C_p is the specific heat capacity ($\text{J/kg}^\circ\text{C}$). T is the unknown temperature of the weld plate ($^\circ\text{C}$). Solving the above equations numerically is very common in engineering and science applications. Solving analytically could only be applied with simple boundary and initial conditions with infinitely large geometries [10]. With advancements in computational methods, the Finite Element method is the most common numerical method used for welding simulations.

Boundary Conditions

To support the above equation, an initial and boundary conditions have been considered.

- I. The initial temperature of the weld specimen is taken as an ambient temperature and is given by $T = T_0$ at $t = 0$, where T_0 is the ambient temperature.
- II. The boundary condition for the weld region is that the total heat will be equal to the total heat supplied

$$Q_n = -Q_{\text{supp}} \text{ or } -Q_n = -k \frac{dT}{dn}$$
- III. The second boundary condition for the rest of the specimen except the weld region is that the heat supplied is all lost due to convection.

$$Q_n = -Q_{\text{conv}}$$

Results & Discussion

Every kind of heat source welding model underwent independent FE modelling. Keep the welding parameters such as welding speed, welding voltage & current, i.e., heat input, etc., constant. Figure 5(a) is the time vs temperature graph at different points on the top surface of the plate in the transverse direction from the weld bead, which has been taken at 5mm, 10mm, 15mm, 20mm, 25mm, and 30mm. The maximum temperature is observed at the nearest point from the heat source, i.e., 5mm, and reaches the maximum temperature of 1289.68°C , while at 10mm, the temperature is 747.271°C . The farthest observation point, i.e., 30mm, has a maximum temperature of 338.5°C ,

which means the temperature keeps decreasing as moving further and further away from the weld line, which are all the functions of time. Figure 5(b) also consists of the contour diagram of temperature distribution on the plate's top surface and across the plate's thickness. The total penetration temperature distribution reaches the melting point of the weld metal and exhibits the effect of the volumetric double ellipsoidal heat source model.

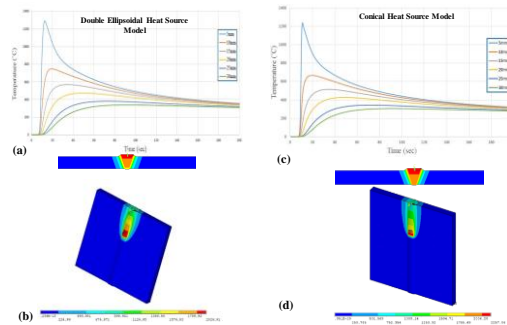


Figure 5 (a) (c) Time-Temperature graph for double ellipsoidal heat source model for the various points on the top surface of the plate across the weld--line away from the weld region (b)(d) Temperature contour diagram on the top surface of the plate and across the plate thickness

Figure 5(c) illustrates the time-dependent thermal profile of the welding process as modelled using a conical heat source. The results are shown for observation points located 5 mm, 10 mm, 15 mm, 20 mm, 25 mm, and 30 mm from the weld centreline on the top surface of the weld plate. Notably, the peak temperature at the 5 mm point reaches approximately 1250°C, with minimal variation. The temperature contours reveal that the conical heat source model enhances heat penetration, as evidenced by the distribution of red and brown colour bands covering the weld bead region in Figure 5(d). As highlighted in section 2.2, this model is particularly suitable for welding processes requiring deep penetration, such as electron beam welding.

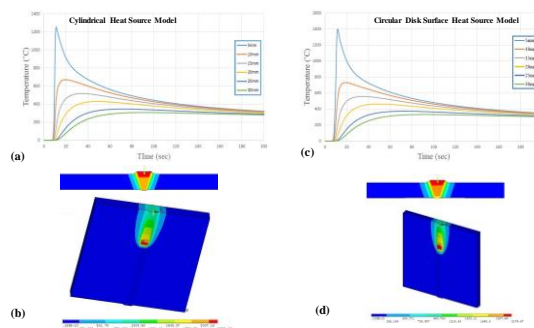


Figure 6 (a) (c) Time-temperature graph for a conical heat source model at various locations on the top surface of the plate, measured along the weld line at increasing distances from the weld region. (b)(d) Temperature contour plot on the top surface of the plate and through the plate thickness.

Furthermore, the thermal gradient across the weld appears more constrained, as depicted in Figure 6. Figure 6(a) and (c) illustrate the time-evolving thermal profile and temperature distribution during the welding process for the cylindrical heat source model. The temperature distribution within the weld zone closely resembles that of the conical heat source model, as the variation in cross-sectional area through the thickness of the plate is minimal. However, heat penetration is visible for the cylindrical heat source. Even the peak temperature on a point 5mm away from the weld centreline approaches the same as the conical heat source model. Therefore, both cylindrical and conical heat source models are extensively used [27], [28], [29] to model laser beam and electron beam welding processes. Nonetheless, the difference may be noticeable for the higher thickness of the plate, where penetration will be a significant parameter.

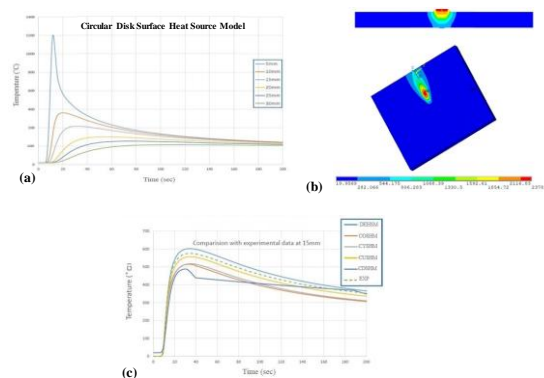


Figure 7 Time-Temperature graph for cylindrical heat source model for the various points on the top surface of the plate across the weld--line away from the weld region (b) Temperature contour diagram on the top surface of the plate and across the plate thickness (c) Comparison of time temperature result with the experiment results for all.

The time-dependent thermal profile and temperature contour plot for the cubic heat source model are shown in Figure 7 (a) respectively. The peak temperature is less in this case for the same parameters which may be because of the equidimensional three axes in x, y and z directions. However, simple mathematical formulations make the cubic heat source model comparatively easy to model. The time-dependent thermal profile and temperature contour for the circular disk

surface heat flux model are shown in Figure 7(b). The effect of surface heat distribution is observed from the through-thickness temperature contour in the weld region. The peak temperature is still achievable on the top surface. Hence, the surface heat flux model may be efficaciously implemented to model the bead-on-plate and thin-plate welding. However, to compare the accuracy of all the heat source models the experimentally obtained temperature-time profile for the submerged arc welding of the AISI 304 steel plate was plotted along with the predicted temperature-time profiles for all the heat source models as shown in Figure 7(c).

Conclusions

The study successfully modeled and simulated single-pass submerged arc welding with different heat sources and boundary conditions. Based on the results, we made a few conclusions as follows below-

1. The analysis shows that the weld bead has a distinct temperature gradient running transversely. The temperature reaches its maximum (1289.68°C) at 5 mm from the heat source and then abruptly reduces to 338.5°C at 30 mm, suggesting that the temperature drops as one gets farther away from the weld line.
2. The temperature rises quickly in all heat source models, including DEHSM (double ellipsoidal), COSHM (conical), CYSHM (cylindrical), CUSHM (curved), and CDSHM (circular disc surface), which closely resembles the experimental data in the early phases. There is potential for improvement in forecasting the highest heat input throughout the welding process, as two models closely captured the experimental peak temperature. This may be because of the same assumptions and ideal conditions that were considered while performing the welding simulation.
3. All models exhibit a slow decrease in the temperature profile's cooling phase, with DEHSM and COSHM fitting the experimental data the best during this phase. This implies that these two models better capture the heat dissipation properties of precision modeling of Arc welding.
4. DEHSM and COSHM seem to be the models that diverge from the experimental data the most, especially during the early cooling phases. This suggests that the ellipsoidal and conical models may more successfully capture the heat transfer mechanisms unique to the precision modeling of SAW than the other heat source models.

Acknowledgments

Authors want to thank the National Institute of Technology Mizoram for providing the computational facility under the seed grant.

References

- [1] S. Kiyoshima, D. Deng, K. Ogawa, N. Yanagida, and K. Saito, "Influences of heat source model on welding residual stress and distortion in a multi-pass J-groove joint," *Comput Mater Sci*, vol. 46, no. 4, pp. 987–995, 2009, doi: 10.1016/j.commatsci.2009.05.002.
- [2] A. Ghosh and H. Chattopadhyay, "Mathematical modeling of moving heat source shape for submerged arc welding process," *International Journal of Advanced Manufacturing Technology*, vol. 69, no. 9–12, pp. 2691–2701, 2013, doi: 10.1007/s00170-013-5154-z.
- [3] F. Hongyuan *et al.*, "New general double ellipsoid heat source model New general double ellipsoid heat source model," vol. 1718, no. 2005, 2013, doi: 10.1179/174329305X40705.
- [4] M. Goldak, J., Chakravarti, A. & Bibby, "A new finite element model for welding heat sources.," *Metallurgical Transactions B*, vol. 15, pp. 299–305, 1984, doi: <https://doi.org/10.1007/BF02667333>.
- [5] X. Pu, C. Zhang, S. Li, and D. Deng, "Simulating welding residual stress and deformation in a multi-pass butt-welded joint considering balance between computing time and prediction accuracy," *International Journal of Advanced Manufacturing Technology*, vol. 93, no. 5–8, pp. 2215–2226, 2017, doi: 10.1007/s00170-017-0691-5.
- [6] Z. Cai and H. Zhao, "Efficient finite element approach for modelling of actual welded structures," *Science and Technology of Welding and Joining*, vol. 8, no. 3, pp. 195–204, 2003, doi: 10.1179/136217103225010916.
- [7] A. Ghosh, "Analytical Solutions for Moving Elliptical Paraboloid Heat Source in Semi-Infinite Plate," vol. 320, pp. 117–133, 2011, doi: 10.4028/www.scientific.net/DDF.319-320.117.
- [8] Y. Z. and Q. Z. . Wang, J. Han, J. P. Domblesky, Z. Yang, "Development of a new combined heat source model for welding based on a polynomial curve fit of the experimental fusion line," *The International Journal of Advanced Manufacturing Technology*, vol. 83, pp. 5–8, 2016.
- [9] C. Chang and L. Wei T. Li, L. Zhang, "A Uniform-Gaussian distributed heat source model for analysis of residual stress field of S355 steel T welding," *Advances in Engineering Software*, vol. 126, pp. 1–8, 2018.
- [10] R. R. and S. C. S. A. Sarkar, A. Datta, P. Dey, "A NUMERICAL APPROACH FOR MODELLING THERMAL PROFILES AND EFFECTS OF PROCESS PARAMETERS ON IT IN SUBMERGED

- ARC WELDING OF AISI 1518 GRADE STEEL,” *Journal of Thermal Engineering*, pp. 505–516, 2018.
- [11] N. S. S. and K. S. S. V. Dhinakaran, “Experimental investigation and numerical simulation of weld bead geometry and temperature distribution during plasma arc welding of thin Ti-6Al-4V sheets,” *J Strain Anal Eng Des*, pp. 30–44, 2016.
- [12] M. S. and J. B. T. Flint, . J. Francis, “Extension of the Double-Ellipsoidal Heat Source Model to Narrow-Groove and Keyhole Weld Configurations,” *J Mater Process Technol*, pp. 123–135, 2017.
- [13] D. M. C. & M. J. Giarollo, “Comparison between two heat source models for wire-arc additive manufacturing using GMAW process,” *Journal of Brazilian Society of Mechanical Science and Engineering*, vol. 44, 2022.
- [14] S. Suman and P. Biswas, “Thermo-mechanical study of single and multi-pass welding of CSEF steel for residual stresses and deformations considering solid state phase transformation,” *Mater Today Proc*, no. xxxx, 2020, doi: 10.1016/j.matpr.2019.12.299.
- [15] S. Suman, A. Tiwari, P. Biswas, and M. M. Mahapatra, “Finite Element Analysis of Thermal-Induced Stresses in Submerged Arc Welded Chromium-Molybdenum Steel and Their Mitigation through Heat Treatment,” *J Mater Eng Perform*, vol. 29, no. 12, pp. 8271–8285, 2020, doi: 10.1007/s11665-020-05262-2.
- [16] S. Suman, P. Biswas, S. Kumar, V. Pratap, A. Kumar, and B. Kuriachen, “Measurement of residual stresses in submerged arc welded P91 steel using surface deformation,” *Mater Today Proc*, vol. 21, pp. 1707–1712, 2020, doi: 10.1016/j.matpr.2019.12.049.
- [17] S. Suman and P. Biswas, “Comparative study on SAW welding induced distortion and residual stresses of CSEF steel considering solid state phase transformation and preheating,” *J Manuf Process*, vol. 51, no. October 2019, pp. 19–30, 2020, doi: 10.1016/j.jmapro.2020.01.012.
- [18] S. Suman and P. Biswas, “Microstructural, Strength and Residual Stress Studies on Single- and Double-Side Single-Pass Submerged Arc Welding of 9Cr–1Mo–V Steel Plate,” *Journal of The Institution of Engineers (India): Series C*, vol. 103, no. 5, pp. 1177–1191, 2022, doi: 10.1007/s40032-022-00870-4.
- [19] S. Suman, P. Pankaj, A. Tiwari, P. Biswas, B. Kuriachen, and A. Sinha, “Effect of pre- and post- welding processes on the distortion pattern in a SAW- welded butt joint of P91 steel plate,” in *Advances in Additive Manufacturing and Joining*, J. Paulo Davim, Ed., Springer

- singapore, 2019, ch. 55, pp. 631–639. doi: <https://doi.org/10.1007/978-981-32-9433-2>.
- [20] S. Suman, P. Biswas, S. Baranwal, and V. Mekala, “Finite Element Modelling of side heating for mitigation of residual stress and distortion in SAW welded P91 steel weld,” *Mater Today Proc*, vol. 28, pp. 2511–2521, 2020, doi: 10.1016/j.matpr.2020.05.004.
- [21] S. Suman and P. Biswas, “Finite element analysis of in- process thermal mitigation of welding induced residual stresses in 9Cr-1Mo-V steel butt joint considering phase transformation,” *J Manuf Process*, vol. 70, no. June, pp. 361–375, 2021, doi: 10.1016/j.jmapro.2021.08.027.
- [22] T. Kik, “Heat source models in numerical simulations of laser welding,” *Materials*, vol. 13, no. 11, pp. 1–24, 2020, doi: 10.3390/ma13112653.
- [23] M. Behúlová and E. Babalová, “Heat source models for numerical simulation of laser welding processes - A short review,” *J Phys Conf Ser*, vol. 2712, no. 1, 2024, doi: 10.1088/1742-6596/2712/1/012018.
- [24] S. Suman, P. Biswas, and P. V. S. S. Sridhar, “Numerical prediction of welding distortion in submerged arc welded butt and fillet joints,” in *International Conference on Design and Manufacturing, IITDM, Chennai*, Chennai, 2016, pp. 1–5.
- [25] S. Suman, P. V. S. S. Sridhar, P. Biswas, and D. Das, “Prediction of welding-induced distortions in large weld structure through improved equivalent load method based on average plastic strains,” *Welding in the World*, vol. 64, no. 1, pp. 179–200, 2020, doi: 10.1007/s40194-019-00805-1.
- [26] S. Suman, P. V. S. S. Sridhar, P. Biswas, and D. Das, “Prediction of welding-induced distortions in large weld structure through improved equivalent load method based on average plastic strains,” *Welding in the World*, vol. 64, no. 1, pp. 179–200, 2020, doi: 10.1007/s40194-019-00805-1.
- [27] C. Pyo, J. Kim, Y. Kim, and M. Kim, “A study on a representative heat source model for simulating laser welding for liquid hydrogen storage containers,” *Marine Structures*, vol. 86, Nov. 2022, doi: 10.1016/j.marstruc.2022.103260.
- [28] B. Huang, X. Chen, S. Pang, and R. Hu, “A three-dimensional model of coupling dynamics of keyhole and weld pool during electron beam welding,” *Int J Heat Mass Transf*, vol. 115, pp. 159–173, 2017, doi: 10.1016/j.ijheatmasstransfer.2017.08.010.

- [29] P. Hartwig, L. Scheunemann, and J. Schröder, “A volumetric heat source model for the approximation of the melting pool in laser beam welding,” *Pamm*, vol. 23, no. 4, pp. 1–9, 2023, doi: 10.1002/pamm.202300173.

Mechanical and Microstructure Analysis of AlSi10Mg Alloy Fabricated by Selective Laser Melting Process

**Sunita K. Srivastava¹ *, N. Rajesh Mathivanan²,
Sunith Babu L.³**

^{1,2} *Department of Mechanical Engineering,
PES University,
Bangalore, INDIA*

³ *Department of Mechanical Engineering,
RIT,
Bangalore, INDIA*

*Corresponding author email: sunita.shri45@gmail.com

Abstract

AlSi10Mg alloy is one of the most extensively used aluminum alloys in additive manufacturing because of its exceptional thermal and dimensional stability. However, the fabrication parameters affect the mechanical properties. Understanding the mechanical properties is of prime importance to characterize the material. The research is focused on examining the microstructure and mechanical properties of the AlSi10Mg alloy manufactured using selective laser melting (SLM) in as-built conditions. The sample is fabricated using specific SLM parameters such as 275 W laser power, 2000 mm/s scan speed, 80 μ m hatch spacing, and 30 μ m layer thickness. To evaluate the material properties, the tensile, hardness, porosity and density measurement tests were performed on the sample. Additionally, SEM (Scanning Electron Microscopy) and EDAX (Energy-Dispersive X-ray Spectroscopy) were employed on the as-fabricated and fractured samples for detailed characterization. The results demonstrate that AlSi10Mg alloy exhibits a tensile strength of 436.95 MPa, yield strength of 58 MPa, elongation of 9.6%, and hardness of HRB 74 as the sample achieved a relative density of 97.43%.

Keywords: Powder Bed Fusion, Additive Manufacturing, AlSi10Mg, Selective Laser Melting, SEM

Introduction

Additive manufacturing (AM) has emerged as a key driver and pioneer of recent industrial innovation in the manufacturing sector. This

manufacturing technique has been customized over several decades to accommodate a wide range of materials which includes metal, polymer, alloy, and composite. Additive manufacturing encompasses various techniques to cater to all ranges of manufacturing requirements including fused deposition modelling (FDM), binder jetting (BJ), powder bed fusion (PBF), and material jetting (MJ). Sheet lamination (SL) etc. Among these, selective laser melting (SLM) and laser metal deposition (LMD) are the most widely used manufacturing processes for metals and metal composites. These techniques offer several advantages that include lesser lead time, complex manufacturing, cost-effectiveness, exceptional part quality, and accuracy. AM processes are quite beneficial in catering to aluminum and aluminum alloys because of its superior strength relative to the weight, which is compatible with additive manufacturing process [1].

However, the laser manufacturing of pure aluminum is quite challenging because of its high reflectivity, which allows it to absorb only 7% of the incident laser. Since silicon exhibits comparatively high laser absorptivity of upto 70% , aluminium- silicon alloys are preferable materials for the laser powder bed fusion process especially selective laser melting [2].

Among the group of aluminium-silicon alloys, AlSi10Mg is among the most popular alloys because of its exceptional mechanical properties, thermal properties, corrosion resistance, and lightweight properties. While the alloy contains Al + Si phase , that might affect the ductility and strength but simultaneously improves the machinability of the material. Its low shrinkage and melting temperature make this alloy suitable for casting and additive manufacturing. However, due to its narrow solidification range and classification as a hypoeutectic group, AlSi10Mg alloy is less prone to crack during the cooling after laser melting, making it a preferable choice for application in automobile and aerospace sectors [3-8].

Various studies have been performed to assess the mechanical and microstructure properties of AlSi10Mg alloy manufactured by SLM at different process parameters lately.

In recent studies, Nirish et. al. [9] investigate the mechanical properties such as ultimate tensile strength, yield point , and deformation (% elongation) of AlSi10Mg alloy produced by selective laser melting (SLM) and results are compared with conventionally casted Al6061 under both preheated and as-built conditions. The SLM manufacturing is done at the specific process parameters (laser spot size of 75 μm , layer height of 30 μm , laser output of 225 W, scan velocity of 500 mm/s, and hatch space of 100 μm). The findings reveal that the

AlSi10Mg shows superior properties compared to cast Al6061. Specifically, the tensile strength of the alloy increased by 2.7%, yield strength increased by 53%, elongation increased by 86%, and hardness increased by 3.2% because the samples were preheated.

Ashwath et. al. [10] investigated the impact of scan rate and build direction on the mechanical and surface properties of the SLM as-built AlSi10Mg comparing with its cast counterpart. The surface micrograph of the as-built samples revealed a refined grain size ranging between 7.2 μm and 5.5 μm as the scanning speed increases, in contrast to that of the cast AlSi10Mg sample ($\sim 9.1 \mu\text{m}$). Due to the fine grained structure and Orowan strengthening mechanism, the as-built sample exhibits a notably high microhardness of 135 HV and tensile strength of 390 MPa (Z) at the scan rate/speed of 500 mm/s and layer thickness of 20 μm .

Prasad et. al. [11] evaluate the mechanical properties of AlSi10Mg alloy produced using the DMLS (Direct Metal Laser Sintering) process at the orientation of 45° and 90°. The samples were produced at 240 W laser power, 1180 mm/s scan speed, 60 μm layer thickness, 0.12 mm hatch distance, and 0.1 mm laser spot size. The tensile strength and compression strength of the sample fabricated at 45° orientation is 428.6 MPa and 642.68 MPa respectively compared to 408.3 MPa and 638.77 MPa of the sample fabricated at 90° orientations.

Mei et. al. [12] examined AlSi10Mg alloy fabricated by SLM at various laser power (300 - 400 W). It was observed that at the 400 W laser power and 1800 mm/s scan speed alloy exhibits very high relative density (99.4%), impressive hardness (147.8 HV), high tensile strength (471.3 MPa) and yield strength (307.1 MPa) along with significant elongation (9.6%). The exceptional properties were achieved due to the unique geometry of the melt pool and the refined microstructure due to high laser power.

Saravana et. al. [13] conducted a mechanical and morphological study of AlSi10Mg alloy fabricated by additively manufactured (AM) and compared it with stir casted samples. It was found that the additively manufactured samples show lower porosity (by 14%) compared with the samples fabricated using stir casted. Furthermore, the tensile strength and the material hardness of the additively manufactured samples also show an increment of 28.6% and 23.69% respectively compared to stir casted samples. The AM samples additionally exhibited a 50% and 32.55% increase in fracture toughness and shear stress respectively.

Expanding the knowledge of the previous findings, this study is focused on the investigation of the mechanical and physical properties of Al-Si-Mg alloy fabricated using the selective laser melting process at the specific process parameters that have not been addressed in the prior studies. The nature of the sample is widely analyzed using a series of tests such as mechanical, surface properties, density, microstructure and porosity using various techniques including universal testing machine (UTM), Rockwell Hardness tester, scanning electron microscopy (SEM), and optical microscopy (OM).

Materials and Methods

Sample Preparation

The AlSi10Mg powder manufactured using the gas atomization process, having an average powder particle size of 20 - 63 μm was used for the fabrication of the samples. The powder consists of upto 10% Silicon primarily, along with a trace amount of other elements as shown in Table 1.

Table. 1. Composition of AlSi10Mg powder (wt%)

Element	Al	Si	Mg	Fe	N	O	Ti	Zn	Mn	Ni	Cu	Pb	Sn
Mass %	Balance	9-11	0.25-0.45	0.25	0.20	0.20	0.15	0.10	0.10	0.05	0.05	0.02	0.02

The samples were manufactured using the RenAM 500E machine by selective laser melting process, with the key manufacturing parameters as shown in Table 2. The fabrication was done with the chamber filled with 99.999% pure Argon gas to prevent oxidation of the powder. The horizontal building direction was maintained throughout the fabrication with the layers oriented at 67° from the preceding layer. The build plate is preheated to 80°C to minimize the temperature difference between the first layer and the plate, which is the common factor contributing to the distortion in 3D printed parts [14]

Table 2: Process Parameters

Printing Parameters	Values
Laser diameter	70 μm
Exposure time	40 μs
Point-to-point distance	90 μm
Hatch spacing	80 μm
Layer thickness	30 μm
Scan speed	2000 mm/s
Laser power	275 W

Flat type sub size tensile test specimen with a total length of 100 mm and thickness of 6 mm along with the 5 mm cube for other analysis was manufactured as shown in Figure 1. The gauge length of 25mm was selected for the tensile sample as per ASTM E8 standard. After fabrication, the as-built samples were kept for the stress-relieving process at 300 °C ±10 °C for 2 hours and then air cooled.

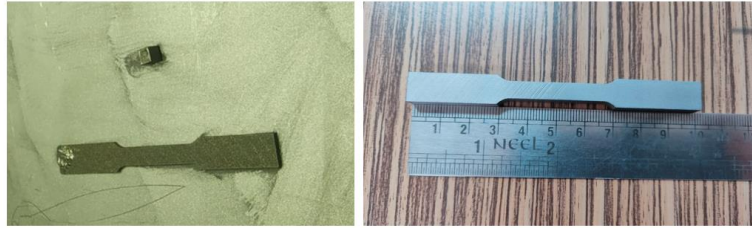


Figure 1: Fabricated Samples

Density and Porosity Measurement

The density of the sample was determined by Archimedes principle using a density measurement kit as shown in Figure 2(a), with the precision upto 0.0001 g. The mass of the cubical sample was first recorded in air and then in distilled water. The samples density was calculated using mass loss principle, according to Equation (1)

$$\rho = \frac{m_a \rho_h}{m_a - m_w} \quad (1)$$

Where m_a is the mass of the sample in air, ρ_h is the density of water (1 g/cm³), m_h is the mass of the sample in water

Hence, The relative density of the sample is $\rho_{RD} = \frac{\rho}{\rho_{TD}} \times 100\%$

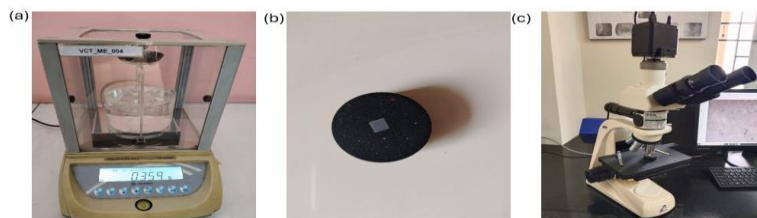


Figure 2: (a) Density Measurement Set-up (b) Sample for Porosity Measurement (c) Porosity Measurement using OM

Porosity tests were conducted on a 5 mm cubical sample using Material Plus 4.5 image analysis software intergraded in Meiji MT7100L Metallurgical Microscope as shown in Figure 2(c). Before the test, the sample was cleaned and etched using emery and velvet cloth for 10 minutes and then mounted on a Bakelite mold for the analysis, as shown in Figure 2(b). Five different images were captured from the surface perpendicular along the scan direction at 200x and 500x magnification and analyzed. The images are fed into the software and converted into to grayscale to help highlight the porosity against the white background. The average of the five readings is used for the final porosity percentage calculation.

Tensile and Hardness Test

Tensile tests were conducted on a universal testing machine, model ETM Wance with a 50 kN capacity and a strain rate of 1mm/min, as shown in Figure 3 (a). The tests were conducted following the ASTM E8 standard procedure. The axial displacement of the sample is cautiously monitored and recorded using computer integrated extensometer.

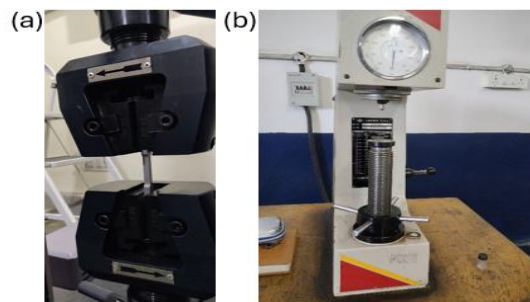


Figure 3: (a) Tensile Test (b) Hardness Test Set-up

A Rockwell hardness tester was used to perform the hardness test using the B scale, equipped with a 1/16 in diameter steel ball indenter, following ASTM E18 standard as shown Figure 3 (b). Initially, a minor load was applied to establish the reference point and ensure proper contact with the sample. Following this, the major load of 100 kgf was applied for 10-15 seconds to create four different indentations. The average value of these four measurements was then recorded.

Microstructural characterization

For the microstructure analysis, the samples were abraded using sand/emery paper and then itched for 30-40 s with Keller's reagent, which is the mixture HNO_3 (5 ml), HCl (3 ml), HF (2 ml) and distilled

Water (190 ml) . The etched samples were then observed using SEM along the scan direction.

Results and Discussion

Powder and Sample Characterization

Figure 4 shows the SEM image of AlSi10Mg powder morphology. The AlSi10Mg alloy powder is predominantly spherical with a minor presence of satellite particles (agglomeration). The presence of these minor agglomerations happens because of the fast solidification of the powder particle during the gas atomization process which can be minimized using a high cooling rate for the finer particles [15].

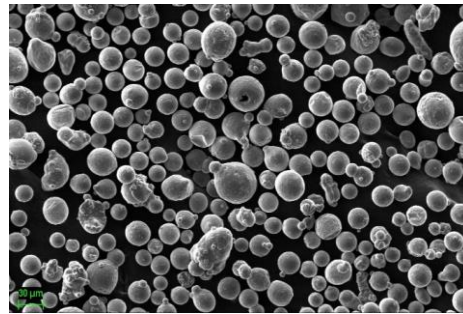


Figure 4: SEM Image of AlSi10Mg Powder

The EDAX spectrum of AlSi10Mg powder, shown in Figure 5, confirms the presence of Aluminium (Al) by 88.4%, Silicon (Si) by 10.6% and Magnesium (Mg) by 1% which is closely aligned with the composition provided by the supplier.

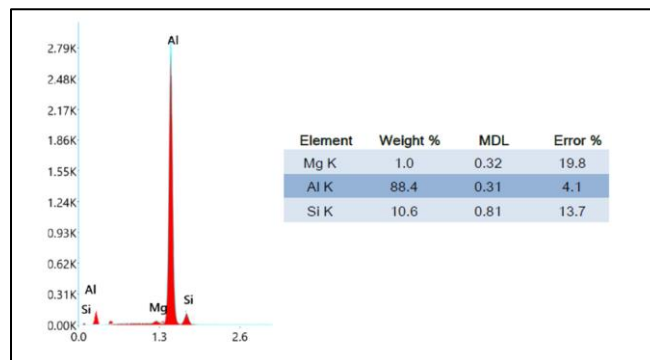


Figure 5:EDAX spectrum of AlSi10Mg powder

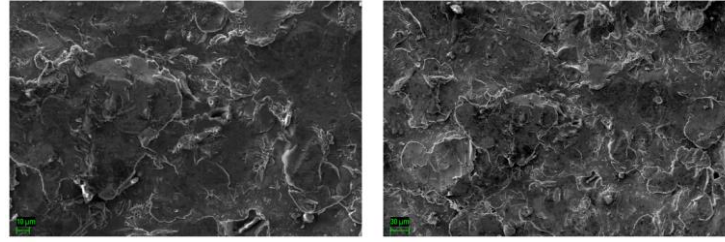


Figure 6: SEM Image of as-built Sample

Figure 6 shows the surface morphology of the as fabricated sample in the plane perpendicular to the build direction (along scan direction). The surface appears rough and irregular primarily due to the layer deposition and the unbelted powder particles. Small pores and voids are visible in the image likely by the gas entrapment or inadequate energy input.

Density and Porosity

The density of the sample was measured at 2.6 g/cm³ against the nominal density of AlSi10Mg alloy at 2.67 g/cm³ [16]. The porosity percentage was recorded at an average value of 0.85% across five locations (0.714 %, 0.853%, 0.819%, 0.904% and 0.959%) as shown in Figure 7. The pores appeared mostly spherical and localized. The OM images show the dispersed, irregular, and interconnected pores mostly due to entrapped gas. The irregular pores were likely due to improper powder spreading, though they were infrequent [1]. No cracks were found in the samples whatsoever, which indicates good formability and successful fabrication using the parameters shown in Table 2.

The sample achieved a relative density (RD) of the sample is 97.43%, calculated using the Archimedes principle at the volumetric energy density (VED) of 57 J/mm³ (as per Equation 1)

$$VED = \frac{\text{Laser power}}{\text{Scan Speed} \times \text{Layer thickness} \times \text{Hatch Spacing}} \quad \text{Eqn (1)}$$

where VED is in J/mm³, the laser power is in W, the scanning speed is in m/s, the layer thickness is in mm and hatch spacing is in mm.

Since the VED is the value of input energy per material volume, it directly impacts the porosity and density. A low VED value is insufficient to melt the powder completely, leading to more porosity and less dense material. Conversely, a high VED value can cause heat turbulence, spatter, and pores formation due to excessive energy, resulting in defective parts [17].

Previous studies have shown that the best combination of properties was found in the range of volumetric energy density (VED) between 49–59 J/mm³ [18]. Further study identifies the optimum range of energy density for SLM-manufactured AlSi10Mg found between 32 J/mm³ - 54 J/mm³ to achieve high density parts. The value of relative density was found above 99% in the range between 30.3 J/mm³ - 55.6 J/mm³ VED except for a few outliers [19]. In additional research, the optimum VED value was found to be close to ~60 J/mm³ to achieve fully dense material [1]. Most fully dense parts (>98%) were achieved in the range of VED of 30-110 J/mm³, with most data lying between 40 J/mm³ and 70 J/mm³ [16].

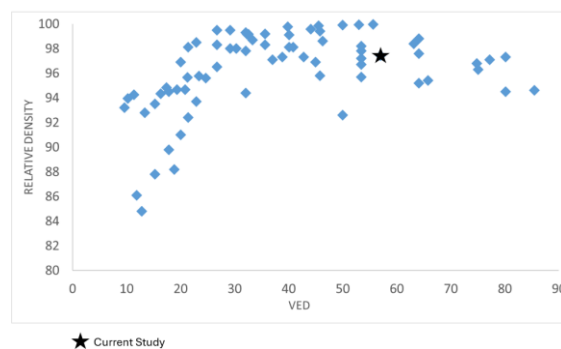


Figure 8: Relationship between RD and VED [17-23]

Maamoun et al. [20] found out that the energy density (VED) value between 50 and 60 J/mm³ can produce the part with the relative density upto 99.7%. The findings of the current research align with the previous studies and extend the work of earlier researchers as shown in Figure 8.

Tensile and Hardness Properties

The tensile and hardness tests of the SLM fabricated specimen were conducted, and the results are presented in Table 3. As shown in Figure 9, the specimen is fractured in the plane right angled to the direction of the applied force. The tensile strength of the specimen is reported as 436.95

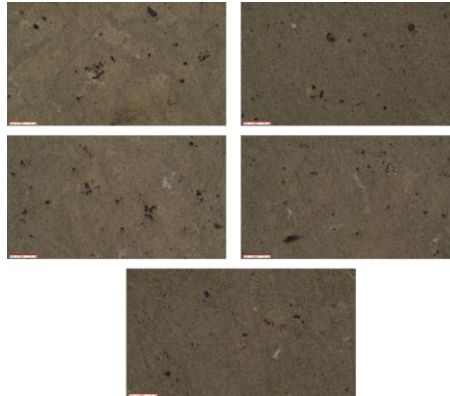


Figure 7 : Optical Images of Porosity

Table 3: Tensile test and Hardness Test results

Mechanical Properties	Values
Yield Stress(MPa)	58
Tensile Strength (MPa)	436.95
Elongation %	9.59
Maximum Force (KN)	15.73
Hardness Test (HRB)	74

MPa under the load of 15.7 KN with the specimen showing elongation of 9.59%. The failure of the specimen is identified as brittle and sudden occurring before the material entered the plastic zone. The stress-strain relationship shows a bi-linear relationship. The initial linear region is the curve used to calculate the yield strength (0.2% proof stress). After yielding the curves continue to show further linear relationships resulting in high maximum tensile strength (UTS) and low yield point (YS). Notably, the data is well aligned with previous findings [11, 12, 24,25,26].

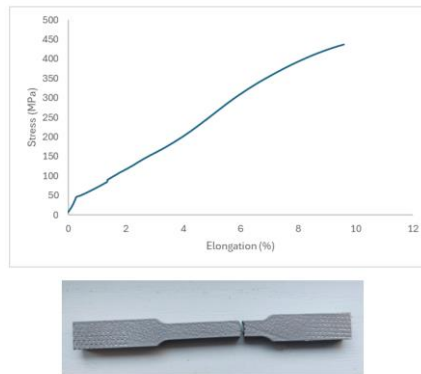


Figure 9: Stress - Strain Diagram and Fractured Specimen

Figure 10, illustrates the variation in the tensile strength (TS) of SLM manufactured AlSi10Mg as a function of different laser power P (along X-direction in Watt) and scan speed V (along Y-direction in mm/s) as per the data collected from the previous research and the current study [9-13][17][20][24-26][28-68]. As shown in the heatmap the highest tensile strength was observed primarily in the range of laser power from 200 to 450 W, and scan rate/speed from 1000 to 2400 mm/s. The trend is due to the high input of the laser energy density or volumetric energy density, which provides an adequate and stable energy density to entirely melt the powder, promoting the formation of a consistent and uniform melt pool.

However, as the scan speed increases after a certain value, the laser energy density decreases, leading to insufficient melting, defects, and porosity. Conversely, the low scan speed increases the energy input causing the melt spattering and entrapment of vaporized gas [12]. The value of tensile strength of the current study falls under the optimum condition highlighted in the heatmap.

Fracture Surface Analysis

The fractured surface observed in SEM (shown in Figure 11) reveals the presence of partially melted powder holes, and porosities due to a lack of fusion and gas entrapment. All these defects have resulted in the brittle fracture of the tensile test specimen. While the dimples present in the fractured surface indicate a ductile failure, the smoother areas exhibit cleavage facets, indicating a brittle fracture [27].

Although the fracture surface of the sample displays a ductile fracture behaviour characterized by micro-void coalescence, some evidence of brittle fracture is also present. The presence of small dimples, voids, columnar grains, and small inclusions is also visible on the fractured

surface. These defects severely impair the mechanical properties of the alloy.

It is evident that the tensile sample showed no plastic deformation and exhibited brittle failure. The fracture mechanism clearly transformed between brittle and ductile fracture, which is evident from the uniform distribution of dimples and the network like pattern in the tear ridge.

The “river pattern-like” stepped cleavage planes show the nature of brittle failure with low ductility.

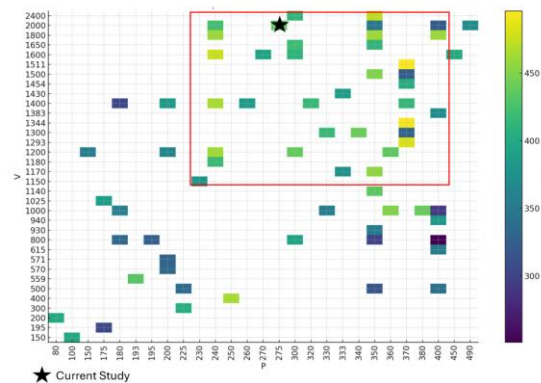


Figure 10: Variation of tensile strength versus SLM process parameters

Microstructure Properties

The selective laser melting possesses very high heating followed by rapid solidification resulting in a very fine microstructure. As reported in the previous studies, the microstructure of Al-Si-Mg alloy fabricated using the selective laser melting process is primarily composed of α -Al and the interdendritic Si-particles [69]. The SEM microstructure image of the as-built sample (Figure 12) revealed the presence of α -Al (light grey) and the eutectic phase with finely dispersed silicon particles (dark grey). The presence of fine Si precipitates and supersaturation of the Al matrix leads to the hardening effect of the alloy, resulting in 30% higher strength than the casting counterpart. Although there is no particular change in the as cast and SLM air cooled as-build sample observed, there is a comparative increase in the ratio of the α -Al phase in the air-cooled SLM sample [70] [71]. The high strength of SLM manufactured AlSi10Mg is attributed to the fine grain structure and different types of precipitated phases formed during the process. The coarse silicon precipitates present in the matrix cause the embrittlement and reduction in the ductility of the material [44].

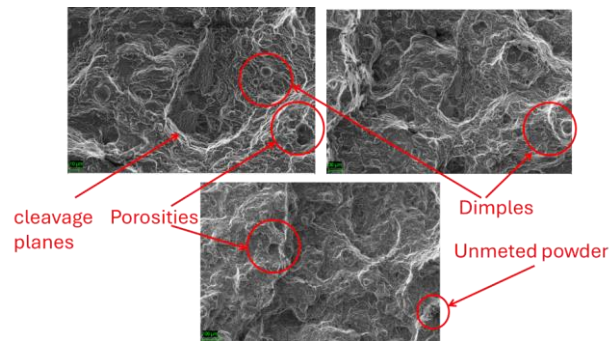


Figure 11: SEM Images of Fractured Surface

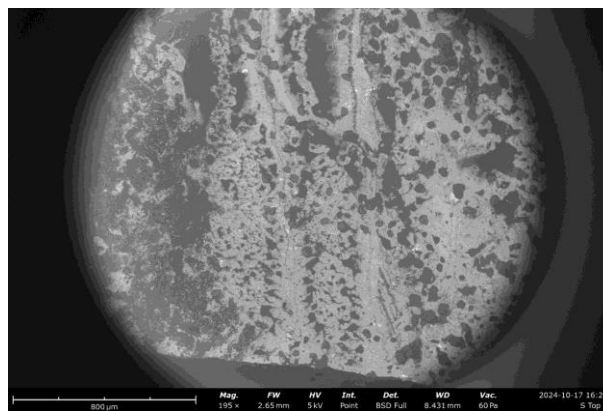


Figure 12: SEM image of as built sample

Declaration

Funding: No financial support was received to conduct this study.

Competing Interests: It was stated that there is no involvement of any competing interests.

Data availability: All data utilized in this study is included within the article or the references.

Author contributions:

SKS contributed to the conceptualization, methodology, experimentation, validation, writing, data collection, and writing of the original draft

NRM contributed to reviewing and editing the article

Conclusion

The paper presents the mechanical (tensile and hardness) and microstructure properties of SLM-manufactured AlSi10Mg alloy in as-

build stress-relieved conditions. The key findings are summarised below:

1. The Al-Si-10%-Mg alloy fabricated using the selective laser melting (SLM) process, demonstrated primarily brittle behavior with some indication of ductile fracture. The material is characterized by a high tensile strength (UTS) of 436.95 MPa, a low yield strength (YS) of 58 MPa, elongation of 9.6%, and a hardness of HRB 74. The sample achieved a relative density of 97.43% with a porosity of 0.85%.
2. The presence of unmelted powder, micro-voids, and porosities caused by lack of fusion of the powder particles and gas entrapment led to the brittle fracture of the tensile test specimen.
3. The presence of coarse silicon precipitates in the matrix contributed to the embrittlement and reduction in the material's ductility.

References

- [1]. Read, Noriko & Wang, Wei & Essa, Khamis & Attallah, Moataz. (2015). Selective laser melting of AlSi10Mg alloy: Process optimisation and mechanical properties development. *Materials & Design*. 65. 417-424. 10.1016/j.matdes.2014.09.044.
- [2]. Quazi, M. & M. A., Fazal & Haseeb, A. S. M. A & Yusof, Farazila & Masjuki, H.H. & Ahmed, Arslan. (2015). Laser-based Surface Modifications of Aluminum and its Alloys. *Critical Reviews in Solid State and Materials Sciences*. 41. 1-26. 10.1080/10408436.2015.1076716.
- [3]. de Damborenea, Juan & Conde, A. & Gardon, M. & Ravi, G.A. & Arenas, M.A.. (2022). Effect of growth orientation and heat treatment on the corrosion properties of AlSi10Mg alloy produced by Additive Manufacturing. *Journal of Materials Research and Technology*. 18. 10.1016/j.jmrt.2022.05.021.
- [4]. Xiao, Haifeng & Zhang, Changchun & Zhu, Haihong. (2022). Effect of direct aging and annealing on the microstructure and mechanical properties of AlSi10Mg fabricated by selective laser melting. *Rapid Prototyping Journal*. 29. 10.1108/RPJ-03-2022-0085.
- [5]. Ammar, Hany & Samuel, A. & Samuel, Fawzy. (2008). Porosity and the fatigue behavior of hypoeutectic and hypereutectic aluminum–silicon casting alloys. *International Journal of Fatigue*. 30. 1024-1035. 10.1016/j.ijfatigue.2007.08.012.

- [6]. Wang, J.Y. & Wang, Bao-Jian & Huang, L.F.. (2017). Structural evolution of Al–8%Si hypoeutectic alloy by ultrasonic processing. *Journal of Materials Science & Technology*. 33. 10.1016/j.jmst.2017.07.018.
- [7]. Aboulkhair, N. T., Maskery, I., Tuck, C., Ashcroft, I., & Everitt, N. M. (2016). The microstructure and mechanical properties of selectively laser melted AlSi10Mg: The effect of a conventional T6-like heat treatment. *Materials Science and Engineering: A*, 667, 139-146. <https://doi.org/10.1016/j.msea.2016.04.092>
- [8]. Biffi, Carlo & Fiocchi, Jacopo & Bassani, Paola & Paolino, Davide S. & Tridello, Andrea & Chiandussi, Giorgio & Rossetto, Massimo & Tuissi, Ausonio. (2017). Microstructure and preliminary fatigue analysis on AlSi10Mg samples manufactured by SLM. *Procedia Structural Integrity*. 7. 50-57. 10.1016/j.prostr.2017.11.060.
- [9]. Nirish, M., & Rajendra, R. (2022). Heat Treatment Effect on the Mechanical Properties of AlSi10Mg Produced by Selective Laser Melting. *Journal of Mechanical Engineering Research and Developments*.
- [10]. Ashwath Pazhani, Dr & Xavior, Anthony & Batako, Andre & Paulchamy, Jeyapandiarajan & J, Joel. (2022). Selective laser melting of Al–Si–10Mg alloy: microstructural studies and mechanical properties assessment. *Journal of Materials Research and Technology*. 17. 2249-2258. 10.1016/j.jmrt.2022.01.135.
- [11]. Prasad M, Kempaiah UN, Mohan RM, Nagaral M (2021) Microstructure, Tensile and Compression Behaviour of AlSi10Mg Alloy Developed by Direct Metal Laser Sintering. *Indian Journal of Science and Technology* 14(45): 3346-3353. <https://doi.org/10.17485/IJST/v14i45.1705>
- [12]. Mei, J., Han, Y., Zu, G., et al. (2022). Achieving Superior Strength and Ductility of AlSi10Mg Alloy Fabricated by Selective Laser Melting with Large Laser Power and High Scanning Speed. *Acta Metallurgica Sinica (English Letters)*, 35, 1665–1672. DOI: 10.1007/s40195-022-01410-w.
- [13]. Saravana K., M., Mohan, E., Robinson, S., et al. (2022). Comparative Study on Morphological, Physical and Mechanical Characteristics of L-PBF Based AlSi10Mg Parts with Conventional Stir Casted Al-10 %SiC Composites. *Silicon*, 14, 2695–2706. <https://doi.org/10.1007/s12633-021-01065-9>
- [14]. Xie, Deqiao & Lv, Fei & Yang, Youwen & Shen, Lida & Tian, Zongjun & Shuai, Cijun & Chen, Bo & Zhao, Jianfeng. (2022). A

Review on Distortion and Residual Stress in Additive Manufacturing. Chinese Journal of Mechanical Engineering: Additive Manufacturing Frontiers. 1. 100039. 10.1016/j.cjmeam.2022.100039.

[15]._Balbaa, M. A., Ghasemi, A., Fereiduni, E., Elbestawi, M. A., Jadhav, S. D., & Kruth, J.-P. (2021). Role of powder particle size on laser powder bed fusion processability of AlSi10Mg alloy. *Additive Manufacturing*, 37, 101630. <https://doi.org/10.1016/j.addma.2020.101630>.

[16]. Giovagnoli, Maverick & Silvi, Giacomo & Merlin, Mattia & Di Giovanni, Maria Teresa. (2020). Optimisation of process parameters for an additively manufactured AlSi10Mg alloy: Limitations of the energy density-based approach on porosity and mechanical properties estimation. *Materials Science and Engineering A*. 802. 140613. 10.1016/j.msea.2020.140613.

[17]. Limbasiya, N., Jain, A., Soni, H., Wankhede, V., Krolczyk, G., & Sahlot, P. (2022). A comprehensive review on the effect of process parameters and post-process treatments on microstructure and mechanical properties of selective laser melting of AlSi10Mg. *Journal of Materials Research and Technology*, 21, 1141-1176. ISSN 2238-7854. DOI: 10.1016/j.jmrt.2022.09.092.

[18]. Pan, Wei & Ye, Zhanggen & Zhang, Yongzhong & Liu, Yantao & Liang, Bo & Zhai, Ziyu. (2022). Research on Microstructure and Properties of AlSi10Mg Fabricated by Selective Laser Melting. *Materials*. 15. 2528. 10.3390/ma15072528.

[19]. Hirata, Tomotake & Kimura, Takahiro & Nakamoto, Takayuki. (2019). Effects of hot isostatic pressing and internal porosity on the performance of selective laser melted AlSi10Mg alloys. *Materials Science and Engineering: A*. 772. 138713. 10.1016/j.msea.2019.138713.

[20]. Maamoun, A. H., Xue, Y. F., Elbestawi, M. A., & Veldhuis, S. C. (2019). The Effect of Selective Laser Melting Process Parameters on the Microstructure and Mechanical Properties of Al6061 and AlSi10Mg Alloys. *Materials*, 12, 12. DOI: 10.3390/ma12010012.

[21]. Hyer, H., Zhou, L., Park, S., & others. (2020). Understanding the laser powder bed fusion of AlSi10Mg alloy. *Metallography, Microstructure, and Analysis*, 9(4), 484–502. <https://doi.org/10.1007/s13632-020-00659-w>

[22]. Li, Chonggui & Sun, Shuai & Zhang, Youfeng & Liu, Chuanming & Deng, Peiran & Zeng, Ming & Wang, Feifei & Ma, Pan & Li, Wenge & Wang, You. (2019). Effects of laser processing

parameters on microstructure and mechanical properties of additively manufactured AlSi10Mg alloys reinforced by TiC. *The International Journal of Advanced Manufacturing Technology*. 103. 10.1007/s00170-019-04001-9.

[23]. Bai, Shigang & Perevoshchikova, Nataliya & Sha, Yu & Wu, Xinhua. (2019). The Effects of Selective Laser Melting Process Parameters on Relative Density of the AlSi10Mg Parts and Suitable Procedures of the Archimedes Method. *Applied Sciences*. 9. 583. 10.3390/app9030583.

[24]. Zhuo, L., Wang, Z., Zhang, H., Yin, E., Wang, Y., Xu, T., & Li, C. (2019). Effect of post-process heat treatment on microstructure and properties of selective laser melted AlSi10Mg alloy. *Materials Letters*, 234, 196-200. ISSN 0167-577X. DOI: 10.1016/j.matlet.2018.09.109.

[25]. Zhou, S., Su, Y., Gu, R., Wang, Z., Zhou, Y., Ma, Q., & Yan, M. (2019). Impacts of Defocusing Amount and Molten Pool Boundaries on Mechanical Properties and Microstructure of Selective Laser Melted AlSi10Mg. *Materials*, 12, 73. DOI: 10.3390/ma12010073.

[26]. Zhang, S., Wei, P., Chen, Z., Li, B., Huang, K., Zou, Y., & Lu, B. (2022). Graphene/ZrO₂/aluminum alloy composite with enhanced strength and ductility fabricated by laser powder bed fusion. *Journal of Alloys and Compounds*, 910, 164941. ISSN 0925-8388. DOI: 10.1016/j.jallcom.2022.164941.

[27]. Ehtemam-Haghighi, Shima & Liu, Yujing & Cao, Guanghui & Zhang, LaiChang. (2016). Phase transition, microstructural evolution and mechanical properties of Ti-Nb-Fe alloys induced by Fe addition. *Materials & Design*. 97. 279-286. 10.1016/j.matdes.2016.02.094.

[28]. Raus, A. A., Wahab, M. S., Shayfull, Z., Kamarudin, K., & Ibrahim, M. (2016). The Influence of Selective Laser Melting Parameters on Density and Mechanical Properties of AlSi10Mg. *MATEC Web Conf.*, 78, 01078. DOI: 10.1051/mateconf/20167801078.

[29]. Casati, R., Hamidi Nasab, M., Coduri, M., Tirelli, V., & Vedani, M. (2018). Effects of Platform Pre-Heating and Thermal-Treatment Strategies on Properties of AlSi10Mg Alloy Processed by Selective Laser Melting. *Metals - Open Access Metallurgy Journal*, 8, 954. DOI: 10.3390/met8110954.

[30]. Chen, B., Moon, S. K., Yao, X., Bi, G., Shen, J., Umeda, J., & Kondoh, K. (2017). Strength and strain hardening of a selective laser melted AlSi10Mg alloy. *Scripta Materialia*, 141, 45-49. ISSN 1359-6462. DOI: 10.1016/j.scriptamat.2017.07.025.

- [31]. Delahaye, J., Tchuindjang, J., Lecomte-Beckers, J., Rigo, O., Habraken, A., & Mertens, A. (2019). Influence of Si precipitates on fracture mechanisms of AlSi10Mg parts processed by Selective Laser Melting. *Acta Materialia*, 175. DOI: 10.1016/j.actamat.2019.06.013.
- [32]. Hitzler, L., Janousch, C., Schanz, J., Merkel, M., Heine, B., Mack, F., Hall, W., & Öchsner, A. (2016). Direction and Location Dependency of Selective Laser Melted AlSi10Mg Specimens. *Journal of Materials Processing Technology*, 243, 48-61. DOI: 10.1016/j.jmatprotec.2016.11.029.
- [33]. Manfredi, D., Calignano, F., Ambrosio, E., Krishnan, M., Canali, R., Biamino, S., Pavese, M., Atzeni, E., Iuliano, L., Fino, P., & Badini, C. (2013). Direct Metal Laser Sintering: An additive manufacturing technology ready to produce lightweight structural parts for robotic applications. *La Metallurgia Italiana*, 105.
- [34]. Li, W., Li, S., Liu, J., Zhang, A., Zhou, Y., Wei, Q., Yan, C., & Shi, Y. (2016). Effect of heat treatment on AlSi10Mg alloy fabricated by selective laser melting: Microstructure evolution, mechanical properties and fracture mechanism. *Materials Science and Engineering A*, 663, 116-125. DOI: 10.1016/j.msea.2016.03.088.
- [35]. Rosenthal, I., Stern, A., & Frage, N. (2017). Strain rate sensitivity and fracture mechanism of AlSi10Mg parts produced by Selective Laser Melting. *Materials Science and Engineering: A*, 682, 509-517. ISSN 0921-5093. DOI: 10.1016/j.msea.2016.11.070.
- [36]. Tang, M., & Pistorius, P. (2017). Anisotropic Mechanical Behavior of AlSi10Mg Parts Produced by Selective Laser Melting. *JOM*, 69. DOI: 10.1007/s11837-016-2230-5.
- [37]. Wang, L., Sun, J., Zhu, X., Cheng, L., Shi, Y., Guo, L., & Yan, B. (2018). Effects of T2 Heat Treatment on Microstructure and Properties of the Selective Laser Melted Aluminum Alloy Samples. *Materials*, 11, 66. DOI: 10.3390/ma11010066.
- [38]. Larrosa, N. O., Wang, W., Read, N., Loretto, M. H., Evans, C., Carr, J., Tradowsky, U., Attallah, M. M., & Withers, P. J. (2018). Linking microstructure and processing defects to mechanical properties of selectively laser melted AlSi10Mg alloy. *Theoretical and Applied Fracture Mechanics*. Advance online publication. DOI: <https://doi.org/10.1016/j.tafmec.2018.09.011>.
- [39]. Manfredi, D., Calignano, F., Krishnan, M., Canali, R., Ambrosio, E. P., & Atzeni, E. (2013). From Powders to Dense Metal Parts: Characterization of a Commercial AlSiMg Alloy Processed through

- Direct Metal Laser Sintering. *Materials*, 6, 856-869. DOI: 10.3390/ma6030856.
- [40]. Tang, M., & Pistorius, P. C. (2017). Oxides, porosity and fatigue performance of AlSi10Mg parts produced by selective laser melting. *International Journal of Fatigue*, 94(Part 2), 192-201. ISSN 0142-1123. DOI: 10.1016/j.ijfatigue.2016.06.002.
- [41]. Zygula, K., Nosek, B., Pasiowiec, H., & Szysiak, N. (2018). Mechanical properties and microstructure of AlSi10Mg alloy obtained by casting and SLM technique. 104, 462-472.
- [42]. Hovig, E. W., Azar, A. S., Mhamdi, M., & Sørby, K. (2020). Mechanical Properties of AlSi10Mg Processed by Laser Powder Bed Fusion at Elevated Temperature. In: TMS 2020 149th Annual Meeting & Exhibition Supplemental Proceedings. The Minerals, Metals & Materials Series. Springer, Cham. DOI: 10.1007/978-3-030-36296-6_37.
- [43]. Tan, Q., Yin, Y., Fan, Z., Zhang, J., Liu, Y., & Zhang, M.-X. (2021). Uncovering the roles of LaB₆-nanoparticle inoculant in the AlSi10Mg alloy fabricated via selective laser melting. *Materials Science and Engineering: A*, 800, 140365. DOI: 10.1016/j.msea.2020.140365.
- [44]. Famodimu, O. H., Stanford, M., Oduoza, C. F., et al. (2018). Effect of process parameters on the density and porosity of laser melted AlSi10Mg/SiC metal matrix composite. *Frontiers of Mechanical Engineering*, 13, 520–527. DOI: 10.1007/s11465-018-0521.
- [45]. Marchese, G., Aversa, A., Lorusso, M., Manfredi, D., Calignano, F., Lombardi, M., Biamino, S., & Pavese, M. (2018). Development and Characterisation of Aluminium Matrix Nanocomposites AlSi10Mg/MgAl₂O₄ by Laser Powder Bed Fusion. *Metals*, 8, 175. DOI: 10.3390/met8030175.
- [46]. Gao, C., Wu, W., Shi, J., Xiao, Z., & Akbarzadeh, A. H. (2020). Simultaneous enhancement of strength, ductility, and hardness of TiN/AlSi10Mg nanocomposites via selective laser melting. *Additive Manufacturing*, 34, 101378. ISSN 2214-8604. DOI: 10.1016/j.addma.2020.101378.
- [47]. He, P., Kong, H., Liu, Q., Ferry, M., Kruzic, J. J., & Li, X. (2021). Elevated temperature mechanical properties of TiCN reinforced AlSi10Mg fabricated by laser powder bed fusion additive manufacturing. *Materials Science and Engineering: A*, 811, 141025. ISSN 0921-5093. DOI: 10.1016/j.msea.2021.141025.

- [48]. Wang, Y., Shi, J., Lu, S., & Xiao, W. (December 14, 2017). Investigation of Porosity and Mechanical Properties of Graphene Nanoplatelets-Reinforced AlSi10Mg by Selective Laser Melting. ASME. J. Micro Nano-Manuf., 6(1), 010902. DOI: 10.1115/1.4038454.
- [49]. Wang, Y., & Shi, J. (2020). Effect of hot isostatic pressing on nanoparticles reinforced AlSi10Mg produced by selective laser melting. Materials Science and Engineering: A, 788, 139570. ISSN 0921-5093. DOI: 10.1016/j.msea.2020.139570.
- [50]. Wei, P., Chen, Z., Zhang, S., Li, B., Han, J., & Lu, B. (2023). Microstructure and mechanical properties of graphene and nano-zirconia reinforced AlSi10Mg composite fabricated by laser powder bed fusion. Materials Science and Engineering: A, 864, 144574. ISSN 0921-5093. DOI: 10.1016/j.msea.2022.144574.
- [51]. Zhang, S., Chen, Z., Wei, P., Liu, W., Zou, Y., Lei, Y., Yao, S., Zhang, S., Lu, B., & Zhang, L. (2022). Wear properties of graphene/zirconia biphasic nano-reinforced aluminium matrix composites prepared by SLM. Materials Today Communications, 30, 103009. ISSN 2352-4928. DOI: 10.1016/j.mtcomm.2021.103009.
- [52]. Yi, J., Zhang, X., Rao, J. H., Xiao, J., & Jiang, Y. (2021). In-situ chemical reaction mechanism and non-equilibrium microstructural evolution of (TiB₂ + TiC)/AlSi10Mg composites prepared by SLM-CS processing. Journal of Alloys and Compounds, 857, [157553]. <https://doi.org/10.1016/j.jallcom.2020.157553>
- [53]. Miao, K., Zhou, H., Gao, Y., Deng, X., Lu, Z., & Li, D. (2021). Laser powder-bed-fusion of Si₃N₄ reinforced AlSi10Mg composites: Processing, mechanical properties and strengthening mechanisms. Materials Science and Engineering: A, 825, 141874. ISSN 0921-5093. DOI: 10.1016/j.msea.2021.141874.
- [54]. Srinivasa Rakesh Ch., A. Raja, Priyanka Nadig, R. Jayaganthan, & N.J. Vasa. (2019). Influence of working environment and built orientation on the tensile properties of selective laser melted AlSi10Mg alloy. Materials Science & Engineering A. DOI: 10.1016/j.msea.2019.01.103.
- [55]. Dong, Z., Zhang, X., Shi, W., Zhou, H., Lei, H., & Liang, J. (2018). Study of Size Effect on Microstructure and Mechanical Properties of AlSi10Mg Samples Made by Selective Laser Melting. Materials, 11, 2463. DOI: 10.3390/ma11122463.
- [56]. Li, X., Shi, S., Han, S., Hu, X., Zhu, Q., Lu, H., Li, W., Shi, Y., & Ding, H. (2020). Microstructure, solidification behavior and

mechanical properties of Al-Si-Mg-Ti/TiC fabricated by selective laser melting. Additive Manufacturing. Advance online publication. DOI: <https://doi.org/10.1016/j.addma.2020.101326>

[57]. Kempen, K., Thijs, L., Van Humbeeck, J., & Kruth, J.-P. (2015). Processing AlSi10Mg by selective laser melting: parameter optimisation and material characterisation. *Materials Science and Technology*, 31(8), 917-923. DOI: 10.1179/1743284714Y.00000000702

[58]. Kim, D.-K., Woo, W., Hwang, J.-H., An, K., & Choi, S.-H. (2016). Stress partitioning behavior of an AlSi10Mg alloy produced by selective laser melting during tensile deformation using in situ neutron diffraction. *Journal of Alloys and Compounds*. DOI: 10.1016/j.jallcom.2016.06.011

[59]. Maskery, I., Aboulkhair, N., Tuck, C., Wildman, R., Ashcroft, I., Everitt, N., & Hague, R. (2015). Fatigue Performance Enhancement of Selectively Laser Melted Aluminium Alloy by Heat Treatment.

[60]. Sun, J., Qiu, L., Wang, F., Yang, Y., & Guo, L. (2019). A new modification effect of eutectic Si in selective laser melted AlSi10Mg. *Materials Science and Technology*, 35(6), 709-715. DOI: 10.1080/02670836.2019.1589740

[61]. Pei, W., Zhengying, W., Zhen, C., Jun, D., Yuyang, H., Junfeng, L., & Yatong, Z. (2017). The AlSi10Mg samples produced by selective laser melting: single track, densification, microstructure and mechanical behavior. *Applied Surface Science*. DOI: <http://dx.doi.org/doi:10.1016/j.apsusc.2017.02.215>

[62]. Zhang, C., Zhu, H., Liao, H., Cheng, Y., Hu, Z., & Zeng, X. (2018). Effect of heat treatments on fatigue property of selective laser melting AlSi10Mg. *International Journal of Fatigue*. <https://doi.org/10.1016/j.ijfatigue.2018.07.016>

[63]. Yang, T., Liu, T., Liao, W., MacDonald, E., Wei, H., Zhang, C., Chen, X., & Zhang, K. (2020). Laser powder bed fusion of AlSi10Mg: Influence of energy intensities on spatter and porosity evolution, microstructure and mechanical properties. *Journal of Alloys and Compounds*. <https://doi.org/10.1016/j.jallcom.2020.156300>

[64]. Song, B., Yan, Q., & Shi, Y. (To appear). Comparative study of performance comparison of AlSi10Mg alloy prepared by selective laser melting and casting. *Journal of Materials Science & Technology*. <https://doi.org/10.1016/j.jmst.2019.08.049>

[65]. Suttay, L. J. (2018). Evaluation of metallurgical and mechanical properties of AlSi10Mg produced by selective laser melting (Graduate

Thesis, Montana Technological University). Digital Commons @ Montana Tech. https://digitalcommons.mtech.edu/grad_rsch/174

[66]. Liu, B., Kuai, Z., Li, Z., Tong, J., Bai, P., Li, B., & Nie, Y. (2018). Performance Consistency of AlSi10Mg Alloy Manufactured by Simulating Multi Laser Beam Selective Laser Melting (SLM): Microstructures and Mechanical Properties. *Materials*, 11, 2354. <https://doi.org/10.3390/ma11122354>

[67]. Murphy, D. M. (2020). Performance evaluation of AlSi10Mg fabricated by a selective laser melting process (Master's thesis). Retrieved from https://scholarsmine.mst.edu/masters_theses/8006

[68]. Zhou, S., Wang, Z., Su, Y., Wang, H., Liu, G., Song, T., & Yan, M. (2020). Effects of Micron/Submicron TiC on Additively Manufactured AlSi10Mg: A Comprehensive Study from Computer Simulation to Mechanical and Microstructural Analysis. *JOM*, 72. <https://doi.org/10.1007/s11837-019-03984-w>

[69]. Thijs, Lore & Kempen, Karolien & Kruth, Jean-Pierre & Humbeeck, Jan. (2013). Fine-structured aluminium products with controllable texture by selective laser melting of pre-alloyed AlSi10Mg powder. *Acta Materialia*. 61. 1809–1819. 10.1016/j.actamat.2012.11.052.

[70]. Sercombe TB, Li X (2016). Selective laser melting of aluminium and aluminium metal matrix composites: review. *Mater Technol Adv Perform Mater* 31(2):77–85. <https://doi.org/10.1179/1753555715Y.00000000078>

[71]. Beder, Murat & Akçay, Serhatcan & Varol, Temel & Çuvalci, Hamdullah. (2024). The Effect of Heat Treatment on the Mechanical Properties and Oxidation Resistance of AlSi10Mg Alloy. *Arabian Journal for Science and Engineering*. 49. 10.1007/s13369-024-08971-1

Improved Bandgap Prediction of 2D Materials using Ensemble of Hyperparameter Optimized Boosting Algorithms

¹Bhuma Chandra Mohan, ²Ch.V.M.S.N.Pavan Kumar,
³K. Ramanjaneyulu

¹*Professor, Department of ECE,
Bapatla Engineering College,
Bapatla*

²*Assistant Professor, Department of ECE,
Bapatla Engineering College,
Bapatla*

³*Professor, Dept. of ECE,
P.V.P Siddhartha Institute of Technology,
Vijayawada*

Abstract

An improved machine learning algorithm for predicting the bandgap of 2D materials is proposed in this work. After successful characterization of graphene, 2D materials with their excellent physical, and chemical properties associated with unique nano sheet structure are gaining importance in recent times. Electrical and optical properties of semiconductors are characterized by its bandgap. Hence, accurate prediction of the bandgap is essential in understanding the material properties. Computational 2D materials database (C2DB) is used to test the proposed algorithm. C2DB contains two sets of data containing 8 and 9(bandgap without spin orbit coupling is added) dimensional features for 3130 materials. The features under consideration include the density of states at the Fermi energy, Heat formation, Sum of atomic masses in unit cell, Number of Atoms, Total Energy, Maximum Force, Volume of unit cell, Maximum stress on unit cell, Gap without Spin Orbit Coupling (SOC). Minimum bandgap is 0 eV and the maximum bandgap is 6.450904 eV. Three boosting algorithms i.e., Light Gradient Boosting-Machine (LGBM), Extreme Gradient Boosting-Machine (XGBM), and Categorical Boosting (CATBoost) with optimized hyper parameters (using Bayesian Optimization) are used in the regression mode to estimate the bandgap. An ensemble of all the three tree-based algorithms (LGBM, XGBM,

CATBoost) is considered wherein, average of the predictions from the optimized three models are considered as final predictions. After adding the bandgap without spin orbit coupling as an additional feature, the Mean Absolute Error (MAE) and Root Mean Square Error (RMSE) in the bandgap prediction are significantly decreased. With a 90% train and 10% test split on the dataset, the coefficient of determination (R^2) value is 0.9864 and 0.9989 for 8 dimensional and 9 dimensional features respectively. Compared to a recent work on the same dataset, all the regression metrics i.e., R^2 , MAE, and RMSE are superior.

Keywords: 2D materials, Bandgap prediction, Ensemble of Boosting Algorithms

Introduction

The bandgap is a crucial electronic property of certain materials that has played a pivotal role in the advancement of semiconductor technology [1]. For over fifty years, Moore's law has guided the path of the chip manufacturing industry. However, recent studies indicate that this trend may be approaching its practical limits. A feasible approach to surpass this imminent limit is to substitute silicon—the main material in chip production—with alternative materials suitable for next-generation electronics [2-3]. Since the groundbreaking isolation and analysis of graphene in 2004 [4], atomically thin two-dimensional (2D) materials have garnered significant attention. These materials are distinguished by their unique nanosheet structure, expansive surface area, and exceptional physical and chemical properties, positioning them as promising candidates for future electronic applications.

Two-dimensional (2D) materials have shown great potential as replacements for silicon in future semiconductor applications. Different 2D materials exhibit unique electrical properties due to their varied structures [5]. For instance, intrinsic graphene lacks a bandgap, meaning it cannot be fully turned off, which limits its applicability in certain devices. In contrast, molybdenum disulfide (MoS_2), belonging to the transition metal dichalcogenide (TMDC) family, is a semiconductor characterized by an indirect bandgap of approximately 1.89 eV [6]. Furthermore, hexagonal boron nitride (h-BN) is an insulator characterized by a large bandgap of roughly 5.9 eV [7]. Because of this range of properties among 2D materials, understanding their electrical characteristics is crucial for their integration into semiconductor devices.

Motivated by this necessity, numerous conceptual and exploratory studies have been conducted to investigate the electronic properties of 2D materials [8]. Although experimental data are often more reliable, testing these ultra-thin materials poses significant practical challenges. Thus, theoretical studies offer a valuable alternative. In recent decades, conventional first-principles calculations have emerged as a powerful tool for analyzing the structures and properties of materials [9]. "These methods have been employed to explore the structural and electronic properties of ideal, doped, and defective 2D materials [10], as well as their interactions with different substrates and contacts. Despite often aligning well with experimental findings, first-principles calculations can be computationally demanding and time-consuming [12].

Recent advancements in machine learning (ML), a data-driven approach, have greatly influenced materials research. ML techniques have been effectively employed to guide chemical synthesis, facilitate material characterization, and enable the design of novel materials. "Significantly, several studies have shown that ML models are exceptionally well-suited for predicting material properties. For example, Cherukara et al. developed the pioneering atomic-level ML model to accurately predict the thermal properties of stanene [15]. Dieb et al. utilized ML to identify the most stable configurations of boron-doped graphene [16]. In addition, Wan et al. developed a convolutional neural network (CNN) model to predict the thermal conductivity of porous graphene [17]. Meanwhile, Dong et al. employed deep learning to predict the bandgaps of hybrid structures composed of graphene and h-BN in various supercell configurations [18]. Baboukani et al. proposed a machine learning (ML) technique to predict nanoscale friction in two-dimensional (2D) materials [19]. ML interatomic potentials demonstrate remarkable efficiency in predicting new materials, modeling lattice dynamics, estimating thermal conductivity, and analyzing the phononic properties of 2D materials [20].

This study employed three boosting algorithms—LGBM, XGBM, and CATBoost—to perform bandgap estimation using regression. Each model was fine-tuned through Bayesian Optimization to achieve optimal hyperparameters, enhancing their predictive accuracy [21]. An ensemble approach combining the three tree-based models (LGBM, XGBM, and CATBoost) was adopted, where the average predictions from the optimized models were taken as the final predictions. Including the bandgap without spin-orbit coupling as an additional feature led to substantial decreases in both MAE and RMSE for bandgap prediction accuracy. With a 90% training and 10% testing

split of the dataset, the R^2 values were 0.9864 for 8-dimensional features and 0.9989 for 9-dimensional features. When compared to GBDT on the same dataset, all regression metrics R^2 , MAE, and RMSE demonstrated superior performance [22-24].

Materials and Methods

Data Collection

We used the Computational 2D Materials Database (C2DB), which offers a detailed dataset encompassing 3,130 materials. This dataset provides two feature sets: an 8-dimensional set and a 9-dimensional set, with the latter including the bandgap without spin-orbit coupling as an additional feature. The features analyzed are as follows:

- Density of states at the Fermi energy
- Heat of formation,
- Atom count,
- Total atomic mass within the unit cell,
- Maximum force, Total energy ,
- Maximum stress in the unit cell,
- Unit cell volume,
- Gap without spin-orbit coupling (SOC).

The dataset's bandgap values starts from a minimum range of 0 eV to a maximum of 6.450904 eV.

Machine Learning Models

Gradient Boosted Decision Tree (GBDT):

The GBDT algorithm is a ML technique that combines decision trees with boosting to create a highly effective prediction model. GBDT is widely used for tasks like regression, classification, and ranking due to its high accuracy and flexibility. GBDT constructs a series of shallow decision trees, typically smaller than individual models, Each tree is trained to correct the errors made by the preceding trees. Boosting, an ensemble technique, combines multiple weak learners (such as small decision trees) into a single, stronger model by iteratively minimizing the errors of the prior learners. GBDT uses gradient descent to minimize a specific loss function, effectively reducing the errors made by prior trees.

In this work, we employed three advanced boosting algorithms for bandgap prediction. The workings of these models were discussed below. The ensemble of the three methods gives better results compared with the GBDT algorithm.

Light Gradient Boosting Machine (LightGBM):

The LightGBM is a ML algorithm within the gradient boosting framework, created with a focus on high speed and efficiency. Developed by Microsoft, it is particularly well-suited for handling large datasets and is optimized for real-time applications. A key distinction between LightGBM and traditional gradient boosting methods is in its tree growth strategy. While conventional algorithms grow trees level by level, LightGBM employs a leaf-wise or depth-first approach. This means it expands the tree by splitting the leaf that has the highest potential for loss reduction, resulting in a more efficient tree structure that can lead to better accuracy and improved performance. One of LightGBM's innovations is its implementation of a histogram-based algorithm. This technique involves transforming continuous features into discrete bins, which enables quicker computation of splits and significantly reduces memory usage. This design makes LightGBM capable of handling very large datasets efficiently, even when they contain millions of samples and numerous features, making it highly scalable for extensive data applications. It is known for performing well with high-dimensional data, as it includes several techniques for feature selection and handling sparsity. It offers GPU support, which can speed up training significantly for large datasets, especially with deep trees and complex models. Techniques such as L1 and L2 regularization, max depth limitation, and early stopping can help reduce overfitting. LightGBM is popular in competitive machine learning due to its speed and high accuracy, especially in tasks with structured/tabular data. It's widely used in platforms like Kaggle, where optimization for large datasets and time efficiency is crucial.

Extreme Gradient Boosting Machine (XGBM):

XGBoost is a high-performance, open-source library for gradient boosting, designed to enhance the efficiency, flexibility, and speed of the gradient boosting framework. Originally developed for structured (tabular) data, XGBoost has become one of the most popular ML algorithms due to its robust performance and versatility in a wide range of applications. It enhances traditional gradient boosting by incorporating both L1 (Lasso) and L2 (Ridge) regularization, helping to reduce overfitting and improving generalization. XGBoost grows trees level by level, as opposed to the leaf-wise growth used in LightGBM. This approach provides more balanced trees and can reduce the risk of overfitting,

especially on smaller datasets. XGBoost can handle missing values directly by learning the best way to treat them. This makes it more flexible when handling datasets with gaps or missing information. It efficiently stores data in a columnar format, which allows for parallelized operations and faster computation. It supports distributed computing, which enables the algorithm to scale across multiple machines for handling large datasets. XGBoost uses a weighted quantile sketch to compute feature splits, which is beneficial for datasets with highly imbalanced target classes. It allows for early stopping based on a validation metric, which helps prevent overfitting and speeds up training. XGBoost remains a popular choice in applied machine learning due to its solid performance and ease of integration with various libraries. While it may not always be the fastest, its reliability and fine-tuning flexibility make it a strong competitor across different machine learning tasks.

Categorical Boosting (CATBoost):

CatBoost is a ML algorithm developed by Yandex specifically designed to handle categorical data effectively. It falls within the family of gradient boosting algorithms and is optimized for speed and accuracy, featuring native support for categorical data—a characteristic that sets it apart from other gradient boosting frameworks such as XGBoost and LightGBM. This technique is specially designed to manage categorical features without extensive preprocessing. It automatically encodes categorical variables using a unique ordered boosting technique that avoids data leakage and reduces overfitting, enabling better model generalization. Instead of the traditional boosting methods, CatBoost introduces ordered boosting, where each new split is determined by excluding information from future observations. This method prevents data leakage during training, resulting in better model performance on unseen data. It constructs symmetric trees, with each tree level splitting the data based on the same feature, resulting in faster and more memory-efficient predictions. This structure also makes CatBoost less prone to overfitting compared to other boosting frameworks that use asymmetric trees. This technique includes built-in methods to handle imbalanced datasets, which can be useful in applications like fraud detection or churn prediction. It inherently supports multiclass classification and multioutput regression, enhancing its versatility for a range of machine learning tasks. It is optimized for both CPU and GPU training, making it well-suited for large datasets and complex problems. It often provides faster inference times compared to other boosting algorithms due to its symmetric trees. CatBoost's advantages

in handling categorical data and its prevention of overfitting make it an appealing choice for structured data problems. "It is extensively utilized in finance, e-commerce, and online recommendation engines, where categorical variables frequently play a crucial role in prediction models.

Hyper parameter Optimization

Hyper parameters for each model were optimized using Bayesian Optimization. This technique intelligently navigates the hyperparameter space to identify settings that minimize prediction error, including adjusting parameters such as learning rate, maximum depth, and the number of estimators.

Ensemble Approach

An ensemble method was utilized, where the predictions from LGBM, XGBM, and CATBoost were averaged to produce the final prediction. This approach combines the strengths of each algorithm, enhancing overall predictive accuracy.

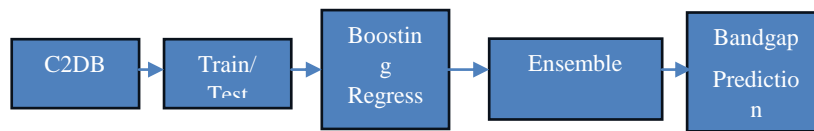


Figure 1. Block diagram representation of the proposed algorithm

The building blocks of the proposed algorithm are shown in Figure 1. The following Figure 2 illustrates the model's use for training, testing, and validating hyperparameter optimization using HyperOpt and K-fold cross-validation.

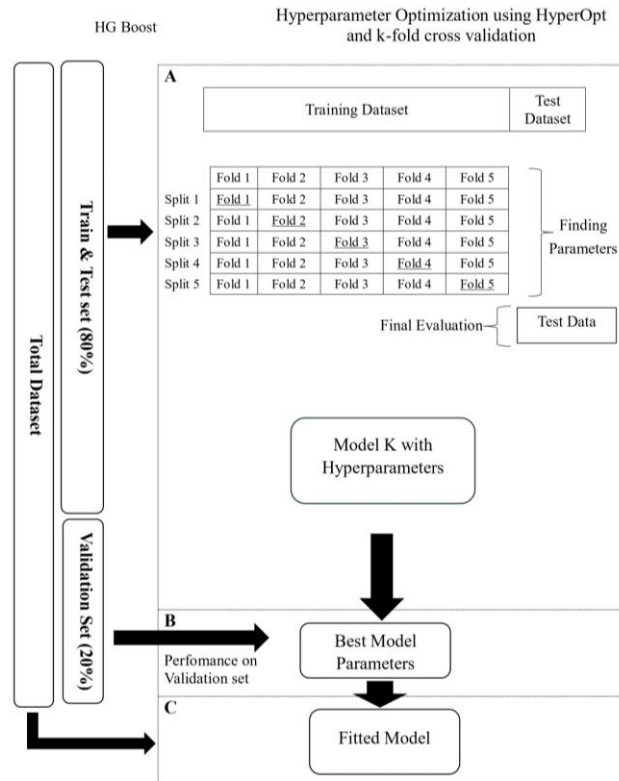


Figure 2: Model used for the hyperparameter optimization

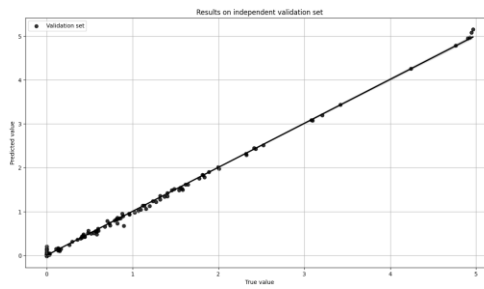
Results and Discussion

All the simulations are carried using Google Colab environment. No GPU (Graphical Processing Unit) was used in the simulations. Python package Hgboost by Taskesen, Eis used for hyperparameter optimization, which in turn utilizes Bayes optimization. Hyperparameters play a key role in the performance of any classification or regression algorithm. For each train test split also the hyperparameters vary over a wide range. Hence, appropriate cross validations are to be performed while optimizing the hyperparameters. In Hgboost package, the entire dataset is split into train, validation and test sets. Further, over several iterations the best hyperparameters are searched with some regression or classification metric as a target. After each boosting algorithm is optimized, the ensemble prediction can be adopted which further increases the performance. The features considered for estimating the bandgap are given below in Table 1.

Table 1. Features considered for estimating the bandgap

Feature No.	Definitions	Feature Name
1.	Density of states at the Fermi energy	Dosef
2.	Heat of formation	Hform
3.	Number of atoms	Natoms
4.	Sum of atomic masses in unitcell	Mass
5.	Total energy	Energy
6.	Maximum force	Fmax
7.	Maximum stress on unitcell	Smax
8.	Volume of unitcell	Volume
9.	Gap w/o soc	Gap_nosoc

To justify the efficacy of the proposed algorithm, various train test splits are considered for experimentation. On an independent validation set which has 20% of the dataset, the difference between true and predicted value of the band gap is plotted below in Figure 3 for XGBoost.

**Figure 3.** Predicted vs True value of the bandgap (XGBoost)

Three important regression metrics are considered in this work. They are briefed below.

The Mean Absolute Error (MAE) is the average magnitude of prediction errors, disregarding their direction (positive or negative). MAE represents the mean absolute difference between predicted and actual values, offering a simple measure of a model's accuracy. This makes it valuable for evaluating predictive performance, as shown in Equation 1.

$$MAE = \frac{1}{n} \sum_{i=1}^n |y_i - \hat{y}_i| \quad (1)$$

The Root Mean Square Error (RMSE) is a commonly used metric for evaluating the accuracy of predictive models, particularly in regression tasks. It measures the average magnitude of errors between predicted and actual values, with greater emphasis on larger errors by squaring

the residuals. RMSE is favored because it provides an error measure in the same units as the target variable, making it easy to interpret.

$$RMSE = \sqrt{\frac{1}{n} \sum_{i=1}^n (y_i - \hat{y}_i)^2} \quad (2)$$

The Coefficient of Determination, commonly referred to as R^2 , is a statistical measure that assesses the fit of a regression model. It indicates the proportion of variance in the dependent variable (target) that is explained by the independent variables (features).

$$R^2 = 1 - \frac{\sum_{i=1}^n (y_i - \hat{y}_i)^2}{\sum_{i=1}^n (y_i - \bar{y})^2} \quad (3)$$

By varying the test size MAE, RMSE and R^2 are computed for all the boosting algorithms. Their ensemble prediction offers lower MAE, RMSE, and higher R^2 and is shown in Figures 4, 5 and 6 respectively.

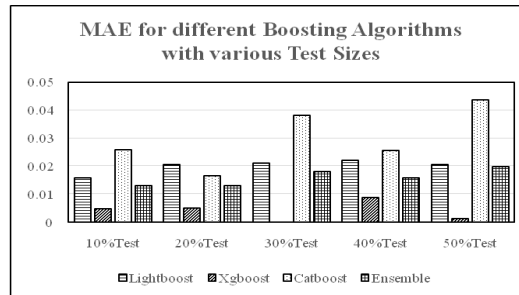


Figure 4. MAE for various boosting algorithms (Various Test splits)

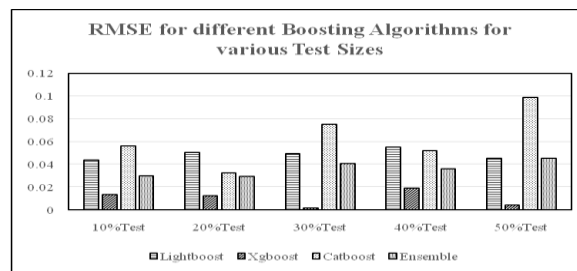


Figure 5. RMSE for various boosting algorithms (Various Test splits)

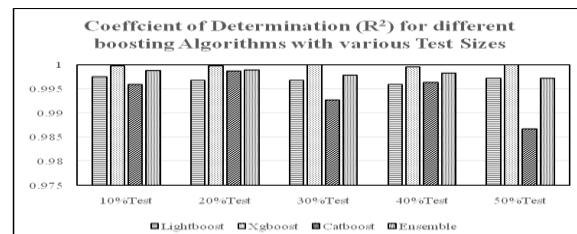


Figure 6. R^2 for various boosting algorithms (Various Test splits)

The results shows that proposed algorithm is giving the coefficient of determination almost equals to unity. The above graphs gives the results for different test sizes from 10% to 50 % respectively.

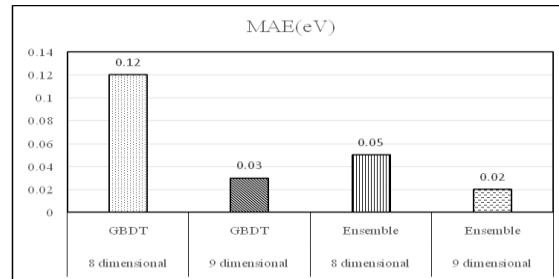


Figure 7: MAE for GBDT and Ensemble methods for 8,9 dimensions.

The Mean Absolute Error the proposed ensemble of three boosting algorithms are compare to the GBDT method for 8 and 9 dimension is shown in Figure 7. The proposed technique is giving the low error rate compared with the GBDT method.

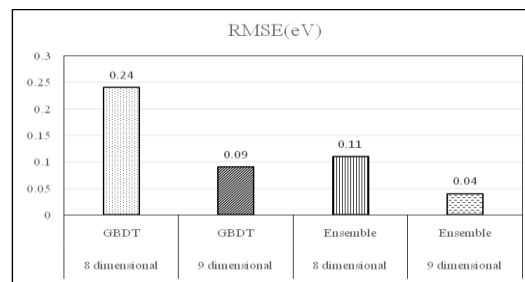


Figure 8: RMSE for GBDT and Ensemble methods for 8,9 dimensions.

The RMSE of the proposed ensemble method is compared to the GBDT method for 8 and 9 dimension is shown in Figure 7. The proposed technique is giving the low error rate compared with the GBDT method.

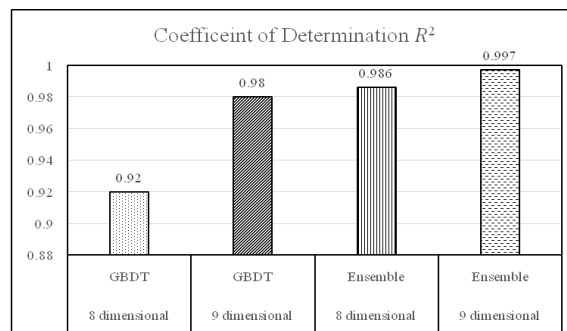


Figure 9: R^2 for GBDT and Ensemble methods for 8,9 dimensions.

The Coefficient of determination (R^2) for the GBDT method and the proposed ensemble method is shown in Figure 9. The proposed technique is giving the better results compared to GBDT method in both 8 and 9 dimensions. Different types of errors are computed and compared in this work with the existing work. The proposed method outperforms well in all the cases. Table 2 describes some of the errors computed for the ensemble method with various test sizes.

Table2: Various Errors for Ensemble Method with different sizes of Test data

Metric	Description	10% Test	20% Test	30% Test	40% Test	50% Test
MAE	Mean Absolute Error	0.01316	0.0132	0.0182	0.01577	0.0199
MSE	Mean Square Error	0.00091	0.00086	0.00167	0.00131	0.00205
RMSE	Root Mean Square Error	0.03014	0.02936	0.04084	0.03619	0.04523
MSLE	Mean Squared Log Error	0.00045	0.00068	0.00143	0.00109	0.00165
MedA E	Median Absolute Error	0.00231	0.00236	0.00224	0.00189	0.00282
MRE	Mean Relative Error	0.06147	0.08526	0.11545	0.20805	0.83536

Compared to the work Zhang et al., on both 8 dimensional and 9 dimensional features, the proposed work offers lower MAE, RMSE and higher R^2 . A comparative analysis is given in Table 2.

Table 3: Comparison between the Ensemble method and GBDT

Reference	Feature Space	Model	MAE(eV)	RMSE(eV)	R^2
Zhang et al., (2021)	8 dimensional	GBDT*	0.12	0.24	0.92
	9 dimensional	GBDT*	0.03	0.09	0.98
Proposed (Ensemble)	8 dimensional	Ensemble**	0.05	0.11	0.986
	9 dimensional	Ensemble**	0.02	0.04	0.997

Conclusion

In this work three boosting algorithms i.e LGBM, XGBM, and CATBoost with optimized hyper parameters (using Bayesian Optimization) are considered in the regression mode to estimate the bandgap of different materials. An ensemble of all the three tree-based algorithms (LGBM, XGBM, CATBoost) is considered wherein, average of the predictions from the optimized three models are considered as final predictions. After adding the bandgap without spin

orbit coupling as an additional feature, the MAE and RMSE in the bandgap prediction are significantly decreased. With a 90% train and 10% test split on the dataset, the R^2 value is 0.9864 and 0.9989 for 8 dimensional and 9 dimensional features respectively. Compared to GBDT on the same dataset, all the regression metrics i.e., R^2 , MAE, and RMSE are giving the better results.

References

- [1] Waldrop MM. The chips are down for Moore's law. *Nature*. 2016; 530(7589):144–147.
- [2] Ghazanfar N, Muhammad K, Sikandar A, Amir A, Ghulam D, Malik R, et al. Gate tunable transport in Graphene/MoS₂/(Cr/Au) vertical field-effect transistors. *Nanomaterials*. 2018;8(01):14.
- [3] Nekrasov N, Kireev D, Omerovi N, Emelianov A, Bobrinetskiy I. Photo-induced doping in a graphene field-effect transistor with inkjet-printed organic semiconducting molecules. *Nanomaterials*. 2019; 9(12):1753.
- [4] Novoselov KS, Geim AK, Morozov SV, Jiang D, Zhang Y, Dubonos SV, et al. Electric Field Effect in Atomically Thin Carbon Films. *Science*. 2004; 306(5696):666–669.
- [5] Wang XX, Shen NF, WuJ, Wang BL, Wan JG. Predicting quantum spin hall effect in graphene/gas band normal strain-controlled band structures. *Applied Surface Science*. 2020; 526:146704.
- [6] Mak KF, Lee C, Hone J, Shan J, Heinz TF. Atomically Thin MoS₂: A New Direct-Gap Semiconductor. 2010; 105(13):136805.
- [7] Yang K, Liu H, Wang S, Li W, Han T. A horizontal-gate monolayer MoS₂ transistor based on image force barrier reduction. *Nanomaterials*. 2019; 9(09):1245.
- [8] Zhao N, Zhu YF, Jiang Q. Novel electronic properties of two-dimensional as xs by alloys studied using DFT. *Journal of Materials Chemistry C*. 2018;6(11):2854–2861.
- [9] Luo BC, Wang XH, Tian EK, Song HZ, Qu HQ, Cai ZM, et al. Mechanism offer ro electric properties of (BaCa) (ZrTi) O₃ from first-principles calculations. *Ceramics International*. 2018; 44(08):9684–9688.
- [10] Rad AS. First principles study of al-doped graphene as nanostructure adsorbent for NO₂ and N₂O: DFT calculations. *Applied Surface Science*. 2015; 357:1217–1224.

- [11] Dai ZH, Liu LQ, Zhang Z. Strain Engineering of 2D Materials: Issues and Opportunities at the Interface. *Advanced Materials*.2019;31(45):1805417.
- [12] Jung JH, Kim SH, Park Y, Lee D, Lee JS. Metal-halide perovskite design for next-generation memories: first-principles screening and experimental verification. *Advanced Science*. 2020; 7(16):2001367.
- [13] Schleder GR, Padilha ACM, Acosta CM, Costa M, Fazzio A. From DFT to machine learning: recent approaches to materials science—are view. *Journal of Physics Materials*. 2019;2(03):032001.
- [14] Butler KT, Davies DW, Cartwright H, Isayev O, Walsh A. Machine Learning for Molecular and Materials Science. *Nature*. 2018; 559(7715):547–555.
- [15] Cherukara MJ, Narayanan B, Kinaci A, Sasikumar K, Gray SK, Chan MKY, et al. Ab-initio based bond order potential to investigate low thermal conductivity of stanene nano structures. *Journal of Physical Chemistry Letters*. 2016; 7(19):3752–3759.
- [16] Dieb MT, Hou ZF, Tsuda K. Structure prediction of boron-doped graphene by machine learning. *Journal of Chemical Physics*.2018;148(24):241716.
- [17] Wan J, Jiang JW, Park HS. Machine learning-based design of porous graphene with low thermal conductivity. *Carbon*.2020; 157:262–269.
- [18] Dong Y, Wu CH, Zhang C, Liu YD, Cheng JL, LinJ. Band gap prediction by deep learning in configurationally hybridized graphene and boron nitride. *Npj Computational Materials*.2019; 5:26.
- [19] Baboukani BS, Ye ZJ, Reyes KG, Nalam PC. Prediction of Nanoscale Friction for Two-Dimensional Materials Using a Machine Learning Approach. *Tribology Letters*. 2020; 68:57.
- [20] Annepu V, et al. Implementation of an efficient IoT enabled automated paralysis healthcare system. In: *Proceedings of the 2023 IEEE 8th International Conference on Engineering Technologies and Applied Sciences (ICETAS)*; 2023 Dec 1-4; Bahrain, Bahrain. New York: IEEE; 2023. p. 1-6. doi: 10.1109/ICETAS59148.2023.10346270.
- [21] Mortazavi B, Novikov IS, Podryabinkin EV, Roche S, Rabczuk T, Shapeev AV, et al. Exploring phononic properties of two-

dimensional materials using machine learning interatomic potentials. *Applied Materials Today*. 2020; 20:100685.

- [22] Taskesen, E. Hgboost is a python package for hyperparameter optimization for xgboost, catboost and lightboost for both classification and regression tasks. (Version 1.0.0) [Computer software]. <https://erdogant.github.io/hgboost>, 2020.
- [23] Zhang Y, Xu W, Liu G, Zhang Z, Zhu J, Li M (2021) Bandgap prediction of two-dimensional materials using machine learning. *PLoS ONE* 16(8): e0255637.
- [24] Bagadi K, et al. Cardiovascular disease prediction using machine learning algorithms. In: *Proceedings of the 2023 IEEE 8th International Conference on Engineering Technologies and Applied Sciences (ICETAS)*; 2023 Dec 1-4; Bahrain, Bahrain. New York: IEEE; 2023. p. 1-8. doi: 10.1109/ICETAS59148.2023.10346353.

Acknowledgments

We thank the principal, management of Bapatla Engineering College for encouraging and sponsoring us to participate in this Conference.

FUSION 360 BASED COMPOSITE LEAF SPRING DESIGN

Duriseti Venkata Srikanth¹, Allam Purushottam²

^{1,2}*Department of Mechanical Engg.*
SNIST,
Hyderabad, Telangana

Abstract

The aim of this study is to create and alter the steel leaf spring design so that it can be used in automobiles for a longer period of time by substituting composite materials. When compared to traditional steel leaf, materials like carbon epoxy, aluminum alloy, and titanium alloy have better mechanical qualities and are more cost-effective. The weight-saving features, deformation and stress characteristics of traditional steel and composite leaf springs were verified and compared. Stiffness was a limitation on the design. The remarkable corrosion resistance and excellent strength to weight ratio make composite leaf springs of utmost interest to the automotive industry. Using Autodesk Fusion 360, the leaf spring was modeled and investigated.

Introduction

A leaf spring's main functions are to support a car and provide the ride a smoother quality by cushioning impacts from potholes in the road. Leaf springs are used to locate the axle and control the vehicle's travel height in addition to keeping the tyres aligned on the road.

A simple type of suspension consisting of steel or composite layers stacked one on top of the other in different diameters is called a leaf spring. The axle is held in place by the straightforward and sturdy construction of the suspension, which serves as a linkage without the need for additional linkage. Depending on where the back axle is located, additional weight and expenses could be decreased. Leaf springs are perfect for heavy commercial vehicles since they regulate axle damping and sustain the weight of the chassis.

According to D.R. Dolas et al. [1], understanding the behavior of a composite leaf spring requires an equal amount of attention to the investigation of the composite material. The purpose of this study was to examine the results of mono composite leaf spring (GFRP) modeling, analysis, and testing. Pro-E (Wild Fire) 5.0 was used for modeling, while ANSYS 10.0 was used for analysis in order to gain a deeper understanding. Using normal eyes and cast eye ends, a

traditional mono leaf spring was developed and analyzed by M.L. Agarwal et al. [2]. CAD modeling was completed in CATIA, and analysis of the deformation, von Mises stress, and normal stress parameters was performed in ANSYS under comparable loading conditions.

D. Rezaei and M. M. Shokrieh [3] presented their work on the design, analysis, and optimization of a leaf spring. The primary objective of this research was to design a spring that could safely handle the designated static external stresses while weighing the least amount of weight. A four-leaf steel spring, which is a component of the rear suspension system of both light- and heavy-duty cars, was modeled using ANSYS. The findings demonstrated that the steel leaf spring was subjected to substantially greater pressures than the composite leaf spring.

With ANSYS14.5, V.K. Jain and Dev Dutt Dwivedi [4] investigated a composite leaf spring. There was an E-glass and epoxy three-layer full-length leaf composite leaf spring. The performance of a composite leaf spring and a conventional steel leaf spring was compared. When it came to weight and strength, the epoxy/e-glass composite performed better than the traditional steel leaf spring. A. Sonani et al. [5] considered deflection and stress in their design for their experiment. Standard steel, E-glass fiber, and composite Epoxy/E-glass were the materials selected for comparison. The solid modeling of the leaf spring that was finished in CATIA V5 was examined using ANSYS. According to the results of the static study, graphite epoxy outperformed the other materials.

M. V. Ramesh et al. [6] researched the structure and design of a glass fiber reinforced polymer (GFRP) composite leaf spring. The study aimed to compare the cost-effectiveness, stiffness, and load-bearing capacity of steel and composite leaf springs.

Pro-E was used to model a multi-leaf spring using finite elements, and ANSYS-11 was utilized to examine it. R.K. Rathore et al. [7] provided evidence of an improved automobile design and application for the usage of parabolic leaf springs as opposed to mono leaf springs. The study's conclusions offered helpful guidance to automakers that wanted to standardize their design and optimization procedures. R.S. Dalu and K. K.

Jadhao's [8] work involved changing the material of a leaf spring. The materials selected for this experiment were polyester resin and glass fiber reinforced plastic (GFRP) (NETPOL 1011).

M. Deepak and G.J. Jacob [9] built and modeled a leaf spring in line with the applied loads. The leaf spring was constructed out of forged steel. In this work, the reinforcing angle was varied to develop the leaf spring for mild steel and composite glass carbon.

The model and fatigue study were also performed using ANSYS and Pro/Engineer. E. Janarthan and M. Venkatesan evaluated the deflection, stress, and mode frequency that the ordinance factory caused in a Sumo leaf spring design [10]. Finite element experimentation and computer-aided analysis were given particular attention in this research.

Materials

Leaf Spring:

Vehicle suspension systems employ leaf springs. Originally, they were referred to as laminated or carriage springs. They are constructed from thin, arc-shaped steel sections that are connected together to resemble a forced bow. The parts are piled with smaller portions of the same material. The bending concept is the foundation for how a leaf spring operates. Even when the structure resists, bending happens when a load is applied to its ends.

Consequently, the reaction force that is produced opposes the applied load, endowing the leaf spring with its characteristic springiness. Because spring steel flexes when pressure is applied at either end and uses its own dampening mechanism to return to its original position, it is typically used in leaf spring setups to create an elliptical shape. Usually, the steel is divided into rectangular pieces and fastened together using a big bolt through the middle of the leaves and metal clips at each head. Big U-bolts are used to secure it to the vehicle's axle. The chosen composite materials' material qualities that were compared to those of steel are listed below.



Figure 1 . Leaf Spring (Semi Elliptical).

Table 1 : LEAF SPRING GEOMETRY AND PROPERTIES:

1	Eye to eye length of the spring	1120 mm
2	Length of Free camber	180 mm
3	Qty. of extra Full Leaves	2
4	Leaf width	50 mm
5	Leaf thickness	6 mm
6	Poisson's Ratio	0.3
7	Modulus of Elasticity of steel	210 gpa
8	No of Graduated Leaves	8

Material Selection:

Steel, aluminum alloy, titanium alloy, beryllium oxide, and epoxy carbon were the materials that were used.

- 1) Epoxy Carbon: High specific strength, modulus, and fatigue strength are all present in this material, along with a low coefficient of thermal expansion.
- 2) Aluminum Alloy: Due to its greater malleability, elastic properties, resistance to corrosion, and lower density, aluminum is a highly sought-after metal.
- 3) Titanium Alloy: A range of alloys make up titanium, which is known for its remarkable strength, rigidity, low density, toughness and remarkable resistance to corrosion. It is the most robust and practical metal available.
- 4) Beryllium Oxide: This white, colorless solid has a higher thermal conductivity than any other non-metal, with the exception of diamond. It also functions as a noteworthy electrical insulator.
- 5) Steel: Typically, leaf springs are composed of 0.90 to 1.0% carbon plain carbon steel. The leaves are heated following the production procedure. Products made of heat-treated spring steel have improved strength, a wider range of deflection, and improved fatigue characteristics, all of which increase the load capacity.

Computational Methodology

Solid Modelling:

Initially, the leaf spring was solidly modeled using Autodesk Fusion 360 in the manner described below. In Fusion 360, the assembly drawing portion is where all of the bolts, clamps, and leaves were put together after being individually designed in the part drawing. By making surface contact between each leaf's upper and lower surfaces, the leaves were put together. After all 8 leaves were constructed in this way, the clamps and bolts were subsequently put together in the leaf spring as shown below

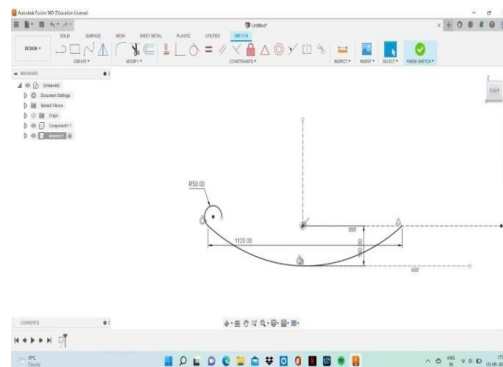


Figure 2.1 : Arc measuring 1120mm

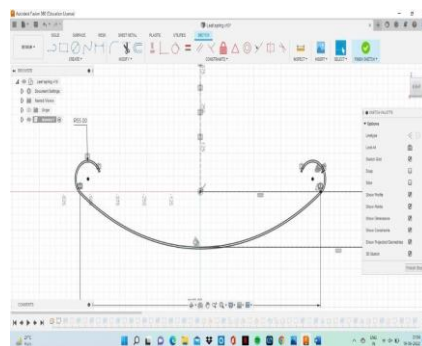


Figure 2.2 : Eye with radius 55mm

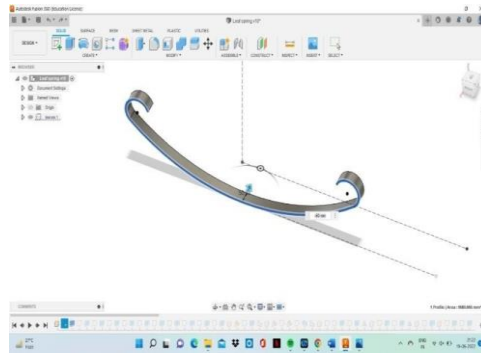


Figure 2.3 : Extrude operation using 50mm

1. As shown in figure 2.1, an arc measuring 1120 mm in length and 180 mm in camber was drawn symmetrically to the construction line.
2. In figure 2.2, an eye with a radius of 55 mm and an offset curve with a length of 6 mm are drawn and connected.. Using a 50 mm dimension, the extrude operation was carried out as shown in figure 2.3.
3. The same techniques as stages 2 and 3 were used to generate the eight graduated leaves and two additional full-length leaves shown in figure 2.4.
4. In Figure 2.5, four circles with a diameter of 10 mm are drawn inside a rectangular box that measures 110 by 70 mm on the bottom leaf.

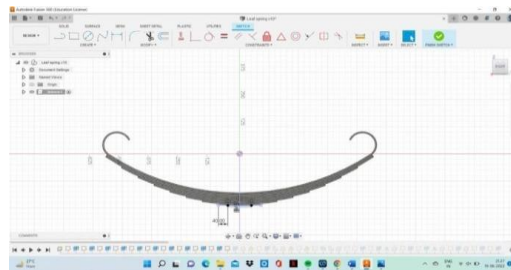


Figure 2.4: 8 graduated and 2 full length leaves

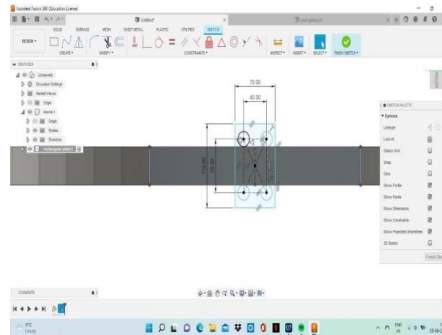


Figure 2.5: 4 circles of 10mm diameter

5. The rectangular box, which was free of the four circles, was extruded to a length of 10 mm before being positioned above the leaves, as seen in figure 2.6, where it measured 76 mm.

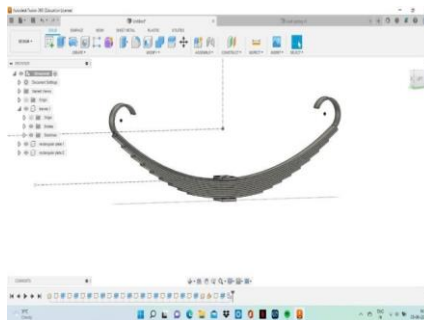


Figure 2.6: Rectangular box measuring 76mm

6. In figure 2.7, a U-bolt was drawn between the two circles with the aid of the sweep operation. It was then moved into the remaining two holes by a length of 75 mm.
- 7.

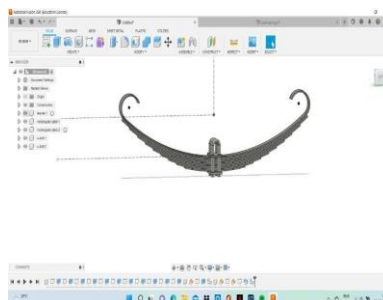


Figure 2.7: U bolt drawn using sweep operation.

8. Using the offset and extrude operations in figure 2.8, a rebound clip of 30 mm length was positioned on one of the leaf edges that was chosen.

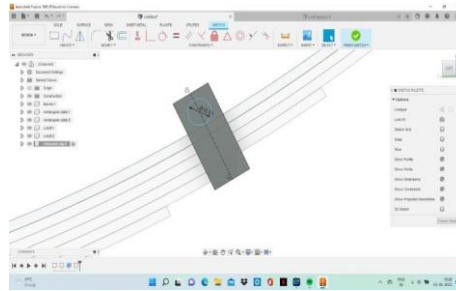


Figure 2.8: Rebound clip positioning

9. The extrude operation was used to create two 10 mm diameter holes on either side of the rebound clip, as shown in figure 2.9. The construction line produced in step 1 was then used to mirror the rebound clip.

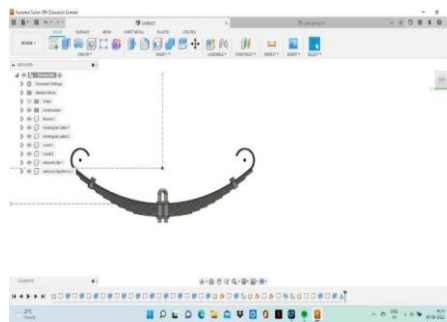


Figure 2.9 : Mirroring of rebound clip

10. The rebound clip depicted in figure 2.10 was created by using the same procedures as in stages 8 and 9

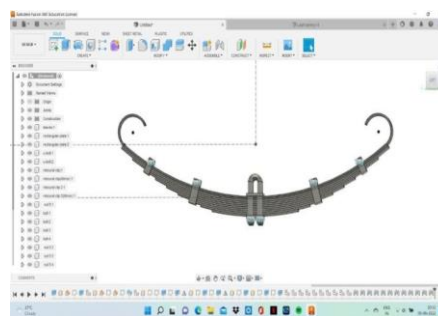


Figure 2.10: Rebound clip

11. As seen in figure 2.11, eight hexagonal nuts and four hexagonal bolts were made. The four hexagonal nuts that surround the U-bolts were subjected to the join operation, while the remaining components were employed at the rebound clips.

This produced the necessary solid leaf spring model.

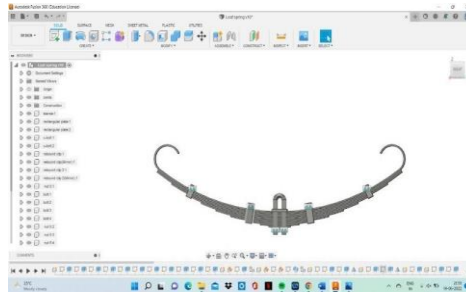


Figure 2.11: Leaf spring model

Simulation Procedure :

The materials used in this analysis of leaf springs included steel, titanium alloy, aluminum alloy, epoxy carbon, and beryllium oxide. These resources were chosen from Autodesk Fusion 360 Software's engineering data repository. Clicking on Create Study selected the static study. A 3200N structural load was placed on the bottom rectangular plate's face. By activating the structural limitations, the spring's two eyes locked. It was designed to create the mesh that splits the drawing into a limited number of pieces. By selecting the "generate results" option, the solutions for the stress, deformation, and elastic strain were found. A comparable verified analysis of the stress and deformation of a thrust bearing pad was conducted by Srikanth et al. using ANSYS.

Results And Discussions:

The tension, elastic strain, and displacement values from Fusion 360 were shown as follows. Plots of the aforementioned parameters for ordinary steel, aluminum alloy, titanium alloy, epoxy carbon, and beryllium oxide leaf springs are shown in Figures 3.1-3.3, 4.1-4.3, 5.1-5.3, 6.1-6.3, and 7.1-7.3, in that order.

The stress, elastic strain, and displacement values for leaf springs made of steel, aluminum alloy, titanium alloy, epoxy carbon, and beryllium oxide (ceramic) are shown in the following table.

Table 2: RESULT ANALYSIS

Element	Weight(G)	Displacement (mm)	Stress (Mpa)	Elastic Strain
Epoxy Carbon	4038.8	0.3556	39.14	0.001883
Titanium Alloy	13258.4	0.01738	6.409	9.02E-05
Aluminium Alloy	8230.9	0.02845	6.256	1.448E-04
Beryllium Oxide	9404.6	0.0069	8.223	2.835E-05
Steel	23930.7	0.01026	6.913	5.095E-05

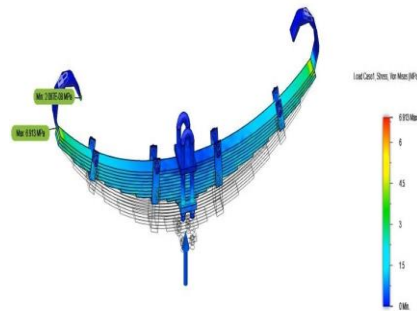
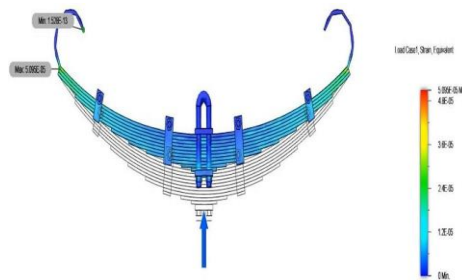
Steel:**Figure 3.1-** Steel stress concentration**Figure 3.2-** Steel elastic strain distribution



Figure 3.3- Steel displacement distribution

For Aluminium Alloy:

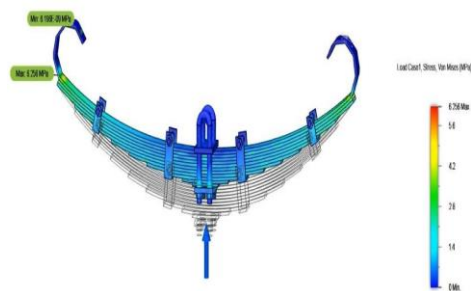


Figure 4.1: Aluminium alloy stress concentration

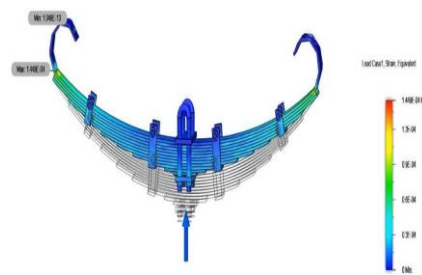


Figure 4.2: Aluminium alloy strain distribution

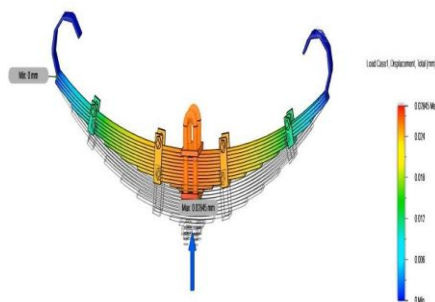


Figure 4.3: Aluminium alloy displacement distribution

For Titanium Alloy:

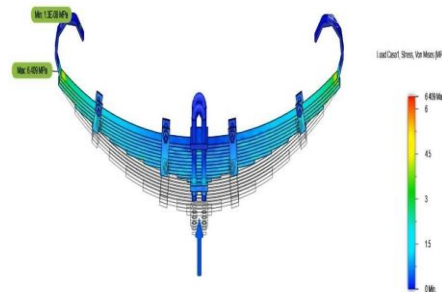


Figure 5.1: Titanium alloy stress concentration

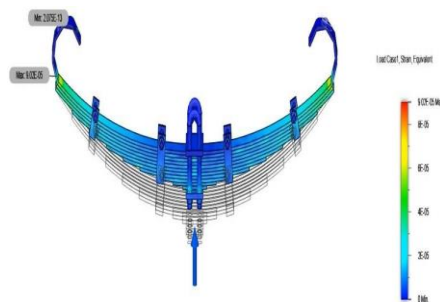


Figure 5.2: Titanium alloy strain distribution

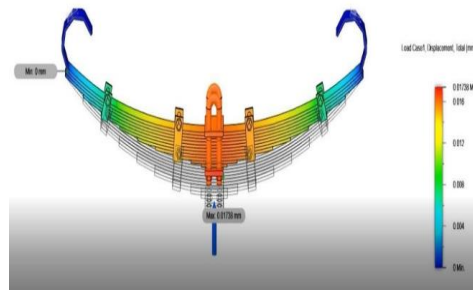


Figure 5.3- Titanium alloy Displacement distribution

For Epoxy Carbon:

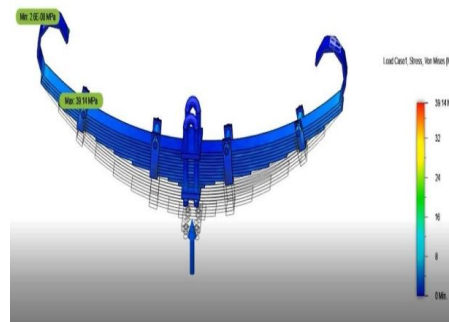


Figure 6.1: Epoxy carbon stress concentration



Figure 6.2- Epoxy carbon Elastic Strain

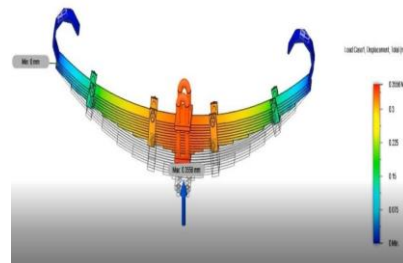


Figure 6.3- Epoxy carbon Displacement

For Beryllium Oxide:

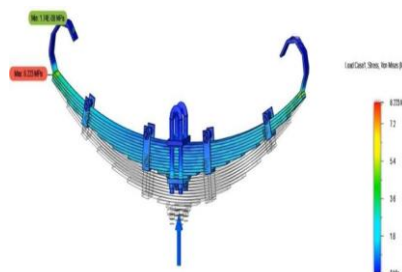


Figure 7.1: Beryllium oxide stress concentration

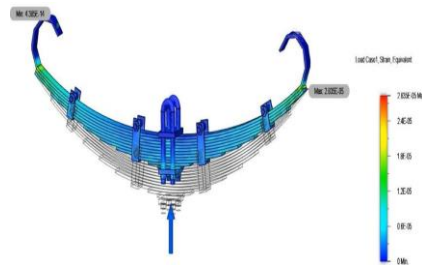


Figure 7.2- Beryllium oxide elastic strain

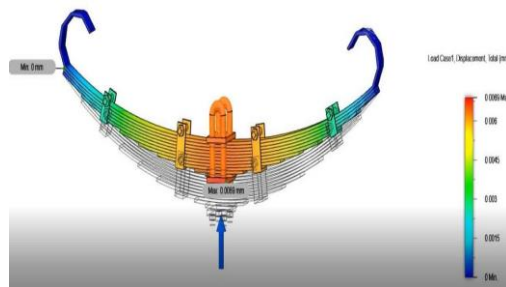


Figure 7.3- Beryllium oxide displacement

Conclusion

A static investigation of the leaf spring was carried out utilizing several material combinations and similar stress conditions for each design scenario. For every one of these leaf spring design cases, results were obtained for individual parameters. For a variety of material combinations in different leaf spring design scenarios, the results of elastic strain, total deformation, Von-Mises stress, and mass were evaluated. An examination of leaf springs constructed of various materials revealed that the composite epoxy carbon exhibits more stress for a given load than ordinary steel material. Since weight was a major factor while building cars, epoxy carbon turned out to be more effective than steel due of its lower weight.

References

1. D.R. Dolas, M.M. Patunkar, Modelling and Analysis of Composite Leaf Spring under the Static Load Condition by using FEA, IJMIE, 1(1), 1-4 (2011).
2. M.L. Aggarwal, G. Bhushan, V. Arora, Eye Design Analysis of Single Leaf Spring in Automotive Vehicles Using CAE Tools, IJAET, 1(1), 88-97 (2011)
3. D. Rezaei, M.M. Shokrieh, Analysis and optimization of a composite leaf spring, Composite Structures, 60(3), 317-325 (2003)
4. V.K. Jain, D.D. Dwivedi, Design and Analysis of Automobile leaf spring, IJCESR, 3(1), 100-105 (2016)
5. A. Sonani, P.H. Desai, D. Kapadia, Design and Analysis of Composite Leaf Spring For Light Weight Vehicle, International Journal Of Engineering Sciences & Research Technology, 5(6), 666-672 (2016)
6. M.V. Ramesh, M.V. Mallikarjun, D. Ashok, Design and Structural Analysis of Composite Multi Leaf Spring, IJETED, 5(2), 30-37 (2012)
7. R.K. Rathore, R.L. Himte, E.N. Karlus, Optimization of Mono Parabolic leaf spring, International Journal of Advances in Engineering & Technology, 7(1), 283-291 (2014)
8. R.S. Dalu, K.K. Jadhao, Experimental investigation & Numerical Analysis of Composite Leaf Spring. International Journal of Engineering Science and Technology, 3(6), 4759-4764 (2011)
9. M. Deepak, G.J. Jacob, Design and Analysis of Leaf Spring in a Heavy Truck, International Journal of Innovative Technology and Research, 5(4), 7041-7046 (2017)
10. M. Venkatesan, E. Janarthan, Design and Experimental Analysis of Leaf Spring Using Composite Materials, International Journal of Engineering Research & Technology, 2(12), 1957-1962 (2013)

Manufacturing of Hollow parts with light weight for Automotive Industry: A case Study

¹Yogesh Dandekar, ²Sanjay Aloni, ³Udayan Pathak,
⁴Prasanna Mahankar

^{1,2}*Assistant Professor,*
Cummins College of Engineering for Women,
Nagpur

³*Executive Director,*
Udayan Pathak & Associates,
Pune

⁴*Assistant Professor,*
Cummins College of Engineering for Women,
Nagpur

Abstract

There are many parts in highway and off highway application transmission which are hollow. Traditionally, these parts are made from costly low Carbon alloy steel either from bar stocks or through forging route. Subsequent to machining, most of these parts undergo heat treatment. In bar stock route there is lot of material wastage in the form swarf generation. Apart from this wastage, there is accumulation of residual stresses due to extensive machining. These stresses get relieved during heat treatment leading to unpredictable distortions.

Alternate method is forging and machining prior to case carburising. There is marked improvement in mechanical properties over bar and avoids accumulation of machining stresses for this route. But it is costly. Also the raw material yield is low. In addition, there is requirement of higher machining stock per face. To retain advantage of superior mechanical properties of forging at the same time to get better yield and avoid machining stresses, there was a need to discover another efficient process route. Seamless tubing is emerging as an efficient process route – from the point of view of both recovery and better mechanical property. It also eliminates accumulation of machining stresses, thus eliminating unpredictable distortion during case carburising.

This paper covers the case studies on actual work done in selection of proper tube size, variety (HFS / CFS), technical requirements for tubes,

on several different transmission parts using seamless steel tubing. The parts covered in the paper, include hollow main drive shaft and shifter sleeve. The average overall cost saving achieved per part was to the tune of 12% for parts converted to CFS & 20% for parts converted to HFS. Post hardening straightening operation was deleted due to elimination of heavy drilling causing accumulation of machining stresses leading to warpage in long shaft. Also, there was marked improvements in the field performance of the part by way of reduction in field failure ppm and phenomenal increase in mean time between failures (MTBF).

Key words: *Hollow parts, Transmission parts, Seamless tubing, Case Carburising, Shifter sleeves, splined hollow shafts, splined couplings etc.*

Introduction

Transmission in highway and off highway applications has many parts hollow in shape. Typically they are gear shifting sleeves, splined hollow shafts, splined couplings, power transmission shaft etc. Fig. 1 & 2 shows some typical parts. Functional and design requirement of these parts is capability for wear resistance and better torsional fatigue strength along with soft core to take care of bending loads. These requirements are best met with, by using low carbon alloy steel of carburising grades like SAE 4820, SAE 8620, SCM 420, 16MnCr5, 20MnCr5 etc. All these are known high cost material. These parts are heat treated for case carburising, hardening and tempering process. Though there is recent trend of switching over to carbo-nitriding with typical case depths of 0.25 to 0.45 mm, this trend is not considered in this article.



Figure 1 Typical transmission parts like shifter sleeves, gear, splined collar, main shaft etc.

Typical design requirements are - surface hardness around 60 HRC, effective case depth of about 0.8 to 1 mm. Few part design and application call for core hardness in the range of 35 to 40 HRC, while

few needs 25 to 30 HRC. These core hardness requirements also at times demand guaranteed hardenability; further increasing cost of raw material. Case carburising heat treatment is also costly. The clearances between the mating parts are maintained as per DIN class 8 for off highway applications while for highway applications DIN class 6 is maintained. All this put together makes the part very costly.



Figure 2 Splined Coupling typical size 35 mm diameter x 45 mm length

Discussions

Traditional process route to manufacture these parts is from the bar stock. The typical process flow is –

Bar Stock → Cutting to the size → Grain refinement (normalizing / iso annealing) → Pre turning → CNC Turning → Stress Relieving → Hobbing / Shaving → Broaching → Carburizing / Hardening Tempering → 100% Inspection / straightening / plug quenching (as required) → Grinding / hard machining → Audit inspection and dispatch.

Though this route is classical and looks most simple with use of conventional machines like lathes, drilling machines etc., the metallic yield is extremely poor. Also, there is an accumulation of machining stresses. These stresses get relieved during case carburising heat treatment, leading to unpredictable distortion during case carburising. This calls for 100 % segregation, size correction by plug quenching, post hardening straightening etc. One of the methods to avoid this problem is, doing an additional stress relieving operation @ 450^o - 550^o C at different stages viz. after pre turning, CNC turning, broaching, hobbing, shaving etc. Though desired, there is limitation to increase the temperature beyond 550^o C. Higher temperature may lead to surface oxidation and scaling which is not permissible on finished parts. This restriction on stress relieving temperature calls for longer stress relieving cycles. Other method is usage of atmosphere-controlled

furnaces and higher stress relieving temperatures. Both options make this stress relieving more costly. This additional stress relieving operation further adds to the part cost and throughput time.

Few gear shifting sleeves were tried using forging route in place of bar stock route. Typical Process flow is –

Bar Stock → Cutting to the size → Pre heating → Forging → Trimming → Grain refinement (normalizing / iso annealing) → Pre turning → CNC Turning Stress Relieving → Hobbing → / Shaving → Broaching → Carburizing / Hardening Tempering → 100% Inspection / straightening / plug quenching (as required) → Grinding / hard machining → Audit inspection and dispatch.

In this case, though there was slight improvement in distortion pattern but the metallic yield was still low. The mechanical properties of forging are optimum in the direction of grain flow. Simulated typical grain flow of tubular part is shown in Fig 3. However, most of the parts were subjected to torsional loads. This has put a challenge for innovation of alternate manufacturing route.

The seamless tube emerged as a better option. The grain flow in seamless tube is typical compared to forging. Fig 4 shows simulated typical grain flow. This makes mechanical properties of tubes isotropic in nature and making suitable to withstand the loads during severe applications.

The part dimensions were care fully studied and suitable tube size from existing product range of Indian Seamless Tubes Limited, Ahamadnagar.

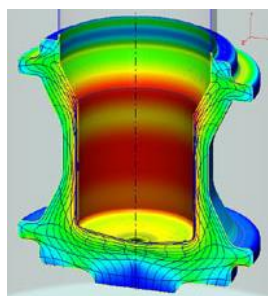


Figure 3 Simulated typical metal flow of forged Tubular part.

(India) was selected. Table 1 gives the dimensions of the parts vs. tube sizes selected. Apart from machining stock, bend inherent in the tube also needs to be considered before finalizing the tube sizes. The choice of hot finished sized vs. hot rolled cold finished tubes was primarily governed by dimensional control required by tube

manufacturer. Table 2 gives the dimensional tolerance on both types of tubes.

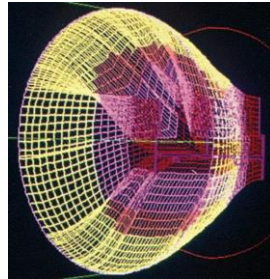


Figure 4 Simulated typical metal flow of Seamless tubing.

Table 1. Part and Seamless Tube Dimensions

S.N .	Part Name	Part Size mm			Tube Size mm		Tube Route
		ID	OD	Length	ID	OD	
1	Drive Shaft	30.8 ± 0.5	$34.67 / 34.57$	262 ± 0.5	26.5	50	Hot Finishe d Seamle ss
2	Coupling	$31.9 / 31.7$	35 ± 0.5	42 ± 0.5			
3	Outer hollow shaft	30.85 ± 0.5	$34.67 / 34.57$	419.25 ± 0.5			
4	Main Drive Shaft	28.25 ± 0.25	47.963 ± 0.013	260 ± 0.5	28.25	52.05	Cold Finishe d Seamle ss
5	Coupling	21.8 ± 0.1	35.0 ± 0.25	42 ± 0.5	19 ± 0.3	35 ± 0.3	Cold Finishe d Seamle ss
6	Coupling	20.1 ± 0.1	35.0 ± 0.5	42 ± 1			
7	Coupling	20.1 ± 0.1	32.0 ± 0.5	46.65 ± 0.1			
8	Shaft Rear	37.20 ± 0.5	40.150 ± 0.5	101.13 ± 0.3	$35 +0 / - 2$	$57 + 2/0$	Hot Finishe d Seamle ss
9	Collar shaft	$36.7 / 36.9$	40 ± 0.5	18.5 ± 0.5			
10	Collar shaft	$36.7 / 36.9$	40 ± 0.5	20.85 ± 0.5			
11	Splined Collar	$36.7 / 36.9$	39.975 ± 0.5	20.85 ± 0.5			
12	Splined Collar	56.35 ± 0.5	$62.35 / 62.25$	20.7 ± 0.5	$43.5 + 0/-2$	$63.5 +2 / 0$	Hot Finishe d Seamle ss
13	Splined Collar	$52.0 / 52.2$	56 ± 0.5	16 ± 0.5	$50.5 + 0/-2$	$77 + 2/0$	Hot Finishe d Seamle ss
14	Shift Collar	$50.2 / 50.0$	55 ± 0.5	18 ± 0.5	$48.5 + 0/-2$	$76 + 2/0$	Hot Finishe d Seamle ss
15	Collar splined	52.015 ± 0.015	73.46 ± 0.5	19 ± 0.5			

Table 2. Dimensional Tolerances of finished tubes

Tube finishing	Outer Diameter (D)	Thickness (t)	Eccentricity	Straightness
Hot rolled D/t = 3.5 – 9.9	± 0.75 %	± 7.5 %	10 % of 't'	1 : 600
Hot rolled D/t > 9.9	± 1.0 %	± 10 %		
Hot Rolled and Cold Finished	± 0.5 % subject to ± 0.25 mm minimum	± 5 %	OD < 125 mm – 5 % 't' OD > 125 mm – 10 % 't'	1: 1000

Case Studies:

Collar / Sleeves – This part is used for gear shifting. Fig. 5 shows typical part.

**Figure 5** Typical shifter sleeves

The process sequence for classical bar stock and seamless tube manufacturing route is –

Bar route

Bar stock → Cutting to the size → Grain refinement (normalizing / iso annealing) → Pre turning → CNC turning → Stress Relieving → Broaching → Tooth chamfering → Carburizing slow cooling → Plug quenching tempering → Shot blasting → Grinding / hard machining → Audit inspection and dispatch.

Seamless tube route

Billet → Hot extrusion → Grain refinement (normalizing / iso annealing) → CNC turning → Stress Relieving → Broaching → Tooth chamfering → Carburizing / hardening tempering → Shot blasting → Grinding / hard machining → Audit inspection and dispatch.

The major areas of concern in the classical bar stock route are the raw material wastage and unpredictable distortion during carburising, hardening and tempering treatment. The distortion was up to 0.3 mm in DIP, while permissible limit was 0.1 mm. The typical

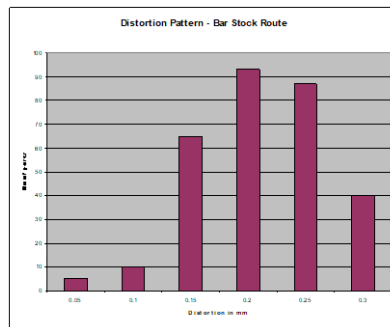


Figure 6 Shifter sleeves - Distortion pattern Bar stock

distribution and spread for the batch of 300 nos. is shown in the Fig 6. The major reason for unpredictable distortion is identified as excessive stresses induced during pre broaching machining. To ensure that the only right parts are shipped, 100% inspection, segregation, re work and re – inspection was required. In spite of this some parts with dimensional discrepancy was shipped leading to assembly line stoppage, tedious online segregation. To avoid this situation, plug quenching was introduced as an additional operation.

Fig 7 and 8 shows plug quenching arrangement. The dimensional discrepancy issue was resolved, but heat treatment throughput time for the batch of 500nos. has gone up from 12 hrs to 26 Hrs. Since this was manual operation, there were issues of hardness variation from piece to piece. Also separate set up and additional man power was required. After tube route was introduced, the dimensional distortion was controlled within 0.075 mm. The typical distribution and spread for the batch of 300 nos. is shown in the fig 9.



Figure 7 Plug Quenching arrangement



Figure 8 Plug quenching arrangement.

Also the plug quenching was deleted reducing throughput time by 14 hrs for the batch of 500 nos. Hence the manufacturing route was switched over to Seamless tubing. The overall cost saving achieved was to the tune of 20%, though the input (seamless tube) price was higher than the bar route.

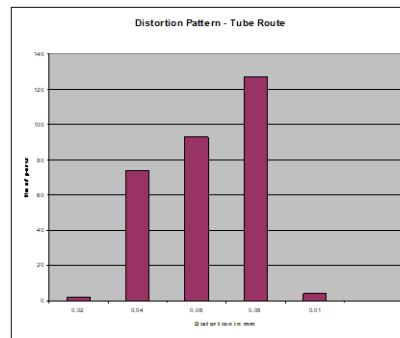


Figure 9 Shifter Sleeves - Distortion pattern Tube route

Main Drive Shaft - This part is used for transmitting the power. Fig. 10 shows typical part.



Figure 10 Main drive shaft.

The process sequence for classical bar stock and seamless tube manufacturing route is –

Bar route

Bar stock → Cutting to the size → Grain refinement (normalizing / iso annealing) → Pre turning (two additional set ups for through hole drilling) → CNC turning → Stress Relieving → Hobbing / shaving → Drilling chamfering (cross holes) → Carburizing → hardening → Straightening and tempering → Shot blasting → Grinding / hard machining → Audit inspection and dispatch.

Seamless tube route

Billet → Hot extrusion → Grain refinement (normalizing / iso annealing) → CNC turning → Hobbing / shaving → Drilling chamfering (cross holes) → Carburizing / hardening tempering → Shot blasting → Grinding / hard machining → Audit inspection and dispatch.

The major problem faced in the classical bar route was heavy rejection to the tune of 30% due to excessive runout. Also straightening was not possible due very thin wall and complex geometry. Runout was found up to 0.35 mm against the specified 0.050 mm. The distribution of runout values of typical batch of 300 nos. is shown in Fig 14. Lot of experimentation for giving support through pipes in heat treatment fixtures, usage of hot quenching oils, higher quenching oil temperatures, stress relieving at various machining stages, straightening at different machining stages etc was carried out but there was only marginal improvement. Another problem was the presence of step at merging point of both side drilling.



Figure 11 Main drive shaft – Run out Pattern Bar route.

Also due to double drilling, there was a wall thickness variation and part ID/OD was like a crown. There were reported cases of field failures to the tune of 1200 ppm, with mtbf (mean time between failure) of 50 hrs in Asian applications which is equal to 150 hrs in Europe and USA applications, due to breakage of shaft at the drilled cross holes. This was attributed to the straightening and poor surface finish during ID drilling. To avoid all these issues seamless tube was introduced as a raw material. With this changeover, the runout was controlled within 0.050 mm as per specification. The distribution of runout values of typical batch of 300 nos. is shown in fig 15. Also the issue of wall thickness variation and crowning effect was also resolved. The field complaints came down to 50 ppm with improvement in mtbf to 2,000 hrs in Asian applications which is equivalent to 6,000 hrs in Europe and USA applications. Over and above this, the overall cost reduction of 12% was achieved.

Conclusion:

There are many thin walled hollow parts used in transmission for highway and off highway applications. Classically, these parts are made through bar stock route or forging route. Both these routes have many limitations from process reliability point of view. During manufacturing

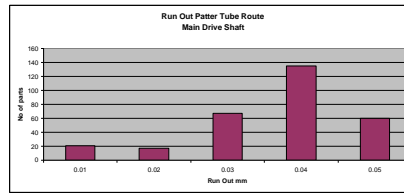


Figure 12 Main drive shaft - Run out Pattern Tube route.

and usage, there are heavy rejections due to distortion so also field reliability issues. There are options of costly processes like deep hole drilling and additional operations like stress relieving. Both these add to the process cost. Manufacturing such parts through seamless route is an innovative solution for the same. Apart from process and product reliability the parts manufactured through this route offers cost saving to the tune of 12 – 20 %.

Acknowledgement:

I am thankful to the management of Tata Motors Limited for granting permission to present this paper in Automotive Symposium of India 2009. Also, we are grateful to Indian Seamless Tubes Limited, Steel Tube Division, for support in developing the required Steel Tubes as per the Technical requirements. Also, our thanks are due to RSB Transmission (I) Limited, Sanaswadi, Pune India, Involute Technologies Private Limited, Pune India and Mahabal Auto Ancillaries Private Limited, Miraj, District Sangli, India for carrying out machining and Heat Treatment of the parts discussed in Case Studies and providing photographs of process equipments.

Modelling and Analysis of Essential Parameters in Green Sand Process to Minimize Shrinkage Porosity in Grey Iron Components

¹Sanjay Aloni, ²Yogesh Dandekar, ³Udayan Pathak,
⁴Prasanna Mahankar, ⁵Vikram Dandekar, ⁶Shailesh Khekale

^{1,2,4,5,6}*Assistant Professor,*

Cummins College of Engineering for Women,
Nagpur

³*Executive Director,*

Udayan Pathak & Associates,
Pune

Abstract

The rejection of casting components because of presence of most challenging defects such as shrinkage porosity which occurs repeatedly in gray iron components with complex geometry like cylinder heads, is the major issue of concern in almost all the green sand foundries engaged in manufacturing of castings for automotive. The shrinkage porosity defect which is persisting in intricate shape casting components produced in gray iron using green sand casting process is difficult to avoid. The present work focused on the identification of parameters which are most influential and responsible for occurrences of such defect, potential parameters that are associated with principal operations in green sand casting process are selected and experiments are performed as per the plan given by the most suitable Taguchi array, L36 OA. Based on the results obtained, the exponential mathematical model is formulated for identification of influential parameters. The study also concluded with reliability and sensitivity analysis which ensures the suitability of the models to predict and avoid the rejections because of variation in respective parameters.

Keywords Green sand process, persisting casting defects, process parameters, Taguchi orthogonal array, Linear and Exponential Model

Introduction

Gray cast iron (GI) is one of the most favorite materials for cast ferrous products and wide range of GI components required in various sectors is produced by using a green sand process. In spite of the

competition from some newer materials in this category, and their promotion, gray cast iron is still dominant amongst all because of its properties have proved it to be the most appropriate material available in many engineering applications and its capacity to cast into intricate shapes comparatively at lower cost [1] Most of the complex cast components used in the automotive industry such as cylinder heads, cylinder blocks, and housings or casings required for different types of transmissions in heavy automobiles such as gearbox housings, axel housings etc. and other miscellaneous items are produced in gray cast irons by using a green sand process. The foundry industries engaged in producing such complex components required in automotive generally uses green sand casting process for mould production, moulds are produced on moulding machines for producing large quantity of such items.

The typical flow of the sequence of operations performed in the production of castings using green sand casting process is shown in Figure 1.1 given below. As shown in the figure principal operations involved in this process and that are carried out on a regular basis in various plants or shops of the foundry industry are as given below.

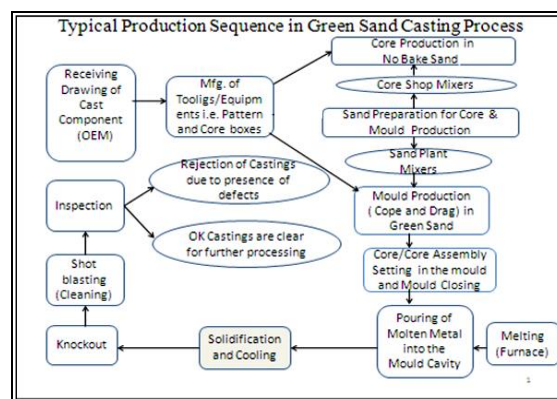


Figure 1.1: Typical production flow in green sand foundry

Casting Defects in Green Sand Process:

Casting produced in green sand casting process is having multi-quality characteristics. The presence of defects is the major concern in the green sand process which affects productivity. The main goal of the foundries is to produce quality castings with no or minimum rejection of castings due to the presence of defects which are most vulnerable in components with complex geometry. Large number of parameters involved in the green sand casting process which are associated with different processes or operations required to perform for producing cast components in green sand process as shown in above figure 1.1. The occurrences of most common

defects in castings produced in the green sand process can be categorized in the following groups, based on their association with a particular process or operation in green sand process [2-4], for example Metallurgical or melting (and pouring) related Defects, Moulding or Mould related Defects, Core related defects, Sand related defects, Fettling and Handling and Tooling's and Equipment's as shown in the table 1.1 .

Table 1.1: Common casting defects associated with different operation's / Processes

Process/ Operations	Associated Defects						
Melting &Pouring	Shrinkage Porosity	Blowhole	Hardness (Low or High)	Cold	Chemical Analysis	Short Pour	Slag Inclusion
Moulding	Blowhole	<u>Mould</u> Broken	<u>Mould</u> Leakage	<u>Mould</u> Mis- Match	<u>Mould</u> Swelling		
Core Making & Core Setting	Blowhole	Core Lift	Core Shift	Core Swelling	Core Scabbing		
Sand Preparation	Sand Inclusion	Scabbing	Sand Fusion
Fettling	Handling Broken	Extra Grinding
Pattern Manufacturing	Rejection of casting components due to the wrong manufacturing of pattern tool equipment & due to Trial and Error method during sample production in the development stage						

Shrinkage Porosity Defect:

Among the various defects, shrinkage porosity defect contribute in significant amount to total foundry rejection, which in turn cause lost in productivity and increases production cost. The defect, shrinkage porosity or closed shrinkage in the complex shaped components for example cylinder head castings used in automotive is very difficult to tackle. This defect affects the final integrity of a casting component and also disturbs mechanical properties. Shrinkage porosity defect in the engine components for example cylinder heads may also affect the performance of such components [5]. In this research work on shrinkage porosity, author stated that, porosity is the most persistent and issue of concern for casting users and contributes customer apprehensions about reliability and quality.

The presence of shrinkage porosity defect at subsurface is visible during the machining of castings as shown in the Figure 1.2 given below. In some cases, the defect is exposed during machining of castings, while it can also be ensured through leak test or pressure test which is compulsory in components like cylinder heads. Though, the presence of porosity is exposed as stated above, the porosity in the

critical sections is so minor which sometimes is very difficult to detect and finally affect the performance of components.

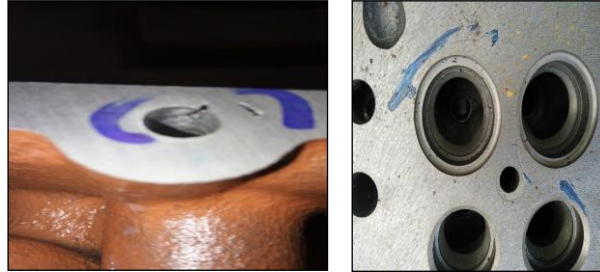


Figure 1.2: Shrinkage porosity in cylinder head castings visible during machining of cylinder head castings

Selection of Process Parameters Responsible for Persisting Defects:

From the reviewed literature [2-3], and through the brainstorming sessions with the skilled foundry personnel the parameters which are responsible for occurrences of persisting defects is identified for further analysis. The parameters at different levels with corresponding values are finalized on the basis of outcome of discussions with skilled foundry personals and of course on the basis of review of previous research work in this regard. Table 1.2 given below, indicates the parameters that are assumed to be responsible for persisting defect shrinkage porosity. The total 19 no. of process parameters are finalized to carry out the experiments using Taguchi's 'Design of Experiments' method and results obtained through experimentation are further investigated using Taguchi's approach for optimization.

Table 1.2: Parameters associated with shrinkage porosity defects

List of Variables					
Independent Variable					
Sr. No.	Name of Variable	Abbreviation	Level 1	Level 2	Level 3
1	Carbon Equivalent	X ₁	3.9	4.0	---
2	Carbon Percentage	X ₂	3.3	3.4	---
3	Pouring Temperature	X ₃	1400	1410	---
4	Inoculants Percentage	X ₄	0.15	0.20	---
5	Steel Scrap Percentage	X ₅	30	40	---
6	Phosphorus Percentage	X ₆	0.08	0.09	---
7	Binder	X ₇	1.8	2.2	---

8	Moisture Percentage	X ₈	4	4.4	4.8
9	Permeability	X ₉	130	140	150
10	Sulphur Percentage	X ₁₀	0.07	0.08	0.09
11	Green Compression Strength	X ₁₁	1.4	1.6	1.8
12	Compatibility Percentage	X ₁₂	40	43	46
13	Moulding Sand Temperature	X ₁₃	30	40	50
14	Squeezing Pressure	X ₁₄	90	100	110
15	Mould Hardness Horizontal	X ₁₅	80	85	90
16	Mould Hardness Vertical	X ₁₆	70	75	80
17	Silica in Sand Percentage	X ₁₇	95	96.5	98
18	Knockout Time	X ₁₈	30	35	40
19	Manganese Percentage	X ₁₉	0.6	0.7	0.8
Dependent Variable					
1	Shrinkage porosity (Closed Shrinkage Defect)	Y1			

Selection of orthogonal array for Taguchi DOE:

The final step of the critical planning phase is the selection of suitable Taguchi's orthogonal array (OA) for conduction of experiments in next phase that is performing the experiments or experimentation. After the completion of the initial steps in the DOE, that is the selection of quality characteristics, selection of the essential parameters that may influence the quality characteristics along with the setting of these parameters at appropriate levels and measurement system for controlling of parameters. In Taguchi method the experiments can be conducted for the optimization of a process by using suitable Taguchi Orthogonal Array (OA) which depends on the number of input parameters identified and there levels [6]. As mentioned in Table 1.2 given below, the number of parameters involved in this study are 19, therefore, L36 OA is as one of the most suitable arrays selected to conduct experiments [7]. The actual design of experimentation is obtained by putting the values of respective parameters at different levels in standard template, as shown in Table 1.3 given below.

Table 1.3: Actual Experimentation Plan

Sr. No.	X ₁	X ₂	X ₃	X ₄	X ₅	X ₆	X ₇	X ₈	X ₉	X ₁₀	X ₁₁	X ₁₂	X ₁₃	X ₁₄	X ₁₅	X ₁₆	X ₁₇	X ₁₈	X ₁₉
1	3.9	3.3	1400	0.15	30	0.08	1.8	4.00	130	0.07	1.4	40.0	30	90	80	70	95.0	30	0.6
2	3.9	3.3	1400	0.15	30	0.08	1.8	4.40	140	0.08	1.6	43.0	40	100	85	75	96.5	35	0.7
3	3.9	3.3	1400	0.15	30	0.08	1.8	4.80	150	0.09	1.8	46.0	50	110	90	80	98.0	40	0.8
4	3.9	3.3	1400	0.15	30	0.09	2.2	4.00	130	0.07	1.4	43.0	40	100	85	80	98.0	40	0.8
5	3.9	3.3	1400	0.15	30	0.09	2.2	4.40	140	0.08	1.6	46.0	50	110	90	70	95.0	30	0.6
6	3.9	3.3	1400	0.15	30	0.09	2.2	4.80	150	0.09	1.8	40.0	30	90	80	75	96.5	35	0.7
7	3.9	3.3	1410	0.20	40	0.08	1.8	4.00	130	0.08	1.8	40.0	40	110	90	70	96.5	35	0.8
8	3.9	3.3	1410	0.20	40	0.08	1.8	4.40	140	0.09	1.4	43.0	50	90	80	75	98.0	40	0.6
9	3.9	3.3	1410	0.20	40	0.08	1.8	4.80	150	0.07	1.6	46.0	30	100	85	80	95.0	30	0.7
10	3.9	3.4	1400	0.20	40	0.08	2.2	4.00	130	0.09	1.6	40.0	50	100	90	75	95.0	40	0.7
11	3.9	3.4	1400	0.20	40	0.08	2.2	4.40	140	0.07	1.8	43.0	30	110	80	80	96.5	30	0.8
12	3.9	3.4	1400	0.20	40	0.08	2.2	4.80	150	0.08	1.4	46.0	40	90	85	70	98.0	35	0.6
13	3.9	3.4	1410	0.15	40	0.09	1.8	4.00	140	0.09	1.4	46.0	40	90	90	80	96.5	30	0.7
14	3.9	3.4	1410	0.15	40	0.09	1.8	4.40	150	0.07	1.6	40.0	50	100	80	70	98.0	35	0.8
15	3.9	3.4	1410	0.15	40	0.09	1.8	4.80	130	0.08	1.8	43.0	30	110	85	75	95.0	40	0.6
16	3.9	3.4	1410	0.20	30	0.09	2.2	4.00	140	0.09	1.6	40.0	30	110	85	80	98.0	35	0.6
17	3.9	3.4	1410	0.20	30	0.09	2.2	4.40	150	0.07	1.8	43.0	40	90	90	70	95.0	40	0.7
18	3.9	3.4	1410	0.20	30	0.09	2.2	4.80	130	0.08	1.4	46.0	50	100	80	75	96.5	30	0.8
19	4.0	3.3	1410	0.20	30	0.08	2.2	4.00	140	0.07	1.8	46.0	50	90	85	75	95.0	35	0.8
20	4.0	3.3	1410	0.20	30	0.08	2.2	4.40	150	0.08	1.4	40.0	30	100	90	80	96.5	40	0.6
21	4.0	3.3	1410	0.20	30	0.08	2.2	4.80	130	0.09	1.6	43.0	40	110	80	70	98.0	30	0.7
22	4.0	3.3	1410	0.15	40	0.09	2.2	4.00	140	0.08	1.8	46.0	30	100	80	70	98.0	40	0.7
23	4.0	3.3	1410	0.15	40	0.09	2.2	4.40	150	0.09	1.4	40.0	40	110	85	75	95.0	30	0.8
24	4.0	3.3	1410	0.15	40	0.09	2.2	4.80	130	0.07	1.6	43.0	50	90	90	80	96.5	35	0.6
25	4.0	3.3	1400	0.20	40	0.09	1.8	4.00	150	0.08	1.4	43.0	50	110	80	80	95.0	35	0.7
26	4.0	3.3	1400	0.20	40	0.09	1.8	4.40	130	0.09	1.6	46.0	30	90	85	70	96.5	40	0.8
27	4.0	3.3	1400	0.20	40	0.09	1.8	4.80	140	0.07	1.8	40.0	40	100	90	75	98.0	30	0.6
28	4.0	3.4	1410	0.15	30	0.08	1.8	4.00	150	0.08	1.6	43.0	30	90	90	75	98.0	30	0.8
29	4.0	3.4	1410	0.15	30	0.08	1.8	4.40	130	0.09	1.8	46.0	40	100	80	80	95.0	35	0.6
30	4.0	3.4	1410	0.15	30	0.08	1.8	4.80	140	0.07	1.4	40.0	50	110	85	70	96.5	40	0.7
31	4.0	3.4	1400	0.20	30	0.09	1.8	4.00	150	0.09	1.8	43.0	50	100	85	70	96.5	30	0.6
32	4.0	3.4	1400	0.20	30	0.09	1.8	4.40	130	0.07	1.4	46.0	30	110	90	75	98.0	35	0.7
33	4.0	3.4	1400	0.20	30	0.09	1.8	4.80	140	0.08	1.6	40.0	40	90	80	80	95.0	40	0.8
34	4.0	3.4	1400	0.15	40	0.08	2.2	4.00	150	0.07	1.6	46.0	40	110	80	75	96.5	40	0.6
35	4.0	3.4	1400	0.15	40	0.08	2.2	4.40	130	0.08	1.8	40.0	50	90	85	80	98.0	30	0.7
36	4.0	3.4	1400	0.15	40	0.08	2.2	4.80	140	0.09	1.4	43.0	30	100	90	70	95.0	35	0.8

Formulation of Mathematical Model:

From the outcomes of the results obtained through experiments conducted as per experimentation plan, it is revealed to develop a mathematical model. In this work, there are 1 dependent and 19 independent variables. It is essential to establish the quantitative correlation between independent and dependent variables which are involved in the experimentation. This correlation is a mathematical model which is useful as a design tool for such complex process where number of parameters involved are more in numbers. However, the exponential mathematical model is more robust; as it gives reasonable precision. Therefore, the exponential model is developed as follows.

MODEL FORMULATION (EXPONENTIAL MODEL)

$$Y_1 = f(X_1, X_2, X_3, X_4, X_5, X_6, X_7, X_8, X_9, X_{10}, X_{11}, X_{12}, X_{13}, X_{14}, X_{15}, X_{16}, X_{17}, X_{18}, X_{19})$$

Considering, dependent and independent parameters have exponential relationship. Hence

$$Y_1 = K \times X_1^a \times X_2^b \times X_3^c \times X_4^d \times X_5^e \times X_6^f \times X_7^g \times X_8^h \times X_9^i \times X_{10}^j \times X_{11}^k \times X_{12}^l \times X_{13}^m \times X_{14}^n \times X_{15}^o \times X_{16}^p \times X_{17}^q \times X_{18}^r \times X_{19}^s$$

Now forming the mathematical model means to find the value of unknowns in the above equation.

Taking log of the both the sides of above equation gives;

$$Y_1 = \log K + a \log X_1 + b \log X_2 + c \log X_3 + d \log X_4 + e \log X_5 + f \log X_6 \\ + g \log X_7 + h \log X_8 + i \log X_9 + j \log X_{10} + k \log X_{11} + l \log X_{12} \\ + m \log X_{13} + n \log X_{14} + o \log X_{15} + p \log X_{16} + q \log X_{17} \\ + r \log X_{18} + s \log X_{19}$$

Above equation is valid for all the readings collected during experimentation. Hence putting summation on both the sides

$$\sum_{i=1}^{i=n} Y_i = \sum_{i=1}^{i=n} (\log K + a \log X_1 + b \log X_2 + c \log X_3 + d \log X_4 + e \log X_5 + f \log X_6 + g \log X_7 + h \log X_8 + i \log X_9 + j \log X_{10} + k \log X_{11} + l \log X_{12} + m \log X_{13} + n \log X_{14} + o \log X_{15} + p \log X_{16} + q \log X_{17} + r \log X_{18} + s \log X_{19})$$

The equation can also be written as;

$$\begin{aligned} \sum_{i=1}^{i=n} Y_1 = & \log K + a \sum_{i=1}^{i=n} \log X_1 + b \sum_{i=1}^{i=n} \log X_2 + c \sum_{i=1}^{i=n} \log X_3 + d \sum_{i=1}^{i=n} \log X_4 + \\ & e \sum_{i=1}^{i=n} \log X_5 + f \sum_{i=1}^{i=n} \log X_6 + g \sum_{i=1}^{i=n} \log X_7 + h \sum_{i=1}^{i=n} \log X_8 + i \sum_{i=1}^{i=n} \log X_9 + \\ & j \sum_{i=1}^{i=n} \log X_{10} + k \sum_{i=1}^{i=n} \log X_{11} + l \sum_{i=1}^{i=n} \log X_{12} + m \sum_{i=1}^{i=n} \log X_{13} + \\ & n \sum_{i=1}^{i=n} \log X_{14} + o \sum_{i=1}^{i=n} \log X_{15} + p \sum_{i=1}^{i=n} \log X_{16} + q \sum_{i=1}^{i=n} \log X_{17} + \\ & r \sum_{i=1}^{i=n} \log X_{18} + s \sum_{i=1}^{i=n} \log X_{19} \end{aligned}$$

$$y_1 = K + ax_1 + bx_2 + cx_3 + dx_4 + ex_5 + fx_6 + gx_7 + hx_8 + ix_9 + jx_{10} + kx_{11} + lx_{12} + mx_{13} + nx_{14} + ox_{15} + px_{16} + qx_{17} + rx_{18} + sx_{19}$$

After multiplying above equation by x_1, x_2, \dots, x_{19} , following matrix is obtained;

p	x1	x2	x3	x4	x5	x6	x7	x8	x9	x10	x11	x12	x13	x14	x15	x16	x17	x18	x19	k	y1
x1	x1x1	x1x2	x1x3	x1x4	x1x5	x1x6	x1x7	x1x8	x1x9	x1x10	x1x11	x1x12	x1x13	x1x14	x1x15	x1x16	x1x17	x1x18	x1x19	a	x1y1
x2	x2x1	x2x2	x2x3	x2x4	x2x5	x2x6	x2x7	x2x8	x2x9	x2x10	x2x11	x2x12	x2x13	x2x14	x2x15	x2x16	x2x17	x2x18	x2x19	b	x2y1
x3	x3x1	x3x2	x3x3	x3x4	x3x5	x3x6	x3x7	x3x8	x3x9	x3x10	x3x11	x3x12	x3x13	x3x14	x3x15	x3x16	x3x17	x3x18	x3x19	c	x3y1
x4	x4x1	x4x2	x4x3	x4x4	x4x5	x4x6	x4x7	x4x8	x4x9	x4x10	x4x11	x4x12	x4x13	x4x14	x4x15	x4x16	x4x17	x4x18	x4x19	d	x4y1
x5	x5x1	x5x2	x5x3	x5x4	x5x5	x5x6	x5x7	x5x8	x5x9	x5x10	x5x11	x5x12	x5x13	x5x14	x5x15	x5x16	x5x17	x5x18	x5x19	e	x5y1
x6	x6x1	x6x2	x6x3	x6x4	x6x5	x6x6	x6x7	x6x8	x6x9	x6x10	x6x11	x6x12	x6x13	x6x14	x6x15	x6x16	x6x17	x6x18	x6x19	f	x6y1
x7	x7x1	x7x2	x7x3	x7x4	x7x5	x7x6	x7x7	x7x8	x7x9	x7x10	x7x11	x7x12	x7x13	x7x14	x7x15	x7x16	x7x17	x7x18	x7x19	g	x7y1
x8	x8x1	x8x2	x8x3	x8x4	x8x5	x8x6	x8x7	x8x8	x8x9	x8x10	x8x11	x8x12	x8x13	x8x14	x8x15	x8x16	x8x17	x8x18	x8x19	h	x8y1
x9	x9x1	x9x2	x9x3	x9x4	x9x5	x9x6	x9x7	x9x8	x9x9	x9x10	x9x11	x9x12	x9x13	x9x14	x9x15	x9x16	x9x17	x9x18	x9x19	i	x9y1
x10	x10x1	x10x2	x10x3	x10x4	x10x5	x10x6	x10x7	x10x8	x10x9	x10x10	x10x11	x10x12	x10x13	x10x14	x10x15	x10x16	x10x17	x10x18	x10x19	x	x10y1
x11	x11x1	x11x2	x11x3	x11x4	x11x5	x11x6	x11x7	x11x8	x11x9	x11x10	x11x11	x11x12	x11x13	x11x14	x11x15	x11x16	x11x17	x11x18	x11x19	=	x11y1
x12	x12x1	x12x2	x12x3	x12x4	x12x5	x12x6	x12x7	x12x8	x12x9	x12x10	x12x11	x12x12	x12x13	x12x14	x12x15	x12x16	x12x17	x12x18	x12x19	j	x12y1
x13	x13x1	x13x2	x13x3	x13x4	x13x5	x13x6	x13x7	x13x8	x13x9	x13x10	x13x11	x13x12	x13x13	x13x14	x13x15	x13x16	x13x17	x13x18	x13x19	l	x13y1
x14	x14x1	x14x2	x14x3	x14x4	x14x5	x14x6	x14x7	x14x8	x14x9	x14x10	x14x11	x14x12	x14x13	x14x14	x14x15	x14x16	x14x17	x14x18	x14x19	n	x14y1
x15	x15x1	x15x2	x15x3	x15x4	x15x5	x15x6	x15x7	x15x8	x15x9	x15x10	x15x11	x15x12	x15x13	x15x14	x15x15	x15x16	x15x17	x15x18	x15x19	o	x15y1
x16	x16x1	x16x2	x16x3	x16x4	x16x5	x16x6	x16x7	x16x8	x16x9	x16x10	x16x11	x16x12	x16x13	x16x14	x16x15	x16x16	x16x17	x16x18	x16x19	p	x16y1
x17	x17x1	x17x2	x17x3	x17x4	x17x5	x17x6	x17x7	x17x8	x17x9	x17x10	x17x11	x17x12	x17x13	x17x14	x17x15	x17x16	x17x17	x17x18	x17x19	q	x17y1
x18	x18x1	x18x2	x18x3	x18x4	x18x5	x18x6	x18x7	x18x8	x18x9	x18x10	x18x11	x18x12	x18x13	x18x14	x18x15	x18x16	x18x17	x18x18	x18x19	r	x18y1
x19	x19x1	x19x2	x19x3	x19x4	x19x5	x19x6	x19x7	x19x8	x19x9	x19x10	x19x11	x19x12	x19x13	x19x14	x19x15	x19x16	x19x17	x19x18	x19x19	s	x19y1

This can also be written as;

$$X * \text{Index} = Y$$

$$X^{-1} * X * \text{index} = X^{-1} * Y$$

$$\mathbf{I} * \text{index} = \mathbf{X}^{-1} * \mathbf{Y}$$

$$\text{index} = \mathbf{X}^{-1} * \mathbf{Y}$$

By solving this following indices are obtained;

	K	X ₁	X ₂	X ₃	X ₄	X ₅	X ₆	X ₇	X ₈	X ₉	X ₁₀	X ₁₁	X ₁₂	X ₁₃	X ₁₄	X ₁₅	X ₁₆	X ₁₇	X ₁₈	X ₁₉
Y ₁	18.690	-8.116	-0.360	2.435	0.019	0.516	0.797	0.240	0.138	-0.485	0.070	-0.212	0.144	-0.091	-0.189	-0.070	0.552	-1.344	-0.213	-0.565

$$Y_1 = 18.690 \times X_1^{-8.116} \times X_2^{-0.360} \times X_3^{2.435} \times X_4^{0.019} \times X_5^{0.516} \times X_6^{0.797} \times X_7^{0.240} \times X_8^{0.138} \times X_9^{-0.485} \times X_{10}^{0.070} \times X_{11}^{-0.212} \times X_{12}^{0.144} \times X_{13}^{-0.091} \times X_{14}^{-0.189} \times X_{15}^{-0.070} \times X_{16}^{0.552} \times X_{17}^{-1.344} \times X_{18}^{-0.213} \times X_{19}^{-0.565}$$

The above mathematical expression can be represented graphically as shown in the fig 1.4 given below;

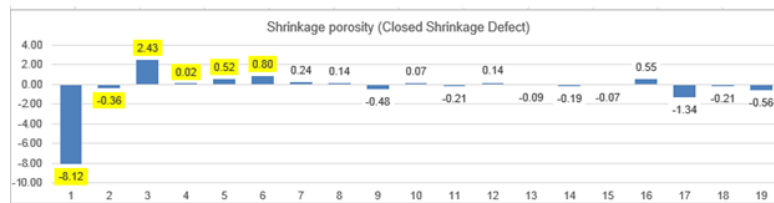


Figure 1.4: Influences of independent variables on shrinkage porosity defect (Y1)

Conclusion

In the occurrences of defect like shrinkage porosity, the most influential parameters among the selected parameters is value of carbon equivalent (CE) and pouring temperature, associated with the melting operation performed in the foundries. The gray cast irons with low value of carbon equivalent (CE) are more susceptible to defect under consideration. Because of low CE value, shrinkage porosity occurs due to an insufficient amount of low density graphite being precipitated and not providing an “expansion” effect to counter the natural solidification shrinkage [8]. The research outcomes will definitely helpful to foundry practitioners to take urgent actions to control the defects such as shrinkage porosity

References:

- [1] Krause, D.E. (1969) Gray Iron – A Unique Engineering Material. Gray, Ductile, and Malleable Iron Castings-Current Capabilities, pp.3–28, ASTM STP 455, American Society for Testing and Materials, Philadelphia.
- [2] American Foundrymen’s Society (AFS) (1966) Analysis of Casting Defects Handbook, 2nd ed., Des Plaines, Illinois.
- [3] ASM International Handbook Committee (1990) ASM Handbook on Casting, 2003, Vol. 15, pp. 1192–1199, ASM International, Materials Park, Ohio, USA.

- [4] Baier, J., Koppen, M. (1994). Manual of casting defects, IKO-Erbsloeh, Marl, Germany
- [5] Monroe, R. (2005) Porosity in Castings, AFS Transactions, Vol. 5, pp.1–28, American Foundry Society, Schaumburg, IL, USA.
- [6] Montgomery, D.C. and Runger, G.C. (2003) Applied Statistics and Probability for Engineers, 3rd ed., John Wiley & Sons Inc., New York.
- [7] Phadke, M.S. (2009) Quality Engineering Using Robust Design, pp.59–60, pp.151–152, Pearson, India.
- [8] Elmquist, L., Diószegi, A. and Björklind, T. (2011) ‘On the formation of shrinkage porosity in gray iron castings’, Key Engineering Materials, Vol. 457, pp.416–421.

Duplex Treatment of Nitriding and PVD coating – An Insight

¹V.K.Bupesh Raja, ²Abel J Francis, ³P D Jeyakumar,
⁴S.Premnath, ⁵Sathish Kannan, ⁶Dinesh. P, ⁷Sabari.C,
⁸D.Lohithanathan

¹*School of Mechanical Engineering,*
Sathyabama Institute of Science and Technology,
Chennai, India

²**Eltechnologies,**
Chennai, India

³*Department of Automobile Engineering,*
B S A Crescent Institute of Science and Technology,
Chennai, 600 048, India.

⁴*Department of Automobile Engineering,*
Sri Venkateswara College of Engineering,
Sriperumbudur, India

⁵**School of Engineering Architecture and Interior Design,**
Amity University, Dubai.

^{6,7,8}*School of Mechanical Engineering,*
Sathyabama Institute of Science and Technology,
Chennai, India

Abstract

This article examines the benefits of duplex surface treatment, which improves the performance of metal components, especially titanium alloys, by combining plasma nitriding and physical vapor deposition (PVD) coating. Plasma nitriding, a thermochemical process, introduces nitrogen into the surface to form hard, wear-resistant nitrides, improving hardness, roughness, friction, and corrosion resistance. PVD coating deposits thin film coatings, such as titanium nitride or chromium nitride, to further enhance surface hardness and reduce friction. The duplex treatment influences the strengths of both methods, resulting in superior surface properties, including improved wear resistance, corrosion protection, and extended component life. This approach is particularly advantageous in applications requiring enhanced wear resistance, corrosion protection, and extended component life, such as in aerospace, automotive, and tooling industries. The combined treatment has shown improved wear

resistance, load-bearing capacity, and fatigue resistance, making it a promising solution for various industrial products, especially in aerospace applications

Introduction

Since the late 1980s and early 1990s, there has been a great deal of study focused on the development of surface treatment (Chang et al., 1999). In a duplex procedure, chromizing and plasma nitriding were carried out.. (Chang et al., 1999).An important area of research has been surface treatment procedures for extending the lifespan of industrial tools and mechanical components. (fesahat et al., 2015). Surface modifications not only improve mechanical properties but also contribute to economic efficiency by prolonging the lifespan of components, reducing maintenance costs, and minimizing failure rates. . Through the thermochemical process of nitriding, nitrogen is added to a metal's surface to create hard nitrides that improve fatigue resistance and hardness. Improving corrosion resistance and tribological characteristics is a promising application of plasma nitriding (fesahat et al., 2015) Diffusion-based duplex surface treatments have been utilized recently to change a variety of surface properties, including wear, corrosion, and friction of ferrous components. (haftlang et al.,2014) The sequential application of two surface modification techniques, known as duplex treatment, is employed in surface engineering to produce a composite surface with integrated properties that are not achievable with either procedure alone. (marcado-solis et al., 2017). Duplex surface treatments have been widely used in tribological applications because of their low friction and appropriate balance of surface hardness, shear stress resistance, fracture toughness, and load bearing capacity.. (marcado-solis et al., 2017). A significant advantage of duplex-treated surfaces is their resilience to abrasive wear. However, because the particles of abrasive material may be even smaller and the PVD coating is only a few micrometers thick, (marcado-solis et al., 2017). Physical vapor deposition (PVD) and chemical vapor deposition (CVD) are two deposition processes commonly used in academic research. Additionally, thermoreactive deposition (TRD) and plasmanitriding (PN) are being used more and more in mass production to increase wear resistance. Research has also been conducted on surface treatment using multicoating techniques and multilayer formation to improve bonding strength and wear resistance. (park et al., 2018)In PN, nitrogen permeates the base material to form a high-hardness nitrided

layer that improves fatigue, corrosion, and wear resistance while offering better thermal stability and reducing base metal deformation. PN in particular offers lower costs, faster processing times, and pollution-free operation. PN enables one to control the nitride phase, unlike conventional nitriding. In general, nitriding worked well to increase the nitrogen content of the substrate surface for multicoating treatment.. (park et al., 2018). The nitrogen concentration of the base material was increased in this work using PN, and a Cr-carbonitride multilayer with exceptional hardness, corrosion resistance, and wear resistance was then created on high-carbon steel by TRD coating. The TRD procedure investigated the integrity of the coating layer, the diffusion behavior of the coating powder components with respect to temperature and time, and the formation behavior of multilayers. (park et al., 2018). The Duplex diffusion treatments make it easier and more efficient to alter the layers' chemical and phase composition, which also help to boost the strength of the layers' adherence to the substrate and decrease flaws like porosity. Making the right coating option could lead to notable performance gains(taktal et al., 2018). The purpose of this review is to provide comprehensive insights into the mechanisms, benefits, and applications of duplex treatments, specifically focusing on the combination of nitriding and PVD coating (hakami et al., 2015).

Surface Treatment Processes:

Nitriding

Nitriding is a surface hardening technique that enhances the qualities of steel and other materials by adding nitrogen to their surface. Surface diffusion, in which nitrogen atoms permeate the material's surface and create hard nitrides (like iron nitrides), is the basis for the nitriding process. Nitriding techniques have been a major surface treatment since the turn of the century. (Zagonel et al. 2006) where the required chemical and structural physical characteristics of the bulk qualities can be greatly customized by adding nitrogen to the steel's surface using plasma. (hakami et al., 2015). Since the turn of the century, nitriding procedures have been a significant surface treatment. (Zagonel et al. 2006).

The hardness dropped as the nitriding temperature was raised to 550 °C. It may have to do with the treated layer becoming thinner at higher temperatures. In order to create carbonitride, plasma nitriding was first carried out by adding nitrogen to the base material that had a high

carbon content. Figure 1a shows a cross-sectional SEM image of the PN specimen. The thickness of the produced nitride was around 10 μm ., and the coating layer's outermost surface showed the characteristic pore defect. The XRD pattern measured on the PN layer's surface is displayed in Figure 1b.(park et al., 2018) .

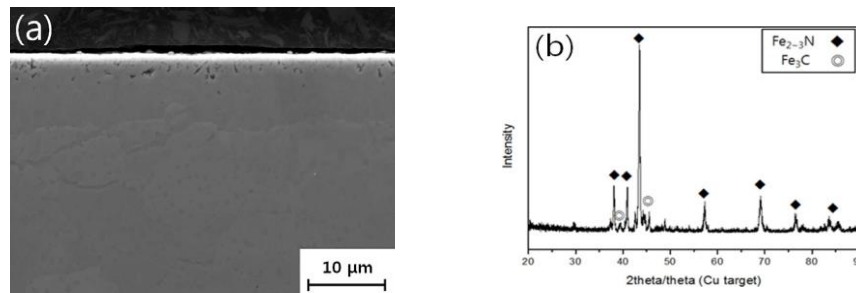


Figure 1. Microstructure of plasma-nitrided specimen: (a) cross-sectional view using SEM; and (b) surface measured using XRD pattern.

After nitriding treatment, a significant proportion of Cr and N can form a CrN compound, which can cause an uneven distribution of Cr. (ping el at., 2019).

Physical Vapour Deposition

Deposition techniques for surface modification do not use the contents of the substrate material; instead, they rely on applying a new substance as a coating to the surface. After being carried from a source metal, the coating material is applied to the substrate surface. A solid source (target) is physically converted into vapor using a variety of vacuum deposition techniques collectively referred to as "physical vapor deposition" (PVD). (gotman et al., 2017). PVD is a vacuum coating method in which a thin layer of material is placed onto the substrate after being vaporized from a solid or liquid source. involves ion bombardment of a target substance, which causes atoms to be dislodged and deposit on the substrate. The PVD sample had the usual appearance of TiN coatings: it was smooth, bright, and gold in color. As anticipated given their increased The plasma nitrided coatings were also golden in color, but they were not as bright or consistent as the PVD coatings due to surface roughness and mixed TiN/Ti₂N structure (Nolan et al., 2006).

Properties and Performance:

Wear Resistance

When titanium specimens' morphology and wear properties were examined, it was discovered that there were notable differences between untreated, plasma nitrided, and TiN-coated samples.. Untreated specimens showed deep ploughing and broad, rough wear tracks because of their decreased surface hardness, which led to significant plastic deformation and adhesive wear fig 2. In contrast, both plasma nitrided and TiN coated specimens exhibited narrower, shallower wear tracks with reduced roughness, indicating improved wear resistance fig 3. The wear rate was significantly lower for the treated specimens, with TiN coated samples showing the least volume loss. The friction coefficient decreased with plasma nitriding and was lowest for TiN coated samples, reflecting smoother interactions during wear testing. Despite having lower surface hardness, the TiN coated specimens benefited from greater coating thickness and density, contributing to their superior wear resistance. These findings challenge previous studies suggesting otherwise, highlighting the influence of different surface treatment techniques, in particular, how well closed-field unbalanced magnetron sputtering (CFUBMS) produces superior TiN films (yo tong et al., 2012).

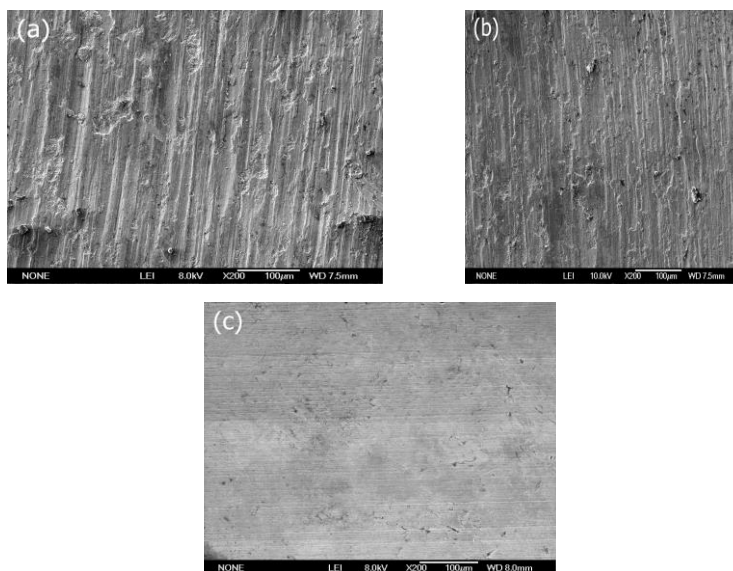


Figure 2 SEM micrographs of wear tracks: (a) TiN coated samples; (b) plasma nitrided samples; (c) untreated Ti

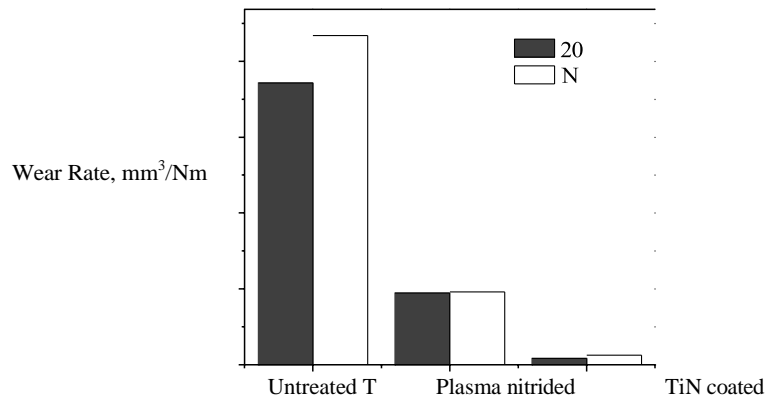


Figure 3 Wear rate of untreated, plasma nitrided and TiN coated samples

Corrosion Resistance

According to the results of corrosion tests, plasma nitriding and TRD (thermal reactive diffusion) treatments both considerably increase the steel samples' resistance to corrosion., as shown in Fig. 4. The current density and corrosion rates decreased with these treatments, particularly with increased plasma nitriding time, attributed to the formation of protective nitride phases, including chromium and iron nitrides. Duplex-treated samples (TRD followed by plasma nitriding) exhibited lower corrosion rates compared to single TRD coatings, indicating improved resistance due to a higher concentration of corrosion-resistant phases. SEM analysis of corroded surfaces revealed that TRD-coated samples showed more significant damage, probably as a result of the presence of carbide phases that are prone to corrosion and their grain boundaries. Plasma nitriding not only reduces residual stress but also enhances the protective coverage over grain boundaries, resulting in less damage in duplex-treated samples compared to those with only TRD coating. (fesahat et al., 2015)

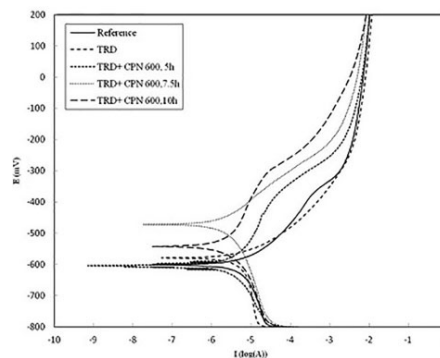


Figure 4 Polarisation curves of specimens

Hardness

The hardness of duplex-treated AISI 1045 steel increases through treatment stages, peaking at 1540 ± 20 HV0.1 at 550 °C. AISI 1020 shows a nitrided layer of 490 HV0.1, while duplex treatment achieves 1400–1500 HV0.1, generally exceeding chromized layers due to CrxN phase formation. figure 5. (hakami et al., 2015) Surface roughness also increases post-treatment (chang et al.,1999).The PN-Al duplex treated specimen achieves a surface hardness of 1284 ± 14 HV0.1, significantly higher than the untreated substrate's 283 HV0.1, due to the hard AlN phase. In contrast, Al-PN specimens show lower hardness from softer Fe4N, with differing hardness profiles attributed to nitrogen's affinity for aluminum. Fig 6 (haftlang et al., 2014). Microhardness, critical loads, and roughness of chromized and duplex-treated steels are shown in Table 1. TRD chromizing yielded microhardness values of approximately 1823 ± 24 and 1769 ± 35 HK0.025, while duplex-treated layers reached 2135 ± 56 and 1976 ± 45 HK0.025, likely due to CrxN phase presence enhancing hardness (taktak et al., 2008). The plasma nitriding increases surface roughness and significantly enhances microhardness in titanium, independent of initial roughness. This improvement results from various titanium nitrides forming a protective coating. AFM images in Figure 7 indicate that plasma nitriding creates a more uniform surface morphology, enhancing adhesion by increasing effective surface area... (fesahat et al., 2015).

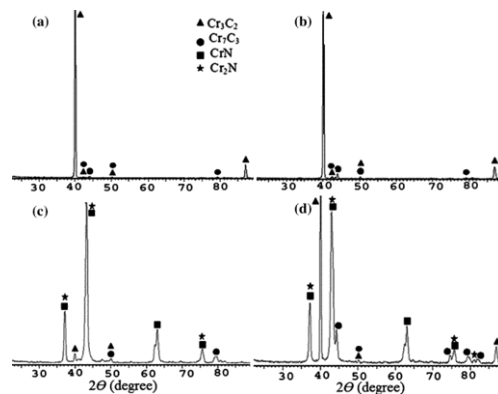


Figure 5. XRD patterns of TRD chromized (a) 52100, (b) 8620 steels and duplex treated (c) 52100, (d) 8620 steels (Taktak, Ulker, and Gunes 2008).

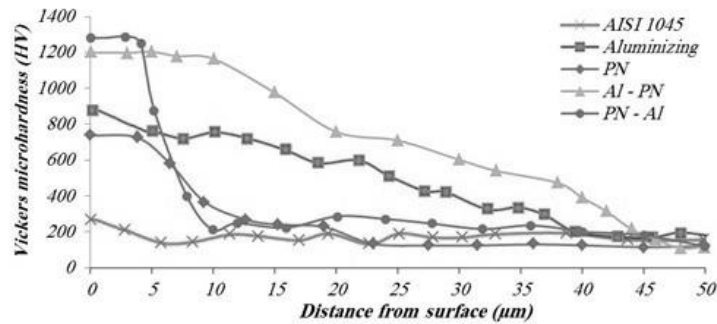


Figure 6

Table 1

Hardness, critical loads and surface roughness values of TRD chromized and duplex treated (TRD+plasma nitriding) AISI 52100 and 8620 steels

Samples	Microhardness, HK _{0.025}	Critical load, N		Surface Roughness, Ra (μm)
		L _{C1} (AE)	L _{C2} (Ft)	
Chromized 52100	1823±24	11.7	76.3	0.42±0.04
Duplex treated 52100	2135±56	29.4	81	0.634±0.1
Chromized 8620	1769±35	21.2	71	0.415±0.06
Duplex treated 8620	1976±45	22	73.8	0.612±0.08

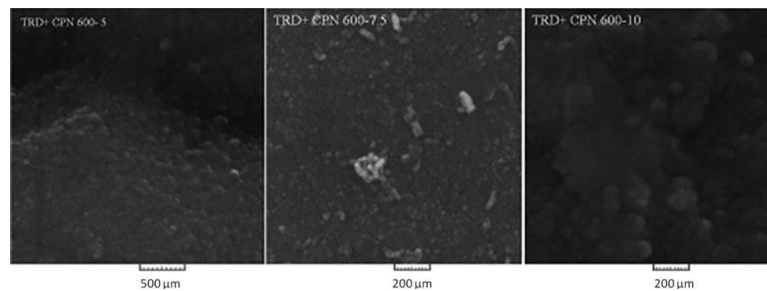


Figure 7 Secondary electron images (SEM) with high magnification of surface of TRD and CPN at 600°C for *a* 5 h, *b* 7.5 h and *c* 10 h

Applications:

1. **Cell-Free Massive MIMO Systems:** In order to increase spectral and energy efficiency, access point configuration and power allocation are optimized for FD communication in a cell-

free massive MIMO system that uses half-duplex devices for uplink and downlink operations.

2. **Multicell Networks:** Discussing power distribution and resource block scheduling in FD multicell networks, emphasizing intercell collaboration to improve performance above conventional single-cell models.
3. **Multi-Band MAC Protocol:** To improve spectral efficiency, a multi-band FD MAC protocol is being proposed for infrastructure-based networks. It uses sub-6 GHz for control and 60 GHz for data.
4. **Fluid-Antenna-Aided Networks:** Using stochastic geometry to analyze large-scale FD cellular networks, considering channel estimation errors and providing expressions for outage probability and average sum-rate performance.
5. **High-Power FD in mmWave IAB::** Designing a high-power FD prototype for mmWave integrated access/backhaul, mitigating self-interference with a corrugated surface for improved system throughput.
6. **Integrated Sensing and Communications (ISAC):** Employing FD ISAC transceivers to maximize communication rates and suppress interference, facilitating simultaneous radar and communication functions.
7. **Jamceiver Technology:** Developing a FD jammer-receiver ("jamceiver") that interferes with incoming signals while receiving them, using frequency-sweeping techniques for self-interference suppression.
8. **Security Applications:** For in-band FD MIMO systems, PHY-based secret key generation techniques are being studied, defects are being addressed, and expressions for secret key capacity against eavesdropping are being derived.
9. **Quantum Communication:** Proposing FD quantum communication protocols for simultaneous information exchange without physical particle transfer, utilizing advanced quantum coding techniques.
10. **Mixed Reality Technology:** Offering an AI-generated contract design to encourage information sharing, examining the consequences of wireless fading and self-interference, and presenting an FD semantic communication framework that improves information sharing (Besma Smida et al., 2023)

Conclusion:

In summary, duplex surface treatment techniques, including physical vapor deposition and nitriding (PVD), have significantly advanced surface engineering by enhancing hardness, wear resistance, and corrosion protection. These methods create composite surfaces that meet the rigorous demands of industrial applications. The synergy between nitriding, which builds a strong nitrided layer, and PVD coatings, which add wear-resistant, dense films, optimizes the durability and longevity of mechanical components. Duplex treatments are essential for applications requiring high-performance materials capable of withstanding mechanical stress and harsh environments, underscoring the importance of continued innovation and application in surface treatment technologies.

References :

- Fesahat, M., Soltanieh, M., & Eivani, A. R. (2015). Effect of plasma nitriding on nanostructure of TRD coating. *Surface Engineering*, 32(8), 547–553. <https://doi.org/10.1179/1743294415Y.0000000094>
- Gotman, I., Gutmanas, E. Y., & Hunter, G. (2017). Wear-resistant ceramic films and coatings. In *Comprehensive Biomaterials II* (pp. 165–203). Elsevier. <https://doi.org/10.1016/B978-0-12-803581-8.09795-2>
- Haftlang, F., Habibolahzadeh, A., & Sohi, M. H. (2014). Comparative tribological studies of duplex surface treated AISI 1045 steels fabricated by combinations of plasma nitriding and aluminizing. *Materials and Design*, 60, 580–586. <https://doi.org/10.1016/j.matdes.2014.04.026>
- Hakami, F., Pramanik, A., & Basak, A. K. (2015). Duplex surface treatment of steels by nitriding and chromizing. *Australian Journal of Mechanical Engineering*, 15(1), 55–72. <https://doi.org/10.1080/14484846.2015.1093256>
- Mercado-Solis, R. D., Mata-Maldonado, J. G., Quinones-Salinas, M. A., Rodriguez-De-Anda, E., & Servín-Castañeda, R. (2017). Micro-scale abrasive wear testing of CrN duplex PVD coating on pre-nitrided tool steel. *Materials Research*, 20(4), 1092–1102. <https://doi.org/10.1590/1980-5373-MR-2016-0757>
- Nolan, D., Huang, S. W., Leskovsek, V., & Braun, S. (2006). Sliding wear of titanium nitride thin films deposited on Ti-6Al-4V alloy by PVD and plasma nitriding processes. *Surface and Coatings*

- Technology*, 200(20–21), 5698–5705.
<https://doi.org/10.1016/j.surfcoat.2005.08.110>
- Park, K., Kim, J. H., Kim, S., & Kang, N. (2018). Multilayer-forming behavior of Cr nitrides and carbides for thermoreactive deposition. *Metals*, 8(6). <https://doi.org/10.3390/met8060400>
- Ping, J., Cui, X., Pu, J., Jiang, X., Zhang, X., & Zhong, Y. (2020). Structural, tribological and corrosion properties of plasma nitrided-chromized-316L stainless steel in air and artificial seawater. *Surface Topography: Metrology and Properties*, 8(1). <https://doi.org/10.1088/2051-672X/ab6438>
- Taktak, S., Ulker, S., & Gunes, I. (2008). High temperature wear and friction properties of duplex surface treated bearing steels. *Surface and Coatings Technology*, 202(14), 3367–3377. <https://doi.org/10.1016/j.surfcoat.2007.12.015>
- Tong, Y., Guo, T. W., Wang, J., Liang, H. F., & Mi, Q. (2013). A comparative study: Effects of two different surface engineering technologies on tribological properties of pure titanium. *Advanced Materials Research*, 602–604, 1646–1651. <https://doi.org/10.4028/www.scientific.net/AMR.602-604.1646>
- Yon Chang, D., Yul Lee, S., & Kang, S.-G. (1999). Effect of plasma nitriding on the surface properties of the chromium diffusion coating layer in iron-base alloys. In *Surface and Coatings Technology* (Vol. 116). www.elsevier.nl/locate/surfcoat
- Smida, B., Sabharwal, A., Fodor, G., Alexandropoulos, G. C., Suraweera, H. A., & Chae, C. B. (2023). Guest Editorial Full Duplex and its Applications. In *IEEE Journal on Selected Areas in Communications* (Vol. 41, Issue 9, pp. 2725–2728). Institute of Electrical and Electronics Engineers Inc. <https://doi.org/10.1109/JSAC.2023.3292659>
- Zagonel, L. F.; Figueroa, C. A.; Droppa, R.; Alvarez, F. Influence of the Process Temperature on the Steel Microstructure and Hardening in Pulsed Plasma Nitriding. *Surf. Coat. Technol.* 2006, 201 (1–2), 452–457. <https://doi.org/10.1016/j.surfcoat.2005.11.137>.

Diamond-Like Carbon Coating – Tribological Applications

¹V.K.Bupesh Raja, ²Abel J Francis, ³K.Duraivelu,
⁴S.Premnath, ⁵Sathish Kannan, ⁶D.Lohithanathan,
⁷Sabari.C, ⁸Dinesh. P

¹*School of Mechanical Engineering,*
Sathyabama Institute of Science and Technology,
Chennai, India

²**Eltechnologies,**
Chennai, India

³*Department of Mechanical Engineering,*
SRM Institute of Science and Technology,
Kattankulathur, Chennai, India

⁴*Department of Automobile Engineering,*
Sri Venkateswara College of Engineering,
Sriperumbudur, India

⁵**School of Engineering Architecture and Interior Design,**
Amity University, Dubai.

^{6,7,8}*School of Mechanical Engineering,*
Sathyabama Institute of Science and Technology,
Chennai, India

Abstract

Diamond-like carbon (DLC) coatings are a metastable form of amorphous carbon with unique properties, including excessive mechanical hardness, chemical inertness, optical transparency, low friction coefficients, high wear resistance, and biocompatibility. DLC coatings can be deposited on various substances using techniques such as Plasma-enhanced chemical vapor deposition (PECVD) and Pulsed laser deposition (PLD), and their properties can be tailored by incorporating elements like nitrogen, hydrogen, silicon, and metals, which have an effect on their hardness, residual strain, and tribological properties. They have been successfully used in various industrial applications, including tribology, optics, electronics, automotive, biomedical, and aerospace, and have shown promising results in reducing abrasion and wear. However, their performance can be affected by factors like lipids, immune cells, and environmental factors, and can be improved by doping, controlling deposition

conditions, and surface modification. DLC coatings are self-lubricating, resistant to erosion, abrasion, and corrosive wear, and offer promising solutions for demanding medical applications.

Introduction

One of the most prevalent and adaptable elements on Earth, carbon serves as the building block for a variety of materials, ranging from soft ones like graphite and polymers to very hard ones like diamonds and carbides. (Erdermir A et al., 2006).

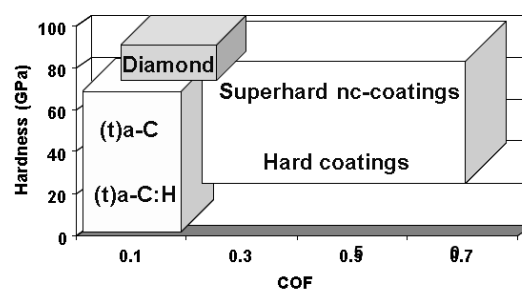


Figure 1. An illustration of the coefficients of friction (COF) and hardness of carbon-based and other hard coatings.

Diamond-like carbon (DLC) coatings have garnered a lot of attention because of their exceptional tribological qualities, which include minimal friction, high heat conductivity, and superhardness. (Erdermir A et al., 2006). Carbon atoms are organized in sp^2 (graphite-like) and sp^3 (diamond-like) links in DLC coatings; the sp^3 presence gives the coating its hardness and resistance to wear, while the sp^2 structure adds flexibility and conductivity. (Al Mahmud et al., 2014). Silicon, titanium, and tungsten are among the elements that can be doped into the coatings to improve their adhesion, wear resistance, and frictional qualities. (Al Mahmud K et al., 2014). There are many opportunities for creating cutting-edge tribological technologies and applications thanks to the discovery of new carbon modifications like fullerenes and graphenes as well as the utilization of carbon-based composite materials and coatings. (Erdermir A et al., 2006; Levchenko V et al., 2019).

There are two types of DLC coatings: hydrogenated and non-hydrogenated. Hydrogenated DLC coatings are very useful in applications that need low friction because they passivate dangling carbon bonds with hydrogen, which lowers friction. (Levchenko V et al., 2019; Al Mahmud et al., 2014). Because of their adaptability, DLC coatings can be used in a range of difficult situations, such as

corrosive, high-temperature, and high-load settings. By lowering the coefficient of friction (CoF), their capacity to create protective transfer layers during wear improves their tribological performance even further. (Al Mahmud et al., 2014). Interestingly, current research shows that DLC coatings are successful in lubricated environments as well, even though the vast majority of studies concentrate on their tribological behavior in dry conditions. (Levchenko V et al., 2019; Al Mahmud et al., 2014). These include studies that demonstrate DLC coatings' strong applicability across a range of sectors by demonstrating their great antiwear and antifriction performance even when lubricants are present. (Levchenko V et al., 2019).

In the automotive sector, DLC coatings are frequently utilized to lower frictional losses in parts like gears, piston rings, and valve trains, greatly enhancing durability and fuel efficiency. (Zahid R et al., 2015). In the biomedical field, DLC coatings provide biocompatibility and wear resistance in medical devices like stents and prosthetics (Levchenko V et al., 2019). Furthermore, DLC coatings are employed in space technology and microelectromechanical systems (MEMS), where long-term durability, low friction, and resistance to extreme environmental conditions are crucial (Levchenko V et al., 2019; Al Mahmud et al., 2014). Their effectiveness under both dry and lubricated conditions has broadened their use, making them an ideal solution for reducing wear and extending the life of critical mechanical systems. The potential uses of DLC coatings are anticipated to grow even more as studies into their tribological behavior in diverse settings continue. (Zahid R et al., 2015).

Classification of DLC Coatings

Different carbon-based materials are depicted in this ternary phase diagram according to their hydrogen concentration, sp^2 (graphitic), and sp^3 (diamond-like) bonding. Materials such as diamond, amorphous carbon (a-C), and hydrogenated a-C (a-CH) are highlighted, demonstrating how their characteristics change depending on bonding and hydrogen levels. (Figure.2)

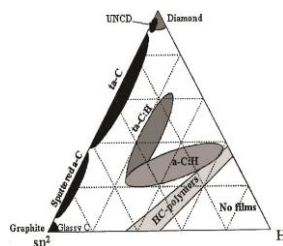


Figure 2 Ternary phase diagram for carbon films.

There are two types of DLC (Diamond-Like Carbon) coatings: doped and non-doped. Doped DLCs can be further classified as non-metal-doped (silicon, fluorine) or metal-doped (titanium, tungsten). Electrical conductivity, wear resistance, surface energy, and adhesion are all enhanced by doping. Non-doped DLCs can be either non-hydrogenated (a-C, ta-C) or hydrogenated (a-C, ta-C). Hydrogenation improves mechanical and chemical properties, decreases reactivity, and passivates dangling carbon bonds, which increases stability.

Multilayer DLC coatings improve load distribution and increase the coating's longevity under extreme stress by alternating between various DLC types (such as a-C/W-DLC). Tribological performance is further improved by surface texturing using methods like ion beam etching or laser machining, which trap wear debris and preserve lubrication. (Kim D W et al.,2014;Kim D W et al.,2013)

For DLC coatings to function well over time, strong substrate adherence is essential. (Ronkainen H et al.,1999).This is often achieved by using interlayers such as chromium or titanium nitride, which promote bonding and evenly distribute mechanical loads, preventing delamination. Pre-treatments like plasma nitriding or surface roughening further enhance adhesion, ensuring the coating's durability even in harsh conditions.

Hydrogen's Effect on DLC Coating

When it comes to the tribological behavior of DLC coatings in various settings, hydrogen inclusion is essential..This Fig represents the atomic structure of Hydrogenated DLC films.According to Erdemir, hydrogenated DLC exhibits lower friction (CoF) in inert environments compared to non-hydrogenated DLC. However, in air-exposed conditions, non-hydrogenated DLC shows a significant reduction in friction, while hydrogenated DLC sees an increase. Environmental elements like water and oxygen strongly influence the frictional properties of these coatings. In dry environments, forces such as van der Waals interactions, covalent bonds, and p-p* interactions dominate, whereas capillary forces play a minimal role. Hydrogen in hydrogenated DLC passivates unbound σ -bonds, lowering surface energy and reducing friction. This continuous passivation, aided by hydrogen atoms embedded in the DLC matrix, prevents cross-linking and reduces p-p* interactions, minimizing friction.(Erdemir A et al., 2006;Al Mahmud K et al.,2014;Erdemir A et al., 2002)

Di-hydrated carbon atoms, which improve surface shielding and increase superlubricity, are frequently included in hydrogenated DLC. Non-hydrogenated DLC, on the other hand, contains more dangling

carbon bonds that, under air-exposed conditions, can be passivated by environmental species like oxygen and water. However, these bonds do not passivate in inert environments, which increases friction because there are more unbound bonds and p–p* interactions present.(Erdermir A et al., 2006; Al Mahmud K et al.,2014;Erdermir et al., 2002).The graph displays the hydrogenated DLC's wear and friction characteristics under testing conditions in a dry hydrogen atmosphere.(Figure.3)

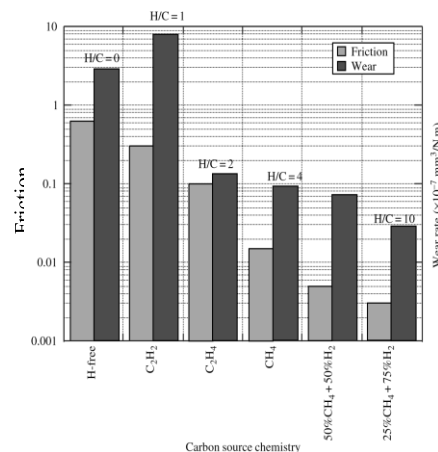


Figure.3 Wear and friction coefficients in dry nitrogen of DLC films made from diverse carbon sources with varied ratios of hydrogen to carbon (H/C)

Effect of sp³/sp² Ratio

The ratio of sp² (graphite-like) to sp³ (diamond-like) carbon bonds largely determines the structure of DLC coatings.(Neuville S et al.,2007;Kim D W et al.,2014)Like diamonds, tetrahedral carbon is represented by the sp³ bonds, which offer superior wear resistance, high hardness, and chemical inertness.(Donnet C et al., 2001; Neuville S et al.,2007).High sp³ DLC coatings, including tetrahedral amorphous carbon (ta-C), which has an 80–88% sp³ concentration, are very hard and perfect for applications that need strength and longevity.(Donnet C et al., 2001; Grill A et al.,1999).In contrast, sp² bonds are planar and are found in graphite, contributing to electrical conductivity and lower hardness (Grill A et al.,1999). Coatings with high sp² content, like amorphous carbon (a-C), with just 5% sp³ content, are softer and more flexible, making them suitable for applications prioritizing flexibility and conductivity (Sullivan J et al.,2001).The tribological performance of hydrogenated variants, such ta-C and a-C, is influenced by hydrogen and has an sp³ concentration

of 70% and 40%, respectively. Additionally, Robertson pointed out that a-C coatings can be divided into two categories according to the amount of hydrogen they contain: hard a-C coatings have 30–40% hydrogen, whereas soft (polymeric) a-C coatings have 40–50%. (Kim D W et al.,2014). While higher sp^3 content correlates with greater hardness, soft a-C, despite its sp^3 content, exhibits lower hardness due to the increased hydrogen levels (Kim D W et al.,2014). It was found that a-C is more prone to graphitization under friction-induced heat, as hydrogen depletion in a-C facilitates the transition to a graphitic structure. (Ronkainen H et al.,2001) In contrast, ta-C remains thermally stable, reducing graphitization and wear, making it more resistant under similar conditions. Additionally, a-C experiences more pronounced electrostatic repulsive forces, aiding in layer slippage during contact. (Kim D W et al.,2014).

Deposition Techniques

The creation of sp^3 bonds from sp^2 -bonded carbon atoms is the main mechanism used in the intricate process of deposition of diamond-like carbon (DLC) films. These films are appropriate for demanding applications due to their remarkable mechanical, thermal, and chemical properties. Physical vapor deposition (PVD) and chemical vapor deposition (CVD) procedures are the two main categories into which DLC deposition methods can be divided.

PVD methods, including plasma vapor deposition, involve the condensation of vapor in a high vacuum, where atoms are deposited onto a substrate. Techniques such as evaporation, sputtering, and ion plating are common, but their line-of-sight nature can pose challenges for uniform coating on complex geometries. CVD methods operate at higher temperatures (800–1000°C) and involve thermochemical reactions that deposit uniform coatings with excellent hardness and adhesion. However, they require careful temperature management to avoid thermal stresses and coating delamination (S. V. Hainsworth et al.,2007; Al Mahmud et al.,2015). The range of suitable substrates is increased by Plasma-Enhanced Chemical Vapor Deposition (PECVD), which enables deposition at lower substrate temperatures. (S. V. Hainsworth et al.,2007).

The formation of sp^3 bonds in DLC films is critically influenced by the energy of bombarding ions, which typically range from 20 to 500 eV. Researchers have explored various ion sources and their configurations to maximize sp^3 bonding and deposition rates. For instance, the

Kaufmann ion source, using thermionic cathodes and a magnetic field, enables high ionization rates, while cathodic arc sources can further enhance deposition rates by creating highly ionized thermal plasma(John Robertson et al.,1991). The methods differ in their efficiency, with cascade arc sources and mass spectrometry ion beam (MSIB) techniques yielding high purity and film quality(John Robertson et al.,1991; Erdemir et al.,2005)

In addition to traditional methods, modern techniques such as PACVD combine advantages from both PVD and CVD processes. These methods allow for low-temperature deposition, accommodating substrates that might be sensitive to high heat(Al Mahmud et al.,2015). Moreover, the deposition gas composition significantly affects the resulting DLC properties. For instance, the hydrogen content in the films is influenced by self-bias voltage and feed gas ratios, impacting tribological behavior(Erdemir et al.,2005). Alloying DLC with elements like silicon, titanium, and tungsten further modifies its mechanical properties, enhancing hardness and wear resistance(Hauert R et al.,2004).

Recent advancements in deposition technologies have focused on achieving smoother and less abrasive films, critical for applications requiring minimal friction and wear. Techniques like laser polishing and the use of modified gas mixtures in CVD have led to smoother nanocrystalline diamond films, characterized by fine grain sizes and reduced roughness(Erdemir et al.,2005). The microstructure of the films, including the presence of non-diamond phases, is vital for their performance in industrial applications.

In conclusion, a range of methods are used in the deposition of DLC films, which affects their tribological and structural characteristics. Optimizing DLC films for a variety of applications requires an understanding of how deposition parameters, such as ion energy, gas composition, and substrate conditions, interact.(Wilfred Mbiombi Mpingi et al.,2014; Hauert R et al.,2004). The ongoing development of these techniques has the potential to advance the real-world industrial uses of DLC coatings.

Tribological Behaviour

The various forms of DLC present cause a wide variety of variations in the tribological characteristics. Researchers also found that the chemical parameters of the test environment, including partial

pressures of hydrogen or oxygen, vacuum or inert gases, and relative humidity, can significantly affect how diamond films wear and friction. The friction and wear rate are also affected by the presence of different gasses and lubricants. Fig 3, portrays different tribo-testing which can be performed in different environments. We can obtain different values as per material being tested and the environment it is performed

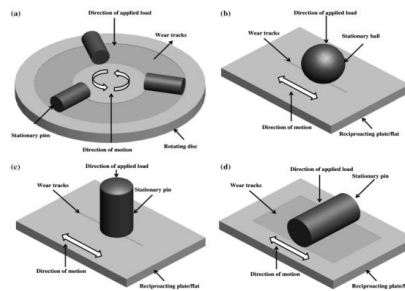


Figure 4 A pin-on-disk, b ball-on-plate, c pin-on-plate (vertical), and d pin-on-plate (horizontal) are the most used geometric configurations for tribo-testing.

The friction and wear behavior of both hydrogenated and hydrogen-free DLC films are strongly influenced by the test environment's composition. Highly hydrogenated DLC sheets can slide against itself with friction coefficients as low as 0.003 in dry air and inert gases. A transfer layer that developed on a steel ball during a sliding test in dry nitrogen is depicted in Figure 5.



Figure 5 On a steel ball, a typical transfer layer generated during a sliding test in dry nitrogen (magnification: 50X).

When sliding against themselves or other counterface materials, such as metals and ceramics, the friction coefficient can rise to 0.15 in humid air. Reactive gases like oxygen and water can also increase friction coefficients in a vacuum. Humidity is ideal for the performance of hydrogen-free DLC. DLC films can be made less

sensitive to humidity by including components like silicon, nitrogen, or fluorine. With a coefficient of 0.06 for a DLC/steel pair, Paulmier et al. discovered that atomic hydrogen reduces friction the most effectively, but molecular hydrogen and air enhanced it. The impact of humidity on hydrogen-free and hydrogenated DLC films is depicted in Figure 6. (Erdemir A et al.,2005)

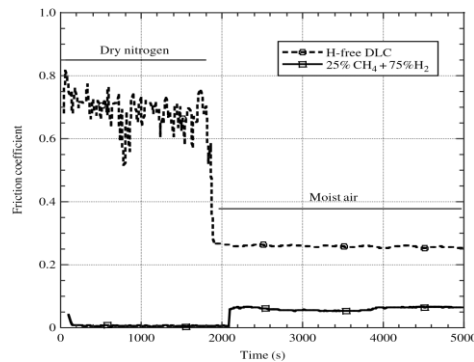


Figure.6 Impact of humid air on the friction coefficient of DLC films that are hydrogenated and those that are not (Erdemir et al.,2005)

According to the still data, the DLC film's friction ranges from 0.001-0.7, which is among the widest variations among the coatings and other materials. (Erdemir et al.,2000; Erdemir et al.,2002) regarding the resistance to wear Certain DLC coatings are quite hard and resistant to wear, whereas other DLC coatings are fragile and readily scratched. The wide variety and variations in the material's wear and friction characteristics rely on the particular film characteristics, the surrounding circumstances, etc. The chemical makeup and structural features of these films have a major impact on their wear and friction behaviors.

In air, dry inert gases, and at moderate temperatures, diamond shows very little wear and friction; in vacuum or at high temperatures, however, wear and friction greatly increase.(Miyoshi K et al.,1993;Chandrasekar S et al.,1992). Researchers have employed appropriate counterface materials like cubic boron nitride and surface engineering techniques like ion implantation to lower friction in vacuum.(Miyoshi K et al.,1999). The high chemical passivity of the diamond's sliding surface, where gaseous adsorbates like oxygen or hydrogen passivate free σ -bonds, reduces adhesion, and achieves smoother sliding, is responsible for this low friction.

Natural and smooth diamond films are self-lubricating mostly because of their high chemical passivity, which allows gaseous adsorbates like

oxygen or hydrogen to passivate free σ -bonds and reduce friction. However, diamond films may experience phase change and frequently generate a graphitic layer when subjected to significant mechanical and thermal loads. This graphitic phase may function as a lubricating coating in moist air or as a source of friction spikes in vacuum or inert gases. The friction and wear performance of diamond films can be greatly impacted by oxidation or graphite transformation at high temperatures. (Erdemir A et al., 2005).

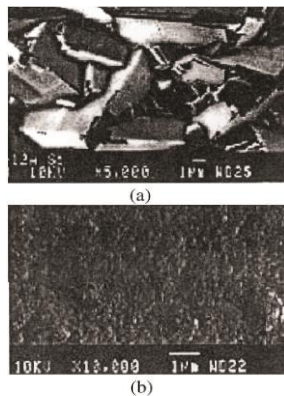


Figure 7 Surface morphology of (a) microcrystalline (rough) and (b) smooth nanocrystalline diamond films

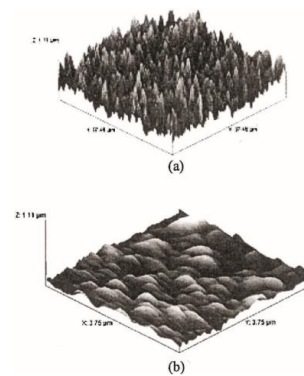


Figure 8 Diamond film AFM pictures of (a) rough and (b) smooth

Depending on their grain size, orientation, and surface morphology, they can seriously wear down mating surfaces. Surface morphology also affects tribo characteristics. A diamond film's surface shape with a microcrystalline and nanocrystalline grain structure is depicted in Figure 7. Atomic force microscopy (AFM) measurements of these films' related surface roughness are shown in Fig. 8. (Erdemir A et al., 2005)

Lubrication

DLC coatings' superior tribological qualities make them popular in high-friction settings, such as engine parts. By forming a barrier between the surface and harsh surroundings, lubricants are essential in shielding these coatings from wear and high temperatures. However, there can be differences in how DLC coatings and lubricants interact, particularly when non-ferrous materials are involved. When additives like MoDTC and ZDDP are present, metal carbides occur, which

lessen wear and friction and improve tribofilm formation and strength in metal-doped DLC coatings like tungsten-doped (W-DLC). These interactions are influenced by surface energy and hydrogen content; hydrogenated DLC (a-C) exhibits less reactivity to additives than non-hydrogenated DLC (a-C), where tribofilms develop more readily. Studies reveal that sunflower oil's unsaturated molecules perform better than mineral (Al Mahmud K et al., 2014)

DLC–Extreme Pressure (EP) Additive Interaction

EP additives are lubricant additives that lessen engine component wear under high pressure. There may be interactions between EP additives and coatings when DLC-coated components are subjected to such pressures. Metal-doped DLCs exhibit greater interaction due to their higher surface energy, whereas non-doped DLCs are often inert. In their study of metal-doped (Ti, WC) and non-doped DLC with EP additives, Kalin et al. discovered that although the oil additives lessen wear, friction largely stays the same. Because of a viscous tribofilm, additives for non-doped DLC improve friction while decreasing wear because the film shields the surface. Metal-doped DLCs show higher reactivity, with Ti-doped coatings forming more phosphorus-rich tribofilms and oxides like TiO₂ due to high frictional heat. As temperature rises, EP additives become more effective, reducing wear by up to 65% at 150°C. WC-doped DLC coatings also demonstrate increasing tribofilm thickness over time, reducing wear during steady-state conditions (Al Mahmud K et al., 2014; M Kalin et al., 2006).

Relative Humidity

The relative humidity has a significant impact on the tribological behavior of DLC coatings. Lower humidity reduces the coefficient of friction (CoF) for hydrogenated DLC (a-C), whereas higher humidity causes oxidation and the creation of carboxylic acid, which increases friction. However, humidity helps non-hydrogenated DLC (a-C) since it reduces CoF by acting as a lubricant. Water molecules can improve sliding between layers and lessen van der Waals forces. Humidity intercalates between layers in ta-C films, reducing CoF. (Al Mahmud K et al., 2014)

Temperature

DLC coatings are greatly affected by temperature, with CoF often increasing as temperatures rise as a result of water evaporation. Higher temperatures (over 250°C) cause hydrogenated DLC to undergo a phase transition from sp³ to sp², creating graphite, which lowers CoF and functions as a solid lubricant. Higher temperatures, however, do not affect the stability of non-hydrogenated DLC. By increasing the

graphitization temperature, silicon doping can improve thermal stability. DLC film oxidation, which affects wear and friction, usually happens at temperatures higher than 350°C.(Al Mahmud K et al.,2014)

Application

Diamond-like Carbon (DLC) coatings have found widespread use in many different industries because of its special qualities, which include reduced friction, remarkable wear resistance, and biocompatibility. An overview of important applications across several industries can be found below.

1. Automotive Applications

In the automotive sector, DLC coatings are used on components like piston pins and rocker arms, where they effectively reduce friction and wear. Their hard and chemically resistant nature protects metal surfaces from scratching and degradation. Research indicates that DLC coatings significantly improve the lifespan of moving parts in engines, thus enhancing overall vehicle performance (Enke K et al.,1980; Naresh Chand et al.,2024)

2. Medical Applications

DLC coatings are increasingly recognized for their suitability in medical applications. Their excellent mechanical properties and biocompatibility make them ideal for surgical tools and prosthetic devices. DLC has shown remarkable bio-similarity, which allows for tissue adherence and a robust interface between implants and biological tissue. Additionally, these coatings prevent blood clot formation, making them advantageous for implants in contact with blood.(Jenkins G M et al.,1977;Naresh Chand et al.,2024)

3. Industrial Parts and Machinery

DLC coatings are widely employed in various industrial applications, including pistons, gears, and mechanical seals. Their ability to withstand high operational temperatures while maintaining low friction is beneficial in environments where traditional coatings might fail. Studies have shown that DLC significantly reduces wear rates in machinery, improving the efficiency and longevity of industrial components.(Hlin M et al.,2001;Naresh Chand et al.,2024)

4. Injection Molding

In the field of injection molding, DLC coatings are applied to dies and ejector pins. These coatings provide enhanced lubricity, which aids in the smooth operation of machinery and extends the life of the molds. The reduced friction results in lower energy consumption during the

injection process, making it an economically favorable choice for manufacturers.(Naresh Chand et al.,2024)

5. Optical Applications

DLC coatings have also been explored in optical applications, such as front surface mirrors for optical devices. However, challenges remain, such as limitations in spectral performance for specific thermal imaging systems. The thin coatings have been found to work effectively only in certain polarization directions, necessitating further development for broader applications.(Cox J T et al.,1975; Naresh Chand et al.,2024)

6. Photothermal Conversion of Solar Energy

DLC coatings contribute to photothermal solar energy conversion, primarily in solar collectors. Their ability to withstand high temperatures enhances the efficiency of solar energy systems. Focusing collectors, which can reach higher operational temperatures, benefit significantly from the protective properties of DLC, minimizing thermal losses.(Naresh Chand et al.,2024)

7. Electronic Devices

DLC films have been investigated for their potential use in electronic devices, serving both as active and passive elements. They have been incorporated into electroluminescent devices and metal-insulator-semiconductor (MIS) structures. Although some initial findings showed limitations due to resistivity issues, ongoing research continues to explore their capabilities in semiconductor applications.(Kim S B et al.,1990;Kapoor V J et al.,1986;Naresh Chand et al.,2024)

8. Tribological Applications

DLC coatings have demonstrated considerable success in tribological applications, including ball bearings and shaving products. Their low friction coefficients enhance performance in these settings, leading to extended lifespans for components like razor blades and improved efficiency in mechanical systems. .(Hlin M et al.,2001;Naresh Chand et al.,2024)

9. Additional Applications

DLC coatings' adaptability also extends to consumer goods where durability and visual appeal are crucial, such as jewelry and watches. The inclusion of other elements, such as silicon, hydrogen, and nitrogen, which affect hardness and residual stress levels, is being researched to improve their qualities. The adhesion qualities of DLC coatings have

improved thanks to the innovative manufacturing of DLC coatings for automotive applications that included PECVD and nanoparticles (WO₃/MoO₃). Overall, because of their many uses, DLC coatings are becoming more popular in a variety of industries. The knowledge of the variables influencing DLC properties and how they are incorporated into different applications will increase as research progresses, opening the door for creative solutions in a wide range of industries. DLC coatings' potential to improve functionality, robustness, and (Kolawole F O et al., 2020; Naresh Chand et al., 2024)

Conclusion

In conclusion, because of their distinct tribological characteristics, diamond-like carbon (DLC) coatings demonstrate exceptional adaptability and efficacy in a wide range of applications. The coatings are ideal for challenging situations because of their hardness, minimal friction, and resistance to wear. The difference between hydrogenated and non-hydrogenated forms is important since their performance is greatly influenced by environmental conditions like temperature and humidity. The mechanical properties of DLC coatings have been improved by developments in deposition processes, such as doping and multilayer designs, which have made it possible to integrate them into the automotive, biomedical, industrial, and electronic industries. DLC coatings are positioned to satisfy changing industrial needs by providing improved durability, efficiency, and environmental resilience as research into these materials progresses.

References

- Al Mahmud, K. A. H.; Kalam, M. A.; Masjuki, H. H.; Mobarak, H. M.; Zulkifli, N. W. M. An Updated Overview of Diamond-Like Carbon Coating in Tribology. *Crit. Rev. Solid State Mater. Sci.* 2015, 40 (2), 90–118. <https://doi.org/10.1080/10408436.2014.940441>.
- Erdemir, A. Friction and Wear of Diamond and Diamond-Like Carbon Films. *Proc. Inst. Mech. Eng., Part J: J. Eng. Tribol.* 2002, 216 (6), 387–400. <https://doi.org/10.1243/135065002762355316>.
- Erdemir, A.; Donnet, C. Tribology of Diamond and Diamond-Like Carbon Films: An Overview. 2005.
- Erdemir, A., & Donnet, C. (2006). Tribology of diamond-like carbon films: Recent progress and future prospects. In *Journal of Physics D: Applied Physics* (Vol. 39, Issue 18). <https://doi.org/10.1088/0022-3727/39/18/R01>

- Hainsworth, S. V.; Uhure, N. J. Diamond-Like Carbon Coatings for Tribology: Production Techniques, Characterisation Methods, and Applications. *Int. Mater. Rev.* 2007, 52 (3), 153–174. DOI: 10.1179/174328007X160272.
- Hauert, R. An Overview on the Tribological Behavior of Diamond-Like Carbon in Technical and Medical Applications. *Tribol. Int.* 2004, 37 (11-12 SPEC. ISS.), 991–1003. DOI: 10.1016/j.triboint.2004.07.017.
- Levchenko, V. A.; Buyanovskii, I. A.; Bol'shakov, A. N.; Matveenkov, V. N. Green Tribology: Orientation Properties of Diamond-Like Carbon Coatings of Friction Units in Lubricating Media. *Russ. J. Appl. Chem.* 2019, 92 (12), 1603–1615. <https://doi.org/10.1134/S1070427219120012>.
- Mpingi, W. M. Structural, Electrical, and Electronic Properties of Diamond-Like Carbon (DLC) and Carbon-Based Materials. 2013..
- Chand, N.; Singh, S.; Sekar, V.; Bharadwaj, R. L.; Mahajan, A. M. Diamond-Like Carbon (DLC) Coatings: Classification, Properties, and Applications. *Int. J. Sci. Res. Sci. Technol.* 2024, 11 (3), 147–168. <https://doi.org/10.32628/ijrst5241131>.
- Robertson, J. Hard Amorphous (Diamond-Like) Carbons. *Mater. Sci. Eng.* 1991, 21.
- Zahid, R.; Masjuki, H. H.; Varman, M.; Mufti, R. A.; Kalam, M. A.; Gulzar, M. Effect of Lubricant Formulations on the Tribological Performance of Self-Mated Doped DLC Contacts: A Review. *Tribol. Lett.* 2015, 58 (2), 32. <https://doi.org/10.1007/s11249-015-0506-5>.
- Kalin, M.; Vižintin, J.; Vercammen, K.; Barriga, J.; Arnšek, A. The Lubrication of DLC Coatings with Mineral and Biodegradable Oils Having Different Polar and Saturation Characteristics. *Surf. Coat. Technol.* 2006. DOI: 10.1016/j.surfcoat.2005.03.016.
- Enke, K.; Dimigen, H.; Hubsch, H. Frictional Properties of Diamond-Like C Layers. *Appl. Phys. Lett.* 1980, 36, 291. DOI: 10.1063/1.91465.
- Hlin, M.; Hedenqvist, P. 'Me-C. H Coatings in Motor Vehicles'. *Wear* 2001, 249, 302–309. DOI: 10.1016/S0043-1648(01)00565-8.
- Cox, J. T.; Hass, G.; Hunter, W. R. Infrared Reflectance of Silicon Oxide and Magnesium Fluoride Protected Aluminium Mirrors at Various Angles of Incidence From 8 μm to 12 μm . *Appl. Opt.* 1975, 14, 1247. DOI: 10.1364/AO.14.001247.

Kim, S. B.; Wager, J. F. Diamond-Like Carbon Films for Electroluminescent Applications. *Surf. Coat. Technol.* 1990, 43, 99. [https://doi.org/10.1016/0257-8972\(90\)90064-J](https://doi.org/10.1016/0257-8972(90)90064-J).

Kapoor, V. J.; Mirtich, M. J.; Banks, B. A. Diamond-Like C Films on Semiconductors for Insulated-Gate Technology. *J. Vac. Sci. Technol.* 1986, 4, 1013. DOI: 10.1116/1.573442.

Kolawole, F. O.; Kolawole, S. K.; Varela, L. B.; Owa, A. F.; Ramirez, M. A.; Tschiptschin, A. P. Diamond-Like C (DLC) Coatings for Automobile Applications. In *Engineering Applications of Diamond*; IntechOpen: London, OH, USA, 2020. DOI: 10.5772/intechopen.95063.

Ronkainen, H.; Varjus, S.; Koskinen, J.; Holmberg, K. Differentiating the Tribological Performance of Hydrogenated and Hydrogen-Free DLC Coatings. *Wear* 2001, 249, 260–266. [https://doi.org/10.1016/S0043-1648\(01\)00558-0](https://doi.org/10.1016/S0043-1648(01)00558-0).

Case Study on repair Welding of Nickel Aluminium Bronze alloy casting (bs1400 ab2- cual10fe5ni5) using Tungsten Inert Gas Welding Process

¹Bhavesh R. Rana, ²Avinash C. Pandey, ³Hemal M. Desai

^{1,2,3}*Welding Engineering & Metallurgy,
Larsen & Toubro Ltd.,
PES IC*

Abstract

Nickel Aluminium bronze (BS1400:1985 AB2) is a copper-based alloy with excellent combination of mechanical strength, pitting corrosion resistance, superior wear resistance along with ease of machinability & weldability. These properties make it outstanding choice for marine, chemical processing, and other industries involving sea water applications. The investigation is focused on centrifugally casted bearing bush of BS 1400:1985 AB2 alloy, where the volumetric defect and lamination were observed on considerable circumferential area, after machining. The defects removal was performed using mechanical grinding. The standard BS1400:1985, does not allow repair of casted material. On the other hand, ASME BPVC. II. B-2023 standard for alternate material ASTM B148 C95800, allows and restricts the repair of defected area to 20 % of the casting section or wall thickness or 4 % of the casting surface area. The mapping of defects indicates; the volumetric defects were present across the cross section of casting thickness. With customer confirmation, the repair of casting across the thickness is allowed. However, the welding procedure need to be established for ensuring that the mechanical and metallurgical properties at transition area i.e. from casted to welded portion shall have similar properties to as casting. The welding of cast AB2 alloy is challenging, when using Gas Metal Arc Welding processes and flux-based arc welding process. The Tungsten Inert Gas welding being a clean and friendly process to perform welding, hence the process was used. This research tries to elaborate issues emerges, while using TIG welding process and focused on developing repair welding procedure to retain the properties of casted bearing bush. The objective of this case study was to successful establish repair welding procedure of Nickel Aluminium bronze alloy casting, focusing on the development of welding parameters (including current, voltage, and travel speed),

techniques and the resultant weld quality, to meet designed properties as casted structure. Microstructural analysis and mechanical testing assessments vis-a-vis casted product were conducted to establish smooth transition between cast to weld portion. This research contributes to a better understanding of BS 1400:1985 AB2 welding processes, benefiting industries that rely on this material for critical applications.

Keywords: Repair welding, Nickel Aluminium Bronze (BS 1400:1985 AB2), Tungsten Inert Gas Welding (TIG), Metallurgical Analysis, Mechanical Analysis, crack formation

Introduction

Nickel Aluminum Bronze (BS1400:1985 AB2) is a versatile and durable alloy that belongs to the family of copper alloys, it is characterized by its excellent combination of strength, corrosion resistance, and wear resistance. The primary alloying elements in nickel aluminum bronze are copper, nickel, aluminum, and often iron. This alloy class is known for its distinctive golden color. Aluminum provides higher strength and improves the corrosion resistance and castings/hot working properties [1]. Nickel improves corrosion resistance, strength and stabilizes the microstructure, while iron refines grains and enhances the alloy tensile strength [2, 3]. The notable properties of Nickel Aluminium Bronze (NAB) are its resistance to corrosion in various environments, including seawater, which makes it exceedingly useful for marine and other corrosive environments. This alloy is prominent for its wear resistance, making it suitable for components subjected to friction, abrasion, and wear. It has good thermal conductivity, making it applicable in heat exchangers and other heat transfer applications. It is generally machinable, allowing for the production of intricate components. In summary, the significance of Nickel Aluminium Bronze (BS1400:1985 AB2) lies in its ability to address the demanding requirements of industries, where corrosion resistance, high strength, and wear resistance are essential. Its versatility makes it a preferred material for critical components in marine, aerospace, defence, oil and gas, chemical processing, automotive, power generation and general engineering applications.

The manufacturing route of Nickel Aluminium Bronze (BS1400 AB2), involves a series of well-defined steps to transform raw materials into the final product. A combination of mechanical properties and corrosion resistance is offered by cast aluminum bronzes. The centrifugal casting, sand casting or investment casting are common manufacturing route for Ni-Al Bronze, which ensures a homogeneous alloy composition. Heat treatment process including annealing or

solution heat treatment with subsequent aging, are employed to optimize mechanical properties, which is depend on final mechanical and metallurgical properties requirement.

The casting process used in the production of aluminum bronze castings has inherent process issues, which can lead to defects. Some common casting defects in aluminum bronze are porosity, inclusion, lamination, shrinkage, misruns, cold shuts, hot tears, blow holes etc. As the Nickel Aluminium Bronze is often considered as specialty alloy with unique properties, and its cost is higher compared to commonly casted materials. The surface defect or volumetric defects can be removed to ready the cast structure for desired application. Welding is commonly used to attend various casting repair due to its ability to effectively restore damaged or worn components. The welding of Nickel Aluminium Bronze, demands meticulous attention to detail. Pre-weld preparations involve exhaustive surface cleaning, and during welding, methods such as gas tungsten arc welding (GTAW) or gas metal arc welding (GMAW) are commonly employed. Choosing an appropriate filler material is crucial to maintain alloy composition and achieve desired properties. Control of welding parameters, such as current, voltage, and travel speed, is essential, and post-weld inspections using non-destructive testing methods ensure weld quality.

Research indicate that the large and clustered defects can be repaired in various ways. Ji et al. [4] used the precision pulsed plasma powder surfacing to repair 9-4-4-2 nickel–aluminum bronze, and the repaired bronze could meet production requirements. Keshavarz and Abbasi-Khazaei [5] used friction stir processing to fabricate a layer of nano-sized aluminum oxide on the surface of the nickel–aluminum bronze alloy, thereby significantly improving the corrosion resistance of the alloy. Davoodi et al. [1] applied a multi-pass gas tungsten arc welding on nickel aluminum bronze, showing that the corrosion resistance of weld parts in the marine environment could not be weakened. Tang et al. [6,7] applied laser surface melting and alloying for as-cast manganese nickel aluminum bronze, resulting in the refinement and homogenization of as-cast microstructure, repairing cast defects. Li et al. [8] used TIG welding for as-cast NAB to refine the microstructure for better corrosion performance. Furthermore, for NAB, it may suffer from surface damage under conditions of extreme flow velocity or fluid turbulence [9]. Since the replacement of these parts with exactly the same material is very expensive, welding repair could be an economical method for the restoration of NAB parts [1]. Meanwhile, this method may lead to increased corrosion due to the occurrence of galvanic couples between the weld and base alloy. However, there

have been few studies dedicated to the corrosion investigation of weld-repaired NAB alloys.

Present research investigation is focused on repair of volumetric defects and lamination, which were observed on considerable circumferential area (at Internal diameter), after machining of centrifugally casted bearing bush made up of BS 1400 AB2 alloy. The defects removal was performed using mechanical grinding. The standard BS1400:1985, does not allow repair of casted material. On the other hand, ASME BPVC. II. B-2023 standard for alternate material ASTM B148 C95800, allows and restricts the repair of defected area to 20 % of the casting section or wall thickness or 4 % of the casting surface area. The mapping of defects indicates; the volumetric defects were present across the cross section of casting thickness. The defected area on casting inner surface is beyond the specified limit of above stated code. With customer confirmation, the repair of casting across the thickness is allowed. However, the welding procedure need to be establish for ensuring that the mechanical and metallurgical properties at transition area i.e. from cast to weld portion shall be similar to that of cast product. The welding of cast BS 1400 AB2 alloy is challenging, when using Gas Metal Arc Welding processes and flux based arc welding process. The Tungsten Inert Gas welding being a clean and friendly process to perform welding, hence the process was used. This research tries to elaborate issues emerges, while using TIG welding process and focused on developing repair welding procedure to retain the properties of casted bearing bush. The objective of this case study was to successful establish repair welding procedure of Nickel Aluminium bronze alloy casting, focusing on the development of welding parameters (including current, voltage, and travel speed), techniques and the resultant weld quality, to meet designed properties as casted structure.

Materials & Method

To explore the research objective, Procedure Qualification Record (PQR) for nickel aluminum bronze welding has been conducted in accordance to applicable code ASME Sec IX: 2023 and base metal acceptance criteria of standard BS 1400:1985, as well as the requirements of the project or application. The performed PQR provides documentation of the specific welding procedure used and the results of testing that demonstrate the procedure's capability to produce sound welds. For this purpose, below mentioned dimension coupon has been used, the geometrical dimension is shown in below fig 1.

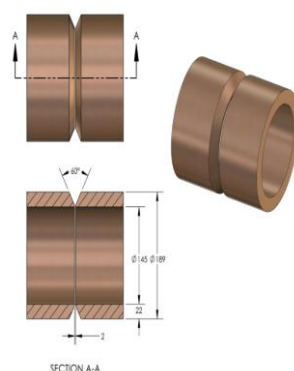


Figure 1. Typical dimension & groove geometry of each welding coupon

The welding was done using the Tungsten Inert Gas welding (GTAW) process. The reasons for selection of this process, is to precisely control the heat input, arc length, and

filler metal deposition. This precision is particularly beneficial when welding of non-ferrous and exotic materials or in applications where weld quality is critical.

Table 1. Chemistry of the Analyzed Base Metal samples

	Specification	Base Metal
%Zn	0.50	0.47
%Pb	0.03	0.02
%Sn	0.10	0.09
%Fe	4.0 – 5.5	4.23
%Ni	4.0 – 5.5	4.24
%Si	0.10	0.02
%Al	8.8 – 10	9.53
%Mn	3.0	0.92
%Mg	0.05	-

Table 2. Used welding Parameter for respective welding process

	Current (A)	Voltage (V)	Travel Speed (mm/min)	Max. Heat Input (KJ/mm)
GTAW	120 – 190	12 - 17	45 – 120	2.10

Table 3. Chemistry of weld metal and Filler wire as per mill TC

	Specification	Mill TC	Weld Metal
%Zn	0.1	0.008	0.005
%Pb	0.02	0.01	0.009
%Fe	3.0 – 5.0	3.45	4.52
%Ni	4.0 – 5.5	4.52	4.83
%Si	0.1	0.07	0.08
%Al	8.5 – 9.5	9.05	8.91
%Mn	0.6 – 3.5	1.55	2.49
UTS (MPa)	480 Min.	620	695
Hardness (BHN)	160-200	185	793

Table 4. Sample extraction plan for welded

Test	Sample Location	Nos. of Sample
Tensile Test (WM)	Along the Weld (Through Thickness)	2
Tensile Test (BM)	Parallel & Perpendicular to Base Plate	2
Bend Test	Through Thickness (Guided Bend)	4
Impact Test	Base Metal, Weld Metal, HAZ	3 Samples from each location
Hardness Test	Through Thickness (Base Metal, Weld Metal, HAZ)	1
Macro / Chemical Test	Through Thickness	1
Microstructure Analysis	Base Metal, Weld Metal and HAZ at depth 0.5mm Top & Bottom and T/2	1

The chemical composition of coupon was confirming to specification of BS 1400:1985, AB2 Nickel Aluminum bronze. The mechanical testing of base metal was performed for comparative study. The tensile test (specimens extracted, perpendicular to circumference) & Hardness test base metal were performed as per BS EN ISO 6892-1:2019 & BS EN ISO 6506-1:2014 standards respectively.

For further investigation, as described in above para, GTAW process was selected for further welding process. The welding parameters like

current, voltage and travel speed etc. are derived and controlled, so as to achieve desired and consistent high quality weld joint. The careful monitoring & adjustment of weld parameters was done to ensure complete fusion of base metal and weld metal. The interpass temperature is maintained 150°C maximum. The detailed welding parameters are mentioned in table no. 2.

Also, the weld consumable selection was done with respect to design requirement & ERCuNiAl filler wire was selected, the chemical and mechanical properties specified as per ASME Sec IIC is closely matching with that of base metal. The chemistry as per mill TC & welded metal at fusion line is depicted in table 3.

As non-destructive testing (NDT) is a crucial aspect of ensuring the quality and integrity of welded joints without causing damage to the tested material. The non-destructive examination was performed in accordance with ASME Sec IX-2023, i.e. Die-Penetration test, Ultrasonic test and Radiography test and the results were found satisfactory. To evaluate the structural change at transition area (i.e. from cast to weld portion) mechanical and metallurgical testing was conducted & the sample extraction plan is being prepared with reference to ASME sec IX-2023 and BS 1400:1985. Refer the below mentioned sample extraction plan for the welded coupon.

Result & Discussion

Mechanical Properties

The Mechanical testing of specimens extracted from welded coupons were carried out. The test results are illustrated in Table 5,

Table 5. Mechanical Properties of Base Metal & Weld Metal

Mechanical Properties	Base Metal	Weld Metal	Heat Affected Zone
Hardness (HV10)	176, 178, 179 (Avg. 178)	182, 195, 197 (Avg. 192)	202, 213, 211 (Avg. 208)
Tensile Strength (MPa)	672, 678, 675 (Avg. 675)	643, 650, 633, (Avg. 640)	-
Yield Strength (MPa)	273, 276, 273 (Avg. 272)	292, 290, 293 (Avg. 291)	-
% Elongation	15, 14, 12 (Avg. 13)	17, 12, 13 (Avg. 14)	-
Yield Ratio, YR	0.40	0.45	-
Toughness (J)	15, 13, 11 (Avg. 12)	15, 21, 19 (Avg. 19)	8, 9, 8 (Avg. 8)
Bend Test	Satisfactory	Bend Test	Satisfactory

Metallurgical Properties

Macro Analysis:

The macro analysis of specimens shows the multi-pass weld is free from in-homogeneities like Porosity, lack of weld penetration, lack of side wall fusion, poor weld profile and undercut and cracks. Also, the weld layers were properly meld in multipass welding.

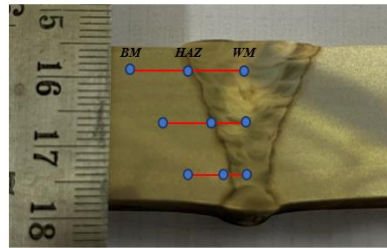


Figure 2. Macro Analysis of Coupons

Micro Analysis:

Microstructure analysis were performed with metallurgical microscope (manufactured by Lica Instruments, Singapore) at 100X, 500X & 1000X with using 1:1 solution of 0.15-0.30% of $\text{AgNO}_3 + \text{HNO}_3$ as etchant. Analyzed location of welded sample is depicted in figure 2. Phase identification and grain size analysis were conducted for three locations different locations, BM, HAZ and Weld Metal as well for each unique samples & unique welding processes as shown in below pictures.

❖ Base Metal:

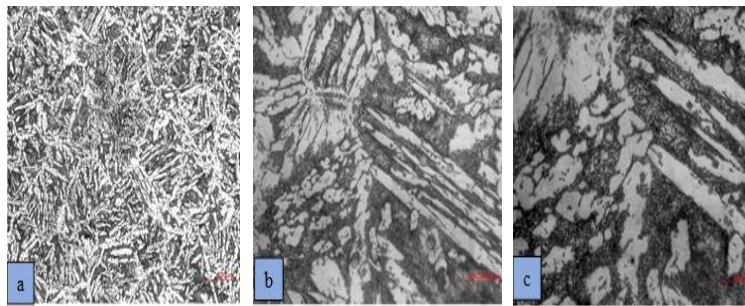


Figure 3. Micro structure of base metal (BM) a) 100X b) 500X c) 1000X

❖ Heat Affected Zone (HAZ):

❖ Weld Metal (WM):

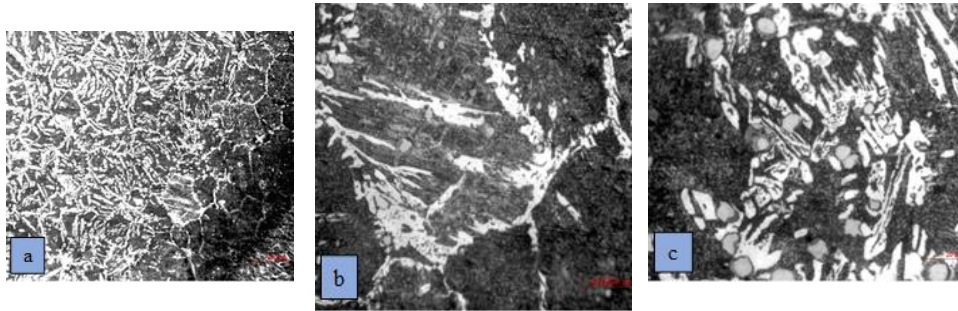


Figure 4. Micro structure of heat affected zone (HAZ) a) 100X b) 500X c) 1000X

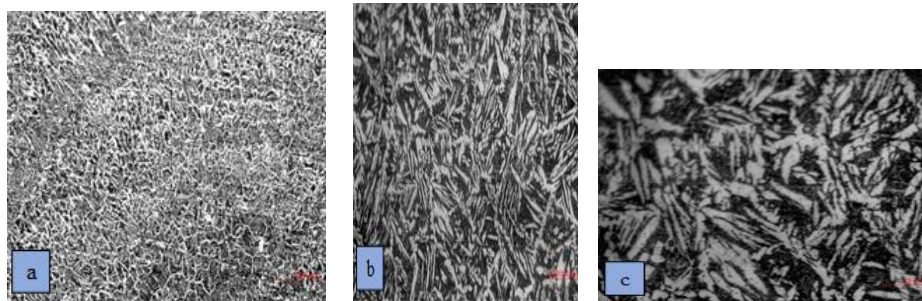


Figure 5. Micro structure of weld metal (WM) a) 100X b) 500X c) 1000X

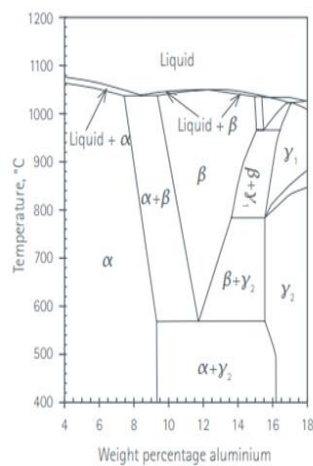


Figure 6. Binary copper-aluminium phase diagram

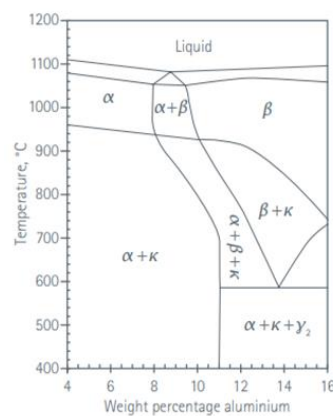


Figure 7. Cu-Al-Ni-Fe phase diagram at 5% each of nickel and iron

Aluminium-bronze alloys can be categorized in three distinct series α series, $\alpha + \beta$ series and $\alpha + \gamma_2$ series, possessing properties entirely different in nature. The wide range of properties that can be obtained by suitable alloying addition. The α aluminium-bronze mostly in the

solid solution range contains about 9.4% aluminium, which can be obtained in casting only on very slow cooling. It is difficult to avoid the hard β formation under normal conditions of cooling, even with 7.4% aluminium in the alloy. From the above equilibrium diagram, it is clear that the β structure is stable only at high temperature and undergoes an $\alpha + \gamma_2$ transformation at about 565°C.

The β phase gives a high hardness combined with relatively high mechanical properties under normal conditions, but severity of cooling results in the formation of β phase with martensitic structure which has lower elongation. The α/β alloys have favorable combination of strength and corrosion resistance. The decomposition of β to $\alpha + \gamma_2$, which occurs during slow cooling or reheating in the temperature range between 550°C and 350°C, has to be avoided. Cooling rates have therefore to be drastic.

The most important aspect is the eutectoid transformation in which the phases are:

1. α Al bronze having FCC lattice similar to iron in its working characteristics.
2. β Al bronze with a b. c. c. structure.
3. β Al bronze which at the eutectoid transformation of 525°C transforms to $\alpha + \gamma_2$.

Alloying elements like nickel, iron and manganese stabilize β and effectively permit slower cooling rate, is very important. When iron and nickel are present at a nominal level of 5% each, they modify the structure of aluminium-bronze and instead of the normal $\alpha + \beta$ an $\alpha + \kappa$ structure with small but tolerable amounts of β is formed.

- Aluminium: Commercial binary alloys of aluminium - bronze usually contain about 8% Al, but the best combination of properties is obtained in the range of 9 to 11% Al. In this range of binary aluminium, advantage can be taken of the characteristic eutectoid transformation in which phase changes occur. This is very important in respect of engineering alloys where suitable heat treatment can confer desired properties in castings.
- Nickel: The addition of nickel has a strong influence in the stabilization of β . The α/β structure is retained at very low cooling rates even with 2 per cent nickel. The addition of nickel to an alloy containing iron has a beneficial effect in modifying the stable structure. The γ_2 formation is suppressed and α solid solution range is extended towards higher aluminium contents.

The combined effect of iron and nickel produces a Kappa phase, which has the same structure as the β aluminium bronze. In alloys containing less than 11% aluminium, the decomposition of β produces $\alpha + \kappa$, when nickel and iron are also present. The size and disposition of Kappa can be controlled from fairly massive to fairly dispersed forms. By regulating the speed of cooling the transformation of $\beta \rightarrow \alpha + \kappa$ can then be arranged to obtain two very important effects (1) hardening by precipitation (of κ in α) and (2) simple martensitic straining to obtain relatively softer phase (β decomposed to α).

In making castings having nickel and iron it is important to see that differential structures are avoided, as indeed should be the case when complex castings are attempted.

Summary of Results & Discussion

The table 1 and 3 shows, the chemical composition of the base metal and deposited weld material respectively, where, it can be noted that the observed chemistry is well within the specification of BS1400:1985 AB2 (For BM) and ASME Sec IIC:2023 SFA no. 5.7 (For WM) respectively. In addition, it is important to observe, the low influence of dilution on the chemical composition in the weld metal center line, where actual analysis was performed (Refer table no. 3).

The Die penetration & radiography test were performed for entire welded seam length and the acceptance criteria for NDE were as per ASME Section IX. The results reveals that the welded joint having excellent fusion between base metal and weld metal.

The macro examination is principally used for checking the quality of welds like Porosity, lack of weld penetration, lack of side wall fusion, poor weld profile and other important defects. The weld bead sequence & other defect was analysed by macro analysis, (as shown in figure 2) and it can be noted that due to multipass welding, the heat affected area can be described easily.

In line with research objective, the mechanical and metallurgical test were performed to ensure the properties at weld metal, base metal and HAZ (fusion line) are within requirements (in terms of microstructure homogeneity).

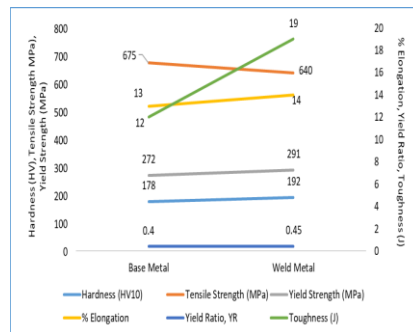


Figure 8. Comparison of base metal and weld metal average mechanical properties

The tensile strength test was performed to determine the yield and tensile strength of WM and BM. The tensile test results are detailed in table 6. The comparisons of average mechanical properties of base metal and weld metal obtained from tensile test is shown in fig.8. The three-point bend test was carried out to identify the tendency to crack during deformation, due to the presence of weld imperfections (such as incomplete fusion at base metal and weld metal) in the area of the face and root of the weld. The impact tests were carried out using a charpy hammer weighing 15 kg to determine the value of shock resistance of WM, HAZ and BM. The result of the test is the amount of energy absorbed to break the sample or its ratio to the cross-sectional area of the sample at the notch location is detailed in table 6. The Vickers micro hardness measurements at 10 kgf indent load were made on the cross section of the welded joint along the measurement line. The result of Hardness test is detailed in table 6. The chemical analysis of base metal and weld metal was performed to understand the change of various alloying element composition due to dilution. The chemical analysis is detailed in table 3. Based on analysis of result, following changes in mechanical properties after successful welding were observed; 7% increase in hardness from base metal to weld metal, 6% increase in yield strength, 3% increase in elongation and 36% increase in impact strength and 5% reduction in tensile strength. The result confirms that there is insignificant change in mechanical properties of base metal & weld metal due to welding and the achieved test results are confirming to specification of weld metal ASME BPVC IIC:2023 and base metal BS1400:1985 AB2.

The microstructure analysis of base metal and weld metal specimen reveals, the structure of base metal (casting) produced in the grains having alpha (α) phase in medium size and fine kappa (K) within alpha grains with fine needle shaped particles in a coarse grained (Beta)

phase, as shown in Figure 3, 4, 5. The presence of kappa phase which is a combination of Fe₃Al and NiAl precipitates is seen in the microstructure greater homogeneity in their microstructure and general refinement of the grains has been observed at fusion line of weld and base metal.

The Nickel Aluminium Bronzes are similar to quench hardening steels in their structural morphology as they also undergo a martensitic transformation if cooled quickly from elevated temperatures. The microstructure at HAZ reveals, fine grains of alpha at the fusion line having significant amount of beta phase present due to slow cooling rate.

Conclusions

1. Based on analysis of result, following changes in mechanical properties after successful welding were observed; 7% increase in hardness from base metal to weld metal, 6% increase in yield strength, 3% increase in elongation and 36% increase in impact strength and 5% reduction in tensile strength. The result confirms that there is insignificant change in mechanical properties of base metal & weld metal due to welding and the achieved test results are confirming to specification of weld metal ASME BPVC IIC:2023 and base metal BS1400:1985 AB2.
2. The decrease in tensile strength is due to increase in aluminum content in diluted weld metal against specified Al % in base metal. The increase in mechanical properties due to appearance of the harder body-centered cubic beta phase. The change in alloying elements composition indicated in chemistry table no. 3, modifies the microstructure structure and thereby increase strength and corrosion resistance; iron improves tensile strength and acts as a grain refiner; nickel improves yield (proof) stress and corrosion resistance and has a beneficial stabilizing effect on the metallurgical structure; manganese also performs a stabilizing function.
3. There is no significant metallurgical change were observed at the transition are (i.e. fusion line) of weld metal and base metal. The base metal and weld metal specimen reveal, the structure of base metal (casting) produced in the grains having alpha (α) phase in medium size and fine kappa (K) within alpha grains with fine needle shaped particles in a coarse grained (Beta) phase.

Acknowledgments

The authors would like to thank Mr. Sanjiv Mulgaonkar, VP & Unit Heat of Larsen & Toubro PES IC, Hazira for his continuous encouragement, support and guidance.

References

1. Eason G., Noble B. and Sneddon I.N., "On certain integrals of Lipschitz-Hankel type involving products of Bessel functions", *Phil. Trans. Roy. Soc. London*, vol. A247, pp. 529-551, Apr. 1955.
2. Sabbaghzadeh, B.; Parvizi, R.; Davoodi, A.; Moayed, M.H. Corrosion evaluation of multi-pass welded nickel–aluminum bronze alloy in 3.5% sodium chloride solution: A restorative application of gas tungsten arc welding process. *Mater. Des.* 2014, 58, 346–356.
3. Wharton, J.A.; Barik, R.C.; Kear, G.; Wood, R.J.K.; Stokes, K.R.; Walsh, F.C. The corrosion of nickel–aluminium bronze in seawater. *Corros. Sci.* 2005, 47, 3336–3367.
4. Alfantazi, A.M.; Ahmed, T.M.; Tromans, D. Corrosion behavior of copper alloys in chloride media. *Mater. Des.* 2009, 30, 2425–2430. [Google Scholar] [CrossRef]
5. Ji, W.X.; Sun, X.F.; Li, Z.M.; Song, W. Repair Feasibility Research of Nickel Aluminum Bronze Surface Corrosion Damage with Precision Pulsed Plasma Powder Surfacing. *Hot Work. Technol.* 2018, 47, 218–226.
6. Abbasi-Khazaei, B.; Keshavarz, S. Nickel-aluminum-bronze/Al₂O₃ surface nanocomposite produced by friction-stir processing: Corrosion properties and microstructure. *Mater. Corros.* 2017, 68, 883–891.
7. Tang, C.H.; Cheng, F.T.; Man, H.C. Effect of laser surface melting on the corrosion and cavitation erosion behaviors of a manganese-nickel-aluminium bronze. *Mater. Sci. Eng. A* 2004, 373, 195–203.
8. Tang, C.H.; Cheng, F.T.; Man, H.C. Laser surface alloying of a marine propeller bronze using aluminium powder Part II: Corrosion and erosion-corrosion synergism. *Surf. Coat. Technol.* 2006, 200, 2594–2601.
9. Li, X.Y.; Yan, Y.G.; Ma, L.; Xu, Z.M.; Li, J.G. Cavitation erosion and corrosion resistance of as-welded nickel aluminum bronze. *J. Shanghai Jiaotong Univ.* 2004, 38, 1464–1467.

10. Kear, G.; Barker, B.D.; Stokes, K.; Walsh, F.C. Flow influenced electrochemical corrosion of nickel aluminium bronze–Part I. Cathodic polarisation. J. Appl. Electrochem. 2004, 34, 1235–1240.

Development of IoT based Real Time Weld Defect Monitoring System For GMAW

¹Harshitsinh Padhiyar, ²Avinash Pandey,
³Hemal Desai

¹*Sr. Engineer, Welding Engineering & Metallurgy,*
L&T PES-IC

harshitsinh.padhiyar@larsentoubro.com

²*Manager, Welding Engineering & Metallurgy,*
L&T PES-IC

avinash.pandey2@larsentoubro.com

³*Sr. DGM, HOD Welding Engineering & Metallurgy,*
L&T PES-IC

hemal.desai@larsentoubro.com

Abstract

Welding is a critical process in various industries, and the quality of the weld is essential to ensure reliability of the final product. The weld quality monitoring, as it stands today, is mainly done by various NDE techniques. These techniques are applied after completion of welding. In case, any weld defects are missed out in Non-destructive test, can lead to catastrophic failures, resulting in significant economic losses and safety hazards. Therefore, to enhance the quality of weld and improve productivity, detection of defects at each weld pass, without involvement of any NDE method will helps to ensure the quality of welded structures.

The real time weld defects monitoring system is based on the concept that different weld defects create unique electrical current and voltage patterns that can be identified through pattern recognition techniques using advancement in data analysis and prediction methodology based on AI/ML. The system uses machine learning algorithms to process the electrical signal patterns and categorize the welds defects. It proposes a unique approach to detect and monitor weld defects such as porosity and lack of fusion in real-time by processing the electrical signal patterns, generated during welding using Gas Metal Arc Welding (GMAW) process.

The system comprises of a sensor, data acquisition hardware and software for data processing and analysis. The sensor is used to generate data of the electrical signal i.e. current and voltage during welding, the data acquisition hardware acquires the data from sensors

and software based on algorithm of AI/ML is used to processes & analysis the data, to identify and classify any defects in the weld. The pilot system allows prompt detection and identification of defects in each weld pass.

Introduction

Gas Metal Arc Welding (GMAW) process is becoming the preferred choice for industries. Its high current density, self-adjusting arc, various modes of metal transfer, and the ability to mix different gases for shielding, coupled with a higher welding speed, make GMAW an ideal solution for industrial applications. Nowadays, the OEMs of welding system are supplying welding system with advance feature like dynamic arc length control, synergic pulse, advanced metal transfer mode etc. These feature makes the GMAW process extremely adaptive to automation. In GMAW process during normal welding, the arc is stable and when a defect is instigated, there will be disturbances in the arc and it will become unstable. Therefore, whenever any deviance occurs, it gets reflected in the signature of output current & voltage, in terms of fluctuates due to change in arc length. These electrical signatures contain valuable information about the quality of the weld and can deliver a good overview, about the quality of welding and possible occurrence of defects. The variations in these signals can indicate different types of weld defect such as porosity and lack of fusion as showed in fig.1.

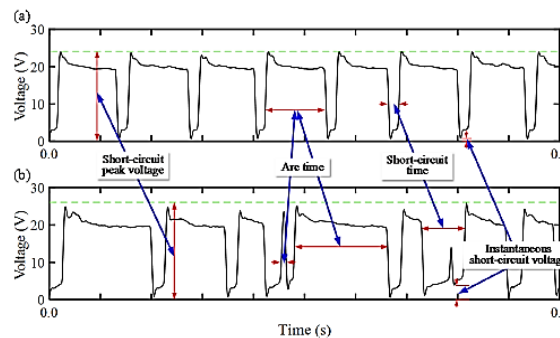


Figure 1: A typical example of change in welding parameter
(a) No Porosity signal and (b) Porosity Signal

Several studies are currently underway to monitor welds and detect welding defects in real-time. These studies focused on parameters like data extraction, thermal analysis, acoustic signals, current/voltage analysis, and X-ray techniques. Some researchers have successfully used welding voltage or welding current to detect defects in the welding process. In present research is focused on development of pilot model for real time welding defect detection system, wherein, the

data will be generated using the IoT edge device (it has ability to collect the sensory information of current and voltage at high frequency rate from the power source). This data will be analyzed in real-time, allows for the rapid and accurate detection and classification of welding defects.

Significant advancements have been made in data analysis and prediction methodologies, particularly in the application of Artificial Intelligence (AI) and Machine Learning (ML). We can make an AI/ML-based system, which can compare the collected data with a master dataset (contains signatures of both defective and non-defective welding data in terms of current and voltage). The system may be able to extract various statistical features from this data, and through signature analysis and pattern detection methods. Using afore data, the Machine Learning model may be trained to provide real- time defect information. The foundation of proposed system lies, in its ability to use sensors for collect welding current and voltage signals during the welding process. These signals are then analyzed using AI/ML algorithms to detect and classify weld defects.

The proposed system will also include a user-interactive interface that provides visualizations of the processed signal information from AI/ML. This interface will deliver real-time feedback to the operator, enabling immediate corrective action after each weld pass. The system can also identify undesirable weld bead quality. The early identification and rectification of welding defect at each pass will drastically reduce the time and effort required for the removal of weld defects (generally the rectification will be performed after completion of welding using Non-Destructive Examination (NDE) of large thickness weld joints).

Experimental Procedure:

A. Procedure for set-up pilot Real-time monitoring:

IoT edge device (fig. 2) (containing Raspberry Pi based dedicated controller with ability to program Arduino & Python also with 16GB of storage, transformer, filters etc.) was precisely connected with GMAW welding Power source Fronius TPS 500i.



Figure 2: IoT device installation & set-up

After connecting IoT Edge device, we need to set-up and execute the program for data fetching & ingestion (fig. 2), which will be transfer the welding data generated by power source to Data storage unit. we have taken bead on plate trials on material SA 516 Gr. 70 with welding consumable ER110S-G to eliminate the initial issues like irregularities

DateTime	pass_no	ID	ACTUAL_CURRENT	ACTUAL_VOLTAGE	ACTUAL_FREQ	ACTUAL_POWER	SERIALNUMBER	ACTUAL_WELD_FREQ	Time
30.01.4	5	95379	40.604	25.848	2.075	1072.454	29177669	0.4	30.18.77
30.01.5	5	95380	263.808	24.340	8.786	7463.020	29177669	0.5	30.18.8
30.01.6	5	95381	271.954	25.096	8.846	7556.624	29177669	0.6	30.18.9
30.01.7	5	95382	247.051	23.955	8.809	6700.604	29177669	0.7	30.19.0
30.01.8	5	95383	233.269	24.041	8.354	6602.208	29177669	0.8	30.19.1
30.01.9	5	95384	231.377	24.339	8.111	6485.030	29177669	0.9	30.19.2
30.02.0	5	95385	221.049	24.848	7.887	6307.762	29177669	1.0	30.19.3
30.02.1	5	95386	208.194	24.839	7.624	5969.030	29177669	1.1	30.19.3
30.02.2	5	95387	195.391	24.597	7.378	5627.812	29177669	1.2	30.19.5
30.02.3	5	95388	181.236	24.669	7.138	5244.540	29177669	1.3	30.19.6
30.02.4	5	95389	177.848	24.122	7.003	5100.374	29177669	1.4	30.19.7
30.02.5	5	95390	173.825	23.389	6.999	4978.730	29177669	1.5	30.19.8
30.02.6	5	95391	169.890	23.876	6.999	4904.832	29177669	1.6	30.19.9
30.02.7	5	95392	165.319	24.575	6.997	4852.594	29177669	1.7	30.20.0
30.02.8	5	95393	161.107	24.011	6.998	4735.881	29177669	1.8	30.20.1
30.02.9	5	95394	157.770	23.294	6.977	4643.040	29177669	1.9	30.20.4
30.03.0	5	95395	170.952	22.580	6.998	4838.257	29177669	2.0	30.20.4
30.03.1	5	95396	161.295	23.585	6.998	4724.426	29177669	2.1	30.20.4
30.03.2	5	95397	170.748	23.220	6.977	4800.321	29177669	2.2	30.20.4
30.03.3	5	95398	161.890	23.538	6.998	4709.465	29177669	2.3	30.20.6
30.03.4	5	95399	153.218	23.795	7.000	4663.327	29177669	2.4	30.20.7
30.03.5	5	95400	159.455	23.853	6.977	4663.614	29177669	2.5	30.20.8
30.03.6	5	95401	152.384	23.822	6.999	4561.347	29177669	2.6	30.20.8
30.03.7	5	95402	160.303	23.122	6.999	4661.406	29177669	2.7	30.20.9
30.03.8	5	95403	161.697	22.597	6.996	4610.456	29177669	2.8	30.21.1
30.03.9	5	95404	148.861	24.469	7.000	4430.000	29177669	2.9	30.21.2
30.04.0	5	95405	155.735	23.716	6.994	4595.228	29177669	3.0	30.21.3
30.04.1	5	95406	173.896	18.362	6.999	4870.574	29177669	3.1	30.21.4
30.04.2	5	95407	173.043	19.428	7.000	4850.218	29177669	3.2	30.21.5
30.04.3	5	95408	160.755	21.765	6.995	4533.228	29177669	3.3	30.21.6
30.04.4	5	95409	161.695	23.766	6.999	4832.842	29177669	3.4	30.21.7
30.04.5	5	95410	153.906	23.344	6.999	4655.723	29177669	3.5	30.21.8

Figure 3: Bead on plate

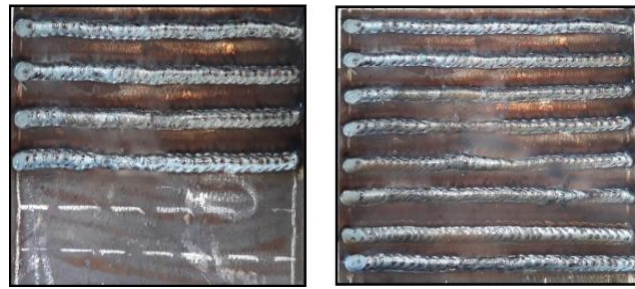


Figure 4: Raw data aggregation

of data, data loss, pass wise data collection, decrease the data ingestion time to nearly zero. After varifying the quality of data, the final trial and extracted raw data as showed in fig. 3 & fig. 4. The raw data contains information of actual time stamp for each weld pass, actual current, actual voltage, total weld pass time with frequency range of 100 milliseconds as .csv file. The pilot system is able to generate separate data files for each weld pass.

The stream lit open-source python library software was used for observation and visualization of the real-time welding data generated by power source. The steps followed for real time data visualization is detailed in figure 5 and figure 6.



Figure 5: Data processing & data aggregation



Figure 6: Real time weld monitoring

B. Welding Trials: Real time weld defect monitoring.

Welding trials conducted using GMAW Fronius power source TPS 500i. The TPS 500i is an advanced powers source with multi control pulse dynamic, arc length control & other advance metal transfer mode. Using Pulse-PMC mode, we had welded 30 nos. of coupons of groove weld using carbon steel material (SA516 Gr. 70) and using consumable ER100S-G, shielding gas mixture of 80% Ar + 20% CO₂ and gas flow rate of 20-22 LPM. The experimental set-up is detailed in fig. 7. We have planned to introduce artificial defect in to the weld and tried to generate different signatures of welding parameters with weld defects, the prime focus shall be on porosity (i.e. surface and sub-surface) & lack of fusion (L/F). We will generate large amount of data sets for good weld passes, weld passes with porosity and lack of fusion (introduce intentionally). The porosity & lack of fusion weld defect will introduce at defined location of the mock ups and the fluctuation of welding signature at the pre-defined location will be compared with RT (Radiographic Testing). The Machine Learning (ML) model will be trained using this data. Total 30nos weld coupon (12 nos, single- & 18 nos double –V groove) were planned to generate the data for welding defects and good welding signatures.

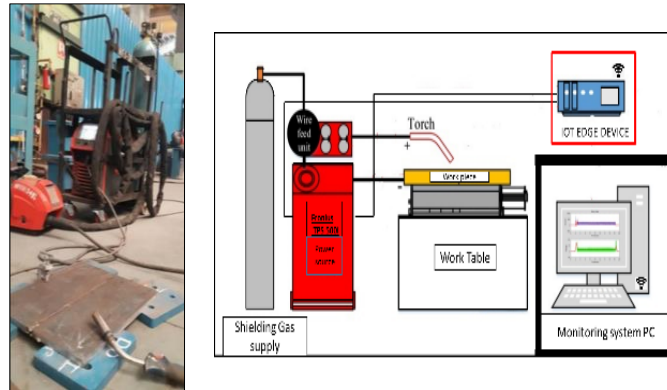


Figure 7: Experimental Set-up

I. Single V weld trials:

The parameter chosen to generate signature of good weld passes are as follows: Current 110-150A, Voltage 18-22V, welding speed 150-200mm/min, shielding gas flow rate 20-22LPM, groove angle 60°, coupon dimension (L-500mm, W-150 mm & T-20 mm) and consumable wire dia.1.2 mm. Total 4 nos. of pass were welded in one coupon, out of which 2 were good welded pass & 2 were weld pass with porosity (refer fig. 8&9). The same was confirmed by RT (refer fig. 10) after each weld pass. To inducing porosity defect, we had abruptly reduced the shielding gas flow rate from 22 LPM to 0-5 LPM, due to this the atmospheric gas has affected with the weld arc and pin hole porosity was induced in the weld joint at defined length.

The fig. 8 & 9 illustrate the signals of current and voltage for 2 good weld pass & 2 weld pass with porosity.

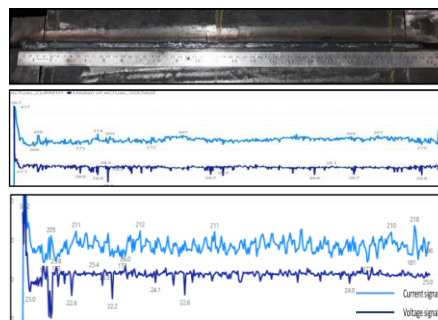


Figure 8: Good weld pass of single-V trails

From the signals, it can be visualized that the good weld pass shows more stable arc signature for the total length of the mock-up. Whereas,

noticeable fluctuation in the signature of weld passes can be observed for the particular time duration, wherein, porosity was introduced.

All single V weld trials were welded with induced porosity at different lengths of weld pass and tried to generate more porosity weld signals to generate a data set of porosity patterns.

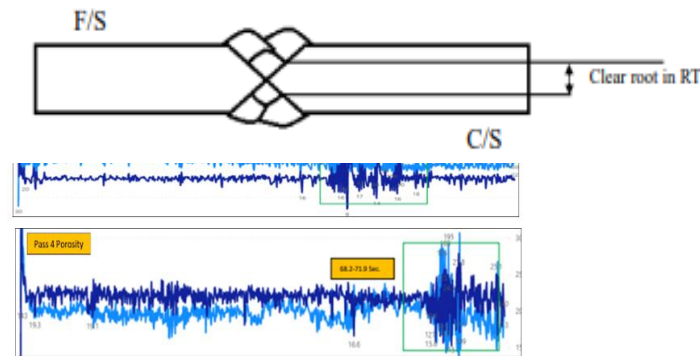


Figure 9: Porosity defect induced weld pass

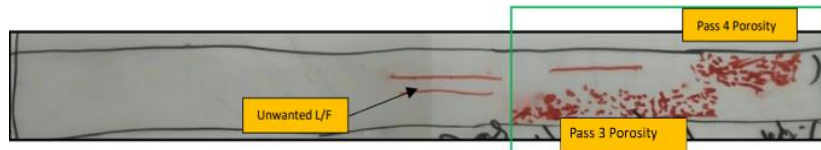


Figure 10: Induced defect confirmed by RT

II. Double V weld trials:

Single-V weld trials were carried out for introducing artificial porosities in various weld passes. Furthermore, the Double-V coupons were used to introduce both porosity & lack of fusion (L/F). The Lack of fusion defect, as defined, is due to improper fusion between weld and base metal or between two adjacent weld beads. It was observed that, whenever there is an improper bead finish or peak/valley on the weld bead, then majorly the Lack of fusion occurs. Using this insight, we tried to introduce lack of fusion defect at the desired location on mock-up coupons. To ascertain that the lack of fusion is present at the desired location, we had carried out RT for each weld pass (refer Fig.1).

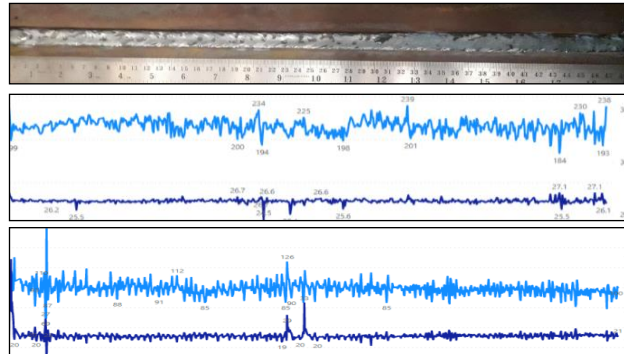


Figure 11: Total pass determination for double-v weld trails

Illustration of Welding signature

1. Fig.12 & 13, shows the signatures pattern of Good welding, when the trials were taken on Double-V joints.
2. Fig. 14 shows the signatures pattern of welding, when the lack of fusion & porosity was introduced during trials taken on Double-V joints:

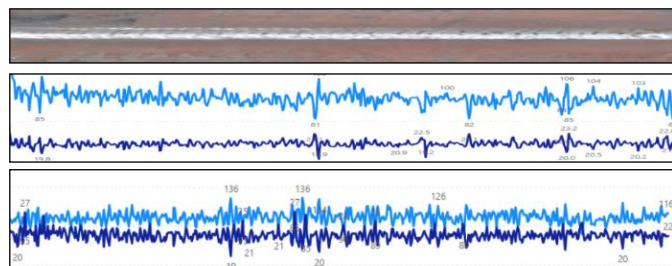


Figure12: Good weld signal trails

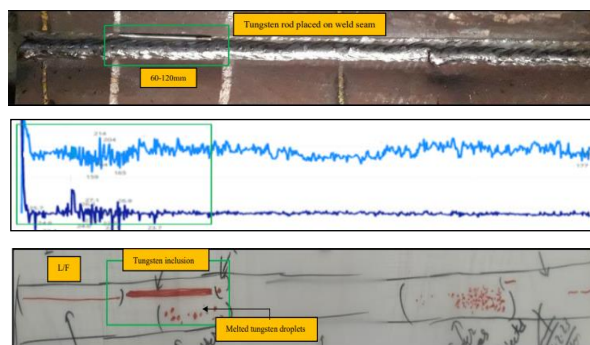


Figure 13: Good weld signal trails

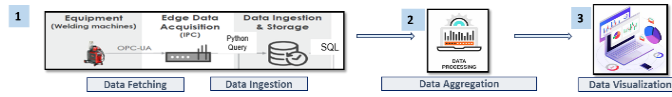


Figure 14: Lack of fusion using tungsten rod

Following methods were used to generate lack of fusion on desired location: 1. Placing tungsten during the progression of welding (as the tungsten rod EWTh-2 has higher melting temperature of $\sim 4000^{\circ}\text{C}$ and does not melt or allow the weld metal to get fused with base metal). 2. Welding using convex bead and improper bead placement, 3. Changing the weaving technique. By using aforesaid method, we had achieved the said defects at the desired location (refer fig. 15 & 16), same was confirmed by RT tracing.

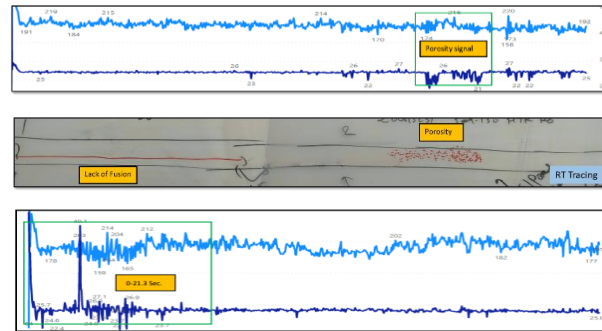


Figure 15: Lack of fusion using improper bead placement

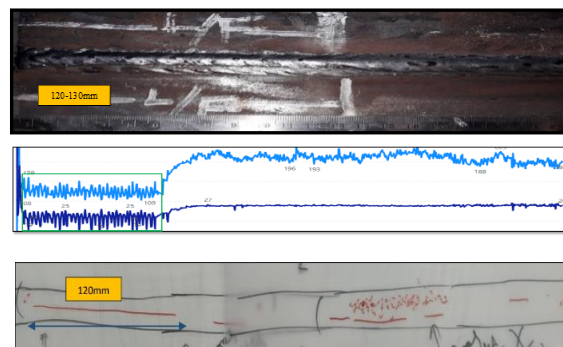


Figure 16: Defected weld signature of porosity & lack of fusion

Experimental Results & Discussion:

With the idea, to reduce the rework at manufacturing shop, the Real time monitoring method was developed. We had generated welding

data, by changing different weld parameters and implementing different weld defect conditions. The signal acquired using IoT edge device was transfer to interactive interface for visualization and processing signal information, to indicated type of defect. The typical set-up of IoT device with interactive interface in detailed in Fig. 17.

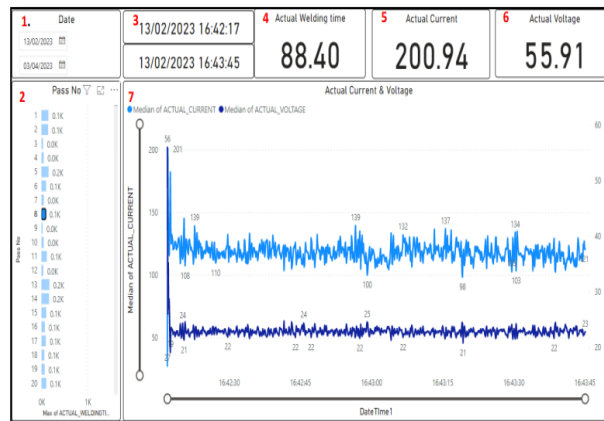


Figure 17: Data processing, aggregation & visualization

Following information in captured in the user interface:

1. Date & Time for signal analysis
2. Pass wise data of signal
3. Date & Time of particular pass
4. Actual welding time
5. Actual (Avg.) Current
6. Actual (Avg.) Voltage
7. Real time monitoring of Current/Voltage signal

The pilot user interface (refer fig. 18) has feature for live and real time data visualization of welding parameter (Current/Voltage). It has capability to store the data of welding process and time stamps. It is helpful for future analysis and tracking the welding performance over the time.

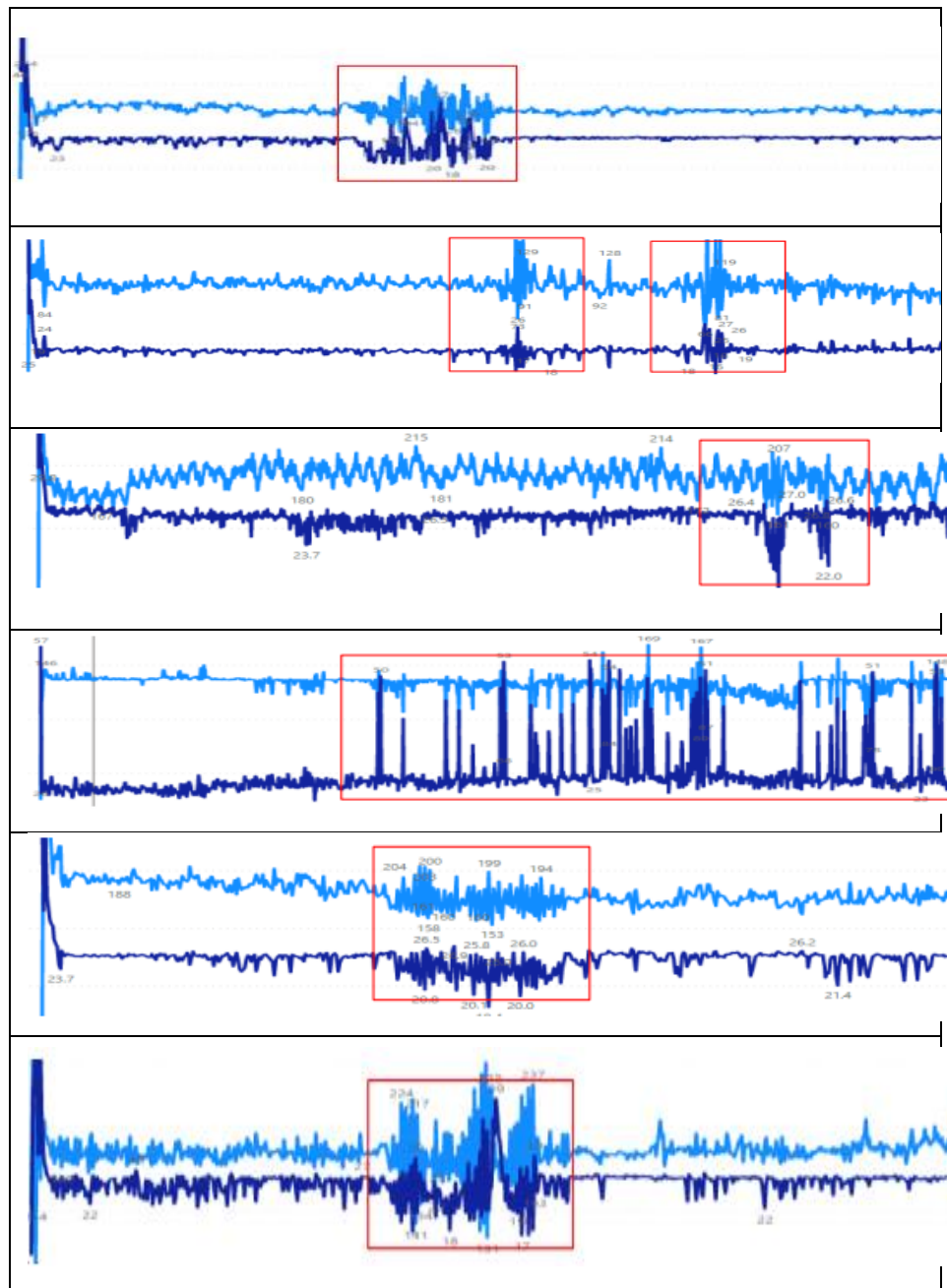


Figure 18: Weld patterns of porosity

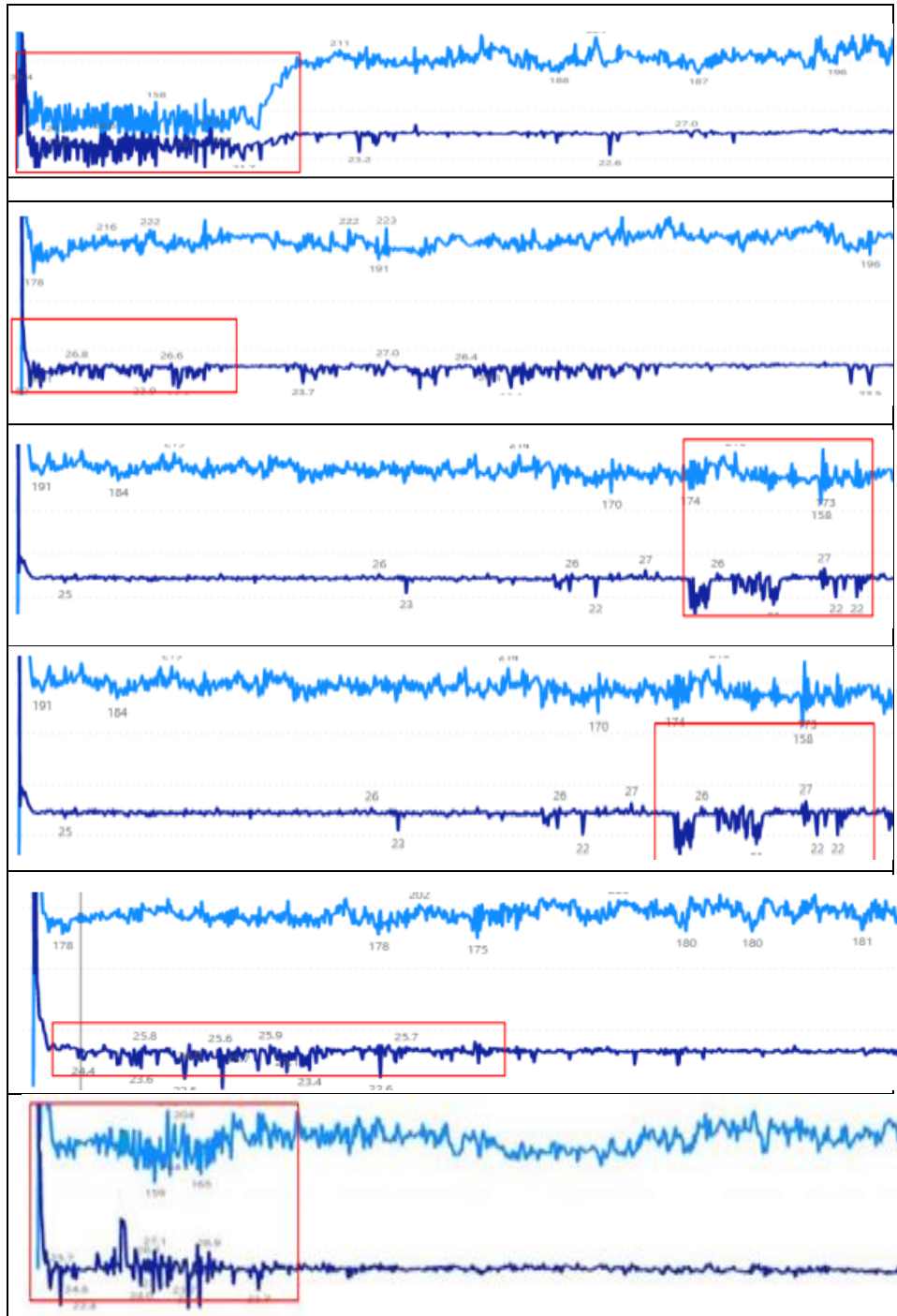


Figure 19: Weld patterns of lack of fusion

Conclusion

The present work was focused on development of Pilot real-time weld defect monitoring system using semi-automatic GMAW. In real time basis, the signal of welding current & voltage signal was generated and with data acquisition device (IoT edge device), the raw data was extracted for good and defective weld signal patterns (Both porosity & lack of fusion).

Various method like decreasing the welding gas for porosity & for lack of fusion changing welding technique, wrong bead placement or lowered the heat input were adopted to generate defective weld signals patterns at intended location of weld pass to create data base for the system.

It is observed that the arc disturbance has major role in creating weld defect and same was visible in obtained signals. Also, it is observed from data that when defect occurs and arc length changes, the welding signature for voltage is more sensitive than current.

The developed pilot model is capable to detect porosity and lack of fusion, while welding using GMAW process and we had welding 5 mock-ups of 1000mm length. The pilot model has successfully indicated the porosity & lack of fusion defect introduce intentionally, which was confirmed by RT.

The model is planned to replicate for multi-pass (up to 250 weld passes in the groove) GMAW welding, for higher thickness jobs. To do the same, we are planned to increase the computation capacity by using higher configuration edge device and developed AI/ML model (with the help of business partner) to study the data of multi-pass welding and indicate the location and type of defects for each pass.

References

1. Decision tree-based weld defect classification using current and voltage signatures in GMAW process: A Sumesha *, Binoy B Nairb, K Rameshkumar C, A Santhakumarid, A Rajae, K Mohandas.
2. Real-Time Detection of Weld Defects for Automated Welding Process Base on Deep Neural Network: Seungmin Shin 1, Chengnan Jin 1, Jiyoung Yu 2 and Sehun Rhee
3. Investigation of feed-forward back propagation ANN using voltage signals for the early prediction of the welding defect: Dinu Thomas Thekkuden1 · Abdel-Hamid Ismail Mourad

4. A study on weld defects classification in gas metal arc welding process using machine learning techniques: Syed Quadir Moinuddina, Syed Shaul Hameedb, Ashok Kumar Dewanganc, K. Ramesh Kumard, A. Shanta Kumarie
5. Sensors for Welding Data Acquisition, Springer Nature, Singapore Pte Ltd. 2019 S. A. Vendan et al., Interdisciplinary Treatment to Arc Welding Power Sources
6. Weld Defect Categorization from Welding Current using Principle Component Analysis, Hayri Arabaci¹ Electric-Electronics Engineering Department Selçuk University Konya, Turkey, (IJACSA) International Journal of Advanced Computer Science and Applications, Vol. 10, No. 6, 2019
7. Prediction of weld porosity (pit) in gas metal arc welds, Seungmin Shin¹ & Min Seok Kim¹ & Sehun Rhee¹ Received: 23 July 2018 /Accepted: 7 May 2019 # Springer-Verlag London Ltd., part of Springer Nature 2019.

Drilling Analysis of Coir Fiber/Pine Needle Powder Reinforced Hybrid Epoxy Composite

¹Rishu Kesharwani, ²Satyavrat, ³Ankit, ⁴Dungali Sreehari*

^{1,2}*UG Student,
Department of Mechanical Engineering,
NIT Uttarakhand, India*

³*Research Scholar,
Department of Mechanical Engineering,
NIT Uttarakhand, India*

⁴*Assistant Professor,
Department of Mechanical Engineering,
NIT Uttarakhand, India*

**Corresponding Author, e-mail: sreehari@nituk.ac.in*

Abstract

Pine Needles are abundantly available in the Himalayan region – Northern region of India and it is a huge forest waste material. The coir fiber obtained from coconut shells is also a waste material which is huge in the Tropical region of India. Considering the two natural waste materials, a coir fiber/pine needle powder reinforced hybrid epoxy composite was fabricated. Drilling is the most common process for joining two materials for structural applications. However, delamination is one of the major concerns in drilling fiber-reinforced composites due to multilayer and multiphase materials. Therefore, in the present study, investigations were carried out to assess the effect of input factors of drilling operation on the delamination factor of the developed composite. The most influencing parameters such as drill diameter, spindle speed and feed rate were considered the input factors at three different levels of each factor. The output factor is the delamination factor. A randomized full factorial was considered to design and perform the experiments. A regression model was generated between the input factors and the output factor. ANOVA was used to analyze the results with a 95% confidence interval. From the analysis, it was witnessed that the feed rate and drill diameter were significant and influencing the delamination factor among the three input factors.

Introduction

Pine needles or *Pinus Roxburghii* Needles (PRNs) are abundantly available in the Himalayan Region of India. The pine needles are forest

bio-waste and can effectively be used in several applications, especially in the preparation of natural fiber composites [1]. The coir fiber is a natural bio-waste material obtained from coconuts, widely available in the Tropical Region of India. Due to several advantages associated with coir fiber in terms of physical, mechanical and structural properties, it has huge potential to prepare a coir fiber reinforced composite [2]. Hybridization of composite, i.e., by reinforcing two or more fibers in a composite significantly improves the properties of the composite [3]. Several combinations of fibers to form hybrid composites were explored by researchers and extensive research has been carried out on pine needle fiber reinforced and coir fiber reinforced composite materials, individually [4-8]. However, the combination of pine needle and coir fiber reinforced hybrid composite is not explored much.

The drilling analysis of natural fiber composites is extremely important for assembling two or more parts by joining method. In the drilling process, the spindle speed, feed rate and depth of cut, tool geometry and tool materials are the most common input parameters that influence the output factors such as thrust force, torque, surface roughness, delamination, and tool wear [9]. Considering the importance of drilling in the composite, researchers explored the effect of different input factors of the drilling process on the performance/output process parameters. Jayabal & Natarajan [10] have investigated the drilling of coir-fiber reinforced polymer composite and optimized the process parameters such as thrust force, torque and tool wear. Box-Behnken design of RSM was used to design the experiment. Feed rate, drill bit diameter, and spindle speed were considered as input variables and the output parameters were the thrust force, tool wear and torque. They developed regression models between the input and output parameters and optimized the process parameters. Tan et al., [11] analyzed the surface roughness of the drilled glass/carbon hybrid composite using RSM and Taguchi methods. In their investigation, the spindle speed, tool geometry and feed rate were considered as input factors each at three levels. It was concluded that lower feed rate, medium spindle speed and step drill geometry gave high surface quality holes. Belaadi et al., [12] performed drilling on bidirectional jute fiber reinforced composite with different drill geometries and materials. The significant process parameters among the input factors such as speed, feed rate and drill diameter were analyzed using ANOVA. Further, ANN and RSM models were generated and validated with the experimental results. They observed that the feed rate is more significant than the other two input factors. Barreno-Avila et al., [13] investigated surface roughness

and delamination parameters while drilling the rice-husk fiber composite. It was reported that the surface roughness was influenced by the spindle speed and type of resin, and delamination was affected by the tool type & resin type. Gaitonde et al., [14] investigated the effect of spindle speed, feed, and drill bit point angle on the delamination factor while drilling the carbon fiber reinforced composite and optimized the process parameters using Taguchi to minimize the delamination factor. They found that the minimum delamination factor was achieved at higher spindle speed, lower feed rate and point angle. Palanikumar, [15] analyzed the delamination factor and surface roughness in drilling glass fiber plastic composite considering the spindle speed, drill diameter and feed rate as process parameters and each at five levels. It was observed that the spindle speed and feed rate were highly influencing the delamination factor. Tsao & Hocheng, [16] used the Taguchi approach and ANOVA to analyze the effect of feed rate, drill diameter and spindle speed in drilling carbon fiber composite with three types of drill bits. They observed that the feed rate and drill diameter were contributing more. Ragunath et al., [17] optimized the drilling process parameters using the RSM and ANOVA during drilling of GFRP/Clay nano-composites considering feed rate, spindle speed, drill diameter and filler content as input process parameters. They concluded that the feed rate was significant than other three process parameters.

Though there are several studies on drilling analysis of hybrid composite with different combinations of fiber reinforcement, no literature has been reported on the drilling analysis of coir fiber/pine needle powder hybrid composite. Therefore, in the present investigation, the coir fiber/pine needle powder hybrid composite was fabricated; drilling operation was performed on the fabricated sample and the effect of input factors such as spindle speed, drill diameter and feed rate were investigated on the exit delamination factor.

Materials and Method

Materials

In the study, pine needle fiber in powder form and coir fiber in mat form were used as reinforcement materials. Epoxy was used as matrix material. Pine needle fibers were collected locally from the hilly region of Srinagar Garhwal, Pauri, Uttarakhand. The coir fiber was procured from the local market. The epoxy resin LY556 and hardener HY951 were supplied by Northern Polymers Pvt. Ltd., New Delhi, India. The properties of fiber materials are as shown in Table 1:

Table 1. Properties of fiber materials

S. No.	Natural fiber material	Tensile strength (MPa)	Young's Modulus (GPa)	% Elongation (at break)	Density (kg/m ³)	Reference
1.	Pine needle fiber	51.48±19.75	1.44±0.67	3.60±0.91	1020±20	[4]
2.	Coir fiber	131-175	4-6	15.40	1150	[8]

Composite Preparation

The pine needles were washed and dried in sunlight for about a week. The sun-dried pine needles were kept in a microwave oven for 5 hours at 70°C to remove any moisture left. The needles were chopped, grounded in a mixer, and sieved using a 300-micron sieve, in order to produce pine needle powder. The coir fiber was compressed under a pressure of 10 MPa with the aid of a compression molding machine and formed into a mat. A 200 mm x 200 mm × 4 mm mold was used to create composites using the handlay-up technique. The sample composite constitutes coir fiber - 30% by wt., pine needle powder (PNP) – 5% by wt., and the remaining 65% matrix (Epoxy). The addition of pine needle powder may increase the adhesion strength between the coir fiber and epoxy resin.

Design of Experiments

A randomized full factorial method was used to design the experiments. The most commonly used factors in drilling such as feed rate, spindle speed and drill diameter each at three levels were considered input factors and the delamination factor was considered as output factor as shown in Table 2. Analysis of Variance (ANOVA) was used to analyze the significant parameters and a regression model was developed between the input and output factors.

Table 2. Input factors and their levels

S. No.	Input Factors	Notation	Units	Levels		
				1	2	3
1.	Feed rate	A	mm/min	10	20	30
2.	Spindle speed	B	rev/min	500	1000	1500
3.	Drill diameter	C	mm	4	6	8

Drilling of Composite

The drilling was performed on the developed coir fiber/pine needle powder hybrid composite using a CNC drill machine. The sample was tightly fixed into the screws in the workpiece holder to avoid any bending while performing the drilling operation. HSS-TiN twist drill bits of different diameters were used as tools. Fig. 1 shows the drilled samples of the composite.

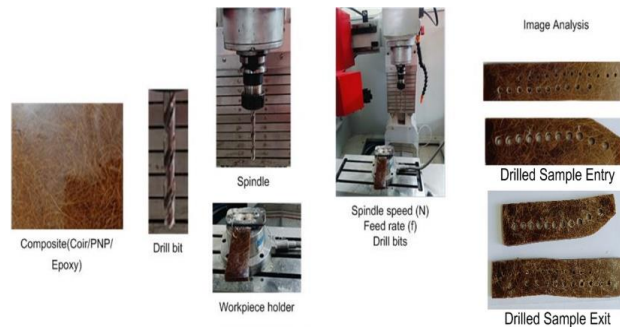


Figure 1 Drilling of coir fiber/pine needle fiber hybrid composite.

Analysis of Delamination Factor

Different approaches like ultrasonic scan, microscopy, x-ray radiography, infrared thermography, eddy current and digital scanning/radiography were reported in the literature for assessing the drilled hole [18]. The microscopy assessment method was considered in the present study using a stereo zoom microscope as shown in Figure 2.



Figure 2 Microscopy assessment method of drilled hole

The delamination occurs at the entry and exit sides of the drilled hole due to peel-up and push-out mechanisms, respectively. However, the effect of the delamination on exit side is more severe than the entry side. The analysis of delamination of the drilled hole of the composite was quantified in different ways by different researchers such as delamination size, conventional delamination factor, shape circularity, adjusted delamination factor, refined delamination factor, minimum delamination factor, and equivalent delamination factor [19-20]. The

conventional delamination factor (F_d) is majorly used in literature to analyze the delamination, and hence, the same is considered here and determined by Eq. 1.

$$F_d = \frac{D_{max}}{D} \quad (1)$$

where D - nominal hole diameter

D_{max} - maximum delamination diameter

Results and Discussion

Analysis of Results

Considering the full factorial design, of DoE, a total of 27 experiments were designed and conducted. The holes of the drilled composite samples were analyzed using image processing software to evaluate the maximum delamination diameter (D_{max}) and nominal diameter (D). The experimental delamination factor was calculated using Eq. 1. and is noted as shown in Table 3.

Table 3. Experimental and Predicted Delamination Factor

Run Order	Coded Input Factors			Experimental Delamination Factor	Predicted Delamination Factor	Error
	A	B	C			
1	2	3	2	1.0175	1.01686	0.0006370
2	3	1	1	1.0140	1.01379	0.0002093
3	1	2	1	1.0120	1.01319	-0.0011880
4	2	2	2	1.0167	1.01702	-0.0003185
5	3	3	2	1.0190	1.01980	-0.0007991
6	1	3	3	1.0157	1.01591	-0.0002130
7	2	3	1	1.0137	1.01343	0.0002704
8	1	2	2	1.0185	1.01773	0.0007704
9	1	1	2	1.0192	1.01897	0.0002343
10	1	3	1	1.0131	1.01234	0.0007593
11	3	2	3	1.0175	1.01758	-0.0000769
12	1	1	1	1.0145	1.01392	0.0005759
13	1	1	3	1.0195	1.01950	0.0000037
14	2	3	3	1.0162	1.01579	0.0004148
15	3	2	2	1.0198	1.01876	0.0010370
16	3	3	1	1.0170	1.01697	0.0000259
17	2	2	1	1.0130	1.01309	-0.0000852
18	2	1	2	1.0160	1.01706	-0.0010630
19	3	1	3	1.0166	1.01693	-0.0003296
20	1	2	3	1.0178	1.01776	0.0000398
21	2	2	3	1.0167	1.01644	0.0002593
22	2	1	1	1.0125	1.01263	-0.0001296
23	1	3	2	1.0154	1.01638	-0.0009824
24	3	1	2	1.0181	1.01762	0.0004843
25	3	3	3	1.0180	1.01811	-0.0001130

26	2	1	3	1.0170	1.01699	0.0000148
27	3	2	1	1.0150	1.01544	-0.0004380

The analysis of variance (ANOVA) at a 95% confidence level was used in the analysis and the results are shown in Table 4.

Table 4. Analysis of Variance (ANOVA) for Delamination Factor

Source	DF	Sum of Squares	Mean Squares	F-value	P-value	Remarks
Regression	9	0.000120	0.000013	27.36	0.000	Significant
A	1	0.000009	0.000009	18.77	0.000	Significant
B	1	0.000000	0.000000	0.97	0.340	Insignificant
C	1	0.000049	0.000049	101.25	0.000	Significant
A*A	1	0.000009	0.000009	18.60	0.000	
B*B	1	0.000000	0.000000	0.04	0.848	
C*C	1	0.000031	0.000031	62.78	0.000	
A*B	1	0.000017	0.000017	35.05	0.000	
A*C	1	0.000004	0.000004	9.16	0.008	
B*C	1	0.000003	0.000003	6.17	0.024	
Error	17	0.000008	0.000008			
Total	26	0.000128	0.000128			
R² = 0.9354, Adj. R² = 0.9012, Pred. R² = 0.8475						
<i>A – feed rate (mm/min), B – spindle speed (rev/min) and C – drill diameter (mm)</i>						

From the ANOVA table 4, the F-value or P-value is analyzed to estimate the significant and insignificant process parameters. The calculated F-values (F_{cal}) corresponding the parameters - feed rate (A) is 18.77 and drill diameter (C) is 101.25. The tabulated F-value (F_{tab}) with level of significance $\alpha = 0.05$, is $F_{0.05,1,17} = 4.45$. In general, if the $F_{cal} > F_{tab}$, then the corresponding process parameter has significant effect on output. Therefore, it is understood that process parameters feed rate and drill diameter had a significant effect on the delamination factor. Further, it was observed that the effect of spindle speed is insignificant (F-value = 0.97 < 4.45).

The regression model relating the input and output factors was developed and is represented in Eq. 2.

$$F_d = 1.00883 - 0.00556 A - 0.00126 B + 0.01292 C + 0.001228 A * A - 0.000056 B * B - 0.002256 C * C + 0.001192 A * B - 0.000608 A * C - 0.000500 B * C \quad (2)$$

The predicted delamination factor was obtained using the regression model Eq. (2). In addition to the experimental delamination factor, the predicted delamination factor and error are shown in Table 2.

In order to check the developed regression model is acceptable or not, it is important to analyze the residuals. The normal probability plot of residuals and fitted values vs residuals are shown in Fig. 3(a) & 3(b), respectively. From Fig. 3(a) it is observed that the residuals fall on a nearly straight line indicating the error distribution is nearly normal. Further, the plot of fitted values vs residuals (Fig. 3(b)) is structure less, demonstrating that the developed regression model is acceptable.

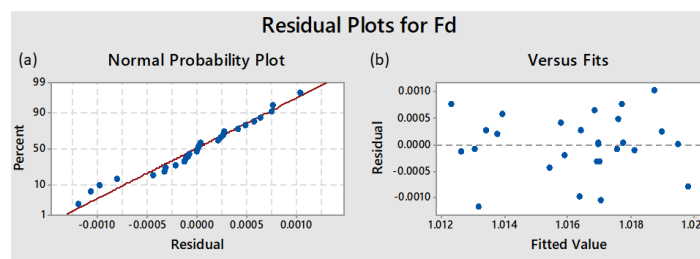


Figure 3 Plots of (a) Normal Probability and (b) Fitted values vs Residuals.

The fitness of the regression model is determined by observing the values of the regression coefficient values R^2 and Adjusted R^2 . The values near unity indicate goodness of fit. Here, the values of R^2 is 0.9354 and adjusted R^2 is 0.9012, indicating that the regression model is a good fit. Further, the predicted value of R^2 is also within the range.

Effect of Input Factors on Delamination Factor

The objective of the study is to minimize the delamination factor. Fig. 4(a) shows the surface plot of the combined effect of feed rate and spindle speed on the delamination factor. From the plot, the minimum delamination factor is observed at low and high levels of feed rate and spindle speed, respectively. Further, observing the surface plots of delamination factor vs spindle speed, drill diameter (Fig. 4(b)) and delamination factor vs feed rate, drill diameter (Fig. 4(c)), it is clear that the delamination factor increases with increasing the feed rate and drill diameter. It is evident from the surface plots that the effect of spindle speed is very much less or insignificant on the delamination factor.

The reason attributed to increase in delamination factor with increase in feed rate may be due to increase in the thrust force. As the drill diameter increases, contact area between the tool and work also

increases and thus the thrust force increases and hence, the delamination factor also increases. The present results are in good agreement with previous studies [17]. Further, it can also be attributed that the addition of pine needle powder in the composite decreases the delamination factor to some extent due to increase in adhesion strength of fiber & matrix and minimized the fiber pull-out.

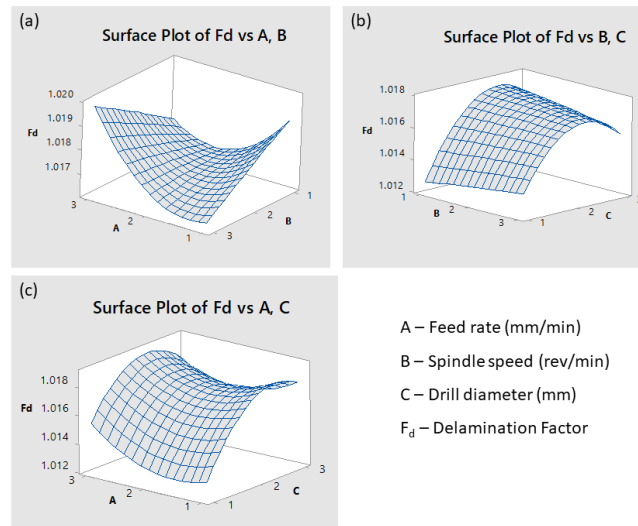


Figure 4 Surface plots of delamination factor vs (a) feed rate and spindle speed (b) speed and drill diameter (c) feed rate and drill diameter

Optimization

The desirability test was performed to optimize the process parameters with the objective of minimizing the delamination factor. The minimum value of the delamination factor was obtained at a desirability value of 0.95682 (near to unity) and optimized factor level settings as feed rate 10 mm/min, spindle speed 1500 rev/min, and drill diameter 4 mm. A confirmation experiment was conducted with the optimized factor settings and the delamination factor was 1.0125 near to the predicted value.

Conclusion

A hybrid composite was developed using Coir fiber and pine needle powder as reinforcement materials and epoxy as a matrix material. A drilling operation was performed on the developed hybrid composite and ANOVA at a 95% confidence level was used to analyze the exit delamination factor. The following conclusions are drawn from the analysis:

- The input process parameters such as feed rate and drill diameter have shown a significant effect on the delamination factor, however, the effect of the spindle speed is insignificant.
- The developed regression model to predict the delamination factor is a good fit with regression coefficient values R^2 and adj. R^2 is 0.9354 and 0.9012, respectively.
- The delamination factor increases with increase in drill diameter and feed rate. Therefore, to achieve minimum delamination, lower feed rate and smaller drill diameter are preferable.

References

- [1] A. Gupta, P. Ghosh, K. Arora, S. Sharma, and S. Kumar, "Valorization potential of pine needle waste biomass: recent trends and future perspectives," *Environ. Sci. Pollut. Res.*, 36136-36151, (2023).
- [2] A. G. Adeniyi, D. V. Onifade, J. O. Ighalo, and A. S. Adeoye, "A review of coir fiber reinforced polymer composites," *Compos. Part B Eng.*, 176, 107305, (2019).
- [3] R. Vinayagamoorthy, "Trends and Challenges on the Development of Hybridized Natural Fiber Composites," *J. Nat. Fibers*, 17(12), 1757–1774, (2020).
- [4] R. Kumar, P. K. Rakesh, D. Sreehari, D. Kumar, and T. P. Naik, "Preparation, characterisation and properties of green composites from *Pinus roxburghii* fibre," *Proc. Inst. Mech. Eng. Part L J. Mater. Des. Appl.*, 1-10, (2024).
- [5] R. Kumar, P. K. Rakesh, D. Sreehari, D. Kumar, and T. P. Naik, "Experimental investigations on material properties of alkali retted *Pinus Roxburghii* Fiber," *Biomass Convers. Biorefinery*, 1-17, (2023).
- [6] R. Kumar, P. K. Rakesh, and D. Sreehari, "Investigation on Physico-Chemical, Mechanical and Thermal Properties of Extracted Novel *Pinus Roxburghii* Fiber," *J. Nat. Fibers*, 20(1), 2157924, (2023).
- [7] V. Sinha, Priyasheel; Mathur, Smita; Sharma, Pradeep; Kumar, "Potential of Pine Needles for PLA-Based Composites," *Polym. Compos.*, 39(4), 1339–1349, (2018).
- [8] S. Jayavani, H. Deka, T. O. Varghese and S. K. Nayak, "Recent Development and Future Trends in Coir Fiber-Reinforced Green

- Polymer Composites: Review and Evaluation,” *Polym. Compos.*, 37 (11), 3296–3309, (2016).
- [9] P. Jagadeesh *et al.*, “Drilling characteristics and properties analysis of fiber reinforced polymer composites: A comprehensive review,” *Heliyon*, 9(3), 14428, (2023).
- [10] S. Jayabal and U. Natarajan, “Optimization of thrust force, torque, and tool wear in drilling of coir fiber-reinforced composites using Nelder-Mead and genetic algorithm methods,” *Int. J. Adv. Manuf. Technol.*, 51(1–4), 371–381, (2010).
- [11] C. L. Tan, A. I. Azmi, and N. Muhammad, “Surface Roughness Analysis of Carbon/Glass Hybrid Polymer Composites in Drilling Process Based on Taguchi and Response Surface Methodology,” *Adv. Mater. Res.*, 1119, 622–627, (2015).
- [12] A. Belaadi, M. Boumaaza, S. Amroune, and M. Bouchak, “Mechanical characterization and optimization of delamination factor in drilling bidirectional jute fibre-reinforced polymer biocomposites,” *Int. J. Adv. Manuf. Technol.*, 111(7–8), 2073–2094, (2020).
- [13] E. Barreno-Avila, E. Moya-Moya, and C. Pérez-Salinas, “Rice-husk fiber reinforced composite (RFRC) drilling parameters optimization using RSM based desirability function approach,” *Mater. Today Proc.*, 49, 167–174, (2022).
- [14] V. N. Gaitonde, S. R. Karnik, J. C. Rubio, A. E. Correia, A. M. Abrão, and J. P. Davim, “A study aimed at minimizing delamination during drilling of CFRP composites,” *J. Compos. Mater.*, 45(22), 2359–2368, (2011).
- [15] K. Palanikumar, “Modeling and analysis of delamination factor and surface roughness in drilling GFRP composites,” *Mater. Manuf. Process.*, 25(10), 1059–1067, (2010).
- [16] C. C. Tsao and H. Hocheng, “Taguchi analysis of delamination associated with various drill bits in drilling of composite material,” *Int. J. Mach. Tools Manuf.*, 44(10), 1085–1090, (2004).
- [17] S. Ragunath, C. Velmurugan, and T. Kannan, “Optimization of drilling delamination behavior of GFRP/clay nano-composites using RSM and GRA methods,” *Fibers Polym.*, 18(12), 2400–2409, (2017).

- [18] P. Patel and V. Chaudhary, “Delamination evaluation in drilling of composite materials – A review,” *Mater. Today Proc.*, 56, 2690–2695, (2022).
- [19] M. M. A. Nassar, R. Arunachalam, and K. I. Alzebdeh, “Machinability of natural fiber reinforced composites: a review,” *Int. J. Adv. Manuf. Technol.*, 88(9–12), 2985–3004, (2017).
- [20] J. Babu, T. Sunny, N. A. Paul, K. P. Mohan, J. Philip, and J. P. Davim, “Assessment of delamination in composite materials: A review,” *Proc. Inst. Mech. Eng. Part B J. Eng. Manuf.*, 230(11), 1990–2003, (2016).

Establishing a process map of microstructural and phase changes through molten pool thermal history for ex-situ and in-situ laser cladding of TiN/ Inconel 625 MMC

¹Dolagobinda Sethi*, ²Prabhat Kumar, ³Suvradip Mullick
^{1,2,3}IIT Bhubaneswar
*a24me09003@iitbbs.ac.in

Abstract

This study aims to develop a process map based on the thermal history of the molten pool to predict the formation of specific phases along with microstructural changes under varying process parameters for laser cladding of TiN/Inconel 625 Metal Matrix Composites (MMCs). TiN/Inconel 625 MMCs were deposited onto SS304 substrates using preplaced laser cladding technique through ex-situ and in-situ deposition methods. For the ex-situ process, a pre-mixed layer of 30% TiN and 70% Inconel 625 (by weight) was irradiated with a continuous-wave (CW) Yb-fiber laser with 220 W power. In the in-situ process, 5% Ti and 95% Inconel 625 (by weight) preplaced powder layer was subjected to laser irradiation in a nitrogen gas environment, leading to the in-situ formation of TiN during deposition. The depositions were carried out under variable line energy conditions by varying the scan speed. Under ex-situ conditions, line energy played a crucial role in the decomposition of TiN and consequent formation of intermetallic Ti-Ni compounds and TiN during solidification. Conversely, in the in-situ process, the nitrogen gas flow rate influenced the amount of TiN formed, while line energy affected Ti-Ni phase formation. The microstructural characteristics and phase formations were correlated with thermal history profiles obtained via infrared pyrometer. Temperature profiles revealed distinct solidification shelves at different temperatures, indicative of specific phase formations. The solidification shelves at 1670-1800°C and 950-1100°C corresponded to TiN re-solidification and Ti-Ni phase formation respectively. Further a specific phase of Fe-Ni was identified and a corresponding solidification shelf was observed at 1420-1500°C in case of ex-situ deposition under specific conditions. Thus, the development of process map can help to identify phase formation based on these solidification shelves and hence minimizing the need for post-processing analysis.

Keywords: Thermal history, Inconel 625, ex-situ, in-situ, MMC

Introduction

Metal Matrix Composites (MMCs) synthesised from Nickel based alloys and hard reinforcement particles have their uses in high temperature and corrosive environments. These MMCs have high strength to weight ratio, high fatigue strength, creep resistant and superior wear resistance. Therefore parts made from these MMCs are used in varied industrial applications like turbine blades, aerospace industry, maritime industry, nuclear reactors and chemical industry [1]. Inconel 625 gains strength from solid solution hardening contributed by alloying elements such as Chromium, Niobium, Molybdenum and Iron. Moreover, precipitation hardening also contribute to its enhanced strength by formation of intermetallic phases involving these elements. Ceramic reinforcement particles such as Oxides (Al_2O_3 , Y_2O_3) [2], Carbides (TiC , WC) [3] and Nitrides (TiN , BN)[4]–[6] have been added to form MMCs.

Powder metallurgy processes have been traditionally employed to produce MMCs. However, these processes have several limitations such as the difficulty in accurately fabricating complex shapes and achieving desired functionalities along with insufficient strength. Fabrication of functionally graded materials using powder metallurgy is still a challenge. These drawbacks have led to exploration of additive manufacturing for MMC fabrication using laser depositions [7], [8].

TiN can be preferred as reinforcement material due to its exceptional properties such as high strength, high melting point (3223 K), high hardness (2400 HV) and excellent thermal conductivity. Moreover, the thermal expansion coefficients of TiN ($9.35 \times 10^{-6} \text{ K}^{-1}$) and Nickel matrix ($13.3 \times 10^{-6} \text{ K}^{-1}$) are close, making TiN effective for reinforcing Nickel based superalloys [9]. However, the research on the studies on laser cladding for fabrication of TiN reinforced Inconel 625 composites are limited.

Fabrication of TiN reinforcement Metal Matrix Composites (MMC) have been achieved by many researchers through ex-situ processes. Mandal et al. [1] fabricated TiN /Inconel 718 MMC by using Laser Powder Bed Fusion. The study focused on effect of reinforcement content in the matrix and laser scan speed on the micro hardness of the MMC. The results showed increase in micro hardness of the MMC with the increase in TiN content in the matrix and decrease the laser scan speed.

Studies have been done for nitriding of the Titanium alloys to produce TiN. Zheng et al. [10] investigated the dynamic interactions between Titanium and Nitrogen gas through Selective Laser Melting (SLM). Under identical laser processing conditions, the nitrogen content on the sample surfaces increased with the concentration of nitrogen in the processing chamber. Moreover, Titanium nitride content decreased with the increase in laser scanning speed. Man et al. [11] fabricated TiN through preplaced laser cladding. Titanium powder was preplaced over the NiTi substrate and laser irradiated in Nitrogen gas environment. The nitrided surfaces resulted in hardness and eventually wear resistant of NiTi substrate.

Researchers have employed post processing techniques to analyse the influence of process parameters and establish a relationship with the properties of the cladding. However there is a lack of comprehensive knowledge about the process and a few studies have reported on the evolution of microstructural changes with the thermal history profile. Laser cladding involves many process parameters and optimization of these parameters is difficult. Sometimes these optimized parameters may not function properly in other contexts due to system specific factors. These factors include laser operating wavelength which controls laser absorptivity on the material as well as the intensity profile of the laser beam. Additionally, the thermo-physical properties of the material and its geometry play a role in determining the rate of heat dissipation. Therefore it is important to study microstructural changes in relation with thermal history of the clad. Moreover developing a relation between microstructural changes and thermal history will eliminate the need of post processing analysis.

Material and Methods

The laser system used for the laser cladding of preplaced TiN/Inconel 625 MMC was continuous wave Yb-fibre laser system which had a maximum working power of 240 W and a wavelength of 1.06 micron. The laser beam had a spot diameter of approximately 750 micron. The temperature during the laser cladding was monitored with the help of IR pyrometer which had working temperature range of 385–1600 °C (non-calibrated temperature range) and a spectral wavelength of 1600 nm. A notch filter with a 1064 ± 25 nm spectral range was used to block the scattered laser radiation. Furthermore, a neutral density filter with an optical density of 1.0 was used along with the notch filter to reduce the intensity of the incoming signal to the pyrometer. Ultrasonic vibrations during the experiments were introduced to prevent agglomerations of reinforcement particles and better distribution of these particles throughout the clad. The ultrasonic

system comprised of a transducer unit consisting of four transducers connected in parallel and a 600 W ultrasonic generator capable of producing vibrations within the frequency range of 26–35 kHz. This transducer unit was designed to deliver vibrations vertically, aligning with the expected direction of grain growth, with amplitudes ranging from 5 to 15 μm . In the experimental setup, the ultrasonic generator maintained a constant power output, resulting in a decrease in vibration amplitude as the frequency increased. Consequently, within the specified frequency range, higher amplitudes were achievable at 28 kHz compared to 34 kHz. The integration of the ultrasonic vibration system with the laser system enabled the provision of vibration to the substrate, as shown in the **Error! Reference source not found..**

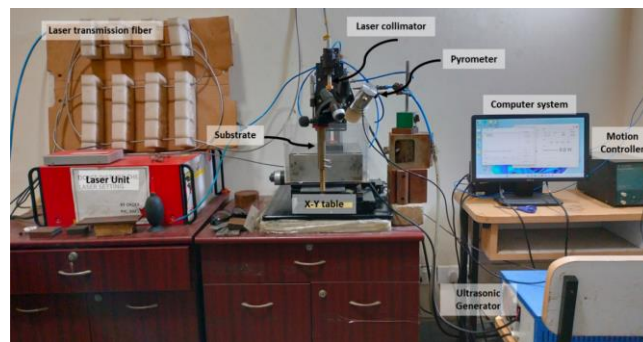


Figure 1: Setup for ex-situ TiN/ Inconel 625 MMC deposition

For in-situ deposition of MMC, a dedicated nitrogen compartment was developed. Acrylic sheets with a thickness of 5 mm were meticulously cut and glued using Chloroform to build a compartment measuring 260 mm x 260 mm x 200 mm. A small window was provided on the top surface of the compartment for the laser beam to pass and incident on the substrate. Two copper tubes were inserted into the chamber (as shown in **Figure 2**) which carried Nitrogen gas. Orifices of 1 mm diameter were drilled in straight line to allow passage of nitrogen to fill the chamber with nitrogen gas. These orifices were adjusted in such a way that the nitrogen gas coming out through these orifices was directed towards the molten pool.

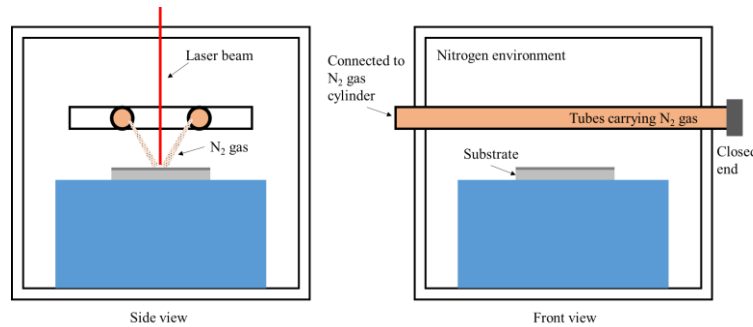


Figure 2: Schematic of the experimental setup for in-situ TiN/ Inconel 625 MMC deposition

The ex-situ and in-situ MMCs were deposited under different process parameters. The operating range of the process parameters (laser power, scan speed and line energy) for both the processes were obtained through trial runs. The operational range of process parameters are mentioned in Table 1.

Table 1: Range of input process parameters

Process	Power (W)	Scan speed (mm/min)	Line energy (J/mm)	Vibration Frequency (kHz)	Amplitude (μm)	N ₂ gas pressure (bar)
Ex-situ	220	120-160	83-110	28-34	15-5	-
In-situ	220	90-120	110-146	28-34	15-5	1-3

Results and Discussions

Ex-situ TiN/Inconel 625 MMC deposition

Microstructure analysis

The microstructural variation for ex-situ 30% TiN/Inconel 625 MMC clad cross sections deposited under variable line energy were analysed and the corresponding microstructures are shown in the **Figure 3**. The SEM images show the presence of reinforcement particles in different forms at different line energies. At lower line energy (higher scan speed), TiN reinforcements are observed to be present in the form of disperoids. As the matrix begin to solidify during cooling, the TiN particles, being solid, becomes embedded within the solidifying Inconel 625 matrix. Due to high cooling rate, these particles do not have sufficient time to coarsen or agglomerate resulting in the fine dispersion of TiN particles within the matrix. In

case of higher line energy (lower scan speed), the reinforcements are seen in the form of dendrites. This is because at lower scan speed, TiN reinforcement particles absorb heat and dissociate. The molten pool lifetime at lower and higher line energies are 382 ms and 594 ms respectively. Due to prolong molten pool life time during solidification, recombine to form TiN rich dendrites.

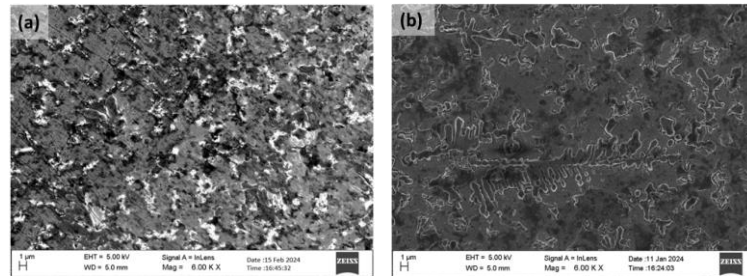


Figure 3: Microstructural variation MMC clads under different line energies (a) 83 J/mm and (b) 110 J/mm

Phase analysis using X-ray diffraction

Phase identification in clads deposited through ex-situ process was done using X-ray diffraction (as shown in **Figure 4**) which confirmed the presence of Titanium nitride phases in higher line energy i.e at 110 J/mm. However nitrides of titanium were not identified through XRD in case of lower line energy. Presence of Ti-Ni phases was observed in both the line energies. In case of lower line energy, Titanium and Nickel are present in maximum quantity and XRD data confirmed the presence of Ti-Ni phase which forms during solidification. Under equilibrium condition, at 942°C, Ti-Ni nucleation takes place with the formation of α Ti, β Ti and Ti_2Ni .

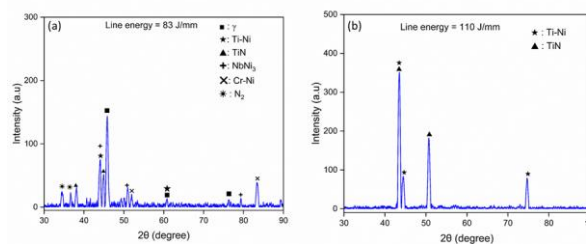


Figure 4: XRD analysis of clads deposited under variable line energies (a) LE = 83 J/mm (b) LE = 110 J/mm

Thermal history analysis

The thermal history graphs acquired using the IR-pyrometer exhibit distinct characteristics linked to the synthesis of nitrides under specified circumstances, indicating the partial decomposition of TiN.

The decomposition process is mainly initiated by the thermal energy generated by the laser, which promotes the dispersion of TiN inside the matrix in the elemental forms of Ti and N. Titanium Nitride (TiN) has a very high melting point, making it challenging to achieve the complete conversion or disintegration of TiN into its constituent elements. However, when the molten pool lasts for a prolonged period of time (at higher line energy), reinforcing particles break down at elevated temperatures higher than the melting point of Inconel 625. Additionally, decomposition might occur at the periphery of larger Ti particles due to element diffusion within the matrix (Inconel 625) under elevated temperatures. Under equilibrium condition, at 942°C, Ti-Ni nucleation takes place with the formation of α Ti, β Ti and Ti₂Ni[12]. At a temperature slightly below the melting point of pure titanium (1670°C), solid β -Ti, α -Ti, and TiN phases are possible depending on the nitrogen concentration[13]. In the temperature profile, a distinct solidification shelf can be seen in between 1670-1800°C which corresponds to TiN nucleation.

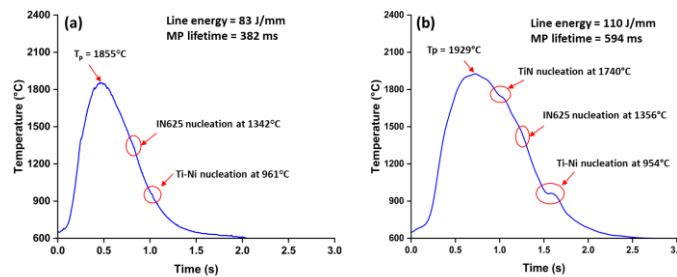


Figure 5: Thermal history profile during MMC depositions through ex-situ process under (a) LE = 83 J/mm (b) LE = 110 J/mm

During the heating cycle, TiN particles gets partially decomposed due to longer time of the molten state, which results in diffusion of Nitrogen and Titanium in the matrix. This further results in the formation of dendrites along with nitride disperoids (containing elements such as Ti, Nb, and Mo) during solidification, as depicted in the SEM image captured for the deposition at line higher line energy. Distinct solidification shelves were observed in **Figure 5(b)** indicating formation of titanium nitride, which also confirms significant decomposition of the TiN particles. However, no distinct solidification shelf is observed in lower line energy indicating no formation of nitride, which also confirms no significant decomposition of the TiN particles. Therefore, the thermal history graphs adequately carry the signature of the micro-structural changes.

TiN/Inconel 625 MMC deposition with acoustic streaming

There are two major non-linear effects of ultrasonic vibrations: cavitation and acoustic streaming. When the pressure within the molten pool drops below its vapor pressure, the liquid begins to vaporize, forming bubbles. These bubbles then break generating shock waves. Shock waves produced due to cavitation effect leads to breaking of the dendrites and refining of the grains. When acoustic wave propagates through the molten pool, it creates regions of high pressure and low pressure. This variations in pressure cause the molten fluid to oscillate back and forth. However due to non-linearity of the fluid properties, the fluid particles do not return to their original positions after each oscillation. This results in net flow or acoustic streaming. Due to acoustic streaming, molten pool gets stirred which results in the homogenizing distribution of the alloying elements in the matrix.

Microstructural analysis

At a constant power generation, vibrational amplitude and vibrational frequency are inversely related. **Figure 6(b)** and **Figure 6(c)** correspond to vibrational amplitude of 5-6 μm (frequency = 34 kHz) and 13-14 μm (frequency = 28 kHz) respectively. Dendrites can be seen under higher line energy without the application of vibration. As the amplitude of vibration is increased, this leads to the generation of intense shock waves which break the dendrites as seen in **Figure 6(b)**. And when the amplitude of vibration is increased further, dispersion of dendrites can be seen along with the formation of refined and equi-axed grains as seen in **Figure 6(c)**.

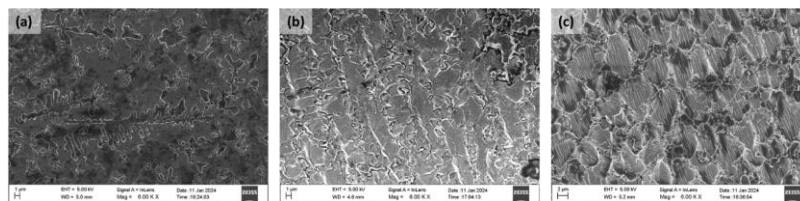


Figure 6: Microstructural variation MMC clads under line energy of 110 J/mm with the application of acoustic streaming

Phase identification through X-ray diffraction

Phase identification in clads deposited through ex-situ process was done using X-ray diffraction which confirmed the presence of Fe-Ni phases along with the presence of TiN and Ti-Ni phases. In case of lower line energy, TiN and Ti-Ni phases were detected significantly along with lower intensity peak of Fe-Ni phase which suggested the presence of Fe-Ni phase in minute amount. However in case of higher

line energy combined with acoustic streaming, considerable amount of Fe-Ni phases were present in the samples along with TiN, Ti-Ni and NbNi₃ phases. When acoustic streaming was coupled with the higher power, the substrate was also affected and the iron content from the substrate move towards clad due to vibration in vertical direction. Moreover due to longer molten pool life time, the Fe-Ni phases were formed during this process. Substantial amount of TiN was detected in the clad samples deposited under higher line energy.

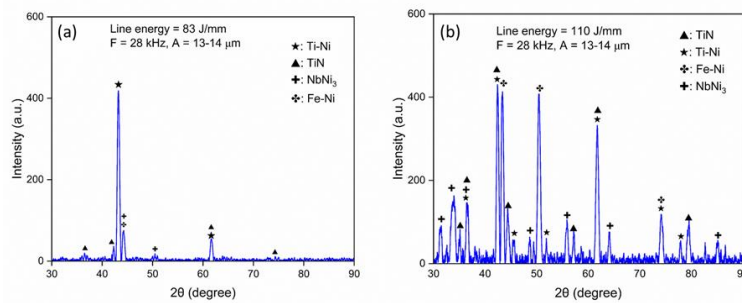


Figure 7: XRD analysis of clads deposited under ex-situ process at (a) LE = 83 J/mm (b) LE = 110 J/mm with the application of vibration

Thermal history analysis

Figure 8 illustrates the thermal history profile of the samples deposited under variable line energy along with the application of acoustic vibration during the MMC deposition. Due to lower line energy, small amount of Fe-Ni phase was detected in the XRD data and a change in slope of the thermal history profile could be observed at a temperature of 1475°C (**Figure 8a**). However at higher line energy, the amount of Iron content in the matrix was significant and as a result Fe-Ni phases were detected in the XRD graphs. Fe-Ni nucleation occurs at 1465°C under equilibrium condition which is distinguished in the temperature history profile as a solidification shelf at a temperature of 1465°C. Moreover, Ti-Ni and TiN solidification shelves corresponding to their nucleation temperatures at 972°C and 1794°C are identified in the thermal history profile. Therefore, the thermal history graphs adequately carry the signatures of the micro-structural changes.

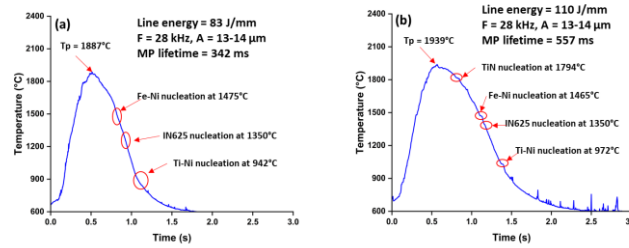


Figure 8: Thermal history profile of MMC depositions through ex-situ process under (a) LE = 83 J/mm (b) LE = 110 J/mm with the application of vibration

In-situ TiN/Inconel 615 MMC

Phase identification through X-ray diffraction

Formation of TiN at higher flow concentration and higher energy could be attributed to two reasons: enhanced nitrogen gas diffusion and increased solubility as reported by Abboudh [14]. Increased pressure signified a denser concentration of nitrogen molecules around the molten titanium droplet. This translated to a higher number of nitrogen molecules bombarding the droplet's surface per unit time. With more nitrogen molecules around, the frequency of collisions between these molecules and the Titanium atoms at the droplet surface increased creating a more favourable condition for nitrogen to diffuse inwards into the molten titanium. **Figure 9(a)** and **Figure 9(b)** shows XRD graphs of clads deposited at same line energy under 1 bar and 3 bar nitrogen gas pressure respectively. At lower flowrate of nitrogen, formation of TiN was minute. However different intermetallic compounds formed (Ti-Ni, NbNi₃, Fe-Mn-Ni, Fe-Ni) along with formation of nitrides. At higher flowrate of nitrogen, formation of TiN was significant which can be confirmed by the increased intensity peaks of TiN. Moreover the additional nitrogen form metal nitrides like Nickel Nitride, Iron Nitride and Molybdenum Nitride.

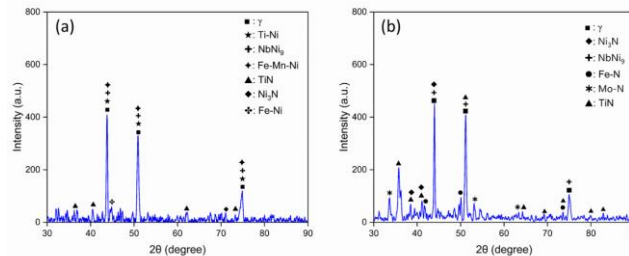


Figure 9: XRD analysis of clads deposited under in-situ process at (a) Pressure = 1 bar and (b) Pressure = 3 bar

Thermal history analysis

When the preplaced specimen was irradiated with laser beam, the Ti and Inconel 625 powder coating efficiently absorbed the laser energy, leading to immediate melting of the Ti and Inconel 625 powders. As the molten metal is exposed to nitrogen and due to the strong affinity of Ti for nitrogen, TiN forms at the interface between the liquid and gas phases. Simultaneously, the Inconel powder absorbed heat transfer and forms Ti-Ni phases. The variation in TiN formation across the depth is determined by the concentration of N₂ and the duration of the liquid phase at different locations within the melt pool [11]. TiN particles formed on the outermost surface were transported and mixed within the molten metal pool, acting as dendritic nuclei and becoming dispersed within the pool. The longer the molten Ti remains in the liquid state, the greater the formation of TiN dendrites. At the outermost surface, where solidification occurs last, TiN forms a continuous and compact structure.

The mechanism of TiN formation during laser melting in nitrogen containing atmosphere was reported by *Labudovic* [15]. It was reported that Labudovic indicates that the following reactions arise during the layer synthesis:

- i. Adsorption: $[\text{Ti}] + \text{N}_2 \rightarrow [\text{Ti}] + [\text{N}_2]$
- ii. Dissociation: $[\text{N}_2] \rightarrow 2 \text{N}$
- iii. Diffusion: $[\text{N}] (\text{surface}) \rightarrow [\text{N}] (\text{surface})$
- iv. TiN formation: $[\text{Ti}(\text{N})] \rightarrow \text{TiN} + [\text{Ti}(\text{N})]$
- v. Solidification: $[\text{Ti}(\text{N})] \rightarrow \text{TiN} + \alpha\text{-Ti}(\text{N})$

Square brackets [] mean in liquid phase. This makes clear, which complex sequences going on during the process. It is shown that besides the TiN, nitrogen dissolution in the pure hexagonal α -titanium also occurs.

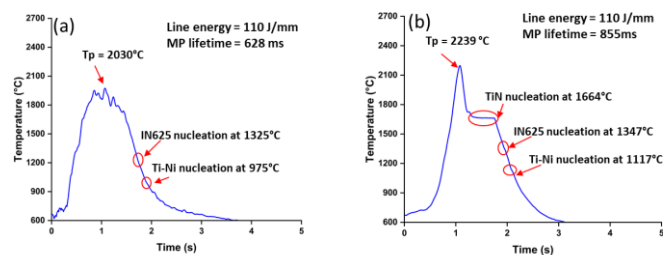
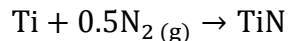


Figure 10: Thermal history of TiN/IN625 MMC depositions under in-situ process at (a) Pressure = 1 bar and (b) Pressure = 3 bar

Titanium reacts with gaseous Nitrogen to form Titanium Nitride which is an exothermic reaction. The chemical reaction is given below:



$$\Delta H = -336 \text{ kJ/mol (exothermic)}$$

As the TiN formation is exothermic, the heat released by TiN formation slightly elevate the temperature around the reacting particles. This helps in melting the surrounding titanium powder particles more efficiently, leading to a more continuous supply of molten metal and hence a longer-lived molten pool is observed with the increase of pressure. From the XRD graphs, it was observed that no formation of nitrides at lower gas pressure. However, at higher nitrogen gas pressure (i.e. at Pressure = 3 bar), significant amount of Titanium nitrides could be identified along with the presence of Ti-Ni phases. Formation of TiN from titanium and nitrogen is an exothermic reaction and the additional energy produced by the exothermic reaction during TiN formation contributes to an increase in the melt pool temperature. Moreover due to significant amount of TiN formation at higher nitrogen gas pressure, distinct solidification shelf corresponding to TiN formation can be seen in the thermal history profile.

Conclusion

- Experiments were conducted through ex-situ method to deposit TiN/ Inconel 625 MMC clads. Keeping the power as constant i.e. 220 W, the operational line energy 83 J/mm to 110 J/mm by varying scan speed. Phase formation under both these processes were identified.
- In ex-situ deposition, TiN were present in particle forms in case of lower line energy and in dendrite forms in case of higher line energy; solidification shelf of TiN can be seen in the temperature profile in case of higher line energy.
- Occurrence of Ti-Ni phases was analysed in both these line energies and their solidification shelves were also identified from the thermal history profiles.
- In in-situ MMC depositions, pressure of nitrogen gas had a significant effect on formation of TiN in the clad. At higher gas pressure (i.e. at 3 bar), TiN phase could be seen, however not in case of lower gas pressure (i.e. at 1 bar). TiN solidification was identified at higher nitrogen gas flowrate (i.e. at 3 bar).

References

- [1] V. Mandal *et al.*, “Fabrication of ex-situ TiN reinforced IN718 composites using laser powder bed fusion (L-PBF): Experimental characterization and high-fidelity numerical simulations,” *Ceram. Int.*, vol. 49, no. 9, pp. 14408–14425,

- 2023, doi: 10.1016/j.ceramint.2023.01.030.
- [2] H. Ahamed and V. Senthilkumar, "Consolidation behavior of mechanically alloyed aluminum based nanocomposites reinforced with nanoscale Y₂O₃/Al₂O₃ particles," *Mater. Charact.*, vol. 62, no. 12, pp. 1235–1249, 2011, doi: 10.1016/j.matchar.2011.10.011.
- [3] Y. M. Youssef and M. A. El-Sayed, "Effect of reinforcement particle size and weight fraction on the mechanical properties of SiC particle reinforced al metal matrix composites," *Int. Rev. Mech. Eng.*, vol. 10, no. 4, pp. 261–265, 2016, doi: 10.15866/ireme.v10i4.9509.
- [4] S. Zhang, L. Wang, X. Lin, H. Yang, and W. Huang, "The formation and dissolution mechanisms of Laves phase in Inconel 718 fabricated by selective laser melting compared to directed energy deposition and cast," *Compos. Part B Eng.*, vol. 239, 2022, doi: 10.1016/j.compositesb.2022.109994.
- [5] X. Li, G. Jin, F. Liu, Y. Sun, S. Guan, and Y. Chen, "Simultaneous enhancements in strength and ductility of hexagonal BN nanosheet reinforced AlSi10Mg composites," *J. Alloys Compd.*, vol. 992, 2024, doi: 10.1016/j.jallcom.2024.174577.
- [6] K. D. Traxel and A. Bandyopadhyay, "Selective laser melting of Ti6Al4V-B4C-BN in situ reactive composites," *J. Mater. Res. Technol.*, vol. 18, pp. 2654–2671, 2022, doi: 10.1016/j.jmrt.2022.03.092.
- [7] N. K. Bhoi, H. Singh, and S. Pratap, "Developments in the aluminum metal matrix composites reinforced by micro/nano particles – A review," *J. Compos. Mater.*, vol. 54, no. 6, pp. 813–833, 2020, doi: 10.1177/0021998319865307.
- [8] S. Hazra, S. Chattopadhyay, S. Chakravarty, and N. kumar Mandal, "Tribology of Mg-B 4 C nanocomposites fabricated following powder metallurgy route," *Eng. Res. Express*, vol. 6, no. 3, p. 035525, Sep. 2024, doi: 10.1088/2631-8695/ad652f.
- [9] M. Xiang *et al.*, "Facile synthesis of high-melting point spherical TiC and TiN powders at low temperature," *J. Am. Ceram. Soc.*, vol. 103, no. 2, pp. 889–898, 2020, doi: 10.1111/jace.16810.
- [10] X. Zhao, Q. S. Wei, N. Gao, E. L. Zheng, Y. S. Shi, and S. F. Yang, "Rapid fabrication of TiN/AISI 420 stainless steel composite by selective laser melting additive manufacturing," *J.*

- Mater. Process. Technol.*, vol. 270, pp. 8–19, 2019, doi: 10.1016/j.jmatprotec.2019.01.028.
- [11] H. C. Man, S. Zhang, F. T. Cheng, and X. Guo, “In situ formation of a TiN/Ti metal matrix composite gradient coating on NiTi by laser cladding and nitriding,” *Surf. Coatings Technol.*, vol. 200, no. 16–17, pp. 4961–4966, 2006, doi: 10.1016/j.surfcoat.2005.05.017.
- [12] H. I. Jeong, D. H. Kim, and C. M. Lee, “Multi-material deposition of Inconel 718 and Ti–6Al–4V using the Ti–Nb–Cr–V–Ni high entropy alloy intermediate layer,” *J. Mater. Res. Technol.*, vol. 29, pp. 3217–3227, 2024, doi: 10.1016/j.jmrt.2024.01.285.
- [13] J. Xu *et al.*, “Diffusion of nitrogen in solid titanium at elevated temperature and the influence on the microstructure,” *J. Mater. Res. Technol.*, vol. 12, pp. 125–137, 2021, doi: 10.1016/j.jmrt.2021.02.073.
- [14] G. I. Silman, “Compilative Fe - Ni phase diagram with author’s correction,” *Met. Sci. Heat Treat.*, vol. 54, no. 3–4, pp. 105–112, 2012, doi: 10.1007/s11041-012-9463-x.
- [15] M. Labudovic, R. Kovacevic, I. Kmecko, T. I. Khan, D. Blečić, and Z. Blečić, “Mechanism of surface modification of the Ti–6Al–4V alloy using a gas tungsten arc heat source,” *Metall. Mater. Trans. A Phys. Metall. Mater. Sci.*, vol. 30, no. 6, pp. 1597–1603, 1999, doi: 10.1007/s11661-999-0096-7.

Fabrication and Analysis of Dual Hardness Steel Through Laser DED

**Sidhartha Sankar Swain ^{1*}, Rohan Ranjan Shandilya ²,
Prabhat Kumar ³, Srikant Gollapudi ⁴, Suhradip Mullick ⁵**

IIT Bhubaneswar

* 23mf06020@iitbbs.ac.in

Abstract

Dual hardness steel, with varying hardness levels, enhances industrial performance. However, traditional methods like roll bonding and forging often cause defects and poor bonding, leading to cracking and compromised integrity. Methods like weld cladding and diffusion bonding are ineffective for large-scale dual hardness steel. This study explores laser DED as an alternative. SS316L and SS420 are chosen as high corrosion and hardness materials respectively suitable for defence applications. The study aims to establish optimal conditions to achieve void-free multilayer deposits of SS316L and SS420 for dual hardness steel using laser direct energy deposition (DED). While DED initially produced voids, optimizing parameters such as line energy, powder feed rate, and using techniques like inter-pass laser re-melting significantly reduced defects. Optimal DED parameters for SS316L include a 220 W laser power, 7 g/min powder feed rate, and 132 J/mm line energy, along with inter-pass re-melting to reduce voids and enhance smoothness. For SS420, using slightly lower power and higher line energy with re-melting further improves results. The highest recorded hardness ranged between 600-650 HV. Ongoing research focuses on further assessing the mechanical strength and surface properties of dual hardness steel, aiming to refine fabrication techniques and expand its industrial applications.

Keywords: Dual hardness steel, Laser direct energy deposition, ultrasonic vibration, re-melting, interfacial bonding.

Introduction

Dual hardness steel has become a popular focus in materials engineering because it combines two different hardness levels in one component, making it highly adaptable to challenging applications. This unique combination of hard and tough areas is typically achieved through advanced manufacturing techniques that allow specific sections of the steel to be hardened while others remain more ductile.

This strategic design means the steel can offer high wear resistance where it's most needed, such as in areas exposed to heavy stress or friction, while retaining toughness in other areas to absorb impact without breaking. These properties make dual hardness steel ideal for demanding industries like automotive, aerospace, and heavy machinery, where components benefit from enhanced durability, longer service life, and reduced maintenance costs. Engineers appreciate the flexibility of dual hardness steel, as it allows them to fine-tune a component's hardness profile to meet the exact needs of modern applications, balancing high performance with cost-effectiveness.

Conventional methods like roll bonding, arc welding, and diffusion bonding are commonly used to fabricate dual-hardness steel, but they often introduce challenges that can compromise the material's structural integrity. For instance, roll bonding, as explored by Jing et al. ^[1], involves hot rolling SUS304 and plain carbon steel at high temperatures. Though the initial interfacial micro-pores decrease with rolling, but bonding issues such as interfacial adhesion, residual stresses, decarburization, and oxide layers, weaken the material. Similarly, Hordych et al. ^[2] highlighted that roll bonding tin-coated steel sheets faces problems like weak bond strength linked to the reduction ratio, oxidation at high temperatures, and the formation of brittle intermetallic layers over 1 μm . Arc welding also presents difficulties, as Rao et al. ^[3] done arc welding of AISI 347 stainless steels onto high-strength low-alloy steel. The process resulted in grain coarsening and decarburization at the interface, which weaken the bond. The key issue across these methods is the microstructural changes that occur during processing, which can reduce both strength and performance. On the other hand, diffusion bonding, when applied to dissimilar steels, such as duplex and austenitic stainless steels with medium-carbon steel, it offers stronger, carbide-rich interfaces, but improper aging or excessive heat can cause defects like lack-of-fill and decohesion. As Khedr et al. ^[4] noted, excessive heat input can also create microstructures like martensite or δ -ferrite, negatively affecting bond integrity.

To overcome these various challenges, several advanced additive manufacturing (AM) techniques are increasingly being used. AM provides many benefits, including the ability to create complex shapes, reduced material and labour costs, and greater precision. Methods like Selective Laser Melting (SLM) and Direct Energy Deposition (DED) are particularly effective for producing dual-hardness steel. However, SLM has limitations, as observed by Bingwei et al. ^[5], including slower feed speeds, unstable processing, powder spheroidization, and issues like warping and cracking in fabrication of

SS316L. Miranda et al. ^[6] also noted surface defects in SS316L fabricated via SLM, which weakened fatigue performance, leading to microcracks and brittle fractures under stress. In contrast, laser DED offers greater advantages, particularly for stainless steel, because it allows for repairs and additions to existing parts, which is beneficial for creating complex and large geometries. Research by Benarji et al. ^[7] on laser-assisted DED for SS316L showed promising results, including high hardness (292 HV) and fast deposition rates. Aydogan et al. ^[8] found that laser-DED of SS420 produced a martensitic structure, resulting in high hardness (555 HV) and tensile strength (1925 MPa), though it had lower ductility. Heer et al. ^[9] successfully fabricated a bimetallic SS316 and SS430 structure using laser-engineered net shaping in DED, creating a strong interface with no visible cracks and improved microhardness. Remelting strategies or in-situ heat treatments improve laser deposition by refining the microstructure, enhancing bonding, and reducing porosity. This leads to better mechanical properties and overall part integrity. For instance, Park et al. ^[10] showed that laser rescanning in L-DED refined grain and cell structures in high-manganese steel, producing nearly defect-free microstructures with enhanced hardness. Similarly, Kahya et al. ^[11] found that remelting during DED of SS316L improves the microstructure, reduces grain size, and enhances properties like Charpy strength. This present study focuses laser DED method with remelting strategy to fabricate dual hardness steel and analysis of grain structure affecting hardness.

Material and Methods

A 30 mm × 30 mm × 8 mm, SS304 substrate polished with abrasive paper (P400 to P600) and a CW mode Yb-fiber laser system shown in Fig 2. with 1.06 μm wavelength, approximate spot diameter of 750 μm and maximum workable power of 240 W used with argon as both shielding and carrier gas for fabrication of dual hardness steel. An austenitic SS316L and martensitic SS420 stainless steels of 45-90 μm spherical powder particles were used for deposition. Powders are co-axially fed through nozzle of hopper (Model: MPF-700) capacity 700 cc, disk rpm of 1-25 having powder feed rate of 2- 90 g/min. Powders are deposited varying Laser power, scan speed and powder feed rate with remelting strategies. For microstructural analysis, laser-cladded samples were cut by wire-EDM perpendicular to the laser scan direction and mounted using cold mounting powder and liquid. Cross-sections were polished with SiC abrasive papers (P400–P1500) and 0.5–1.5 μm diamond polish, then ultrasonically cleaned for 5–10 minutes. The polished surfaces were etched with a 1:3:3 HNO₃: HCl

solution for 30 seconds and the grain structures are seen through optical microscopy. Micro-hardness was measured along the depth of the cross-section using a Vickers tester (Zwick Roell ZHV) with a 200-gf load and a 10-second dwell time at the top and bottom layers.

Table 1: Composition of SS420 and SS316L material

Material/Elements	Cr	Ni	Mo	C	Mn	Si	P	S	Fe
SS316L	16.5	10.25	1.95	0.02	1.85	1.0	0.045	0.03	Bal
SS420	12.65	0.28	0.04	0.31	0.67	0.79	0.03	0.021	Bal

Table 2: Property comparison of SS316L and SS420

Property	S S316L	SS420
Tensile Strength	550-620 MPa	650-800 MPa
Hardness (HV)	152	247
Thermal conductivity	15 W/m K	24.9 W/m K
Linear Coefficient of Thermal Expansion	16.5×10^{-6} m/m-k	10.3×10^{-6} m/m-k

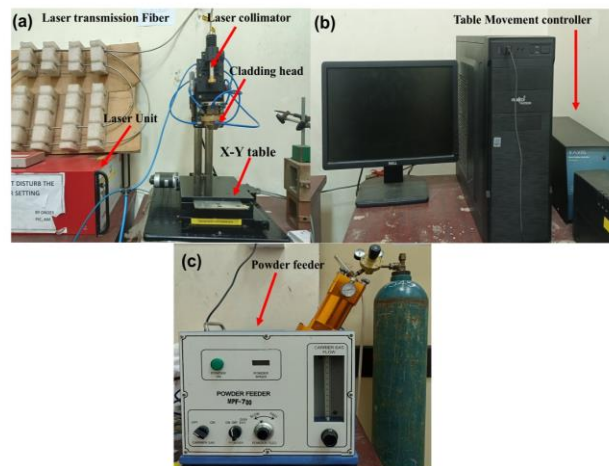


Figure 2 Experimental set up (a) laser setup, (b) X-Y table movement controller, (c) Powder feeder

Result and Discussion

Optimisation of process parameters for SS316L

Primarily for optimisation, single-track deposition of SS316L done. Process parameters such as laser power, scan speed, carrier gas flow rate, and powder feed rate were optimized to achieve target dilution (10–20%) and wetting angle (45–60°). The power variation 200–220W, scan speed 100–132 mm/min, carrier gas flow rate 7.5 to 9.5 lit/min and powder feed rate 5.5 g/min to 8.8 g/min varying disk rpm 0.7–1.2 in the powder feeder, used to decide the optimum process parameters. The best results observed at 220 W laser power, 100 mm/min scan speed, 8.5 L/min carrier gas flow rate. Analysis showed that lower scan speed increases dilution due to longer interaction time, causing more substrate and powder to melt. Conversely, higher scan speed increases the wetting angle by reducing molten pool lifetime, resulting in less effective spreading of the molten material. Optimal dilution and wetting angle are crucial for achieving desired intermixing and bonding, ensuring good adhesion and mechanical integrity of the deposited SS316L layer. Further in Fig 3. multi-track, multilayer deposition (5 track and 3 layer) with optimised overlap percentage of 25%, varying powder feed rate are experimented and 7.4 g/min powder feed rate gave better result in terms of less interlayer voids and cracks. K Saeidi et al. ^[12] investigated cracks form in SS316L due to brittle glass nano-inclusions from Si and Cr's oxygen affinity and stress from dislocation pile-ups, especially around Mo-rich sub-grain boundaries. Cr-silicate inclusions block dislocation movement, leading to stress buildup. Additionally, thermal expansion mismatch around inclusions causes further stress, promoting crack formation.

Table 3: Selected optimized parameters for as-deposited SS316L

Process Parameters	Power(W)	Scan Speed (mm/min)	Carrier Gas flow (lit/min)	Powder flow rate (g/min)
Experimental Range	200-220	100-132	7.5-9.5	5.5-8.8
Selected Parameter	220	100	8.5	7

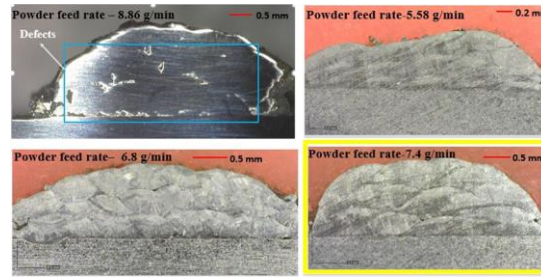


Figure 3 multi-track, multi-layer deposition of SS316L varying powder feed rate

To make the powder feed rounding off, 7 g/min at 0.95 disk rpm set to be the optimised value for multi-track, multi-layer SS316L deposition. In Fig 4. to further improve surface quality, reducing micro voids and enhancing bonding between interlayers, Re-Melting strategy used by keeping the as-deposited condition same, varying line energy from 30 J/mm to 45 J/mm and experimented with power 220 W. The best result was observed with 45 J/mm (re-melting speed 293 mm/min) with less crack and interlayer voids.

Table 4: Selected optimized parameters for remelting of SS316L

Process parameters	Power(W)	Speed (mm/sec)	Line energy (J/mm)
Experimental range	200-220	293-440	30-45
Selected parameters	220	293	45

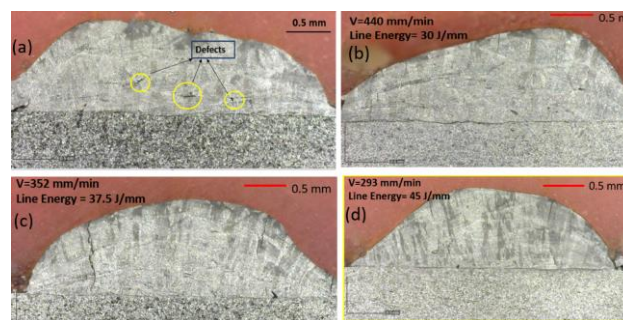


Figure 4. Multi-track, multi-layer deposition of SS316L varying Re-melting Line energy where (a) As-deposited at 7 g/min, (b) As-deposited +Re-melting (30 J/mm) (c) As-deposited +Re-melting (37.5 J/mm), (d) As-deposited +Re-melting (45 J/mm).

Optimisation of process parameters for SS420

For SS420, in Fig 5. similarly, the single track and multi-track deposition done by the variation of process parameters i.e. power 200-240 W, scan speed 75-110 mm/min, carrier gas flow rate 7.5-9.5 lit/min and powder feed rate 5.5-7 g/min for 0.8-1.2 disk rpm of powder feeder respectively. The optimum values came up with 230 W power, 80 mm/min scan speed, 8.5 lit/min career gas flow rate and 6 g/min powder flow rate at 0.9 disk rpm with 35% over lap shows the best results. Further to enhance more surface quality and improving bonding by reducing voids and cracks, inter-pass re-melting strategy applied with same as-deposited condition, 45-55 J/mm line energy at same laser power 230 W with varying scan speed. The best outcome came up with 55 J/mm (re-melting speed 251mm/min).

Table 5: Selected optimised parameters for as-deposited SS420

Process Parameters	Power(W)	Scan Speed (mm/min)	Carrier Gas flow (lit/min)	Powder flow rate (g/min)
Experimental Range	200-240	75-110	7.5-9.5	5.5-7
Selected Parameter	220	100	8.5	6

Table 6: Selected optimized parameters for remelting of SS420

Process parameters	Power(W)	Speed (mm/sec)	Line energy (J/mm)
Experimental range	200-240	251-306	45-55
Selected parameters	230	251	55

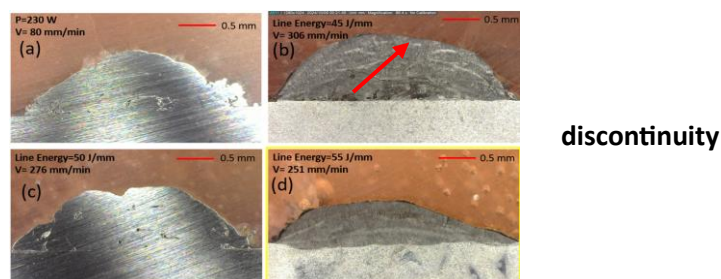


Figure 5. Multi-track, multi-layer deposition of SS420 varying Re-melting Line energy where (a) As-deposited at 6 g/min, (b) As-

deposited +Re-melting (45 J/mm) (c) As-deposited +Re-melting (50 J/mm), (d) As-deposited +Re-melting (55 J/mm).

Dual Hardness steel deposition

By using the above optimised process parameters, both steels deposited on the substrate SS304 (10 tracks and 6 layers) in Fig 6 i.e.- on the substrate 3 layers of SS316L and then 3-layer SS420 using as-deposited and inter pass re-melting strategy. Remelting condition showing better inter layer bonding and defect free surface.

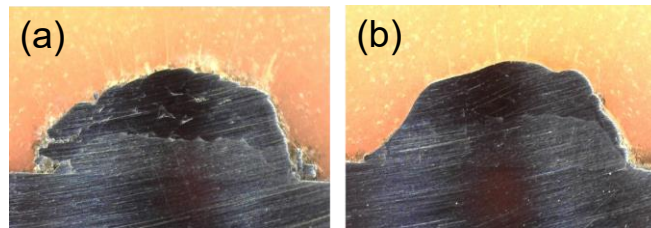


Figure 6. Multi-track, multi-layer deposition of Dual hardness steel where (a) As-deposited (b) Inter-pass remelting

Grain structure analysis

Laser deposition creates distinct grain structures due to localized heating, rapid cooling, and thermal gradients characteristic of additive manufacturing. In Fig 7. Image (a), fine and uniform grains result from rapid cooling and limited heat input, typical in initial or peripheral deposition layers that are farther from the heat-affected zone. Image (b) shows larger, irregular grains, suggesting higher energy input due to re-melting in areas closer to the laser path or where layers overlap, leading to thermal gradients and grain growth. Image (c) displays elongated grains, reflecting directional solidification caused by the laser's movement, with grains aligned opposite to heat dissipation. Image (d), with a mix of fine and coarse grains, likely indicates variable cooling rates and thermal cycling near deposited layers or interfaces, where multiple passes cause some grains to coarsen or recrystallize. The melt pool depth for SS316L varies from 0.27 mm to 0.30 mm and for SS420, it varies from 0.31 to 0.48 mm due to inter-pass laser re-melting.

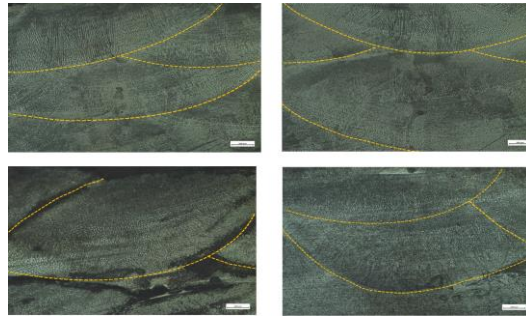


Figure 7. Grain structure of dual hardness steel where (a) as-deposited SS316L (b) Re-melted SS316L (c) as-deposited SS420 (d) re-melted SS420

Micro Hardness Analysis

The micro-hardness test has been done to find out the hardness value of sample which is deposited at different conditions. Hardness value is taken on the top and bottom of each layer along the center line. It is observed that hardness value is maximum for sample deposited with as-deposited (Fig. 7) i.e. 627 HV. Though Re-melting produces good inter-layer bonding and void free surface but there is a slight compromise in hardness i.e. 614 HV. Remelting reduces hardness by promoting grain growth, which leads to a coarser and softer structure. It also relieves residual stresses introduced during rapid cooling of the initial deposition. Additionally, hard phases formed initially can dissolve or transform into softer phases, further lowering hardness.

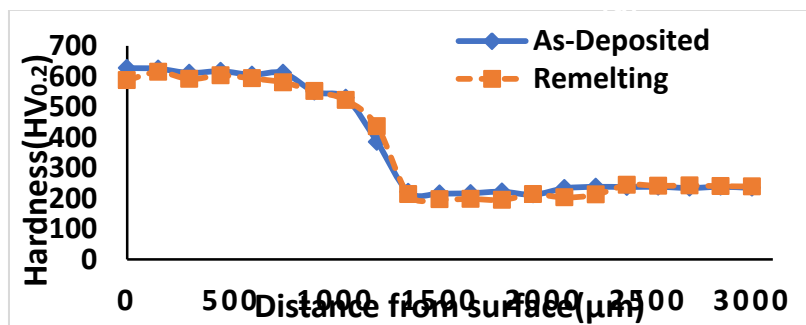


Figure 8. Micro hardness of Dual hardness steel

Conclusion

In this study, the optimization of laser deposition parameters for SS316L and SS420 was successfully achieved, resulting in improved surface quality and mechanical properties. The optimised parameters

for SS316L included a laser power of 220 W, a scan speed of 100 mm/min, and a powder feed rate of 7 g/min, which minimised voids and enhanced interlayer bonding. For SS420, the optimal conditions were identified as a power of 230 W, scan speed of 80 mm/min, and powder flow rate of 6 g/min. Inter-pass remelting strategies effectively enhanced surface quality and reduced defects, leading to better interlayer bonding in dual hardness steel deposits. While remelting improved the overall structural integrity and surface finish, it resulted in a slight reduction in microhardness due to grain growth and the dissolution of hard phases. Overall, the findings underscore the importance of carefully optimizing process parameters to balance surface quality, adhesion, and mechanical properties in laser-based additive manufacturing.

Acknowledgments

This work was conducted under the guidance and funding of the Indian Institute of Technology, Bhubaneswar. The authors express their gratitude to the institute for its continuous support

References

1. Yuan Jing, Yi Qin, Xiaoming Zang, Ying Hong Li, The bonding properties and interfacial morphologies of clad plate prepared by multiple passes hot rolling in a protective atmosphere, *Journal of Materials Processing Technology*, Volume 214, Pages 1686-1695.2 (2014)
2. Illia Hordych, Khemais Barianti, Sebastian Herbst, Florian Nürnberger, Cold Roll Bonding of Tin-Coated Steel Sheets with Subsequent Heat Treatment, *Metals*, 11, 917, (2021)
3. N. Venkateswara Rao, G. Madhusudhan Reddy, S. Nagarjuna, Weld overlay cladding of high strength low alloy steel with austenitic stainless steel – Structure and properties, *Materials and Design*, 32: 2496-2506 (2011)
4. Mahmoud Khedr, Atef Hamada, Antti Jarvenpaa, Sally, Elkatatny and Walaa Abd-Elaziem, Review on the Solid-State Welding of Steels: Diffusion Bonding and Friction Stir Welding Processes, *Metals*, 13, 54 (2023)
5. Bingwei Gao, Hongjian Zhao, Liqing Peng and Zhixin Sun, A Review of Research Progress in Selective Laser (SLM), *Micromachines*, 14, 57 (2023)
6. Georgina Miranda, S. Faria, Flávio Bartolomeu, Predictive models for physical and mechanical properties of 316L stainless steel

produced by selective laser melting, *Materials Science and Engineering A* 657 (2016)

7. K. Benarji, Y Ravi Kumar, CP Paul, and KS Bindra, Parametric investigation and characterization on SS316 built by laser-assisted directed energy deposition, *Institute of Mechanical Engineers*, Vol. 234(3) 452–466 (2020)
8. Beytullah Aydogan, Aaron O'Neil, Himanshu Sahasrabudhe, Microstructural and mechanical characterization of stainless steel 420 and Inconel 718 multi-material structures fabricated using laser directed energy deposition, *Journal of Manufacturing Processes* 68,1224–123 (2021)
9. Bryan Heer, Amit Bandyopadhyay, compositionally graded magnetic-nonmagnetic bimetallic structure using laser engineered net shaping, *Materials Letters*, 216,16–19 (2018)
10. Young Keun Park, Hyun Ji Nam, Yong Ho Park and Wook jin Lee, Laser Rescanning for Enhancing Mechanical Properties of Laser-Directed Energy-Deposited High-Manganese Steels, *Micromachines*, 15(2), 176 (2024)
11. Harun Kahya, Hakan Gurun and Gokhan Kucukturk, Experimental and Analytical Investigation of the Re-Melting Effect in the Manufacturing of 316L by Direct Energy Deposition (DED) Method, *Metals*, 13(6), 1144 (2023)
12. K. Saeidi, X. Gao, Y. Zhong, Z.J. Shen, Hardened austenite steel with columnar sub grain structure formed by laser melting, *Materials Science & Engineering*, 625 221–229 (2015)

Graphite Oxide Embedded Polyaniline Hybrids For High Frequency Electromagnetic Wave Attenuation and EMI Shielding

**¹T N Girisha, ¹R Thulasi, ²N Maruthi N, ³Raghavendra
Narasimha and ¹Faisal Muhammad***

*¹Research Center-Physics,
PES University-Electronic City Campus,
Bangalore- 560100, Karnataka, India*

*²Department of Physics,
Faculty of Engineering and Technology, Jain University,
Bangalore - 562112, Karnataka, India.*

*³Department of Chemistry,
K.L.E Societies P.C. Jabin Science College
Hubballi-580031, Karnataka, India*

*Correspondence to: E-mail: *muhammadfaisal@pes.edu
(Muhammad Faisal)*

Abstract

With the ever-growing use of smart electro/electrical devices and systems, electromagnetic interference (EMI) has become highly sensitive issue and needs to be suppressed. The adverse effects of, EMI, the silent invisible pollution cannot be underestimated as it is associated with the operational efficiency of the devices and also the living beings. In this study composites of conducting polyaniline (PAni) dispersed with graphite oxide (GO) have been synthesized by in-situ chemical oxidative polymerization and tested for broadband electromagnetic (EM) wave attenuation and EMI shielding. These composite hybrids have been characterized by X-ray diffraction (XRD), Fourier transform infrared spectroscopy (FTIR), scanning electron microscopy and high-resolution transmission electron microscopy (TEM) for structural and morphological features. SEM and TEM results showed modified morphological features of conducting network of PAni matrix in the presence of dispersant GO. The EM wave attenuation and EMI shielding properties have been investigated using transmission line waveguide technique in the frequency range of

8 to 12 GHz (microwave X-band). The composite samples have shown EMI shielding efficiency (EMI SE) in the range of -26 dB to -30 dB which demonstrates that more than 99% of the incident EM energy has been attenuated. The observed absorption coefficient was in the range of 77 to 84 % clarifying that polyaniline-coated graphite oxide composites can be optimized as potential broadband electromagnetic wave absorbers and shields. These EMI shielding results can be primarily attributed to the modified complex dielectric permittivity of polyaniline in the presence of graphite oxide. These composites combine the morphological and electrical properties of both polyaniline (PAni) and graphite oxide (GO), and can effectively absorb electromagnetic waves across a wide frequency range with very high EMI SE.

Keywords: Polyaniline, graphite oxide, X-ray diffraction, electron microscopy, Electromagnetic interference, shielding efficiency.

Introduction

The current era we are living with our surroundings exposed to exhaustive usage of electronic gadgets, primarily mobile phones, wireless devices and computers, other portable smart electronics devices and systems. This exposure to electromagnetic energy causes the ever-increasing electromagnetic radiation pollution. This issue of electromagnetic interference (EMI) needs very relevant attention with the rapid proliferation of the electro/electronic gadgets and also increase the wireless transmission technology (5G) [1]. This electromagnetic radiation pollution causes very harmful effect on the living beings with very specific negative impact on human health. Long-term and prolonged electromagnetic energy exposure radiation raises the risk of various chronic heart disease, brain dysfunctionalities, asthma, migraines, and pregnancy complications [2, 3]. In addition to this, the problem of EMI causes electrical devices to malfunction and produce various other performance issues. Thus, it is very important to minimize the electromagnetic radiation pollution to safe guard the diverse domain of electro/electrical devices and systems and to protect the healthy well-being of living beings. Thus, EMI shielding is extremely significant in guaranteeing the proper operation of electrical devices and prevents malfunctions [4].

Polymer composites and metals were the most commonly utilized shielding materials for the suppression of the broad array of electromagnetic pollution [4, 5]. From the literature documentation, it is evidenced that metals and metal-based materials have been broadly investigated for EMI shielding because of their high conductivity and

diverse dielectric attributes. However, metal based EMI shields have various drawbacks like heavy, sensitive to corrosion and poor processability [6, 7]. Other EMI shielding materials based on ferrite and its derivatives have shown promising results but they have exhibited drastic decrease in the magnetic loss at high frequency with other morphological irregularities [8]. For productive and efficient shielding applications, recent studies have clearly demonstrated that polymer based conducting composites especially the diverse family of conjugated polymers (CP) and CP based composites (CPCs) are highly efficient and versatile. CPCs have the unique advantages of diverse properties of conducting polymers blended with the specific properties of the dispersed phase. These materials have been found to be less corrosive, light weight, have a tunable thickness and they are very good EM wave absorbing characteristics suitable for various frequency bandwidths [9, 10]. Some of the most practically relevant and promising conducting polymers are polyaniline, polypyrrole, PEDOT, and polythiophene. Composites based on these polymers have dominant shielding characteristics enabling as replacement for the traditional metal, metal based and ferrite based shielding materials.

The current work addresses polyaniline (PAni)/graphite oxide (GO) composite as a promising broad band EMI shielding material. Graphite oxide is highly stable with diverse electrical characteristics with good thermoelectric properties [11,12] and it can be optimized as an efficient dispersant to modify the properties of polyaniline/GO composites.

Experimental

Materials

Aniline, ammonium peroxy-disulfate (APS), and hydrochloric acid (HCL) were procured from Sigma-Aldrich (India) Ltd. Graphite oxide powder (research grade) was purchased from Indiamart, India.

Sample preparation

Synthesis of polyaniline and polyaniline/GO composites have been carried out using oxidative polymerization, which is one of the most economically feasible and environmentally friendly synthesis method [13, 14]. Starting with aniline monomer and hydrochloric acid mixture in beaker with constant stirring, at a well-maintained temperature 0-4° C. 5 g of ammonium peroxydisulfate was dissolved in the 1.0 molar concentrated hydrochloric acid and incorporated this dissolved solution to the above aniline hydrochloride. The polymerization reaction has been allowed to carry out for 7 hours,

maintaining the reaction temperature 0-4°C. After completion of the polymerization, the obtained polyaniline was extracted by filtration accompanied by thorough rinsing using hydrochloric and double distilled water. This process of filtration has been continued until the filtrate become colorless. Polyaniline is thus extracted and processed for characterization. In a similar way polyaniline composites with 10 and 20 weight percentage (w%) of incorporated graphite oxide (PG1 and PG2) has also been carried out and processed for further studies.

Characterizations

Structural features of the samples have been investigated by XRD (PANalytical X'pert Pro - Cu K α radiation at 40kV with step size 0.02°). The morphological features of the samples have been investigated by scanning electron microscopy (Philips SEM, model-XL30 ESEM, Nether lands) and HRTEM (JOEL JEM 2100, Japan). Frequency dependent conductivity measurements has been carried out at room temperature over the frequency range 100 Hz to 1 MHz, using Hioki LCR meter (model: 3532-50, Japan). The EMI shielding measurements have been carried using transmission line two-port network analysis with X-band waveguide in a Vector Network Analyzer (HP VNA - model 8510C; in the range of 50 MHz to 25 GHz, USA). The incident X-band (8 to 12 GHz) electromagnetic (EM) energy range onto the samples generated the parameters of EM energy scattering (two port S-parameters) responsible for the transmission (S12/S21) and reflection (S11/S22) of the EM energy. These scattering parameters have been utilized for the evaluation of EMI shielding efficiency of the samples.

Results and Discussion

XRD studies

Powder XRD technique was used to analyze the structural features of the polyaniline/GO composites. The diffractogram of pure polyaniline was found to exhibit the typical polyaniline semi-crystalline nature with broad peaks around 2 θ equal to 14° to 24°. [11, 15]. X-ray diffraction analysis helps in the identification of various structural modifications in the resulting composites in comparison with the individual phases. This modifications in turn influences the phase boundaries in the conductive network resulting modified electrical responses. The diffractograms of the composite samples have shown distinct modifications (2 θ values slightly shifted to 19° to 25° with GO peaks around 43° to 75°) indicating the interaction forming composite network. The coating of polyaniline over GO is anticipated to improve

the various physical and electrical characteristics of the resulting composites [16, 17].

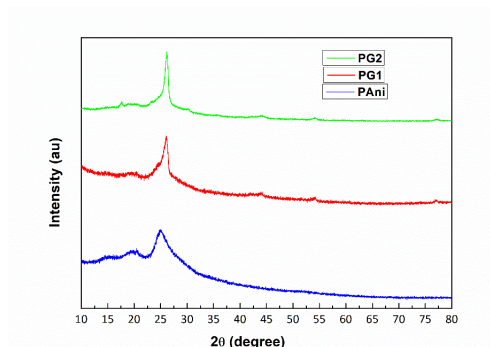
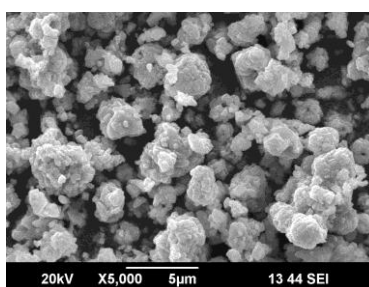
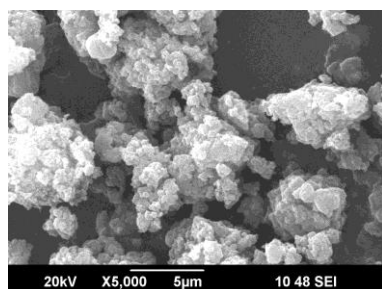


Figure 1: X ray diffraction pattern of pristine PAni and PAni/GO composites (PG1 and PG2).

Morphological features

Electron microscopy technique has been used to analyze the morphological features of the samples. SEM micrograph of pure PAni has shown typical morphology with a dominant agglomeration of the polymeric chain. Pure GO has shown specific irregular spherical morphology [16, 18] and incorporation of GO as a dispersant in PAni matrix can implement distinct morphology modification of the composite network leading to various property transitions. The composite morphology shown in Fig. 2c shows the coating of polyaniline over GO conforming to the XRD pattern. The incorporation of GO into PAni is evidenced in the HRTEM image shown in Fig. 2d [19]. The defined morphological features of GO in the presence of polyaniline result in modified interconnected morphological features that might facilitate better electromagnetic wave interaction characteristics for efficient shielding [17, 20 - 22]



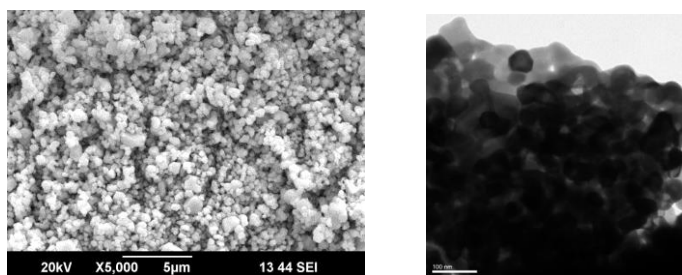


Figure 2 (a, b, c, &d): Morphological features of samples - SEM images of pure polyaniline, PG1 and PG2, HRTEM image of PG2

Electrical Conductivity

Electrical characterization of conducting polymer composites is very relevant as the analysis explains the charge transport mechanisms in these composites. The frequency-dependent AC conductivity helps to extract the inputs on mobility of charge carriers and the compatibility of the chosen conducting polymer matrix and the dispersant materials. An effective composite network will have a modified microstructure leading to stabilized distribution and connectivity of conductive pathways. In the present study, the composites have a marginal increase in the resultant conductivity compared to pure polyaniline indicating the suitability of GO content in the tunability of electrical properties. The increase in AC conductivity at higher frequencies clarifies that charge carriers have dominant movement under oscillating electric fields[21]. This nature of conductivity modification can hence facilitate better electromagnetic wave interaction possibilities favoring effective EMI shielding. The observed non-linear conductivity variation clearly indicates that the conductivity mechanism obeys power law and has the effects of charge carrier hopping with percolation effects of the dispersed phase. A possible electrical behavior is modeled with the bulk resistance of the polymer represented as R1, the resistance through the conductive filler with R2, and the capacitive effects of the composite network due to dielectric properties with C.[23], [24], [25]

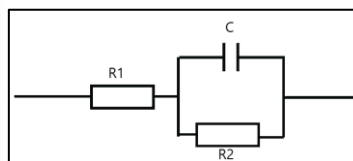
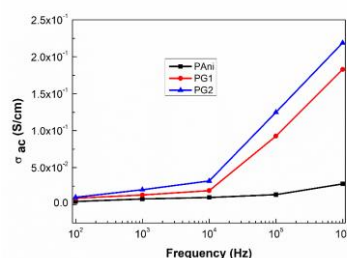


Figure 3: Frequency-dependent ac conductivity of pure polyaniline, PG1, and PG2 with equivalent circuit for PG1 and PG2.

This frequency-dependent electrical conductivity of CPs and their composites is a very relevant parameter as electromagnetic energy interaction with induced currents can absorb and dissipate energy leading to better attenuation. In general, the high conductivity of materials enables better shielding dominantly by the mechanism of reflection. Moderate conductivity observed in these PANi/GO composites facilitates shielding by the mechanism of absorption. Also, the balanced interaction between electrical conductivity and dielectric attributes of conducting polymer-based composites also influences electromagnetic wave attenuation in moderate conductivity composites. [14], [22], [26]

EMI shielding studies

In the development and optimization of EMI shielding materials, the most distinct parameter is the ability of attenuation by suitable specific mechanisms including reflection, absorption, and multiple reflections which is schematically shown in Fig. 4. As per the theory of EM energy propagation through transmission line, we can say that the intersection between the electromagnetic wave by the positioning of shielding material can be treated as two port network in the transmission line where the shielding material acts as a receiver and the electromagnetic wave acts as the source [27].

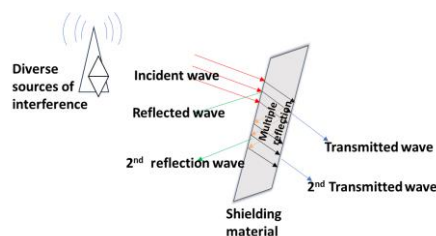


Figure 4: Mechanisms of attenuation by shielding materials

Basic shielding equations for the analysis of shielding efficiency (SE) is described below. The shielding efficiency of a sample can be evaluated in terms of the power ratio of incident and transmitted EM energy and is expressed in dB. The total shielding efficiency is considered as the sum of efficiency by the contribution of reflection of EM energy and that of absorbed EM energy [28-30]. The relevant formulae for the calculation of the EMI SE in terms of incident power (P_1), reflected power (P_2) and transmitted power (P_3) can be expressed as

$$\text{EMI SE (Total)} = \text{SE (reflection)} + \text{SE (absorption)} \quad \text{-----1}$$

$$\text{SE (reflection)} = 10 \log \frac{p_1}{p_1 - p_2} \quad \text{-----2}$$

$$\text{SE (absorption)} = 10 \log \frac{p_1 - p_2}{p_3} \quad \text{-----3}$$

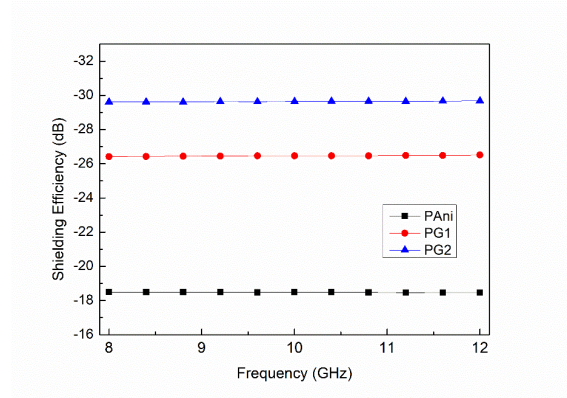


Figure 5: EMI shielding efficiency of PANi and PANi/GO composites (PG1, and PG2) as a function of a X-band frequency

Figure 5 shows the observed EMI shielding efficiency in the microwave frequency range of 8 – 12 GHz (X-band) and the corresponding absorbed EM power of PANi/GO composites are shown in Fig. 6. Compared to pure polyaniline, the composites have shown very relevant shielding efficiency clarifying the synergy between PANi and GO. High shielding efficiency in X-band is significant as this microwave broadband has various applications. Radar and communication systems, aerospace, and defense applications are very major domains exhaustively utilizing X-band frequencies. Also, many popular consumer electronics like microwave ovens, wireless routers, and mobile phones use X-band electromagnetic energy. Some medical equipment and devices also operate in X-band frequencies. Thus, effective EMI shielding is essential in microwave X-band to protect these systems from interference, ensuring accurate signal processing and data integrity. Also, shielding is essential for enhanced device performance and to ensure compliance with regulatory standards.[31], [32]

Composite materials of polyaniline with suitable type and concentration of conductive dispersants can modify the electrical properties and correlated shielding performance. Higher dispersant content within percolation limit can facilitate marginal increase in conductivity but the crowding effect strongly influences the structural

consistency of the composite network. The observed results in the present shielding analysis conforms this where the higher concentration of the dispersant GO resulted in the marginal decrease in absorption of EM energy as shown in Fig. 6. Thus, the observed highly relevant shielding efficiency of PANi/GO composites can be primarily justified attributed to the modified electrical properties with compatible composite network. The enhanced shielding efficiency was found to be primarily due to dominant absorption process and these PANi/GO composite samples can be further optimized for various broadband EMI shielding applications in diverse electro/electrical domains.

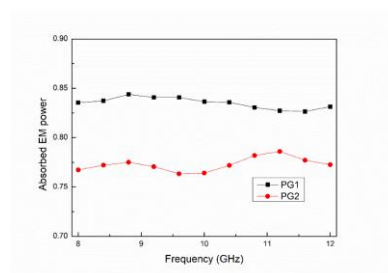


Figure 6: Absorbed electromagnetic power of PG1 and PG2 at X-band frequencies

Conclusion

In-situ polymerization method has been adopted for the synthesis of polyaniline/GO composites and a study has been carried out to investigate the suitability as a broadband electromagnetic interference shielding material. The structure and morphological modifications revealed the modified features of the composites and the frequency-dependent ac conductivity has shown distinct conductivity modification supporting better EMI shielding properties. Lower concentration of GO in the polyaniline has contributed better absorption dominant shielding while the increased concentration GO has resulted in increased shielding efficiency with a marginal reduction in the contribution of attenuation by absorption. The results clearly revealed that graphite oxide has played a major role as a compatible dispersant in polyaniline introducing effective conductivity tunability enabling highly valid shielding efficiency. The overall charge transport modification with modified phase boundaries resulted in the trapping of incident electromagnetic energy. Thus these composites can be further optimized for EMI shielding applications in broad frequency range and also it can be explored for various multifunctional applications like supercapacitor and corrosion inhibition.

Acknowledgment

Authors greatly acknowledge and would like to thank the Management of PES University, Electronic city Campus, Bangalore- 560100, Karnataka, India for their support and encouragement towards carrying out this work.

References

- [1] L. Ma, M. Hamidinejad, L. Wei, B. Zhao, and C. B. Park, "Absorption-dominant EMI shielding polymer composite foams: Microstructure and geometry optimization," *Mater. Today Phys.*, vol. 30, p. 100940, 2023, doi: <https://doi.org/10.1016/j.mtphys.2022.100940>.
- [2] "manna-srivastava-2021-reduced-graphene-oxide-fe₃o₄-polyaniline-ternary-composites-as-a-superior-microwave-absorber-in."
- [3] K. Nath, S. K. Bhattacharyya, and N. Ch. Das, "Chapter 10 - Biodegradable polymeric materials for EMI shielding," in *Materials for Potential EMI Shielding Applications*, K. Joseph, R. Wilson, and G. George, Eds., Elsevier, 2020, pp. 165–178. doi: 10.1016/B978-0-12-817590-3.00010-5.
- [4] D. D. L. Chung, "Materials for electromagnetic interference shielding," *Mater. Chem. Phys.*, vol. 255, p. 123587, Nov. 2020, doi: 10.1016/j.matchemphys.2020.123587.
- [5] S. Iqbal and S. Ahmad, "Chapter 16 - Conducting polymer composites: An efficient EMI shielding material," in *Materials for Potential EMI Shielding Applications*, K. Joseph, R. Wilson, and G. George, Eds., Elsevier, 2020, pp. 257–266. doi: 10.1016/B978-0-12-817590-3.00016-6.
- [6] S. P. Gairola, V. Verma, L. Kumar, M. A. Dar, S. Annapoorni, and R. K. Kotnala, "Enhanced microwave absorption properties in polyaniline and nano-ferrite composite in X-band," *Synth. Met.*, vol. 21–22, no. 160, pp. 2315–2318, 2010, doi: 10.1016/j.synthmet.2010.08.025.
- [7] J. Kruželák, A. Kvasničáková, K. Hložeková, and I. Hudec, "Progress in polymers and polymer composites used as efficient materials for EMI shielding," *Nanoscale Adv.*, vol. 3, no. 1, pp. 123–172, 2021, doi: 10.1039/D0NA00760A.
- [8] "(PDF) Microwave absorbing characteristics of Fe₃O₄@SiO₂ core-shell polyaniline-based composites." Accessed: Oct. 08,

2024. [Online]. Available: https://www.researchgate.net/publication/350703900_Microwave_absorbing_characteristics_of_Fe_3_O_4_SiO_2_core-shell_polyaniline-based_composites
- [9] N. Maruthi, M. Faisal, and N. Raghavendra, "Conducting polymer based composites as efficient EMI shielding materials: A comprehensive review and future prospects," *Synth. Met.*, vol. 272, p. 116664, Feb. 2021, doi: 10.1016/j.synthmet.2020.116664.
- [10] H. Lu *et al.*, "Electromagnetic shielding of ultrathin, lightweight and strong nonwoven composites decorated by a bandage-style interlaced layer electropolymerized with polyaniline," *J. Mater. Sci. Mater. Electron.*, vol. 30, Dec. 2019, doi: 10.1007/s10854-019-02379-6.
- [11] "(PDF) Facile preparation of polyaniline/graphene oxide composite towards electrode materials." Accessed: Oct. 26, 2024. [Online]. Available: https://www.researchgate.net/publication/367343137_Facile_preparation_of_polyanilinegraphene_oxide_composite_towards_electrode_materials
- [12] Y. Zhao, G.-S. Tang, Z.-Z. Yu, and J.-S. Qi, "The effect of graphite oxide on the thermoelectric properties of polyaniline," *Carbon*, vol. 50, no. 8, pp. 3064–3073, Jul. 2012, doi: 10.1016/j.carbon.2012.03.001.
- [13] M. J. Almasi, T. Fanaei Sheikholeslami, and M. R. Naghdi, "Band gap study of polyaniline and polyaniline/MWNT nanocomposites with in situ polymerization method," *Compos. Part B Eng.*, vol. 96, pp. 63–68, Jul. 2016, doi: 10.1016/j.compositesb.2016.04.032.
- [14] T. Mutalib, S. J. Tan, K. L. Foo, L. Ming, H. Yong, and M. M. A. B. Abdullah, "Properties of polyaniline/graphene oxide (PANI/GO) composites: effect of GO loading," *Polym. Bull.*, vol. 78, Sep. 2021, doi: 10.1007/s00289-020-03334-w.
- [15] M. Mitra *et al.*, "Reduced graphene oxide-polyaniline composites—synthesis, characterization and optimization for thermoelectric applications," *RSC Adv.*, vol. 5, no. 39, pp. 31039–31048, 2015, doi: 10.1039/C5RA01794G.
- [16] A. Ibarra-Hernández, A. Vega-Rios, and V. Osuna, "Synthesis of Graphite Oxide with Different Surface Oxygen Contents Assisted Microwave Radiation," *Nanomaterials*, vol. 8, no. 2, p. 106, Feb. 2018, doi: 10.3390/nano8020106.

- [17] M. Mupit, M. A. Azam, M. R. Islam, R. Yunus, O. S. Kooi, and M. A. F. Mohd Szali Januddi, "Facile preparation of polyaniline/graphene oxide composite towards electrode materials," *Energy Environ.*, vol. 35, no. 5, pp. 2476–2496, Aug. 2024, doi: 10.1177/0958305X221150431.
- [18] H. Wei, J. Zhu, S. Wu, S. Wei, and Z. Guo, "Electrochromic polyaniline/graphite oxide nanocomposites with endured electrochemical energy storage," *Polymer*, vol. 54, pp. 1820–1831, Mar. 2013, doi: 10.1016/j.polymer.2013.01.051.
- [19] D. Shao, G. Hou, J. Li, T. Wen, X. Ren, and X. Wang, "PANI/GO as a super adsorbent for the selective adsorption of uranium(VI)," *Chem. Eng. J.*, vol. 255, pp. 604–612, Nov. 2014, doi: 10.1016/j.cej.2014.06.063.
- [20] M. Faisal and S. Khasim, "Electrical Conductivity, Dielectric Behavior and EMI Shielding Effectiveness of Polyaniline-Yttrium Oxide Composites," *Bull. Korean Chem. Soc.*, vol. 34, no. 1, pp. 99–106, Jan. 2013, doi: 10.5012/BKCS.2013.34.1.99.
- [21] M. Faisal and S. Khasim, "Broadband electromagnetic shielding and dielectric properties of polyaniline-stannous oxide composites," *J. Mater. Sci. Mater. Electron.*, vol. 24, no. 7, pp. 2202–2210, Jul. 2013, doi: 10.1007/s10854-013-1080-y.
- [22] M. Faisal and S. Khasim, "Polyaniline–antimony oxide composites for effective broadband EMI shielding," *Iran. Polym. J.*, vol. 22, no. 7, pp. 473–480, Jul. 2013, doi: 10.1007/s13726-013-0149-z.
- [23] "Effect of Morphology on the Electrical Conductivity of Polyaniline as Potential Photocatalyst | Polymer Science, Series B." Accessed: Oct. 28, 2024. [Online]. Available: <https://link.springer.com/article/10.1134/S1560090424600086>
- [24] A. H. Majeed *et al.*, "A Review on Polyaniline: Synthesis, Properties, Nanocomposites, and Electrochemical Applications," *Int. J. Polym. Sci.*, vol. 2022, no. 1, p. 9047554, 2022, doi: 10.1155/2022/9047554.
- [25] N. Khalid *et al.*, "A short review on polyaniline (PANI) based nanocomposites for various applications: enhancing the electrical conductivity," *IOP Conf. Ser. Mater. Sci. Eng.*, vol. 957, no. 1, p. 012028, Oct. 2020, doi: 10.1088/1757-899X/957/1/012028.
- [26] A. Boublia *et al.*, "The curious case of polyaniline-graphene nanocomposites: a review on their application as exceptionally

- conductive and gas sensitive materials,” *Crit. Rev. Solid State Mater. Sci.*, vol. 49, no. 5, pp. 973–997, Sep. 2024, doi: 10.1080/10408436.2023.2274900.
- [27] L. Ma, M. Hamidinejad, L. Wei, B. Zhao, and C. B. Park, “Absorption-dominant EMI shielding polymer composite foams: Microstructure and geometry optimization,” *Mater. Today Phys.*, vol. 30, p. 100940, Jan. 2023, doi: 10.1016/j.mtphys.2022.100940.
- [28] Y. Ahmadi, S. Iqbal, and S. Ahmad, “Chapter 4 - Significance of naturally derived materials for potential EMI shields,” in *Materials for Potential EMI Shielding Applications*, K. Joseph, R. Wilson, and G. George, Eds., Elsevier, 2020, pp. 63–72. doi: 10.1016/B978-0-12-817590-3.00004-X.
- [29] M. H. Al-Saleh and U. Sundararaj, “Electromagnetic interference shielding mechanisms of CNT/polymer composites,” *Carbon*, vol. 47, no. 7, pp. 1738–1746, Jun. 2009, doi: 10.1016/j.carbon.2009.02.030.
- [30] S. B. Kondawar and P. R. Modak, “Chapter 2 - Theory of EMI shielding,” in *Materials for Potential EMI Shielding Applications*, K. Joseph, R. Wilson, and G. George, Eds., Elsevier, 2020, pp. 9–25. doi: 10.1016/B978-0-12-817590-3.00002-6.
- [31] R. Pal, S. L. Goyal, I. Rawal, and A. K. Gupta, “Tailoring of EMI shielding properties of polyaniline with MWCNTs embedment in X-band (8.2–12.4 GHz),” *J. Phys. Chem. Solids*, vol. 169, p. 110867, Oct. 2022, doi: 10.1016/j.jpcs.2022.110867.
- [32] K. Zubair *et al.*, “Study of mechanical, electrical and EMI shielding properties of polymer-based nanocomposites incorporating polyaniline coated graphene nanoparticles,” *Nano Express*, vol. 2, no. 1, p. 010038, Mar. 2021, doi: 10.1088/2632-959X/abe843.
- [33] W. Kong *et al.*, “Polyaniline-decorated carbon fibers for enhanced mechanical and electromagnetic interference shielding performances of epoxy composites,” *Mater. Des.*, vol. 217, p. 110658, May 2022, doi: 10.1016/j.matdes.2022.110658.
- [34] P. Das, Ashish. B. Deoghare, and S. R. Maity, “Enhanced Morphological, Mechanical and Dielectric Properties of Paraffin Wax Incorporated with Polyaniline (PANI) and Reduced Graphene Oxide (RGO) nanocomposites,” *Diam. Relat. Mater.*, vol. 139, p. 110361, Nov. 2023, doi: 10.1016/j.diamond.2023.110361.

Identifying The Advancements Of Friction Stir Welding: Innovations In Numerical Modeling And Simulation

¹Urmila H. Dakave, ²Dr. Vivek V. Kulkarni

¹*Research Scholar, Mechanical Engg. Dept.,
Sanjay Ghodawat University,
Atigre, Maharashtra*

²*Professor, Mechanical Engg. Dept.,
Sanjay Ghodawat University,
Atigre, Maharashtra*

Abstract

Numerical modeling has played a pivotal role in advancing Friction Stir Welding technology, enabling process optimization, predicting weld quality, and enhancing our understanding of material behavior. This paper provides an overview on the advancement of numerical modeling techniques employed in FSW of various materials. It offers a comprehensive analysis of various modelling approaches, emphasizing their strengths, limitations, and recent advancements. The review assesses the challenges faced by numerical modeling in FSW, such as the complexity of physical phenomena, the need for robust validation, and computational demands. It emphasizes the role of numerical modeling in addressing these challenges and driving innovation in FSW technology. A critical aspect of the review is the exploration of material-specific modeling, simulation software's approaches considering the distinct behaviors of different materials. It underscores the importance of these techniques in advancing FSW technology, reducing costs, and promoting sustainability. By recognizing the evolving trends and challenges, this review provides a basis for further research and improvement efforts needed in pursuit of even more precise and efficient FSW processes for joining of different materials

Keywords: FSW, Numerical modelling, Simulation software's, FEM, Materials, FSW challenges

Introduction

In the field of manufacturing and aerospace industries predominantly for joining aluminum alloy one of the significant solid state weld process is Friction Stir Welding [1]. The Welding Institute TWI was

developed this process in 1991 and has since revolutionized the way aluminum alloys are joined [2]. FSW is considered a breakthrough technology because it offers several advantages over traditional welding methods, making it highly significant in the industry. When it comes to joining aluminum alloys, FSW is important because it can solve a lot of the problems with traditional fusion welding techniques like tungsten inert gas and metal inert gas welding, which require melting and solidifying the materials [3]. FSW does not melt the base materials because it is a solid-state welding technique. In order to facilitate the formation of a joint, it uses frictional heat generated by a rotating tool to soften and stir the material. Fusion welding has a low heat input, which reduces the likelihood of distortion, warping, and heat-affected zone issues [4]. FSW gives the weld joint better mechanical qualities because it doesn't produce a molten pool. The weld's strength and toughness are enhanced by the lack of solidification cracks and decreased grain growth in the heat-affected area [6]. FSW creates joints with outstanding fatigue performance, which makes them perfect for use in the automotive, aerospace, and other sectors where long-term durability and structural integrity are crucial [7]. It can be used to join dissimilar aluminum alloys that are difficult to fuse together using traditional fusion welding techniques. This capability opens up new possibilities for creating materials with better properties for specific applications [8]. During solidification, FSW can lessen common welding flaws like porosity and inclusion cracks, producing a higher-quality and more dependable welded joint [9]. Because FSW uses less energy than fusion welding, it is more environmentally friendly. Additionally, it eliminates the need for shielding gases and reduces emissions and fume production [10]. Long term benefits like reduced rework and improved product quality can eventually result in cost savings, even though FSW initially requires a specialized equipment investment [11]. Friction stir welding is one of the most significant technologies in the field of joining aluminum alloys. It is a well-liked choice for industries like aerospace, automotive, and marine applications that require aluminum structures that are dependable, lightweight, and high-performing due to its solid-state nature and numerous advantages.

Advances in FSW

Friction stir welding (FSW) has already made significant strides in joining aluminum alloys. Manufacturers and researchers have created and employed advanced tool materials for FSW. Composite tools composed of materials like polycrystalline cubic boron nitride (PCBN), for instance, have been shown to extend tool life [12]. Real-

time process monitoring and control systems have improved. Torque, force, and temperature are among the parameters that these systems use sensors to measure while welding [13]. Advanced algorithms and machine learning techniques are used to optimize the FSW process and ensure high quality welds. FSW automation has increased, especially in fields where precision and consistency are crucial. Robotic FSW systems have made it possible to accurately weld large, complex structures [14]. Better joint characteristics and shorter cycle times are two advantages of hybrid processes. FSW has successfully joined these advanced aluminum alloys, providing improved mechanical properties and reducing the likelihood of weld defects [16]. FSW continues to be a key factor in the light weighting of structures, such as parts for cars and airplanes, as industries seek to reduce weight for improved performance and fuel efficiency [19]. Keeping up with the latest research and industry developments is essential to fully understanding the current state of FSW for joining aluminum alloys.

Role of Numerical modelling in FSW

Numerical modeling is crucial to understanding and refining the Friction Stir Welding (FSW) process. The process of FSW, a dynamic and intricate solid-state welding technique that enables engineers and researchers to modify parameters and improve weld quality, is better understood through numerical simulations [20]. Numerical simulations provide a visual representation of the FSW process, allowing researchers to observe and analyze the temperature distribution, material flow, and deformation inside the workpiece [21]. This visualization helps identify potential issues and optimize process parameters. Numerical models are a reliable way to predict temperature profiles during FSW. This knowledge is essential for minimizing the heat-affected zone preventing overheating or under heating, and comprehending the material's thermal history [22].

As the rotating FSW tool passes through the workpiece, simulation models replicate the material's plastic deformation. In addition to predicting defects like tunneling or voids, this aids in the study of material flow patterns and the optimization of tool geometry and traverse speed [23]. Predicting residual stresses and distortions in the weld and surrounding areas is made possible by numerical modeling [24]. Designing compensation strategies and evaluating the weld's structural integrity require this information. Researchers can virtually test various tool geometries and materials with simulation tools. This enhances tool life, reduces wear, and optimizes tool designs for particular applications [25]. Common flaws in FSW, like voids, tunneling, and kissing bonds, can be predicted using numerical

simulations. Researchers can create preventative measures and improve the quality of the weld by comprehending the underlying causes of these defects [27].

Furthermore, modeling can predict the microstructural alterations in the weld and HAZ, which directly affect the mechanical properties of the joint. This knowledge can be used to tailor the welding procedure to yield the required material qualities [28]. Numerical modeling saves time and money by removing the need for drawn-out experimental trials. By using simulations, engineers can reduce the parameter space and conduct physical experiments more efficiently [29]. Numerical modeling enhances process control, reduces trial-and-error experimentation, and ultimately leads to improved weld quality, efficiency, and reliability in a number of industries, including manufacturing, automotive, and aerospace.

The different FSW aspects that were previously discussed will be accomplished with the aid of this article's critical comparative overview of numerical modeling techniques. Additionally, it talks about how future research and development efforts can be shaped by numerical modeling techniques, which will ultimately lead to better weld quality, reduced costs, and improved performance in a range of applications. This makes it possible for researchers to weigh the benefits and drawbacks of different approaches and choose the most appropriate one for their specific research objectives. Researchers and institutions worldwide can work together more effectively by exchanging information about numerical modeling techniques in FSW of aluminum alloy.

Numerical Modeling Techniques

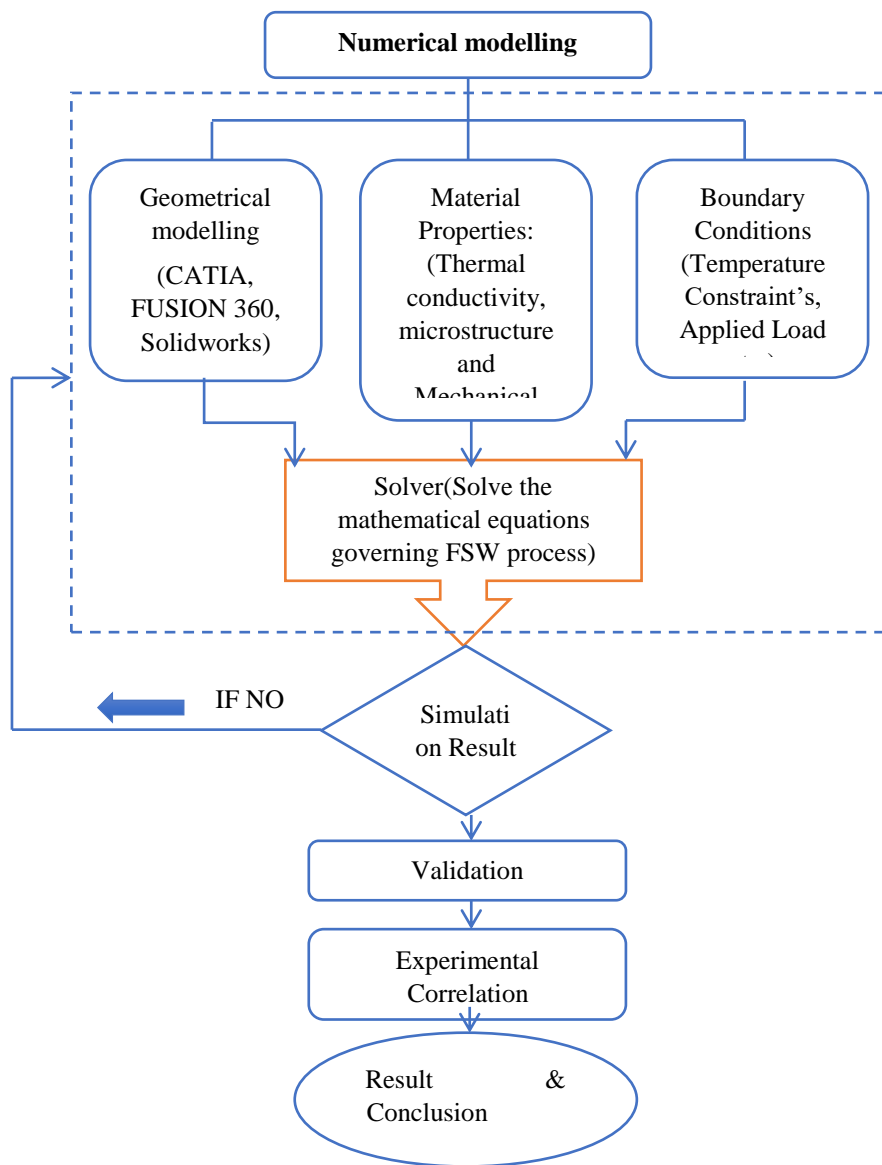
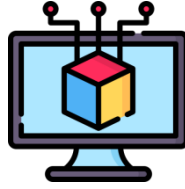


Figure 1: Numerical Modelling Process Flow

Above Figure 1 shows the flow of process carried out for modelling using different techniques, software packages used to give input of 3D model along with mechanical properties and boundary conditions to solver to get simulation result. Then the result will be compared or validate by actual experimentation and finding out the result out of it. Different techniques specially used for simulate result of FSW joining of aluminium alloy. One of the method is finite element analysis is actively used for simulating FSW process. It helps in predicting temperature distribution, material flow, and stress/strain fields during welding. FEA accounts for factors such as heat generation, thermal conductivity, and material behavior to simulate the process accurately [31]. Other method is Computer fluid dynamics that is CFD which is used to model the flow of material in the area near of the tool during FSW. This helps in understanding the complex material flow patterns, mixing of alloying elements, and heat transfer within the workpiece. Heat Transfer models are one of the models mostly focused on temperature profiles developed during FSW. These models consider heat generated at the zone of Tool and workpiece interfaces along with conduction of heat by the material. Finite difference method as well as Finite element method both can be utilized for heat transfer simulation [33]. Some of the models are material flow models basically predicts the deformation and the material flow during the process of joining of materials by FSW. These models study the redistribution of alloying elements and weld nugget formation. Approaches used in these models are Lagrangian or Eulerian approaches [34]. Microstructural evolution models often used to simulate the evolution of microstructure, grain size of particles and texture during and after the FSW joining process. It provides the view on how the process parameters affect the final material properties and help to optimize the weld conditions [35]. Numerical techniques plays vital role in predicting residual stresses and distortion in the welded components. This is crucial for assessing the structural integrity of the weld and designing appropriate post weld heat treatments [36].

Comprehensive numerical models that couple various physical phenomena like heat transfer, fluid flow, material deformation, and phase transformation are increasingly used to provide a holistic view of the FSW process [37]. In addition to physics-based models, empirical and data-driven models can be employed to predict FSW outcomes based on experimental data. Machine learning and artificial intelligence techniques can play a role in developing such models [38].

Numerical modeling have an essential role in predicting residual stresses and distortion in friction stir welding joints. Residual stresses

and distortion are substantial concerns for welding processes, as the structural integrity and dimensional accuracy of the final product affected by them.

Different FSW process based research work has presented here which easily expresses comparative aspects of numerical modelling techniques for FSW used for joining aluminium alloys.

Nikola Sibalic and Milan Vukcevic [39] utilized DEFORM 3D software package with Lagrangien formulation for simulating FSW Process at Welding Aluminium Alloy AA6082-T6. They found that the geometric parameter i.e. shoulder diameter have the major impact on the Fz value and the Welding forces attained through numerical simulation was approximately 10% greater than experimental forces, it means that the FEM simulation can be successfully implemented for FSW. ANSYS Workbench 15.0 software is used for finite element analysis. The Heat Source Modeling-Circular Disc model was employed. Transient temperature distribution under convective boundary conditions Plotting temperature distribution curves reveals that the curves in experimental and numerical simulation temperature data are similar in nature. The air's heat transfer coefficient and the measuring device's thermal inertia cause a very slight variation in the numerical simulation results. Yifu Shen and Jingming Tang [45] Experimental study and numerical simulation of friction stir lap welding between aluminum alloys AA2024 and AA7075 Using the FLUENT three-dimensional nonlinear heat transfer equation as a model, Results from calculations and experiments also demonstrated that location has an impact on temperature distribution. Both the experimental and numerical results clearly show an asymmetric temperature distribution between the RS and the AS. The asymmetry arises because the radiating surface area and resultant vector values in the AS are comparatively greater than those in the RS. B.

S. Mohanty, D. K. Sahoo*, and G. B. Bhaskar [46] ABACUS software Microstructural grain development during inductive-based friction surfacing of aluminum AA6063: a multi-phase-field simulation study using the Johnson-Cook model The multi-phase field model (MFM) and the constructive material model (CMM) were used to forecast grain development. Coordinates for CMM images with an error of less than 10%, derived from calculations and experiments. Grain structure development during recrystallization was significantly impacted by increasing the coating strength, which was assumed to be inversely proportional to the average coating's grain diameter. Laszlo I. Kiss, Kirk Fraser, and Lyne St-Georges [48] A Solid-Mechanics Method Without Meshes for Modeling the Friction Stir-Welding of

Aluminum The joint multi-GPU parallelization strategy of Alloy Complex Lagrangian SPH residual deformation and stresses. It is easy to calculate the significant plastic deformation that occurs during FSW. Mesh-based methods struggle to capture all the physics of the process due to discretization errors and mesh distortion. The model can predict defects (free surface changes), which is different from other numerical methods. Numerical modeling techniques for dissimilar aluminum alloy FSW are continuously evolving due to the increasing number of diverse materials that need to be welded for a range of applications. Researchers and engineers use these tools to better understand the welding process, optimize parameters, and ensure the quality of joints in dissimilar alloy combinations, all of which contribute to the advancement of materials science and engineering. While mesh-based Finite Element Analysis FEA is commonly used for numerical simulations in friction stir welding (FSW), other numerical modeling methods do not depend on meshing. These strategies are widely used in simulation techniques such as computational fluid dynamics CFD. SPH, or smoothed particle hydrodynamics, is a method for simulating FSW without meshing.

Complexity of Physical Phenomena

Thermal and Mechanical Interactions

The complex thermal and mechanical interactions involved in FSW can have a significant impact on the weld quality. The process generates localized heat through friction, which influences material flow, microstructural changes, and mechanical characteristics. To capture these interactions, multi-physics modeling involving thermal, metallurgical, and mechanical phenomena is required.

Material Behavior

In addition to temperature, variables like strain rate and tool geometry also affect how materials behave during FSW. The modeling process is complicated by the material flow around the tool and the ensuing microstructural evolution. The intricacy is increased by variations in material characteristics like viscosity and yield strength.

Tool Interaction

Additional difficulties arise from the interaction between the workpieces and the rotating tool. To effectively predict joint quality and integrity, simulations must accurately depict tool wear, deformation, and the heat produced at the tool-workpiece interface.

Strong Validation Experimental Data Challenges Are Necessary

Numerical models must undergo thorough validation in order to be considered credible. Nevertheless, it can be difficult to get high-fidelity experimental data. Real-time measurements of crucial parameters like temperature, material flow, and mechanical properties are made more difficult by the transient nature of FSW.

Comparability of Models and Experiments

It is necessary to carefully evaluate boundary conditions, material properties, and the particular configurations used in experiments when validating models against experimental results. Assumptions made during modeling may cause differences between simulated and experimental results, making robust validation a difficult and frequently iterative procedure.

Computational Demands

Resource Intensiveness

FSW numerical models, especially those that try to capture the fine details of the mechanical and thermal behavior, can be computationally demanding. For many researchers, high-resolution simulations that include a variety of physical phenomena can be prohibitively computationally demanding.

Time-Dependent Simulations

Time-dependent simulations that address abrupt variations in temperature and material properties are required due to the dynamic nature of the FSW process. Finding a balance between accuracy and computational viability is crucial because this requirement increases computational demands.

Strategies for Overcoming Challenges

Development of Simplified Models

The creation of simplified models that capture key elements of the FSW process while lowering computational demands is one strategy for handling complexity. These models can be used as a foundation for more intricate simulations and offer insightful information about the behavior of processes.

Enhanced Experimental Techniques

Improvements in experimental methods, like in-situ measurements and high-speed imaging, can aid in acquiring more thorough data for model validation. Numerical models can be better understood and improved with improved data collection techniques.

Parallel Computing and Machine Learning

Numerical simulation efficiency can be greatly increased by utilizing machine learning and parallel computing techniques. By speeding up calculations and fine-tuning model parameters, these technologies can enable more thorough simulations with greater fidelity.

Conclusions

Numerical modeling will continue to lead FSW developments as computing power increases, promoting sustainability, efficiency, and quality in aluminum alloy joining. By evaluating the viability of joining disparate aluminum alloys using numerical modeling, engineers can create novel structures that maximize material qualities for particular uses. Numerical modeling enables optimized FSW processes, which can minimize the environmental impact and contribute to sustainability goals by reducing material waste and energy consumption. The formation of residual stresses and distortion during FSW is precisely predicted by numerical models. Achieving the required mechanical properties of aluminum alloys requires an understanding of and ability to control their microstructure. Engineers can precisely control grain size, texture, and phase composition by using numerical modeling to predict how process parameters affect microstructural changes. The development of FSW technology for aluminum alloys depends heavily on numerical modeling. With the help of its predictive capabilities, engineers and researchers can control material behavior, optimize processes, and create novel, lightweight, high-performance aluminum alloy structures for a variety of uses. The intricacy of physical phenomena, the requirement for strong validation, and the high computational requirements make numerical modeling of friction stir welding extremely difficult. Improving the precision and dependability of simulations requires addressing these issues. Overcoming these obstacles and improving our knowledge and use of FSW will require continued research, cooperation between experimentalists and modelers, and developments in computational techniques.

References

- [1] Khedr, M.; Abd-Elaziem, W.; Hamada, A.; Järvenpää, A.; Elkatatny, S. Review of Friction Stir Welding and Diffusion Bonding Techniques for Solid-State Steel Welding. *Metals* 13, 54 (2023).

- [2] Thomas WM, Needham JC, Murch MG, Temple-Smith P, Nicholas ED, and Dawes CJ. Stir butt welding with friction. Application for International Patent No. PCT/GB92/02203; 1991.
- [3] Z.Y. Ma and R.S. Mishra Processing material and friction stir welding pp. 1–78 in Sci Eng R: Rep, 50 (2005)
- [4] Shalin Marathe. THE FRICTION STIR WELDING REVIEW PAPER (FSW). Advances in Engineering, Science, and Management: An International Journal, 2 (2016).
- [5] Somil Dubey, Aman Singh, Subodh Kumar, Rudra Pratap Singh, an analysis of the friction stir welding procedure, Materials Today: Proceedings, Volume 38, Part 1, 2021, Pages 6-11, ISSN 2214-7853.
- [6] Kumar, S.D. and Kumar, S.S., 2019. Examination of the mechanical properties of aluminum alloys AA5083 and AA6063 friction stir welded joints. Mechanical Engineering & Mechanics, 23(1).
- [7] Texier, D., Atmani, F., Vadesse, N., Bocher, P., Nadeau, F., Chen, J., Zedan, Y., and Demers, V. (2018). The fatigue performance of GMAW and FSW aluminum alloy welded joints: competition between structural-contact-fretting crack initiation and microstructural cracks. 116, pp. 220-233, International Journal of Fatigue.
- [8] Boopathi, S., Asif, M.M., and Haribalaji, V. (2022). Friction stir welding process optimization for joining dissimilar aluminum alloys AA2014 and AA7075. Today's Materials: Proceedings, 50, pp.2227-2234.
- [9] Kah, P., Suoranta, R., Rajan, R., and Martikainen, J. (2015). examination of weld flaws in aluminum alloys welded by fusion and friction-stir. 10(1), pp. 1–10, International Journal of Mechanical and Materials Engineering.
- [10] Ciarapica, F.E., Simoncini, M., Forcellese, A., and Bevilacqua, M., 2020. Comparison of the effects of fusion and solid state welding techniques on the environment when joining aluminum alloys. Section B: Journal of Engineering Manufacture, Proceedings of the Institution of Mechanical Engineers, 234(1-2), pp. 140-156.
- [11] Cheeseman, B.A., Yen, C.F., Hariharan, A., Pandurangan, B., Arakere, G., and Grujicic, M. (2011). Creation of a reliable and reasonably priced friction stir welding method for use in cutting-edge military vehicles. Materials engineering and performance journal, 20 (pp. 11–23).

- [12] In 2018, Miles, M.P., Liu, F.C., Hovanski, Y., Sorensen, C.D., and Nelson, T.W. An overview of the properties, microstructure, material flow, and tool used in friction stir welding of steels. *Materials Science & Technology Journal*, 34(1), pp. 39–57.
- [13] In 2020, Misra, P., Pal, S.K., Chakravarty, D., Pal, S., Chakravarty, T., Pal, A., Gupta, A., Raj, P., Kumar, A., Anwer, S., and Pal, S.K. Using a number of sensors, the friction stir welding process is monitored and controlled in real time. 30 pp. 1–11 in the *CIRP Journal of Manufacturing Science and Technology*.
- [14] Gibson, B.T., Cook, G.E., Dharmaraj, K.J., Prater, T.J., Longhurst, W.R., Cox, C.D., Ballun, M.C., Lammlein, D.H., and Strauss, A.M. (2014). Process, automation, and control of friction stir welding. *Manufacturing Processes Journal*, 16(1), pp. 56–73.
- [16] Cam, G. and Mistikoglu, S., 2014. Recent developments in friction stir welding of Al-alloys. *Journal of Materials Engineering and Performance*, 23, pp.1936-1953.
- [18] Lemos, G.V.B., Hanke, S., Dos Santos, J.F., Bergmann, L., Reguly, A. and Strohaecker, T.R., 2017. Progress in friction stir welding of Ni alloys. *Science and Technology of Welding and Joining*, 22(8), pp.643-657.
- [19] Kumar, A.P., Dirgantara, T. and Krishna, P.V. eds., 2020. *Advances in Lightweight Materials and Structures: Select Proceedings of ICALMS 2020*. Springer.
- [20] Singh, H., Mehta, A., Sharma, Y. and Vasudev, H., 2023. Role of expert systems to optimize the friction stir welding process parameters using numerical modelling: a review. *International Journal on Interactive Design and Manufacturing (IJIDeM)*, pp.1-17.
- [21] Neto, D.M. and Neto, P., 2013. Numerical modeling of friction stir welding process: a literature review. *The International Journal of Advanced Manufacturing Technology*, 65, pp.115-126.
- [22] Vignesh, R.V., Padmanaban, R., Arivarasu, M., Thirumalini, S., Gokulachandran, J. and Ram, M.S.S.S., 2016, September. Numerical modelling of thermal phenomenon in friction stir welding of aluminum plates. In *IOP conference series: materials science and engineering* (Vol. 149, No. 1, p. 012208). IOP Publishing.
- [23] Gao, E.Z., Zhang, X.X. and Liu, C.Z., 2018. Numerical simulations on material flow behaviors in whole process of friction stir welding. *Transactions of Nonferrous Metals Society of China*, 28(11), pp.2324-2334.

- [24] Costa, M.I., Leitão, C. and Rodrigues, D.M., 2019. Parametric study of friction stir welding induced distortion in thin aluminium alloy plates: A coupled numerical and experimental analysis. *Thin-Walled Structures*, 134, pp.268-276.
- [25] Iqbal, M.P., Jain, R., Pal, S.K. and Mandal, P., 2022. Numerical modelling of friction stir welding of pipes: Effect of tool shoulder on mechanical property and metallurgical characterization. *Journal of Manufacturing Processes*, 79, pp.326-339.
- [26] MohammadiSefat, M., Ghazanfari, H. and Blais, C., 2021. Friction Stir Welding of 5052-H18 aluminum alloy: Modeling and process parameter optimization. *Journal of Materials Engineering and Performance*, 30, pp.1838-1850.
- [27] Zhu, Y., Chen, G., Chen, Q., Zhang, G. and Shi, Q., 2016. Simulation of material plastic flow driven by non-uniform friction force during friction stir welding and related defect prediction. *Materials & Design*, 108, pp.400-410.
- [28] allais, C., Denquin, A., Bréchet, Y. and Lapasset, G., 2008. Precipitation microstructures in an AA6056 aluminium alloy after friction stir welding: Characterisation and modelling. *Materials Science and Engineering: A*, 496(1-2), pp.77-89.
- [29] Pandian, V. and Kannan, S., 2020. Numerical prediction and experimental investigation of aerospace-grade dissimilar aluminium alloy by friction stir welding. *Journal of Manufacturing Processes*, 54, pp.99-108.
- [30] Nirmal, K. and Jagadesh, T., 2021. Numerical simulations of friction stir welding of dual phase titanium alloy for aerospace applications. *Materials Today: Proceedings*, 46, pp.4702-4708.
- [31] El-Sayed, M.M., Shash, A.Y. and Abd-Rabou, M., 2018. Finite element modeling of aluminum alloy AA5083-O friction stir welding process. *Journal of Materials Processing Technology*, 252, pp.13-24.
- [33] Yaduwanshi, D.K., Bag, S. and Pal, S., 2015. Heat transfer analyses in friction stir welding of aluminium alloy. *Proceedings of the Institution of Mechanical Engineers, Part B: Journal of Engineering Manufacture*, 229(10), pp.1722-1733.
- [34] Yang, X., Feng, W., Li, W., Xu, Y., Chu, Q., Ma, T. and Wang, W., 2018. Numerical modelling and experimental investigation of thermal and material flow in probeless friction stir spot welding process of Al 2198-T8. *Science and Technology of Welding and Joining*, 23(8), pp.704-714.

- [35] Marzbanrad, J., Akbari, M., Asadi, P. and Safaee, S., 2014. Characterization of the influence of tool pin profile on microstructural and mechanical properties of friction stir welding. *Metallurgical and Materials Transactions B*, 45, pp.1887-1894.
- [36] Draup, A.J.A., 2017. Numerical simulation of the structural response of friction stir welded aluminium 2139-T8 alloy subjected to complex loading configurations. The University of Manchester (United Kingdom).
- [37] Hamilton, R., MacKenzie, D. and Li, H., 2010. Multi-physics simulation of friction stir welding process. *Engineering Computations*, 27(8), pp.967-985.
- [38] Andrade, D.G., Leitão, C., Dialami, N., Chiumenti, M. and Rodrigues, D.M., 2020. Modelling torque and temperature in friction stir welding of aluminium alloys. *International Journal of Mechanical Sciences*, 182, p.105725.
- [39] Sibalic, N. and Vukcevic, M., 2019. Numerical simulation for FSW process at welding aluminium alloy AA6082-T6. *Metals*, 9(7), p.747.
- [41] Sahooa, D.K., Mohanty, B.S. and Bhaskar, G.B., 2022. Multi phase-field simulation study on microstructural grain development during inductive-based friction surfacing of aluminium. *DIGEST JOURNAL OF NANOMATERIALS AND BIOSTRUCTURES*, 17(1), pp.263-284.
- [42] Jamshidi Aval, H., 2023. Smoothed-Particle Hydrodynamics (SPH) Simulation of AA6061-AA5086 Dissimilar Friction Stir Welding. *Metals*, 13(5), p.906.
- [43] Fraser, K., St-Georges, L. and Kiss, L.I., 2016. A mesh-free solid-mechanics approach for simulating the friction stir-welding process. *Joining technologies*, pp.27-52.
- [44] Iftikhar, S.H., Mourad, A.H.I. and Guessoum, M., 2022, February. Numerical modeling of friction stir welding of thermoplastic materials—An overview. In *2022 Advances in Science and Engineering Technology International Conferences (ASET)* (pp. 1-5). IEEE.
- [45] Derazkola, H.A., Eyvazian, A. and Simchi, A., 2020. Modeling and experimental validation of material flow during FSW of polycarbonate. *Materials Today Communications*, 22, p.100796.
- [46] Marode, R.V., Pedapati, S.R., Lemma, T.A. and Awang, M., 2023. A review on numerical modelling techniques in friction stir

processing: current and future perspective. Archives of Civil and Mechanical Engineering, 23(3), p.154.

[47] Dialami, N., Chiumenti, M., Cervera, M. and Agelet de Saracibar, C., 2017. Challenges in thermo-mechanical analysis of friction stir welding processes. Archives of Computational Methods in Engineering, 24, pp.189-225.

[48] Meyghani, B., Awang, M. and Wu, C.S., 2020. Finite element modeling of friction stir welding (FSW) on a complex curved plate. Journal of Advanced Joining Processes, 1, p.100007.

[49] Nie, L., Wu, Y.X. and Gong, H., 2020. Prediction of temperature and residual stress distributions in friction stir welding of aluminum alloy. The International Journal of Advanced Manufacturing Technology, 106, pp.3301-3310.

[50] Chandra, D., Satria, E. and Yusoff, N., 2021, February. Buckling Analysis of Curve Stiffened Fuselage Panel of Very Light Jet Aircraft. In IOP Conference Series: Materials Science and Engineering (Vol. 1062, No. 1, p. 012049). IOP Publishing.

[51] Yoon, J.W., Bray, G.H., Valente, R.A.F. and Childs, T.E.R., 2009. Buckling analysis for an integrally stiffened panel structure with a friction stir weld. Thin-Walled Structures, 47(12), pp.1608-1622.

[52] Sun, W., Tong, M., Guo, L. and Dong, D., 2008, October. Post-buckling simulation of an integral aluminum fuselage panel subjected to axial compression load. In 2008 Asia Simulation Conference-7th International Conference on System Simulation and Scientific Computing (pp. 893-897). IEEE.

[53] Neto, E.L., Monteiro, F.A. and Ruela, H.H., 2010. A Comparison of Buckling Performance of Rivet and Friction Stir Welding Stiffened Panels. Mecánica Computacional, 29(49), pp.4967-4975.

SUSTAINABLE MACHINING OF NITINOL SHAPE MEMORY ALLOY USING NEAR-DRY ELECTRICAL DISCHARGE MACHINING PROCESS

**Ramver Singh ¹, Tanmay Tiwari ^{2*}, T.S Srivatsan ³,
Akshay Dvivedi⁴, Pradeep Kumar ⁵**

¹ *H2power energy Pvt. Ltd,*
IIT Kanpur Outreach Center
Sector 62-Noida, INDIA

² *Center of Precision Manufacturing,*
Department of Mechanical Engineering
The University of Akron
Akron, Ohio, USA 44325

³ *Department of Mechanical Engineering*
The University of Akron
Akron, Ohio, USA 44325

^{4,5} *Advanced Manufacturing Processes Laboratory*
Indian Institute of Technology Roorkee [IIT R]
Roorkee 247667, INDIA

* Corresponding author email: ttiwari@uakron.edu

Presenting author: tss1@uakron.edu

Abstract

Micro-electrical discharge machining (micro-EDM) is vital for the purpose of high-precision manufacturing. Yet, its sustainability is hindered by the health risks posed by the traditional fossil fuel-based dielectric fluids. While dry-electrical discharge machining (EDM) with air offers a potential solution, it lacks in adequate machining performance. This research study tackles this problem by exploring the near-dry micro-EDM milling of nickel-titanium (NiTi) shape memory alloy, commonly known as Nitinol, using a water-air mist, an approach that has not as yet been widely investigated. In this research study, micro-grooves were machined, and the performance of the near-dry method are compared to the dry variant. The effects of various process parameters to include (i) peak current, (ii) pulse on time, (iii) pulse off

time, and (iv) gas pressure, on process performance metrics, such as (a) material removal rate (MRR), (b) surface roughness (Sa value), and (c) width overcut (WOC), were analyzed using response surface methodology. The near-dry variant demonstrated a machining speed more than twice that of dry-electrical discharge machining (EDM) with air. This study confirms that micro-EDM with water-air mist is a more sustainable alternative for the purpose of enabling improved energy efficiency, resource utilization, and reducing waste generation.

Introduction

Nickel-titanium (Nitinol) shape memory alloys (SMAs) are extensively used across various industries to include (i) aerospace, (ii) biomedical, and (iii) electronics [1]. These industries demand materials that exhibit a healthy combination of high precision, durability, and compatibility with other materials. Nitinol is particularly valued for its properties, such as (i) shape memory effect, and (ii) super-elasticity, which does enable precise actuation in applications ranging from stents to actuators. However, machining Nitinol presents significant challenges due on account of its high toughness and poor machinability when using the conventional techniques [2]. Consequently, advanced machining methods are increasingly essential to effectively process Nitinol while concurrently leverage its exceptional properties in practical applications.

Despite the numerous advantages of Nitinol for the purpose of selection and use in various applications, its machining remains problematic. Traditional machining techniques often result in a combination of (i) excessive tool wear, (ii) poor surface finish, and (iii) dimensional inaccuracies. Electrical Discharge Machining (EDM) has emerged as a potentially viable alternative for machining difficult materials like Nitinol [3]. However, traditional electrical discharge machining (EDM) processes rely on hydrocarbon-based dielectric fluids, which often pose both environmental and health risks [4]. While dry EDM offers a more sustainable option [5], it typically underperforms in terms of material removal rate (MRR) and surface quality when compared one-on-one with the conventional wet EDM methods. There does exist a critical need to explore alternative machining strategies, such as Near-dry EDM (ND-EDM), to enhance performance while concurrently addressing concerns specific to sustainability [6].

The near-dry electrical discharge machining [ND-EDM], a relatively newer variant of the EDM process, replaces conventional dielectric oil with a compressed air-water mixture [7]. This method

addresses environmental concerns associated with traditional electrical discharge machining (EDM), which does use hydrocarbon-based dielectric fluids that often generate harmful emissions and waste. Researchers have reported that near-dry wire EDM (ND-WEDM) does provide an enhanced machining results for the hard materials while maintaining environmental sustainability [8]. The minimal use of deionized water along with a large proportion of compressed air was found to improve performance while concurrently maintaining an eco-friendly machining environment. Previous studies have indicated an overall effectiveness of near-dry EDM in machining the Nitinol shape memory alloy (SMA) [9].

For example, Chaudhary et al. (2022)[10] examined the impact of electrical pulse characteristics (on and off times and peak current) on the machining performance during near-dry Wire-EDM of Nitinol shape memory alloy. Their independent study utilized a teaching-learning-based optimization (TLBO) algorithm to perform the optimization. The Single-response optimization achieved a maximum material removal rate (MRR) of 66.84 mm³/minute at a parametric setting (95 μ s & 9 μ s, and 6 A). The minimum surface roughness (Ra value) of 2.81 μ m was obtained for a parametric setting of 35 μ s & 27 μ s, and 2 A. Notably, the near-dry Wire-EDM process demonstrated an 8.94% reduction in material removal rate (MRR) when compared to wet Wire electrical discharge machining (WEDM) while improving surface roughness (SR) by 41.56%. It was inferred that the air-water mist enhanced flushing efficiency and reduced thermal energy at the inter-electrode gap (IEG), resulting in better surface quality with fewer defects.

Near-dry EDM has also shown much promise with other difficult materials. For example, Dhakar et al. (2019)[11] demonstrated that near-dry EDM (ND-EDM) did improve the machining performance while concurrently addressing environmental sustainability. Their findings indicated increased material removal rate (MRR) for high-speed steel (HSS), with peak pulse current being the most significant factor. Similarly, Yadav et al. (2020)[12] studied rotary tool near-dry EDM (RT-ND-EDM) using a water-air dielectric for deep hole machining of high-speed steel (HSS), and did find that a higher current and pulse-on time increased surface roughness (SR) and resulted in the formation and presence of surface defects like fine microscopic cracks. In 2021, they explored how tool electrode geometry impacts the performance of RT-ND-EDM, revealing that the double-start helical electrodes significantly enhanced material removal rate (MRR), accuracy, and surface quality by improving the flushing of debris [7]. Yadav et al. (2022) further investigated debris

characteristics in RT-ND-EDM, discovering that glycerin-air dielectrics produced larger debris and a much higher material removal rate (MRR), but with much rougher surfaces when compared to water-air [9]. Boopathi et al. (2012)[13] found that moderate air-mist pressure in near-dry electrical discharge machining (EDM) of HSS-M2 increased the material removal rate (MRR) while concurrently reducing the surface roughness. Gholipoor et al. (2015)[14] showed that near-dry EDM yielded surfaces with fewer microscopic cracks when compared to the wet method and dry method. Kao et al. (2007)[15] investigated the use of a liquid-gas mixture as the dielectric medium in near-dry wire-electrical discharge machining (EDM). Their experiments comparing the dry, wet, and near-dry EDM processes showed that near-dry EDM achieved a higher MRR, suggesting the near-dry to be a promising alternative for enhancing productivity while concurrently minimizing environmental impact. Boopathi and Sivakumar [16] optimized near-dry WEDM for high speed steel (HSS) using a multi-objective evolutionary algorithm. They found current to be the most significant factor influencing both material removal rate (MRR) and surface roughness (SR), with moderate air-mist pressure improving both outcomes.

In summary, prior research demonstrates that near-dry electrical discharge machining (EDM) holds great potential for improving both sustainability and surface quality while maintaining or enhancing productivity. By reducing the reliance on fossil fuel-based dielectrics, near-dry EDM presents an environmentally friendly alternative to conventional methods, particularly for the machining of hard-to-machine materials, such as Nitinol. However, almost no research has been studied in the micromachining domain.

Micro-electrical discharge machining (micro-EDM) is a key technology in high-precision and high-value manufacturing, and is being widely used for fabricating intricate micro-features in hard-to-machine electrically conductive materials [17]. It has become particularly significant in industries, such as (i) aerospace, (ii) biomedical, and (iii) electronics, where the demand for precision, miniaturization, and material compatibility is often high [18]. Despite its precision and effectiveness, traditional micro-electrical discharge machining (EDM) systems rely heavily on fossil fuel-based dielectric fluids, such as hydrocarbon-based EDM oils, posing both environmental concern and health concern [19]. These dielectric fluids generate (i) harmful fumes, (ii) increase carbon footprints, and (iii) contribute to hazardous waste generation, challenging the overall sustainability of the process.

In recent years, dry micro-EDM variant, which uses gas as a dielectric medium, has emerged as a potentially viable alternative for the purpose of reducing reliance on liquid-based dielectrics. However, dry micro-EDM variant has struggled to match the performance of conventional methods, particularly in terms of material removal rate (MRR) and surface quality. To overcome these limitations, near-dry electrical discharge machining (EDM) does offer a promising solution. This technique combines the environmental benefits of dry-EDM with improved machining performance by introducing a minimal amount of liquid dielectric to aid in both spark generation and removal of the debris.

This paper investigates the application of near-dry micro-EDM milling on nickel-titanium (NiTi) shape memory alloy, commonly known as Nitinol. To date, limited studies have explored the potential of using near-dry micro-EDM with a water-air mist on Nitinol. This research study aims to fill this gap by analyzing the effects of key process parameters, namely (i) peak current, (ii) pulse on time, (iii) pulse off time, and (iv) gas pressure—on performance metrics, such as (a) MRR, (b) surface roughness (Sa), and (c) width overcut (WOC).

The findings from this research study could establish near-dry electrical discharge machining (EDM) to be a more sustainable and effective alternative to traditional methods, contributing to (i) improved energy efficiency, (ii) better resource utilization, and (iii) reduced waste generation in high-precision manufacturing.

Research Methodology

A custom-designed micro-EDM system equipped with a water-air mist dielectric delivery system was used for the experiments. The system allowed precise control over both gas pressure and liquid flow rate, maintaining a consistent formation of mist during machining. Nickel-titanium (Nitinol) was selected as the workpiece material due to its widespread use in both biomedical and aerospace applications, coupled with its challenging machinability. The tool electrode was made of tungsten, known for its high melting point, ensuring consistent machining conditions throughout the experiments.

The process parameters investigated were the following: (i) current (A), (ii) pulse-on time (μs), (iii) Pulse off time (μs), and (iv) gas pressure (psi). The pulse current controls the energy intensity released during each discharge, influencing both the material removal rate (MRR) and surface integrity. Pulse on time defines the duration of each electrical pulse, directly exerting an impact on the total discharge energy input. Pulse off time (μs) is the time between successive

discharges, that affects both cooling and debris removal. Gas pressure (bar) regulates the generation of mist and dielectric properties of the medium. The performance of the process was evaluated based on the following response variables: (i) material removal rate (MRR), (ii) Surface roughness (Sa), and width overcut (WOC). The material removal rate (MRR) was measured to assess the throughput of the machining process. The surface roughness (Sa) value was measured to evaluate the surface finish of the machined micro-grooves. The width overcut (WOC) was measured to determine the accuracy of the machining process in terms of dimensional deviations.

A central composite design (CCD) under RSM was used to systematically vary the process parameters and observe their effects on the response variables. The design provided a structured approach to optimize the process and to concurrently enable in understanding the interaction between the parameters. After machining, each sample was analyzed using a surface profilometer [white light interferometer, WLI] to measure surface roughness, while a microscope was used to examine the width overcut (WOC). The material removal rate (MRR) was calculated based on the material removed per unit time. The experimental results were analyzed using RSM to develop empirical models correlating the process parameters with the response variables. Equations 1-3 express the developed empirical regression models for (i) material removal rate (MRR), (ii) surface roughness (Sa), and (iii) width overcut (WOC) in terms of coded process parameters, such as (i) current (A), (ii) pulse-on time (B), (iii) pulse-off time (C), and (iv) gas pressure (D).

$$\begin{aligned} \text{MRR} = & 0.0175161 - 0.00200538 \times A - 0.00191935 \times B + \\ & 0.00263441 \times C + 0.000693548 \times D + 0.000322581 \times AB \\ & + 0.000120968 \times AC - 1.6129 \times 10^{-5} \times AD + \\ & 0.000290323 \times BC + 0.000233871 \times BD + \\ & 0.000145161 \times CD + 0.0010672 \times A^2 + 0.000994624 \times B^2 \\ & + -0.000844086 \times C^2 - 3.76344 \times 10^{-5} \times D^2 \dots \end{aligned} \quad (1)$$

$$\begin{aligned} \text{Sa} = & 5.91167 + 1.72917 \times A + 0.4625 \times B + -0.145833 \times C + \\ & 0.220833 \times D + -0.09375 \times AB + -0.13125 \times AC + \\ & 0.28125 \times AD + 0.06875 \times BC + 0.08125 \times BD + \\ & 0.06875 \times CD + -0.0872917 \times A^2 - 0.0372917 \times B^2 + \\ & 0.0127083 \times C^2 - 0.249792 \times D^2 \dots \end{aligned} \quad (2)$$

$$\begin{aligned} \text{WOC} = & 72.6667 + 3.83333 \times A + 5.16667 \times B - 3.5 \times C - \\ & 1.58333 \times D + 0.25 \times AB - 0.25 \times AC + 0.375 \times AD - \\ & 0.25 \times BC - 0.125 \times BD - 0.875 \times CD + 0.666667 \times A^2 + \\ & 1.16667 \times B^2 + 1.41667 \times C^2 + 4.16667 \times D^2 \dots \end{aligned} \quad (3)$$

Results and Discussion

1.1. Effect on Material Removal Rate (MRR)

Table 1 provides the summary of ANOVA analysis for the material removal rate (MRR) response. The ANOVA results reveal that the developed model is highly significant, with a p-value of 1.999×10^{-12} and an F-value of 107.24, indicating that the model successfully captures the response variability. Among the input factors, (i) Current, (ii) Pulse-on time, and (iii) Pulse-off time have a significant effect on material removal rate (MRR), with p-values of 2.186×10^{-7} , 9.44×10^{-8} , and 0.00018, respectively. This suggests that these three factors are the primary drivers influencing the values of material removal rate (MRR). In contrast, gas pressure was found to be insignificant ($p = 0.892$), showing a minimal impact on the response under the conditions tested.

The model's non-significant Lack of Fit ($p = 0.677$) indicates that the model fits the data well, with minimal unexplained variance. The low residuals and pure error further confirm both the accuracy and consistency of the model. Overall, the analysis highlights Current, Pulse-on time, and Pulse-off time to be the key factors for process optimization, while Gas pressure plays a less critical role. The interaction and quadratic effects offer a valuable insight into fine-tuning the process parameters for the purpose of improved performance.

The influence of different process parameters on the material removal rate (MRR) during near-dry micro-EDM of Nitinol is shown in **Figure 1**. A significant decrease in the material removal rate (MRR) was observed with an increase in current, while keeping other parameters at their central levels. For a current setting of 1 A, the highest material removal rate (MRR) was recorded at $25.75 \times 10^{-3} \text{ mm}^3/\text{min}$. However, as the current was increased to 4 A, the MRR dropped sharply by approximately 36%, reducing to $16.51 \times 10^{-3} \text{ mm}^3/\text{min}$. This suggests that higher current settings negatively impact the efficiency of material removal. This is essentially due to the adverse effects on the machining conditions.

Table 1. A summary of ANOVA analysis for the Material Removal Rate [MRR] response

Source	Sum of Squares	df	Mean Square	F-value	p-value	
Model	0.0005	14	0.0000	107.24	< 0.0001	significant
A-Current	0.0000	1	0.0000	79.64	< 0.0001	
B-Pulse-on time	0.0000	1	0.0000	90.73	< 0.0001	
C-Pulse-off time	7.324E-06	1	7.324E-06	24.22	0.0002	
D-gas pressure	5.791E-09	1	5.791E-09	0.0192	0.8918	
AB	1.665E-06	1	1.665E-06	5.51	0.0331	
AC	2.341E-07	1	2.341E-07	0.7743	0.3928	
AD	4.162E-09	1	4.162E-09	0.0138	0.9082	
BC	1.349E-06	1	1.349E-06	4.46	0.0519	
BD	8.751E-07	1	8.751E-07	2.89	0.1095	
CD	3.371E-07	1	3.371E-07	1.11	0.3077	
A ²	0.0000	1	0.0000	103.31	< 0.0001	
B ²	0.0000	1	0.0000	89.73	< 0.0001	
C ²	0.0000	1	0.0000	64.63	< 0.0001	
D ²	3.885E-08	1	3.885E-08	0.1285	0.7250	
Residual	4.536E-06	15	3.024E-07			
Lack of Fit	2.715E-06	10	2.715E-07	0.7454	0.6770	not significant
Pure Error	1.821E-06	5	3.642E-07			
Cor Total	0.0005	29				
R ²						0.99
Adjusted R ²						0.98
Predicted R ²						0.96
Adeq Precision						43.52

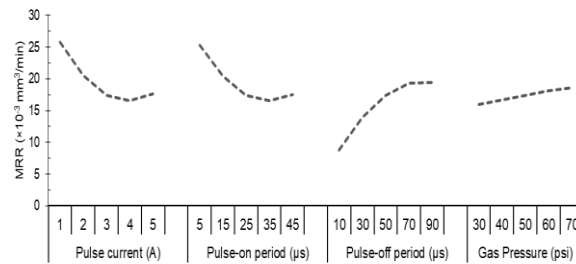


Figure 1. Effect of varying process parameters on material removal rate (MRR).

A similar trend was observed when varying the pulse-on time, another critical parameter affecting the material removal rate (MRR). As the pulse-on time was increased from 5 μs to 45 μs , the MRR followed the same pattern of an initial decline. This was followed by stabilization at a lower value. This further indicates that prolonged pulse durations do not necessarily improve material removal efficiency. In fact, it can lead to reduced performance in the near-dry micro-electrical discharge machining (EDM) process. These results highlight the importance of optimizing both the current and pulse-on time to achieve higher MRR in micro-EDM of Nitinol. While lower settings of current and pulse-on time promote faster material removal, increasing these parameters beyond a certain threshold does reduce the material removal rate (MRR).

The observed decrease in material removal rate (MRR) with increasing pulse current or pulse-on time in the near-dry micro-electrical discharge machining (EDM) process is an intriguing deviation from typical macroscopic EDM behavior. While Sundrayal et al. (2020) [20] attribute their findings to an increased volume of material removal at the lower pulse-on times essentially due to more frequent discharges and uniform heat distribution. This rationale seems less applicable in the microscopic domain. Their macroscopic tool, which likely encounters broader thermal diffusion areas, may experience more significant material removal for lower pulse-on times. However, in the case of microscopic-sized tools, such as those chosen for use in near-dry micro-EDM, the dynamics are fundamentally different.

In the near-dry electrical discharge machining (EDM) process with deionized (DI) water as the liquid phase of the dielectric medium, the formation of an electrical double layer (EDL) assumes a pivotal role. The electrical double layer (EDL), which forms at the interface between the tool and the deionized (DI) water, requires a certain amount of time to charge fully before it can conduct current for the

water electrolysis process. This delay becomes particularly critical as the pulse-on time increases, thereby allowing more time for this layer to stabilize and initiate electrolysis. However, at shorter pulse-on times, the time window for electrical double layer (EDL) charging is reduced, potentially obstructing the onset of water electrolysis. This can, in turn, suppress the secondary effects of gas production while concurrently hindering material removal.

This theory aligns with the observations of Chung et al. (2015) [21] and Li and Natsu (2020) [22], who reported the involvement of water electrolysis in micro-electrical discharge machining (EDM). Their study does provide the necessary foundation to suggest that in the micro-EDM regime, where tool size and discharge time are both constrained, the behavior of the electrical double layer (EDL) and the corresponding electrochemical phenomena become more pronounced, driving an anomalous reduction in the material removal rate (MRR) at higher pulse-on times and current. This interplay of the electrochemical effect and the thermal effect distinguishes microscopic electrical discharge machining (EDM) from its macroscopic counterpart, offering a fresh lens to view the micro-machining process.

As the pulse-off period increased from 10 μs to 90 μs , the material removal rate (MRR) exhibited a steady rise. At a pulse-off period of 10 μs , the material removal rate (MRR) was 8.78 mm^3/min , which progressively increased as the pulse-off period was extended, reaching a peak value of 19.42 mm^3/min at 90 μs , representing a 121% increase from the initial value. The material removal rate (MRR) increased significantly between 10 μs and 70 μs , reaching a value of 19.28 mm^3/min at 70 μs , which was a 119.5% increase from the 10 μs setting. However, the increase was only marginal beyond 70 μs , with only a 0.7% rise between 70 μs and 90 μs . This suggests that while extending the pulse-off period initially enhanced the material removal rate (MRR), it approached a near-saturation point at around 70 μs . The trend indicated that the pulse-off period did allow for sufficient cooling time while enabling in improving spark initiation, contributing to higher material removal rate (MRR) values, though the benefits diminished with an extension of the period.

When the gas pressure was increased from 30 psi to 70 psi, the material removal rate (MRR) consistently improved. At 30 psi, the MRR was 15.96 mm^3/min , which increased by 4.95% to 16.75 mm^3/min at 40 psi. As the gas pressure rose to 50 psi, the material removal rate (MRR) further increased to 17.46 mm^3/min , representing a 9.4% increase when compared to 30 psi. At 60 psi, the material removal rate (MRR) reached 18.09 mm^3/min , a 13.4% increase from

the initial value. Finally, at the highest tested pressure of 70 psi, the material removal rate (MRR) peaked at 18.64 mm³/min, resulting in a total increase of 16.8% from the 30-psi setting. This trend does indicate that higher gas pressure promote better flushing of debris while concurrently enhancing the sparking efficiency, leading to increased material removal rate. However, the rate of improvement diminished at higher pressures, suggesting that the process approached optimal conditions at around 70 psi

The interaction between current and pulse-on time is statistically significant ($p = 0.033$), indicating that their combined effect is important in optimizing the process. Other interactions, such as AC, AD, and BD, are not significant (p -values > 0.05), suggesting that they do not notably influence the outcome. Additionally, the quadratic terms for current (A^2), pulse-on time (B^2), and pulse-off time (C^2) are also significant, reflecting upon the nonlinear relationship between these factors and the response. These findings suggest the presence of an optimal operating range for these factors, beyond which performance can decline. Additionally, the interaction effects between current and pulse-on time were visualized (see **Figure 2**), highlighting upon the optimal conditions for material removal rate (MRR) to occur when both parameters are balanced. The combined influence of these factors suggests that while increasing either parameter does enhance the material removal rate (MRR), the most efficient operation occurs within specific ranges. Moreover, the data illustrates that the material removal rate (MRR) values were highest when the current was maximized, and the pulse-on time was moderately high. For instance, the maximum recorded material removal rate (MRR) of 0.02542 mm³/min was achieved for a current of 3 A and a pulse-on time of 50 μ s, affirming the optimal performance conditions identified through the surface plots.

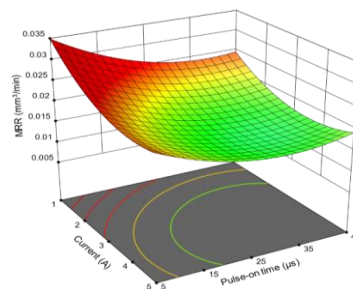


Figure 2. Surface and contour plots displaying the effect of process parameters (current and pulse-on time) Interaction on MRR

Effect on Surface Roughness (SR)

The ANOVA analysis for surface roughness reveals that the overall model is highly significant, with an F-value of 109.98 and a p-value of 1.66×10^{-12} , indicating that the model effectively explains the variation in surface roughness. Among the individual factors, current and gas pressure were found to have a significant impact on surface roughness, with p-values of 0.00637 and 0.0112, respectively. The F-value for current is 10.04, and for the gas pressure it is 8.36, highlighting their strong influence on the response. In contrast, both Pulse-on time and Pulse-off time were not significant ($p > 0.05$), suggesting that these factors do not significantly affect the surface roughness in the given experimental range.

The quadratic effect of gas pressure (D^2) was found to be significant, with a p-value of 4.57×10^{-5} and an F-value of 31.99. This clearly suggests that the relationship between gas pressure and surface roughness is non-linear, and there is an optimal range for this factor. The quadratic terms for both Current (A^2) and Pulse-on time (B^2) show marginal significance, while the Pulse-off time (C^2) is not significant. The non-significant Lack of Fit ($p = 0.0892$) does clearly indicate that the model fits the experimental data well. Overall, these results suggest that both current and gas pressure are the primary factors influencing surface roughness, with significant interactions and quadratic effects, while Pulse-on time and Pulse-off time play a less critical role.

As the pulse current increased, the Sa values also increased as is shown in **Figure 3**. At a current of 1 A, the surface roughness was 2.06 μm . When the pulse current was raised to 2 A, the surface roughness increased sharply to 4.05 μm , reflecting a 96.6% increase. The roughest surface (around 9 μm) was formed at a current setting of 5 A. The overall trend does demonstrate a significant rise in the surface roughness, culminating in an increase of approximately 336% from the lowest current setting to the highest current setting. This trend suggests that intense discharges does result in greater material removal irregularities on the workpiece surface.

Table 2. A summary of ANOVA analysis for the surface roughness (Sa)

Source	Sum of Squares	df	Mean Square	F-value	p-value	
Model	82.39	14	5.88	109.98	< 0.0001	significant
A-Current	0.5370	1	0.5370	10.04	0.0064	
B-Pulse-on	0.0357	1	0.0357	0.6679	0.4266	

time						
C-Pulse-off time	0.0316	1	0.0316	0.5912	0.4539	
D-gas pressure	0.4472	1	0.4472	8.36	0.0112	
AB	0.1406	1	0.1406	2.63	0.1258	
AC	0.2756	1	0.2756	5.15	0.0384	
AD	1.27	1	1.27	23.65	0.0002	
BC	0.0756	1	0.0756	1.41	0.2530	
BD	0.1056	1	0.1056	1.97	0.1804	
CD	0.0756	1	0.0756	1.41	0.2530	
A ²	0.2090	1	0.2090	3.91	0.0668	
B ²	0.0381	1	0.0381	0.7129	0.4117	
C ²	0.0044	1	0.0044	0.0828	0.7775	
D ²	1.71	1	1.71	31.99	< 0.0001	
Residual	0.8026	15	0.0535			
Lack of Fit	0.7025	10	0.0703	3.51	0.0892	not significant
Pure Error	0.1001	5	0.0200			
Cor Total	83.19	29				
R ²						0.99
Adjusted R ²						0.98
Predicted R ²						0.94
Adeq Precision						42.28

Increasing gas pressure resulted in an increasing and then decreasing trend in the surface roughness (Sa) value of the machined surface. At a gas pressure of 30 psi, the surface roughness was measured to be 4.43 μm . When the gas pressure increased to 40 psi, the surface roughness rose significantly to 5.40 μm , indicating a 21.9% increase. Further increase of the gas pressure to 50 psi resulted in a marginal increase in roughness to 5.87 μm , reflecting an 8.7% rise from the previous setting. However, at gas pressures of 60 psi and 70 psi, the surface roughness values decreased to 5.83 μm and 5.30 μm , respectively. Overall, the results indicate an initial increase in the surface roughness with rising gas pressure. This is followed by a decrease, suggesting that while moderate gas pressures can enhance material removal irregularities, excessively high pressures can lead to too much water in the IEG causing electrochemical dissolution and resulting polishing effects on the surface irregularities.

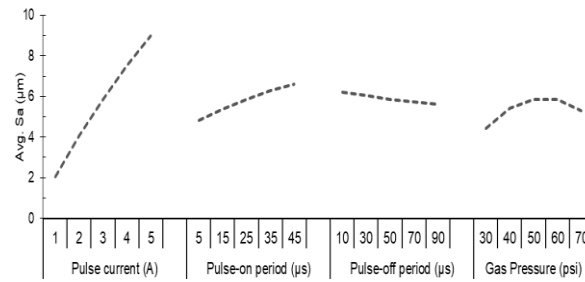


Figure 3. Effect of varying process parameters on average surface roughness (Sa)

In terms of interaction effects, the interaction between Current (A) and Gas pressure (D) is highly significant for a p-value of 0.00021 and an F-value of 23.65. This does indicate that the combined influence of these factors does have a considerable effect on surface roughness. Additionally, an interaction between current and pulse-off time shows significance ($p = 0.0384$). However, the effect is less pronounced than an interaction between current and gas pressure (as shown in **Figure 4**). Other interactions, such as (i) current - pulse on time, (ii) pulse-on and pulse-off times, and (iii) pulse-off time and gas pressure, were found to be non-significant ($p > 0.05$), implying that the combined effects of these factors do not meaningfully impact the surface roughness.

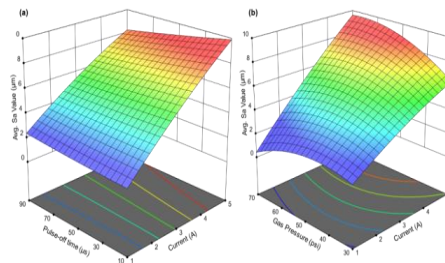


Figure 4. Surface and contour plots displaying the effect of process parameters interaction on MRR:
 (a) Current and pulse-off time, and
 (b) Current and gas pressure.

Effect on Width Overcut (WOC)

The ANOVA results for width overcut (WOC) analysis show that the developed model is highly significant, with an F-value of 121.84 and a p-value of 7.79×10^{-13} , confirming that the model effectively explains the variation in width overcut (WOC). Among the

input factors, Current (A), Pulse-on time (B), Pulse-off time (C), and Gas pressure (D) are all highly significant, with p-values well below 0.05. Specifically, Pulse-on time has the highest F-value of 585.38 ($p = 1.97 \times 10^{-13}$), followed by Current (A) with an F-value of 322.23 ($p = 1.50 \times 10^{-11}$), indicating these factors have the most substantial impact on width overcut (WOC). Similarly, Pulse-off time (C) and Gas pressure (D) are also significant, with F-values of 268.63 and 54.97, respectively.

Table 3. A summary of ANOVA analysis for the width overcut (WOC)

Source	Sum of Squares	df	Mean Square	F-value	p-value	
Model	1866.78	14	133.34	121.84	< 0.0001	significant
A-Current	352.67	1	352.67	322.23	< 0.0001	
B-Pulse-on time	640.67	1	640.67	585.38	< 0.0001	
C-Pulse-off time	294.00	1	294.00	268.63	< 0.0001	
D-gas pressure	60.17	1	60.17	54.97	< 0.0001	
AB	1.00	1	1.00	0.9137	0.3543	
AC	1.0000	1	1.0000	0.9137	0.3543	
AD	2.25	1	2.25	2.06	0.1721	
BC	1.0000	1	1.0000	0.9137	0.3543	
BD	0.2500	1	0.2500	0.2284	0.6396	
CD	12.25	1	12.25	11.19	0.0044	
A ²	12.19	1	12.19	11.14	0.0045	
B ²	37.33	1	37.33	34.11	< 0.0001	
C ²	55.05	1	55.05	50.30	< 0.0001	
D ²	476.19	1	476.19	435.10	< 0.0001	
Residual	16.42	15	1.09			
Lack of Fit	3.08	10	0.3083	0.1156	0.9979	not significant
Pure Error	13.33	5	2.67			
Cor Total	1883.20	29				
R ²						0.99
Adjusted R ²						0.98
Predicted R ²						0.98
Adeq Precision						38.07

The non-significant Lack of Fit ($p = 0.998$) suggests that the model fits the experimental data well, with minimal unexplained variance. The small residuals and pure error does confirm accuracy of the model. The results clearly indicate that (i) pulse-on time, (ii) current, and (iii) pulse-off time are the key factors influencing width overcut (WOC) (as shown in **Figure 5**), with significant quadratic effects, while an interaction between certain factors, particularly C and D, also plays a role. The findings suggest that optimizing these parameters can effectively minimize the width overcut (WOC) in the process.

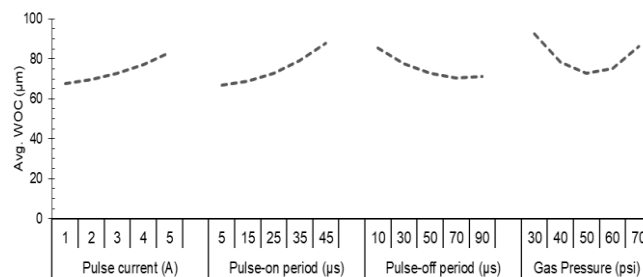


Figure 5. Effect of varying process parameters on width overcut (WOC)

The interactions between the factors, such as AB, AC, AD, and BC, show no significant effect on width overcut (WOC) (p -values > 0.05), suggesting that the combined influence of these factors does not significantly affect the response. However, an interaction between the pulse-off time (C) and gas pressure (D) is significant, with an F-value of 11.19 and a p -value of 0.00443. This clearly indicates that the combined effect of these two factors has a notable impact on width overcut (WOC), as shown in **Figure 6**. Additionally, the quadratic terms for current (A^2), pulse-on time (B^2), pulse-off time (C^2), and gas pressure (D^2) are highly significant, especially Gas pressure (D^2), which has the highest F-value of 435.10 ($p = 1.71 \times 10^{-12}$), showing a strong non-linear effect on width overcut (WOC).

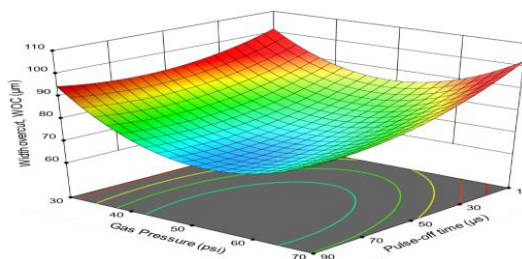


Figure 6. Surface and contour plots displaying the effect of process parameters interaction (pulse-off time and gas pressure) on width overcut (WOC).

Conclusions

1. Material removal rate (MRR) was significantly influenced by current and pulse-on time, with the highest MRR observed at the lower current settings. Increasing the current from 1 A to 4 A resulted in a 49% reduction in material removal rate (MRR), emphasizing the sensitivity of MRR to current variations.
2. Current and gas pressure were the most significant factors affecting surface roughness, while pulse-on time and pulse-off time had a lesser impact. An interaction between current and gas pressure showed a strong influence on surface roughness, requiring careful optimization to minimize roughness.
3. Width overcut (WOC) was predominantly influenced by pulse-on time, current, and pulse-off time, with significant quadratic effects observed for these parameters. An interaction between pulse-off time and gas pressure significantly affected width overcut (WOC), highlighting the need to consider combined parameter effects.
4. Quadratic terms for current, pulse-on time, pulse-off time, and gas pressure were highly significant, especially gas pressure, indicating strong non-linear relationships with surface roughness and width overcut (WOC).

References

- [1] Singh, R., Dvivedi, A., and Kumar, P., 2021, "Evaluation of the Surface Integrity of Titanium Nitride Coating Deposited on the Ni-Ti Substrate Through the Near-Dry Electrical Discharge Surface Coating Process," *TMS 2021 150th Annual Meeting & Exhibition Supplemental Proceedings*, Springer, Cham, pp. 421–429.
- [2] Velmurugan, C., Senthilkumar, V., Dinesh, S., and Arulkirubakaran, D., 2018, "Machining of NiTi-Shape Memory Alloys-A Review," ***Mach. Sci. Technol.***, **22**(3), pp. 355–401.
- [3] Singh, R., Singh, R. P., and Trehan, R., 2021, *State of the Art in Processing of Shape Memory Alloys with Electrical Discharge Machining: A Review*.
- [4] Singh, R., Yadav, V. K., Dvivedi, A., and Kumar, P., 2023, "Evaluating the Feasibility of Using Biodegradable Castor Oil as a Dielectric Medium during Micro-Electrical Discharge Machining of Inconel 718," ***J. Mater. Eng. Perform.***, **32**(14), pp. 6465–6477.

- [5] Singh, R., Tiwari, T., Dvivedi, A., and Kumar, P., 2023, “Assessing the Performance of Air, Argon, and Oxygen as Dielectric Mediums during Dry-Micro-EDM of Ti6Al4V Alloy: A Comparative Study,” **Mater. Manuf. Process.**, **38**(7), pp. 859–877.
- [6] Yadav, V. K., Ramver, Kumar, P., and Dvivedi, A., 2020, “Investigation on the Effect of Input Parameters on Surface Quality During Rotary Tool Near-Dry EDM,” *Recent Advances in Mechanical Infrastructure, Lecture Notes in Intelligent Transportation and Infrastructure*, A.K. Parwani, and P. Ramkumar, eds., Springer, Singapore, IITRAM Ahmedabad, pp. 41–47.
- [7] Yadav, V. K., Singh, R., Kumar, P., and Dvivedi, A., 2021, “Performance Enhancement of Rotary Tool Near-Dry EDM Process through Tool Modification,” **J. Brazilian Soc. Mech. Sci. Eng.**, **43**(2), p. 72.
- [8] Muniraju, M., and Talla, G., 2024, *Exploring Sustainable Machining Processes for Nitinol Shape Memory Alloy: A Review of Eco-Friendly EDM and Other Techniques*, Springer Berlin Heidelberg.
- [9] Yadav, V. K., Singh, R., Kumar, P., and Dvivedi, A., 2022, “Investigating the Performance of the Rotary Tool Near-Dry Electrical Discharge Machining Process through Debris Analysis,” **J. Mater. Eng. Perform.**, **31**(10), pp. 8405–8417.
- [10] Chaudhari, R., Kevalramani, A., Vora, J., Khanna, S., Patel, V. K., Pimenov, D. Y., and Giasin, K., 2022, “Parametric Optimization and Influence of Near-Dry WEDM Variables on Nitinol Shape Memory Alloy,” *Micromachines*, **13**(7), pp. 1–19.
- [11] Dhakar, K., Chaudhary, K., Dvivedi, A., and Bembalge, O., 2019, “An Environment-Friendly and Sustainable Machining Method: Near-Dry EDM,” **Mater. Manuf. Process.**, **34**(12), pp. 1307–1315.
- [12] Yadav, V. K., Kumar, P., and Dvivedi, A., 2019, “Effect of Tool Rotation in Near-Dry EDM Process on Machining Characteristics of HSS,” **Mater. Manuf. Process.**, **34**(7), pp. 779–790.
- [13] Boopathi, S., and Sivakumar, K., 2012, “Experimental Comparative Study of Near-Dry Wire-Cut Electrical Discharge Machining (WEDM),” **Eur. J. Sci. Res.**, **75**(4), pp. 472–481.
- [14] Gholipoor, A., Baseri, H., and Shabgard, M. R., 2015,

- “Investigation of near Dry EDM Compared with Wet and Dry EDM Processes,”* **J. Mech. Sci. Technol.**, **29**(5), pp. 2213–2218.
- [15] Kao, C. C., Tao, J., and Shih, A. J., 2007, “Near Dry Electrical Discharge Machining,” **Int. J. Mach. Tools Manuf.**, **47**(15), pp. 2273–2281.
- [16] Boopathi, S., and Sivakumar, K., 2013, “Experimental Investigation and Parameter Optimization of Near-Dry Wire-Cut Electrical Discharge Machining Using Multi-Objective Evolutionary Algorithm,” **Int. J. Adv. Manuf. Technol.**, **67**(9–12), pp. 2639–2655.
- [17] Ramver, Yadav, V. K., Kumar, P., and Dvivedi, A., 2020, “Experimental Investigation on Surface Morphology of Micro-EDMed Ti-6Al-4 V Alloy,” *Recent Advances in Mechanical Infrastructure, Lecture Notes in Intelligent Transportation and Infrastructure*, A.K. Parwani, and P. Ramkumar, eds., Springer Nature Singapore Pte Ltd., IITRAM Ahmedabad, pp. 69–74.
- [18] Singh, R., Tiwari, T., Rakurty, C. S., Dvivedi, A., and Kumar, P., 2024, “Fluoride-Ion Enhanced the Electrochemical Surface Texturing of Ti6Al4V Alloy via in Situ EDM and ECM with Patterned Tool,” **Int. J. Adv. Manuf. Technol.**, **134**, pp. 3217–3236.
- [19] Singh, R., Rakurty, C. S., Dvivedi, A., and Kumar, P., 2024, “Editors’ Choice—Improving Quality of EDMed Micro-Holes on Titanium via In Situ Electrochemical Post-Processing: A Transient Simulation and Experimental Study,” **J. Electrochem. Soc.**, **171**(1), p. 013501.
- [20] Sundriyal, S., Yadav, J., Walia, R. S., Vipin, and Kumar, R., 2020, “Thermophysical-Based Modeling of Material Removal in Powder Mixed Near-Dry Electric Discharge Machining,” **J. Mater. Eng. Perform.**, **29**(10), pp. 6550–6569.
- [21] Chung, D. K., and Chu, C. N., 2015, “Effect of Inductance in Micro EDM Using High Frequency Bipolar Pulse Generator,” **Int. J. Precis. Eng. Manuf.** - Green Technol., **2**(3), pp. 299–303.
- [22] Li, G., and Natsu, W., 2020, “Realization of Micro EDM Drilling with High Machining Speed and Accuracy by Using Mist Deionized Water Jet,” **Precis. Eng.**, **61**(August 2019), pp. 136–146.

ADDITIVE MANUFACTURING

Study on Deposition Characteristics of Ti6Al4V alloy fabricated through Wire Arc Additive Manufacturing using TIG and MIG-CMT Mode

¹Kadiri Sai Siddhartha, ²P Kavinaya, ³V M Kaoushik, ⁴S Natarajan

^{1,2,3,4}Larsen & Toubro Ltd-
Precision Engineering System,
Coimbatore.

Abstract

The present work aims to study the effect of arc source on the microstructure changes and tensile properties of Ti6Al4V alloy fabricated using wire arc additive manufacturing (WAAM) through Tungsten Inert Gas (TIG) and Cold Metal Transfer-Metal Inert Gas (CMT-MIG) welding method. The specimens are extracted from X and Z orientation for both the welding methods subsequent to solution annealing at 910° C followed by ageing at 540° C. The microstructure results shows the as-built microstructure is acicular α which got decomposed after heat treatment. After solution annealing and ageing, the microstructure appears to be lamellar α and β under both welding methods. The size of lamellar α is finer in CMT mode resulting in higher tensile properties than TIG mode. The tensile properties are approximately 7.5% more in horizontally extracted specimens and approximately 10% more in vertically built specimens in CMT mode of deposition.

The development and refinement of WAAM techniques for Ti6Al4V alloy is expected to motivate the exploration for manufacturing of critical parts for space applications with lower cost and with lesser lead time compared to conventional forging routes.

Keywords - wire arc additive manufacturing, Ti6Al4V, lamellar α and β .

Introduction

L&T is involved in manufacturing of various structural assemblies and sub-systems for variety of space launch vehicles. L&T has pioneered in manufacturing rocket motor casings, and booster segments for these launch vehicles.

Titanium and its alloys finds variety of application in aerospace and defence sectors. Few of the current applications include motor casings, and high pressure gas bottles which are used for launch vehicles and satellites [1, 2]. Ti6Al4V alloy is one variety of titanium alloy which exhibits α/β dual phase alloy which is beneficial in many of the critical applications as stated above. These titanium alloys are weldable, heat treatable and can be used up to 400° C [3]. Processing at high temperature and the subsequent rate of cooling results in the microstructure which possess superior properties of the Ti6Al4V alloy. The mechanical properties depend on the parameters such as volume fraction of α/β , grain morphology, alpha colony width, grain boundary alpha width, and lamella width [4, 5]. The microstructure of Ti6Al4V alloy can be manipulated to achieve desired properties as per applications. There are numerous manufacturing methodologies available which are predominantly thermo-mechanical treatment for Ti6Al4V alloy to obtain the desired mechanical properties. There are growing amount of interest to manufacture titanium alloys as components/sub-assemblies near net shape to reduce the manufacturing lead time and to reduce the manufacturing costs.

Additive manufacturing (AM) is an emerging technology to make the complex profiles to their near net shape with less manufacturing time. The input raw material source can be in the powder or wire form. In Powder bed fusion (PBF) or Powder direct energy deposition (P – DED) process the powder is used as a raw material. In wire direct energy deposition (W-DED) inclusive of wire arc additive manufacturing (WAAM) the input raw material used is wire [6]. In the WAAM process, an arc source is used to melt the wire feedstock and to deposit it sequentially, layer after layer, to produce near net shape components on a substrate. Each additive manufacturing method has merits and de-merits, which requires consideration while selecting the optimum approach for the specific applications. Powder bed fusion techniques like laser powder bed fusion (LPBF) and electron beam melting (EBM) are capable of producing finer resolution in the range of 0.2 to 0.3 mm. But the disadvantage of LPBF is the slower deposition rate combined with limitation in the build envelope size. DED process like electron beam based additive manufacturing (EBAM) require a vacuum chamber which limits the maximum permissible build envelope. Arc based W-DED such as WAAM can be used for producing larger structures and near net shaped components using CNC based machines or robot based welding machines. One limitation of WAAM is the resolution that can be achieved which is typically above 5 mm necessitating further machining to attain the finished part geometry. The key advantages of WAAM are higher

deposition rate, which are typically 3-5 kg/hour and the lack of constraints in the build envelope which help in producing larger components, faster and at a lower cost.

There are numerous studies carried out on powder bed fusion process of titanium alloys for print parameter optimizations and post-processing heat treatment techniques to optimize the microstructure and to achieve desired mechanical properties. Likewise, numerous studies are being carried out on development of W-DED for various engineering alloys through TIG and CMT based processes for single wall deposition. TIG based technique is preferred for depositing using larger filler diameters wire which results in higher heat input which in turn results in higher residual stresses. CMT based deposition is ideal for use with lesser diameter filler wires ensuring optimum energy output for melting without high heat input, as in the case of TIG, resulting in lower residual stresses

In the present work, a comparative study is undertaken on the impact of different arc modes in the output for multi pass deposition of Ti6Al4V alloy. Titanium alloy in bulk volume is deposited using TIG mode and CMT mode and investigation is carried out using non-destructive techniques, microstructural analysis and mechanical property evaluations.

Experimental Procedure

Materials

Ti6Al4V alloy of size 210x170x150 mm was fabricated using a 6-axis KUKA robot with TIG source and subsequently with MIG source using the filler wire of dia 1.6 mm and 1.2 mm respectively. The composition of filler wire is shown in Table 1 which meets the specifications of AMS 4954. The substrate used is of same composition with plate thickness of 25 mm.

Table 1. Chemical composition (wt. %) of Ti6Al4V filler wire

Element	Ti	Al	V	Fe	C	O	N	H	Y
Composition in wt %	Balance	6.03	4.15	0.13	0.018	0.13	0.006	0.001	0.001

Methods

The first sample block of Ti6Al4V alloy is manufactured using a 6 axis KUKA robot with Fronius TIG welding head and the second

sample using CMT-MIG welding machine. The Fixture setup with welding source used for wire arc deposition is shown in Fig. 1 along with deposited block. The sample block was deposited layer by layer as per pre-determined sequence with the weld parameters as shown in Table 2 and Table 3 for TIG and CMT modes respectively. High purity (99.999%) argon is used as shielding gas during TIG mode of deposition and high purity helium (99.999%) is used as shielding gas during CMT mode of deposition to avoid oxidation of weld pool. A custom localized trailing setup is implemented to ensure the weld pool is not oxidized during cooling period. High purity argon is used as trailing gas. CMT deposition of Ti6Al4V alloys requires higher energy for melting because of the resulting aspect ratio of bead geometries. Ivan et al [7]. has shown the usage of helium as shielding gas for Ti6Al4 alloy based on the bead characteristics. The higher aspect ratio of bead geometry achieved in CMT method leads to lack of fusion at edges of beads. In order to overcome the overlapping issue, the bead on plate is carried out with high purity shielding gasses like 100 % argon and 100 % helium. Visual observations on the bead geometries founds that the bead deposited using 100% helium appears to be defect free.

Table 2. Deposition Parameters for TIG mode

Parameter	Value
Welding Current	170-220 A
Welding Voltage	10-13 V
Weld speed	100 mm/min
Filler Wire Feed Rate	700-900 mm/min
Shielding gas flow rate (Argon)	15 lpm
Trailing gas flow rate(Argon)	30 lpm

Table 3. Deposition Parameters for CMT mode

Parameter	Value
Welding Current	150 A (Peak)
Welding Voltage	10-13 V
Weld speed	400 mm/min
Filler wire feed rate	10.5m/min
Shielding gas flow rate (Helium)	15 lpm
Trailing gas flow rate(Argon)	30 lpm

**Figure 1.** TIG and CMT setup with Fixture

The deposited block along with base plate were heat treated as per the cycle of AMS 4999A. The HT cycle is shown in Table 4:

Table 4. Heat treatment cycle for TIG and CMT mode deposited blocks

Parameter	Value
Solution Annealing cycle	
Loading temperature	Room temperature
Soaking temperature	910° C
Soaking time	240 minutes
Vacuum level	1 x 10 ⁻⁴ mbar
Cooling media	Nitrogen purging at 0.2 bar
Ageing cycle	
Loading temperature	Room temperature
Soaking temperature	540° C
Soaking time	240 minutes
Vacuum level	1 x 10 ⁻⁴ mbar
Cooling media	Nitrogen purging at 0.2 bar

Characterization

The deposited block is separated from the base plate using EDM wire cutting and then rough machined in order to assess and characterize the soundness of block using visual and NDT techniques. Thereafter, the specimens are extracted for microstructure analysis, micro-Vickers hardness testing, and tensile testing in horizontal(X) & vertical (Z) direction, fracture toughness testing in both horizontal(X) & vertical (Z) directions.

NDT Techniques

The deposited block is assessed through Balteau 210 KV X-ray radiography technique with focal size of 2.5 x 2.5 mm with sensitivity of 2 %. The film used was AGFA D5 film with exposure time optimized to obtain the sensitivity as per ASTM E1742 technique. After Radiography, the blocks were assessed with ultrasonic technique using TR-0° probe as per AMS 2631 technique to validate the presence of defects in the deposited blocks.

Microstructure Analysis

The samples are extracted in post heat treated condition for microstructure analysis. The samples are mounted using thermoset polymer and prepared with standard metallographic technique of ASTM E3 practice and then etched with kroll's reagent (1% HF, 3% HNO₃, 96% water). The optical microscope is used to analyze the microstructure. Image J is used for analysis of lamellar size calculation.

Mechanical Property studies

Micro- Hardness (Vickers scale)

The samples are analyzed for micro-hardness in Vickers scale under 500 gf load for dwell time of 10 s. The hardness is taken in the samples deposited by both TIG and CMT method post heat treatment.

Tensile strength

The samples are machined as per ASTM E8M for tensile testing and then tested using UTM machine for both TIG mode and CMT mode specimens. Gauge length of 25 mm is used for evaluation of tensile properties. The strain rate of 0.005 mm/mm/minute is used up to 0.2 % Proof stress calculation and then strain rate is increased till breakage. The elongation properties were studied after specimens were broken.

Fracture toughness

The samples (Compact-tensile) are machined as per ASTM E399 for fracture toughness test as per the dimensions in Fig. 2. The loading rate maintained is 4mm/min during testing. The specimens are taken in horizontal and vertical orientations for both the conditions of deposition.

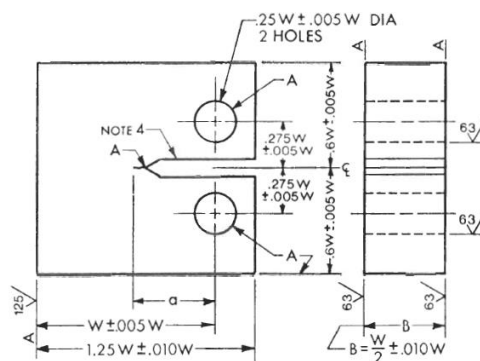


Figure 2. Fracture Toughness test specimen; W=40 mm, B=20 mm

Results and Discussions

The samples extracted are found to be radiographically & ultrasonically defect free for all the specimens extracted in X & Z-direction for both TIG and CMT mode.

NDT Analysis:

The deposited block is non-destructively assessed using high energy X-ray radiography and ultrasonic technique (TR-0°) probe. In both the NDT techniques, there were minor observations in the form of porosities approximately 1mm in size in both the modes of depositions. There were minor regions exhibiting lack of fusion, particularly in the area of deposition stoppage at the edges of blocks.

Microstructure Analysis:

The heat treated samples microstructure of both the methods of welding are shown in Figure 3. The microstructure appears to be lamellar α and β . The lamellar α/β region and grain boundary α is marked in the optical micrographs. The width of α seems to be finer in CMT mode compared to TIG mode of deposition. Image J is used to analyze the size of lamellar α and grain boundary α and the same is formulated in Fig.4. The average width of lamellar alpha for the samples built using TIG mode is 1.1 μm and the average width of primary alpha of CMT based samples is 0.6 μm . The width of prior β or grain boundary α is finer in CMT mode of deposition (0.8 μm), whereas, the width of grain boundary alpha of TIG mode appears in the range of 1.3 μm . The reason behind this is the heat input achieved by CMT method is very low because of lesser heat input involved in CMT along with higher welding speed required for deposition.

The digital process control in CMT helps to detect the short circuit which results to detach the weld droplets by retracting the wire during deposition. During the short circuit the wire moves forward and backward and then pulled back again. As a result, the arc only introduces heat for a very short period of time during arc burning phase. The short circuit is controlled resulting in a spatter free material transfer. The stability of arc is superior to that in TIG which results in spatter free bead deposition. The finer lamellar α width increases the difficulty for dislocation movement with results in improved tensile properties [8].

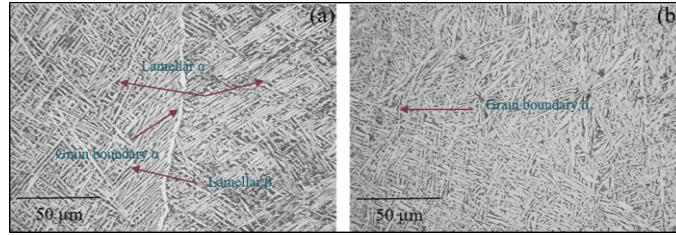


Figure 3. Optical Micrographs of (a) TIG mode deposited WAAM sample, (b) CMT mode deposited WAAM sample

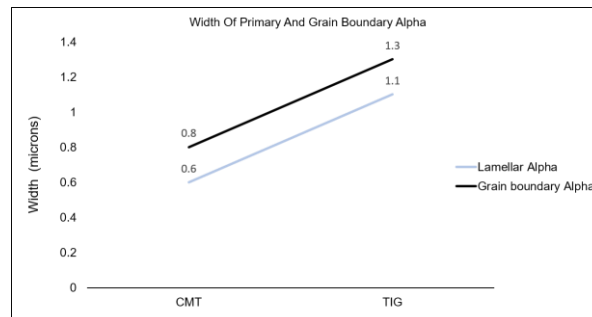


Figure 4. Width of lamellar alpha and grain boundary alpha for CMT and TIG mode of deposition

Micro-Vickers Hardness

The Vickers hardness for both the conditions of deposition is formulated in Figure 5. The hardness of heat treated samples after TIG mode of deposition ranges from 313-360 HV, whereas, CMT deposited samples ranges from 400-422 HV. During solution annealing process, the acicular α decomposed into lamellar α/β , because of the heating at 2 phase region which results in decomposition of α along with transformed β . Various authors have shown that additive manufactured Ti6Al4V alloy post heat treatment above 800° C decomposes acicular α into lamellar α and β and results in superior tensile properties [11]. The hardness comparison shows that the hardness of CMT deposited samples are more than the TIG deposited samples. The reason behind this is the smaller size of lamellar α , and the grain boundary α being finer in CMT deposition mode than in the TIG mode of deposition.

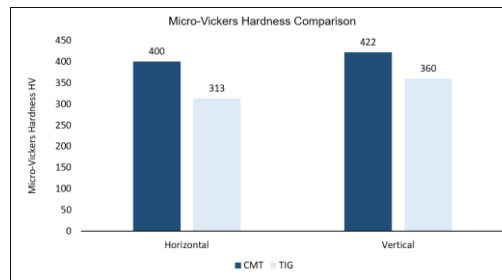


Figure 5. Micro-Vickers Hardness comparison for TIG and CMT mode of deposition

Tensile Properties

The tensile properties for both the condition of deposition is schematically shown in the Figure 6. The trend of tensile properties is similar to that of Vickers Hardness. The average tensile properties of CMT deposited samples in horizontal orientation exhibited 1006 MPa for UTS, and 896 MPa for 0.2 % proof stress, both of which are at least 10 % more than the TIG mode deposited horizontal specimens which resulted 936 MPa for UTS, 823 MPa for 0.2% PS). Likewise, the vertically extracted specimens for CMT showed UTS of 980 MPa, and 0.2 % PS of 878 MPa which are approximately 7.5 % higher than the vertical specimens for TIG mode of deposition. The increase in tensile properties of CMT deposited samples are due to the fact that the lamellar α/β and grain boundary α are finer than the samples deposited in TIG mode.

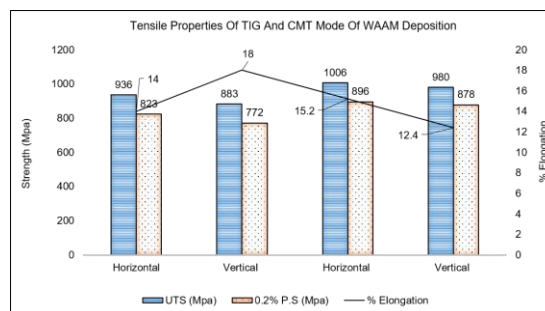


Figure 6. Tensile testing comparison for TIG and CMT mode of deposition

The reason behind this is the lower amount of heat input which is used in CMT process and also faster cooling rate after each layer of deposition. The CMT cycle consist of arching phase and short-circuiting phase. Sun et al [9] has shown that the waveform of 1 CMT cycle consists of arc burning phase and short circuiting phase which results in minimal amount of time for peak current during deposition

which results in reduced heat input. There is a current pulse which appears in the short-circuiting phase which increases the output energy distribution which is essential for stability of arc in CMT process. The lesser heat input also reduces the melting of previous layer deposited which eliminates melting of previously formed grains and thus results in finer microstructure.

Fracture Toughness Properties

To obtain Plane-strain fracture toughness, the following conditions are to be met to consider the obtained K_Q to be considered as K_{IC} .

$$P_{max}/P_Q < 1.10$$

$$2.5 \left(\frac{K_Q}{\sigma_{ys}} \right)^2 < (W - a)$$

The thickness (B) is 20 mm for all the specimens tested for FTT and the results are formulated in Fig.7. Fracture toughness results of CMT and TIG mode of deposition are meeting the minimum requirements of 75 MPa.m^{1/2} as per AMS 4999A. Moreover, FTT results are almost similar for both the mode of deposition. Generally, fracture toughness depends on the size of lamellar α and the size of each colony width. The coarser colony width and lamellar α makes crack propagation difficult and the trade-off should be done with respect to required tensile properties. Zhang et al. has shown that the coarser α colony size results in higher fracture toughness compared to finer microstructures.

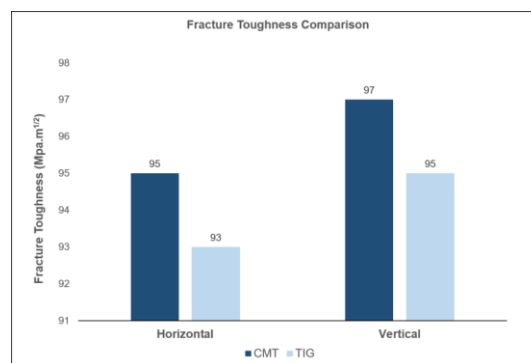


Figure 7. Fracture toughness testing comparison for TIG and CMT mode of deposition

To summarize, Ti6Al4V alloy blocks were fabricated using TIG mode and MIG-CMT mode of wire arc additive method and systematically

characterized for the soundness for deposition through non-destructive testing, microstructure analysis, mechanical property studies including micro-Vickers hardness and tensile properties. Even though the TIG method of deposition meets the minimum requirements of AMS 4999A, CMT mode of deposition offers the advantages of faster deposition rate and increased mechanical properties.

Conclusions

In this work, the effect of different arc modes through Tungsten inert gas (TIG) and MIG-cold metal transfer (CMT) mode of deposition is evaluated in systematic way utilizing non-destructive techniques, microstructure analysis and mechanical property. The following points are concluded:

1. Both TIG and CMT mode deposited samples are sound in terms of radiography and ultrasonic test with minor observations on porosities and lack of fusion at edges of blocks.
2. The microstructure appears to be free of cracks, no lack of fusion or micro porosities.
3. The acicular α is decomposed into lamellar α/β during heat treatment at 910° C and subsequent ageing. The reason behind this is due to the heating of the deposited block at two phase (α/β) region which decomposes the acicular α .
4. Samples from CMT mode of deposition appears to have finer α width in both lamellar α and grain boundary α which makes it difficult for the dislocation to glide.
5. Owing to the above reasons, the mechanical properties of CMT mode of deposition are superior to TIG mode of deposition. It is observed that the tensile properties are typically 10 % more in horizontal extracted samples and 7.5 % more in vertically extracted samples.

With the soundness of CMT mode of deposition being similar to that of TIG mode of deposition samples and further considering the superior mechanical properties, higher deposition rate and lower cost of CMT method over TIG method, it is established that the CMT method of deposition is better suited for manufacturing large critical aerospace components through WAAM.

References

1. M. Wollmann, J. Kiese, and L. Wagner, "Properties and applications of titanium alloys in transport," *Ti 2011 - Proc. 12th World Conf. Titan.*,
2. C. Murgau Charles, *Microstructure model for Ti-6Al-4V used in simulation of additive manufacturing.*
3. H. Tan *et al.*, "Achieving superior ductility for laser solid formed extra low interstitial Ti- 6Al-4V titanium alloy through equiaxial alpha microstructure Scripta Materialia Achieving superior ductility for laser solid formed extra low interstitial Ti-6Al-4V titanium al," *Scr. Mater.*
4. D. Thoguluva, R. Vijayaram, T. R. Vijayaram, M. P. Natarajan, M. Ramarao, and D. Ananthapadmanaban, "Titanium and Titanium Alloys: Advanced Materials for Engineering Industries,"
5. G. Lütjering, "Influence of processing on microstructure and mechanical properties of ($\alpha + \beta$) titanium alloys," *Mater. Sci. Eng. A*,
6. W. J. Evans, "Optimising mechanical properties in alpha + beta titanium alloys," *Mater. Sci. Eng. A*,
7. I. Tabernero "Study on Arc Welding processes for High Deposition Rate Additive Manufacturing" Conference on Electro Physical and Chemical Machining
8. J. Gou *et al.* "Microstructure and mechanical properties of as-built and heat treated Ti6Al4V alloy prepared by cold metal transfer additive manufacturing" *journal of Manufacturing proces.*
9. G. Lutjering, J. C. Williams, and A. Gysler, *Microstructure and mechanical properties of titanium alloys.* Springer, 2000
10. AMS 4999 A- Titanium alloy direct deposited products Ti6Al4V Annealed.
11. S. Cao *et al.*, "Role of martensite decomposition in tensile properties of selective laser melted Ti-6Al-4V, *J. Alloys Compd.*

Optimizing WAAM Process Parameters to Enhance Microstructure and Mechanical Properties of Aluminum 1050: An Experimental Approach

**Sujata Sahoo^{1*}, Prashant Veer², Somashekara M A³,
Anbukkarasi Rajendran⁴**

*^{1,2,3,4} Department of Mechanical, Materials and Aerospace
Engineering (MMAE), IIT Dharwad, Karnataka, India*

Abstract

Wire Arc Additive Manufacturing (WAAM) is a cutting-edge technique utilizing arc welding processes to create complex geometries with aluminum alloys, particularly aluminum 1050. This study focuses on optimizing WAAM process parameters, such as current, travel speed, and standoff distance (SOD) to enhance deposition quality and bead geometry consistency. Extensive parameter studies were conducted to determine optimal ranges, including interactions between parameters and their impact on bead shape, aspect ratio, and deposition volume. Analysis of the bead area and deposition consistency confirmed that specific parameter combinations minimize defects, enhance layer stability, and improve aspect ratio uniformity. For thin-wall structures, optimized parameters were crucial for achieving straight, defect-free walls, essential for load-bearing capacity and dimensional accuracy. The findings provide valuable insights for aerospace and automotive industries where precise, high-quality additive manufacturing is crucial. This research advances understanding of WAAM's potential, paving the way for innovative solutions in large-scale metal additive manufacturing applications.

Keywords: Wire Arc Additive Manufacturing (WAAM), Aluminum 1050, Parameter optimization, Bead geometry, Thin-wall deposition.

Introduction

Additive Manufacturing (AM) has revolutionized the production of complex components across various industries by providing innovative solutions that traditional manufacturing methods cannot achieve. In AM process objects are build layer-by-layer, thereby minimizing material wastage and allow for the fabrication of intricate geometries which significantly helps in reducing the weight of the components without compromising in their strength. [1]. The ability of fabricating

intricate geometries is especially beneficial for industrial applications like aerospace and automotive industries, where weight of the component plays a critical role, and reduction in weight significantly improves enhance the fuel efficiency and performance of the component.

Wire-Arc Additive Manufacturing (WAAM) has emerged as a prominent method in the field of AM, particularly for fabricating metallic components. WAAM employs an arc welding process to deposit material layer by layer, making it an efficient method for producing large-scale structures with complex geometries. This manufacturing process is especially beneficial for Al-alloys, which are widely employed in numerous sectors owing to their light weight, elevated strength, and outstanding resistance to corrosion. Among these alloys, aluminum 1050 is known for its exceptional conductivity and ductility, which makes it a preferred choice for aerospace, automotive, and marine applications [2].

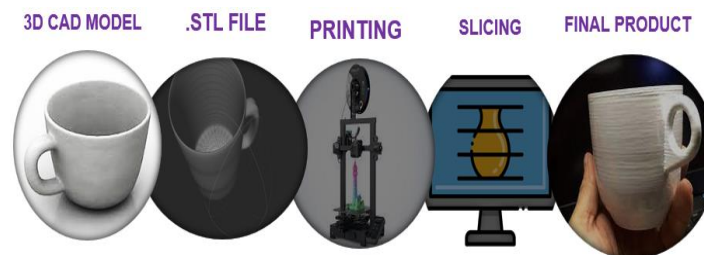


Figure1. Schematic of Additive Manufacturing Process

The mostly extensively utilized alloy for the production of aircraft structural components (including skins, wings and ribbed beams) are high strength Al-alloys. As compare to other alloys, High-strength Al-alloys have high specific strength, exceptional specific stiffness and fatigue and corrosion resistance. [3]. However, traditional manufacturing methods often fall short of producing components that fulfill the demands for high overall performance, cost-effectiveness, and sustainable environmental practices [[4], [5], [6]]. AM technology has the potential to address these challenges by integrating design with manufacturing, as well as combining structure with function [7,8]. Specifically, for large-scale structural elements made from aluminum alloys, wire arc additive manufacturing (WAAM) presents notable advantages, such as a low buy-to-fly ratio, reduced equipment costs, shorter production times, and a high deposition rate [[9], [10], [11], [12]].

The CMT-based Wire Arc Additive Manufacturing (WAAM) process is known for its reduced heat input and minimal spatter, attributed to its short-circuits transition mechanism [15,16]. However, the broader

adoption of CMT-based WAAM is constrained by issues related to the quality of the formation and the properties of the produced components [17-19]. These factors are influenced by the presence of internal defects and the quality of the surface finish.

The additive manufacturing (AM) process facilitates the fabrication of geometrically complex components by constructing them layer-by-layer, directed by acquiring three-dimensional data from either using designing software or scanning tangible objects [18]. Wire Arc Additive Manufacturing (WAAM) represents a particular variant of AM in which an arc is used to create a thermal energy to melt and deposit filler wire sequentially along a predetermined trajectory [19, 20]. The WAAM Process is schematically represented in Figure 2. In contrast to conventional manufacturing techniques, such as equal and subtractive operations, which frequently experience challenges associated with intricate processes, restricted manufacturing versatility, low material efficiency, and extended production durations, WAAM is remarkably well-suited for fabricating large near-net-shape metallic components due to its superior material efficacy and structural adaptability [21].

In recent years, there has been a rising interest among researchers in exploring the use of WAAM (Wire Arc Additive Manufacturing) manufacturing technology to fabricate various Al-alloys, such as Al-Mg, Al-Cu, and Al-Si alloys, which are known for their good weldability [22-28]. With the aerospace industry's rising demand, the strength necessities for WAAM produced Al-alloys are becoming increasingly stringent. Conventional aluminum alloys, however, fall short of meeting the demands for ultra-high strength [29].

Currently, two primary methods exist for producing Al-Zn-Mg-Cu aluminum alloys through WAAM. The initial approach involves using multiple wires as feedstocks for the process. For instance, Chen et al. [30] succeeded in fabricating Al-6.6Zn-2.6Mg-2.6Cu components of Al-alloy by concurrently supplying Zn, ER2319, and ER5356 filler wires into the molten pool utilizing a gas tungsten arc welding (GTAW) system. However, they observed weld hot cracks occurring 40–60 mm away from the base after depositing over 40 layers, as the internal stress escalated with increased deposition height, leading to the formation of macro-cracks. Similarly, Yu et al. [31] reported that the microstructures of their as-deposited components predominantly featured columnar grains alongside many pores and microcracks, which led to tensile strengths of 241 MPa horizontally and 160 MPa vertically, respectively indicative of anisotropic behavior. This literature underscores the inadequacy of using numerous wires as

feedstocks for WAAM process for Al-Zn-Mg-Cu Al-alloys owing to the inopportune chemical compositions and dissimilar microstructures, making the resultant components highly prone to hot cracks which adversely affects their mechanical properties.

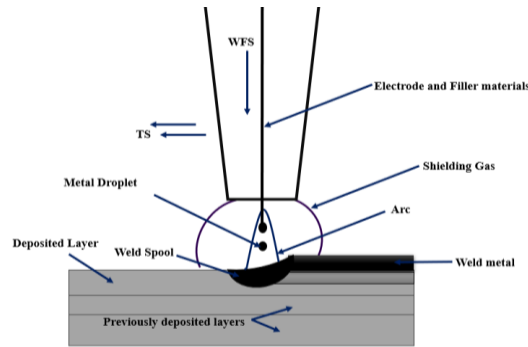


Figure 2. Schematic view of WAAM Process

A promising methodology to alleviate these challenges is to utilize commercially accessible or self-fabricated Al-alloy wires as raw material directly. Dong et al. [32] examined the microstructural attributes in conjunction with the mechanical characteristics of 7055 Al-alloy produced via a GTAW process employing a commercially used 7055 Al filler wire. Although their microstructure remained comprised of coarse columnar grains, their horizontal tensile strength was constrained to 230.7 MPa, attributable to elevated porosity and persistent secondary phases. Using a commercial 7055 wire as the raw material, Fu et al. [33] used the hot wire WAAM process to reduce heat input, producing components devoid of cracks with a microstructure primarily composed of big equiaxed grains and a small number of columnar grains. Their tensile strength reached 563 MPa after three phases of solution and aging thermal treatment. By altering the compositions of Al-Zn-Mg-Cu Al-alloy (Al-3.6Zn-5.9Mg-0.3Cu), Klein et al. [34] created a filler wire and used the cold metal transfer (CMT) technique to create components free of cracks. Their tensile strength reached 477 MPa subsequent to a two-stage aging treatment. They subsequently developed an Al-5.5Zn-Mg-Cu (ML7075) wire and fabricated thin-wall structure component by WAAM which is crack-free by CMT approach, achieving a tensile strength of 558 MPa post T6 heat treatment [35].

Notwithstanding these advancements yielding substantial enhancements in strength, the prevailing tensile strength levels continue to fall short of the ultra-high strength criteria for Al-Zn-Mg-Cu Al-alloys employed in specific structural applications within the aerospace sector, which necessitate tensile strengths surpassing 614 MPa in accordance with the AMS4206C [36]. Consequently,

augmenting the mechanical properties of Al-Zn-Mg-Cu Al-alloys produced via WAAM persists as a pivotal domain of inquiry. Figure 3 shows the methodology of the Study.

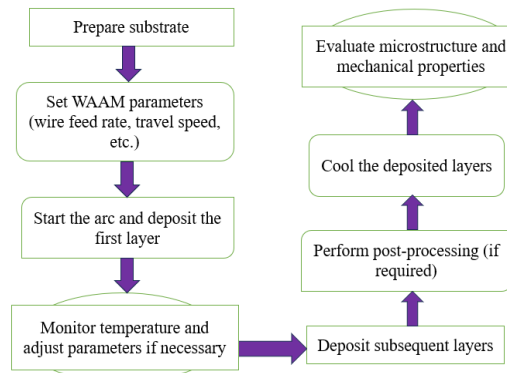


Figure 3. Methodology of Study

Materials and Methods

Material

Feedstock Materials

Due to its advantageous properties, the 1050 aluminum alloy is widely employed as a filler material in WAAM. As a high-purity Al-alloy, with a minimum aluminum content of 99.5%, 1050 alloy offers excellent ductility, making it well-suited to accommodate the thermal expansion and contraction inherent in WAAM processes without introducing cracking or structural flaws. This characteristic is crucial for maintaining integrity in complex or layered geometries. Additionally, 1050 alloy's high electrical and thermal conductivity provides stability to the molten pool during deposition, effectively dissipating heat and reducing thermal stresses, which aids in achieving uniform and defect-free layer deposition. Its inherent corrosion resistance further enhances the longevity and reliability of WAAM-produced parts, especially in environments exposed to moisture or other atmospheric conditions. Figure 4 is image of Al 1050 wire spool.

The 1050 alloy's relatively low melting point (~650°C) and high ductility contribute to its ease of deposition, resulting in smooth layer formation and minimizing risks such as porosity or cracking. This ease of processing enhances the efficiency and consistency of the WAAM process. Cost-effectiveness is another advantage; as a commercially pure aluminum, 1050 alloy is more affordable than many other alloys, making it ideal for large-scale manufacturing or prototyping, where material costs are a consideration. Moreover, 1050 alloy exhibits

strong metallurgical compatibility with AA6101 substrates, supporting robust bonding and a cohesive interface, essential for achieving high-quality, structurally sound components. Collectively, these attributes make 1050 aluminum alloy a strategic choice in WAAM applications, where its electrical and thermal properties, corrosion resistance, and process efficiency contribute to producing durable and reliable components.

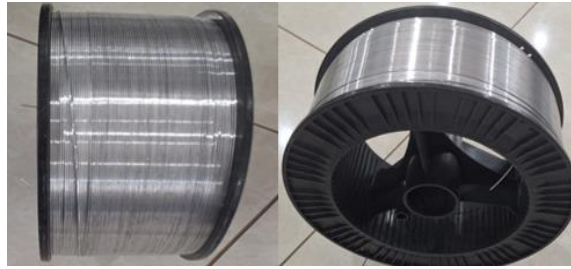


Figure 4. Al 1050 wire spool

The material utilized in this investigation was commercially available 1050 aluminum alloy filament, acknowledged for its high purity and ductility. The chemical constitution is presented in Table 1.

Table 1: Chemical composition of 1050 aluminum alloy.

Element	Al	Cu	Iron	Mn	Mg	Si	Ti	Vn	Zn
%	99.5%	0.05%	0.4%	0.05%	0.05%	0.25%	0.03%	0.05%	0.05%
	min	max	max	max	max	max	max	max	max

Base Materials (Substrate)

AA6101 T65 is an excellent choice as a substrate material in WAAM for depositing 1050 Al-alloy due to its advantageous combination of properties. Its high electrical conductivity (52–58% IACS) and thermal conductivity (160–190 W/m·K) make it ideal for applications where efficient heat dissipation is critical, such as in WAAM processes. This thermal management minimizes thermal gradients, reducing the risk of warping or distortion in the deposited layer. Additionally, AA6101 T65 offers a favorable strength-to-weight ratio, with yield strength values ranging from 170 to 220 MPa, providing a strong, lightweight substrate that enhances structural integrity without adding excessive weight. The material's corrosion resistance ensures durability under atmospheric and environmental exposure, which is essential for applications where both the substrate and the deposited alloy may be exposed to harsh conditions.

Moreover, AA6101 T65 demonstrates excellent compatibility with 1050 aluminum alloy, resulting in improved bonding and minimizing

the risk of delamination between the substrate and the deposited material. This compatibility also supports metallurgical bonding, enhancing the mechanical stability of the interface. Known for its good weldability, AA6101 T65 facilitates a strong and stable fusion with the deposited 1050 alloy, which is crucial for achieving a high-quality build in WAAM processes. Additionally, the alloy's high dimensional stability and stiffness provide a stable base that resists deformation, thereby aiding in maintaining dimensional accuracy and minimizing residual stresses in the deposited layers. Collectively, these attributes make AA6101 T65 a highly suitable substrate material for WAAM, optimizing both process stability and final part performance in applications utilizing 1050 aluminum alloy.

Table 2: Chemical composition of Substrate (AA6101 T65).

Element	Composition (%)
Aluminum (Al)	Balance
Magnesium (Mg)	0.35–0.8
Silicon (Si)	0.3–0.7
Iron (Fe)	0.5 max
Copper (Cu)	0.1 max
Manganese (Mn)	0.03 max
Zinc (Zn)	0.1 max
Titanium (Ti)	0.03 max
Other Elements (each)	0.03 max
Other Elements (total)	0.15 max

Table 3: Properties of AA6101 T65

Property	Value
Density	2.70 g/cm ³
Melting Point	580–650 °C
Electrical Conductivity	52–58% IACS
Thermal Conductivity	160–190 W/m·K
Ultimate tensile strength	200–240 MPa
Yield Strength	170–220 MPa
Elongation at Break	5–12%
Modulus of Elasticity	69 GPa
Hardness (Brinell)	~75 HB

WAAM Process Parameters

The WAAM process was conducted using a specialized WAAM system, specifically a Fronius Trans-Steel setup, which included an attached welding torch integrated with a Vertical Machining Center (VMC). This configuration enabled precise control over the arc deposition process, ensuring consistent layer buildup and high-quality metallurgical bonding between deposited layers. The Fronius Trans-Steel system, known for its stability and adaptability in various welding applications, provided an ideal platform for achieving uniform deposition, optimized for the specific needs of the 1050 aluminum alloy on the AA6101 T65 substrate. The parameters were optimized to achieve consistent bead formation. The process parameters are listed in Table 4. Shielding Gas Argon (100%), the flow rate is 12 L/min, Wire Feed Speed (WFS) is 2–4 m/min, inter-pass temperature is 120°C, layer thickness approximately 6.0 mm per pass.

Table 4: Range of WAAM Process parameters

Parameter	Range
Current (I)	80–120 A
Travel Speed (TS)	100–200 mm/min
Standoff Distance (SD)	8–12 mm
Wire Feed Speed (WFS)	2–4 m/min
Inter-pass Temperature	100–150°C
Arc Voltage (V)	18–22 V
Shielding Gas	Argon (100%)
Shielding Gas Flow	12–20 L/min

WAAM Equipment and Setup

In the experimental Setup for wire weld deposition, a Vertical Machining Center (VMC) equipped with an integrated welding torch was utilized to ensure precise control over the WAAM process. The setup included a Fronius Trans Steel welding system, which provided stable arc performance and adaptability to meet the specific requirements of aluminum 1050 deposition on an AA6101 T65 substrate. The VMC integration enabled fine positioning and controlled movement of the welding torch, which is critical for achieving consistent layer buildup and uniform bead geometry throughout the deposition.



Figure 5. WAAM Experimental setup

The welding torch, connected to the VMC, facilitated real-time adjustments in travel speed, current, and standoff distance (SOD), essential for maintaining optimal deposition conditions. With a flow rate of 12 L/min, argon was utilized as a shielding gas to stop oxidation and guarantee a clean welding environment. The wire feed speed (WFS) was adjusted between 2–4 m/min, depending on the specific current and travel speed settings, to maintain a stable melt pool and consistent deposition rate. Additional control of inter-pass temperature, held at approximately 120°C between layers, minimized thermal stress and supported dimensional accuracy. This setup provided the necessary precision and flexibility to optimize WAAM parameters for high-quality aluminum alloy structures, essential for applications requiring complex geometry and robust mechanical performance.

Results and Discussion

Parameters study {Range of optimization}

In the Parameters Study (Range of Optimization), this research explores the effect of current, travel speed, and standoff distance (SOD) on the WAAM process for aluminum 1050, with each parameter playing a critical role in defining the quality, stability, and uniformity of deposited layers. Current, as a primary heat source, directly affects the melt pool size and bead width. Lower currents generate smaller melt pools and narrower beads, which are advantageous for finer details but may lead to underfill and layer instability. In contrast, higher currents increase bead width and deposition rate; however, they can cause overheating, leading to distortions or irregular layers. The study's images suggest that mid-range current values are optimal, providing balanced deposition with minimal defects and stable layer formation.

Travel speed significantly impacts deposition rate and bead height by controlling the rate at which the torch moves. Slower speeds allow

more material to accumulate, forming taller and thicker beads. However, excessive heat accumulation at slow speeds can widen the bead and negatively impact structural consistency. Higher travel speeds lead to thinner beads, favoring precision but potentially weakening the interlayer bonding due to reduced bead height. The images demonstrate that achieving a balanced travel speed results in ideal bead height and width, crucial for consistent layer stacking and preventing localized overheating.

The standoff distance (SOD), or the gap between the torch tip and substrate, also influences the arc's spread and deposition stability. Closer torch positions (small SOD) yield a more concentrated arc and finer bead geometry but may introduce spatter and irregularities due to high energy density. A larger SOD disperses the arc over a broader area, resulting in smoother layers and moderate bead width, beneficial for consistent layer bonding. The visual data suggest that maintaining SOD within a specific range promotes optimal bead contour and surface smoothness without compromising interlayer adhesion.

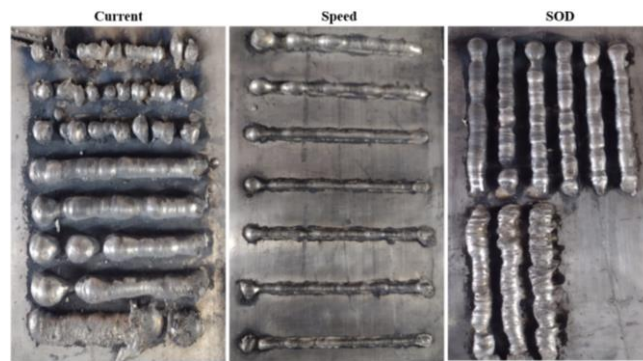


Figure 6. Parameters study bead image of Current, Speed, and SOD

Furthermore, interaction effects among current, travel speed, and SOD highlight the importance of parameter synergy. For instance, a combination of high current and low travel speed produces wider and more robust beads but risks defects from excessive heat. Adjusting SOD within an optimal range can help distribute the heat evenly, enhancing deposition quality. The images underscore that fine-tuning these parameters in tandem reduces common WAAM issues such as porosity and cracking, maintaining dimensional stability and layer uniformity critical for producing high-quality WAAM components.

Interaction Effects Between Parameters:

The results also detail significant interactions between current, travel speed, and SOD, which together influence the bead's microstructural quality and the WAAM process's overall stability. For instance, the

study notes that the combined effect of current and travel speed impacts bead uniformity, influencing microstructural consistency and reducing anisotropy in the layers. Figure 7 shows the Interaction Effects Between Current, speed, and SOD. These parameter interactions are crucial in minimizing common WAAM-related defects such as porosity, cracking, and dimensional instability, thus enhancing the reliability of the WAAM process for aluminum 1050.

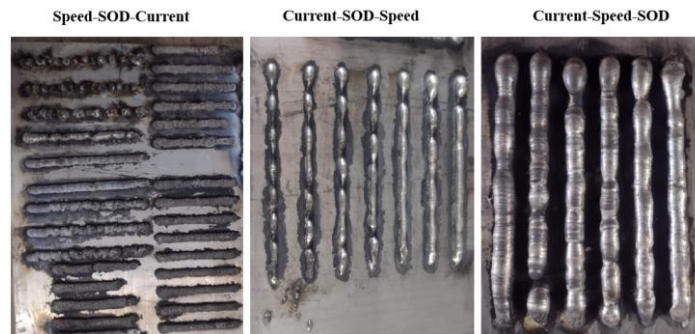


Figure 7. Interaction Effects Between Current, speed, SOD

L27 Full factorials study

Parameter Impact on Bead Geometry and Formation

The study's full factorial analysis reveals how variations in WAAM parameters, specifically current, travel speed, and standoff distance (SOD), influence the bead geometry, including width, height, and aspect ratio. The results show that higher current values result in wider beads due to increased heat input, while higher travel speeds tend to produce narrower beads. Such parameter adjustments are crucial for achieving precise bead dimensions, which directly affect the structural stability of WAAM-fabricated components. The findings highlight that an optimal current setting, paired with a moderate travel speed, ensures desirable bead width and height, balancing deposition rate with thermal stability. Table 4 shows L27 WAAM process parameters and Figure 8 expressions the Beads Images of deposited in L27 DOE.

Table 4: L27 WAAM process parameters

	Current	Speed	SOD
1	80	300	8
2	80	300	10
3	80	300	12
4	80	400	8
5	80	400	10

6	80	400	12
7	80	500	8
8	80	500	10
9	80	500	12
10	95	300	8
11	95	300	10
12	95	300	12
13	95	400	8
14	95	400	10
15	95	400	12
16	95	500	8
17	95	500	10
18	95	500	12
19	110	300	8
20	110	300	10
21	110	300	12
22	110	400	8
23	110	400	10
24	110	400	12
25	110	500	8
26	110	500	10
27	110	500	12

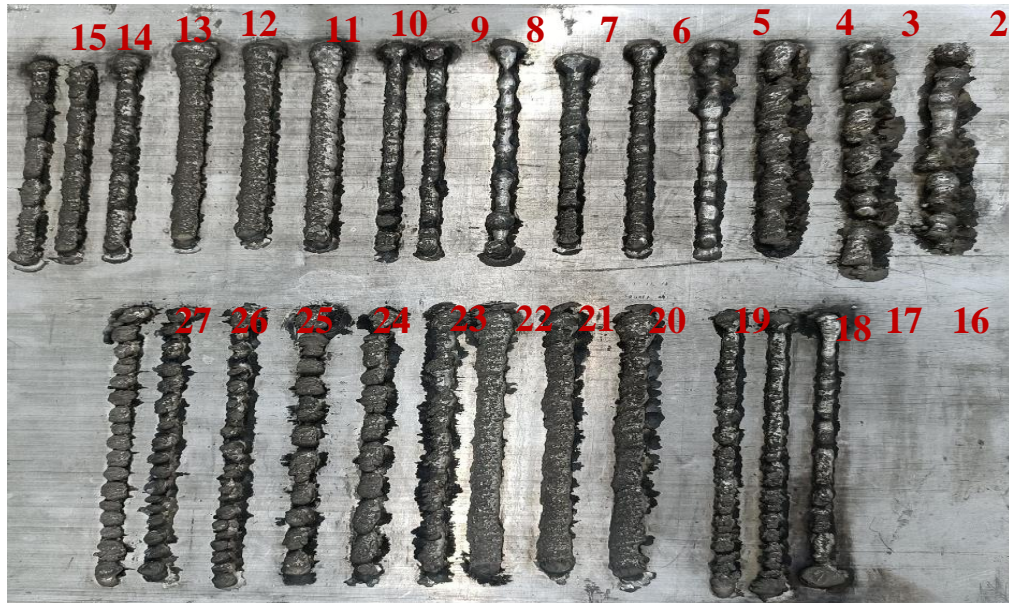


Fig.8. Beads Images of deposited in L27 DOE

Figure 9(a) presents the Key Effects Plot for Signal-to-Noise (SN) Ratios for current, travel speed, and standoff distance (SOD) in the WAAM process, illustrating the effect of these parameters on the stability and quality of deposition. SN ratios are used to assess the robustness of the process by analyzing how different parameter levels impact the consistency of results. Higher SN ratios indicate parameter settings that reduce variability and improve process reliability. The plot reveals that certain levels of current, travel speed, and SOD significantly enhance the SN ratio, suggesting optimal values for each parameter that minimize disturbances, such as heat fluctuation or irregular bead formation, thus contributing to a stable WAAM process.

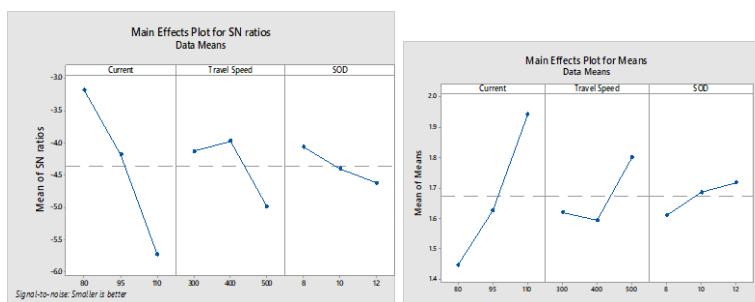


Fig.9(a)& (b) Main effects plot for SN ratios and Main effects plot for Means of Current, Travel Speed, SOD

In Figure 9(b), the Main Effects Plot for Means shows the average impact of current, travel speed, and SOD on deposition quality. This plot helps identify the parameter settings that most consistently

produce desirable bead geometry and deposition characteristics. The means plot highlights the trends in how each parameter, at various levels, affects the average outcome, allowing for precise tuning of the WAAM process. Adjustments in current levels, for instance, show a noticeable impact on bead width and height consistency, while travel speed directly influences the layer thickness and bonding. Optimal settings in SOD, as indicated by the means plot, enhance layer adhesion and uniformity. Together, these plots provide a comprehensive view of how to adjust each parameter to achieve high-quality, reliable deposition results in WAAM.

Aspect Ratio (AR) Insights

Aspect ratio analysis, illustrated through contour plots, indicates how parameter combinations affect bead height-to-width proportions. Lower SOD values combined with moderate current levels achieve a favorable aspect ratio, reflecting stable and well-shaped beads essential for uniform layering. Achieving the right aspect ratio is vital for mechanical stability, as it minimizes dimensional inconsistencies and supports the overall strength of the structure. High aspect ratios could lead to excessive height and uneven layering, while lower ratios might compromise structural density.

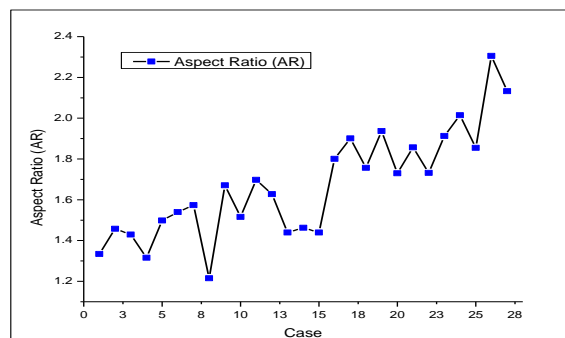


Figure 10. Aspect Ratio (AR) of Deposited Beads

Fig. 10 illustrates the Aspect Ratio (AR) of deposited beads, which is the ratio of the height to the width of the beads formed during the deposition process. A higher AR indicates a more elongated bead, while a lower AR signifies a flatter or wider bead. This parameter is important for assessing the quality of the deposited material, as it influences factors such as bead bonding, surface finish, and the overall mechanical properties of the final product. Maintaining an optimal AR ensures better adhesion between layers and contributes to the structural integrity of the deposit.

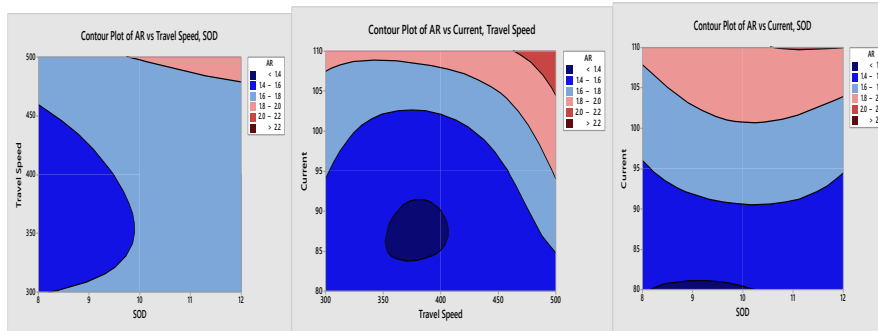


Fig.11(a), (b) &(c) Contour plot of AR vs of Current, Travel Speed, SOD

Figure 11(a), (b), and (c) display contour plots illustrating the relationship between the aspect ratio (AR) and various process parameters: current, travel speed, and standoff distance (SOD). In these plots, the x-axis represents the different levels of the process parameters, while the y-axis corresponds to the aspect ratio of the weld or deposition. The contour lines show how AR changes with respect to each parameter, allowing for an easy visualization of the optimal conditions for achieving a desired AR.

In Figure 11(a), which represents the influence of current on AR, we can observe how variations in the applied current affect the geometry of the weld. Higher currents may lead to an increase or decrease in AR depending on other interacting parameters. Similarly, Figure 11(b) shows how travel speed influences AR. The contour lines in this plot help identify the optimal travel speed for achieving the desired aspect ratio, with slower or faster speeds impacting the final deposition characteristics. Finally, Figure 11(c) focuses on the effect of the standoff distance (SOD) on AR. This parameter plays a crucial role in heat distribution and material deposition, as seen in the contour plot, where variations in SOD can either enhance or reduce the aspect ratio of the welded or deposited material. Overall, these contour plots provide a comprehensive overview of how process parameters interact to influence the aspect ratio, which is a critical factor in determining the quality and properties of the final product.

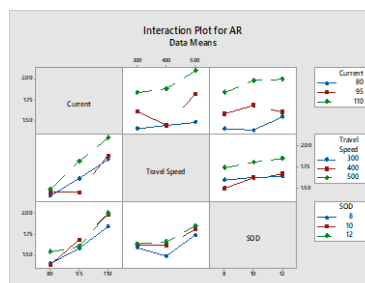


Figure 12. Interaction plot of Current, Travel Speed, SOD

Fig. 12 displays the interaction plot for current, travel speed, and standoff distance (SOD). This plot illustrates how the combined effects of these parameters influence the response variable. The interaction between current and travel speed shows how changes in one can affect the impact of the other on the outcome. Similarly, the relationship between SOD and other parameters reveals its role in optimizing the process, as different SOD values can either enhance or reduce the effect of current and speed on the final result. This interaction plot helps in understanding the complex interdependencies among these factors and aids in optimizing them for desired performance.

Bead Area and Deposition Volume

The bead area, derived from the profile of the deposition, is crucial for assessing deposition volume and consistency. Observations reveal that higher current values, coupled with slower travel speeds, produce larger bead areas, ensuring better fusion between layers and fewer porosity issues. However, excessively large areas can indicate potential overheating, which might lead to grain coarsening or distortion of the deposited material. By balancing current and travel speed, the study achieves optimal bead areas that promote material integrity and layer cohesion without overheating or excessive material buildup.

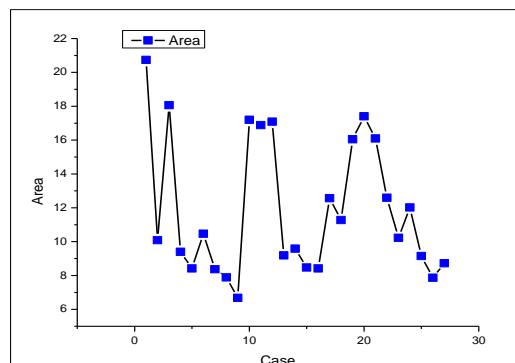


Figure 13. Areas of Deposited Beads

Fig. 13 illustrates the areas where deposition of beads has occurred during the manufacturing process. These beads represent the material that has been deposited layer by layer, forming a structure in additive manufacturing or welding. The distribution and pattern of the deposited beads are critical in determining the concluding properties of the material, such as its strength, density, and surface quality. By analyzing the areas of the deposited beads, researchers can assess the uniformity, consistency, and effectiveness of the deposition process, which directly impacts the performance of the final product.

Figures 14(a), (b), and (c) present contour plots illustrating the relationship between various process parameters, current, travel speed, and standoff distance (SOD), and the resulting areas. These plots visually represent how changes in these parameters influence the size or extent of the affected area during a particular manufacturing or welding process. The contour lines within each plot show the regions where the combined influence of the parameters results in specific values of the area, highlighting the optimal zones for the process. In Figure 14(a), the contour plot for current indicates how variations in the applied current affect the area, with higher or lower currents influencing the thermal input and, consequently, the size of the affected zone. In Figure 14(b), the travel speed's influence on the area is depicted, showing that varying the speed affects the duration of energy application and, thus, the heat distribution and area size. Similarly, Figure 14(c) shows how changes in standoff distance impact the area, as it alters the heat intensity received by the material, which directly affects the resulting area. Collectively, these contour plots are useful for optimizing the process parameters to achieve desired outcomes in terms of area control.

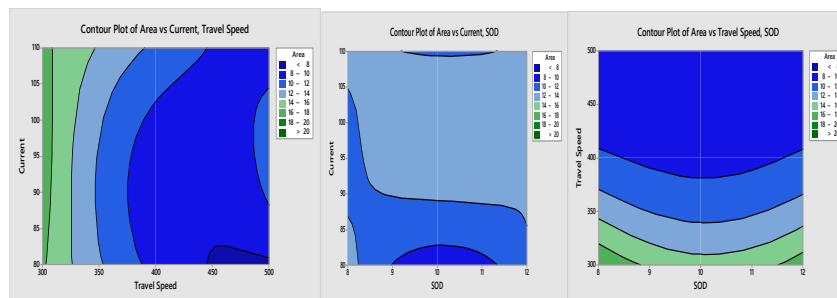


Figure 14(a), (b) & (c) Contour plot of Areas vs of Current, Travel Speed, SOD

Figure 15 shows the interaction plot of three key factors: Current, Travel Speed, and SOD (Stand-Off Distance). The plot visually represents how the combination of these variables influences the outcome of the process being studied. It helps to identify how changes in one factor, such as Current, affect the result at different levels of Travel Speed and SOD. For example, if the Current is increased while keeping Travel Speed constant, the plot may show a rise or fall in the outcome depending on the SOD, suggesting a complex relationship between these parameters. This interaction can indicate the optimal operating conditions for achieving desired results, such as improved efficiency, quality, or performance in manufacturing processes. By observing these interactions, engineers and researchers can make more

informed decisions about how to fine-tune process parameters for better control over the system

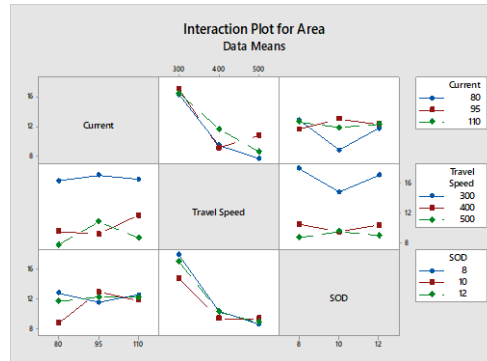


Figure 15. Interaction plot of Current, Travel Speed, SOD

Thin-Wall Deposition and Structural Consistency

When applied to thin-wall structures, optimized parameters are shown to produce straight, uniform walls with minimal internal defects. This outcome is essential for applications requiring precise, lightweight structures, such as aerospace components. The study confirms that maintaining consistency in thin-wall depositions relies on careful balancing of parameters, as thin-walled sections are more sensitive to minor fluctuations in heat input and deposition speed. Achieving uniform thin-wall deposition is fundamental to ensuring load-bearing capacity, dimensional precision, and overall structural reliability in WAAM-fabricated parts.

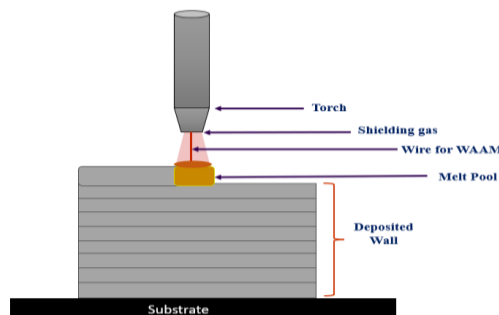


Figure 16. Process of depositing wall

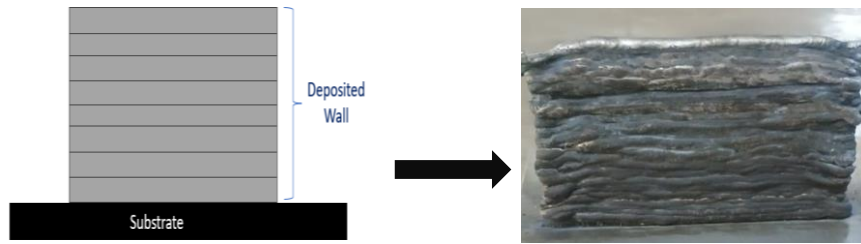


Figure 17. WAAM deposited thin wall

Summary and Conclusion

This research demonstrates that optimizing WAAM process parameters for aluminum 1050 significantly improves microstructure and mechanical properties, making it suitable for applications in industries requiring lightweight and durable materials. Key conclusions include:

- WAAM optimization effectively enhances grain refinement, contributing to improved mechanical properties.
- Optimized parameters result in a balance of lightweight and strength, essential for aerospace and automotive applications.
- This study provides a foundation for further exploration of WAAM as a viable manufacturing technique for aluminum alloys.

Future Work

Future studies should investigate post-WAAM heat treatments to further refine the microstructure and boost mechanical properties. Exploring other aluminum alloys or hybrid materials may expand WAAM's applicability in more demanding structural applications, potentially advancing its adoption in aerospace and other critical industries.

References

1. T. Dursun, C. Soutis Recent developments in advanced aircraft aluminium alloys
2. Mater Des, 56 (2014), pp. 862-871, [10.1016/j.matdes.2013.12.002](https://doi.org/10.1016/j.matdes.2013.12.002)
3. M.M. Tawfik, M.M. Nemat-Alla, M.M. Dewidar Enhancing the properties of aluminum alloys fabricated using wire + arc additive manufacturing technique - a review J Mater Res Technol, 13 (2021), pp. 754-768, [10.1016/j.jmrt.2021.04.076](https://doi.org/10.1016/j.jmrt.2021.04.076)
4. A. Heinz, A. Haszler, C. Keidel, S. Moldenhauer, R. Benedictus, W.S. Mille Recent development in aluminium alloys for aerospace

- applications Mater Sci Eng (2000), [10.1016/S0921-5093\(99\)00674-7](https://doi.org/10.1016/S0921-5093(99)00674-7)
5. B. Cong, X. Cai, Z. Qi, B. Qi, Y. Zhang, R. Zhang, *et al.* The effects of ultrasonic frequency pulsed arc on wire + arc additively manufactured high strength aluminum alloys Addit Manuf, 51 (2022), Article 102617, [10.1016/j.addma.2022.102617](https://doi.org/10.1016/j.addma.2022.102617)
 6. J. Gu, M. Gao, S. Yang, J. Bai, J. Ding, X. Fang Pore formation and evolution in wire + arc additively manufactured 2319 Al alloy Addit Manuf, 30 (2019), Article 100900, [10.1016/j.addma.2019.100900](https://doi.org/10.1016/j.addma.2019.100900)
 7. H.A. Colorado, E.I.G. Velásquez, S.N. Monteiro Sustainability of additive manufacturing: the circular economy of materials and environmental perspectives J Mater Res Technol, 9 (4) (2020), pp. 8221-8234, [10.1016/j.jmrt.2020.04.062](https://doi.org/10.1016/j.jmrt.2020.04.062)
 8. X. Zhang, K. Zhang, L. Zhang, W. Wang, Y. Li, R. He Additive manufacturing of cellular ceramic structures: from structure to structure–function integration Mater Des, 215 (2022), Article 110470, [10.1016/j.matdes.2022.110470](https://doi.org/10.1016/j.matdes.2022.110470)
 9. S.C. Renjith, K. Park, G.E. Okudan Kremer A design framework for additive manufacturing: integration of additive manufacturing capabilities in the early design process Int J Precis Eng Manuf, 21 (2) (2020), pp. 329-345, [10.1007/s12541-019-00253-3](https://doi.org/10.1007/s12541-019-00253-3)
 10. C. Wang, Y. Li, W. Tian, J. Hu, B. Li, P. Li, *et al.* Influence of ultrasonic impact treatment and working current on microstructure and mechanical properties of 2219 aluminium alloy wire arc additive manufacturing parts J Mater Res Technol, 21 (2022), pp. 781-797, [10.1016/j.jmrt.2022.09.055](https://doi.org/10.1016/j.jmrt.2022.09.055)
 11. S. Srivatsav, V. Jayakumar, M. Sathishkumar Recent developments and challenges associated with wire arc additive manufacturing of Al alloy: a review Mater Today Proc, 46 (2021), pp. 8561-8566, [10.1016/j.matpr.2021.03.542](https://doi.org/10.1016/j.matpr.2021.03.542)
 12. T.A. Rodrigues, V. Duarte, R.M. Miranda, T.G. Santos, J.P. Oliveira Current status and perspectives on wire and arc additive manufacturing (WAAM) Materials, 12 (7) (2019), p. 1121, [10.3390/ma12071121](https://doi.org/10.3390/ma12071121)
 13. S. Chen, M. Xu, T. Yuan, X. Jiang, H. Zhang, X. Zheng Thermal–microstructural analysis of the mechanism of liquation cracks in wire-arc additive manufacturing of Al–Zn–Mg–Cu alloy J Mater Res Technol, 16 (2022), pp. 1260-1271, [10.1016/j.jmrt.2021.12.016](https://doi.org/10.1016/j.jmrt.2021.12.016)

14. S. Selvi, A. Vishvaksenan, E. Rajasekar Cold metal transfer (CMT) technology - an overview Defence Technology, 14 (1) (2018), pp. 28-44, [10.1016/j.dt.2017.08.002](https://doi.org/10.1016/j.dt.2017.08.002)
15. C.G. Pickin, K. Young Evaluation of cold metal transfer (CMT) process for welding aluminium alloy Sci Technol Weld Join, 11 (5) (2013), pp. 583-585, [10.1179/174329306X120886](https://doi.org/10.1179/174329306X120886)
16. S.T. Selvamani Microstructure and stress corrosion behaviour of CMT welded AA6061 T-6 aluminium alloy joints J Mater Res Technol, 15 (2021), pp. 315-326, [10.1016/j.jmrt.2021.08.005](https://doi.org/10.1016/j.jmrt.2021.08.005)
17. B. Cong, Z. Qi, B. Qi, H. Sun, G. Zhao, J. Ding A comparative study of additively manufactured thin wall and block structure with Al-6.3%Cu alloy using cold metal transfer process Appl Sci, 7 (3) (2017), p. 275, [10.3390/app7030275](https://doi.org/10.3390/app7030275)
18. C.R. Cunningham, J.M. Flynn, A. Shokrani, V. Dhokia, S.T. New man Invited review article: strategies and processes for high quality wire arc additive manufacturing Addit Manuf, 22 (2018), pp. 672-686, [10.1016/j.addma.2018.06.020](https://doi.org/10.1016/j.addma.2018.06.020)
19. S.C. Altıparmak, V.A. Yardley, Z. Shi, J. Lin Int. J. Lightweight Mater. Manuf., 4 (2021), pp. 246-261
20. S.W. Williams, F. Martina, A.C. Addison, J. Ding, G. Pardal, P. Colgrove Mater. Sci. Technol., 32 (2016), pp. 641-647
21. D.H. Ding, Z.X. Pan, D. Cuiuri, H.J. Li Int. J. Adv. Manuf. Technol., 81 (2015), pp. 465-481
22. M. Köhler, S. Fiebig, J. Hensel, K. Dilger Metals, 9 (2019), p. 608
23. Z.W. Qi, B.Q. Cong, B.J. Qi, H.Y. Sun, G. Zhao, J.L. Ding J. Mater. Process. Technol., 255 (2018), pp. 347-353
24. S. Li, L.J. Zhang, J. Ning, X. Wang, G.F. Zhang, J.X. Zhang Addit. Manuf., 34 (2020), Article 101206
25. Z.W. Qi, B.Q. Cong, B.J. Qi, G. Zhao, J.L. Ding Mater. Lett., 230 (2018), pp. 275-278
26. Q.Y. Miao, D.J. Wu, D.S. Chai, Y. Zhan, G.J. Bi, F.Y. Niu, G.Y. Ma Mater. Des., 186 (2020), Article 108205
27. B.Q. Cong, J.L. Ding, S. Williams Int. J. Adv. Manuf. Technol., 76 (2014), pp. 1593-1606
28. J.Y. Bai, C.L. Yang, S.B. Lin, B.L. Dong, C.L. Fan Int. J. Adv. Manuf. Technol., 86 (2015), pp. 479-485

29. S.Y. Zhou, K. Wu, G. Yang, B. Wu, L.Y. Qin, H. Wu, C.Y. Yang
Mater. Charact., 189 (2022), Article 111990
30. A. Gloria, R. Montanari, M. Richetta, A. Varone
Metals, 9 (2019), p. 662
31. S.J. Chen, M. Xu, T. Yuan, X.Q. Jiang, H.D. Zhang, X. Zheng J.
Mater. Res. Technol., 16 (2022), pp. 1260-1271
32. Z.L. Yu, T. Yuan, M. Xu, H.D. Zhang, X.Q. Jiang, S.J. Chen J.
Manuf. Process., 62 (2021), pp. 430-439
33. B.L. Dong, X.Y. Cai, S.B. Lin, X.L. Li, C.L. Fan, C.L. Yang, H.R.
Sun Addit. Manuf., 36 (2020), Article 101447
34. R. Fu, W.J. Lu, Y.L. Guo, H.S. Lei, Y.A. Cui, J.R. Wang Addit.
Manuf., 58 (2022), Article 103042
35. T. Klein, M. Schnall, B. Gomes, P. Warczok, D. Fleischhacker, P.J.
. Morais Addit. Manuf., 37 (2021), Article 101663
36. T. Klein, L. Reiter, M. Schnall Mater. Lett., 313 (2022),
Article 131841
37. 36 Aluminum Alloy, Plate (7055-T7751) 8.0Zn-2.3Cu-2.0Mg-
0.16Zr Solution Heat Treated, Stress Relieved, and Overaged,
Aerospace Material Specification AMS 4206C
SAE International, Warrendale, PA (2017)SS

Steady-State Thermal analysis of Inconel Material lab manufactured 3D Metal Printed Exhaust valve for IC Engines: An Innovative Approach

Sarabjit Singh¹, Harmesh Kumar Kansal^{2*}, Rajesh kumar³

¹*Research Scholar,*
UIET Panjab University,
Chandigarh

^{2, 3}*Professor,*
UIET Panjab University,
Chandigarh

**Corresponding Author Email: harmeshkansal@gmail.com,*

Abstract

This investigation examines 3D metal printer manufacturing, focusing on laser powder bed fusion (LPBF), to assess its capability to produce functional internal combustion (IC) engine components for the automotive and defence industries. The exhaust valve of a commercially available Diesel-engine is the subject of this study, which focuses on Steady-State. The metal exhaust valve has been manufactured in our Advance Manufacturing Lab, using LPBF technique. Thermal analysis of 3D metal printed exhaust valve. Using a video measuring machine, the exhaust valve model was prepared using Inconel 718 material. In steady state conditions, a diesel engine's exhaust valve was thermally analyzed. The ANSYS software has been used to create the model in order to perform under Steady-state thermal analysis via Finite Element Method (FEM). The simulation has been performed and the results of thermal analysis were carried out on the exhaust valve under Steady-state conditions. It has been observed that the exhaust valve head has the highest temperature, while the valve stem tip experiences the lowest temperature. For Inconel 718 material, the lowest and maximum total heat fluxes recorded are 0.0016767W/mm^2 and 0.22504W/mm^2 , respectively. It has been observed that the area around the exhaust valve head and closest the tip of engine's exhaust valve stem's exhibits minimum total heat flux. In contrast, the highest total heat-flux is noticed in the bottom portion of valve stem's. The directional heat flux ranges from a minimum of -0.22312W/mm^2 to a maximum of 0.00217W/mm^2 . It has been observed that the highest directional heat flux occur in the region

around the exhaust valve head and closer to the valve stem's tip. Conversely, the lowest directional heat-flux is found in the bottom portion of the valve stem.

Keywords: *3D Metal Printer, Exhaust Valve, Internal combustion engine, Inconel 718, Thermal analysis*

Introduction

Now a days modern technology, automakers may employ additive manufacturing to quickly prototype and create component that fulfil demanding specifications, such as needs for personalization, increased fuel efficiency and supply chain problems following the pandemic [1]. In today's automobile industry, additive manufacturing improves energy efficiency, speeds up production, reduces material waste, and simplifies the supply chain [2,3]. Automotive engineering could benefit from additive manufacturing and generative design. This approach employs computational models and algorithms to streamline the traditional design-review-refine stages into a single, efficient workflow that meets design goals and specifications[4–6].

Among the various types of additive manufacturing are material extrusion [7], binder jetting, sheet lamination, powder bed fusion [8], vat photopolymerization, directed energy deposition and material jetting [9]. Each of these techniques has its own advantages and disadvantages, including factors such as material expenses, production rates, component durability, and reliability [10–12]. In the field of additive manufacturing, a variety of materials, such as metals, polymers, and ceramics, are utilized to produce composite materials, materials with functional grades (FGMs), and hybrids [13]. Common raw materials used in metal additive manufacturing are liquids form, wire, powder and foil strips [14]. Direct bonding of materials is accomplished by high energy density sources including lasers, electron beams, plasma arcs, and ultrasonic waves. Binder jetting is an alternative method that fuses metal powder to produce the required strength by means of post-build heating and sintering [11,12]. Additive manufacturing has several applications in the military. Enhancing the structural and aerodynamic efficiency of unmanned aerial vehicles (UAVs) through improved design is one significant usage [15]. Internal combustion (IC) engines are commonly utilized in many UAVs, and there is a growing interest in employing additive manufacturing (AM) to enhance engine designs [16]. Compared to consumer products, military vehicles typically have smaller production runs, making additive manufacturing (AM) a more cost-effective option than traditional methods. In some cases, even when producing more units, AM can still save money. Laureijs et al. found that an AM-

designed engine bracket was less expensive to produce and more fuel-efficient than the original forged one on [17]. Additive manufacturing (AM) minimizes the need to overproduce critical spare parts or store molds and dies, as it only needs build files and powder to reproduce components. Moreover, AM enables quicker production of small-batch new parts, removing the necessity for creating machine programs or expensive molds when they are not readily available [18]. Furthermore, AM can manage a variety of sizes and shapes due to its versatility. Because a single machine can fabricate both simple components like brackets and complex ones like engine blocks, as long as they fit within the producing area, this versatility reduces the need for different [19]

The complete AM process employing LPBF and the difficulties of producing IC engine components with this technology will be covered in this paper due to its potential advantages.

A Hyundai verna Diesel engine was selected for this investigation. A 3D metal printed exhaust valve manufactured in our lab using (DMLS) Direct metal laser sintering techniques EOSINT M280. Inconel 718 superalloys materials with superior strength-to-weight ratios and resistance to corrosion and high-temperature properties ability to withstand extreme conditions [20–22]. Here's a detailed breakdown of how the 3 D printed inconel material based exhaust valve is manufactured:

1. Design Phase of exhaust valve

- (CAD Modeling) - Create a detailed 3D model of the exhaust valve using computer aided design software.
- Simulation – use simulation tools to design performance and manufacturability, reducing weight and maintaining strength.

2. Material selection (Inconel Alloy)

Inconel 718 superalloys materials with superior strength-to-weight ratios and resistance to corrosion and high-temperature properties ability to withstand extreme conditions

3. 3D Printing Process:

- Preparation : Convert the the 3D model of exhaust valve converted to a Stereolithography (STL file) and slice the model into layers.
- Printing : The exhaust valve is produced using 3 D metal printer method Direct metal Laser Sintering (DMLS)

4. Post- Processing :

- Heat Treatment : Apply heat treatment processes to relieve stresses and enhance the mechanical properties of 3 D printed exhaust valve.
- Surface Finishing : Perform Machining or surface finishing techniques to achieve the required surface smoothness and dimensional accuracy.

5. Inspection and Tesing : Use non destructive testing method such as micro CT scan analysis to ensure the quality of 3D metal printed exhaust valve.

The main objective was to study the Steady-State Thermal analysis of Inconel Material Based on 3D Metal Printed Exhaust valve for IC Engines.

The purpose of this study is to use ANSYS software to examine the exhaust valve's thermal performance in a diesel engine. The dimensions and morphology of an exhaust valve are video copied from a commercial available exhaust valve of hyundai car are shown in Fig. 1.



Figure 1 The dimensions and morphology of an exhaust valve are video copied from a commercial available exhaust valve of hyundai car

Methodology

Exhaust valve of diesel engine (Hyundai Verna) drawing prepared on video measuring machine an industrial area in Panchkula near Chandigarh as shown in Fig. 2.



Figure 2 Exhaust Valve Drawing Prepared On Video Measuring Machine

The dimensions and detailing of exhaust valve prepared on Video Measuring Machine as shown in Fig. 3 and Table 1.

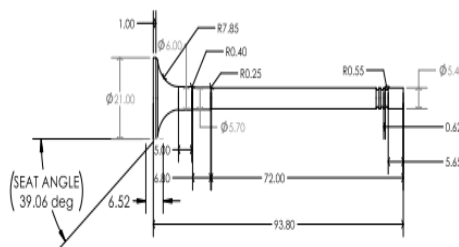


Figure 3 Dimensions and detailing of exhaust valve drawing prepared on Video Measuring Machine

Table 1. Dimensions and detailing of exhaust valve drawing

Valve Diameter (mm)	21
Seat Angle	39.06 ⁰
Seat width (mm)	0.67
Stem Diameter (mm)	5.40
Length of exhaust valve (mm)	93.80

The exhaust valve model for the CI engine was designed using SolidWorks., as shown in Figure 4

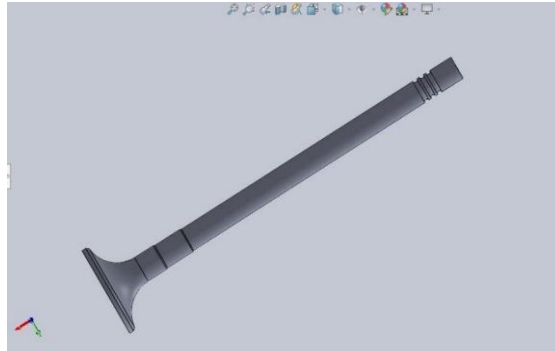


Figure. 4 Model of the exhaust valve

We used ANSYS software to create a mesh over the model for steady-state thermal analysis based on FEM. This mesh was made using tetrahedral elements, with 4538 nodes and 2322 elements.



Figure 5 Mesh generation

Thermal analysis has been conducted using ANSYS for this study. The exhaust valve is made of Inconel 718 material. The Inconel alloy 718 used in this study is a precipitation hardened Nickel-Iron alloy with a nominal composition as listed in Table 2.

Table 2. Chemical Composition of Inconel 718 [23]

Element	Ni	Cr	Nb	Mo	Ti	Co	Al	Fe
%	50-55	17-21	4.8-5.5	2.8-3	0.65-1.15	1	0.2-0.8	Balance

The alloy has exceptional properties at high temperatures (around 973 K), including superior fatigue life, good strength, and improved creep resistance. Moreover, its slow precipitation kinetics make it easy to weld. These remarkable properties make it a popular choice for a wide range of high-temperature applications, such as aircraft, liquid-fuelled rockets, gas turbines and nuclear reactors other structural and

applications. There are several different varieties of Inconel 718 alloy goods available, including as wrought, powder metallurgy, and cast items. For example, a large number of aviation engine components, including pressure containers, aerofoils, supporting structures, and essential rotating elements, significantly utilize the alloy. Indeed, it makes up more than thirty percent of the weight of a contemporary airplane engine [24]. The properties of Inconel-718 as shown in Table 3 [23,25,26,26]

Table 3. The properties of inconel 718

Density g/cm ³	Young's Modulus GPa	Poisson's Ratio	Bulk Modulus	Shear Modulus GPa	Tensile Strength Ultimate MPa	Tensile Strength Yield MPa	Melting Point °C
8.19	199.9	0.284	240	139	1375	1100	1260- 1336

The information about the materials used is manually added to the library. To conduct a steady-state thermal analysis, the exhaust valve must be subject to boundary conditions. Combustion gasses leave the combustion chamber as the exhaust valve open during the exhaust stroke. Thus, it can be said that the hot combustion gases exiting the cylinder cause a thermal load on the exhaust valve. The exhaust gases can be considered to have temperature ($T_g=700$ °C) and convective heat transfer coefficient ($h_g=1e^{-005}W/mm^2$ °C) for the purpose of our investigation. A formula will be used to determine the convective heat transfer coefficient's value as shown in Eq. 1.

$$Nu = \frac{hD}{k} = 0.18(Re)^{0.62} Re = \frac{\rho UD}{\mu} \quad 1$$

In this study, h_g is one of the boundary condition parameters. The coefficient is determined using the following parameters: (i) μ (exhaust gas viscosity), (ii) ρ (Density of exhaust gases), (iii) U (velocity of exhaust gases), (iv) k (exhaust valve's material thermal conductivity), and (v) D (Diameter of exhaust valve stem's).

Additive Manufacturing Process

The laser bed fusion process involves heating, melting, and solidifying a layer of powder with the CAD file. As shown in Fig. 6, these processes, while different, have similar technical features.

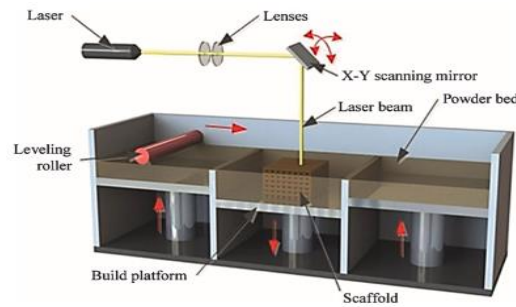


Figure 6. LPBF system schematic [27]

Along predefined pathways, the laser scans the powder bed selectively in certain locations. A new product layer is formed when the melting powder cools and solidifies. The powder dispenser platform rises when the first layer is finished to supply materials for the subsequent layer. To create a new layer, the recoater transfers material over the building platform, lowering it by the thickness of the layer. Until the required shape is achieved, this process is repeated [28,29]. The Inconel 718 exhaust valve was fabricated using the LPBF technique, a common AM method for high-temperature alloys. It employs a high-energy laser and selectively melts Inconel powder layer by layer, allowing for precise control over the geometry and microstructure. The 3D metal printed machine EOSINT M 280 as shown in Fig. 7.



Figure 7 3D metal printed machine

The exhaust valve were manufactured on an EOSINT M280 in 40 μm layers. The process Parameters for 3D Metal Printed exhaust valve as shown in table 4.

Table 4. Machine Parameters for 3D Metal Printed exhaust valve

Component	Layer Thickness μ	Laser Power [W]	Laser Speed [mm/s]	Hatch spacing mm
3D Metal Printed Exhaust Valve	40 μ	280 W	960	0.11

The newly Inconel 718 3D metal printed exhaust as shown in Fig. 7.

**Figure 7** New 3D Metal printed exhaust valve

Results and discussion

In this part, the results of thermal analysis carried out on the exhaust valve under steady-state conditions has been discussed. The analysis consider INCONEL 718 material different parameters: Total heat flux, Temperature, and Directional heat-flux along x-axis.

Figure 6 shows temperature distribution across the engine's exhaust valves using Inconel 718 material. The lowest and highest temperatures for Inconel 718 material are 225.15°C and 700°C, respectively. It has been observed that the highest temperature occurs around the exhaust valve head, while the minimum temperature is near the engine's exhaust valve stem tip. It is because the exhaust valve head comes in direct contact with hot combustion gasses during the engine's exhaust stroke, resulting in the maximum temperature around it. When exhaust gases pass the exhaust valve on their way out of the combustion chamber, a considerable quantity of heat is transferred to the valve head. The extremely high temperatures of the combustion process, which in certain situations may exceed 650 °C, are closest to the valve.

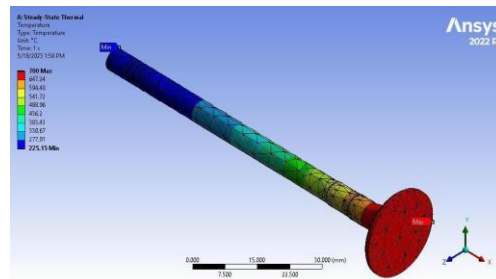


Figure 6 Temperature distribution Inconel 718

Further, the exhaust valve stem tip is located further away from the combustion chamber and is frequently cooled by the engine's surrounding parts. Heat dissipation is aided by the stem's passing through the valve guide. Further helping in maintaining a lower temperature in that area include lubricants surrounding the valve stem and contact with comparatively colder components, such as the cylinder head and valve springs. As a result, the temperature gradient along the valve is greater at the head and progressively lowers as it approaches the stem tip.

Figure 7 (below) represents total heat flux for the engine exhaust valve under steady-state conditions for Inconel material.

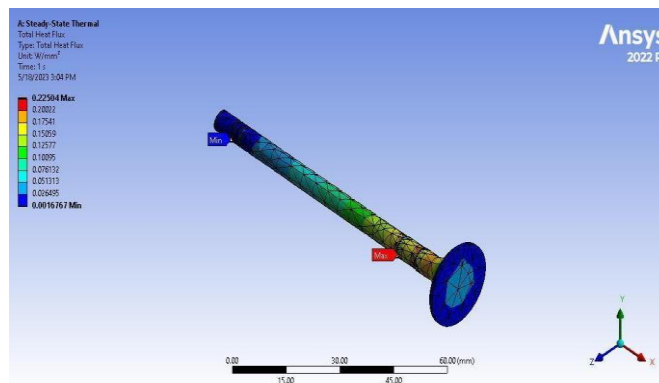


Figure 7 Total Heat Flux Inconel 718

The respective lowest and highest total heat flux observed for Inconel 718 material are 0.0016767 W/mm^2 and 0.22504 W/mm^2 . It has been observed that the area near the exhaust valve stem's tip and around the exhaust valve head, experiences the least total heat flux. In contrast, the highest total heat-flux is noticed in the bottom portion of valve stem's due to differences in heat dissipation and surface area exposure

for heat conduction, convection, and radiation. Due to a lack of conductive pathways, the valve head does not experience a large total heat flux even if it is exposed to high combustion temperatures. Convection from the hot gases is mostly responsible for this heat transfer, but the overall heat transfer is kept at a low level because the valve head and valve seat are in intermittent contact, which causes some heat to be conducted away.

Additionally, a large surface area on the valve head reduces the total heat flow by distributing the heat load across a larger area. Components that cool the valve stem tip include the rocker arm/cam followers and the valve springs. The heat intake to the stem tip is limited by this cooling, and the heat transmission mechanisms there are less effective. This results in a reduced overall heat flux in this region. Furthermore, because of the cooling from nearby components, heat conduction is mostly impacted in this area, which is further away from the hot combustion gasses. The combination of conduction and convection causes the most total heat flux in the lower portion of the valve stem, which travels through the valve guide. Heat is transferred to the cylinder head by conduction, which occurs when the valve stem and valve guide come into close contact. The cooler guide and the hotter upper portion of the stem have different temperatures, which encourages substantial heat conduction. This part may also benefit from air or cooling oil flow, which would increase the overall amount of heat transferred by convection. Lubrication in the valve guide facilitates heat dissipation even more.

In conclusion, the valve head and stem tip have larger surface areas and less effective heat transfer mechanisms, which limits the overall heat flow in those locations. In contrast, the bottom portion of the valve stem is more effective in transferring heat (via conduction and convection).

Fig. 8 depicts Directional heat flux for the engine exhaust valve within the x-direction under steady-state conditions for Inconel 718 material,.

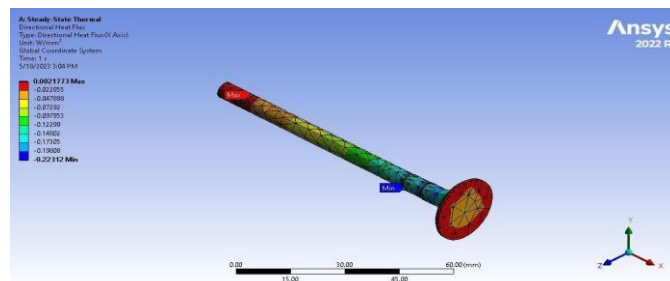


Figure 8 Directional Heat Flux Inconel 718

The respective lowest and highest directional heat flux observed for Inconel 718 material are -0.22312W/mm^2 and 0.00217W/mm^2 . It has been observed that the area near the exhaust valve stem's tip and around the exhaust valve head, experiences the highest directional heat flux. Conversely, the bottom portion of valve stem's experiences minimum directional heat flux. This is because of the large temperature differences and heat-transfer processes in these areas. Usually, the surrounding engine parts, such as the rocker arms or cam followers and the valve springs, cool the stem tip. A sharp temperature differential is produced between the stem tip and the surrounding areas as a result of the cooling. As heat moves away from the hotter parts of the valve stem, this gradient creates a higher directional heat flux.

On the other hand, minimum directional heat flux in the lower section of valve stem is because of smaller temperature gradient. The portion that passes through the valve guide experiences minimal directional heat flow. Heat transfer is slower in this part because of the guide's and the surrounding components' cooling impact, as well as the valve stem's increased insulation from the valve guide. As a result, there is less of a temperature differential between the valve stem and its surroundings, which lowers the directional heat flux.

Conclusion

Steady state thermal analysis conducted on the exhaust valve of a CI engine manufactured by 3D printing process from Inconel 718 materials. Based on the study, the following conclusions were drawn.

- The exhaust valve of commercial 4-wheeler passenger vehicle is manufactured using LPBF technique of 3D printing in the Lab.
- The exhaust valve head is the location of the maximum temperature, $700\text{ }^{\circ}\text{C}$, and the valve stem tip is the location of the lowest temperature, $225.15\text{ }^{\circ}\text{C}$.
- The lowest heat flux is observed area near the exhaust valve stem's tip and around the exhaust valve head.
- The highest total heat-flux is noticed in the bottom portion of valve stem's for Inconel 718 material is 0.22504W/mm^2 , while the minimum for total heat flux is 0.0016767W/mm^2 .
- Maximum directional heat flux is observed in the head region and close to tip of the valve stem's of engine exhaust valve.
- Minimal directional heat flux is observed near the bottom portion of valve stem's

Acknowledgements

We would like to thanks to Central Tool Room and Training Centre (CTTC), Bhubaneswar India for manufacturing 3D printed valve and Praka Engineering, Panchkula-Haryana, India for providing the drawing prepared video measuring machine facility to this research.

References

1. J. C. Vasco, Addit Manuf 505 (2021).
2. I. Gibson, D. Rosen, B. Stucker, and M. Khorasani, Additive Manufacturing Technologies 379 (2021).
3. R. E. Laureijs, J. B. Roca, S. P. Narra, C. Montgomery, J. L. Beuth, and E. R. H. Fuchs, Journal of Manufacturing Science and Engineering, Transactions of the ASME **139**, (2017).
4. N. A. Fountas, J. D. Kechagias, and N. M. Vaxevanidis, Machines 2023, Vol. 11, Page 95 **11**, 95 (2023).
5. M. M. Francois, A. Sun, W. E. King, N. J. Henson, D. Turret, C. A. Bronkhorst, N. N. Carlson, C. K. Newman, T. Haut, J. Bakosi, J. W. Gibbs, V. Livescu, S. A. Vander Wiel, A. J. Clarke, M. W. Schraad, T. Blacker, H. Lim, T. Rodgers, S. Owen, F. Abdeljawad, J. Madison, A. T. Anderson, J. L. Fattebert, R. M. Ferencz, N. E. Hodge, S. A. Khairallah, and O. Walton, Curr Opin Solid State Mater Sci **21**, 198 (2017).
6. S. M. Hashemi, S. Parvizi, H. Baghbanijavid, A. T. L. Tan, M. Nematollahi, A. Ramazani, N. X. Fang, and M. Elahinia, <https://doi.org/10.1080/09506608.2020.1868889> **67**, 1 (2022).
7. J. Kechagias, D. Chaidas, N. Vidakis, K. Salonitis, and N. M. Vaxevanidis, Materials and Manufacturing Processes **37**, 963 (2022).
8. J. Kechagias, Rapid Prototyp J **13**, 316 (2007).
9. G. B. Kannan and D. K. Rajendran, in *Advances in 3D Printing and Additive Manufacturing Technologies* (2016).
10. M. Yakout, M. A. Elbestawi, and S. C. Veldhuis, Solid State Phenomena **278**, 1 (2018).
11. A. Lores, N. Azurmendi, I. Agote, and E. Zuza, <https://doi.org/10.1080/00325899.2019.1669299> **62**, 267 (2019).
12. H. A. Youssef, H. A. El-Hofy, and M. H. Ahmed, 925 (2011).
13. P. Kumar, S. K. Sharma, and R. K. R. Singh, Materials and Manufacturing Processes **38**, 1033 (2023).

14. W. E. Frazier, *J Mater Eng Perform* **23**, 1917 (2014).
15. G. D. Goh, S. Agarwala, G. L. Goh, V. Dikshit, S. L. Sing, and W. Y. Yeong, *Aerosp Sci Technol* **63**, 140 (2017).
16. G. Belgiorno, A. Boscolo, G. Dileo, F. Numidi, F. C. Pesce, A. Vassallo, R. Ianniello, C. Beatrice, and G. Di Blasio, *SAE Int J Adv Curr Pract Mobil* **3**, 672 (2020).
17. R. E. Laureijs, J. B. Roca, S. P. Narra, C. Montgomery, J. L. Beuth, and E. R. H. Fuchs, *Journal of Manufacturing Science and Engineering, Transactions of the ASME* **139**, (2017).
18. S. H. Khajavi, J. Partanen, and J. Holmström, *Comput Ind* **65**, 50 (2014).
19. S. A. Haba and G. Oancea, *International Journal of Advanced Manufacturing Technology* **80**, 747 (2015).
20. J. Ding, S. Xue, Z. Shang, J. Li, Y. Zhang, R. Su, T. Niu, H. Wang, and X. Zhang, *Materials Science and Engineering: A* **804**, 140718 (2021).
21. Y. Zhang, L. Lan, and Y. Zhao, *Materials Science and Engineering: A* **864**, 144598 (2023).
22. O. Pereira, A. Celaya, G. Urbikain, A. Rodríguez, A. Fernández-Valdivielso, and L. Noberto López de Lacalle, *Journal of Materials Research and Technology* **9**, 8459 (2020).
23. E. Hosseini and V. A. Popovich, *Addit Manuf* **30**, 100877 (2019).
24. H. Qi, M. Azer, and A. Ritter, *Metall Mater Trans A Phys Metall Mater Sci* **40**, 2410 (2009).
25. N. Metal, N. Alloy, P. Properties, M. Properties, T. Strength, T. Strength, R. Strength, and P. Hardened, 9 (1960).
26. ASM Material Data Sheet, (n.d.).
27. C. Vyas, G. Poolagasundarampillai, J. Hoyland, and P. Bartolo, *Biomedical Composites*, Second Edition 261 (2017).
28. M. Dadkhah, J. M. Tulliani, A. Saboori, and L. Iuliano, *J Eur Ceram Soc* **43**, 6635 (2023).
29. V. Bhavar, P. Kattire, V. Patil, S. Khot, K. Gujar, and R. Singh, *Additive Manufacturing Handbook* 251 (2017).

POLYMERS
AND
BIOMATERIALS

**Bio-inspired Synthesis of Metal oxide Nanoparticles
from *Neltuma juliflora* (Sw.) Raf. Leaf Extract for
Antimicrobial and Antioxidant activities**

Nagaraja H^{1*}, Monica K.J. Nidhi¹, Hanumanthagouda B²,
Kotresh M G³, Uma Reddy B¹

¹Department of Botany,
Vijayanagara Sri Krishnadevaraya University,
Ballari - 583105, Karnataka, India.

²Department of Physics,
Kishkinda University,
Ballari - 583104, Karnataka, India.

³Department of Physics,
Vijayanagara Sri Krishnadevaraya University,
Ballari - 583105, Karnataka, India.

*Email: nagarajah@vskub.ac.in

Abstract

The current study presents a bio-inspired method for synthesizing metal oxide nanoparticles (MONPS) CaO, MgO and NiO using *Neltuma juliflora* (Sw.) Raf. leaf extract as a reducing and stabilizing agent. The nanoparticles were characterized using FTIR, X-ray diffraction, and FE-SEM, confirming their chemical and physical characteristics. The antimicrobial activities of the nanoparticles were assessed against Gram-positive (*Enterococcus faecalis*, *Staphylococcus aureus*), and Gram-negative (*Pseudomonas aeruginosa*, and *Escherichia coli*) bacterial strains, demonstrating significant inhibition of microbial growth. Further, the haemolytic test combined with DPPH analysis, demonstrated that the NiO nanoparticles had excellent biocompatibility and robust antioxidant activity. These findings emphasized the potential of NiO NPs as multifunctional agent in biomedical applications and underscore the suitability of *N. juliflora* (Sw.) Raf. for the eco-friendly fabrication of biocompatible nanoparticles with therapeutic potential.

Keywords: Calcium oxide, Magnesium oxide, Nickel oxide NPs, Antimicrobial, Antioxidant.

Introduction

The emergence of multi-drug resistant (MDR) bacteria has become a significant global health concern, rendering conventional antibiotics ineffective against various infections ([World Health Organization \(WHO\). 2017](#)).

Nanotechnology is one of the most groundbreaking and promising technologies of the 21st century, offering vast applications in human health. This field focuses on the study of nanoparticles, typically ranging in size from 1 to 100 nm ([Kumar et al., 2017](#)). A particularly exciting aspect of nanotechnology lies in its application within healthcare and medicine, where nanoparticles have shown significant potential. Due to their size similarity to biomolecules, metallic NPs have widespread recognition as therapeutic agents in recent years ([Sharma et al., 2009](#)). The characterizations of nanomaterials such as shape, size, method of synthesis, metal type, and the use of encapsulating agents—can be modified, allowing for versatility in their applications ([Jain et al., 2017](#)).

Nanoparticles are highly effective in interacting with pathogenic bacteria due to their high surface-area-to-volume ratios, making them valuable in drug delivery systems as well ([Patra et al., 2018](#)). In nanomedicine, therapeutic agents can be delivered in a controlled manner to specific targeted locations in the body. Among the various metals used for nanoparticle synthesis, silver nanoparticles (AgNPs) have attracted considerable attention due to their remarkable, broad-spectrum antibacterial properties. This has led to their extensive use against drug-resistant bacterial strains, and they have also been manifested antiviral, antifungal, anti-inflammatory, and anti-biofilm effects ([Burduşel et al., 2018](#)). With the rise in drug resistance, AgNPs are increasingly considered a promising alternative for treating drug-resistant, multidrug-resistant, and extensively drug-resistant strains of TB, as they offer improved and targeted drug delivery ([Seung et al., 2015](#)).

Plant-mediated synthesis of metal oxide nanoparticles (MONPs) has gained attention due to its eco-friendly, cost-effective, and efficient nature ([Iravani et al., 2014](#)). *Prosopis juliflora*, a medicinal plant rich in bioactive compounds, has been analyzed for its antimicrobial activities ([Kumar et al., 2013](#)).

This study aims to synthesize CaO, MgO and NiO NPs using *N. juliflora* plant leaves as a reductant and investigate their potential

against MDR bacteria. The bio-synthesized MONPs NPs will be characterized using various techniques, and their antimicrobial efficacy will be evaluated against pathogenic bacterial strains.

Several studies have reputed that NiO NPs have unveiled effective antimicrobial activity against various pathogens, including bacteria (*E. coli*, *S. aureus*, *P. aeruginosa*), fungi (*C. albicans*), and viruses (HIV, HSV) (Srivastava et al., 2019). Antibacterial activity of NiO NPs was reported to be that the Ni⁺ ions reacts with bacterial membrane and disrupts the cell, causes DNA damage and oxidative stress leading to cell destruction (Jafarirad et al., 2016; Haq et al., 2021; Suresh et al., 2024). NiO NPs have been investigated to exhibit antioxidant activity by scavenging free radicals and reducing oxidative stress (Saikia et al., 2010),

Our study also emphasizes with this hypothesis as the experimental data reveals NiO NPs as potent antibacterial and antioxidant agent when compared to CaO and MgO NPs. This is a novel approach evaluating two different plant micronutrients calcium and magnesium and a non specific metal nickel in the form of nanoparticles synthesised by green route method using *N. juliflora* for the evaluation of therapeutic properties.

Materials and Methods

Materials

Calcium chloride (CaCl₂, purity 98%, MW 110.99g/mol), Magnesium chloride (MgCl₂.6H₂O, Purity 98%, MW 203.30), Nickel sulphate (NiSO₄.6H₂O, 99%, MW 262.86), Sodium chloride (NaCl, purity 99.5%, MW 58.44g/mol) and Crystal violet were attained from Sigma-Aldrich Ltd., Agar Bacteriological grade, (HIMEDIA GRM026-500G), Nutrient broth (HIMEDIA M002-500G), Sodium Dodecyl Sulphate (SDS) (NaC₁₂H₂₅SO₄, purity 90%, MW 288.38g/mol), Ethanol (C₂H₅OH, purity 99.9%), Streptomycin (HIMEDIA (25 µg) SD031-1VL), 2,2- Diphenyl-1- picrylhydrazyl (DPPH) (C₁₈ H₁₂N₅O₆, purity 85.0%, MW 394.32g/mol), L-Ascorbic acid (C₆H₈O₆, purity 99.0%, MW 176.13g/mol) MTT(3-[4,5-dimethylthiazol-2-yl]-2,5 diphenyl tetrazolium bromide), DMEM (Dulbecco's Modified Eagle Medium) were used for therapeutic Study. Graph generation, and characterization analysis was done using OriginPro8.5 software and ImageJ software.

Methodology

Green synthesis of CaO/MgO/NiO Nps from *Neltuma juliflora* (Sw.) Raf.

The fresh, and healthy leaves of *N. juliflora* were collected from Vijayanagara Sri Krishnadevaraya University campus, Ballari, Karnataka, India. The leaves were thoroughly washed, and shade dried for 2-3 days, and pulverized using an electric blender. 20g leaf powder in 100mL of MilliQ water was used to make leaf extract (LE). Metal salts CaCl_2 , $\text{MgCl}_2 \cdot 6\text{H}_2\text{O}$ and $\text{NiSO}_4 \cdot 6\text{H}_2\text{O}$ at concentration of 0.1M, were dissolved independently in 100mL of MilliQ water to form salt solution. The salt solution was volumetric analysis against plant extract maintained at a pH 10.5, until the visible color change from green color to white for CaO, yellowish white for MgO and greenish white for NiO NPs.

Characterization Methods

X-ray diffraction (XRD) analysis was performed with a Smartlab SE diffractometer ($\lambda = 0.15406 \text{ nm}$) to determine the crystallite size and structure of nanoparticles (NPs) over a 0° – 90° scan range. Field emission scanning electron microscopy (FE-SEM) with EDX (Zeiss EVO LS 15) provided surface morphology and elemental analysis at 10–15 kV. FTIR spectra (400 – 4000 cm^{-1} , 2 cm^{-1} resolution) were recorded using a PerkinElmer Frontier spectrometer with KBr discs, and UV-Vis spectroscopy was employed to assess optical properties and band-to-band absorption.

Turbidometric Assay For Evaluating Antibacterial Activity

The antibacterial assay followed a modified protocol by (Tótoli et al., 2015), using *N. juliflora* MONPs at concentrations of 50, 100, 150, $200 \mu\text{g/mL}$ in nutrient broth with standardized inoculum. Streptomycin ($25 \mu\text{g/mL}$) served as a positive control, while nutrient broth alone and broth with inoculum acted as blank and negative controls, respectively. After a 24-hour incubation at room temperature, bacterial growth was halted with 12% formaldehyde, and absorbance was measured at 530nm using a UV-Vis spectrophotometer.

$$\text{Inhibition of Bacterial growth (\%)} = \frac{\text{Absorbance of control} - \text{Absorbance of sample}}{\text{Absorbance of control}} \times 100 \text{ ---- (1)}$$

Assessment Of Antibiofilm Activity Using The Crystal Violet Staining Technique

The biofilm inhibitory effect of MONPs was assessed using a modified crystal violet staining method (Andersson et al., 2009; Singh et al., 2013). Cultures of *E. faecalis*, *P. aeruginosa*, *S. aureus*, and *E. coli* (OD 0.5 at 600nm) were incubated with MONPs (50, 100, 150, $200 \mu\text{g/mL}$) in nutrient broth for 24 hours at room temperature. After

incubation, tubes were rinsed, stained with 1% crystal violet, and destained with ethanol. Absorbance was measured at 590nm with a UV-Vis spectrophotometer. Experiments were performed in triplicate, and the mean absorbance values were recorded.

Antibiofilm activity (%) =

$$\frac{\text{Absorbance of control} - \text{Absorbance of sample}}{\text{Absorbance of control}} \times 100 \text{ ---- (2)}$$

DPPH assay for Evaluating Antioxidant Activity

The antioxidant activity was investigated using the DPPH assay. A 0.14mM DPPH solution in ethanol was combined with different concentrations of MONPs (50, 100, 150, 200µg/mL) and incubated in the dark place for 30 minutes. L-ascorbic acid and PBS served as positive and negative controls, respectively. Absorbance was measured at 517nm, and the radical scavenging activity (RSA) of MONPs was calculated ([Baliyan et al., 2022](#)).

Radical Scavenging Ability (%) =

$$\frac{\text{Absorbance of control} - \text{Absorbance of sample}}{\text{Absorbance of control}} \times 100 \text{ ---- (3)}$$

Hemolytic assay on human RBC

Around 5 mL of entire blood was collected from a healthy volunteer, washed with saline, and centrifuged to isolate red blood cells (RBCs), which were re-suspended in PBS (pH 7.4). The MONPs sample, prepared in PBS, was combined with 1 mL of RBC suspension at concentrations of 50, 100, 150, 200µg/mL. SDS (1%) and PBS served as positive and negative controls, respectively. After incubation at RT for 120 minutes, samples were centrifuged, and the supernatant's absorbance was calculated at 540nm to determine hemolysis percentage ([Wang et al., 2019](#)).

Haemolysis (%) =

$$\frac{\text{Absorbance of the sample treated with MONPs}}{\text{Absorbance of positive control treated with 1\% SDS}} \times 100 \text{ ---- (4)}$$

Results and Discussion

X-Ray Diffraction Analysis of CaO, MgO and NiO nanoparticles

The structural properties and crystallinity of NiO, MgO, and CuO nanoparticles synthesized using *Neltuma juliflora Raf* leaf extract through a conventional method were examined by XRD spectroscopy, as depicted in [Fig. \(1\)](#). The XRD data provide that each sample exhibits pronounced, sharp peaks, indicative of high crystallinity. For

NiO, the diffraction peaks observed at 2θ values of 37.28° , 43.53° , 63.05° , 75.51° , and 79.42° , corresponding to the (111), (200), (220), (311), and (222) crystal planes, confirm a face-centered cubic (FCC) structure as per JCPDS file no. 4-835. The absence of any extraneous peaks confirms the purity of the NiO phase. (Ezhilarasi et al.,2016) Similarly, the XRD pattern of MgO nanoparticles reveals sharp peaks, indicating a highly crystalline structure. Based on JCPDS file no. 39-7746, the Bragg reflections observed correspond to the (111), (200), and (220) planes, affirming the FCC phase structure of MgO. (Suresh et al.,2018) In the case of CaO nanoparticles, XRD patterns display reflection peaks at 2θ values of 29.32° , 34.10° , and 47.27° , corresponding to a monophasic cubic crystal structure was confirmed by XRD analysis ,consistent with JCPDS data No. 77-2376. A trace amount of CaCO_3 formation is noted, likely due to the rapid carbonation of Ca(OH)_2 and CaO by atmospheric CO_2 , with the carbonation rate increasing with the surface area. (Marquis et al., 2016 & Osuntokun et al., 2018)

The crystallite size of the prepared nanocrystals was estimated from higher intense peak of XRD pattern using Debye Scherer's equation,

$$D = \frac{k\lambda}{\beta \cos \theta} \text{-----(5)}$$

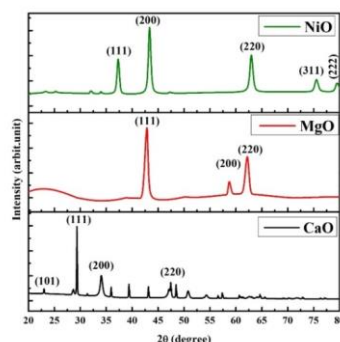


Figure (1): The X-ray diffraction pattern of NiO, MgO, and CaO NPs synthesized via green route method using *Neltuma juliflora* leaf extract.

The crystallite sizes of NiO, MgO, and CuO nanoparticles were determined to be 14.03 nm, 11.31 nm, and 56.55 nm, respectively. The reduced crystallite sizes observed for NiO and MgO may be ascribe to the synthesis method employed, where the plant essence acts as both a

fuel and a capping agent, thereby minimizing particle size. Consequently, it is anticipated that the smaller crystallite size, combined with high crystallinity, will significantly enhance the biological efficacy of the synthesized nanoparticles (Ezhilarasi et al.,2016).

FT-IR Analysis Of Green Synthesis of CaO, MgO and NiO NPs

FTIR analysis was commanded to identify the functional groups within the synthesized NiO, MgO, and CaO nanoparticles and the obtained spectrum is displayed in Fig. (). From the spectrum, the broad absorption peaks between $3424\text{--}3644\text{ cm}^{-1}$ and $1432\text{--}1456\text{ cm}^{-1}$ correspond to the deformation vibration of adsorbed water molecules (O-H stretching) and the vibrational modes of chemically bonded hydroxyl groups, respectively (Olajire et al., 2019). Weak bands between $1628\text{--}1799\text{ cm}^{-1}$ suggest C=O bond stretching vibrations. Distinct peaks in the fingerprint region ($877\text{--}1090\text{ cm}^{-1}$) are attributed to in-plane C-H bending of aromatic compounds, potentially resulting from the adsorption of atmospheric water and CO₂ or from the plant extract, indicating a high surface area. Additionally, metal-oxygen stretching frequencies observed within $400\text{--}800\text{ cm}^{-1}$ are associated with Ni-O (625 cm^{-1}), Mg-O (665 cm^{-1}), and Ca-O (706 cm^{-1}) bonds (Jadhav et al.,2022 & Umaralikhan et al.,2016)

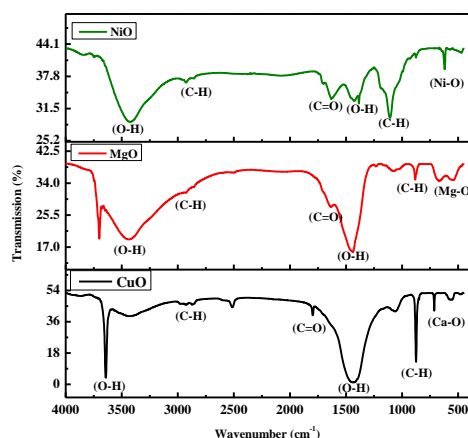


Figure (2): The FT-IR spectrum of NiO, MgO, and CaO Nanoparticles synthesized using *Neltuma juliflora* leaf extract.

SEM-EDX analysis of CaO, MgO and NiO nanoparticles

SEM analysis of the phyto-synthesized CaO, MgO and NiO nanoparticles revealed spherical shaped MgO and NiO NPs, whereas

CaO NPs were observed to be like flakes Fig. (3 (a-c)). Further their EDX reported the presence of respective elements and oxygen attention of the MONPs Fig. (3 (d-f)).

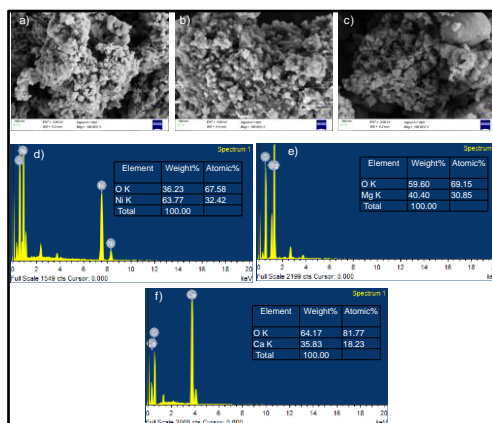


Figure (3): The FE-SEM & EDX analysis of Phyto-synthesized NiO, MgO, and CaO NPs using *Neltuma juliflora* leaf extract. (a-c): FE-SEM micrographs of NiO, MgO and CaO NPs; (d-f): Graphs representing the EDX profile of the NiO, MgO and CaO NPs.

NiO Nanoparticles Exhibited Promising Antibacterial Efficacy

Antibacterial activity of CaO, MgO and NiO was assessed on gram-positive (*Enterococcus faecalis*, *Staphylococcus aureus*) and gram-negative (*Pseudomonas aeruginosa*, and *Escherichia coli*) strains via turbidometric method. It was notable that only NiO NPs had significant impact on bacterial growth as it showed notable reduction in bacterial growth when compared to CaO and MgO NPs Fig. (5 (A-D)). IC₅₀ value was found to be 150 µg/mL of NiO NPs against all the test pathogens. Comparing these results with a similar study, NiO NPs demonstrated antibacterial activity against *E. coli*, *P. aeruginosa*, and methicillin-resistant *Staphylococcus aureus* (MRSA), with a time and dose-dependent reduction in cell viability. The antibacterial mechanism of NiO NPs involves Ni⁺ ions released in aqueous suspension. As these ions can disrupt essential bacterial enzymes by interfering with thiol groups, and by radicals that interacting with the anionic bacterial cell surface, impairing respiration and replication and Triggering cell demise (Haq et al., 2021 & Suresh et al., 2024).

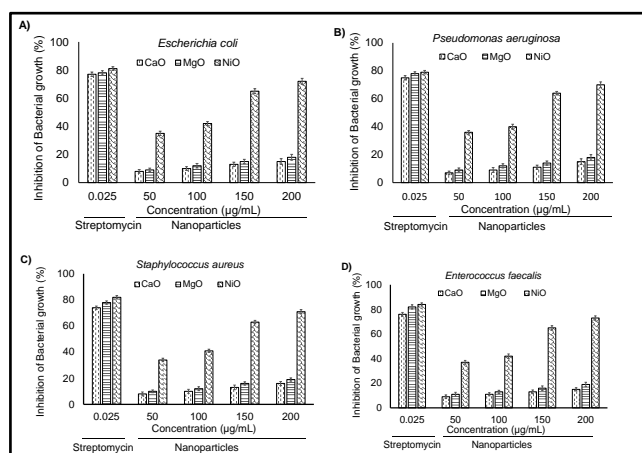


Figure (5): Antibacterial efficacy of CaO, MgO and NiO NPs. (A-D): Bactericidal effect of CaO, MgO and NiO NPs on *Escherichia coli*, *Pseudomonas aeruginosa*, *Staphylococcus aureus* and *Enterococcus faecalis* respectively.

NiO nanoparticles: Potent antibiofilm agent

The concentration dependent (50, 100, 150 and 200 µg/ml) biofilm inhibition was evident in NiO NPs, whereas CaO and MgO did not exhibit promising antibiofilm property when compared to standard streptomycin. NiO NPs showed an IC₅₀ value of 150 µg/ml and MIC of 50 µg/ml [Fig. \(6 \(A-D\)\)](#). Comparable findings have been reported in earlier studies that NiO NPs have greater efficacy in the suppression of bacterial biofilm as observed in *Pseudomonas aeruginosa* ([Maruthupandy et al., 2020](#)), MRSA ([L. Argueta-Figueroa et al., 2014](#)), *E. coli* and *P. mirabilis* ([Rajivgandhi et al., 2018](#)).

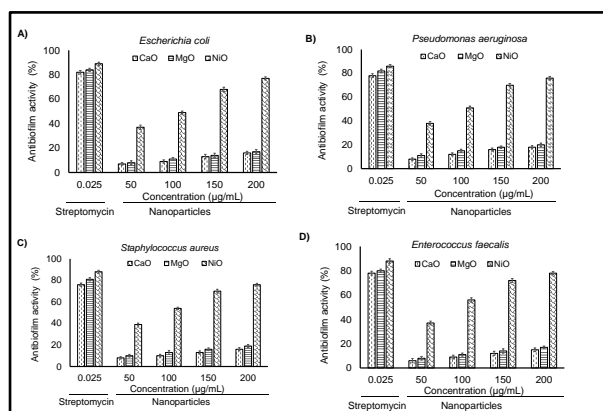


Figure (6): Antibiofilm property of CaO, MgO and NiO NPs. (A-D): Effect of CaO, MgO and NiO NPs on bacterial biofilm of *E. coli*, *P. aeruginosa*, *S. aureus* and *E. faecalis* strains respectively.

Efficient antioxidant agent- NiO nanoparticles

Radical scavenging activity (RSA) analysed by DPPH assay against CaO, MgO and NiO NPs revealed that NiO NPs exhibited 87% of RSA at a concentration of 200 µg/ml, while standard L-ascorbic acid showed 92% antioxidant activity at the same concentration. It was also observed that RSA increased with increased concentration (Figure 7 (A)). These findings are consistent with earlier studies, where NiO NPs synthesized from *Z. spina-christi* plant extract exhibited remarkable antioxidant potential surpassing the standard reference L-ascorbic acid (Saikia et al.,2010 & Suresh et al.,2024)

Hemocompatible photosynthesized NiO nanoparticles

A hemolysis rate below 2% indicates that the nanoparticle is hemocompatible, while a rate above 5% suggests it is not blood-compatible (Neun et al., 2020). As per this reference NiO NPs are compatible agents to RBC as they have shown only upto 1.102% of hemolysis of RBCs at the highest test dose of 200 µg/ml. Whereas, CaO and MgO were found to be slightly toxic as they exhibited 1.236 and 1.17% at the lowest concentration of 50 µg/ml (Figure 7 (B)), thus they may not be considered as competent drugs for internal medicine.

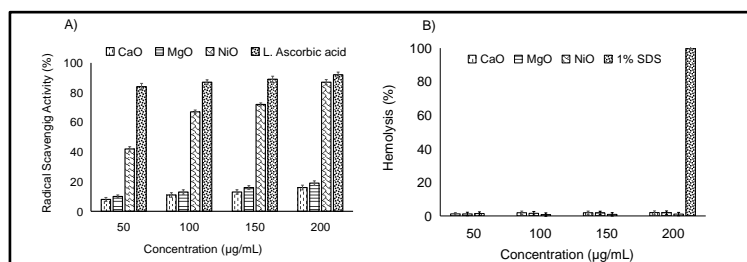


Figure (7): Antioxidant potential and Hemocompatibility of CaO, MgO and NiO NPs. (A): Rate of radical scavenging activity of CaO, MgO and NiO NPs with reference to standard L-ascorbic acid. (B): Hemolytic activity of CaO, MgO and NiO NPs, using 1% SDS as standard exhibiting maximum lysis.

Summary and Conclusion

In Summary and conclusion, among the three nanoparticles tested, NiO NPs demonstrated superior antibacterial, antibiofilm, antioxidant, and hemocompatibility properties, positioning them as the most promising avenue for novel therapeutic applications. NiO NPs shows a exhibited substantial reduction in bacterial growth across various strains, including gram-positive and gram-negative bacteria, with a potent IC₅₀ value of 150 µg/mL and MIC of 50 µg/mL.

Additionally, NiO NPs exhibited effective biofilm inhibition and high radical scavenging activity, reaching 87% at a high dose of 200 µg/mL, comparable to the standard antioxidant L-ascorbic acid. Importantly, hemolysis assays confirmed their blood compatibility, with only 1.102% hemolysis at the highest concentration, making them safer than CaO and MgO NPs, which displayed higher hemolysis levels even at lower concentrations. These results underscore the therapeutic potential of NiO NPs, supporting their application as a viable antimicrobial and antioxidant agent for clinical use.

Acknowledgements

The financial support from “NFST Fellowship by Ministry of Tribal Affairs, GOVT OF INDIA”, and “KSTEPS, DST, GOVT. OF KARNATAKA” is greatly acknowledged. The physico-chemical characterization portions of the research were performed using facilities at CeNSE, Indian institute of Science, Bengaluru, Centre for Excellence for Multidisciplinary Advanced Research Facility, Vijayanagara Sri Krishnadevaraya University, Ballari. The authors thank to Dr. Gajendra Verma, VIMS, Ballari for gifting the ATCC Bacterial strains, and Dr. Shringeswara A N, Mahathma Gandhi Botanical Garden, University of Agricultural Sciences, Gandhi Krishi Vigyana Kendra, Bangalore for plant identification, and authentication.

References

1. Antibacterial, antioxidant and physicochemical investigations of tin dioxide nanoparticles synthesized via microemulsion method. Haq S, Ahmad P, Khandaker MU. Mater Res Express., 8, 35013. (2021)
2. Antibacterial, antioxidant and physicochemical investigations of tin dioxide nanoparticles synthesized via microemulsion method: Haq S, Ahmad P, Khandaker MU. Mater Res Express.; 8, (2021).
3. Anti-biofilm activity of zinc oxide nanosheets (ZnO NSs) using *Nocardia* sp. GRG1 (KT235640) against MDR strains of gram negative *Proteus mirabilis* and *Escherichia coli*: G. Rajivgandhi, M. Maruthupandy, T. Muneeswaran, M. Anand, N. Manoharan, Process Biochem. 67, 8-18. (2018).
4. Antimicrobial properties of ZnO nanomaterials: A review: Kumar, Rajesh, et al. Ceram. Int., 43, 3940-961. (2017).
5. Anti-quorum sensing and anti-biofilm activity of nickel oxide nanoparticles against *Pseudomonas aeruginosa*. Maruthupandy, M.,

- Rajivgandhi, G. N., Quero, F., & Li, W. J. Environ. Chem. Eng., 8, 104533. (2020).
6. Biofabrication of zinc oxide nanoparticles using fruit extract of *Rosa canina* and their toxic potential against bacteria: A mechanistic approach: Jafarirad S, Mehrabi M, Divband B, Kosari-Nasab M. Mater Sci Eng C Mater Biol Appl., 59, 296-02. (2016).
 7. Biomedical applications of silver nanoparticles: an up-to-date overview: Burduşel, A. C., Gherasim, O., Grumezescu, A. M., Mogoantă, L., Fica, A., & Andronescu, E. Nanomater., 8, 681. (2018).
 8. Characterization of extracellular polymeric substances from denitrifying organism *Comamonas denitrificans*: Andersson, S., Dalhammar, G., Land, C. J., & Kuttuva Rajarao, G. Appl. Microbiol. Biotechnol., 82, 535-43. (2009).
 9. Cis-9-octadecenoic acid from the rhizospheric bacterium *Stenotrophomonas maltophilia* BJ01 shows quorum quenching and anti-biofilm activities: Singh, V. K., Kavita, K., Prabhakaran, R., & Jha, B. Biofouling., 29, 855-867. (2013).
 10. Determination of antioxidants by DPPH radical scavenging activity and quantitative phytochemical analysis of *Ficus religiosa*: Baliyan, S., Mukherjee, R., Priyadarshini, A., Vibhuti, A., Gupta, A., Pandey, R. P., & Chang, C. M. Molecules., 27, 1326. (2022).
 11. Green synthesis of metal oxide nanoparticles: A review: Singh, S., Singh, M., & Kumar, V. J. Nanopart. Res., 20, 271. (2018).
 12. Green synthesis of zinc oxide nanoparticles using *Rhus coriaria* extract and their anticancer activity against triple-negative breast cancer cells: Mongy, Y., Shalaby, T. Sci Rep., 14, 13470. (2024).
 13. Medicinal plant leaf extract and pure flavonoid mediated green synthesis of silver nanoparticles and their enhanced antibacterial property: Jain, M.S. Mehata. Sci. Rep., 7, (2017).
 14. Nano based drug delivery systems: recent developments and future prospects: J. K. Patra, G. Das, L.F. Fraceto, E.V.R. Campos, M.D.P. Rodriguez-Torres, L.S. Acosta-Torres, L.A. Diaz-Torres, R. Grillo, M.K. Swamy, S. Sharma, S. Habtemariam, H.S. Shin J. Nanobiotechnol., 16, 1-33. (2018).
 15. NCL Method ITA-5.2. NCI Hub: Neun, B., Cedrone, E., & Dobrovolskaia, M. Bethesda, MD, USA. (2020).

16. Nickel oxide nanoparticles: A novel antioxidant. Colloids and surfaces. Saikia, Jyoti & Paul, Samrat & Konwar, Bolin & Samdarshi, S K. B, Biointerfaces. 78. 146-8. (2010).
17. Nickel oxide nanoparticles: a novel antioxidant. Saikia JP, Paul S, Konwar BK, Samdarshi SK. Colloids Surf. B Biointerfaces., 78,146–148. (2010).
18. Nickel oxide nanoparticles: A review on their synthesis, characterization, and antimicrobial applications: Srivastava, P., Kumar, A., & Singh, S. J. Nanosci. Nanotechnol., 5, 1-13. (2019).
19. Phytosynthesis of Nickel Oxide Nanoparticles and Their Antioxidant and Antibacterial Efficacy Studies: Suresh, L., Snega, R., Geetha Sravanthy, P., & Saravanan, M. Cureus, 16, (2024).
20. Phytosynthesis of Nickel Oxide Nanoparticles and Their Antioxidant and Antibacterial Efficacy Studies: Suresh, L., Snega, R., Geetha Sravanthy, P., & Saravanan, M. Cureus., 16, (2024).
21. Plants in nanoparticle synthesis: Iravani, S., Korbekandi, H., Mirmohammadi, S. V., & Mekanik, H. Rev. Adv. Sci. Eng., 3, 261-74. (2014).
22. Prosopis juliflora: A plant with immense medicinal potential: Kumar, S., Kumar, V., & Prakash, O. M. J. Pharm. Res., 6, 133-39. (2013).
23. Protective effects of the flavonoid fraction obtained from pomelo fruitlets through ultrasonic-associated microwave extraction against AAPH-induced erythrocyte hemolysis: Wang, Q., Luo, J., Liu, H., Brennan, C. S., Liu, J., & Zou, X. RSC Adv., 28, 16007-17. (2019).
24. Rapid green synthesis of silver nanoparticles (AgNPs) using (Prunus persica) plants extract: exploring its antimicrobial and catalytic activities: R. Kumar, G. Ghoshal, A. Jain, M. Goyal J. Nanomed. Nanotechnol., 8, 1-8. (2017).
25. Rapid turbidimetric assay to determine the potency of daptomycin in lyophilized powder: Tótolí, E. G., & Salgado, H. R. N. Pharm., 7, 106-21. (2015).
26. Rich Multidrug-resistant tuberculosis and extensively drug-resistant tuberculosis Cold Spring Harbor perspectives in medicine: K.J. Seung, S. Keshavjee, M.L5,(2015).

27. Silver nanoparticles: green synthesis and their antimicrobial activities: V.K. Sharma, R.A. Yngard, Y. Lin Adv. Colloid Interface Sci., 145, 83-96. (2009).
28. Synthesis, characterization and antibacterial activity of copper, nickel and bimetallic Cu–Ni nanoparticles for potential use in dental materials. Progress in Natural Science: L. Argueta-Figueroa, R.A. Morales-Luckie, R.J. Scougall-Vilchis, O.S. OleaMejía, Mater. Intl., 24, 321–328. (2014).
29. World Health Organization (WHO). (2017). Global priority list of antibiotic-resistant bacteria to guide research, discovery, and development of new antibiotics. (2017).
30. World Health Organization (WHO). Global priority list of antibiotic-resistant bacteria to guide research, discovery, and development of new antibiotics. (2017).

Enhancing Polyoxymethylene (POM) Strength for Gearing Applications through Alumina Reinforcement and Comprehensive Testing

**K. Karthik¹, A N Kaarthik², Atchaya B³, Mahalakshmi P⁴,
Manoj U⁵, Sathish Kumar N⁶**

¹²³⁴⁵⁶ *Department of Mechanical Engineering,*
Coimbatore Institute of Technology,
Tamil Nadu, India, 641014

Abstract

One of the most important parts of mechanical power transmission systems is the gearing. Plastic gears have a number of advantages for drive designers, such as reduced noise, flexible design, and lubrication-free operation. Additional advantages consist of reduced weight and cost, increased effectiveness, and chemical resistance. Even though plastics have many advantages, the major drawback is their strength when compared to metals. So our objective is to improve the strength of polyoxymethylene (POM) thermoplastic by adding alumina (ceramic filler) of 5 and 10% to the POM and analyzing the variations in the property by conducting various tests such as tensile, flexural, hardness, wear test, and FESEM. After that, design and analysis of spur gear pairs is done on ANSYS software for the obtained property to study the variations among the materials. If the obtained variation in the properties suits our objective, then we can use the material for gearing applications such as gear pumps, etc.

Keywords: Polymer, Alumina, Analysis, Gears.

Introduction

Gear transmission

Systems for gear transmissions are crucial to numerous sectors. Monitoring and managing the gear transmission system requires an awareness of mesh gear behavior, including work conditions, distortion, and stress distribution. It's common for gears to have to run at high speeds and torque levels while still being reasonably cheap and incredibly dependable. The strength and service circumstances, such as wear and noise, determine the gear materials used in gear manufacturing. The materials used to make the gears could be metallic

or non-metallic. Cast iron's superior machineability, good wear qualities, and ease of creating intricate geometries using a sting process make it a popular material for gear manufacturing. In order to reduce weight and noise, gears are made of non-metallic materials such as wood, rawhide, compressed paper, and plastics like nylon, acrylic, and polycarbonate. High strength, superior wear resistance, strong mechanical and abrasion resistance, chemical resistance, and self-lubricating properties characterize nylon materials. Materials made of polycarbonate have excellent dimension stability, great impact strength, and heat resistance. Plastic spur gears are replacing the cast iron spur gears of sugarcane juice cans because, as previously said, nylon and polycarbonate have good qualities. Although plastic materials can result in significant cost savings, they are not necessarily more economical than their cast iron equivalents.[3]

Because spur gears have complicated geometry, there is a need for improved analysis using numerical methods that provide more accurate solutions than the theoretical methods. One such method is finite element analysis, which has been widely used in the analysis of components used in various mechanical systems. The spur gears are subjected to several stresses when they are in operation, but of all, two types of stresses—bending stress and contact stress—are important from the design point of view. The bending stresses are theoretically analyzed by the Lewis equation, and the contact stresses by the Hertz equation.

Polymers

Polymers are essentially large molecules made up of repeating units called monomers. Picture them as a string of beads, where each bead represents a monomer. These monomers are linked together through chemical bonds, forming long chains or networks. These molecules can be found everywhere in our daily lives, from natural sources like proteins, cellulose, and DNA to synthetic materials like plastics, synthetic fibers, and rubbers. Their properties vary widely depending on factors such as their composition, structure, and how they're processed.

Because of their diverse properties and applications, polymers are used in countless industries. They're crucial in packaging, textiles, automotive manufacturing, construction, electronics, and even in healthcare for things like medical devices and drug delivery systems. Their versatility and adaptability make them indispensable in our modern world.

Composites

Composites are materials formed by combining two or more components with different properties to create a new material that exhibits enhanced characteristics. These components typically include a reinforcement phase, which provides strength and stiffness, and a matrix phase, which holds the reinforcement in place and distributes loads. Composites can be tailored to meet specific performance requirements, offering advantages such as lightweight construction, corrosion resistance, and improved mechanical properties. They find extensive applications in industries such as aerospace, automotive, marine, construction, and sports equipment manufacturing, where their versatility and performance benefits are highly valued. [2]

Polymer Matrix Composites (PMC)

Polymer matrix composites (PMCs) are materials made by embedding reinforcing fibers within a polymer matrix. These composites combine the high strength and stiffness of the fibers with the lightweight and corrosion-resistant properties of the polymer matrix. In PMCs, the polymer matrix serves to hold the fibers in place, transfer loads between them, and protect them from environmental factors such as moisture and chemicals. The reinforcing fibers, which can be made of materials like carbon, glass, or aramid, provide the composite with its mechanical properties, such as strength and stiffness. [7] PMCs are widely used in the aerospace, automotive, marine, and sporting goods industries due to their high strength-to-weight ratio, corrosion resistance, and design flexibility. They are utilized in applications where lightweight and durable materials are essential, offering advantages such as reduced fuel consumption, improved performance, and enhanced structural integrity.

Selection of Material and Methods

The selection of material for the design of gear plays a vital role in gear overall performance and efficiency. So the material for the gear for the specific application has to be selected wisely in order to get the optimum output for the given standard inputs. The materials may be either metallic or non-metallic material. Cast iron is widely used for gears for better performance. But here polymer material is chosen over cast iron because when it is exposed to water or saltwater, rusts occur and it is painted to provide extended protection. If exposed to chemicals or high-pressure washing, the paint will peel off. For gears where weight is the primary consideration, thermoplastics are the ideal

material. Plastic gears can be machined similarly to metallic gears, while injection molding is a preferable method of production for some thermoplastics. Acetal is one of the most widely used thermoplastics for injection molding. Other names for this substance are polyoxymethylene (POM) and polyacetal. There are two types of polyoxymethylene that can be found on the market: copolymers (POM-C) and homopolymers (POM-H). Either polymer can be used to create gears. Spur gears, helical gears, worm wheels, bevel gears, and gear racks are a few examples of these.

Table 1. Material property of POM

PROPERTY	VALUE
Density	1.41 g/cm ³
Melting point	165 °C
Tensile yield stress	62 MPa
Tensile modulus	2700 MPa
Elongation at yield	2.5 %
Tensile breaking stress	67 MPa
Young's Modulus	3.9 MPa

Injection Moulding

Injection molding is a process of heating the raw materials in the form of granules in the hopper and then injecting the liquid into the die with constant pressure and then allowing it to cool to produce the component with the required size and shape.[4]

Samples

S1: 100% POM (100 grams POM).

S2: 95% POM & 5% AlO₃ (95 grams POM & 5 grams AlO₃).

S3: 90% POM & 10% AlO₃ (90 grams POM & 10 grams AlO₃).

Molding process

POM granules + aluminum powder + coconut oil (dispersing agent) + stirring → blended POM.

Blended POM → pour in hopper → melting (200 °C) → molding → die rejection → Required sample



Figure 1. POM Tensile test specimen (95% POM)

GEAR ANALYSIS

Static Analysis

Static analysis in SolidWorks is a simulation technique for evaluating the structural integrity of a design without physical testing [5]. It assesses how a model responds to applied forces, identifying stress points and potential deformation. This helps engineers optimize designs before building physical prototypes, saving time and resources. The analysis assumes gradual force application and static equilibrium. It provides insights into stress distribution, deformation, and factors of safety, aiding in creating robust and reliable products. Keep in mind that static analysis may not capture dynamic effects or material nonlinearities.[6]

Stress Analysis

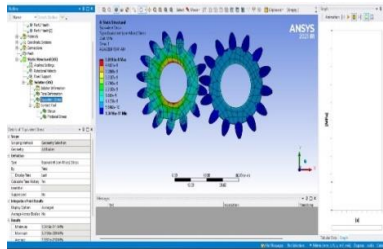


Figure 2. Stress Analysis of 90% POM and 10% alumina composition gear.

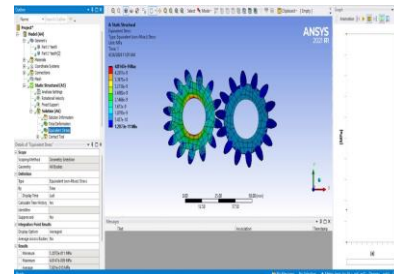


Figure 3. Stress Analysis of 95 % POM and 5% Alumina Composition Gear.

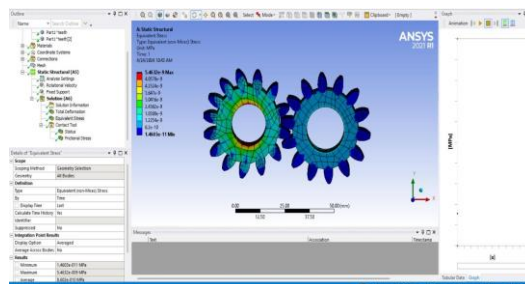


Figure. 4. stress analysis of 100% POM gear

Deformation Analysis

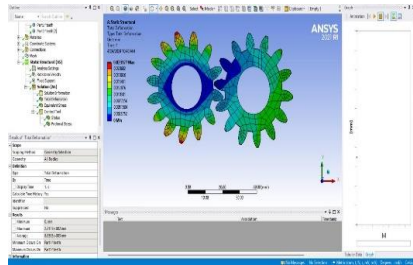


Figure 5. Deformation Analysis of 90% POM and 10% alumina composition

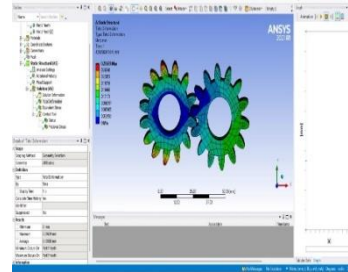


Figure 6. Deformation Analysis of 95% POM and 5% alumina composition gear.

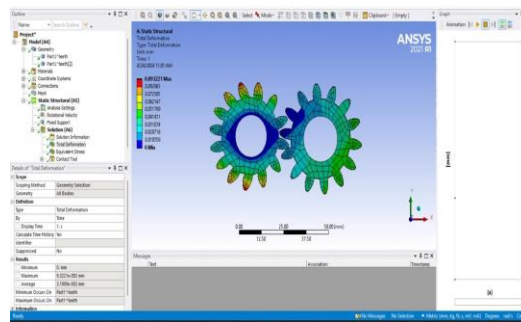


Figure 7. Deformation Analysis of 100% POM gear

The boundary conditions for the stress and deformation analysis in Ansys are carried out by keeping one gear (the driver) fixed and the other gear (the driven) rotating gear in the opposite direction to the driver gear. The gear that is on the left side of the above-mentioned figures is fixed gear, and the contacting gear on the right side is driven gear for all stress and deformation analysis.

Table 2. Stress and deformation result

MIXTURE	MAXIMUM STRESS (MPa)	MAXIMUM DEFORMATION (mm)
S1	4.8147e ⁻⁹	0.093
S2	5.4632e ⁻⁹	0.296
S3	5.0193e ⁻⁹	0.0231

Table 3. Hardness test result

MIXTURE	TRIAL 1	TRIAL 2	TRIAL 3	AVERAGE
S1	94	94	93	93.66(1)
S2	91.5	93	92	92.16 (3)
S3	92	95.5	90.5	92.66(2)

Hardness value decreases and increases due to lack of interfacial bond and effect of filler content. Due to loose bonding, hardness decreases and increases when enough bond and sufficient filler content is added.

Table 4. Tensile test result

Mixture	Tensile Strength (mpa)	Break Strength (mpa)	Break Force (n)	Elongation (%)	Modulus of Elasticity (n/m ²)
S1	1.75	1.4	5.13	3.70	0.71
S2	1.44	1.5	5.38	1.78	0.24
S3	1.58	1.6	5.63	0.62	2.88

Similar to the hardness result due to a lack of bonding and filler content, tensile strength decreases and increases, but breaking strength keeps on increasing, and elongation keeps on decreasing due to hardness and toughness of material, which increases and reaches optimized condition. Similarly, the elastic modulus of S3 has a huge difference due to the optimized value of stiffness property and large surface interaction between the filler and the polymer.

Table 5. Flexural test result

MIXTURE	FLEXURAL STRENGTH (N/mm ²)	MAX FORCE (N)
S1	15.00	30.00
S2	19.55	39.11
S3	17.38	34.76

On seeing the flexural test results, the flexural strength is slightly deviating, and this may happen due to the following reasons:

Compatibility affects the adhesion between the ceramic particles and the polymer, which in turn influences the load transfer mechanism and ultimately the flexural strength.

The manufacturing process used to fabricate the composite can also influence flexural strength. Different compositions of ceramic powder may require adjustments in processing parameters such as temperature, pressure, and mixing time to achieve optimal dispersion and mechanical properties.

SEM Analysis

Scanning electron microscopy is an effective technique for analyzing the microstructure of materials. This technique involves using a concentrated electron beam to scan a material's surface in order to get high-resolution images that can reveal particulars of the microstructure and surface properties. By changing the magnification, working distance, and electron high tension, a SEM was used to analyze the distribution of aluminum, its alloying elements, and the uniform grain structure. [7]

Table 6. Different parameters for SEM

Magnification (in x)	150x, 250x, 500x
Working distance (WD) (in mm)	8.7 mm, 9.2 mm
Electron High Tension (EHT)	20kV
Magnification (in μm)	20 μm , 100 μm

Particles Distribution

During the SEM process, there is a slight possibility that pores or voids could occur, which could weaken the material's mechanical qualities. The number, distribution, and size of these pores can be observed and quantified using SEM. The SEM image data can be used to optimize the processing parameters and enhance the material's properties.

Table 7. Weight Percentage

Mixture	Carbon (C)	Oxygen (O)	Aluminium(Al)	Silica(Si)	Calcium (Ca)
Weight %					
S1	44.40	55.50	0.10	-	-
S2	44.43	55.35	0.22	-	-
S3	47.20	50.69	1.24	0.47	0.40

Surface Roughness

SEM can be used for assessing and examining the surface topography and roughness, which affect the quality of a material's surface. According to the findings, it is evident that the layer-by-layer melting process is the factor that causes the surface to be rough. This outcome can be used to optimize the processing parameters, and depending on the need, the material's attributes can be enhanced.

SEM can be used for assessing and examining the surface topography and roughness, which affect the quality of a material's surface. According to the findings, it is evident that the layer-by-layer melting process is the factor that causes the surface to be rough. This outcome can be used to optimize the processing parameters, and depending on the need, the material's attributes can be enhanced.

Table 8. Wear parameters

PARAMETERS	VALUES
Sliding velocity	1 m/s
Sliding distance	200 m
Applied load	10 N

Table 9. Wear Rate Results

MIXTURE	WEAR RATE (Microns)
S1	-2.58
S2	-3.03
S3	-3.21

From the wear test results, we can clearly say that adding alumina to POM is enhancing the wear property by reducing the wear rate, and it is an important property for gear applications. Coefficient of friction and frictional force are increasing while adding alumina.⁷

RESULT

From the design and analysis of polymer gears, we found the various results.

Pure POM with the percentage variation of alumina is chosen for the initial stage.

By using injection molding specimens for tensile, flexural, hardness, wear, and FESM were obtained.

In a tensile test, values obtained increase with the effective dispersion of ceramic particles within the polymer matrix, which reinforces the material and enhances elastic modulus. Higher concentrations of well-dispersed ceramic particles generally result in greater reinforcement and increased modulus, contingent upon achieving proper dispersion and bonding between the phases.

Observing hardness test results among three samples with varying compositions, from 100% POM to 90% POM and 10% alumina, reveals a slight decrease in hardness. This decline in hardness can be attributed to factors including dilution of the polymer matrix, weak bonding between ceramics and polymers, non-uniform distribution of particles causing stress concentration, reduced flexibility of polymers, and processing conditions affecting ceramic dispersion.

Compatibility affects the adhesion between the ceramic particles and the polymer, which in turn influences the load transfer mechanism and ultimately the flexural strength.

From the wear test results, we can clearly say that adding alumina to POM is enhancing the wear properties, such as the coefficient of friction and frictional force increasing while adding alumina.

SEM can be used for assessing and examining the surface topography and roughness, which affect the quality of a material's surface, and it plays the major role in determining the mechanical properties of samples.

From the result of static analysis using Ansys the deformation at the point of contact and other teeth it is clear that the POM-ALUMINA composition pair is less deformed from the values obtained using deformation simulation by keeping the boundary conditions as one gear is fixed and other gear is allowed to rotate.

Conclusion

By designing and analyzing the gears, the following conclusions are made from project phase 2. Selecting parameters by the rpm and volume flow rate from the gear pump and designing the gear is done for the polymer gears, and the obtained gear dimensions are true.

The design number of teeth and face width of gear are obtained by the gear calculations, and static analysis is successfully done in the Ansys software.

Hardness value may decrease or increase due to lack of interfacial bond and effect of filler content.

In a tensile test, values obtained increase with the effective dispersion of ceramic particles within the polymer matrix, which reinforces the material and enhances elastic modulus.

The coefficient of friction and frictional force increasing while adding alumina is obtained from the wear test results.

By comparing POM-ALUMINA and POM-PPOM gear pairs, the stress developed by the POM-ALUMINA is less than the value obtained from the result of the Ansys analysis on the point of contact of the tooth.

The 90% POM–10% ALUMINA gear pair has less deformation from the analysis result.

From the SEM result, we can conclude that surface texture is more for 90% POM and

10% ALUMINA

From the above results, due to less stress concentration, total less deformation, and low displacement, the POM-ALUMINA gear pair is more stable, rigid, and stronger than the POM-POM gear pair.[1]

References

- [1] <https://www.geartechnology.com/articles/22621-a-comparative-study-of-polymergears-made-of-five-materials>
- [2] Andrzej K. Bledzki , Abdullah A. Mamun , Maik Feldmann (*Polyoxymethylene composites with natural and cellulose fibres: Toughness and heat deflection temperature*). *Volume 72, Issue 15, 12 October 2012, Pages 1870-1874* <https://doi.org/10.1016/j.compscitech.2012.08.004>
- [3] Akant Kumar Singh, Siddhartha, and Prashant Kumar Singh (*Polymer spur gears behaviors under different loading conditions*) *Volume 232, Issue 2* <https://doi.org/10.1177/1350650117711595>
- [4] Gurjeet Singh, Ajay Verma. (*A Brief Review on injection moulding manufacturing process*) *Volume 4, Issue 2, Part A*, 2017, Pages 1423-1433 <https://doi.org/10.1016/j.matpr.2017.01.164>
- [5] K Senthilnathan, S Bharani Kumar, G Suresh, Rajesh Ravi, T Srinivasan, G Sai Krishnan (*Design and analysis of gear testing kit and static structural analysis of spur gear using ANSYS software.*). IOP Conference Series: Materials Science and Engineering, Volume 988, International Conference on Recent Developments in Material Science and Applications (ICRDMSA 2020) 25 – 26 September 2020, Chennai, India. DOI 10.1088/1757-899X/988/1/012004
- [6] M. KEERTHI1, K. SANDYA2, K. SRINIVAS3 .(*Static & Dynamic Analysis of Spur Gear using Different Materials*) *Volume: 03 Issue: 01 / Jan-2016* [IRJET](https://doi.org/10.17993/IRJET)
- [7] Azzam D. Hassan1, Usama J. Naeem2 and Imad O. Bachi1. (*Processing and Evaluation of Ceramic Filler Reinforced Polymer Matrix Composites*) Publishing Ltd, Journal of Physics: Conference Series, Volume 2361, 2022 8th Asia Conference on Mechanical Engineering and Aerospace Engineering (MEAE 2022) 09/06/2022 - 11/06/2022 Wuhan, China. Citation Azzam D. Hassan et al 2022 J. Phys.: Conf. Ser. 2361 012009. DOI 10.1088/1742-6596/2361/1/012009.

Biodegradable Microneedle patches for Enhanced and Efficient Transdermal Drug Delivery

¹Sanjana S Kanguri, ²Pradyumna J

^{1,2}*Department of Centre for Sensors & Vision Technology,
Central Manufacturing Technology Institute,
Bengaluru*

Abstract

The skin serves as a primary interface for transdermal drug delivery systems (TDDs), which offer a non-invasive and controlled release of therapeutic agents, presenting a sophisticated alternative to conventional drug administration routes. This study focuses on the fabrication and characterization of biodegradable microneedle arrays composed of carboxymethyl cellulose (CMC), selected for its high biocompatibility, reinforced with amylopectin to enhance structural integrity. Dissolving microneedles (DMNs) are engineered to mechanically penetrate the skin and dissolve, facilitating a novel and efficient pathway for transdermal drug delivery. Microneedles were fabricated through a micromolding technique, achieving consistent geometries with precise dimensions and uniform distribution, essential for reliable skin penetration. The integration of amylopectin significantly improved the mechanical properties of the DMNs, facilitating effective penetration. Microneedle penetration evaluation demonstrated the microneedles in facilitating effective drug release. This study demonstrates that CMC-amylopectin-based microneedles hold significant potential as a transdermal drug delivery platform, highlighting the promise of carbohydrate-based microneedles as innovative tools for topical therapeutic applications.

Introduction

Transdermal drug delivery (TDD) involves administering therapeutic agents through the skin to enable drug entry into the systemic circulation, producing a systemic effect. TDD offers a compelling alternative to traditional administration routes like oral or intravenous delivery by providing sustained and controlled drug release, which can enhance patient compliance. One of the key benefits of TDD is that it bypasses challenges such as gastrointestinal irritation, enzymatic degradation, and low absorption by delivering the drug directly through the skin into the bloodstream (Motia et al., 2020).

Additionally, TDD circumvents first-pass metabolism, leading to improved bioavailability and often requiring a lower dosage.

The skin, the body's largest organ, is composed of three primary layers: (1) the epidermis, (2) the dermis, and (3) the hypodermis. Within the epidermis are five layers, with the outermost being the stratum corneum. This layer, which is approximately 10-20 μm thick, is highly hydrophobic and comprises dead keratinized cells called corneocytes. The stratum corneum acts as a barrier, preventing drugs and other compounds from easily penetrating into the systemic circulation. Various methods, such as iontophoresis, chemical penetration enhancers, sonophoresis, prodrugs, and micro needles can help to overcome this barrier and facilitate drug delivery through the skin (Lyndsey et al., 2022).

Microneedle (MN) technology is an innovative method that offers a painless, minimally invasive alternative to conventional transdermal patches and injections. Microneedles, typically 50-900 μm in length, can penetrate the epidermis or dermis, delivering therapeutic agents without reaching deeper layers where nerves and blood vessels reside. First proposed in the 1970s, microneedles advanced significantly in the 1990s due to microfabrication breakthroughs that allowed for the development of microneedle arrays. Solid microneedles were initially used to create microchannels in the skin, enhancing drug permeability (Park et al., 2016). Since then, microneedle technology has evolved to include dissolving, coated, hollow, and hydrogel-forming microneedles, expanding their applications to drug delivery, vaccines, cosmetic treatments, and even diagnostics.

Microneedles can be classified into four types: solid, hollow, coated, and dissolving. Solid microneedles, often made from materials like silicon, stainless steel, or titanium, are primarily used to create skin microchannels, facilitating enhanced drug permeation. Coated microneedles, similar in structure and typically fabricated from stainless steel or titanium, are coated with a drug solution that dries onto the needle surface, enabling drug release upon insertion (Yonghun et al., 2016). Hollow microneedles contain an inner cavity for direct liquid drug injection, allowing controlled fluid infusion at a rate similar to traditional needle but with minimal penetration depth. Dissolving microneedles, made from biodegradable and biocompatible materials such as maltose, polyvinylpyrrolidone, chondroitin sulfate, dextran, hyaluronic acid, albumin, carboxymethyl cellulose, and amylopectin, dissolve in contact with skin fluids, releasing the drug payload as they degrade (Kevin et al., 2017).

Selecting the appropriate microneedle type and application method is critical for successful transdermal drug delivery. Polymer materials are particularly valued in biotechnology and medicine due to their affordability, biocompatibility, dissolvability, swellability, biodegradability, and reduced contamination risk. Additionally, polymers are easy to machine and allow high reproducibility for large-scale production (Demir et al., 2013). Unlike many conventional microneedles, polymeric microneedles offer unique benefits, making them preferable to materials like silicon, which can be brittle and non-biocompatible (Juha et al., 2015). This study focuses on selecting polymer materials and optimizing their fabrication parameters, classifying them by dissolution characteristics such as dissolvable, swellable, and degradable behaviors to meet patient-specific requirements while minimizing contamination risks.

Dissolvable microneedles (MNs) are particularly promising for delivering macromolecules rapidly. They need sufficient robustness to penetrate the skin effectively, and their fabrication process should exclude organic solvents and take place under ambient conditions. This ensures targeted drug delivery with immediate uptake, making dissolvable microneedles ideal for short-term applications. Made from water-soluble materials like maltose, polyvinylpyrrolidone, chondroitin sulfate, dextran, hyaluronic acid, and albumin, dissolving microneedles deliver drugs with a simple press against the skin (Lee et al., 2008). Composed of biocompatible, water-soluble substances like cellulose derivatives and sugars, these microneedles fully dissolve within the skin, eliminating biohazardous sharp waste. Upon penetration, they soften and dissolve in biological tissues, reducing damage from application forces. This advantage positions dissolvable microneedles above silicon and metal types, which may break in vivo. They are versatile, easy to use, inexpensive, and suitable for self-administration, a critical benefit for developing countries. The materials used in dissolving microneedles are cost-effective, widely available, and processed under mild conditions without harsh treatments like high temperatures (Wu et al., 2022).

This study centers on developing biodegradable microneedle arrays made from carboxymethyl cellulose (CMC), a biocompatible polysaccharide, and amylopectin, which enhances microneedle structural integrity. Although dissolving microneedles are gaining attention, challenges remain in optimizing their mechanical properties and ensuring penetration efficiency. This research aims to fabricate and evaluate the mechanical strength and penetration efficiency of CMC-amylopectin microneedles, demonstrating that these materials,

when combined in optimal ratios, can produce robust and effective microneedles, paving the way for skin penetration efficiency.

Materials & Methodology

Materials

PDMS (polydimethyl siloxane), CMC (carboxymethyl cellulose) and amylopectin were purchased from Sigma Aldrich Chemical co, positive mold of stainless steel fabricated from N. R Industries, Bangalore.

Fabrication of mold using PDMS

Dissolving Microneedles (MNs) can be fabricated using various techniques, including drawing lithography, photolithography, micromolding, and droplet-born air blowing. Among these, micromolding is extensively utilized for producing dissolving microneedles. In this process, the MN mold is either filled with a melted polymer that then hardens or with a concentrated polymer solution that is left to dry. Typically, the drug-loaded polymer solution is cast onto the surface of a female microneedle mold made of polydimethylsiloxane (PDMS), which is then drawn into the micropores. To enhance this process, techniques like vacuumization and centrifugation are often applied. The polymer solution is usually injected into the microcavities of female molds, filled under pressure or vacuum, and allowed to dry naturally. In most cases, a PDMS micromold is prepared using a master structure.

PDMS is selected as the mold material due to its flexibility and minimal surface adhesion, which facilitates the easy removal of the polymer microneedle from the mold. Specifically, the Sylgard 184 PDMS kit is used, containing a base and a curing agent. For the fabrication of PDMS mold a positive mold made up of stainless steel with 25×25mm array mold was fabricated, with the help of that mold negative mold of PDMS was fabricated. To prepare the negative mold by micromolding, the PDMS pre-polymer and curing agent is mixed in a 1:1 ratio. This solution is poured into the positive mold, filling it completely, and then degassed in a vacuum chamber to remove any air bubbles. After degassing, the solution is cured at 80°C for 40 minutes. Finally, the cured PDMS mold is carefully separated from the positive mold, creating a 25 × 25 mm array with 225 needles, each with a base width of 300 μm and a height of 700 μm.

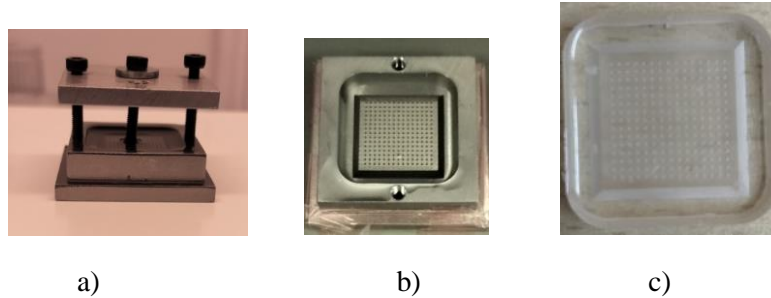


Figure 1 a) &b) Positive mold made of stainless steel, c) negative mold fabricated with PDMS

Fabrication of dissolving Microneedle

In this study, dissolving microneedles (DMNs) were fabricated using carboxymethyl cellulose (CMC), a biocompatible polysaccharide, and amylopectin, which enhance both the strength and structural integrity of the microneedles. To prepare the microneedle solution, CMC and amylopectin were each dissolved in deionized water at a 5% (w/v) concentration. This mixture was then poured into a PDMS (polydimethylsiloxane) mold, which had been created using a stainless-steel master mold to form precise microneedle shapes. Once the solution was poured into the mold, it was placed in desiccator and subjected to vacuum degassing. This step ensured that the mixture fully filled each microneedle cavity within the mold and effectively removed any trapped air bubbles, which could otherwise compromise the structural quality and consistency of the microneedles. After degassing, the mold containing the microneedle formulation was cured on a hot plate at 60°C for approximately 4 hours. The curing process enabled the microneedles to solidify and achieve the necessary mechanical properties required for successful skin penetration. Following the curing process, the solidified microneedles were carefully removed from the PDMS mold and prepared for subsequent characterization. This characterization step involved evaluating the mechanical strength, dissolution behavior, and drug release efficiency of the fabricated microneedles to confirm their suitability for transdermal drug delivery applications. The entire fabrication process, from mixing to curing, was optimized to ensure the development of reliable, structurally sound dissolving microneedles for efficient and effective transdermal administration.

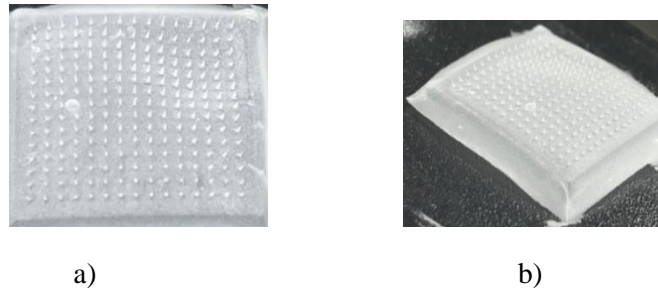


Figure 2 a) &b) dissolving microneedles fabricated using CMC and amylopectin

Characterization of dissolving microneedle

Scanning electron microscopy (SEM)

Scanning electron microscopy (SEM) is one important method of analyzing microneedle morphology, which provides high resolution imaging that is necessary for evaluating structural traits like texture of the surface and homogeneity among the microneedle array. These morphological characteristics are crucial in the production of microneedle because of direct impact on the effectiveness of drug administration, mechanical strength and skin penetration.

Therefore, the surface morphology of the microneedles was done using SEM. The samples were mounted on an aluminium mount and sputtered with a layer gold-palladium. Then the samples were placed into the SEM vacuum chamber and observed at various magnifications with accelerating voltage of 8 kV.

Confocal Microscopy Imaging

Confocal microscopy is an advanced imaging technique crucial for evaluating the morphology of microneedles, particularly their, sharpness, and uniformity, in a non-destructive manner. Unlike traditional microscopy, confocal microscopy provides (1)high-resolution imaging wherein both lateral and axial planes, that enables detailed visualization of microneedle structure, (2)three-dimensional imaging, as it collects images at multiple focal planes as this feature helps visualize the depth structure and alignment of individual microneedles capabilities, allowing researchers to assess the microneedles' dimensions, and spatial distribution in intricate detail. The confocal microscopy imaging of microneedles was done to study about the geometrical dimensions such as base width, height and tip width of the microneedle fabricated.

Mechanical strength

Mechanical strength is used to measure and understand the mechanical properties of a material, structure or component. This is a process of evaluating the physical strength, resilience and response to various types of mechanical forces such as compression, tension, fracture and bending test. The Bending test is a standard method of assessing the mechanical strength flexibility of microneedles, especially those meant for transdermal applications where they must ensure insertion forces without breaking. The robustness of microneedles was assessed to a controlled bending test to determine their resilience under a force of 4N. This force range is consistent with earlier research showing that indicates that effective microneedles must withstand forces up to 4N. The bending test was conducted to ensure that the microneedles are able to withstand force of up to 4N without structural failure into the skin.

Penetration efficiency

Penetration efficiency measures how effectively a microneedle can enter a target surface, such as skin, with minimal resistance, damage, or deformation. To assess microneedle penetration efficiency, an established in vitro model was employed. In this method, Parafilm M was folded into eight layers (without stretching) and placed on a flat plate. The microneedle patch was then applied to the layered parafilm and pressed manually for 30 seconds. The parafilm penetration test is widely used as a reliable in vitro method for evaluating the penetration capability of microneedles, as it simulates interaction with skin and assesses both mechanical strength and penetration depth. Parafilm's layered structure serves as a practical skin model, with each layer roughly corresponding to a specific depth in the outer skin layers, allowing for quantification of microneedle insertion effectiveness under controlled conditions. In this study, carboxymethyl cellulose (CMC) microneedles reinforced with amylopectin were pressed onto the parafilm membrane to simulate skin penetration resistance, with amylopectin used to enhance structural integrity.

Results and Discussion

Fabrication of PDMS mold

The microneedle array mold was fabricated using the micromolding process to create square pyramidal-shaped cavities within a PDMS sheet. This method allowed us to successfully produce cavities with diameters ranging from 200 to 300 μm and depths between 600 and 700 μm . The resulting PDMS mold features a 25×25 array, with each cavity measuring approximately 300 μm in

diameter and 700 μm in depth. Figure.3(a) illustrates the fabrication process of the PDMS mold. Using micromolding for mold fabrication offers significant advantages in terms of both time and cost efficiency compared to other methods. Unlike photolithography or etching techniques, micromolding does not require the use of hazardous chemicals, making it a safer and more environmentally friendly option. Traditional photolithography techniques, which involve complex steps to create non-vertical, pyramid-shaped cavities, are often resource-intensive and require specialized equipment. In contrast, micromolding provides a simplified, reliable approach to achieving the desired cavity shapes, making it ideal for rapid prototyping of microneedles. The micromolding process not only reduces the complexity and duration of fabrication but also facilitates consistent production of high-quality molds suitable for dissolvable microneedle applications. Figure.3(b) showcases the final PDMS mold, highlighting the well-defined square pyramidal cavities essential for producing microneedles.

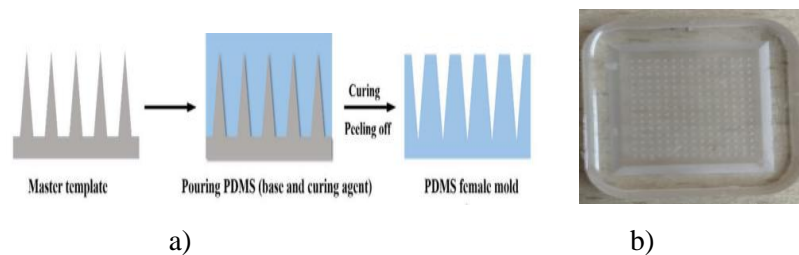


Figure 3 a) Fabrication process of PDMS mold, b) final PDMS mold

Fabrication of dissolving microneedle

Figure 4 shows the fabrication process of the microneedles, where a solution of carboxymethyl cellulose (CMC) and amylopectin is poured into a polydimethylsiloxane (PDMS) mold. This casting process involves filling the mold's square-pyramidal cavities, each designed with sharp edges, followed by curing the solution to form solid microneedles. Upon curing, the solution hardens, creating an array of microneedles, each with a height of approximately 700 μm and a base diameter of around 300 μm , accurately replicating the geometry of the mold.

One advantage of using CMC and amylopectin as base materials is that their fabrication does not require harsh or toxic organic solvents, which could potentially degrade or contaminate any active substances incorporated into the microneedles. This solvent-free approach ensures that sensitive biomolecules or other active agents encapsulated within the microneedles remain stable and uncontaminated, making CMC-

based microneedles an excellent choice for applications requiring the delivery of sensitive therapeutic agents.

While advanced microfabrication techniques can yield microneedles with extremely high precision, the micromolding process used here provides a simpler yet effective means of achieving relatively high uniformity in the microneedle structure. This level of reproducibility is sufficient for practical applications in transdermal drug delivery, where consistent mechanical and functional properties are essential for reliable performance.

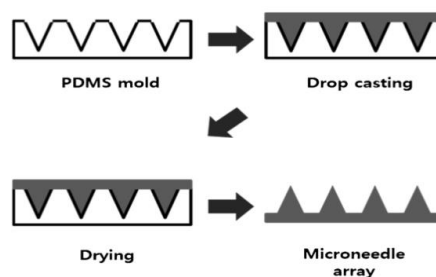


Figure 4 Fabrication process of microneedles.

Morphology of dissolving microneedle

The structural morphology of the CMC-amylopectin microneedles was examined using scanning electron microscopy (SEM). SEM images confirmed that the dimensions and shapes of the fabricated microneedles closely matched the theoretical geometry of the square-pyramidal cavities in the master mold, demonstrating successful replication. The microneedles exhibited uniformly sharp tips and a rough base substrate, which are advantageous for enhancing adhesion to the skin upon application.

The SEM analysis also highlighted in the fig and the high reproducibility of the microneedles, with consistent structural characteristics across multiple samples. This reproducibility is critical for ensuring uniform performance in applications, particularly in transdermal drug delivery, where consistency in microneedle dimensions can influence the dosage and release rate of the encapsulated therapeutic agents. +SEM supports the potential of CMC-amylopectin microneedles for consistent, reliable performance in biomedical applications.

Fig.5 indicates the study of microneedle array covered a surface area of 25 mm² and contained a total of 225 individual microneedles arranged in a precise 15×15 configuration, providing an even

distribution across the patch. Under higher magnification, the structure of each needle became clearly visible, showcasing the precise, well-defined edges and tips necessary for efficient skin penetration and dissolution. This detailed observation of morphology under SEM supports the potential of CMC-amylopectin microneedles for consistent, reliable performance in biomedical applications.

Scanning electron microscopy (SEM) provides key insights into the morphological and structural properties of microneedles made from carboxymethyl cellulose (CMC) and amylopectin. CMC's hydrophilic nature facilitates strong binding with polysaccharides like amylopectin, forming a cohesive, enhanced structural matrix. The branched structure of amylopectin integrates well within the CMC network, contributing to improved mechanical stability and durability. SEM analysis typically reveals a smooth, interconnected surface morphology, indicative of strong bonding interactions. The dense microstructure observed under SEM suggests minimal phase separation, likely due to hydrogen bonding between the components, highlighting their potential for applications in biodegradable films or structural materials where strength and flexibility are required.

The structural dimensions of the microneedles were analyzed using confocal microscopy, which allowed precise measurement of microneedle height, base diameter, and tip width. The imaging confirmed that the square-pyramidal geometry of the PDMS mold was faithfully reproduced in the fabricated microneedles. These measurements closely aligned with the intended dimensions set by the mold design, indicating successful replication through the micromolding process. Fig,6

The results, presented in a detailed table, indicate that each microneedle has a height of approximately 700 μm and a base diameter of around 300 μm , with a sharp tip width of about 30 μm . This combination of measurements underscores the capability of the fabrication process to achieve well-defined microneedle structures, which are essential for effective skin penetration and subsequent dissolution in transdermal applications.

By ensuring consistency in height, base diameter, and tip sharpness, this confocal microscopy analysis validates the precision of the micromolding process and confirms the structural uniformity across the microneedle array. These dimensions are critical parameters that influence the microneedles' mechanical strength, skin penetration efficacy, and controlled drug release performance, making them well-suited for transdermal delivery applications.

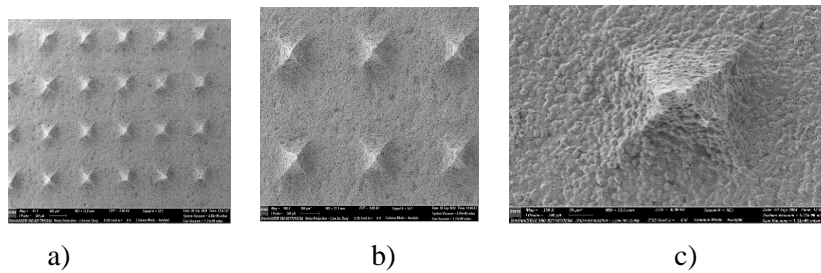


Figure 5 a) represents the sem image of dissolving microneedle at 45x magnification, b) represents the sem image of dissolving microneedle at 100x magnification and c) represents the sem image at 350x magnification.

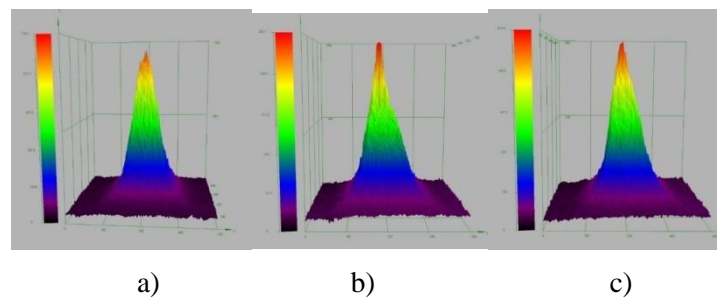


Figure 6 a)-c) represents the confocal imaging of dissolving microneedle with desired height, base width and tip width of the microneedles.

Table.1 Fabricated microneedle dimensions obtained from confocal microscopy.

Sl.no	Height (μm)	Base width (μm)	Tip Width (μm)
a	607.075	254.167	26.667
b	632.363	231.667	23.33
c	608.154	220.833	21.667

Evaluation for mechanical strength of dissolving microneedle

To ensure successful skin penetration without fracture, microneedles must exhibit adequate mechanical strength. The mechanical robustness of the dissolving microneedles was evaluated

using a bond tester under controlled parameters for force limit, test distance, and speed. This testing approach is non-destructive, allowing for accurate assessment of the microneedles' strength without compromising their structural integrity.

The test was conducted on two sample groups, each subjected to a constant test speed and force limit, while varying the test distance to observe any impact on mechanical strength. These conditions were carefully chosen to simulate real-world application forces that microneedles might experience during skin insertion. The results, summarized in the accompanying table, reveal the mechanical response of each sample group under the specified parameters, highlighting the microneedles' durability and resistance to deformation or breakage. The microneedles can sustain up to the force range of 4N.

By maintaining consistent test speed and force limit, the experiment provides insights into how different insertion depths (represented by test distance) affect the structural stability of the microneedles. This testing is crucial in validating the mechanical reliability of dissolving microneedles for transdermal drug delivery, ensuring that they can withstand the necessary forces for safe and effective application.

Table. 2 Parameters and results evaluating mechanical strength of dissolving microneedle.

Sl.no	Force limit (N)	Test distance (μm)	Test speed ($\mu\text{m}/\text{sec}$)	Result
a)	3	-2000	3000	3.4N
b)	3	-3000	3000	4N

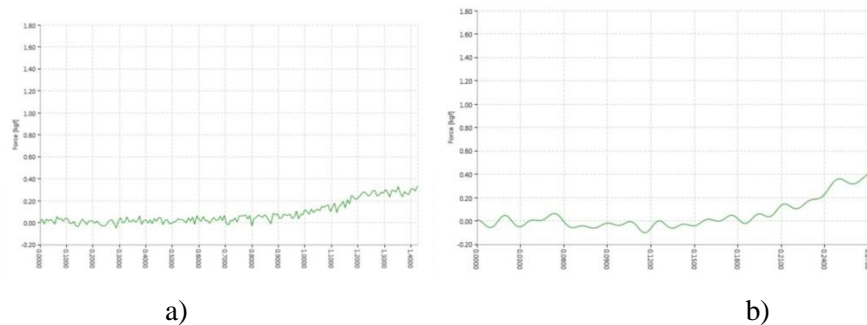


Figure 7 Graph represents force (Kgf) VS Time (Sec)

Penetration Efficiency

An in vitro study was conducted to evaluate the penetration efficiency of the microneedles using Parafilm M as an experimental model in place of human skin. Parafilm M serves as a practical model for testing microneedle insertion, as its layered structure can simulate the mechanical resistance of skin, providing an accessible means of assessing penetration depth and efficiency.

In this study, the penetration depth achieved on Parafilm M demonstrated a minimum insertion depth of approximately 300 μm and the results are represented in the below table. When tested across eight layers of Parafilm M, the microneedles achieved partial penetration through the layers, indicating that while effective, there is room for optimization to enhance the depth and consistency of insertion. Fig

Given the partial penetration results, the addition of amylopectin or similar strengthening agents to the CMC matrix is suggested as a means to reinforce the mechanical strength of the microneedles. By improving the structural integrity of the microneedles, this modification could lead to increased insertion efficiency and depth, allowing for more reliable skin penetration. Optimizing the formulation in this way would make the microneedles more suitable for transdermal drug delivery, where consistent penetration into the skin is crucial for effective therapeutic application.

This approach to strengthening the microneedles with amylopectin or other reinforcing agents holds potential for developing robust microneedle arrays capable of overcoming the natural resistance of the skin, thus enhancing the overall efficacy of the microneedle-based drug delivery system.

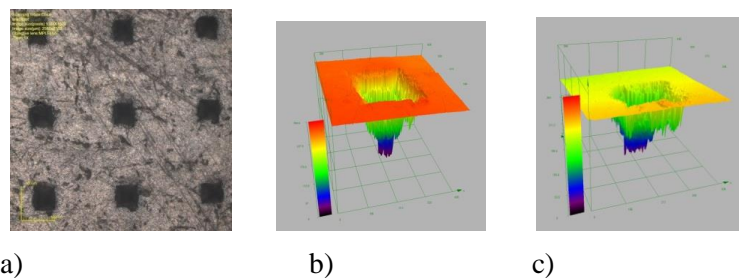


Figure 8 a) Needle Penetration onto parafilm, b)-c) penetration depth.

Conclusion

In this study, fabrication and characterization of microneedle patches using carboxymethyl cellulose (CMC) and amylopectin successfully demonstrated the desired mechanical strength and performance for transdermal applications. By optimizing the CMC-to-amylopectin ratios, we achieved robust structural integrity, ensuring both durability and effective penetration necessary for efficient drug delivery. Characterization confirmed that the microneedles retained sufficient strength to meet the requirements for successful skin insertion, validating the effectiveness of this biodegradable system. These findings confirm the potential of CMC-amylopectin microneedles as a reliable, patient-friendly solution for transdermal drug delivery, with promising applications in delivering a range of therapeutic agents. The successful optimization also establishes a foundation for future exploration into formulation adjustments to further enhance delivery profiles and therapeutic outcomes.

Acknowledgement

We acknowledge and express our sincere gratitude to our institution Central Manufacturing Technology Institute and our director of the Institute, Dr. Nagahanumaih, for providing the necessary facilities to conduct this research. We also acknowledge the Indian Institute of Science, Bengaluru, for their support and for providing characterization facilities essential for this study.

References

1. Motia Azmana, Syed Mahmood, Ayah Rebhi Hilles, Uttam Kumar Mandal, Khater Ahmed Saeed Al-Japairai, Subashini Raman, Transdermal drug delivery system through polymeric microneedle: A recent update, *Journal of Drug Delivery Science and Technology*, Volume 60, 2020.
2. Lyndsey E. Moore, Sonja Vucen, Anne C. Moore, Trends in drug- and vaccine-based dissolvable microneedle materials and methods of fabrication, *European Journal of Pharmaceutics and Biopharmaceutics*, Volume 173, 2022.
3. Kevin Ita, Dissolving microneedles for transdermal drug delivery: Advances and challenges, *Biomedicine & Pharmacotherapy*, Volume 93, 2017.
4. Park, YH., Ha, S.K., Choi, I. *et al.* Fabrication of degradable carboxymethyl cellulose (CMC) microneedle with laser writing

and replica molding process for enhancement of transdermal drug delivery. *Biotechnol Bioproc E* **21**, 110–118 (2016)

5. Yonghun Park, Kyu Sik Kim, Minsub Chung, Jong Hwan Sung, Bumsang Kim, Fabrication and characterization of dissolving microneedle arrays for improving skin permeability of cosmetic ingredients, *Journal of Industrial and Engineering Chemistry*, Volume 39, 2016
6. Juha Mönkäre, M. Reza Nejadnik, Khalil Baccouche, Stefan Romeijn, Wim Jiskoot, Joke A. Bouwstra, IgG-loaded hyaluronan-based dissolving microneedles for intradermal protein delivery, *Journal of Controlled Release*, Volume 218, 2015, Pages 53-62, ISSN 0168-3659,
7. Lee, J. W., Park, J. H., & Prausnitz, M. R. (2008). Dissolving microneedles for transdermal drug delivery. *Biomaterials*, 29(13), 2113–2124.
8. Wu, M., Xia, T., Li, Y., Wang, T., Yang, S., Yu, J., Liang, Q., Shen, T., Yu, M., & Zhao, B. (2022). Design and fabrication of r-hirudin loaded dissolving microneedle patch for minimally invasive and long-term treatment of thromboembolic disease. *Asian journal of pharmaceutical sciences*, 17(2), 284–297.
9. Demir, Y. K., Akan, Z., & Kerimoglu, O. (2013). Characterization of polymeric microneedle arrays for transdermal drug delivery. *PloS one*, 8(10), e77289.
10. Bahmani, S., Khajavi, R., Ehsani, M. *et al.* Transdermal drug delivery system of lidocaine hydrochloride based on dissolving gelatin/sodium carboxymethylcellulose microneedles. *AAPS Open* **9**, 7 (2023)
11. Oh, N. G., Hwang, S. Y., & Na, Y. H. (2022). Fabrication of a PVA-Based Hydrogel Microneedle Patch. *ACS omega*, 7(29), 25179–25185.
12. J.L. Yang, X. Fu, Y. Song, Recent advances of microneedles for biomedical applications: drug delivery & beyond, *Acta Pharm. Sin. B* **9** (3) (2019) 469.
13. J.C. Norman, S. Tong, N.T. Aiyar, A.R. Patel, S.R. Prausnitz, M.R. Allen, M. G. Hollow, Microneedles for Intradermal Injection Fabricated by Sacrificial Micromolding and Selective Electrodeposition, *Biomed. Microdevices* **15** (2) (2014) 203–2010.

14. P. Van Damme, et al., Safety and efficacy of a novel microneedle device for dose sparing intradermal influenza vaccination in healthy adults, *Vaccine* 27 (3) (2009) 454–459.
15. I. Leroux-Roels, et al., Seasonal influenza vaccine delivered by intradermal microinjection: A randomised controlled safety and immunogenicity trial in adults, *Vaccine* 26 (51) (2008) 6614–6619.
16. Y. Li, H. Zhang, R. Yang, Y. Laffitte, U. Schmill, W. Hu, M. Kaddoura, E. J. Blondeel, B. Cui, Fabrication of sharp silicon hollow microneedles by deepreactive etching towards minimally invasive diagnostics, *Microsyst. Nanoeng.* 5 (2019) 41–52.
17. Y. Levin, et al., Intradermal vaccination using the novel microneedle device MicronJet600: Past, present, and future, *Hum. Vacc. Immunotherapeut.* 11 (4) (2015) 991–997.
18. C. O'Mahony, Structural characterization and in-vivo reliability evaluation of silicon microneedles, *Biomed. Microdevices* 16 (3) (2014) 333–343. [8] J.B. Carey, et al., Microneedle array design determines the induction of protective memory CD8⁺ T cell responses induced by a recombinant live malaria vaccine in mice, *PLoS ONE* 6 (7) (2011) e22442.
19. S.R. Vućen, et al., Improved percutaneous delivery of ketoprofen using combined application of nanocarriers and silicon microneedles, *J. Pharm. Pharmacol.* 65 (10) (2013) 1451–1462.
20. R. Paleco, et al., Enhancement of the in vitro penetration of quercetin through pig skin by combined microneedles and lipid microparticles, *Int. J. Pharm.* 472 (1–2) (2014) 206–213.
21. K. Malinovskaja-Gomez, H.I. Labouta, M. Schneider, J. Hirvonen, T. Laaksonen, Transdermal iontophoresis of flufenamic acid loaded PLGA nanoparticles, *Eur. J. Pharm. Sci.* 89 (2016) 154–162.
22. G. Aggarwal, S. Dhawan, S.L. HariKumar, Natural oils as skin permeation enhancers for transdermal delivery of olanzapine: in vitro and in vivo evaluation, *Curr. Drug Deliv.* 9 (2) (2012) 172–181.
23. J. Manikkath, A.R. Hegde, G. Kalthur, H.S. Parekh, S. Mutalik, Influence of peptide dendrimers and sonophoresis on the transdermal delivery of ketoprofen, *Int. J. Pharm.* 521 (1–2) (2017) 110–119.

24. A.P. Morris, K.R. Brain, C.M. Heard, Skin permeation and ex vivo skin metabolism of O-acyl haloperidol ester prodrugs, *Int. J. Pharm.* 367 (1–2) (2009) 44–50.
25. Y. Cao, Y. Tao, Y. Zhou, S. Gui, Development of sinomenine hydrochlorideloaded polyvinylalcohol/maltose microneedle for transdermal delivery, *J. Drug Deliv. Sci. Tech.* 35 (2016) 1–7.
26. J. W.Z. Li, M.R. Huo, J.P. Zhou, Y.Q. Zhou, B.H. Hao, T. Liu, Y. Zhang, Super-short solid silicon microneedles for transdermal drug delivery applications, *Int. J. Pharm.* 389 (1–2) (2010) 122–129.

Transport, EMISE and Humidity Sensing studies of Polyaniline-Cobalt Ferrite Nanocomposites

**Raghavendra Naik¹, M. Revanasiddappa^{1*}, S. Manjunatha²,
Y. T. Ravikiran³**

¹*Department of Chemistry,
PES University,
Electronic city campus, Bangalore - 560100, India*

²*Department of Physics,
Kishida University,
Ballari, 583104, India*

³*Department of Physics,
Government Science College,
Holalkere, 577526, India*

**E-mail:raghavendranaik334@gmail.com*

Abstract

Polyaniline-CoFe₂O₄ nanocomposite thin films and pellets were prepared by incorporating varying amounts of CoFe₂O₄ in the matrix of polyaniline (PANI) through an in-situ polymerization technique. Morphology of the composites were examined using SEM, XRD studies exhibited crystalline nature of the composites and FTIR analysis revealed cobalt ferrite was homogeneously mixed in the matrix of PANI. AC Conductivity, dielectric and electric modulus studies exhibited the regular behavior of PANI composites were studied in the range 10 Hz – 7 MHz Thin films of PANI- CoFe₂O₄ nanocomposites when exposed to a broad Frequency range: 2–3 GHz. showed electromagnetic interference in the range of -4 dB to -9 dB, indicating effective attenuation of electromagnetic energy and serving as evidence for EMI shielding. Conductivity measurements were investigated and showed that PANI exhibits a more effective conducting mechanism in CoFe₂O₄-PANI composites. The humidity sensitivity experiment revealed a variation in resistance in response to relative humidity when the pellets were exposed to a broad humidity range from 11% to 97% RH.

Introduction

These days, PANI becoming more popular because of its special qualities, which include low weight, flexibility, ease of use, and

inexpensive production. They are utilized in products like energy storage devices and super capacitors due to their special qualities, such as conductivity [1], [2]. Polymers that are generated by oxidative polymerization processes can have their conductivity increased and utilized in advanced technologies of the future by mixing them with metal oxide nanoparticles [3], [4].

Reconstituted aniline monomer is the building block of PANI, which is composed of alternate arrangements of a single (σ) and double (π) bond. The polymer's charge carriers polarons and solitons, are insufficient on their own to give the polymer conductivity [5], [6], [7]. CoFe₂O₄ nanoparticles that have been blended increase conductivity by producing holes and electrons, which act as charge carriers. Holes made by electrons travelling to nearby holes and jumping of electron forms new holes [8], [9]. CoFe₂O₄ nanoparticles are a form of semiconductor with both conducting and magnetic characteristics [10]. These nanocomposites improve the electromagnetic interaction by absorbing and reflecting radiation. It is beneficial in preventing increased radiation pollution and lowering undesired radiation in electronic and communication devices [11]. PANI is porous nature so allowing water molecules to enter it. This feature makes it suitable for use in humidity sensors in agriculture and the food industry [12].

Our work focused on producing several composites of PANI/CoFe₂O₄ nano composite, which were then evaluated using XRD, Fourier transform IR, and scanning electronic microscopy techniques.

Experimental

Materials and Methods:

Every chemical utilized in this investigation was research-grade purity. Aniline (C₆H₅NH₂), Ammonium persulfate (APS), Hydrochloric acid (HCl), cobalt ferrite (CoFe₂O₄). To create nanocomposite, aniline underwent two-fold distillation and deionized water was used in the purification of polymer nanocomposites.

Preparation polyaniline:

The oxidizing agent used in the oxidative polymerization process to produce polyaniline was ammonium persulfate (APS). After dissolving aniline in HCl solution, ammonium persulfate solution was added drop wise to aniline and hydrochloric acid solution at lower temperature. The entire liquid was continuously stirred for four to five hours using a magnetic stirrer in order to create powder of dark green color polyaniline. Polyaniline was purified by repeatedly washing it in ethanol and deionized water.

Preparation of polymer cobalt ferrite nanocomposites:

By using the in-situ polymerization process, varying amounts of 2, 4, 6, 8, and 10% CoFe_2O_4 nanocomposite with aniline were added to create PANI/ CoFe_2O_4 nanocomposites.

Initially, 1 ml of aniline and 40 ml of HCl solution are mixed with a known percentage of cobalt ferrite and maintained in an ice bath at a temperature lower than 5 °C. A 40 ml HCl solution mixed with APS in different beaker and resulting solution is then introduced drop wise in to first solution. after 4–5-hour continuous stirring precipitate was obtained. Wash the resultant precipitate with double-distilled water and ethanol, which is then dried for ten hours at 70°C.

Characterization:

FT-IR spectroscopic data was obtained using Nicolet 750 FTIR instrument in the frequency range 250 - 4000 cm^{-1} . Surface morphology of the composite was examined with the assistance of scanning electron microscope (SEM) of [make: Zeiss Ultra 60]. XRD data was obtained by using Malvern analytical aeris bench top model.

Ac conductivity measurement:

A mortar and pestle were used to grind a synthesized PANI/ CoFe_2O_4 nanocomposite for an hour. By subjecting the nanocomposite to five tons of hydraulic pressure, a thin pellet was prepared. AC response parameters of the nanocomposite pellet were recorded in the frequency range 10 Hz - 7 MHz using a digital LCR meter [make: Hioki model 3532-50].

Humidity sensing measurement:

The silver paint-coated pellets were used for humidity sensing studies. A digital Multimeter (HIOKI DT4282) was used to measure the resistance of these pellets under relative humidity environments at room temperature.

EMI shielding measurement:

PANI/ CoFe_2O_4 nanocomposites EMI shielding was investigated using the S band frequency range 2–3 GHz. The wave guide was filled with films of PANI/ CoFe_2O_4 nanocomposites. The Tektronix spectrum analyzer receives the output from the signal generator (RIGOL), which is coupled to the input of a rectangular wave guide. The analyzer captures the residual frequency. Additionally, a computer-interfaced data recorder has been used to record frequency[13].

Result and discussion

FTIR analysis:

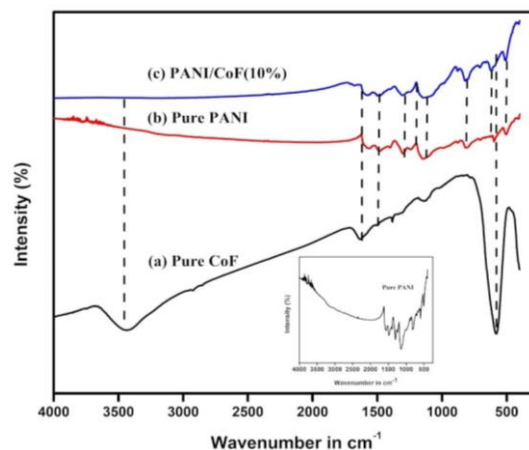


Figure 1. FTIR spectra of (a)Pure CoFe_2O_4 , (b) Pure PANI, (C)10% PANI/ CoFe_2O_4 .

The FT-IR spectra of pure polyaniline, pure CoFe_2O_4 and its 10% composite of PANI/ CoFe_2O_4 composite are displayed in Fig.1. It displays stretch at 590 cm^{-1} , which is the frequency at which the CoFe_2O_4 spinel structure stretches as a result of Fe-o vibration, whereas C-H bending out of the plane in the substitute benzene ring is seen at 780 cm^{-1} . The large peak at 1150 cm^{-1} indicates the presence of the $\text{N}=\text{Q}=\text{N}$ (Q=quinoic) ring in vibration mode. The $-\text{C}=\text{N}$ imine group found in polyaniline is represented by the vibration seen in 1507 cm^{-1} . It displays an N-H stretching vibration caused by protonation in the 3500 cm^{-1} regions. The strong peak at 570 cm^{-1} found in pure PANI is absent in CoFe_2O_4 nanocomposites due to disturbance in the random configurations of PANI chains caused by CoFe_2O_4 and the PANI matrix, resulting in a more amorphous area and undetectable vibrations. This further extends or dilutes the intensity of FT-IR peaks.[14], [15].

XRD Studies:

X-RD analysis confirms nature of pure PANI with pure cobalt ferrite and 10% PANI/ CoFe_2O_4 composite. The pattern of pure cobalt ferrite and polyaniline composite is depicted in Fig .2. The broad diffraction peaks at $2\theta - 19^\circ$ and 20° in the XRD pattern of PANI indicate that it is semicrystalline in nature. A sharp peak may be seen at $2\theta - 19^\circ, 30^\circ$,

36°, 43°, 54°, 57°, and 63° in the CoFe_2O_4 XRD pattern. The cobalt ferrite's crystallinity is confirmed by these pointed peaks. PANI composite the X-RD pattern of PANI/ CoFe_2O_4 nanocomposites displays peaks at 20 - 30°, 32°, 36°, 43°, 54°, 57°, and 63°. This shows that pure CoFe_2O_4 distributed in polyaniline shows interaction and create an ionic link with the polyaniline's amide group[16] [17], [18].

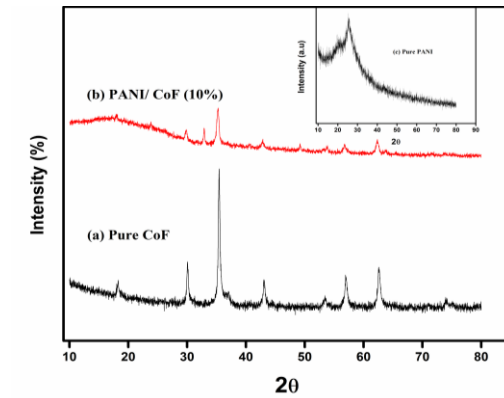


Figure 2. XRD images of (a)Pure CoFe_2O_4 , (b) 10% PANI/ CoFe_2O_4 , (c) Pure PANI.

SEM analysis:

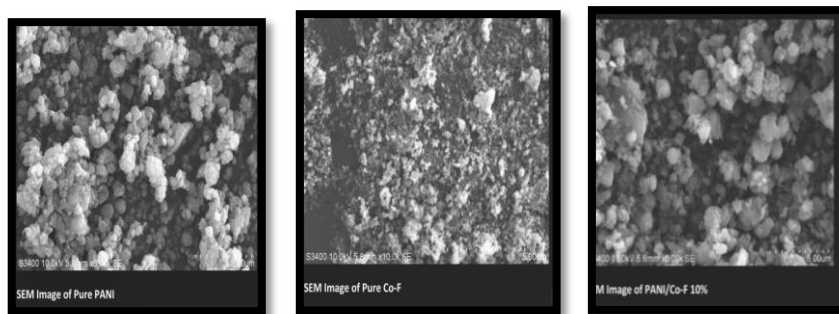


Figure.3. SEM pictures of (a) Pure PANI, (b) Pure CoFe_2O_4 , (c)10% PANI/ CoFe_2O_4 .

PANI, cobalt ferrite and their composite has been investigated using a scanning electron microscope (SEM). It shows surface features, shown in Fig.3. (a) That a globular agglomeration was formed and interconnecting polymer chain bonds caused a chemically heterogeneous morphology to be dispersed unevenly. In Fig.3 (b) Pure CoFe_2O_4 typical structure of cobalt ferrite is granular, non-uniform, spherical with low crystallinity that appears uneven and porous. Fig .3.

(c) composites shows the formation of microstructure agglomerated clusters of dispersant metal oxide in PANI matrix [19] [20], [21].

AC conductivity:

Different PANI/ CoFe₂O₄ composites were subjected to 50 Hz to 1 MHz in order to perform the AC conductivity experiment. Conductivity values are measured by using the formula Eq.1. $\sigma(f) = \sigma'(f) - \sigma''(f) \dots\dots\dots (1)$

The real and imaginary components of AC conductivity are denoted by $\sigma''(f)$ and $\sigma'(f)$. The measurement of AC conductivity is shown in Fig.4. (a) and (b).

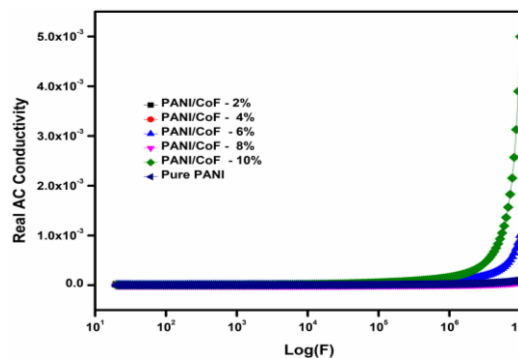


Figure 4 (a) Measurement of real AC conductivity for PANI/CoFe₂O₄ at frequencies of 2, 4, 6, 8, and 10%.

Figure 4. (a) The composition demonstrates how the frequency of the different composite changes as the applied electric field increases. 10% and 6% composites exhibit the highest ac conductivity as compared to other composites; their frequency increases linearly. It indicates that charge carriers take longer at the interface at low frequencies, whereas polarization rises at high frequencies due to the charge's inability to keep up with the rapid changes in the electric field. A material will therefore display different electric characteristics based on the frequency of the applied field [22].

An imaginary portion of AC conductivity is depicted in Figure .4. (b) There is diversity in the AC conductivity of different composites when an external electric field is introduced. All composites initially exhibit the same AC conductivity at low frequencies; at higher frequencies, conductivity increases by 10% and 6%, respectively. Accept these two composites at higher frequencies; other composites don't change at high frequencies.

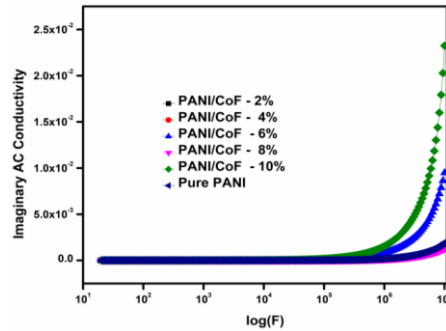


Figure 4. (b) Measurement of imaginary AC conductivity for PANI/CoFe₂O₄ at frequencies of 2, 4, 6, 8, and 10%.

Dielectric studies:

The dielectric constant measures a material's ability to polarize when an electric field is applied. The manner in which a material transmits and stores external electric energy determines this. The dielectric constant is plotted against the applied electric field in the Fig.5. (a) Due to space charge polarization, composite concentrations of 2%, 6%, and 10% exhibit at lower frequencies, the dielectric constant decreases sharply as frequency increases. CoFe₂O₄ nanocomposites exhibit various electrical characteristics in PANI. A high-frequency electric field exhibits a rapid change in the electric field and reduces charge accumulation at the interface, while larger concentrations cause charge carriers to concentrate at the interface, increasing the dielectric constant. There was less polarization[23],[24].

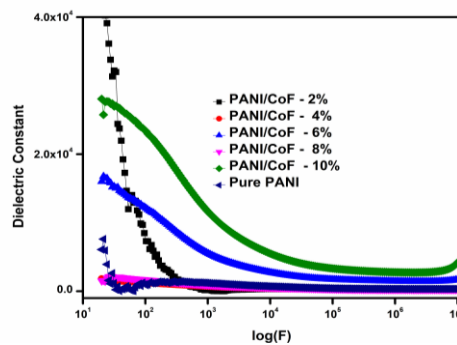


Figure 5. (a) The real dielectric constant for PANI/CoFe₂O₄ varies by 2, 4, 6, 8, and 10% depending on the frequency applied.

The imaginary dielectric constant is displayed in Fig.5. (b) It depicts the energy loss as heat brought on by the trailing dipole's dielectric loss. 2%, 4%, 6%, 8%, and 10% polymer composites were subjected to the frequency. Lower frequencies have a lesser imaginary dielectric constant; as the frequency rises, it falls. This demonstrates that it takes

time for the dipole to align itself with an applied external electric field. The dipole is currently in charge of energy release and dissipation in the form of heat, phase lag raises the amount of energy wasted as heat, which causes dielectric loss and lowers the material's storage capacity efficiency[22].

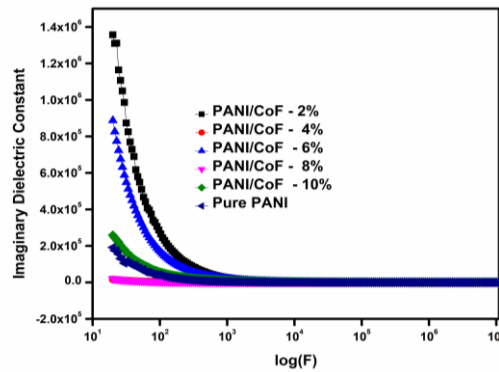


Figure 5. (b) The imaginary dielectric constant for PANI/CoFe₂O₄ varies by 2, 4, 6, 8, and 10% depending on the frequency applied.

The dielectric modulus with frequency is displayed in Fig .6. which analyzes the permittivity.

$$\text{Eq .1} \quad M^* = M' + jM'' \dots\dots\dots (1)$$

In this case, M' and M'' stand for the real and imaginary parts of the dielectric modulus, respectively. The composite exhibits frequency variation in Fig .6. (a) 6% and 10% of nanocomposites do not exhibit change when the applied electric frequency increases, indicating greater polarization. This is because modulus and material polarization are inversely correlated, indicating that the material can store more energy in an applied electric field. In other composites, short-range charge carriers are demonstrated by the dielectric modulus increasing with frequency[24].

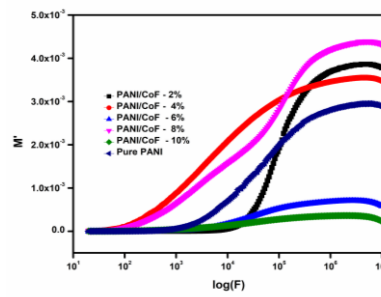


Figure 6. (a) shows the real dielectric modulus M' of 2, 4, 6, 8, and 10% PANI/CoFe₂O₄ composites as a function of applied frequency.

The imaginary dielectric modulus is displayed in Fig.6. (b) It depicts interfacial polarization-induced relaxation is represented by the imaginary electric modulus. As the frequency increases, the electric modulus of 10% composites decreases. Variation appears in other composites more frequently. Because the 10% composite contains more nanocomposites, is larger in surface area, exhibits greater contact, and has fewer charge carriers, more charge builds up at the interface, increasing polarization.

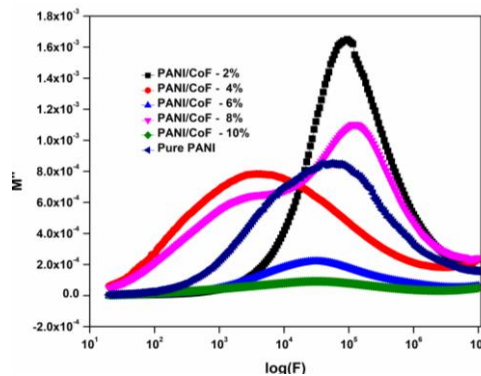


Figure 6. (b) shows the imaginary dielectric modulus M'' of 2, 4, 6, 8, and 10% PANI/CoFe₂O₄ composites as a function of applied frequency.

EMI shielding Effectiveness Measurement:

Electromagnetic interference is becoming more prevalent as people rely more and more on contemporary wireless technological devices. Unwanted electromagnetic radiation from external sources is referred to as EMI interference [25]. It can create a variety of issues, including increased current flow in circuits, voltage fluctuations, and noise in electronic devices [2],[26]. EMI shielding is essential to the effectiveness of the gadgets we use, including phones, laptops, TVs, and medical and military equipment[27]. Materials with the ability to prevent interference Using waveguide transmission line technology, the efficacy of EMI shielding for PANI/CoFeO₄ nanocomposite films has been evaluated here.

The results are used to Illustrate a frequency (GHz) vs. EMI shielding (dB) graph, and it is found that the EMI shielding of various polymer nanocomposites is nearly identical. The composites exhibit a -4 dB to -9 dB range of EMI shielding. All these composites show the same trend in shielding the EMI in S band.

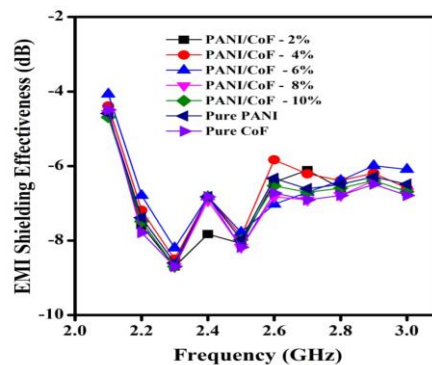


Figure 7. Frequency vs. EMI SE of PANI/CoFe₂O₄ composites of 2,4,6,8 and 10%.

It's evident from the Fig.7. fluctuations that conductivity and EMI shielding efficacy are correlated. PANI is a conjugated conductive polymer that initially exhibits conductivity because of the π electrons' delocalization. Different concentrations of cobalt ferrite (CoFe₂O₄) nanocomposites are added to the polyaniline, creating an interconnecting network that increases the number of holes and electrons and facilitates easy electron mobility within the network of the polyaniline nanocomposite [28]. Conductivity is raised by this. Higher conductivity composites protect from electromagnetic radiation by absorbing more of it and producing a heating effect [29]. Reduced reflection results from a rise in EMI radiation absorption level with an increase in nanocomposite quantity. Because of the highest absorption at -9 dB, it appears that interfering electromagnetic radiation can be blocked in this range [30], [31].

$$\text{Eq.1. } FSPL = 20 \log 10(d) + 20 \log 10(f) + 20 \log 10(4\pi/C) - GTX - GRX \dots\dots\dots (1)$$

The aforementioned formula, which takes into account factors like film thickness (t), electrical conductivity and (σ) frequency (f) in MHz, can also use to calculate the effectiveness of EMI shielding.

Humidity Sensing Measurement:

PANI exhibits both the reduced form (-NH-) and the oxidized form (-N=) during synthesis because ammonium persulfate (APS), an oxidizing agent, is used in the process. $N \rightarrow NH^+$ and $N \rightarrow NH_2^+$ are the reduced and oxidized forms of nitrogen, respectively, due to the one unbonded electron pair on nitrogen [32]. It exhibits an electron hopping mechanism as it transitions from the protonated reduced form (NH₂⁺) to the protonated oxidized form (NH⁺). It is not until the proton is

removed from (NH_2^+) that the electrons are lost. The proton transfer process is hampered when there is an increase in water adsorption in the polymer nanocomposite. As a result, resistance rises in tandem with humidity absorption.

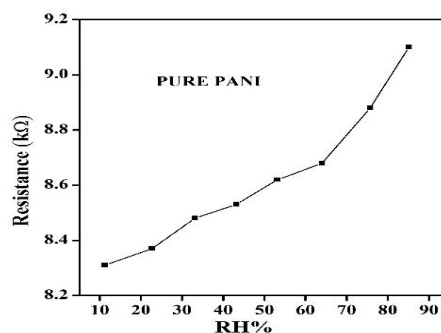


Figure 8. (a) Resistance of pure PANI/ CoFe₂O₄ composites varies with percentage relative humidity.

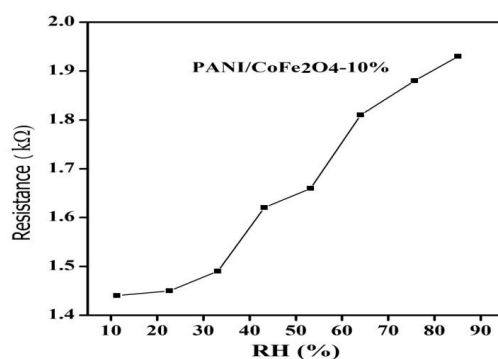
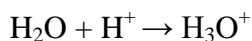


Figure 8. (b) Resistance of 10% PANI/ CoFe₂O₄ composites varies with percentage relative humidity.

As may be seen clearly from looking at the Fig. 8. (a) and (b) that resistance rises in tandem with humidity levels. SEM has already demonstrated the porous nature of the use PANI composite. As water molecules come into contact with the PANI/CoFeO₄ surface, they are physically adsorbed and a chemisorption mechanism is subsequently displayed [33]. H^+ and OH^- hydroxide ions are first formed when water molecules collide on the surface[34], [35]. At this point, the polymer nanocomposites surface double hydrogen bond is adsorbed with the water molecules. The adsorption process begins when the OH^{+3} ion attracts the OH^- .

Water molecules combine with OH⁻ ions to generate HO⁺ ions as physisorption rises. These ions then begin to migrate between two water molecules, further boosting absorption.



More water vapor starts to accumulate between the polymer nanocomposites layers as a result of this process. It is the Grotthuss mechanism this explains hopping mechanism[36].

The humidity response of 10% PANI/ CoFe₂O₄ varies with polyaniline, as shown in Fig .8. (a) and (b). The main cause of the resistance change in PANI/ CoFe₂O₄ nanocomposites is the presence of cobalt ferrite, which results in better conductivity than pure polyaniline. Polymer chains and silver particles separate due to the adsorption of water molecules when exposed to a humid environment, which results in low electrical conductivity. This indicates that the chemical makeup of the polymer and its composites affects humidity sensing[37].

Conclusion

In situ polymerization was used to successfully create PANI/CoFe₂O₄ nanocomposites. The crystalline structure of natural polymers and CoFe₂O₄ is revealed by XRD. A polymer's characteristic frequency for identification. FT-IR was used to determine the composites. SEM is used for surface morphology analysis. This polymer composite's conducting ability was investigated under applied frequency, and the results indicate that conductivity rose as the composite's CoFe₂O₄ content increased. Composites exhibit effective absorption when EMI shielding performance is tested between 2 and 3 GHz frequencies, and this is correlate with AC conductivity. It demonstrates its suitability for EMI shielding in electronic instruments. With a rise in CoFe₂O₄ concentration, humidity sensitivity rose, and sensor devices were made possible by the rapid reaction in humidity sensitivity.

Acknowledgement:

The authors would like to express their gratitude to the management of PES University, Electronic city Campus, Bangalore and the Vision Group on Science and Technology for their support in carrying out research work, under the grant PESUIRF/Chemistry-ECC/2020/14 dated 30-09-2020.

References:

- [1] “Critical review on recent developments in conducting polymer nanocomposites for supercapacitors - ScienceDirect.” Accessed: Oct. 24, 2024. [Online]. Available: <https://www.sciencedirect.com/science/article/abs/pii/S0379677923000486>
- [2] L. T. Zegebreale, N. A. Tegegne, and F. G. Hone, “Recent progress in hybrid conducting polymers and metal oxide nanocomposite for room-temperature gas sensor applications: A review,” *Sensors and Actuators A: Physical*, vol. 359, p. 114472, Sep. 2023, doi: 10.1016/j.sna.2023.114472.
- [3] “Conducting polymers prepared by oxidative polymerization: polyaniline - ScienceDirect.” Accessed: Oct. 25, 2024. [Online]. Available: <https://www.sciencedirect.com/science/article/abs/pii/S0079670098000082>
- [4] “Conductive Polymer-Assisted Metal Oxide Hybrid Semiconductors for High-Performance Thin-Film Transistors | ACS Applied Materials & Interfaces.” Accessed: Oct. 25, 2024. [Online]. Available: <https://pubs.acs.org/doi/10.1021/acsami.0c21134>
- [5] “Role of conducting polymer and metal oxide-based hybrids for applications in amperometric sensors and biosensors - ScienceDirect.” Accessed: Oct. 25, 2024. [Online]. Available: <https://www.sciencedirect.com/science/article/abs/pii/S0026265X18318587?via%3Dihub>
- [6] “Rev. Mod. Phys. 60, 781 (1988) - Solitons in conducting polymers.” Accessed: Oct. 25, 2024. [Online]. Available: <https://journals.aps.org/rmp/abstract/10.1103/RevModPhys.60.781>
- [7] “Polarons, bipolarons, and solitons in conducting polymers | Accounts of Chemical Research.” Accessed: Oct. 25, 2024. [Online]. Available: <https://pubs.acs.org/doi/abs/10.1021/ar00118a005>
- [8] N. K and C. Sekhar Rout, “Conducting polymers: a comprehensive review on recent advances in synthesis, properties and applications,” *RSC Advances*, vol. 11, no. 10, pp. 5659–5697, 2021, doi: 10.1039/D0RA07800J.

- [9] “Review on Optical and Electrical Properties of Conducting Polymers - Bajpai - 2016 - Indian Journal of Materials Science - Wiley Online Library.” Accessed: Oct. 25, 2024. [Online]. Available: <https://onlinelibrary.wiley.com/doi/10.1155/2016/5842763>
- [10] “Magnetic and electrical properties of In doped cobalt ferrite nanoparticles | Journal of Applied Physics | AIP Publishing.” Accessed: Oct. 25, 2024. [Online]. Available: <https://pubs.aip.org/aip/jap/article-abstract/112/8/084321/375811/Magnetic-and-electrical-properties-of-In-doped?redirectedFrom=fulltext>
- [11] S. Dabas, M. Chahar, and O. P. Thakur, “Electromagnetic interference shielding properties of CoFe₂O₄/polyaniline/poly(vinylidene fluoride) nanocomposites,” *Materials Chemistry and Physics*, vol. 278, p. 125579, Feb. 2022, doi: 10.1016/j.matchemphys.2021.125579.
- [12] B. Chethan, V. Prasad, S. Mathew, and H. Jan, “Polyaniline/Graphene oxide composite as an Ultra-Sensitive humidity sensor,” *Inorganic Chemistry Communications*, vol. 166, p. 112633, Aug. 2024, doi: 10.1016/j.inoche.2024.112633.
- [13] M. Mishra, A. P. Singh, V. Gupta, A. Chandra, and S. K. Dhawan, “Tunable EMI shielding effectiveness using new exotic carbon: Polymer composites,” *Journal of Alloys and Compounds*, vol. 688, pp. 399–403, Dec. 2016, doi: 10.1016/j.jallcom.2016.07.190.
- [14] “(PDF) The Effect of a Small Amount of Water on the Structure and Electrochemical Properties of Solid-State Synthesized Polyaniline.” Accessed: Oct. 26, 2024. [Online]. Available: https://www.researchgate.net/publication/258684418_The_Effect_of_a_Small_Amount_of_Water_on_the_Structure_and_Electrochemical_Properties_of_Solid-State_Synthesized_Polyaniline
- [15] E. Tanrıverdi, A. ÜZÜMCÜ, H. Kavas, A. Demir Korkmaz, and A. Baykal, “Conductivity Study of Polyaniline-Cobalt Ferrite (PANI-CoFe₂O₄) Nanocomposite,” *Nano-Micro Letters*, vol. 3, pp. 99–107, Jul. 2011, doi: 10.1007/BF03353658.
- [16] N. Maruthi *et al.*, “Polyaniline/V₂O₅ composites for anticorrosion and electromagnetic interference shielding,” *Materials Chemistry and Physics*, vol. 259, p. 124059, Feb. 2021, doi: 10.1016/j.matchemphys.2020.124059.

- [17] M. A. Ahmed, R. M. Khafagy, S. T. Bishay, and N. M. Saleh, "Effective dye removal and water purification using the electric and magnetic $\text{Zn}_{0.5}\text{Co}_{0.5}\text{Al}_{0.5}\text{Fe}_{1.46}\text{La}_{0.04}\text{O}_4$ /polymer core-shell nanocomposites," *Journal of Alloys and Compounds*, vol. 578, pp. 121–131, Nov. 2013, doi: 10.1016/j.jallcom.2013.04.182.
- [18] C. Shekhar Joshi, R. C. Srivastava, and A. Joshi, "Polyaniline/Manganese-Cobalt ferrite nanocomposite as an efficient material for crystal violet dye degradation under sunlight irradiation," *Materials Today: Proceedings*, May 2023, doi: 10.1016/j.matpr.2023.04.462.
- [19] S. S. Menon, M. Thomas, and M. T. Ramesan, "Synthesis, characterization, gas sensing, and electrical property evaluation of polyaniline/copper-alumina nanocomposites," *Polymer Composites*, vol. 41, no. 3, pp. 900–910, 2020, doi: 10.1002/pc.25421.
- [20] B. Ünal, "The Electrical Properties of Polyaniline (PANI)- $\text{Co}_{0.5}\text{Mn}_{0.5}\text{Fe}_2\text{O}_4$ Nanocomposite," *Journal of Inorganic and Organometallic Polymers and Materials*, Jan. 2013, Accessed: Oct. 26, 2024. [Online]. Available: https://www.academia.edu/106413187/The_Electrical_Properties_of_Polyaniline_PANI_Co0_5Mn0_5Fe2O4_Nanocomposite
- [21] S. Naseem, "Synthesis of Polyaniline/ Fe_2O_3 Nanocomposites and Study of their Structural and Electrical Properties", Accessed: Oct. 26, 2024. [Online]. Available: https://www.academia.edu/33417973/Synthesis_of_Polyaniline_%CE%B3_Fe_2_O_3_Nanocomposites_and_Study_of_their_Structural_and_Electrical_Properties
- [22] "Nanoclay-based conductive and electromagnetic interference shielding properties of silver-decorated polyaniline and its nanocomposites - Materials Advances (RSC Publishing)." Accessed: Oct. 25, 2024. [Online]. Available: <https://pubs.rsc.org/en/content/articlelanding/2023/ma/d3ma00393k>
- [23] S. B. Aziz, A. Marf, E. Dannoun, M. Brza, and R. Abdullah, "The Study of the Degree of Crystallinity, Electrical Equivalent Circuit, and Dielectric Properties of Polyvinyl Alcohol (PVA)-Based Biopolymer Electrolytes," *Polymers*, vol. 12, Sep. 2020, doi: 10.3390/polym12102184.

- [24] “Interfacial Polarization-Induced Loss Mechanisms in Polypropylene/BaTiO₃ Nanocomposite Dielectrics | Chemistry of Materials.” Accessed: Oct. 25, 2024. [Online]. Available: <https://pubs.acs.org/doi/abs/10.1021/acs.chemmater.6b01383>
- [25] A. Kausar and I. Ahmad, “Conducting Polymer Nanocomposites for Electromagnetic Interference Shielding—Radical Developments,” *Journal of Composites Science*, vol. 7, p. 240, Jun. 2023, doi: 10.3390/jcs7060240.
- [26] “Progressive Review of Functional Nanomaterials-Based Polymer Nanocomposites for Efficient EMI Shielding.” Accessed: Oct. 26, 2024. [Online]. Available: <https://www.mdpi.com/2504-477X/7/2/77>
- [27] “(PDF) Electromagnetic Interference Impacts on Electronic Systems and Regulations.” Accessed: Oct. 26, 2024. [Online]. Available: https://www.researchgate.net/publication/377181966_Electromagnetic_Interference_Impacts_on_Electronic_Systems_and_Regulations
- [28] “Superflexible Interconnected Graphene Network Nanocomposites for High-Performance Electromagnetic Interference Shielding | ACS Omega.” Accessed: Oct. 26, 2024. [Online]. Available: <https://pubs.acs.org/doi/10.1021/acsomega.8b00432>
- [29] “Polymer Nanocomposites for Electromagnetic Interference Shielding...: Ingenta Connect.” Accessed: Oct. 26, 2024. [Online]. Available: <https://www.ingentaconnect.com/content/asp/jnn/2018/00000018/00000011/art00055;jsessionid=w0dn349nrf3i.x-ic-live-03>
- [30] “Chemically reduced versus photo-reduced clay-Ag-polypyrrole ternary nanocomposites: Comparing thermal, optical, electrical and electromagnetic shielding properties | CoLab.” Accessed: Oct. 26, 2024. [Online]. Available: <https://colab.ws/articles/10.1016%2Fj.materresbull.2016.05.024>
- [31] “Preparation of silver-plated polyimide fabric initiated by polyaniline with electromagnetic shielding properties - Dan Yu, Yu Wang, Tianqi Hao, Wei Wang, Baojiang Liu, 2018.” Accessed: Oct. 26, 2024. [Online]. Available: <https://journals.sagepub.com/doi/full/10.1177/1528083717692592>

- [32] S. Manjunatha, T. Machappa, Y. T. Ravikiran, B. Chethan, and A. Sunilkumar, "Polyaniline based stable humidity sensor operable at room temperature," *Physica B: Condensed Matter*, vol. 561, pp. 170–178, May 2019, doi: 10.1016/j.physb.2019.02.063.
- [33] "Humidity sensing properties of poly-vanadium-titanium acid combined with polyaniline grown in situ by electrochemical polymerization - ScienceDirect." Accessed: Oct. 25, 2024. [Online]. Available: <https://www.sciencedirect.com/science/article/abs/pii/S0925400518309110?via%3Dihub>
- [34] "Chemisorption and Physisorption of Water Vapors on the Surface of Lithium-Substituted Cobalt Ferrite Nanoparticles | ACS Omega." Accessed: Oct. 25, 2024. [Online]. Available: <https://pubs.acs.org/doi/10.1021/acsomega.0c04784>
- [35] "Full article: Humidity-sensing properties of conducting polypyrrole-silver nanocomposites." Accessed: Oct. 25, 2024. [Online]. Available: <https://www.tandfonline.com/doi/full/10.1080/17458080802512494>
- [36] "Grotthuss mechanism." Accessed: Oct. 25, 2024. [Online]. Available: <https://water.lsbu.ac.uk/water/grotthuss.html#alt>
- [37] L. Kabir, A. R. Mandal, and S. K. Mandal, "Humidity-sensing properties of conducting polypyrrole-silver nanocomposites," *Journal of Experimental Nanoscience*, vol. 3, no. 4, pp. 297–305, Dec. 2008, doi: 10.1080/17458080802512494.

Transport properties and EMI SE studies of Silver decorated Polyaniline-Banana carbon ternary nanocomposites

¹K. R. Hemantha Kumar*, ²M. Revanasiddappa,
³S. Manjunatha, ⁴Y. T. Ravikiran, ⁵S.B. Naidu Krishna,
⁶V. Srinivasa Murthy

^{1,6}*Department of Chemistry, School of Engineering,
Dayananda Sagar University,
Bangalore – 560068, India*

²*Department of Chemistry,
PES University, Electronic city campus,
Bangalore, 560100, India*

³*Department of Physics,
Kishkinda University,
Ballari, 583104, India*

⁴*Department of Physics,
Government Science College,
Holalkere, 577526, India*

⁵*Institute for Water and Wastewater Technology,
Durban University of Technology,
Durban-4000, South Africa.*

*E-mail: hemanthdhanya@gmail.com, and vsmurthy-chem@dsu.edu.in

Abstract

EMI shielding effectiveness plays a vital role in ensuring the reliability and performance of electronic devices in a highly packed electromagnetic environment. In this regard, conducting polymer composites have emerged as potential candidates to mitigate EMI. Natural ingredients like green tea extract and banana peels were used in the synthesis of Silver-PANI-Banana carbon (Ag-PANI/BC) ternary nano composites. In-situ chemical polymerization method was adopted to synthesize the varied composition of banana carbon (BC) in the PANI matrix. FTIR bands evidenced the formation of composites. Amorphous nature of PANI and Ag-PANI, semicrystalline form of Ag-PANI/BC ternary composite was confirmed from XRD studies. SEM studies of Ag-PANI-BC (8%) composite revealed the granular structures with inhomogeneous surfaces. AC conductivity of the composites found to be 10^{-6} to 10^{-4} S/cm measured in the frequency

range 20 Hz to 10 MHz. Interestingly, 6 and 8 wt.% composites have exhibited excellent EMI shielding effectiveness of around 25 to 26 dB measured in s-band which suits pertinent practical applications in electronic systems functioning in frequency range (2.1 to 3 GHz).

Introduction

Conducting polymers have seen fascinating applications in the field of electronics and electrical appliances as they can easily combine their chemical and mechanical properties with the electrical properties of metals and semiconducting materials [1,2]. PANI (polyaniline) a prominent conducting polymer due to its ease of synthesis, processibility, economic viability and environmental stability have found many applications in sensors, opto-electronic and electrochromic devices [3]. Further, chemical stability and mechanical strength were found via synergistic effects when these conducting polymer constituents are assorted with metals, metal oxides, organic compounds, non-metals, and other polymers which were prepared by physical mixing/blending, chemical processes, and other electrochemical pathways [4]. Interestingly, upon embedding PANI with silver nano particles, it has exhibited a remarkably enhanced electrical and electronic properties [5]. In addition, Ag-PANI composite has shown effective application as antibacterial agent, and synergetic effectiveness over traditional antibiotic reagents in the broad range of pathogenic bacteria [6]. With emerging novel materials, PANI was incorporated with carbon nanotubes, graphene oxide, graphene and graphene analogues [7,8], to note TMDs (Transition metal dichalcogenides) for example WS₂ [9] and MoS₂ has shown promising utility in opto-electronics, CO₂ reducers, H₂ evolution and gas sensing areas [10,11] have also been composited with PANI. Among the varieties of applications of these intrinsic polymer composites, EMI (Electromagnetic Interference) shielding has emerged as one of the promising areas as far as their applications are concerned [12]. EMI shielding effectiveness in S band (2-4 GHz) has garnered its significance in radar, wireless sensors, IOT devices, aerospace & defense, medical devices wearable and automotive electronics [13,14].

Very recently, an excellent application of carbon incorporated with conducting polymer research was reported [12], carbon being most essential and common element present in environment [15]. Research on carbon composite materials has gained special emphasis on adopting materials for greener technology, using waste material from natural sources and eventually advancing such materials for electronic

applications [16]. In this regard, we have extracted the carbon from the banana peels, to realize its potential in EMISE. To enhance the conducting behavior of the composite, silver extracted from green tea has been incorporated to the composite. Recently, we have studied such ternary composites of conducting polymers to increase the conductivity [17]. Banana peel reported here, is cost effective and a highly efficient, as well as eco-friendly method to produce carbon. Banana peels essentially contain organic components which includes, starch, lignin, cellulose proteins, and pectin. It is also reported that the banana peels are efficient adsorbents to remove organic and inorganic pollutants, this is because of range of functional groups present in it, along with the well-established internal microporosity and higher surface to volume ratio [18]. In our earlier studies, polypyrrole - banana carbon composite prepared via green chemistry approach has shown an excellent corrosion resistance and effective electromagnetic shielding properties [12].

Hence, in view of these excellent properties of this novel binary composite, in this present study, we have explored the AC conductivity studies and EMI shielding effectiveness of the composites prepared via in situ chemical polymerization method, in which both the silver and the carbon are extracted using soft green chemistry. As obtained ternary composite with varying wt.% of banana carbon were characterized with the help of XRD, FT-IR and SEM techniques. AC conductivity measurements and EMI shielding properties of the composites were also studied to explore their pertinent practical applicability for electrical and electronic devices.

Experimental

Materials and Methods

Aniline ($C_6H_5NH_2$) monomer and concentrated HCl (hydrochloric acid) were obtained from S.D. Fine Chemicals, Mumbai, India. Ammonium persulphate was procured from Sigma-Aldrich, Bengaluru, India. Aniline was doubly distilled before taking it for use in the synthesis of the composites. All through the synthesis of PANI and Ag-PANI-BC composites, distilled water was used. Banana carbon (BC) was prepared by initially drying banana peels at room temperature (~ 300 K), followed by cutting them in to smaller pieces. These pieces were burned by placing them on the iron pan covered with a lid to obtain a blackish powder. Finally, it was ground to a fine powder using pestle and mortar, then used for the further synthesis of the composites.

Preparation of banana carbon powder:

Banana peels were kept for drying at room temperature (300 K), upon complete drying, and then chopped into smaller pieces. On the top of iron pan, banana peels were placed and burned under air by closing the lid until obtaining a black powder. Fig.1 depicts preparation of banana carbon (BC) powder.

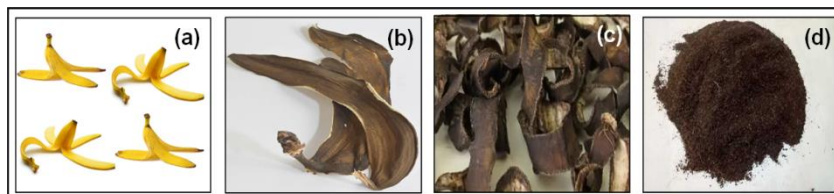


Figure.1, Schematic diagram for preparation of banana carbon from banana peels, (a) banana peels, (b) banana peels after drying at 300 K, (c) chopped banana peels, and (d) black banana carbon powder.

Preparation of Ag-PANI-BC composites:

Composites were prepared using Aniline (2M) dissolved in 2N HCl in a beaker. 0.1M of $(\text{NH}_4)_2\text{S}_2\text{O}_8$ with green tea extract and AgNO_3 solutions were added separately dropwise along the sides of the beaker. Then known concentrations of BC (2%, 4%, 6%, 8% & 10%) in to the above solution in a controlled flow to start oxidation reaction under cooling. Obtained product after the in-situ polymerization was allowed to dry in an oven at 60 °C until to reach a constant weight and then powdered using a pestle-mortar. For EMI shielding measurements, Ag-PANI-BC (6%) and (8%) composites were mixed with known concentration of aqueous PVA solution separately to prepare the substrate-free films of the said composites as shown in Fig. 2.

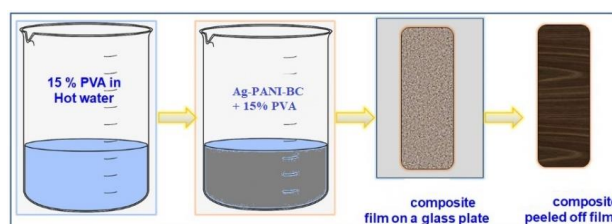


Figure 2, Preparation of Ag-PANI-BC composites thin films for EMI-SE measurements.

Characterization

Fourier-transform infrared spectroscopic (FTIR) data was obtained using Nicolet 750 FTIR instrument in the range 250 - 4000 cm^{-1} . Surface morphology of the composite was analyzed with the assistance of scanning electron microscope (SEM) of make Zeiss Ultra 60 instrument which uses an aluminium tape to load samples. Energy dispersive X ray spectroscopy (EDX) was helpful to gather elemental composition of the prepared ternary composites. XRD spectra of PANI, BC and Ag-PANI-BC composite were performed in the range $2\theta = 10^\circ$ to 80° by Siemens D-5000 powder XRD (Germany) with Cu $K\alpha$ radiation ($\lambda=1.54 \text{ \AA}$).

AC conductivity measurements:

Before measuring AC conductivity readings, samples were processed with the help of pestle and mortar to get fine granular powder. Silver doped PANI pellet and Ag-PANI/BC composite pellets measuring 13.4 mm diameter and 0.4 mm thickness were obtained with the help of 7-ton pressure in a hydraulic pressing machine. AC readings were collected with the frequency range 20 Hz - 10 MHz, data were obtained with instrument model Hioki 3532-50 LCR meter (Japan) built with a programmable computer.

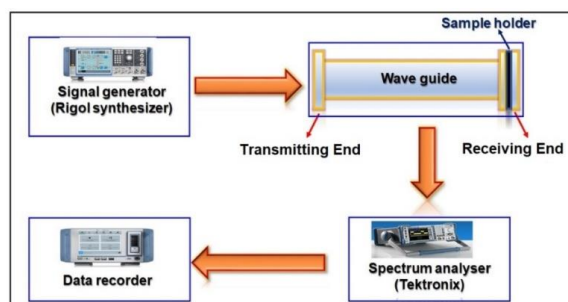


Figure 3, Schematic diagram of the instrument setup for measuring electromagnetic interference shielding effectiveness

EMI shielding measurements:

EMI shielding effectiveness (EMI SE) of ternary composites containing BC (6%) and BC (8%) were measured in a frequency range 2.1 - 3 GHz (S band) using the lab fabricated experimental set up as shown in Fig. 3. The signal generator (of make RIGOL) is connected to input of a wave guide and the output is fed to a Tektronix spectrum analyzer records the residual frequency. This frequency has been recorded through a computer interfaced data recorder.

EMI shielding effectiveness (in dB) of the sample can be measured by logarithmic ratio of input power to the out power of the signal. Mathematically, EMI shielding effectiveness is a negative quantity as the output power is always less than the input power. When a microwave radiation is incident on the EMI material, reflection, absorption, and transmission of the signal occurs. Hence, the effectiveness of the shield is logically due to the reflection and the absorption parts which can be expressed mathematically as in Eq. 1. [19]

$$SE_t = SE_r + SE_a = 10 \log \left(\frac{P_t}{P_i} \right) \quad (1)$$

Results and Discussion

FTIR Studies:

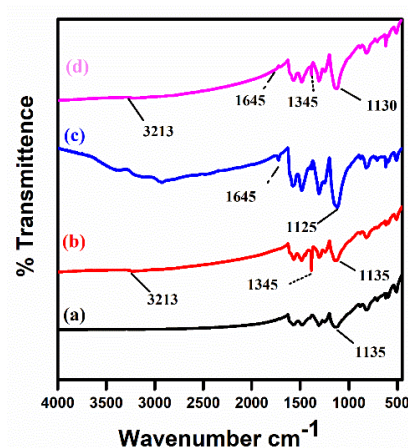


Figure 4, FTIR spectra of (a) PANI, (b) Ag-PANI, (c) BC and (d) Ag-PANI-BC (8%) composite.

FTIR spectral absorption band of PANI is represented in Fig.4a, the distinctive peak at 1135 cm^{-1} is owing to aromatic C-N tertiary vibrations and band at 1301 cm^{-1} is corresponding to primary C-N and secondary vibrations [20]. Broad band around $3450 - 3200 \text{ cm}^{-1}$ is due to NH stretching vibrations. Bands at 1567 and 1478 cm^{-1} are assigned to the C=C stretching in quinoid ring, and C=C stretching in benzene ring respectively. Also, the band at 1242 cm^{-1} may be assigned for the C-N stretching of the benzenoid ring. The para substituted aromatic ring specific vibrations can be observed at 810 cm^{-1} and can be ascribed to the out-of-plane bending vibrations. The above frequency bands are in par with earlier reported values [21].

Fig. 4b, depicts IR absorption spectrum of Silver-PANI (Ag-PANI), in which absorption peak around 1305 cm^{-1} is due to polaronic form of PANI. The signal at 1245 cm^{-1} is assigned to the vibration of PANI in protonated linkage, upon silver particles doping in to the PANI matrix and these peaks shifts to 1230 cm^{-1} . As silver ions are reduced to silver, $-\text{NH}-$ (amine) functional group of PANI backbone chain changes to $-\text{N}=$ (imine) by oxidation [22]. Presence of silver nano particles in the composite matrix was clearly defined with the bands 494 and 422 cm^{-1} .

Fig.4c, depicts FTIR spectrum of BC, band at 1125 cm^{-1} suggest C-C absorption, the band at 1645 cm^{-1} indicate C=C stretching vibrations suggesting presence of other allotropes of carbon. Fig. 4d, shows signature peaks of PANI and the band at 3213 cm^{-1} suggesting NH stretching vibrations of PANI, band at 1645 cm^{-1} was observed with minor variation in its absorption intensity, indicating the presence of BC in the composite.

XRD Studies:

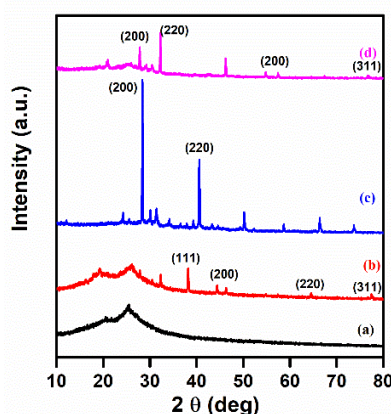


Figure 5 XRD pattern of (a) PANI, (b) Ag-PANI, (c) BC and (d) Ag-PANI-BC (8%).

XRD spectrum of Polyaniline, Silver-PANI (Ag-PANI), BC and Silver-PANI-BC ternary composites are shown in Fig. 5. Fig 5a, depicts the X ray diffraction (XRD) spectral information for polyaniline (PANI), which clearly evidences two broad peaks at 21.3° and 25.5° , they can be attributed to the lattice periodicity in the direction along the PANI chains which are normal to the polymer chains[21]. These two broad peaks of polyaniline represent the chain ordering to a short range. Fig. 5b bear diffraction spectral pattern of Silver-PANI (Ag-PANI) providing the Bragg reflections at 19.2° and 26.1° which are attributed to organization of periodicities along the

backbone chain of PANI and orthogonal to the polymer chains, respectively. Other three diffraction peaks at 38.1° , 44.3° and 64.5° are assigned as (111), (200) and (220) Bragg reflection planes related to face centered cubic (fcc) structure of silver. These peaks of silver have relatively low intensity to those of PANI chains [22]. XRD patterns of the synthesized banana carbon (BC, Fig. 5c) has been matched with the PDF card No. 000411476 corresponding to potassium chloride (KCl), with space group (Pm-3m), revealing its crystalline structure. XRD of BC shows characteristic peaks at 28.3° related to (200) and 40.6° corresponding to (220) planes [16]. Also, a small peak at 24.2° corresponding to carbon (002) plane, indicating the presence of amorphous carbon in the BC sample. XRD pattern of Ag-PANI-BC ternary composites (Fig. 5d) displayed sharp peaks at $2\theta = 29^\circ$ which showed the incorporation of BC in the composite. Characteristic peaks corresponding to Ag-PANI and BC is evidenced in Ag-PANI-BC composite, which clearly reveals the formation of the composite. Peaks of BC which are seen in the composite are with reduced intensity, showing its crystalline nature and hence deducing that the banana carbon has been entrenched in to the matrix of Silver-Polyaniline polymer chains. It is imperative that, with the increase in wt.% of BC in the composite, their crystalline nature too found to increase. Thus, supporting the evidence for the crystallinity of the synthesized tertiary composites.

SEM and EDX studies:

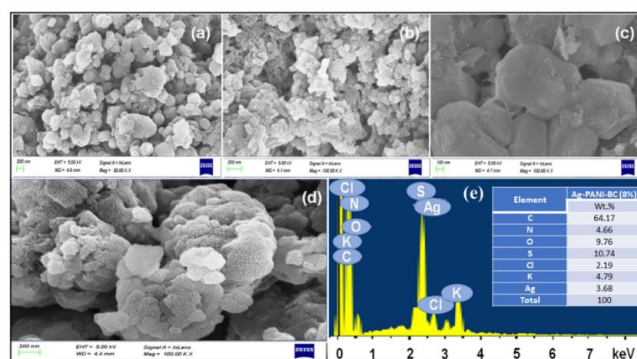


Figure 6, Scanning electron micrographs of (a) PANI, (b) Ag-PANI, (c) BC and (d) Ag-PANI-BC (8%) and (e) EDX spectrum of Ag-PANI-BC (8%).

Fig. 6 shows the SEM and EDX images of the sample. In Fig.6a, depicts the uniform distribution of granular structures of PANI with

average size in the 100 - 500 nm range [23]. Fig. 6b, shows Ag-PANI particles in granular structures of comparatively smaller sizes around 50 to 300 nm. Fig. 6c, shows a SEM image of BC, wherein flakes like structures with sizes in the range 200 to 800 nm with uneven surface morphology. Fig. 6d, represents morphology of Ag-PANI-BC (8%), wherein granular shaped uneven structures with nonuniform surfaces of sizes in the range 90 - 180 nm were observed. Incorporation of BC in the composite is evident from the surface morphology of the composite.

Fig. 6e, shows EDX (Energy dispersive X-ray spectrum, revealing carbon, nitrogen, and chlorine peaks of the polymer PANI and BC in the anticipated proportion. Thus, these peaks confirm the ternary composite formation and the elemental composition in it was found to be in accordance with the components of known composition taken during the preparation of the ternary composite Ag-PANI-BC (8 %). The particulars of the elemental constituents found by EDX is listed in inset table and it clearly evidences the incorporation of BC in the composites.

AC Conductivity studies:

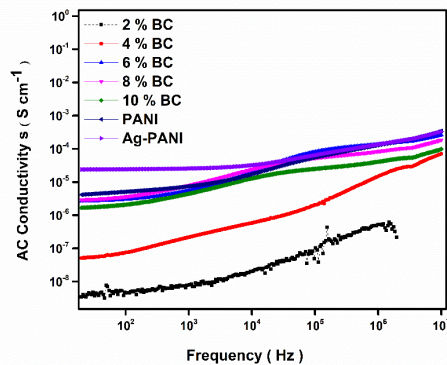


Figure 7, AC Conductivity measurements with variation of applied frequency

AC conductivity in the disordered materials can be obtained by using the equation 1

$\sigma(f) = \sigma'(f) - i\sigma''(f)$ Eq.1 $\sigma'(f)$ is for real AC Conductivity part and $\sigma''(f)$ represents the imaginary conductivity of the composites. Measured AC conductivity results are shown in Figure.7. AC conductivity measurements with varied frequency from 20 Hz to 10 MHz. Conductivity curves for composites 2 to 6 % and 10 % show slight increase in conductivity with the applied frequency, this behavior is

ascribed may be due to lower surface charge of composite suppressed by carbon present within the ternary composite and the noticeable conducting behavior exhibited is due to the presence of Silver (Ag) and Polyaniline (PANI) in the composite which is also very much closely correlating with the conductivity values PANI and Ag-PANI as such. In addition, carbon is neither creating charge carriers nor possesses conjugation essential for conducting behavior of the composite. There are no significant surface charge carriers with BC doping in the composites suggesting no polaron hopping frequency is noticed and polarons and bipolarons exists in the composites are mainly constituted from PANI which can clearly observed with very narrow variation of conductivity values of PANI /Ag-PANI with that of BC composites. For transfer of the charges, applied frequency is insufficient to surpass the carbon's insulating behavior. As the frequency increases it aids the ion movement in the composite and enhancing surface charge carrier capacity leading to improve ion mobility and better conduction.

It is important to note different allotropes of carbon, synthesis methodology, concentration, all these factors play a significant role in the conductivity behavior of the composites. It is well understood from the conductivity plots that, addition of BC in to PANI/Ag-PANI framework is not uniformly distributed, thus causing bad conducting network, hopping, barrier inhibition is ineffective, which in turn leading to the poorer interactions between polymer and BC resulting in the weaker movement of carriers and yielding a low electrical conductivity.

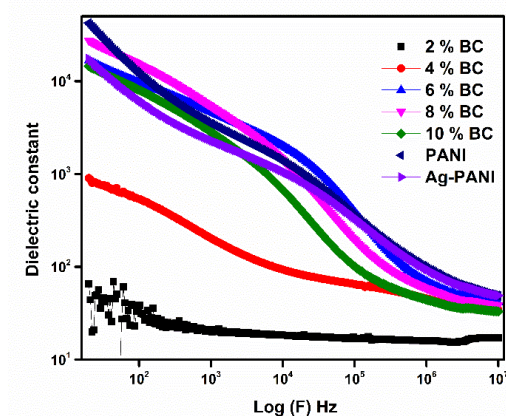


Figure 8, Variation of dielectric constant as a function of applied frequency for 2,4,6,8, and 10 % Ag-PANI/BanC composites

Dielectric constant and dielectric tangent loss of the composites were measured as a function of applied frequency obtained for all the varied % of BC. Figure 8, demonstrates the change in dielectric constant vs. applied AC frequencies for Ag-PANI/BC composites. Dielectric constant was found to be in the order of 10^4 at lower frequency for composites of concentration 4 %, 6 %, and 10%, the value found to decrease with increasing frequency. On the other hand, 8 % composite has shown 10^3 at 20 Hz and exhibiting very slow decreasing trend reaching to 10^2 at 10 MHz. This linear fashion of gradually decreasing dielectric constant, demonstrating the characteristic dielectric properties of the conducting polymer nano composites, which is in accordance with the recent studies reported [24]. Electrode polarization and space charge polarization can be attributed with greater permittivity values at lower applied frequencies [25]. Decrease in dielectric constant as frequency increases can be explained by Maxwell–Wagner–Sillars polarization effect [26]. Change in dielectric constant vs. applied frequencies can be detailed on the base of charge carrier's hopping frequency. As the hopping frequency of the charge carriers follows frequency of the applied field, which marks in larger dielectric constant values. In contrast, at higher applied frequencies, applied frequency of the AC field lags due to hopping frequency, which makes lower dielectric constant values due to the random dipolar orientation [27]. Noticeably, 2% composite shown anomalous behavior over other and plateau values across all the frequency range under the study.

Tangent loss vs. the increase in applied frequency for the ternary composites are depicted in Figure 9. All varied wt.% composites exhibited abnormal dielectric behavior attributed by dielectric relaxation peaks, which can be more understood by Rezlescu model [29].

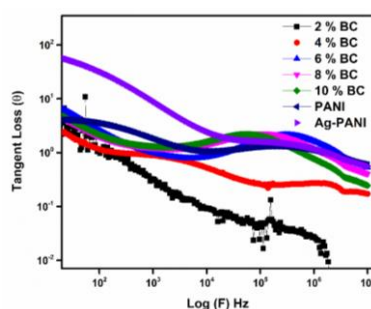


Figure 9, Variation of Tan θ as a function of frequency for Ag-PANI/BanC composites with different concentration of BanC of 2, 4, 6, 8 and 10 %

Also, this kind of distinctive dielectric nature be described by the advance of small polarons which are important for the charge polarization [30]. Upon resonance phenomena occurs with externally applied frequencies, it induces the formation of dielectric relaxation peaks [31]. In addition, the results of $\tan \theta$ are larger at lower applied frequencies which indicate the relaxation peaks. Except 2%, all other composites demonstrated linear fashion of decreasing trend of $\tan \theta$ as applied frequency increases. Whereas, 2 % composite shown ambiguous behavior around 20 Hz frequency then followed by the rapid decrease of loss with rise in applied frequency. Higher $\tan \theta$ values at lower applied frequencies will be useful in designing devices functioning in medium frequencies.

Higher dielectric loss values noted at the lower applied frequencies in all the different wt.% composites can be interrelated to the loss of DC conduction. Thus, the obtained results have expanded implication with that of the tendencies noted with the decrease in dopant concentration.

The difference of the real electrical modulus (M') with function of $\log(F)$ of the composite system are shown in Figure 10. As we can notice from figure, the results of (M') can be fragmented in to two segments. The first segment corresponds to 2, and 4% composites show flattened pattern ascribing to very narrow changes in the M' values at applied frequency range, suggesting that the electrode polarization to M' make a constant contribution to the nanocomposite ternary materials. The second segment corresponding to 6, 8 and 10% composite, there is a linear increase of (M') with applied frequency. Above data can be evaluated in accordance to the conduction phenomenon linked to the short-range mobility of charge carriers (especially ions). Electrical modulus behavior, the complex permittivity (ϵ^*) related to the electrical modulus (M' and M'') is obtained using reported formulae [32-35]

Figure 10(b), depicts the results for the imaginary part (M'') of the electrical modulus with variation of applied frequency. The lower imaginary (M'') values for 6, 8 and 10 % composite at the lower applied frequency are the sign of ions transport. Ver much resolved relaxation peaks are originated for these curves ascribed to the imperfections within the crystalline phase. It is to note that, the M'' peak intensity is increasing with increase of $\log(F)$ ascribed by BC which plays to the relaxation process. In contrast, other two composites 2 and 4 % are contradictory to observation obtained for 6%, 8%, and 10%.

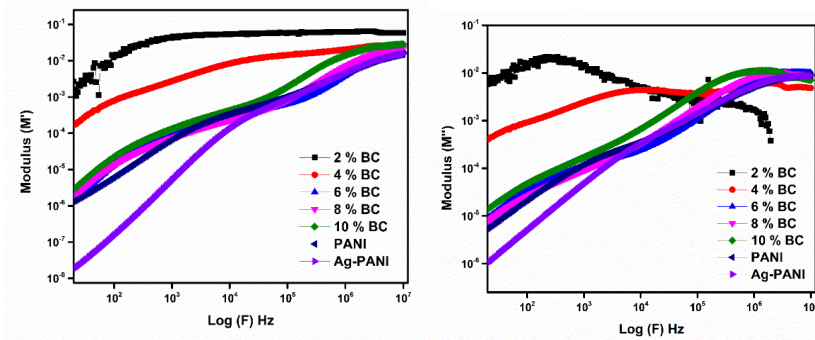


Figure 10(a)& (b) the electric modulus M' & M'' of 2,4,6,8 and 10 % Ag-PANI/BC composites as a function of applied frequency in the range from 20 Hz to 10 MHz

EMI Shielding effectiveness:

It is well known from reported literature, with the basis of EMI shielding theory SE is directly proportional to electrical conductivity of the nanocomposites [36]. Hence Ag-PANI-BC (6 and 8%) have shown better conductivities compared to other composites. EMI SE of Silver-Polyaniline-BC, Ag-PANI-BC-6 % and with 8% exhibited a good shielding effectiveness of around 25 and 26 dB in the frequency range of 2.1 GHz to 3.0 GHz (S band) as shown in Figure 11. This kind of EMI SE is useful for the protection of the electronic gadgets working in S band as reported in our earlier literature [37]. Shielding mechanism in case of PANI is primarily due to the orientational polarization and the space charge polarization. In any intrinsic conducting polymers like PANI has got conjugated double bonds in their polymer chains. These conjugated polymers contain free charges and the bound charges which involve in the transport properties. Polarons/ bipolarons account for free charges which move along the polymer chains.

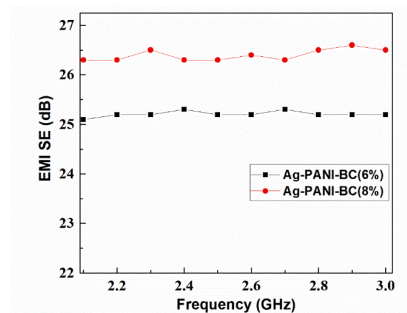


Figure 11. Frequency versus EMI SE of Ag-PANI, BC and Ag-PANI-BC composites of 6 & 8 %

Dipoles in PANI account for the bound charges possessing limited mobility contributing to the strong polarization [38]. When the samples of Ag decorated PANI composited with carbon obtained from the banana peel subjected to EMI shielding effectiveness studies do exhibit the similar charge transfer mechanism. Ag-PANI-BC (6 and 8%) composites exhibited a good shielding effectiveness involving such space-charge polarization effects as in PANI [12].

Conclusions

Ag-PANI-BC composites were prepared using in situ polymerization method. In the prepared composites the fillers Ag and BC were successfully extracted using green chemistry approach. FTIR studies support the incorporation of BC in the composite. X-Ray diffraction pattern obtained for the composite was clearly evidences the retention of crystallinity nature of BC which encompasses the well interfacial arrangement of the BC in Ag-PANI conducting polymer chains. Surface morphology information obtained with the help of SEM analysis supports fine unification of BC in the nano composite. EDX analysis, evidences the presence of carbon extracted from the banana peel in the ternary composite. Conductivity data revealed the enhancement of conductivity in the composites. Upon gathering AC conductivity data, it clearly suggests the composite revealed and undoubtedly comprehends the power law well in alignment with the applied frequency. 2% and 4% composites shown very linear increase of conductivity with the applied frequency. Whereas, 6%, 8% and 10% composites conductivity are independent of applied frequency and higher values which are close to Ag-PANI exhibited clearly suggesting the effective concentration. Though addition of BanC is not helpful in enhancing the conductivity of the ternary composites, these can be used for insulating application involving electrical devices. EMI SE obtained are very well in correlation with conductivity measurements. Ag-PANI-BC composites (6 and 8 wt.%) exhibiting good shielding effectiveness of around 26 dB in S-band can have potential applications. Further, the authors wish to explore this material to other bands such as C-band, X-band and Ku bands of the electromagnetic spectrum having technological implications.

Acknowledgement

The authors are thankful to of PES university management, Electronic city campus, Bangalore, and Vision group -science and technology, to support in carry out the research work, PESUIRF/Chemistry-ECC/2020/14 dated 30-09-2020. Author, Hemantha Kumar K R wish

to acknowledge Syngene International Limited for providing permission to do the research.

References

- [1] H.R. Mahadevaswamy, M. Revanasiddappa, and S. Manjunatha, Chem. Pap. 78,1435-1
- [2] B.M.B.B. Patel, M. Revanasiddappa, D.R. Rangaswamy, S. Manjunatha, and Y.T. Ravikiran, Mater. Today. Proc. 49, (2021), 2253–2259. <https://doi.org/10.1016/j.matpr.2021.09.337>.
- [3] V. Babel, and B.L. Hiran, Polym. Compos. 42 (2021) 3142–3157. <https://doi.org/10.1002/pc.26048>.
- [4] M. Beygisangchin, S.A. Rashid, S. Shafie, A.R. Sadrolhosseini, and H.N. Lim, Polymers (Basel). 13 (2021) 2003. <https://doi.org/10.3390/polym13122003>.
- [5] K. Vinay, M. Revanasiddappa, S. Manjunatha, K. Shivakumar, and Y.T. Ravikiran, Mater. Res. Express. 6 (2019) 104003.
- [6] S.G. Mohammad, D.E. Abulyazied, and S.M. Ahmed, Desalin. Water Treat. 170 (2019) 24694. <https://doi.org/10.5004/dwt.2019.24694>.
- [7] P. Vishnoi, S. Rajesh, S. Manjunatha, A. Bandyopadhyay, M. Barua, S.K. Pati, and C.N.R. Rao, ChemPhysChem. (2017). <https://doi.org/10.1002/cphc.201700789>.
- [8] S. Manjunatha, B. Chethan, Y.T. Ravikiran, and T. Machappa, AIP Conf. Proc. 1953 (2018) 030096. <https://doi.org/10.1063/1.5032431>.
- [9] S. Manjunatha, S. Rajesh, P. Vishnoi, and C.N.R. Rao, J. Mater. Res. 32 (2017) 2984–2992. <https://doi.org/10.1557/jmr.2017.224>.
- [10] S. Manjunatha, T. Machappa, A. Sunilkumar, and Y.T. Ravikiran, J. Mater. Sci. Mater. Electron. 29 (2018) 11581–11590. <https://doi.org/10.1007/s10854-018-9255-1>.
- [11] A. Sunilkumar, S. Manjunatha, T. Machappa, B. Chethan, and Y.T. Ravikiran, Bull. Mater. Sci. 42 (2019) 271. <https://doi.org/10.1007/s12034-019-1955-5>.
- [12] C.K. Madhusudhan, K. Mahendra, N. Raghavendra, and M. Faisal, J. Mater. Sci. Mater. Electron. 13 (2021) 1366–1382.

- <https://doi.org/10.1007/s10854-021-07466-1>.
- [13] A. Sedighi, R.A. Taheri, and M. Montazer, *Ind. Eng. Chem. Res.* 59 (2020) 12774–12783. <https://doi.org/10.1021/acs.iecr.0c02141>.
- [14] N. Maruthi, M. Faisal, and N. Raghavendra, *Synth. Met.* 272 (2021) 116664. <https://doi.org/10.1016/j.synthmet.2020.116664>.
- [15] J. Gómez, M.V. Sulleiro, D. Mantione, and N. Alegret, *Polymers (Basel)*. 13 (2021) 745.
- [16] L. Zheng, B. Sun, S. Mao, S. Zhu, P. Zheng, Y. Zhang, M. Lei, and Y. Zhao, *ACS Appl. Bio Mater.* 1 (2018) 496–501. <https://doi.org/10.1021/acsabm.8b00226>.
- [17] R. Megha, Y.T. Ravikiran, S.C.V. Kumari, H.G.R. Prakash, M. Revanasiddappa, S. Manjunatha, S.G. Dastager, and S. Thomas, *J. Mater. Sci. Mater. Electron.* 31 (2020) 18400–18411. <https://doi.org/10.1007/s10854-020-04386-4>.
- [18] S.G. Mohammad, S.M. Ahmed, A.F.M. Badawi, and D.S. El-Desouki, *J. Appl. Life Sci. Int.* 3 (2015) 77–88. <https://doi.org/10.9734/JALSI/2015/16652>.
- [19] M. Mishra, A.P. Singh, V. Gupta, A. Chandra, and S.K. Dhawan, *J. Alloys Compd.* 688 (2016) 399–403. <https://doi.org/10.1016/j.jallcom.2016.07.190>.
- [20] S. Manjunatha, R. Megha, B. Chethan, M. Prashantkumar, Y.T. Ravikiran, and T. Machappa, *J. Mater. Eng. Perform.* 30 (2021) 1885–1894. <https://doi.org/10.1007/s11665-021-05526-5>.
- [21] S. Manjunatha, T. Machappa, Y.T. Ravikiran, B. Chethan, A. and Sunilkumar, *Phys. B Condens. Matter.* 561 (2019) 170–178. <https://doi.org/10.1016/j.physb.2019.02.063>.
- [22] B. Massoumi, and S. Fathalipour, *Polym. Sci. Ser. A.* 56 (2014) 373–382. <https://doi.org/10.1002/app.39448>.
- [23] L.B. Gunjal, S. Manjunatha, B. Chethan, N.M. Nagabhushana, Y.T. Ravikiran, T. Machappa, and S. Thomas, *MRS Commun.* 13 (2023) 248–255. <https://doi.org/10.1557/s43579-023-00336-3>.
- [24] S. Manjunatha, T. Machappa, A. Sunilkumar, and Y.T. Ravikiran, *J. Mater. Sci.*, 29, 11581 (2018)
- [25] H.M. Kim, C.Y. Lee, and J. Joo, *J. Korean Physical Society*, 36 (6), 371–375, (2000)

- [26] Z.Yua, and C.Angb,Maxwell-Wagner polarization in ceramic composites BaTiO₃-NiO.3ZnO.Fe₂IO₄, J. Appl. Phys. 91(2),(2002)
- [27] S.Sinha,S.K.Chatterjee,J.Ghosh, and A.K.Meikap, Polym.Compo.,38,287 (2017)
- [28]. N. Rezlescu, and E. Rezlescu, Phys. Status Solidi 23, 575 (1974).
- [29]. J.Bao, J.Z.Zhenxing, Y.Longtu and L.Z.Gui, J. Magn. Magn. Mater. 250, 131-137, (2002).
- [30]. I. Sadiq, S.Naseem, M.N.Ashiq, M.A. Khan, S.Niaz , and M.U. Rana, Progress in Natural Science: Materials International,25, 5, 419-424, (2015).
- [31]. V.R. Ramani, B.M. Ramani, A.D. Saparia, D. Dhruv, and J.H. Markna, J. Nano Res, 37,68-73, (2016).
- [32]. T.A. Hanafy, K. Elbanna, and El.S. Sayed, J. Appl Polym Sci,21,3306-13, (2011).
- [33]. P. Maji, P.P. Pande, and R.B. Choudary, Bull. Mater Sci,38,417-24, (2015).
- [34]. N.S.Alghunaim, J.Materials Research and Technology,8, 3596-3602, (2019)
- [35]. M. Rahaman, T. K. Chaki, and D. Khastgir, J. Mater Sci, 46,3989–3999, (2011).
- [36] A. Sunilkumar, S. Manjunatha, R. Yaled Thippeswamy, and S. Thomas, Chem. Pap. (2023). <https://doi.org/10.1007/s11696-023-02828-x>.
- [37] L.L. Wang, B.K. Tay, K.Y. See, Z. Sun, L.K. Tan, and D. Lua, Carbon N. Y. 47 (2009) 1905–1910. <https://doi.org/10.1016/j.carbon.2009.03.033>.
- [38] C.K. Madhusudhan, K. Mahendra, B.S. Madhukar, T.E. Somesh, and M. Faisal, Polym. Sci. Ser. B. 63 (2021) 280–290. <https://doi.org/10.1134/S156009042103009X>.

Adjustable Prosthetic Feet for the Age Group of 5-10 Years

**Khushi H. Sharma¹, Aryan S. Nandgaonkar², Arin A. Thale³
Ankita J. Sartape⁴, Sunny Sarraf⁵, Afzal Ansari⁶**

*^{1, 2, 3, 4, 5, 6} Department of Mechanical Engineering,
Fr. C. Rodrigues Institute of Technology,
Vashi, India.*

Abstract

Traditional prosthetic feet fail to meet the dynamic requirements of active pediatric users with respect to physical and developmental demands and thus experience a huge rate of replacement due to wear, fatigue, and growth. The aim for this new adjustable, high-resilience prosthetic foot prototype is to present an idea specifically to accommodate children in the 5-10 age bracket with rate growth and demands of activity. With advanced 3D printing applied, the design incorporates a strong framework of biocompatible materials that improve modularity and will permit incremental size changes, reducing the replacement interval. The biomechanical flexibility of the design, with respect to load-bearing stability, optimized weight, and user comfort over extended usage cycles, is also given importance.

Initial evaluations have yielded promising outcomes, including but not limited to mechanical robustness, ergonomic comfort, and functional performance under simulated activity. Further refinement of the prototype will be made with close cooperation between pediatric specialists on the advice of experts. This iteration will validate the design's possibility and feasibility for clinical trials and potential utilization in the future.

Introduction

Development of prosthetic devices, especially in children, is crucial for improved mobility and living standards of young amputees. Current solutions frequently fail to accommodate the special requirements of growing children, particularly those related to adjustability, comfort, and durability [1]. Conventional prosthetic feet may need to be replaced several times due to natural growth and high activity levels of young users; hence, adaptable designs will address these specific needs [2][3].

Recent breakthroughs in materials science and additive manufacturing have brought new opportunities in the design of pediatric prosthetics that are not only functional but also cost-effective and customizable [4][5]. The project focuses on the design of an adjustable prosthetic foot for children aged 5-10 years to be able to adapt and feel comfortable through the use of lightweight and biocompatible materials along with 3D printing technology [6]. The paper fills the gap between functionality and affordability by providing a durable solution that grows along with its young users, by exploring innovative design techniques, such as the integration of adjustable mechanisms and improved material choices [7][8].

This research continues established methodologies and recent innovations in prosthetics, using computational modeling and practical testing to ensure reliability and performance under diverse conditions [9]. A multidisciplinary approach will be taken in this study to address both the mechanical and biomechanical challenges inherent in pediatric prosthetic design, ultimately enhancing the independence and overall well-being of children who rely on these devices [10].

Aim and Objective

This prosthetic foot is a totally new concept with versatility and light weight in the design and its uniqueness in the creation basis for the child user belonging to the age group 5-10 years of active lifestyles, functionality, and comfort in adapting themselves toward the changing phases. This could help to improve mobility accompanied by independence with a lot of confidence in users coming from the young group, and thus enable them fully to take part in the activities.

Objectives of project:

A Growth-Incorporating Adjustable Prosthetic Foot: Acceptance is based on recognition that a child grows at the pace where his or her body changes continuously, which calls for the prosthetic foot to be one accommodating growth features in order to be modified periodically without always having to be changed frequently such that there will be sustainment of fit and functionality on the child's side.

Advanced Materials: The prosthetic foot should be made from advanced, durable, and biocompatible materials that would resist the wear and tear associated with an active child's life without irritating or discomforting him or her.

Light Prosthetic Foot for Daily General Living Activities: The structure shall be light so that it can be easy to move around with. Therefore, the comfortability factor will be essential in case the child is to be moving around for long hours in wearing the prosthetic. Thus, for children, it will be all about being comfortable because they will wear the prosthetic for extended periods, and thus, on ergonomic comfort, features are also to be maximized to increase usability.

Use 3D printing to design custom prosthetic feet specifically tailored for the needs of a child: Develop prosthetic feet, specifically with the aid of 3D printing technology, so that every child will have tailored options according to his or her needs and desires. Then it will be fitted and customized precisely so that the design will be an aesthetic part of personal style or personality.

Testing the prosthetic foot in real life performances and designing the final design through iterative processes based on user experience: The prosthetic foot shall be extensively tested in various conditions of daily life to establish its working. User experiences both from children and their care givers shall feed in further development to be assured that at the last stage, not only the prosthetic limbs look functional but could also achieve real life requirements and expectations of a child with his family.

Material Selection and Properties

The major materials used for the development of the adjustable prosthetic feet for the children of 5-10 years are selected based on the factors such as strength, flexibility, weight, and biocompatibility.

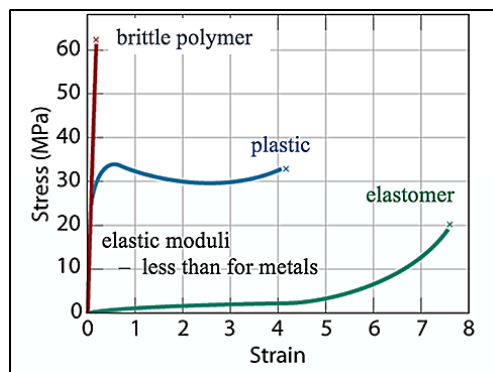


Figure 1. Stress-strain diagram of brittle, plastic, and elastomer polymers (Callister and Rethwisch, 2018) [22].

UV-Curable (SUV) Elastomers: These elastomers were chosen because of excellent elongation at break which can go as high as 1100%, and therefore they are tough enough to use in applications requiring flexibility as well as strength. Mechanical properties can be tuned such that they are tailored according to desired performance. Their curing by UV also allows a very high level of precision in the development of intricate designs that may be suited for prosthetic use, and this is very critical for developing customized prosthetic components for children [21].

Poly Lactic Acid (PLA): PLA is a biodegradable thermoplastic derived from renewable resources, including corn starch. PLA has stiffness and can be easily printed for applications such as 3D printing and biomedical use. Since PLA is biocompatible and available in abundance, it may become an economical way to create strong yet lightweight prosthetic parts. For instance, it is suitable for parts that may have to undergo some amount of stress without breaking [2].

Thermoplastic Polyurethane: This material is known to offer flexibility, impact strength, and comfort. When using prosthetics, for instance, TPU in parts where the prosthetic foot comes into contact with the skin is very cushiony and durable.[6][7]

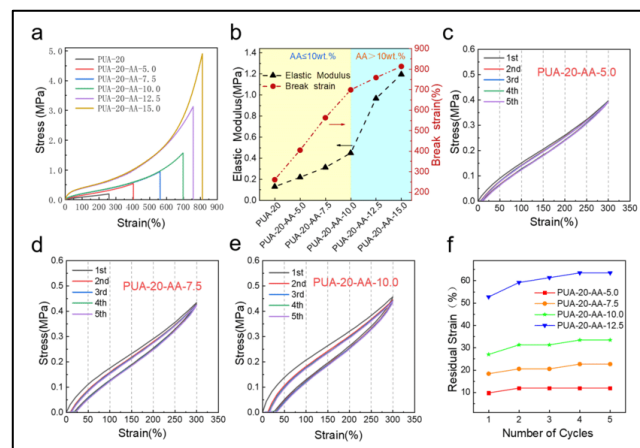


Figure 2. Mechanical Properties of UV-Curable Elastomers [24]

The following table gives a general overview of the significant properties of UV-curable elastomers used for the prosthetic design:

Table 1. Properties of UV curable (SUV) elements.

Property	Typical Range / Max Value	Example Value
Hardness (Shore A)	20 - 90 Shore A	50 Shore A
Tensile Strength (MPa)	5 - 25	12
Elongation at Break (%)	100% - 800%	300%
Young's Modulus (MPa)	0.1 - 10	2
Tear Strength (kN/m)	10 - 50	30
Compression Set (%)	<30%	25
Flexural Modulus (MPa)	0.1 - 10	1.5
Glass Transition Temperature (°C)	-40 to 100	20
Thermal Conductivity (W/(m·K))	0.1 - 0.5	0.3
Coefficient of Thermal Expansion (µm/(m·K))	100 - 300	200
Water Absorption (%)	<5% (after 24 hours)	3
UV Transparency	Transparent to UV light	N/A
Cure Depth (mm)	Up to several mm	3
Curing Time	Seconds to minutes	30 seconds

This table shows that a great deal of mechanical properties is available in UV-curable elastomers. Such high elongation at break for flexibility should accompany tensile strength and tear resistance to ensure the prosthetic foot can endure dynamic loads associated with a child's movements [21][5].

Methods

a. Computer-Aided Design Modeling and Stress Analysis

The preliminary design was based on the design of detailed CAD models for the prosthetic foot and, in particular, was interested in the adjustable attachment mechanism that changes the size of the foot in the length and width directions. The design was visualized and optimized by using a CAD software tool such as SolidWorks or Autodesk Inventor [1].



Figure 3: CAD Design

The figure 3 presents a 3D rendering of a prosthetic foot, showcasing its various components when assembled. The different colors represent distinct parts, each meticulously designed to replicate the function and form of a biological foot [9]. The rendering provides a clear view of the prosthetic's structure, highlighting the intricate connections and mechanical design that allow for mobility and support, essential for individuals relying on such devices for their daily activities.

Stress Analysis

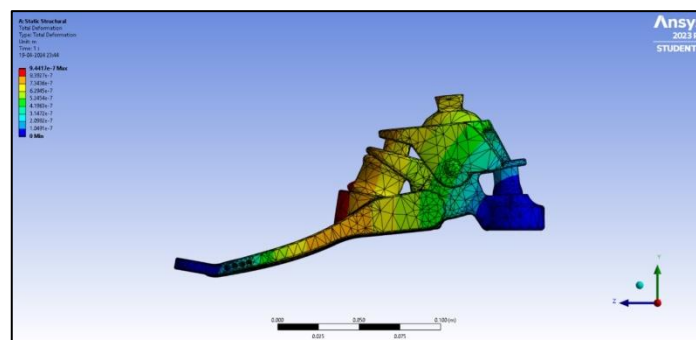


Figure 4: Total deformation

ANSYS was used to carry out finite element analysis stress testing to determine how the materials would perform in actual conditions. The figure 4 shows tests simulated the following:

Total Deformation Analysis: This was a test that determined the degree of deformation resulting from the application of different loads on the prosthetic foot. The aim was that the material should deform to safe limits, thereby averting discomfort and injury to the user [2].

Equivalent (von Mises) Stress Analysis: The experiment would provide the values for stress level under loading and the design team would, therefore be able to crosscheck the optimally stressed condition along with failure areas. More robust, longer-lasting design of a prosthetic has lesser values for equivalent stress [15].

b. 3D Printing

The prototyping was done of the prosthetic foot with the use of 3D printing technology. This incorporated the utilization of PLA as well as TPU in making of the same. This is because each 3D printing will give a distinct prototype suitable to the child's prosthetics. To achieve strength yet flexibility in the created prototype, optimal settings for infill density, layer height, and wall thickness for the utilized printer were chosen. Therefore, adjustments made on these prototypes included detailed adjustments about fit and comfort in support of children's ever-changing needs [11][7].

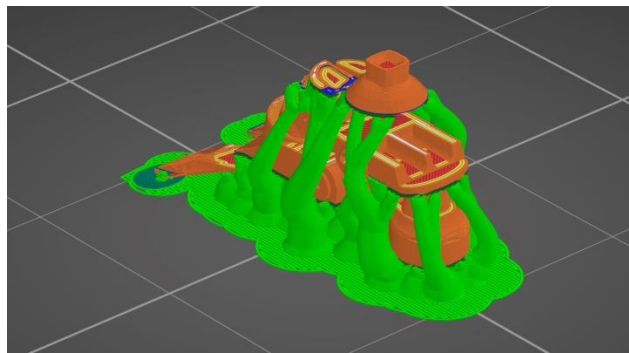


Figure 5: Total deformation 2d

Results

Stress and deformation simulations reveal information on the performance of elastomers, as well as other materials, within the context of a dynamic prosthetic application.

Deformation-According to the FEA results, it was determined that the total deformation of the prosthetic foot using SUV elastomers does not exceed the value of 0.944 μm . For prostheses made for children, however, this is usually around 1-1.5 μm . With such deformation

being easily achieved within this limit, the design permits a natural bending movement when required without endangering the structure's or the user's comfortable experience.

Equivalent stress: The equivalent (von-Mises) stress analysis shows that the maximum stress level reaches 7.5582 MPa. When using SUV elastomer for pediatric applications, the commonly acceptable stress value is roughly 10 MPa. Given that the stresses experienced are lower than that level and uniform in nature, it reduces the ability of the materials to experience fatigue failure, allowing the prosthetic foot to be used by kids on a daily basis [2] [15].

These results confirmed material selections and suitability of a design as shown in a comparative table below:

Table 2: Comparison Chart of Elastomers

Property	UV-Curable (SUV) Elastomers	Silicone Elastomers	Thermoplastic Elastomers (TPEs)
Elongation at break	High (e.g., up to 1100%)	Moderate to High	Variable depending on type
Flexibility	Excellent flexibility and resilience	Flexible and resilient	Flexible
Biocompatibility	Generally biocompatible	Biocompatible	Varies by specific material
Curing Method	UV radiation	Room temperature cure	Heat or chemical activation
Mechanical Properties	Tune able by adjusting mixing ratio	Generally consistent	Varies widely
Chemical Resistance	Resistant to UV exposure	Good resistance to chemicals	Varies by type
Cost and Availability	Cost-effective for mass production	Available but may be more expensive	Widely available
Complexity of Design	Capable of intricate designs	Capable of intricate designs	Capable of complex shapes
Durability	Durable under repeated stress	Durable and long-lasting`	Varies based on formulation

The characteristics of performance of UV-curable elastomers and other available elastomers are analyzed in Table 2 which demonstrates their

applicability in terms of flexibility, mechanical properties and durability [21][24].

Discussion

The design of the prosthetic foot integrates successfully all the aspects including lightweight feature, biocompatibility and durability essential for children. Dynamic and inexpensive prosthetics are best done using UV curable elastomers with their high elongation and flexible properties. This material makes it possible for the prosthetic to withstand normal daily activities and forces normally exerted on children by the prosthetic while still providing comfort and resilience [7][5].

Implications: This design can be step forward by incorporating things such as energy-return mechanisms, further improving the already existing 3D printed design in terms of its functional purposes and efficient use of material [1]. Along this line, research in plenty of elastomer's compositions can further help in enhanced customization especially in pediatric prostheses where individual fit is imperative [11].

In conclusion of this study, we investigate the advantages offered by UV curable elastomers in the manufacture of children's prosthesis, providing optimal durability and comfort at a reasonable price with suitable means of production being 3D printing for such prostheses.

Summary

The focus of this work is on the conception, design, and analysis of an adjustable prosthetic foot for young children aged between five and ten years [1]. The aim was to provide an adjustable artificial limb which is strong, flexible and offers comfort designing prosthetics for growing children [2]. The combination of UV cured elastomers, thermoplastic polyurethane (TPU), and Poly Lactic Acid (PLA) was used in the design, as light weight and biocompatible materials that could withstand wear and tear plus most importantly, flexible [21].

The Materials and Methods section elaborated on how the materials were selected based on some properties, for instance, tensile strength, elongation, and biocompatibility [7]. A design verification structural stress analysis has been done using Finite Element analysis and developed using ANSYS Cesium software and the results confirmed that the design is structurally sound; there was minimal deformation and stress concentration was within reasonable limits [15][9]. The advanced 3D printing processes used allowed the speed of production

to enhance incorporation of different designs for different users as well as giving them comfort [11][5].

The Results showed that UV cured elastomers had a very good performance with very high elongation and flexibility which is important for a prosthetic device that is to be used by a hyper dynamic active child. Further review established UV cured elastomers as the preferable material and the most cost-effective option, standing out above every other material in terms of flexibility and longevity.

Conclusion

The Adjustable prosthetic foot for kids of 5-10 years in age is a progressive step towards the enhancement of prosthetic design in children where there is prosthetic sonification for comfort and durability as well as more for flexural grooving. This study aimed at overcoming the challenges associated with the traditional prosthetic treatment, which is often rigid and impractical tailored to the needs of active and growing children [21]. For this reason, UV curable elastomers, thermoplastic Polyurethane (TPU), and Poly Lactic Acid (PLA) was selected in this design which achieved the best performance structure that is light lover, flexible, and biocompatible in nature [24].

The finite Element Analysis (FEA) of an orthopedic device was conducted with the aid of ANSYS software to gain deep insight into the behaviors of materials based on realistic assumptions and it was found out that UV curable elastomers offer the best compromise of elasticity versus tensile stress [16]. The wear resistance of the foot prosthesis and its even stress distribution when loads are applied dynamically show that such material is fit for children's prosthetics [9]. Moreover, stress-strain analysis showed that these types of elastomers can retain their elasticity at high elongation at break which is a necessary property in devices that will be impact loaded as well as subjected to various motions.

In this context, individual components would be first produced as various prototypes adapted to make an exact fit using 3D printing method. This method of manufacturing is also affordable and increase its scope so that mass production of customized prosthetics can be undertaken at a cheaper cost than the conventional norms.

Acknowledgement

We are grateful for the immense support offered to us by our Principal Dr. S. M. Khot, Head of the Department Dr. Aqleem Siddiqui, and faculty members of the Mechanical Department. We sincerely express our deep sense of gratitude to our guide Mr. Sunny Sarraf & Mr. Afzal

Ansari for their continuous support and guidance throughout our project work. We are thankful to the teaching and non-teaching staff of Fr. C. Rodrigues Institute of Technology, Vashi, Navi Mumbai for their cooperation. We also wish to express our sincere thanks to all those who helped us directly or indirectly in our project.

References

- [1] M. Bourgain, T. Provot, and X. Bonnet, "Design and manufacturing of prosthetic feet for children as a multidisciplinary project for mechanical engineering students," (2020).
- [2] J.K. Hitt, R. Bellman, M. Holgate, T.G. Sugar, and K.W. Hollander, "The sparky (spring ankle with regenerative kinetics) project: Design and analysis of a robotic transtibial prosthesis with regenerative kinetics," International Design Engineering Technical Conferences and Computers and Information in Engineering Conference, vol. 4806, pp. 1587-1596, 2007.
- [3] M.L. Stills, "Partial foot prostheses/orthoses," Clin Prosthet Orthot, vol. 12, no. 1, pp. 14-18, 1987.
- [4] J.K. Oleiwi and A.N. Hadi, "Properties of materials and models of prosthetic feet: A review," IOP Conference Series: Materials Science and Engineering, vol. 1094, no. 1, p. 012151, IOP Publishing, 2021.
- [5] R. Versluys, A. Desomer, G. Lenaerts, P. Beyl, M. Van Damme, B. Vanderborght, I. Vanderniepen, G. Van der Perre, and D. Lefeber, "From conventional prosthetic feet to bionic feet: a review study," 2008 2nd IEEE RAS & EMBS International Conference on Biomedical Robotics and Biomechatronics, pp. 49-54, IEEE, 2008.
- [6] C. Curtze, A.L. Hof, H.G. van Keeken, J.P.K. Halbertsma, K. Postema, and B. Otten, "Comparative roll-over analysis of prosthetic feet," Journal of Biomechanics, vol. 42, no. 11, pp. 1746-1753, 2009.
- [7] M.S. Scholz, J.P. Blanchfield, L.D. Bloom, B.H. Coburn, M. Elkington, J.D. Fuller, M.E. Gilbert, et al., "The use of composite materials in modern orthopaedic medicine and prosthetic devices: A review," Composites Science and Technology, vol. 71, no. 16, pp. 1791-1803, 2011.
- [8] B. Rochlitz, D. Pammer, and R. Kiss, "Functionality and load-bearing analysis of 3D-printed prosthetic feet," Materials Today: Proceedings, vol. 5, no. 13, pp. 26566-26571, 2018.
- [9] K. Sasaki, J. Pinitlertsakun, P. Nualnim, G. Guerra, Y. Sansook, S. Kaewdoug, et al., "The reversible adjustable coupling: a

- lightweight and low-cost alignment component for the lower limb prosthesis," *Journal of Rehabilitation and Assistive Technologies Engineering*, vol. 4, p. 2055668317706427, 2017.
- [10] G.F. Waluyono, B. Suhardi, and E. Pujiyanto, "The Design of Shoe Sizes for Boys Aged 4-6 Years Old Based on Foot Anthropometric Data: Length Foot, Width Foot, and Foot Ball Circumference," *IOP Conference Series: Materials Science and Engineering*, vol. 598, no. 1, p. 012056, IOP Publishing, 2019.
- [11] Y. Tang, G. Dong, Y. Xiong, and Q. Wang, "Data-driven design of customized porous lattice sole fabricated by additive manufacturing," *Procedia Manufacturing*, vol. 53, pp. 318-326, 2021.
- [12] J.R. Engsborg, K.G. Tedford, M.J.N. Springer, and J.A. Harder, "Weight distribution of below-knee amputee and able-bodied children during standing," *Prosthetics and Orthotics International*, vol. 16, no. 3, pp. 200-202, 1992.
- [13] V. Vijayan, S. Arun Kumar, S. Gautham, M. Mohamed Masthan, and N. Piraichudan, "Design and analysis of prosthetic foot using additive manufacturing technique," *Materials Today: Proceedings*, vol. 37, pp. 1665-1671, 2021.
- [14] D. Tomassoni, E. Traini, and F. Amenta, "Gender and age related differences in foot morphology," *Maturitas*, vol. 79, no. 4, pp. 421-427, 2014.
- [15] A.H. Hansen, "Microprocessor-Control of Foot/Ankle Prostheses - Focus on Function," *The Academy Today*, 2015.
- [16] V. Prost, H.V. Peterson, and A.G. Winter, "Multi-Keel Passive Prosthetic Foot Design Optimization Using the Lower Leg Trajectory Error Framework," *Journal of Mechanisms and Robotics*, vol. 15, no. 4, p. 041001, 2023.
- [17] V. Prost, W.B. Johnson, J.A. Kent, M.J. Major, and A.G. Winter, "Biomechanical Evaluation of Prosthetic Feet Designed Using the Lower Leg Trajectory Error Framework," unpublished, 2021.
- [18] S. Müller, A. Carlsohn, J. Müller, H. Baur, and F. Mayer, "Static and dynamic foot characteristics in children aged 1-13 years: a cross-sectional study," *Gait & Posture*, vol. 35, no. 3, pp. 389-394, 2012.
- [19] D. Atamturk and I. Duyar, "Age-related factors in the relationship between foot measurements and living stature and

body weight," *Journal of Forensic Sciences*, vol. 53, no. 6, pp. 1296-1300, 2008.

- [20] V.R. Sastri, "Other Polymers: Styrenics, silicones, thermoplastic elastomers, biopolymers, and thermosets," in *Plastics in Medical Devices-Properties, Requirements, and Applications*, 2nd edition, Elsevier Inc., Waltham, MA, USA, 2014, pp. 215-261
- [21] D.K. Patel, A.H. Sakhaei, M. Layani, B. Zhang, Q. Ge, and S. Magdassi, "Highly stretchable and UV curable elastomers for digital light processing based 3D printing," *Advanced Materials*, vol. 29, no. 15, p. 1606000, 2017.
- [22] W.D. Callister and D.G. Rethwisch, *Fundamentals of Materials Science and Engineering*, vol. 471660817, Wiley London, 2000.
- [23] C. Pollard, A. Harray, A. Daly, and D. Kerr, "Nutrition monitoring survey series 2012 key findings," WA Health, Perth, Australia, 2015.
- [24] Q.N. Jun Zhou, H. Yan, C. Wang, H. Gong, and Y. Long, "3D printing highly stretchable conductors for flexible electronics with low signal hysteresis," *Virtual and Physical Prototyping*, vol. 17, no. 1, pp. 19-32, 2022, doi: 10.1080/17452759.2021.1980283.

Fabrication And Characterization Of Biodegradable Composite Materials Using Bamboo Fibers As Reinforcement And Natural Binder As Matrix

Adarsh Jaiswal¹, Krishnakant Dhakar^{1*}, T. S. Srivatsan²

¹: *Department of Industrial and Production Engineering*
Shri G.S. Institute of Technology and Science
Indore, Madhya Pradesh 452003, INDIA

* Krishnakant Dhakar, E-Mail: krishnakant.dhakar@gmail.com

²: *Department of Mechanical Engineering*
The University of Akron
Akron, OHIO 44325, USA

Corresponding author: E-Mail:
*krishnakant.dhakar@gmail.com

Abstract

In recent years, there has been a growing emphasis on sustainable and eco-friendly approach or alternative to conventional plastics and non-biodegradable materials. One promising avenue is the fabrication of biodegradable materials utilizing bamboo fibers as the reinforcement and starch as the matrix. Bamboo fibers are rich in cellulose, making them an excellent reinforcement material. Starch, on the other hand, serves as an environmentally friendly matrix due on account of its biodegradable and renewable properties. Through a process of blending and compounding, the bamboo fibers were integrated into a starch matrix, resulting in the engineering of composite material. The bamboo fibers reinforce the starch matrix, thereby enhancing the mechanical properties, such as flexural strength and wettability, of the composite materials. The maximum value obtained in a flexural strength test, in accordance with ASTM Standard D790, for a bamboo fiber-reinforced starch-based sample, that measured 127 x 12.7 x 3.2 mm, was 33.872 N/mm². The bamboo fibre-reinforced starch-based composite displayed an average water absorption percentage of 3.96% obtained very much in conformance with the standard ASTM D-570-98. Additionally, this approach does promote an effective utilization of the waste materials and thereby contributing to reducing the overall

environmental impact associated with their disposal. The resultant biodegradable composite material does show great promise for the production of disposable items. Items like (i) utensils, (ii) packaging materials, and (iii) single-use containers can be easily fabricated from this composite material and thus take on the role of potentially viable alternative to conventional disposable plastics. Further, these biodegradable items have the advantage of natural degradation, and thereby minimizing pollution and contributing to a more sustainable and environment conscious future.

Keywords: Composites, Natural Fiber Reinforced Composites (NFRCs), Bamboo Fiber, Natural binders, Starch, Mechanical Testing.

Introduction

In the prevailing era, plastics have become ubiquitous due on account of their unmatched convenience, significantly enhancing the daily life of the people. However, this widespread use did come about at a considerable cost, manifesting in the consumption of energy during production and severe environmental problems due to non-degradable nature of the plastics. Consequently, there is an urgent need to explore potentially viable alternatives to plastics, particularly materials that are fully biodegradable, to mitigate these issues. Starch has emerged as a promising candidate to address this need and potentially replace synthetic polymers in certain aspects of packaging. Starch, a natural polymer found in various plants, to include (i) corn, (ii) potatoes, and (iii) rice, does possess biodegradable properties, making it an attractive alternative to traditional plastics. When used in packaging, starch-based materials can offer comparable functionalities, such as (i) barrier properties, and (ii) structural integrity, while being environment friendly [1].

Starch-based bioplastics can be processed into films, trays, bags, and other packaging forms, thereby presenting both a versatile and sustainable solution. The use of starch in packaging not only offers a renewable and biodegradable option but also contributes to reducing the overall environmental impact associated with plastic waste. A noticeable advancement in research and technology continues to enhance the properties and processing capabilities of starch-based materials, their integration into the packaging industry is expected to noticeably increase, thereby both facilitating and enabling a more sustainable and eco-conscious approach to packaging materials. This shift towards biodegradable alternatives like starch does underscore the collective commitment to addressing the challenges posed by traditional plastics while concurrently fostering a more sustainable

future. Indeed, there is a notable trend in various industries, to essentially include the following: (i) textile, (ii) automotive, (iii) packaging, (iv) construction, and more, towards incorporating natural fiber composites as a more sustainable and eco-friendlier alternative to traditional plastics. This shift is driven by (i) environmental concerns, (ii) sustainability goals, and (iii) the need to reduce the reliance on non-renewable resources [2].

The advantages of natural fiber composites include the following: (i) biodegradability, (ii) reduced carbon footprint, (iii) lower production costs, and (iv) comparable or even superior properties to traditional plastics. However, challenges like moisture sensitivity, standardization of properties, and scaling up production need to be addressed for a broader adoption of the natural fiber composites. Natural fibers primarily come from plants and are abundant in cellulose, a complex carbohydrate. Cellulose is a polymer composed of glucose units linked together, providing strength and rigidity to plant cell walls. Due to its chemical structure, cellulose has hydrophilic properties, meaning it has an affinity for water. This hydrophilicity enables natural fibers to readily absorb and interact with water molecules [3]. When exposed to moisture, such as (i) humid environments, and (ii) during contact with liquids, these fibers tend to gradually swell and retain water. This inherent hydrophilic nature of natural fibers is crucial in various applications, to include textiles, as it allows for effective moisture absorption, breathability, and overall comfort. Additionally, this characteristic is essential for both biodegradability and sustainability, making the natural fibers an environment friendly alternatives when compared with the synthetic counterpart. In this novel research study, the technique of compression molding was used to create composite materials using bamboo fiber as the reinforcement and starch as the matrix. Physical techniques were used to explore how cornstarch and bamboo fiber affected the mechanical testing to obtain flexural strength and impact resistance of the composite material [4].

Materials and Methods

Materials

The research involves utilizing key raw materials, such as corn starch, water, natural fibers and bamboo fibers. Starch, a renewable resource serves as a fundamental component in creating bioplastics, thereby offering a sustainable alternative to the traditional plastics. Water, an essential solvent, aids in the processing and blending of these materials. Bamboo fibers, known for their strength and eco-

friendliness, contribute to the project by providing a sustainable and versatile natural fiber. Together, these raw materials form the foundation for developing eco-friendly products like (i) biodegradable plates, (ii) food cutlery, and (iii) few other environmentally conscious innovations.

Sample Preparation

A process of mixing the bamboo fiber, starch, and water in different proportions to create a homogeneous solution. The solution could then be used in various applications, depending on the specific ratio(s) and the intended end-use. This novel research study involves creating a solution by combining bamboo fiber, starch, and water in varying proportions. The first step was to carefully measure and select the desired quantities of bamboo fiber, corn starch, and water based on the intended formulation. The raw materials are then combined in a container, and a stirring mechanism was used to thoroughly mix the components together. During the mixing process, the stirrer is carefully adjusted to ensure proper integration of the bamboo fiber, starch, and water. The stirring continues until the solution reaches a state of homogeneity, where all the ingredients are both evenly distributed and well blended. Achieving a homogeneous solution is crucial for obtaining consistent properties and characteristics in the final product. The specific proportions of bamboo fiber, starch, and water can be adjusted to tailor the solution for different purposes and to concurrently optimize the properties of the resulting material [5]. Composition of the is provided in **Table 1**.

Table 1: Tabular representation of parameter related to fabrication of plates.

PARAMETER	L1	L2	L3
CONCENTRATION	40:60	45:55	50:50
FIBER SIZE	1	3	5
TEMPERATURE	140	160	180

The Taguchi L9 approach, part of the Taguchi Method developed by Genichi Taguchi, is a design of experiments (DOE) technique used for optimizing processes and products by minimizing variation while concurrently enabling in improving quality. The "L9" in the Taguchi

L9 approach represents the number of experimental runs or trials, which is nine in this case.

Table 2. Tabular representation of Design of Experiment

SI NO. (Design of Experiment)	P1	P2	P3
1	1	1	1
2	1	2	2
3	1	3	3
4	2	1	2
5	2	2	3
6	2	3	1
7	3	1	3
8	3	2	1
9	3	3	2

Fabricating a die for the composite materials did involve the creation of a specialized tool that can form the composite materials into the shape desired or product desired. All the samples in the die were subsequently heated and then compressed using a Compression Molding machine at various temperatures. Details are provided in Table 3.

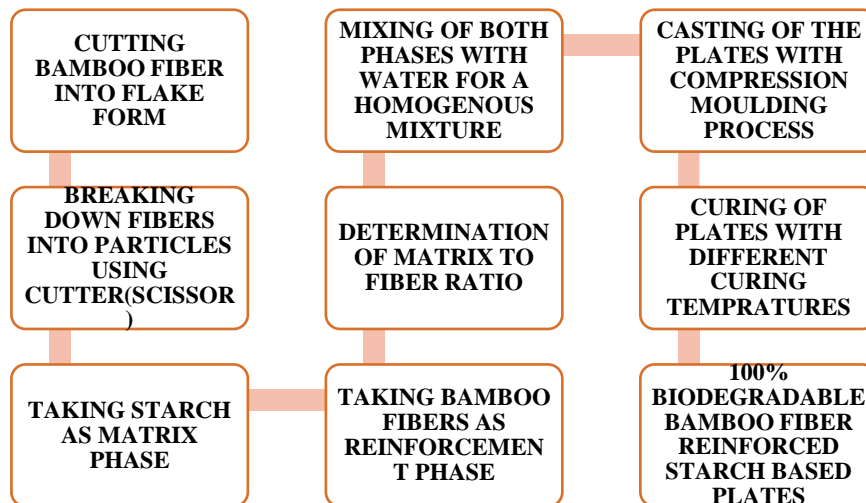
Table 3. Tabular representation of parameter according to design of experiment (Taguchi L9)

SI No	P1 (Concentration)	P2 (Fiber Length)	P3 (Temperature) °C)
1	40:60	1	140
2	40:60	3	160
3	40:60	5	180
4	45:55	1	160
5	45:55	3	180
6	45:55	5	140
7	50:50	1	180
8	50:50	3	140
9	50:50	5	160



Figure 1. Compression molding machine

Flow chart of process



Procedure for Flexural strength test

The test was conducted in accordance with the ASTM D790 Standard using a Universal Test Machine (UTM) in order to extract the data on flexural strength of composite material. It was used to provide data of the force acting per millimeter square of the composite material. Under the ASTM D790 Standard the sample dimensions for a rectangular cross-section was a length of 127 mm, width of 12.7 mm, and a thickness of 3.2 mm. The total number samples to be tested was 9 [6].

Procedure for Wet ability Test of bamboo Fiber Reinforced starch-based Composites

The ASTM D570-98 Standard is a widely recognized test method for evaluating the water absorption characteristics of a variety of materials, to include the composite materials. This test measures the tendency of a material to absorb water and the degree of water absorption, which is essential for developing an understanding on how the material can perform in real-world applications. The procedure essentially involves immersing a test specimen in water for a specified duration of time. The change in weight of the chosen test specimen was then carefully measured to determine the extent of water absorption. This information is crucial for assessing the suitability of a composite material for applications where exposure to moisture or water is of concern. Ability of the test to measure the percentage weight gain of a test sample upon exposure to water does help in quantifying how much water a material can absorb, and the rate at which it does the absorption. It is essential for assessing both the performance and durability of materials in various environment conditions, as water absorption does exert an influence on properties, such as (i) mechanical strength, (ii) dimensional stability, and (iii) electrical properties. The overall flexibility of the standard in allowing for adjustments in immersion duration and temperature is crucial since different materials have distinctly different water absorption characteristics. For example, polymers and natural fibers, which are commonly used in composite materials, are often susceptible to water absorption, and the test should be tailored to suit the specific material in question. Overall, the ASTM D570-98 Standard is a valuable tool for the purpose of characterizing materials and to concurrently help in understanding how they will respond to moisture or water exposure, which is vital in a wide range of applications, to include (i) engineering, (ii) civil construction, and (iii) manufacturing [7].

Results and Discussion

Flexural Strength

The test was meticulously executed following the rigorous procedure detailed in the ASTM D790 Standard, and using a Universal Test Machine (UTM), to extract crucial data pertaining to flexural strength of the chosen composite material. This test aids in determining the force acting per square millimeter of the composite material. In strict compliance with the ASTM D790 Standard, the test samples were thoughtfully prepared in a rectangular cross-sectional shape, having the dimensions of 127 mm in length, 12.7 mm in width,

and 3.2 mm in thickness. A comprehensive evaluation did involve testing a total of nine samples, yielding a useful insight into the chosen and studied composite material's ability to withstand bending forces and to concurrently distribute the stress. The test data gathered does hold much importance in diverse applications and industries.

Table 4: Flexural Strength value of Bamboo Fiber reinforced Starch Composite.

S No.	Name of the test	Test Method	Unit	Test value obtained
Bamboo fiber Composite, Sizes 127x12.7x3.2 mm				
1	Flexural strength	ASTM D 790	N/mm ²	5.4
2	Flexural strength	ASTM D 790	N/mm ²	13.1
3	Flexural strength	ASTM D 790	N/mm ²	20.33
4	Flexural strength	ASTM D 790	N/mm ²	7.07
5	Flexural strength	ASTM D 790	N/mm ²	14.94
6	Flexural strength	ASTM D 790	N/mm ²	20.32
7	Flexural strength	ASTM D 790	N/mm ²	17.28
8	Flexural strength	ASTM D 790	N/mm ²	31.34
9	Flexural strength	ASTM D 790	N/mm ²	33.82

The Wettability Test

Objective of the water absorption test was to evaluate how much water a test specimen will absorb under fixed and predefined conditions over a given period of time. As per ASTM D570-98 Standard, the test sample conditioning involved heating of the sample to eliminate any potential moisture content. There are numerous assessment settings and durations available following conditioning. This experimental investigation was conducted using the same protocol. The method used in this research study is known as the “half

hour Water test”. In **Table 5** displays the weight of the extracted samples after the process and weight of the conditioned samples. Three samples were averaged in order to determine the percentage of water absorption.

The produced bamboo fiber-reinforced starch-based composite exhibited an average water absorption percentage of 3.96%, as can be inferred from the details contained in **Table 5**.

Table 5. Tabular Representation of Weight and Water Absorption percentage of the test specimens.

Sample Number	WEIGHT OF CONDITIONED SAMPLES W1 (IN GRAMS)	WEIGHT OF SAMPLES AFTER IMMERSION W2 (IN GRAMS)	WATER ABSORPTION $[(W2-W1)/W1] \times 100$ (%)	AVERAGE WATER ABSORPTION (%)
Tap water (27° C)	49.7466	51.2551	3.03	3.96
Cold water (8° C)	58.8585	61.4273	4.36	
Hot water (80° C)	57.3826	59.9682	4.50	

Conclusions

1. Starch-based materials have emerged as a promising alternative to natural binders like corn starch, while concurrently offering a more environment friendly solution for various applications, particularly in packaging.
2. Starch is a natural polymer that can be found abundantly in many plants. It possesses several advantageous properties, to include biodegradability, low cost, and a renewable source, making it an attractive candidate for replacing synthetic plastics in certain applications.
3. One of the key advantages of starch-based materials is their biodegradability.

4. The natural fibers are chosen for their low cost, biodegradability, and excellent mechanical performance. When combined with corn starch-based materials, these natural fibers can strengthen the composite, making it suitable for a broader range of applications, to include food cutlery, packaging. The maximum value obtained in the flexural strength test, in accordance with ASTM D790 Standard, for a bamboo fiber-reinforced starch-based sample measuring 127 x 12.7 x 3.2 mm, was 33.872 N/mm². The result obtained does serve as a critical indicator of the material's ability to resist both bending stresses and flexural stresses, highlighting on both its strength and structural integrity for use in applications where it will experience such loads.
5. The high flexural strength of the bamboo fiber-reinforced starch-based sample, as demonstrated by this result, makes it well-suited for applications that require reliable load-bearing capabilities and resistance to bending forces.
6. The bamboo fiber-reinforced starch-based composite displayed an average water absorption percentage of 3.96%. This information suggests that the composite material can absorb and retain about 3.96% of its weight in water under specific test conditions.
7. Water absorption properties are significant in assessing a material's suitability for various applications, especially when exposure to moisture, or water, is of critical need and does merit consideration.

References

- [1] Duane W. M., Swanson C. L., and Fanta G. F: American Chemical Society, (1992), pp.197-230.
- [2] Zeng, G., Lin, R., Meng, C., Chen, L., 201, "*Properties of Bamboo Fiber Reinforced Cornstarch-based Composites*," **Trans Tech Publications, Applied Mechanics and Materials**, Vol. 200(2012) pp 237-242.
- [3] Nadya P., *Rapid Prototyping of Green Composites*, University of Amsterdam (2008)
- [4] Yusuf, F., Wahab, N., Rahman, N., Kalam, A., Mahatma., Taib, C., 2017, "*Properties of treated bamboo fiber reinforced tapioca starch biodegradable composite*," "**Materials today**".

- [5] Manalo A.C., Wani E., N. A. Zukerman N. A., Karusena W., *Effects of alkali treatment and elevated temperature on the mechanical properties of bamboo fibre-polyester composites*, **Composites Part B** 80 (2015) 73-83.
- [6] Veda Narayanan, V., Kumar, B. S. P., Karuna, M. S., Jayanthi, A., Kumar, K. V. P., Radha, A., Ramkumar, G., & Christopher, D. (2022). *Experimental Investigation on Mechanical Behaviour of Kevlar and Ramie Fibre Reinforced Epoxy Composites*. **Journal of Nanomaterials**, 2022, 1–10.
- [7] Bhat, Ritesh & Mohan, N. & Sharma, Sathya Shankar and Pratap, Ashu & Keni, Agastya & Sodani, Dev. (2019). *Mechanical testing and microstructure characterization of glass fiber reinforced isophthalic polyester composites*. **Journal of Materials Research and Technology**. 8. 10.1016/j.jmrt.2019.06.003.

The Mechanical Properties of Epoxy Based Bamboo Fibre Reinforced Composite: An Experimental Study

**Shrivardhan Bhargava¹, Krishnakant Dhakar^{1*},
T. S. Srivatsan²**

¹ *Department of Industrial and Production Engineering*
Shri G.S. Institute of Technology and Science
Indore, Madhya Pradesh 452003, INDIA

² *Department of Mechanical Engineering*
The University of Akron
Akron, OHIO 44325, USA

Corresponding Author: krishnakantdhakar@gmail.com

Abstract

Recently, there has been an increased emphasis on finding sustainable and eco-friendly alternatives to traditional non-biodegradable materials. One promising approach involves the development of biodegradable composites using natural fibers. In this paper is presented a useful collection of results of a recent study on the fabrication, evaluation, and analysis of a composite material that is reinforced with bamboo fibers and paired with various polymer matrices. Recognized for its impressive combination of mechanical properties, bamboo fiber is explored as a potentially viable and economically affordable reinforcement, as an attractive alternative in the field of research specific to composite materials. In this research study, bamboo fiber serves as the reinforcement phase, while epoxy resin functions as the matrix phase. The composite material was fabricated using the hand-layup technique, with chopped bamboo fibers of 5-10 mm length and having a random orientation that was combined with epoxy resin and a hardener in a 2:1 ratio, and subsequently cured for 24 hours. The mechanical properties of the bamboo fiber-reinforced composite were determined through mechanical tests, to include both the impact test and tensile test. The test results clearly indicate that the composite materials containing 15 weight percentage of bamboo fiber reinforcement did reveal an observable enhancement in hardness, tensile strength, and impact resistance. The mechanical properties, to include tensile properties, of

the bamboo-epoxy composites did reveal considerable improvement for high fiber content. In this paper is presented the following: (i) intricacies specific to the fabrication process, (ii) factors affecting the composite properties, and (iii) mechanical tests used to assess their performance. The key findings highlight the potential of bamboo fiber-reinforced composite materials having polymer matrices as being suitable for a spectrum of industrial applications while concurrently providing valuable insights into future research in this area.

Keywords: Reinforced Composites, Natural Fibre, Bamboo Fibre, Epoxy Resin, Hand-layup Process, Mechanical Testing

Introduction

Natural fibre composites (NFCs), made from fibres like bamboo, banana, sisal, hemp, and cotton, are becoming both a viable and sustainable alternative in materials science. Known for their lightweight, renewable, and biodegradable properties, they are often combined with both thermoplastic resins and thermosetting resins, offering environmental benefits and lower density when compared one-on-one with the traditional composite counterparts [1]. Contemporary improvements, notably in genetic engineering, have contributed to increasing fibre quality, with bamboo acquiring popularity because of its high tensile strength and low cost. [2] Despite challenges from environmental factors, like humidity and temperature, the bamboo, known as the "natural glass fibre," shows great potential for use in applications that require high tensile strength. Industries, such as (i) automotive, (ii) aerospace, and (iii) construction, are increasingly adopting Natural Fibre Reinforced Composites (NFRCs), with bamboo fibre composites emerging as a lighter, stronger alternative to synthetic materials [3]. Bamboo's antibacterial, ultra-violet (UV)-resistant, and moisture-wicking properties have also attracted interest in the textile industry, presenting significant untapped potential as eco-friendly production methods continue to evolve [4].

Preparation of Bamboo Fiber Reinforced Composite

The Reinforcement Phase Used

The reinforcement phase in composite materials plays a critical role in enhancing mechanical properties, such as (i) strength, and (ii) stiffness. In this experimental study, bamboo fiber flakes were used as the reinforcement material due on account of their renewable nature, high strength-to-weight [σ/ρ] ratio, and environmental sustainability. The bamboo fibers were cut into tiny flakes around 10mm in length to ensure consistent distribution within the chosen matrix. The

incorporation of these natural fibers is expected to significantly improve the overall tensile properties of the resultant composite, offering a sustainable alternative to the synthetic reinforcements for environment-conscious applications.



Figure 1. The Bamboo Fibres

Matrix Phase Used

The matrix phase in composites serves to bind the reinforcement, transfer loads, and provide structural integrity [6]. In the current study, a 2:1 epoxy-hardener mixture was used as the matrix material. This epoxy formulation was chosen because of the following reasons: (i) its superior adhesion, (ii) mechanical strength, and (iii) overall resilience to environmental conditions. The proportion of 2:1 promotes proper curing, resulting in a strong bond among the bamboo fiber flakes. This combination contributes to enhancing the overall mechanical performance of the composite, making it suitable for applications requiring the following: (i) high strength, (ii) durability, and (iii) environmental sustainability.



**Figure 2. Epoxy Resin and Hardener
Processing of Bamboo Fiber-Reinforced Composites**

A closed mould with dimensions of 250 x 25 x 10 mm was used to prepare the composite specimens. A thin layer of release agent (commonly SPMRA) was applied to the interior surface of the mould to facilitate easy removal. Dow Epoxy Resin (DER) 331, known for its excellent adhesion, strength, low density, and chemical resistance, was chosen for this study due to its superior mechanical properties.

The matrix mixture, composed of resin and hardener in a 2:1 ratio, was uniformly mixed using a simple stirrer and subsequently poured into the mould, to form a thin and even layer of the resin. Mechanically and chemically-treated bamboo fibers were then uniformly distributed over the resin layer using steel rollers to ensure uniformity. Preventing air bubbles and voids was crucial. To ensure this, the mold was placed under compression molding with 2000–3000 psi for 15-20 minutes, and then placed under a 10 kg dead load for 24 hours.

Three different compositions of the composite samples were prepared with fibre contents of 5 weight percent, 10 weight percent, and 15 weight percent. A second layer of epoxy resin and hardener (2:1 ratio) was then applied over the fibres. This process was repeated until the mould reached a thickness of 10 mm. Once the slurry was fully deposited into the mould, a thin steel plate was placed on top. A pressure of up to 5 KPa was applied to the plate to release any remaining air bubbles. The composite block was then left to cure at ambient temperature of 28.5 °C for 24 hours, with constant pressure being maintained on the mould throughout the curing process.



Figure 3. Pictorial Depiction of the Mould

Three different compositions of the composite samples were prepared with fibre contents of 5wt%, 10wt%, and 15wt%. A second layer of epoxy resin and hardener (2:1 ratio) was applied over the fibres. This process was repeated until the mould thickness reached 10 mm. Once the slurry was fully deposited into the mould, a thin steel plate was placed on top. A pressure of up to 5 KPa was applied to the plate to release any remaining air bubbles. The composite block was left to cure at ambient temperature of 28.5 °C for 24 hours, with constant pressure maintained on the mould throughout the curing process.

Mechanical Characterization of the Bamboo Fiber-Reinforced Composites

Tensile Test

The tensile test of composites evaluates their ability to withstand uniaxial tension, providing critical data on mechanical properties such as tensile strength, stiffness, and elongation [5]. In this experimental investigation, all three sample batches were tensile tested in conformance with procedures detailed in the standard ASTM D3039 [5]. Flat test specimens were used and a uniaxial load was then applied through the ends. The dimensions of the test section was 250 mm × 25 mm. According to ASTM standards, the test specimens containing fibers aligned parallel to the loading direction should be 10mm wide. This test configuration ensures accurate measurement of the tensile behavior and performance of the chosen composite material.

Table 1: Designation of Composites Samples for Tensile Testing

Composites Samples	Compositions
MB-1	Matrix + Bamboo Fiber (5 wt%)
MB-2	Matrix + Bamboo Fiber (10 wt%)
MB-3	Matrix + Bamboo Fiber (15 wt%)

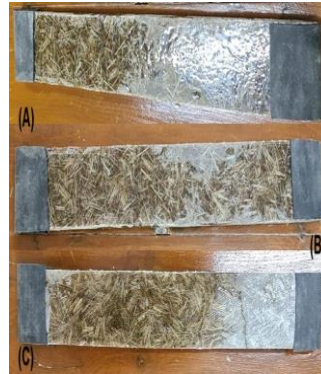


Figure 4. BFRC Samples for Tensile Testing-(A) MB-1, (B) MB-2, (C) MB-3.



Figure 5. Pictorial Illustration of Universal Testing Machine

Results and Discussion

Tensile Test Result of MB-1 (5% Bamboo Fibre Reinforced Composite)

Table 2. Outcomes of Tensile Testing for BFRC (5%)

Fiber Percentage	Sample No.	UTS (in MPa)	Avg. UTS (in MPa)
5% wt.	1	25.17	25.084
	2	24.9	
	3	25.2	
	4	25.05	
	5	25.1	

Ultimate tensile strength of the bamboo fibre reinforced composite (BFRC) test specimen was carried out on a 600 KN

Universal Test Machine (UTM). The average and maximum ultimate tensile strength of bamboo fiber composite of 5% concentration was found to be 25.170 N/mm² and 25.084 N/mm² respectively.

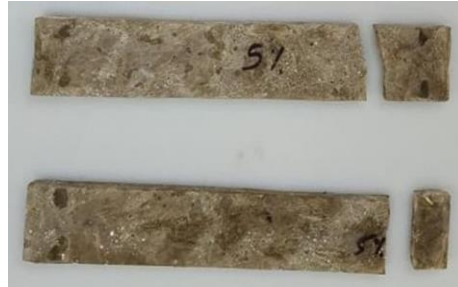


Figure 6. MB-1 (5% BFRC) after the tensile test.

Tensile Test Result of MB-2 (10% Bamboo Fibre Reinforced Composite)

Table 3. Outcomes of Tensile Testing for BFRC (10%)

Fiber Percentage	Sample No.	UTS (MPa)	Average UTS (MPa)
10% wt.	1	27.5	27.42
	2	27.1	
	3	27.35	
	4	27.6	
	5	27.55	

Tensile strength of the BFRC test specimen was carried out on a 600 KN universal test machine. The average and maximum ultimate tensile strength of bamboo fiber composite of 10% concentration was found to be 27.420 N/mm² and 27.600 N/mm².



Figure 7: MB-2 (10% BFRC) After Tensile Test

Tensile Test Result of MB-3 (15% BFRC)

Table 4. Outcomes of Tensile Testing for BFRC (15%)

Fiber Percentage	Sample No.	UTS (in MPa)	Avg. UTS (in MPa)
15% wt.	1	31.00	31.398
	2	31.74	
	3	30.92	
	4	31.68	
	5	31.65	

Tensile strength of the BFRC specimen was carried out on a 600KN Universal test machine (UTM). The average tensile strength and maximum ultimate tensile strength of the bamboo fiber composite of 10% concentration was found to be 31.398N/mm² and 31.740N/mm² respectively. Upon comparison of the test results, it was concluded that in this research the composite with 15% fiber concentration showed the maximum tensile strength.



Figure 8. MB-3 (15% BFRC) After Tensile Test

Effect of Fiber Loading on Ultimate Tensile Strength of the Composite

Material

Influence of fiber weight fraction on tensile strength of the composite material is shown in **Figure 9**. As the fiber content increases from 5 wt.% to 15 wt.%, the tensile strength goes from a value of 25.170 N/mm² to 31.740 N/mm².

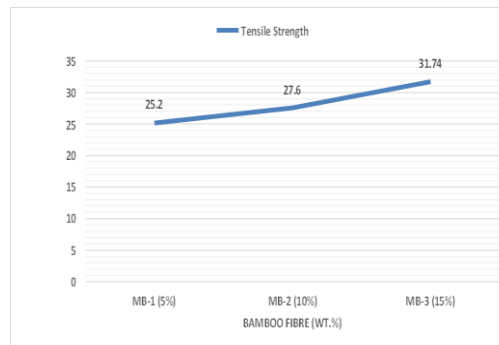


Figure 9. Effect of Fibre Loading on Tensile Strength of the composite material

Conclusions

The key finds of this novel research study are the following:

1. This study clearly demonstrates that bamboo fiber reinforcement in an epoxy-hardener matrix significantly enhances the mechanical properties of the composite, with optimal results achieved for the 15% fiber weight loading.
2. The hand-layup process, while effective, presented challenges in eliminating voids, which negatively impact the composite materials performance, particularly in tensile strength.
3. The tensile strength was observed to improve with an increase in bamboo fiber content, although the presence of porosity and insufficient interfacial bonding limited the mechanical gains.
4. These bamboo-epoxy composites exhibit promising potential for various industrial applications, to include (i) coal dust distribution pipes, (ii) helicopter fan blades, and (iii) affordable housing.

Future research should focus on incorporating other natural fibers to further improve performance and expand application possibilities.

References

1. Lucintel Brief. *Opportunities in Natural Fibre Composites*. **Lucintel** March 2011.
2. Omar Faruka, D., Andrzej, K., Bledzkia, C., Fink, H.P. and Mohini, S., (2012), "Biocomposites reinforced with Natural Fibres," **Journal Program Polymer Science**, 37, pp.1552-1596.

3. Khalil, H.A., Bhat, I.U.H., Jawaid, M., Zaidon, A., Hermawan, D. and Hadi, Y.S., (2012), "*Bamboo fibre reinforced bio-composites: A review*," **Materials and Design**, 42, pp.353-368.
4. Besi, M.K.S., (2013), "*A review on mechanical properties of bamboo fibre reinforced polymer composite*," **Australian Journal Basic Applied Science** ([8) pp.247-253.
5. Wani, R.S. and Shitole, R.R., 2017. *Tensile testing of Bamboo Fibre Reinforced epoxy composite*. **IOSR J. Mech. Civ. Engg**, 17, pp.7-11.
6. Ramachandran, M., Bansal, S., Fegade, V. and Raichurkar, P., (2015), "*Analysis of bamboo fibre composite with polyester and epoxy resin*," **International Journal on Textile Engineering and Processes**, 1(4), pp.18-21

Dynamic Mechanical and Tribological Properties of Multimaterial Hydrogel Film Under Physiological Solutions for Biomedical Applications

¹Devara Venkata Krishna* , ²Palivela Bhargav Chandan,
³Mamilla Ravi Sankar

*Department of Mechanical Engineering,
Indian Institute of Technology,
Tirupati, India*

**Presenter e-mail : me21d501@iittp.ac.in*

Abstract

Hydrogels are progressively familiar for their potential in biomedical applications due to their biocompatibility and customizable properties. Developing hydrogel films with tailored mechanical and tribological properties is critical for their successful application in biomedical fields, such as tissue engineering and wound healing. Numerous studies have reported hydrogel films for articular cartilage and wound healing applications. Prior studies have not assessed the performance of hydrogel films under physiological solutions that mimic the biological environment. The present study evaluates the dynamic mechanical and tribological properties of the quaternary blended multimaterial hydrogel under different physiological solutions such as ringer lactic solution (RLS) and artificial synovial fluid (ASF). The dynamic mechanical behavior of the developed hydrogel film was assessed for storage and loss modulus of the film under the influence of oscillatory strain and frequency. Additionally, creep and stress relaxation behaviors were evaluated. Oscillating tribology was carried out concurrently to appraise the hydrogel film surface frictional characteristics, which are crucial for applications requiring prolonged contact with biological tissues. The outcomes highlight the feasibility of these multimaterial hydrogel films for use in biomedical devices and implants by showing that they maintain mechanical stability and have low friction coefficients in various physiological fluids. This thorough analysis of hydrogel films in different physiological settings advances the development of materials intended for biomedical use.

Keywords: Film, artificial synovial fluid, multimaterial, coefficient of friction

Introduction

Hydrogels are rapidly emerging as essential materials in biomedical engineering due to their remarkable ability to mimic biological tissue properties, high water content, biocompatibility, and tunability [1, 2]. The films made from the hydrogels have potential biomedical applications, including wound dressings [3], biosensors [4], bone repair [5], actuators [6], drug delivery [7], and antibacterial applications [8] etc. Various researchers have developed hydrogel films from different biomaterials. For instance, Mojally et al. [9] developed a hydrogel film from corn starch (CS), polyvinyl alcohol (PVA), silver nanoparticles (SNP), and castor oil (CO) that were crosslinked with glutaraldehyde for wound dressings. Ulvan hydrogel films, a natural polymer derived from sulfated polysaccharides found in green seaweed, were prepared using a facile method involving ionic crosslinking with boric acid and adding glycerol as a plasticizer for wound dressing applications. These films demonstrated favorable properties, including optimal viscosity, swelling degree, moisture content, and water vapor transmission, making them suitable for effective wound management [10]. Glycerol, Chitosan, and PVA were formulated into wound dressing materials and evaluated for various properties, including water vapor transmission, absorption, tensile strength, biodegradability, and antibacterial activity. The findings indicated an optimal dressing ratio for enhanced performance, with silver nanoparticle (AgNP) dressing exhibiting superior antibacterial activity compared to the other formulations, making it a promising candidate for effective wound management [11]. Nanocomposite hydrogel films (NHF) were developed using hydroxypropyl methylcellulose (HPMC) loaded with Cu nanoparticles (CuNPs) for antibacterial wound dressing applications, with ascorbic acid acting as a nucleating agent [12]. A hydrogel film was developed with glycol oxidized hyaluronic acid/chitosan for the dual ophthalmic delivery of levofloxacin (Lev) and dexamethasone (Dex). This dual drug delivery system demonstrated effective performance, particularly with Lev-loaded hydrogel films, which exhibited a potent capacity to inhibit bacterial growth against various strains, including *Staphylococcus aureus* and *Escherichia coli*. These findings highlight the hydrogel's suitability for ophthalmic applications, combining anti-inflammatory and antibacterial properties in a single formulation [7]. Hydrogel films composed of carboxymethyl tamarind gum (CMTG) and polyvinyl alcohol (PVA) were developed with citric acid (CA) as a crosslinking agent to improve wound healing capabilities. The films were characterized for permeability, total carboxyl content (TCC), protein adsorption, swelling behavior, tensile strength, hemocompatibility, and

the controlled loading and release of moxifloxacin (MXF) [13]. While significant progress has been made in developing hydrogel films [14], a critical need remains to deepen understanding of how these materials behave under physiological conditions that closely mimic the in vivo environment. Most existing studies have focused on optimizing hydrogel formulations for their mechanical strength [15], flexibility [16], and biocompatibility [17]. Still, relatively few have systematically evaluated their dynamic mechanical and tribological properties when exposed to biological fluids. Since many biomedical applications involve continuous interaction between the hydrogel material and biological tissues, such as cartilage replacements [18], implants [19], or long-term wound dressings [20], assessing these properties under relevant conditions is of primary importance.

The present study evaluated the dynamic mechanical and tribological properties of the quaternary blended multimaterial hydrogel under different physiological solutions such as ringer lactic solution (RLS) and artificial synovial fluid (ASF). Multi-material hydrogel film (MMHF) was developed from chitosan, gelatin, PVA, and guar gum-based biomaterials. Oscillatory strain, frequency sweep, and stress relaxation tests were conducted to evaluate the dynamic mechanical performance of the produced hydrogel film under dry and swallow conditions. Oscillating tribology was performed concurrently to evaluate the hydrogel film's surface frictional properties, which are critical for applications requiring prolonged interaction with biological tissues.

Experimental Protocol

Materials and Fabrication of Multimaterial Hydrogel Film (MMHF)

Gelatin (Type B, 120 g Bloom), Chitosan with low molecular weight, Glyoxal 40% aqueous solution, acetic acid glacial extrapure AR, 99.9%, Guar gum extrapure, and PVA (MW 14 kDa) were procured from SRL PVT Ltd, India. The hydrogel films were fabricated using the solvent-casting technique. Chitosan solution was prepared by dissolving one gram of Chitosan in 10 ml of acetic acid solution, continuously stirring for 2 hours at 90°C. Meanwhile, an 8% w/v PVA solution was created by dissolving PVA in deionized water (DIW) and stirring at 90°C for 1 hour, followed by the adding of 15% (w/v) of gelatin and continued stirring at 60 for 45 minutes. The chitosan and PVA/Gelatin solutions were mixed, and stirring continued for 10 minutes. After that, 3% (w/v) of guar gum was added to the

chitosan/PVA/gelatin solution, and stirring continued for 10 min. Thereafter, glyoxal crosslinker was added in the ratio of 1:10 (crosslinker: DIW), poured into the Petri plates, and left to dry at room temperature for three days. Once dried, the films were carefully peeled off and stored in a desiccator for further use.

Dynamic Mechanical Analysis

The prepared hydrogel film's dynamic mechanical analysis (DMA) was evaluated using the Anton Paar modular compact rheometer (MCR) 302, Austria. Quantitatively, the loss modulus (G'') and storage (G') of the dried and swollen MMHF were evaluated considering the influence of shear strain (0.001 to 1000%) and frequency (0.01 to 100 Hz). The shear strain sweep is intended to mimic dynamic tissue conditions, replicating movements typically associated with facial expressions, such as smiling. Given this, a higher frequency may better represent these motions. Therefore, the frequency was set to 1 Hz for optimal relevance [21]. The phase angle (δ) in viscoelastic materials is a critical parameter that indicates the balance between elastic (solid-like) and viscous (liquid-like) behavior during deformation, which is calculated as mentioned in equation 1. The combination effect of elastic (storage) and viscous (dissipative) energy was uttered by complex modulus (G^*) and complex viscosity (η^*), which were calculated using equations 2 and 3, respectively [22]. The stress relaxation behavior of MMHF was conducted at the constant strain of 10% for 1000 seconds.

$$\delta = \tan^{-1} \left(\frac{G''}{G'} \right) \quad (1)$$

$$G^* = (G'^2 + G''^2)^{0.5} \quad (2)$$

$$\eta^* = \frac{\sqrt{G'^2 + G''^2}}{\text{Oscillating frequency}} \quad (3)$$

Oscillatory Tribological Behavior

Tribological measurements were conducted using a Tribo-cell mounted on a rheometer (Anton Paar modular compact rheometer (MCR) 302, Austria). The geometry of the turbo-cell includes three-cylindrical pin geometry and a cup that houses a 60 mm diameter disc-shaped polytetrafluoroethylene (PTFE). The hydrogel films were attached to the cylindrical pins, as shown in Figure 1. The cup is attached to a bottom plate adapter secured to the base. In this setup, the

three pins are attached to the rotating bar (tool master), and the bottom plate remains stationary during measurements, as shown in Figure. 1. The pins and substrate interaction is designed to mimic the hard-soft contact. The measurements were conducted at 25 °C under the lubrication of RLS and ASF at the 5 N normal load. Sliding speed varied from 1-10 mm/s, and corresponding COF was observed. ASF was prepared as per the procedure reported in the previous studies [23]. Approximately 10 mL of liquid was loaded into the cup to ensure adequate coverage of the substrate's surface. The tool master with pins was lowered onto the substrate until the zero gap was attained. During the test, normal load (N), coefficient of friction (COF), sliding speed (mm/s), and time (s) were recorded.

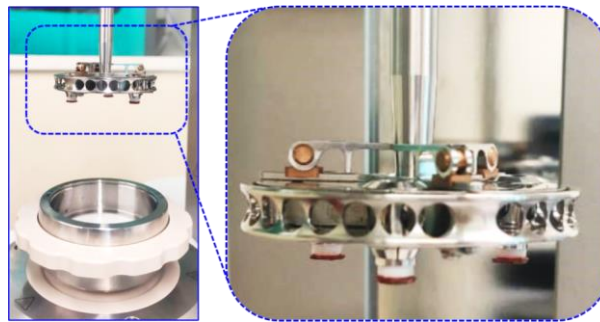


Figure 1. Oscillatory tribology experimental setup

Outcomes and Interpretation

Infrared Spectroscopy of film

The FTIR spectroscopy information of the MMHF is shown in Figure 2. The notified peaks of polyvinyl alcohol were 3285 cm^{-1} , 2933 cm^{-1} , 1636 cm^{-1} , 1054 cm^{-1} , and 872 cm^{-1} , representing the hydroxyl groups, C-H, C=O, C-H, and C-C, respectively. The major peaks observed for the Chitosan include 3285 cm^{-1} , 2933 cm^{-1} , 1636 cm^{-1} , 1544 cm^{-1} , 1380 cm^{-1} , 1313 cm^{-1} , 1150 cm^{-1} , 1054 cm^{-1} , and 901 cm^{-1} , indicating the N-H and O-H stretching, C-H stretching, OC-NHR, NH_2 , C-N, C-O, C-O-C bridge, N-H, and C-H, respectively [24]. The wavenumbers 3285 cm^{-1} , 1636 cm^{-1} , 1544 cm^{-1} , and 1255 cm^{-1} represent Amide A, Amide I, Amide II, and Amide III concerning the gelatin [25]. The peaks at 1636 cm^{-1} represent the CONH_2 in Chitosan and gelatin [26]. The various peaks, such as 3390.71 cm^{-1} (O-H), 2933 cm^{-1} (C-H), 2875 cm^{-1} (C-H), 1636 cm^{-1} (C=O), 1347

cm^{-1} (O-H), 1037 cm^{-1} (C-O), and 872 cm^{-1} (galactose and mannose) [27] were confined for the guar gum.

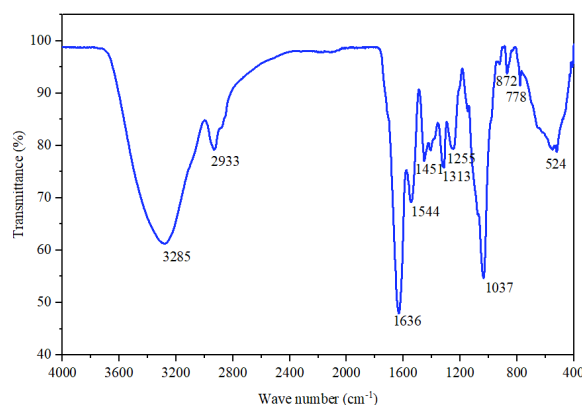


Figure 2. Viscoelastic properties variation with the shear strain

Strain sweep behavior of hydrogel film

Figure 3 illustrates the G' and G'' as a function of shear strain (γ) for MMHF under dry and swollen conditions based on dynamic strain sweep tests. All dry and swollen MMHFs exhibit typical elastic behavior. The dynamic strain sweep test identifies the critical point where the hydrogel film transitions between solid and fluid states. The dry film exhibited a G' of 535.59 kPa at the lower shear strain (0.001%). A reduction of 15.92% and 30.91% in the G' was noticed at the lower shear strain (0.001%) for the swollen films in the ASF and RLS, respectively. The swollen hydrogel films exhibited evident weak strain overshoot behavior. The weak overshoot typically occurs in the early stages of the nonlinear viscoelastic region when the hydrogel film has not fully transitioned to a fully viscous state. It often indicates internal rearrangements, leading to a localized hydrogel film structure flow [28]. Therefore, the local maximum of G'' (overshoot) can be interpreted as a result of the equilibrium between the formation and breakdown of network junctions [29]. The dry film also exhibited similar behavior; however, the peak observed in the curve G'' is relatively small. In the case of the dry film, the G' curve intersects the G'' curve at approximately a shear strain of 57.65%, marking the critical point. Beyond this strain, G' rapidly decreases and falls below G'' , indicating the collapse of the film network and its transition from a quasi-solid to a quasi-liquid state. For film swollen in RLS and ASF for 30 h, the G' curve intersects the G'' curve at approximately 59.93% and 96.21%, marking the critical point, respectively. This suggests that

the hydrogel film, under swollen conditions, was able to withstand the deformation. Additionally, when γ is below the critical point, the G' values of the film swollen in ASF exhibited higher than that of the swollen in RLS.

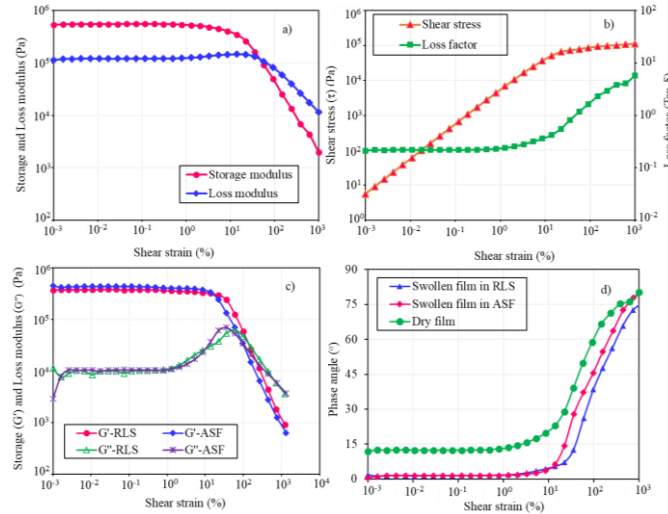


Figure 3. Viscoelastic properties variation with the shear strain

The dry film exhibited a phase angle of 11.92° at the 0.001% shear strain. Meanwhile, swollen films in RLS and ASF exhibited a phase angle of 1.77° and 0.34° , respectively, as shown in Figure 2 (d). It indicates that the swollen films were more capable of storing the energy at the lower shear strains. At the higher shear strains, both dry and swollen films show similar phase angles (75° - 80°), indicating the dominant viscous behavior. The region that signals that the material behavior is mechanically stable is known as the linear elastic region (LVR) [21]. The shear strain (1%) was identified from the LVR region and used as input for the frequency sweep. Beyond the linear viscoelastic region (LVR), the film is undergoing deformation beyond its ability to recover its original shape, transitioning from solid-like to liquid-like behavior.

Frequency sweep behavior of hydrogel film

Frequency sweep tests were conducted within the linear viscoelastic region (LVR), where the structural integrity of the samples remained intact, using frequencies ranging from 0.1 to 100 Hz. These experiments effectively assess the mechanical behavior of hydrogel film without disturbing its structure [30]. The moduli of the dry and

swollen films were evaluated under the influence of frequency at the 1% of shear strain, and the results are depicted in Figure 4.

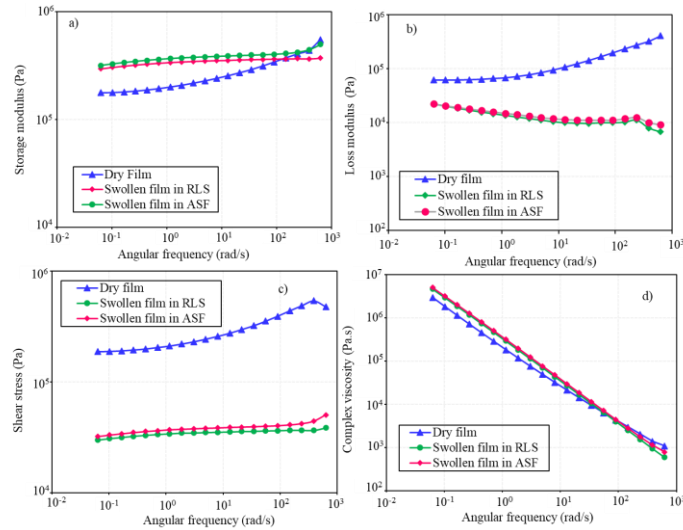


Figure 4. Viscoelastic properties variation with the frequency

At 100 Hz, the dry film exhibited a higher G' (549.06 kPa) than the swollen films in RLS and ASF because the film maintains a more rigid and compact structure in dry conditions than in a swollen state. The film swollen in ASF shows relatively higher G' (496.02 kPa) than the film swollen in RLS ($G'=369.88$ kPa) at 100 Hz for a 30h swollen period. It is attributed to the interaction between the biomolecules, such as hyaluronic acid in the ASF, and biopolymers of the hydrogel film. The G' and G'' of both dry and swollen hydrogel film were increased as the frequency increased. The rise in G' with increasing frequency can be attributed to the formation of macromolecular structures in the higher frequency range [31]. Similarly, the increase in loss modulus with frequency is likely due to bond rupture, leaving insufficient time for the structure to recover. No crossover was observed in the frequency sweep tests, indicating that the hydrogel film exhibits solid-like behavior [32, 33]. The complex viscosity of the hydrogel film was evaluated with the varied frequency, as shown in Figure 3 (d). The reduction in complex viscosity with increasing frequency is attributed to the weakening and disruption of attractive forces. This behavior is characteristic of shear-thinning, pseudoplastic hydrogel film [47]. The swollen film in ASF showed the highest complex viscosity, followed by the swollen film in RLS and the dry

film at the lowest frequency. At 100 Hz, the dry film exhibited the highest complex viscosity, followed by the swollen film in ASF and the swollen film in RLS. This is due to the compact structure of the dry film at the higher frequency [34].

Stress Relaxation Behavior

Understanding stress relaxation is crucial when selecting biomaterials for biomedical applications, such as artificial tissues, as prolonged exposure to stress can lead to tissue failure. The developed hydrogel films were tested under a constant 10% strain for 1000 seconds to study this behavior, as shown in Figure 5 (a-b). When comparing the relaxation behavior of the dry and swollen hydrogel film, the dry film experiences more stress (~ 51.47 kPa) due to the compact polymer network structure. In the case of the swollen film, the polymer chains become flexible and have great mobility due to the presence of fluid, resulting in lower stress experiences. The film is swollen in the RLS, and ASF experiences a stress of ~ 27.64 kPa and ~ 35.97 kPa, respectively. The interaction of biomolecules such as protein and hyaluronic acid present in the ASF with the film's polymer chains betters the film's mechanical structure, resulting in the experience of higher stress.

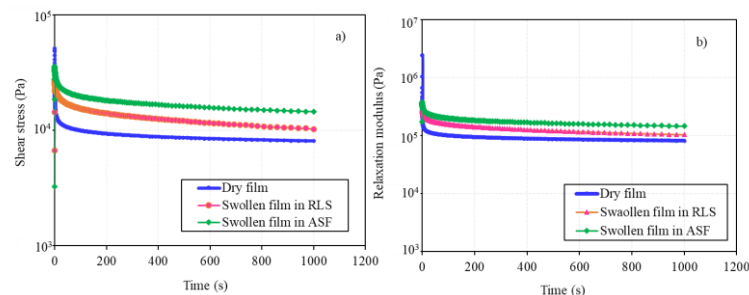


Figure 5. Stress relaxation behavior of multimaterial hydrogel film

In contrast, ions in the RLS affect the osmotic balance and hydration rather than forming bonds with the film's polymer chains. In the initial period (fast relaxation stage), the stress relaxation of the dry film was observed at 81.76%, whereas swollen films in ASF and RLS were revealed at 47.89% and 49.24%, respectively. The initial stress relaxation occurs much more rapidly in the dry film than in the swollen film. A similar trend was reported in the prior studies [35]. In the 1000s, dry, swollen film stress relaxation in RLS and ASF was noticed as 84.29%, 63.50%, and 59.58%, respectively.

Oscillatory tribology

Figure 6 illustrates the variation of the coefficient of friction (COF) with the sliding speed of a normal load of 5 N under the lubrication of RLS and ASF. A decrease in the COF was noticed in the presence of ASF compared to the RLS lubrication. Under lubrication conditions, the interstitial fluid of hydrogel is replenished through re-swelling in the surrounding lubricant. This process sustains interstitial fluid pressurization and helps re-form liquid films during sliding [36, 37].

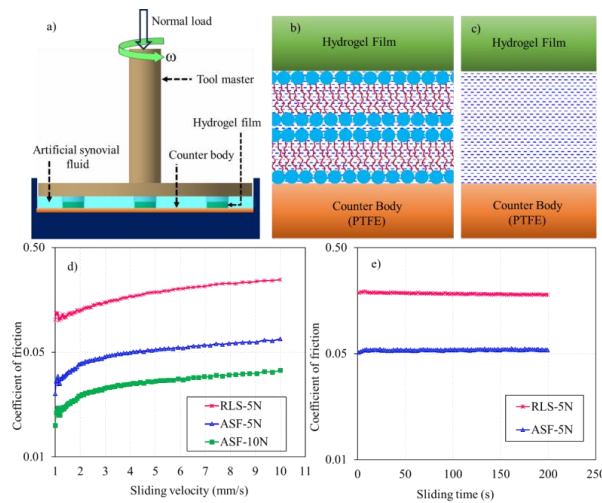


Figure 6. Oscillatory frictional behavior of hydrogel film, a) schematic representation of experimental setup, b) interface between the hydrogel film and PTFE counter body in the presence of ASF during the test, c) interface between the hydrogel film and PTFE counter body in the presence of RLS during test, d) COF variation with the sliding velocity at the different normal loads, e) COF variation with the sliding time at 5 mm/s

The ability of the hydrogel to re-swell and replenish interstitial fluid may vary, causing fluctuations in the lubrication effectiveness and, thus, the COF. The two components of ASF, hyaluronic acid (HA) and phospholipids, play a significant role in the lubrication of the hydrogel surface [38]. This lubrication occurs due to hydration lubrication, where slip is facilitated by the hydrated lecithin headgroup interface exposed on the HA-phospholipid surface [39], as illustrated in Fig. 5 (b). ASF works by providing boundary lubrication, where molecules like hyaluronic acid interact with the surface and form a hydrated layer [23]. This mechanism reduces direct surface contact, whereas RLS lacks such specific lubricating molecules and mainly relies on

hydrodynamic lubrication, which is less effective in reducing COF. Figure 5(d) depicts the variation in coefficient of friction (COF) with sliding speed under various normal loads. As sliding speed rises, COF decreases little at first, then increases across all loads [40]. This phenomenon mostly results from the porous nature of hydrogel film, which increases resistance and causes pressure building within the material. As the normal load increases, so does the internal pressure, allowing a greater load to be borne by the liquid phase, resulting in a lower COF [41]. The film exhibited a greater COF at lower speeds (1 mm/s), followed by a decreasing and increasing trend. Due to the lack of effective lubrication at the interface at the lower sliding speed result in higher COF. As the sliding speed rises, fluid enters the contact area, reducing COF [42, 43]. The lowest COF point on each curve corresponds to the transition from mixed to hydrodynamic lubrication [44]. However, if the sliding speed increases, the coefficient of friction may climb again. This increase is explained by elastohydrodynamic lubrication theory, which states that at greater speeds, viscous drag rises, resulting in a larger friction coefficient [42, 43]. Over the sliding time of 200s, the change in the COF was nearly constant, with slight fluctuations under the lubrication of both ASF and RLS. This may be due to the minimal changes in the surface of the hydrogel film in the considered period.

Conclusion

The dynamic mechanical and tribological properties of the quaternary blended multimaterial hydrogel film in two physiological solutions, such as ringer lactic solution (RLS) and artificial synovial fluid (ASF), were assessed. The dry film exhibited a G' of 535.59 kPa at the lower shear strain (0.001%). A reduction of 15.92% and 30.91% in the G' was noticed at the lower shear strain (0.001%) for the swollen films in the ASF and RLS, respectively. At 100 Hz, the dry film exhibited a higher G' (549.06 kPa) than the swollen films in RLS and ASF. The film swollen in ASF shows relatively higher G' (496.02 kPa) than the film swollen in RLS (G' =369.88 kPa) at 100 Hz for a 30h swollen period. When comparing the relaxation behavior of the dry and swollen hydrogel film, the dry film experiences more stress (~51.47 kPa) for the same period due to the compact polymer network structure. The film under the lubrication of ASF exhibited lower COF as it provides boundary lubrication, where molecules like hyaluronic acid interact with the surface and form a hydrated layer—this thorough analysis of hydrogel films in physiological conditions suggested material for biomedical use.

Acknowledgment

The authors are grateful to the Department of Science and Technology (DST)-Innovation in Science Pursuit for Inspired Research (INSPIRE) for fellowship support (IF190716).

References

1. Xue, X., Hu, Y., Deng, Y., Su, J.: Recent Advances in Design of Functional Biocompatible Hydrogels for Bone Tissue Engineering. *Adv. Funct. Mater.* 31, (2021). <https://doi.org/10.1002/adfm.202009432>.
2. Vedadghavami, A., Minooei, F., Mohammadi, M.H., Khetani, S., Rezaei Kolahchi, A., Mashayekhan, S., Sanati-Nezhad, A.: Manufacturing of hydrogel biomaterials with controlled mechanical properties for tissue engineering applications. *Acta Biomater.* 62, 42–63 (2017). <https://doi.org/10.1016/j.actbio.2017.07.028>.
3. Natori, N., Shibano, Y., Hiroki, A., Taguchi, M., Miyajima, A., Yoshizawa, K., Kawano, Y., Hanawa, T.: Preparation and Evaluation of Hydrogel Film Containing Tramadol for Reduction of Peripheral Neuropathic Pain. *J. Pharm. Sci.* 112, (2023). <https://doi.org/10.1016/j.xphs.2022.05.013>.
4. Ahmad, N., Colak, B., Zhang, D.W., Gibbs, M.J., Watkinson, M., Remzi Becer, C., Gautrot, J.E., Krause, S.: Peptide cross-linked poly (Ethylene glycol) hydrogel films as biosensor coatings for the detection of collagenase. *Sensors (Switzerland)*. 19, (2019). <https://doi.org/10.3390/s19071677>.
5. Fadeeva, I. V., Trofimchuk, E.S., Forysenkova, A.A., Ahmed, A.I., Gnezdilov, O.I., Davydova, G.A., Kozlova, S.G., Antoniac, A., Rau, J. V.: Composite polyvinylpyrrolidone–sodium alginate—Hydroxyapatite hydrogel films for bone repair and wound dressings applications. *Polymers (Basel)*. 13, (2021). <https://doi.org/10.3390/polym13223989>.
6. Dong, Y., Wang, J., Guo, X., Yang, S., Ozen, M.O., Chen, P., Liu, X., Du, W., Xiao, F., Demirci, U., Liu, B.F.: Multi-stimuli-responsive programmable biomimetic actuator. *Nat. Commun.* 10, (2019). <https://doi.org/10.1038/s41467-019-12044-5>.
7. Bao, Z., Yu, A., Shi, H., Hu, Y., Jin, B., Lin, D., Dai, M., Lei, L., Li, X., Wang, Y.: Glycol chitosan/oxidized hyaluronic acid hydrogel film for topical ocular delivery of dexamethasone and levofloxacin. *Int. J. Biol. Macromol.* 167, (2021).

<https://doi.org/10.1016/j.ijbiomac.2020.11.214>.

8. Li, Q., Ai, R., Fan, J., Fu, X., Zhu, L., Zhou, Q., Chen, L., Ma, W., Li, Y., Liu, L.: AgNPs-loaded chitosan/sodium alginate hydrogel film by in-situ green reduction with tannins for enhancing antibacterial activity. *Mater. Today Commun.* 38, (2024). <https://doi.org/10.1016/j.mtcomm.2023.107927>.
9. Mojally, M., Sharmin, E., Obaid, N.A., Alhindi, Y., Abdalla, A.N.: Polyvinyl alcohol/corn starch/castor oil hydrogel films, loaded with silver nanoparticles biosynthesized in *Mentha piperita* leaves' extract. *J. King Saud Univ. - Sci.* 34, 101879 (2022). <https://doi.org/10.1016/j.jksus.2022.101879>.
10. Sulastri, E., Zubair, M.S., Lesmana, R., Mohammed, A.F.A., Wathoni, N.: Development and Characterization of Ulvan Polysaccharides-Based Hydrogel Films for Potential Wound Dressing Applications. *Drug Des. Devel. Ther.* Volume 15, 4213–4226 (2021). <https://doi.org/10.2147/DDDT.S331120>.
11. Samadi, A., Azandeh, S., Orazizadeh, M., Bayati, V., Rafienia, M., Karami, M.: Fabrication and characterization of glycerol/chitosan/polyvinyl alcohol-based transparent hydrogel films loaded with silver nanoparticles for antibacterial wound dressing applications. *Adv. Biomed. Res.* 10, 4 (2021). https://doi.org/10.4103/abr.abr_211_20.
12. Jayaramudu, T., Varaprasad, K., Pyarasani, R.D., Reddy, K.K., Akbari-Fakhrabadi, A., Carrasco-Sánchez, V., Amalraj, J.: Hydroxypropyl methylcellulose-copper nanoparticle and its nanocomposite hydrogel films for antibacterial application. *Carbohydr. Polym.* 254, 117302 (2021). <https://doi.org/10.1016/j.carbpol.2020.117302>.
13. Mali, K.K., Ghorpade, V.S., Dias, R.J., Dhawale, S.C.: Synthesis and characterization of citric acid crosslinked carboxymethyl tamarind gum-polyvinyl alcohol hydrogel films. *Int. J. Biol. Macromol.* 236, 123969 (2023). <https://doi.org/10.1016/j.ijbiomac.2023.123969>.
14. Serro, A.P., Silva, D.C., Fernandes, A.I.: Hydrogel-Based Novel Biomaterials: Achievements and Prospects. *Gels.* 10, 436 (2024). <https://doi.org/10.3390/gels10070436>.
15. Mohammad Mehdipour, N., Kumar, H., Kim, K., Sundararaj, U., Shor, R.J., Natale, G.: Manipulating mechanical properties of PEG-based hydrogel nanocomposite: A potential versatile bio-adhesive for the suture-less repair of tissue. *J. Mech. Behav.*

- Biomed. Mater. 150, 106285 (2024).
<https://doi.org/10.1016/j.jmbbm.2023.106285>.
16. He, Q., Cheng, Y., Deng, Y., Wen, F., Lai, Y., Li, H.: Conductive Hydrogel for Flexible Bioelectronic Device: Current Progress and Future Perspective. *Adv. Funct. Mater.* 34, (2024).
<https://doi.org/10.1002/adfm.202308974>.
 17. Qureshi, M.A. ur R., Arshad, N., Rasool, A., Islam, A., Rizwan, M., Haseeb, M., Rasheed, T., Bilal, M.: Chitosan and Carrageenan-Based Biocompatible Hydrogel Platforms for Cosmeceutical, Drug Delivery, and Biomedical Applications. *Starch - Stärke.* 76, (2024).
<https://doi.org/10.1002/star.202200052>.
 18. Chuang, E.-Y., Chiang, C.-W., Wong, P.-C., Chen, C.-H.: Hydrogels for the Application of Articular Cartilage Tissue Engineering: A Review of Hydrogels. *Adv. Mater. Sci. Eng.* 2018, (2018). <https://doi.org/10.1155/2018/4368910>.
 19. Cong, Y., Fu, J.: Hydrogel–Tissue Interface Interactions for Implantable Flexible Bioelectronics. *Langmuir.* 38, 11503–11513 (2022). <https://doi.org/10.1021/acs.langmuir.2c01674>.
 20. Zivari-Ghader, T., Rashidi, M.-R., Mehrali, M.: Biological macromolecule-based hydrogels with antibacterial and antioxidant activities for wound dressing: A review. *Int. J. Biol. Macromol.* 134578 (2024).
<https://doi.org/10.1016/j.ijbiomac.2024.134578>.
 21. Öhrlund, Å.: Evaluation of Rheometry Amplitude Sweep Crossover Point as an Index of Flexibility for HA Fillers. *J. Cosmet. Dermatological Sci. Appl.* 08, (2018).
<https://doi.org/10.4236/jcdsa.2018.82008>.
 22. Vildanova, R.R., Sigaeva, N.N., Kukovinets, O.S., Kolesov, S.V.: Preparation and rheological properties of hydrogels based on N-succinyl chitosan and hyaluronic acid dialdehyde. *Polym. Test.* 96, (2021).
<https://doi.org/10.1016/j.polymertesting.2021.107120>.
 23. Venkata Krishna, D., Ravi Sankar, M.: Bioinspired artificial synovial fluid for in vitro frictional behavior of bovine articular cartilage and auxiliary biomaterials. *J. Mol. Liq.* 122836 (2023).
<https://doi.org/10.1016/j.molliq.2023.122836>.
 24. Abilova, G.K., Kaldybekov, D.B., Ozhmukhametova, E.K., Saimova, A.Z., Kazybayeva, D.S., Irmukhametova, G.S.,

- Khutoryanskiy, V. V.: Chitosan/poly(2-ethyl-2-oxazoline) films for ocular drug delivery: Formulation, miscibility, in vitro and in vivo studies. *Eur. Polym. J.* 116, (2019). <https://doi.org/10.1016/j.eurpolymj.2019.04.016>.
25. Hassan, N., Ahmad, T., Zain, N.M., Awang, S.R.: Identification of bovine, porcine and fish gelatin signatures using chemometrics fuzzy graph method. *Sci. Rep.* 11, (2021). <https://doi.org/10.1038/s41598-021-89358-2>.
 26. Thombare, N., Mahto, A., Singh, D., Chowdhury, A.R., Ansari, M.F.: Comparative FTIR Characterization of Various Natural Gums: A Criterion for Their Identification. *J. Polym. Environ.* 31, (2023). <https://doi.org/10.1007/s10924-023-02821-1>.
 27. Elsaed Shima, S.M., Zaki, E.G., Omar, W.A.E., Ashraf Soliman, A., Attia, A.M.: Guar Gum-Based Hydrogels as Potent Green Polymers for Enhanced Oil Recovery in High-Salinity Reservoirs. *ACS Omega* 6, (2021). <https://doi.org/10.1021/acsomega.1c03352>.
 28. Sim, H.G., Ahn, K.H., Lee, S.J.: Three-dimensional dynamics simulation of electrorheological fluids under large amplitude oscillatory shear flow. *J. Rheol. (N. Y. N. Y.)* 47, (2003). <https://doi.org/10.1122/1.1582854>.
 29. Hyun, K., Wilhelm, M., Klein, C.O., Cho, K.S., Nam, J.G., Ahn, K.H., Lee, S.J., Ewoldt, R.H., McKinley, G.H.: A review of nonlinear oscillatory shear tests: Analysis and application of large amplitude oscillatory shear (LAOS), (2011). <https://doi.org/10.1016/j.progpolymsci.2011.02.002>.
 30. Shakeel, A., MacIver, M.R., van Kan, P.J.M., Kirichek, A., Chassagne, C.: A rheological and microstructural study of two-step yielding in mud samples from a port area. *Colloids Surfaces A Physicochem. Eng. Asp.* 624, (2021). <https://doi.org/10.1016/j.colsurfa.2021.126827>.
 31. Razi, S.M., Motamedzadegan, A., Shahidi, S.A., Rashidinejad, A.: Basil Seed Gum Enhances the Rheological and Physical Properties of Egg Albumin Foams. *Food Nutr. J.* 8, (2018). <https://doi.org/10.29011/2575-7091.100092>.
 32. Jannatamani, H., Motamedzadegan, A., Farsi, M., Yousefi, H.: Rheological properties of wood/bacterial cellulose and chitin nano-hydrogels as a function of concentration and their nano-films properties. *IET Nanobiotechnology* 16, (2022). <https://doi.org/10.1049/nbt2.12083>.

33. Rafe, A., Razavi, S.M.A.: Dynamic viscoelastic study on the gelation of basil seed gum. *Int. J. Food Sci. Technol.* 48, (2013). <https://doi.org/10.1111/j.1365-2621.2012.03221.x>.
34. Gong, J., Wang, L., Wu, J., Yuan, Y., Mu, R.J., Du, Y., Wu, C., Pang, J.: The rheological and physicochemical properties of a novel thermosensitive hydrogel based on konjac glucomannan/gum tragacanth. *LWT.* 100, (2019). <https://doi.org/10.1016/j.lwt.2018.10.080>.
35. Hazur, J., Endrizzi, N., Schubert, D.W., Boccaccini, A.R., Fabry, B.: Stress relaxation amplitude of hydrogels determines migration, proliferation, and morphology of cells in 3-D culture. *Biomater. Sci.* 10, (2022). <https://doi.org/10.1039/d1bm01089a>.
36. Caligaris, M., Ateshian, G.A.: Effects of sustained interstitial fluid pressurization under migrating contact area, and boundary lubrication by synovial fluid, on cartilage friction. *Osteoarthr. Cartil.* 16, 1220–1227 (2008). <https://doi.org/10.1016/j.joca.2008.02.020>.
37. Shi, Y., Xiong, D.: Microstructure and friction properties of PVA/PVP hydrogels for articular cartilage repair as function of polymerization degree and polymer concentration. *Wear.* 305, (2013). <https://doi.org/10.1016/j.wear.2012.12.020>.
38. Zhu, L., Seror, J., Day, A.J., Kampf, N., Klein, J.: Ultra-low friction between boundary layers of hyaluronan-phosphatidylcholine complexes. *Acta Biomater.* 59, (2017). <https://doi.org/10.1016/j.actbio.2017.06.043>.
39. Lin, W., Klein, J.: Hydration Lubrication in Biomedical Applications: From Cartilage to Hydrogels. *Accounts Mater. Res.* 3, (2022). <https://doi.org/10.1021/accountsmr.1c00219>.
40. Krishna, D.V., Sankar, M.R., Sarma, P.V.G.K., Samundeswari, E.L.: Synergistic Effects of Psidium Guajava and Copper Nanoparticles Reinforced Hybrid Hydrogel for Tissue Engineering. *Adv. Ind. Eng. Polym. Res.* (2024). <https://doi.org/10.1016/j.aiepr.2024.10.001>.
41. Furmann, D., Nečas, D., Rebenda, D., Čípek, P., Vrbka, M., Krupka, I., Hartl, M.: The effect of synovial fluid composition, speed and load on frictional behaviour of articular cartilage. *Materials* (Basel). 13, (2020). <https://doi.org/10.3390/ma13061334>.
42. Qiu, X., Yan, Y., Zhang, G., Huang, J., Zhao, Y., Xia, X., Cui,

- X., Zhang, X.: Investigation of the time-dependent friction behavior of polyacrylamide hydrogels. *Colloids Surfaces A Physicochem. Eng. Asp.* 659, (2023). <https://doi.org/10.1016/j.colsurfa.2022.130753>.
43. Cuccia, N.L., Pothineni, S., Wu, B., Harper, J.M., Burton, J.C.: Pore-size dependence and slow relaxation of hydrogel friction on smooth surfaces. *Proc. Natl. Acad. Sci. U. S. A.* 117, (2020). <https://doi.org/10.1073/pnas.1922364117>.
44. Feng, D., Shen, M., Peng, X., Meng, X.: Surface Roughness Effect on the Friction and Wear Behaviour of Acrylonitrile–Butadiene Rubber (NBR) Under Oil Lubrication. *Tribol. Lett.* 65, 10 (2017). <https://doi.org/10.1007/s11249-016-0793-5>.

Fabrication and Characterization of Biodegradable Composite Disposable Plates using Natural Fibers and Starch

Adarsh Jaiswal¹, Krishnakant Dhakar^{1*}, T. S. Srivatsan²

¹ *Department of Industrial and Production Engineering*
Shri G.S. Institute of Technology and Science
Indore, Madhya Pradesh 452003, INDIA

² *Department of Mechanical Engineering*
The University of Akron
Akron, OHIO 44325, USA

Corresponding Author: krishnakantdhakar@gmail.com

Abstract

A revolutionary product has the potential to bring the 3R concept, namely **R**educe, **R**ecycle and **R**euse, to the mainstream, i.e., one-hundred percent [100%] biodegradable disposable plates made of eco-friendly bamboo and straw stubble fiber, which is noticeably pocket - friendly. A discussion on the ban of single use plastics in India resulted in an idea to develop a viable replacement to disposable plates and cutlery. The primary concern specific to banning the use of plastics is that it has the tendency to harm the terrestrial ecosystem. To overcome this problem, natural fiber using matrix phase as natural binders, such as starch (used for making different type of food packing and cutlery item), is suggested. The use of these non-disposable plates can be considered to be both harmful to the environment and not biodegradable. Finally, a combination of bamboo fiber, straw stubble fiber, and natural binder was found to be an ideal option. Not only are these cutting-edge plates biodegradable, they also offer a combination of excellent strength and durability. This technical presentation will highlight all aspects specific to the fabrication of a biodegradable composite plate using natural binder as the matrix phase and natural fiber as the reinforcement phase. Tests were then performed, to include the following (i) the water absorption test (wet ability), and (ii) the flexural test. Compression molding can also cause deformation and a shift in orientation when utilizing long fibers. For this approach, only components having a constant wall thickness can be used. Many geometrical characteristics, to include undercuts, were difficult to produce using this procedure due to the matching metal tooling.

Further, size of the processed portion is limited. Since only one direction of pressure is applied during the processing technique, the shaped part can tend to consolidate unevenly. However, on the surfaces that are parallel to the direction of closure, there does occur a large amount of consolidation. A comparison of the different types of natural fiber used as the reinforcement phase and natural binder as the matrix phase for the engineered composite materials can be utilized for biodegradable plates since it offers the advantages of being both eco-friendly and cost-effective. Due on account of its low cost, biodegradability, and superior mechanical performance, natural fiber has been chosen for use as the binder resulting in better aesthetic features and binding properties at the different temperatures.

Keywords: Composites, Natural Fiber Reinforced Composites (NFRCs), Bamboo Fiber, Natural binders, Starch, Mechanical Testing.

Introduction

The growing concern over plastic waste and its harmful impact on the environment has provided the much-needed impetus for a global shift towards sustainable materials. Traditional plastics, commonly used in disposable tableware, contribute significantly to pollution, thereby affecting both the land ecosystem and marine ecosystem. In response, countries like India have gradually implemented a total ban on single-use plastics, thereby driving the need for biodegradable alternatives. This research explores an innovative solution by creating disposable plates from biodegradable composites and made using natural fibres and starch-based binders. The widespread use of single-use plastics has noticeably contributed to environmental degradation, especially in terrestrial ecosystems. According to a United Nations report, millions of tons of plastic waste enter the oceans annually, and thereby contributing to devastating both wildlife and marine habitats. To address this issue of concern, the 3R framework [Reduce, Recycle, and Reuse] has emerged as a viable strategy for promoting sustainability [1].

The use of natural fibres like bamboo and straw stubble does offer a potentially viable eco-friendly alternative while concurrently improving both strength and durability of the composite materials. This study focuses on exploring how these biodegradable plates can be made, while concurrently determining their mechanical performance, and the environmental benefits they have to offer. With the growing need to replace single-use plastics, the primary objective of this research is to develop disposable plates using sustainable bamboo and straw stubble fibres. By incorporating natural starch-based binders, the

goal is to create a product that does meet consumer expectations while contributing to a significant reduction in environmental footprint [2].

Review of the Literature

Biodegradable Materials

Research on biodegradable materials has demonstrated that composites made from natural fibres and biodegradable polymers can serve as effective alternatives to conventional plastics [3]. Starch, in particular, proves to be a highly effective natural binder for these materials. Its biodegradable nature coupled with an ability to improve mechanical strength make it a perfect choice for applications where reducing environmental impact is a priority. When used alongside with natural fibres, starch can produce composites that are not only durable but also environment friendly. Starch-based binders are known for their ability to enhance the mechanical properties of these composites while concurrently maintaining their biodegradability [4].

Biodegradable materials tend to break down naturally, helping to lessen their impact on the environment. Research by Smith et al. [5] highlights the crucial need to develop sustainable alternatives to conventional plastics, which can take hundreds of years to degrade while continuing to pollute the environment during that time.

Natural Fiber Reinforced Composites (NFRCs)

Natural fibres have become increasingly popular in composite materials due on account of their renewable nature and strong mechanical properties. Research shows that natural fibre-reinforced composites (NFRCs) can offer strength comparable to synthetic fibre composites, while concurrently being more environment friendly [6]. These materials have a wide range of applications, from packaging to construction. Fibers like bamboo and straw present promising alternatives because of their biodegradability and excellent mechanical properties. Studies have shown that the bamboo fibres, in particular, offer an attractive combination of high tensile strength and low density, making them highly advantageous for composite materials [7]. Meanwhile, straw stubble fibres, as an agricultural by-product, does provide a cost-effective and eco-friendly option [8].

Single-Use Plastics

The environmental impact of single-use plastics is significant, and does contribute to pollution and thereby damaging both the land eco-system and the marine ecosystem [9]. In response, many countries, to include India, have introduced a total ban on single-use plastics with

the fond hope of reducing or minimizing these harmful effects, thereby highlighting the urgent need for sustainable alternatives [10].

Methodology

Materials

Bamboo fibres were sourced from local suppliers in Jhabua, Madhya Pradesh, while the straw stubble fibres were obtained from local agricultural practices. Starch was chosen as the natural binder due to its excellent binding properties and biodegradability. The fibrous form of bamboo and straw stubble is shown in **Figure 1(a)** and **Figure 1 (b)**. The starch in powdered form is shown in **Figure 1 (c)**.

Fabrication of the Composite

The biodegradable disposable plates were fabricated using the compression moulding process. The fibres were mixed with the starch binder in a specific ratio [example: 60% fibre to 40% binder] and then compressed at 180°C using a pressure of 2000-3000 psi for 10-15 minutes. The compression moulding process was optimized to ensure the following:

- (a) Mitigate issues, such as deformation, and
- (b) Ensure a near uniform wall thickness.

Using a heated hydraulic press under high pressure, this method does consolidate the moulded parts. Typically, this method has been used to create fibre-reinforced thermoplastic, chopped thermoplastic fibres, and thermosetting preregs. This method is also used to produce sandwich constructions having a honeycomb core and polymeric foam. There are several advantages to this strategy. The continuous fibres that have been compression-moulded have significantly improved mechanical properties. With the exception of flat mouldings, each moulding loses its viability for low production numbers. The machined tool is quite expensive. Along with these advantages, there are a few disadvantages. Compression moulding can also cause deformation and orientation shift when utilizing long fibres. For this approach, only components having a constant wall thickness can be used. Many geometrical characteristics, to include undercuts, were difficult to produce using this procedure due to the matching metal tooling. The size of the processed portion is limited. Since only one direction of pressure is applied during this process, a shaped part can consolidate unevenly. Nevertheless, on surfaces that are parallel to the direction of closure, there does occur a large amount of consolidation. In comparison to injection moulding, compression moulding is an

inexpensive method for the mass making of specimens [11]. Fabrication of biodegradable disposable plates is shown in **Figure 2**.

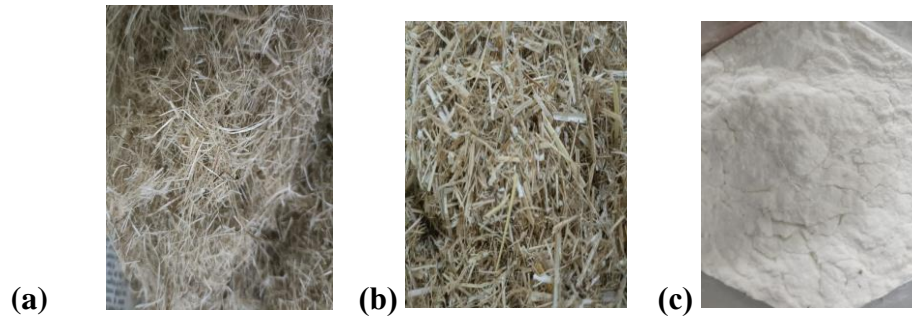


Figure 1.(a) Bamboo fibre, (b) Straw Stubble, and (c) Starch

Mechanical Testing

Two primary mechanical tests were conducted:

1. **Water Absorption Test:** To evaluate the wet ability of the biodegradable disposal plates they were initially submerged in water for full 30 minutes, and then the weight gain was measured. The water absorption test objective was to evaluate how much water a biodegradable disposal plate will absorb under fixed, predefined conditions over a given period of time. There are numerous assessment settings and durations available following conditioning. This experimental investigation was conducted using the same protocol. The method used in this research study is known or referred to as the “half hour Water test”.
2. **Flexural Test:** The flexural strength was measured using a universal testing machine. This testing process aimed at determining the force acting per square millimetre of the chosen composite material.

Observations

The compression moulding process effectively produced uniform plates. However, some deformation was observed in samples having a complex geometry. An optimization of the moulding parameters can help in enhancing the overall quality of the final product.

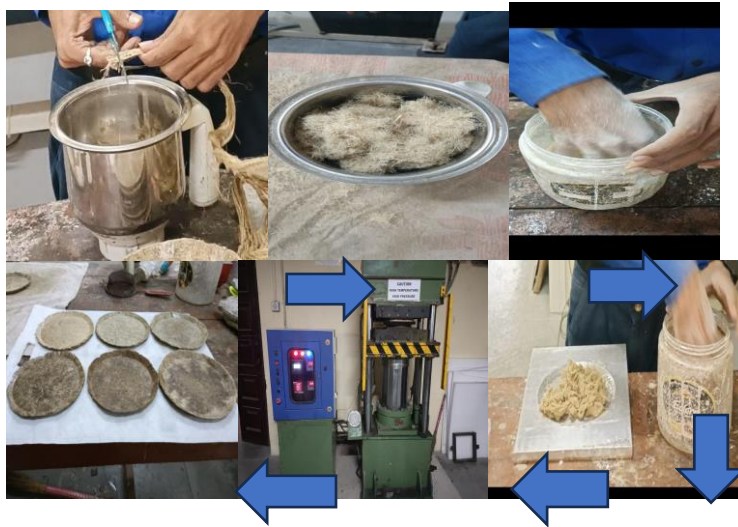


Figure 2. Illustrative Representation of Fabricated Composite disposable plates.

Discussion

The results indicate that the developed biodegradable plates did exhibit promising mechanical properties, making them suitable for various applications. When compared to the conventional plastics, these composites offer the advantage of being biodegradable, and thereby addressing the urgent need for being both sustainable and viable alternatives.

A comparison with existing materials does clearly reveal that a combination of bamboo and straw fibres, reinforced with starch, does significantly enhance the mechanical performance while concurrently maintaining cost-effectiveness. Future work could focus on long-term biodegradation studies and commercial applications.

Conclusions

The following are the key findings of this novel research study:

1. This research highlights the potential of bamboo and straw stubble fibres, combined with natural binders, to create 100% biodegradable disposable plates.
2. The findings support the viability of these materials as sustainable alternatives to single-use plastics, contributing to environmental conservation.
3. Additional research is needed to explore additional applications and optimize production processes.

4. Due to its low cost, biodegradability, and superior mechanical performance, natural fibre has been employed in natural binders with better aesthetic features and binding properties at different temperature zones.

References

1. UNEP. (2021). "Global Plastics Outlook: Economic Drivers, Environmental Impacts, and Policy Options." United Nations Environment Programme.
2. Chamas, A., et al. (2020). "Degradation Rates of Plastics in the Environment." **Environmental Science & Technology**, 54(1), 28-40.
3. Reddy, R. R., et al. (2013). "Biodegradable Polymers and Their Applications." **Materials Science and Engineering: R: Reports**, 74(1), 1-19.
4. Thygesen, A., et al. (2005). "The Role of Starch in the Biodegradability of Natural Fiber Composites." **Composites Science and Technology**, 65(11-12), 1812-1822.
5. Smith J., Brown T., and Taylor M., "Biodegradable alternatives to plastic: An analysis of natural fibre composites," **Environmental Science and Technology**, vol. 54, no. 12, pp. 7542-7553, 2020.
6. R. Patel, V. Sharma, and R. Singh, "Mechanical properties of natural fibre composites: A review," **Composites Science and Technology**, vol. 207, p. 108757, 2021.
7. Mohanty, A. K., et al. (2005). "Natural Fibers, Biopolymers, and Bio composites." *CRC Press*.
8. Alvarez, V. H., et al. (2016). "Natural Fibers in Bio composites." **Journal of Cleaner Production**, 112, 4526-4533.
9. Geyer, R., et al. (2017). "Production, Use, and Fate of All Plastics Ever Made." **Science Advances**, 3(7), e1700782.
10. Bhat, S., et al. (2021). "Impact of Single-Use Plastic Ban in India." **Waste Management & Research**, 39(8), 925-934.
11. Satishkumar, G. et al. (2020) "Synthesis and Mechanical Properties of Natural Fiber Reinforced Epoxy/Polyester/Polypropylene Composites, **Journal of Natural Binders**.

Fault Tree Analysis of FDM 3 D Printer for Improved Maintainability

¹Sayli M. Jadhav, ²Dr. Vinay Kulkarni

D. Y. Patil. College of Engineering,
Akurdi, Maharashtra, India

Abstract

Additive manufacturing, particularly FDM 3D printing, has future scope for the manufacturing industry. However, Problem of nozzle clogging is a major issue in using FDM Printer and it reduces production. The absence of early warning systems emphasizes the importance of efficient maintenance solutions for using FDM Printers in Industry 4.0. Real-time monitoring and online process control are critical to increasing productivity of FDM Printers. This paper involves fault tree Analysis of FDM printers performed during working. Maintainability and real time maintenance improves the effectiveness of FDM printers. Real time maintenance improves adaptability to industries and mass manufacturing systems in industry 4.0 A diagram of the system's main flaws and their root causes is provided. Boolean algebra is utilized to determine the governing reliability models for FDM printers and to evaluate fault tree (FT) diagrams.

Keywords— Fault Tree Analysis, FDM Printers, Nozzle Clogging

Introduction

The FDM process has the advantages of being simple to set up, easy to install, easy to maintain, inexpensive initial setup operating costs, and low material consumption costs (Kadir Günaydın et al., 2018) [2]. FDM technology, has revolutionized manufacturing processes. which provides unmatched adaptability and efficiency in producing complicated geometries and bespoke items. However, inherent maintenance issues that might cause operational disruptions and lower print quality are impeding the mainstream adoption of FDM 3D printing. To solve these problems and guarantee the dependability and functionality of FDM 3D printers in a range of applications, better maintainability techniques are crucial. Fault Tree Analysis (FTA) stands out among these tactics as a potentially effective technique for methodically locating and reducing possible failure modes in the FDM printing process. Researchers can improve the operating efficiency and fault tolerance of FDM 3D printers by incorporating FTA into maintenance procedures. This will expand the potential of additive manufacturing in Industry 4.0 and beyond.

General Description of FDM 3D printer-

Thermoplastic filament is melted and deposited layer by layer in an FDM 3D printer to create objects. A filament spool for material supply, an extruder assembly for filament melting and deposition, a frame for stability, a build platform for printing, motion systems for accurate movement, a bed leveling mechanism for print consistency, heating elements for filament melting, cooling fans for material cooling, and a control system for printing process management are some of its constituent parts. All things considered, FDM 3D printers are adaptable devices that can create functioning components, prototypes, and even finished goods using a variety of thermoplastic materials. Because of their ease of use and very straightforward construction, they are well-liked by professionals, companies, and hobbyists for small-scale production, customized manufacturing, and quick prototyping.

Literature Review

Several work progress done by the researchers on the basis of finding issues and challenges

Patil, R. B., Mhamane, D. A et.al[1]- They studied Fault Tree Analysis of CNC Machine-In this paper the authors studied fault tree analysis (FTA) for CNC machine reliability study. The faults associated with the CNC machine and their causes The CNC turning center's reliability is analyzed using this method. The main issues with the system are examined, as are the reasons behind them. The FTA diagram for CNC machine is drawn and governing reliability of CNC machine is calculated .AndrijaVolkanovski ,Marko Cepin et al^[2]. - They applied Fault Tree analysis for calculating the reliability of power system. The for different power system and quantitative data is evaluated to study the reliability of power stations 3.FAULT TREE ANALYSIS. Mr. S. B. Herwade Prof. A. M. Naniwadekar studied FTA for vertical broaching machine quantitatively and Reliable failure data is analysed to provide reliable information for the design of the equipment.to management. **R Zagidullin*, D Antipov**^[5]They studied FEMA analysis of FDM 3 D printer with the help of failure Tree. They Carried failure mode analysis for design failures of FDM printers. Lambos, N. et.al. studied the printer extrusion for nozzle clogging with less cost using sensors. They analyzed an automated monitoring system for study the maintenance issues of FDM Printers and designed a system to analyze driver gear slippage of filament with acoustic signals'. A. Watson developed one of the reliability analysis techniques, fault tree analysis (FTA), at Bell Laboratories in 1962. A

graphical structures were used to study failure into different levels as per occurrence of the events, and Boolean gates are used to simulate how these events interact. Fault trees are used for risk analysis and study of reliability .

Methodology

Determine the Main Types of Faults observed in the working of FDM Printer

Design Consideration- Based on survey of Different Industries the issues are Sort out to get the maximum focused area according to the issues raised by the FDM Users.

The survey is focused on PLA material used in FDM ender 3D printer.

The following are often the main fault types that lead to a top-level failure in FDM 3D printers:

1 .Problems with Material Handling and Extrusion: Nozzle Cloggingjamming of the spool or filament feed.failure of the extruder motor.,Nozzle clogging as a result of inconsistent temperature or filament contaminants.

2..Problems with Thermal Control:The print head is not consistently heated or cooled. Changes in bed temperature have an effect on adhesion.,problems with thermal runaway (overheating).

3.Issues with the Print Bed and Alignment:..Poor adherence of the initial layer due to improper bed leveling, problems with Z-axis alignment,Print displacement is being caused by debris on the bed surface,Failures of the Control System and Software:

4.Incorrect motions or extrusion are caused by firmware or G-code issues,faults in the control board's and other components' communication,malfunctioning sensors (such as end-stop and temperature sensors).

5.Operational and environmental conditions:changes in the surrounding temperature or humidity,Variations in power

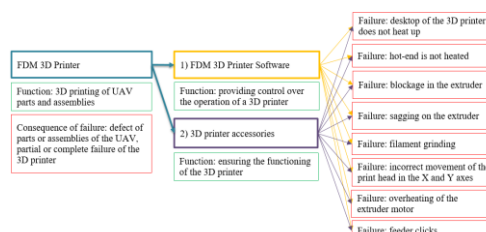


Figure 1.1 Fragment of the “failure tree” of the FDM 3D printer design^[5]

Construction of Fault Tree for FDM 3 D printer

Building a Fault Tree- When creating a fault tree diagram, the choice of useful symbols and how they are used are crucial. The fundamental FTA symbols are divided into three categories: gates, events, and transfer symbols.

Using logical gates to map dependencies, a fault tree graphically depicts the relationship between the top-level failure and the fundamental flaws that could cause it. An example of an FTA structure in FDM 3D printing is shown I fig 1.2

Top level Failure Event in FDM Printer is system failure or Printer Stop .This is due to Nozzle Clogging. This event means printer cannot finish the Print or not able to produce quality product Event at the Top Level: Total Print Failure OR Gate: One or more of the following subsystems failing could result in the failure:

1. Filament is not moving Mechanical Blockages in Nozzle : Extruder motor failure

AND filament jamming.

OR Gate: Filament Quality is Poor

2. Failure of the Thermal Controller

Issues with the bed warmer and the print head heater.

OR Gate: Incorrect Temperature Setting Mechanical Problems

OR Gate: Failure to level the bed OR misalignment of the Z-axis.

AND Gate: Vibration problems AND loose frame parts.

System/Software Failure

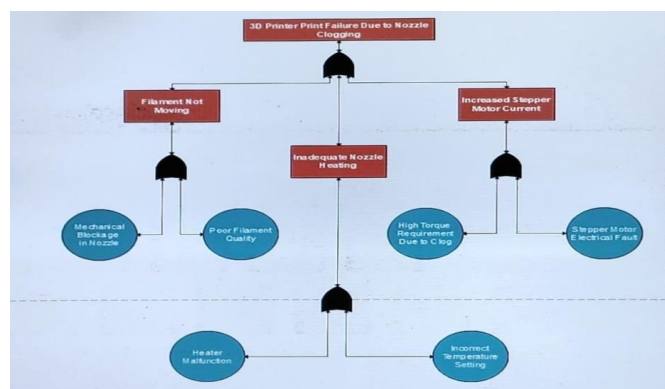


Figure 1.2 Fault Tree of Nozzle Clogging in FDM Printer

Conclusion

An FDM 3D printer's possible failure locations can be found and fixed with the aid of the FTA technique. The reliability and output quality of the FDM printing process can be greatly increased by comprehending and addressing these issues, which will make it more appropriate for tasks involving consistent manufacturing and prototyping. An FDM 3D printer's possible failure locations can be found and fixed with the aid of the FTA technique. The reliability and output quality of the FDM printing process can be greatly increased by comprehending and addressing these issues, which will make it more appropriate for tasks involving consistent manufacturing and prototyping. This Study need failure probability data for every defect event, which can be hard to get for consumer-grade FDM printers because of numerous models and brands, variable production standards, or a lack of trustworthy data. Hence to improve the maintainability of FDM printers RPN study can be carried out in future study

FutureScope: FTA can be used Investigate the possibilities of combining with real-time monitoring and sensor data to predict failures and guide maintenance through predictive maintenance FTA with Machine Learning Models: Use machine learning to help FDM operators detect upcoming failures before they affect print quality by dynamically modifying fault tree probabilities based on usage data.

References:

1. Patil, R. B., Mhamane, D. A., Kothavale, P. B., & Kothavale, B. (2018). Fault Tree Analysis: A Case Study from Machine Tool Industry. SSRN Electronic Journal.
2. Volkanovski, A., Čepin, M., & Mavko, B. (2009). Application of the fault tree analysis for assessment of power system reliability. *Reliability Engineering & System Safety*, 94(6), 1116–1127.
3. Waghmode, L. Y., Patil, R. B., (2013) “An Overview of Fault Tree Analysis (FTA) Method for Reliability Analysis.” *Journal of Engineering Research and Studies*, Volume 4, pp. 6-8.
4. Che, J., Lv, M., Yang, Z., Wang, Z., Xu, F., (2012) “Equipment Systems Reliability Analysis Based on FTA”, *Air Defence Forces Academy Zhengzhou, China IEEE* pp. 293-296.
5. Zagidullin, R., Antipov, D., Dmitriev, A., & Zezin, N. (2021). Development of a methodology for eliminating failures of an FDM 3D

printer using a “failure tree” and FMEA analysis. *Journal of Physics Conference Series*, 1925(1), 012085.

6. Nikolaos Lambos, George-Christopher Vosniakos, George Papazetis Low-cost automatic identification of nozzle clogging in material extrusion 3D printers. *Volume 51*, 2020.

6. Kadir Günaydın, Prof. Dr. Halit Süleyman Türkmen. COMMON FDM 3D PRINTING DEFECTS. 2018

7. Sachini Wickramasinghe, ORCID, Truong Do and Phuong Tran. FDM-Based 3D Printing of Polymer and Associated Composite: A Review on Mechanical Properties, Defects and Treatments. *Polymers* 2020, 12(7), 1529

8. Peeters, J. F. W., Basten, R. J. I., & Tinga, T. (2018). Improving failure analysis efficiency by combining FTA and FMEA in a recursive manner. In *Reliability Engineering & System Safety* (Vol. 172, pp. 36–44). Elsevier BV.

9. Guohua Gao; Han Ren; Yunsong Du; Hao Wang. Research and Development of Stiffness Regulator by 3D Printing. May 2018

10. Mirko Kariz, Milan Sernek, Murčo Obućina, Manja Kitek Kuzman. Effect of wood content in FDM filament on properties of 3D printed parts. *Volume 14*, March 2018, Pages 135-140

11. M. Randermann, T. Hinrichs, R. Jochem, Development of a Quality Gate Reference Model for FDM Processes, (2023)

12. G. Hsiang Loh, E. Pei, J. Gonzalez-Gutierrez, M. Monzón, An Overview of Material Extrusion Troubleshooting, *Appl. Sci.* 10(14) (2020) 4776.

13. G.D. Goh, Y.L. Yap, H.K.J. Tan, S.L. Sing, G.L. Goh, W.Y. Yeong, Process–Structure–Properties in Polymer Additive Manufacturing via Material Extrusion: A Review, *Crit. Rev. Solid State Mater. Sci.* 45(2) (2019) 113-133.

14. W. Lee, J. Fritsch, A. Maqsood, S. Liu, T. Bourassa, R. Calara, W.S. Kim, Adaptive 3D Printing for In Situ Adjustment of Mechanical Properties, *Adv. Intell. Syst.* 5(1) (2022) 2200229.

Structure property co-relation of automotive grade recycled Polypropylene: Towards reducing the carbon footprint

**Santu Panja¹, Nithin Madhav², Arun Nagarkatti³,
Manish Gopal⁴**

^{1,2,3,4}R&D Materials Science Group,
TVS Motor Company Limited,
Hosur, India

Abstract

Polypropylene (PP) is the most widely used general purpose plastic in automotive, packaging, furniture, and domestic appliances due to their low cost, environmental friendliness, recyclability, and excellent strength per weight ratio. Today, plastic recycling and reuse is a hot topic with growing concerns about carbon footprint reduction to save the environment. The polymer recycling process involves various stages such as plastic sorting, cleaning, and reprocessing. This whole recycling process potentially influences the material structure and properties. This work mainly deals with the effect of introduction of recycled polypropylene into the virgin polypropylene composition blends and its effect on various properties such as physical properties, mechanical properties, and thermal properties. Analysis of multiple virgins and recycled polypropylene polymer blends were done by increasing the recycled content up to half of the original mass of the virgin material and characterization of the property changes were done. Additionally, aimed to establish the correlation between recycled percentage and properties of the recycled blend which may be used as a standard guide or standard operating procedure for characterizing the blends.

The knowledge gained from this study will not only contribute to the fundamental insights into the behavior of recycled polypropylene but also support the development of sustainable materials with improved performance for a wide range of industries. Ultimately, bridging the gap between virgin PP and recycled PP properties will facilitate the adaptation of recycling practices and further promote the circular economy, leading to a more environmentally responsible and resource-efficient automotive industry.

Introduction

The United Nations (UN) has adopted seventeen sustainable development goals related to the global challenges, such as poverty, inequality, climate change, environmental degradation, peace, and justice for achieving a better and more sustainable future for all. The 17 Goals are all interconnected, and it is critical that we achieve them all by 2030 in order to leave no one behind (United Nations, 2015). Sustainable Development Goal (SDG) number 12 calls for responsible consumption and production practices. TVS Motor Company, being a sustainable manufacturing 2-Wheeler and 3-Wheeler global company, has taken various initiatives in the field of innovation in recycling technologies and sustainable materials, further promoting eco-friendly design for its vehicle production, and adopting a circular economy model, resulting in reducing carbon footprint and addressing significant environmental impacts due to resource consumption and waste generation targeting UN SDG 12, UN SDG 13, & UN SDG 9.

The target of recycling is not only material conservation, but also to reduce the carbon footprint, and energy footprint as shown in the Figure 1.

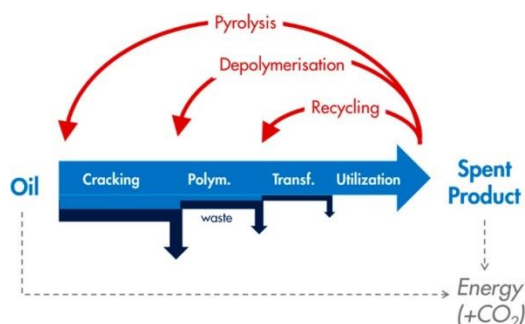


Figure 1: Various routes for plastic recycling from waste
(Lange et.al, 2021)

Based on the quality and state of the end-of-life of the product, priority should be first given to reuse, second to reprocessing, third to depolymerization of plastic to the monomer, fourth is conversion of plastic to a hydrocarbon feedstock and, last option is the energy recovery. This priority number is referred as waste hierarchy, the objective is to maximize the recycling and minimize the energy waste from the carbon footprint perspective (Lange et.al, 2021).

Generally, three types of plastic recycling processes are available: mechanical recycling, chemical recycling and thermal recycling (Kalali et.al, 2023). As per literature, mechanical recycling is the

widely used plastic recycling process due to its rapid process and high efficiency (Kalali et.al, 2023). Other advantages of the mechanical recycling process are that it is a straightforward process, and the facility required for the recycling process is simple, economical, and uses less energy and resources (Salahuddin et.al, 2023). The main disadvantage of the mechanical recycling process is the downcycling of the mechanical properties, that's why it is very difficult to use the recycled polymer in the critical or high load bearing application. But in the chemical recycling process, mechanical properties upcycling is possible with the addition of some special filler. So, recycled polymer obtained from the chemical recycling process has very good mechanical properties that can be applied in critical applications. The main disadvantage of the chemical recycling process is the high capital investment involved in developing the infrastructure and processes. And another disadvantage is that the feasibility to recycle material through chemical recycling process is yet to be established. The thermal recycling process is melting the plastic waste to a higher temperature, and then casting or injection moulding into a desirable product shape. In this process only lower order mechanical properties products are feasible. In this work we have focused on the mechanical recycling process. As this process is simple, economical and feasible for large scale production, it is required for the automotive market.

The mechanical recycling process involves various stages, the first stage is identification of good scrap sources. Then separation of various polymer or other materials mixture from the identified scrapped material. Separation process can be done by various methods like density separation where after carefully washing the scrapped different materials can be separated as per material density. Other methods of different material mixture separation are optical sorting (colour based), tribo electrostatic separation (effective surface work function based), and floatation (surface property based) (Kalali et.al, 2023). Next stage of the recycling process is washing and shredding of the sorted polymer from the scrap. After that the shredded polymer goes for the drying process. Finally, the material is fed into the extruder for the material compounding where different percentage of virgin and recycled materials are added together with other various additives as per environmental and application requirement. After that the compounded material is moulded as per requirement.

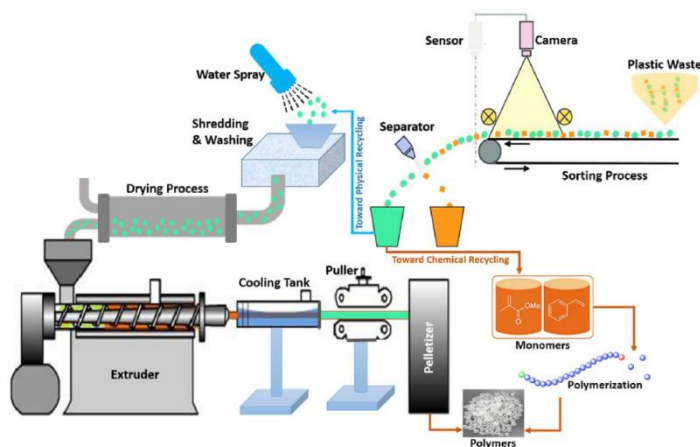


Figure 2: Schematic process flow diagram of mechanical and chemical recycling (Kalali et.al, 2023).

Two types of plastic scrap are commonly available for recycling: Post-Industrial Recycled (PIR) material and Post-Consumer Recycled (PCR) material. PIR material is derived from industrial sources, such as production defects or leftover materials from manufacturing processes. In this case, the scrap originates from a known and controlled source, typically involving only a single round of thermal processing. The material type and its original application are well-defined, which makes it easier to reprocess and use the recycled material for the same or similar applications without significant quality concerns.

On the other hand, PCR material is sourced from consumer products after their end-use lifecycle. The main challenge with PCR material lies in its heterogeneous nature, as it often consists of a mixture of various polymers and unknown additives from different applications. The quality of PCR materials is harder to control because the scrap typically includes contaminants, different grades of plastic, and potential degradation from prolonged use or environmental exposure. As a result, maintaining consistent quality, performance, and mechanical properties in recycled products becomes far more challenging with PCR material than with PIR material.

In recycling, addressing the quality issues with PCR material involves complex sorting and cleaning processes, as well as incorporating advanced additive systems to stabilize the recycled polymer during reprocessing. Technological advancements in separation, purification, and chemical recycling methods are critical to overcoming these challenges and improving the reliability of PCR plastics. Ensuring that PCR meets the necessary performance standards for applications like

packaging, automotive, or consumer goods requires careful blending, material characterization, and sometimes the use of virgin material to achieve the desired balance of properties.

Overall, while PIR materials offer a more straightforward recycling process due to their known source and composition, PCR materials present a significant challenge in terms of maintaining the quality of the recycled product, necessitating advanced recycling technologies and robust quality control measures.

As polypropylene material is extensively used material for the automotive industry, almost 3-6 kg of polypropylene material is being used in 2Wheeled vehicles. So, our first focus is on recycling polypropylene material to reduce the carbon footprint as well as reduction of virgin raw material usage to full fill our sustainability goal. In this work we have studied various properties of the polypropylene material that change after the addition of recycled polypropylene material to virgin polypropylene material. Characterized property from purely virgin PP material to the half of virgin and half of recycled material after increasing with significant amount of recycled content in each step.

In the preceding section we have discussed the necessity of plastic recycling, the advantages of the use of recycled material, various stages of recycling process, the path for reaching the sustainability goal. Although plastic recycling is needed to meet UN sustainability goals, various challenges are there for plastic recycling like-

- Recycled material has varying material composition due to mixture of various types of materials in the scrap sources. After carefully sorting the material mixture, some trace amount of other materials are usually present in the final composition (Sormunen et.al, 2019).
- Identifying good quality post-consumer recycled scrap sources and continuous supply of scrap material.
- Lower mechanical properties of the recycled polymer, as the addition of recycled material in virgin material does not have a continuous polymer chain which leads to lower mechanical properties.
- No testing methodology is available to estimate the percentage of recycled material in virgin and recycled blends to backtrack the composition.

So, in order to fulfill our goal and make our future more sustainable, this is the right time for academia, industry, and

research institutes to come together and develop recycling technologies and materials.

Materials and methods:

Materials:

Recycled Polypropylene (RPP) and virgin Polypropylene (PP) serve as the primary materials in this context, sourced from a plastic raw material supplier in pellet form. The post-consumer PP, identifiable by its resin code '5,' is meticulously separated from solid waste originating from various sources such as households, industries, automotive, and medical utilities. To ensure a clean and uncontaminated material, the post-consumer PP undergoes thorough washing and drying process, effectively eliminating any impurities. Next step involves the compounding of the cleaned post-consumer PP with virgin PP in an extruder, followed by the palletization process. This results in the production of Recycled Polypropylene pellets (RPP). By employing this recycling approach, the material is given a new life cycle, contributing to sustainability efforts while minimizing the environmental impact associated with plastic waste.

3.2 Methods:

3.2.1 Material processing and specimen preparation:

The recycled and virgin polymer blend is prepared as per the composition table. Sample specimens for various tests have been manufactured by Injection Molding process, employing carefully crafted dies adhering to ASTM standards. The Injection Molding machine used for this sample preparation from Deesha Impex, specifically the InjKON model, with temperature variations ranging from 220 °C to 250 °C. The significance of injection parameters, including injection pressure, injection time, packing time, among others, is paramount as they directly influence the quality of the resulting specimen. The parameters for the injection molding process are listed in Table -1.

Table-1: Processing parameters of injection moulding chamber (Satya et.al, 2020)

Recycled PP processing parameters	Parameters	Zone 1	Zone 2	Zone 3	Zone 4
	Melt temperature (°C)	240	235	235	230
	Injection pressure (bar)	90	100	120	120
	Injection speed (rpm)	90	90	90	90
	Cooling time (s)	5	8	8	10
	Holding time (s)	5	8	8	10
	Holding pressure (bar)	80	90	100	110

Blending composition of virgin and recycled PP materials has been done as per the below Table -2.

Table – 2: Material recycling plan

Sl No	Material Code	% of virgin PP	% of recycled PP
1	I	100 - 92	0 - 2
2	II	92 - 88	8 - 12
3	III	82 - 78	18 - 22
4	IV	72 - 68	28 - 32
5	V	62 - 58	38 - 42
6	VI	52 - 48	48 - 52

Melt flow index (MFI) study:

Different polymer blends were prepared as per material composition table and characterized the melt flow changes at room temperature as per ASTM D1238 using Instron melt flow tester.

Density characterization:

The change in the polymer blend density after the addition of recycled material was measured by weighing a sample in air medium, and in a test liquid (water), using a balance and pan straddle as per ASTM D792 test procedure.

Tensile property characterization:

Tensile testing was conducted at room temperature following the ASTM 638 Type V standards. The experiments were executed using the Zwick Z010 Universal tensile testing machine, and the resultant data was gathered through the Zwick software. The specimens under investigation adhered to nominal dimensions of $165 \times 13 \times 2.5$ mm, featuring a gauge length of 70 mm. A total of five samples were subjected to testing for each material condition, and the reported results represent the average values derived from the tests.

Impact property characterization:

Impact tests were conducted in compliance with ASTM 256-02 standards within a controlled environment at room temperature, specifically at 28°C. The impact strength values were determined by averaging the results from five rectangular specimens, each measuring $124.5 \times 14 \times 5$ mm. These tests were executed using the Instron Izod impact testing machine. The V-Notch, with a depth of 2.5 mm at a 45-degree angle, was precisely obtained using a Notch cutter. The impact tests were performed with a hammer force delivering 2.71 J of energy.

Thermal property characterization:

The change in the crystallinity of the PP blend material (after mixing virgin and recycled PP) is calculated by differential calorimetry (DSC) method using PerkinElmer DSC-6000 instrument. A small amount of sample (5-10 mg) was heated from 30°C to 200°C at a heating rate of 10°C/min with the aim of determining the melting peak temperature (T_m). From the area of melting point, crystallinity of the material is calculated.

Results and Discussion

The melt flow of the polymer blend has been increased after increasing the recycled material content. Because the recycling process can lead to the degradation of the polymer chains, resulting in shorter polymer chains and reduced molecular weight. Shorter polymer chains flow more easily when melted, leading to a higher MFI value compared to virgin PP.

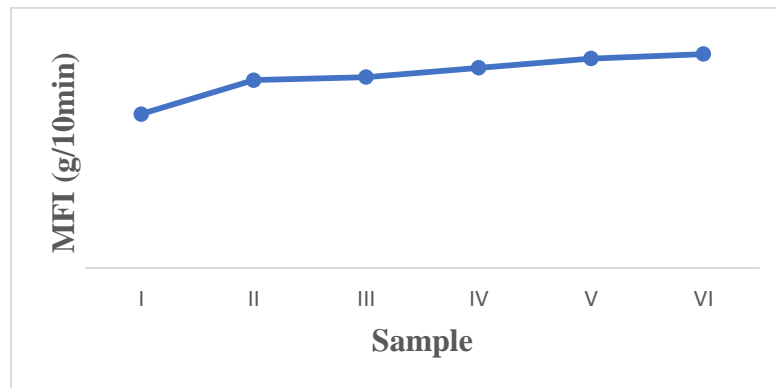


Figure 3: Melt flow index of different recycled polymer grades

The density of the polypropylene blend remains unchanged after increasing the recycled content in the virgin material, as during sorting time enough care has been taken to separate the different polymer material. As both virgin and recycled material have the same density, the overall density of the blend remains unchanged.

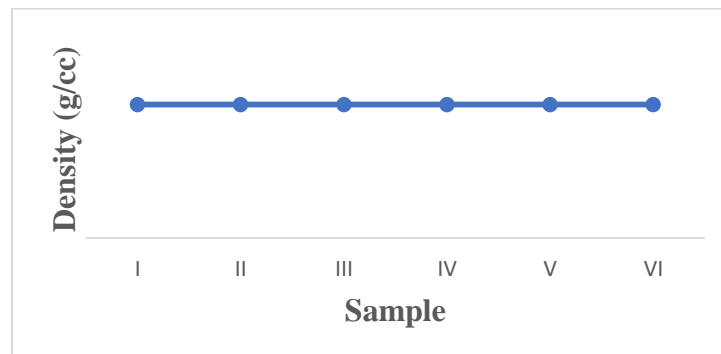


Figure 4: Density study of different recycled polymer grades

Stress-strain diagram of recycled PP blend is shown in figure-5. From the graph it has been seen that there is not much change in the tensile strength after increasing the recycled material content but there is minor change in the elongation property. In general, the tensile strength decreases after the addition of recycled material with the virgin material. But in this case, the tensile strength remains constant due to the good quality of the scrap source, implying that previously used material has gone into the minimal thermal degradation. Also, virgin and recycled PP are well-mixed, and the processing conditions are optimized (e.g., temperature, pressure), that helped to maintain consistent mechanical properties. Proper blending minimizes defects and ensures an even distribution of recycled content, which helps keep

tensile strength stable. Also, properly maintained the composition of various additives like antioxidants, coupling agents, reinforcement agents, UV additives etc. to maintain constant tensile strength after increasing the recycled material content.

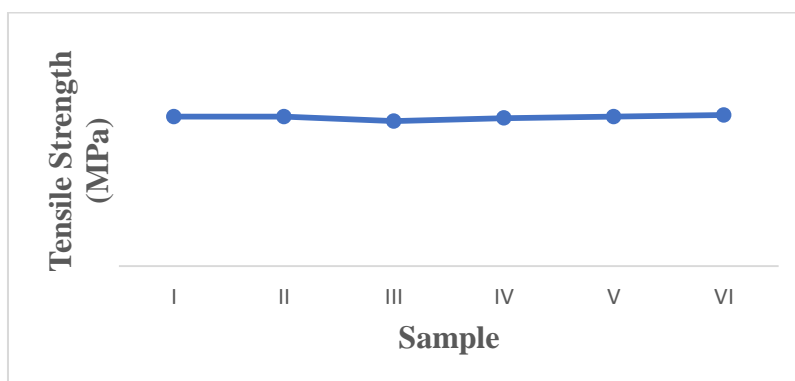


Figure 5: Tensile strength study of different recycled polymer grades

In general, the impact property of the recycled material decreases over increasing the recycled material content. During our compounding stage of the virgin and recycled material, enough care has been taken and optimized the composition of different additives, so it helped to maintain the uniform impact property of the blend. There is no much change in the impact property of the blend.

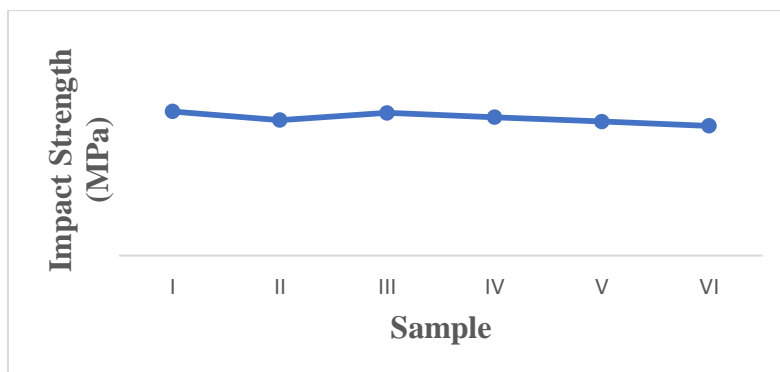


Figure 6: Impact strength study of different recycled polymer grades

From the preceding section we have observed that after carefully moulding the recycled and virgin material with proper composition of additives, mechanical properties can be controlled. But in the case of thermal property, the crystallinity of the material has dropped after increasing the recycled content. The main reason for the decrease in the crystallinity would be degradation of polymer chain, presence of

traces of impurities, and contaminants. All these contribute to an increase in the amorphous (non-crystalline) phase in the material. As the crystalline phase decreases, the proportion of amorphous regions, where polymer chains are randomly arranged and grow, further reducing the overall crystallinity of the blend.

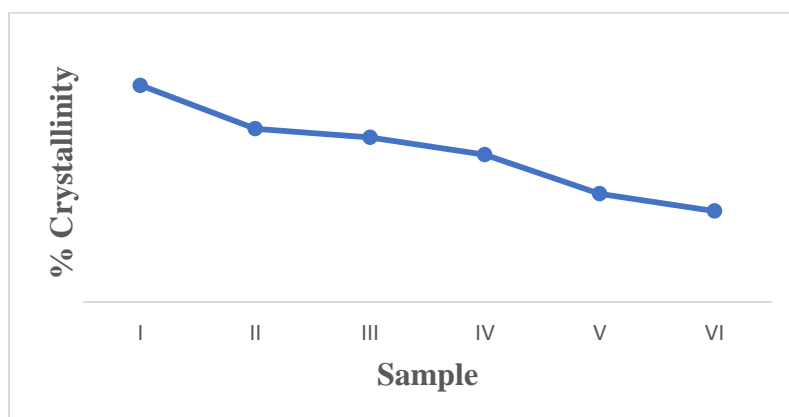


Figure 7: Crystallinity study of different recycled polymer grades

Conclusion

The study investigates the impact of incorporating recycled polypropylene (PP) into virgin PP blends, focusing on key material properties changes such as Melt Flow Index (MFI), density, tensile strength, and crystallinity. The MFI property of the polymer has changed after increasing the recycled content due to breakdown of the polymer chain during the reprocessing of the polymer blend. Density of the blended material remains constant after adding the recycled material due to the similar type of polymers blended. There is not much change of mechanical properties like tensile strength and impact properties due to proper maintenance of polymer blending and additive dosage. The main change in the property after the addition of recycled material is the crystallinity of the blend material. Significantly, crystallinity of the blend material has decreased after increasing the recycled material percentage due to increasing the randomly orientation of shorter polymer chain.

This study confirms that after properly maintaining the blending of the recycled and virgin polymer blend with proper dosage additives, the mechanical properties can be maintained as like virgin material. But the thermal property of the material like crystallinity change would be there. So, to differentiate between the recycled and virgin material crystallinity study can be consider as a main distinguish study. And further study is required to backtrack the percentage of recycled

polymer present in an unknown polymer blend to maintain the product quality.

Acknowledgement

The authors would like to acknowledge the authority of TVS Motor Company Limited for the financial and motivational support to conduct the study. The authors also would like to acknowledge all the people from TVSM and outside TVSM who are directly and indirectly involved in this work.

References

- [1] United Nations, <https://www.un.org/sustainabledevelopment/development-agenda/>, accessed on 16-Aug-2024.
- [2] J.-P. Lange, ACS Sustainable Chemistry & Engineering 9 (2021) 15722–15738.
- [3] E.N. Kalali, S. Lotfian, M.E. Shabestari, S. Khayatzadeh, C. Zhao, H.Y. Nezhad, Current Opinion in Green and Sustainable Chemistry 40 (2023) 100763.
- [4] U. Salahuddin, J. Sun, C. Zhu, M. Wu, B. Zhao, P. Gao, Advanced Sustainable Systems 7 (2023).
- [5] P. Sormunen, T. Kärki, Journal of Building Engineering 24 (2019) 100742.
- [6] S.K. Satya, P.S.R. Sreekanth, Materials Today Proceedings 27 (2020) 920–924.



Published & Printed by :

(Since 1973)

TANEJA SALES CORPORATION

20, Satnam Park, Krishna Nagar, Delhi - 110051.

#9312231302